

<b>REPORT DOCUMENTATION PAGE</b>			1 Form Approved OMB NO. 0704-0188	
<p>The public reporting burden for this collection of information is estimated to average 1 hour per response, including the time for reviewing instructions, searching existing data sources, gathering and maintaining the data needed, and completing and reviewing the collection of information. Send comments regarding this burden estimate or any other aspect of this collection of information, including suggestions for reducing this burden, to Washington Headquarters Services, Directorate for Information Operations and Reports, 1215 Jefferson Davis Highway, Suite 1204, Arlington VA, 22202-4302. Respondents should be aware that notwithstanding any other provision of law, no person shall be subject to any penalty for failing to comply with a collection of information if it does not display a currently valid OMB control number.</p> <p>PLEASE DO NOT RETURN YOUR FORM TO THE ABOVE ADDRESS.</p>				
1. REPORT DATE (DD-MM-YYYY) 31-08-2014		2. REPORT TYPE Ph.D. Dissertation		3. DATES COVERED (From - To) -
4. TITLE AND SUBTITLE Laser cooling and slowing of a diatomic molecule			5a. CONTRACT NUMBER W911NF-12-1-0242	
			5b. GRANT NUMBER	
			5c. PROGRAM ELEMENT NUMBER 611102	
			5d. PROJECT NUMBER	
6. AUTHORS John Barry			5e. TASK NUMBER	
			5f. WORK UNIT NUMBER	
7. PERFORMING ORGANIZATION NAMES AND ADDRESSES Yale University 47 College Street, Suite 203  New Haven, CT 06520 -8047			8. PERFORMING ORGANIZATION REPORT NUMBER	
9. SPONSORING/MONITORING AGENCY NAME(S) AND ADDRESS (ES) U.S. Army Research Office P.O. Box 12211 Research Triangle Park, NC 27709-2211			10. SPONSOR/MONITOR'S ACRONYM(S) ARO	
			11. SPONSOR/MONITOR'S REPORT NUMBER(S) 61945-PH.4	
12. DISTRIBUTION AVAILABILITY STATEMENT Approved for public release; distribution is unlimited.				
13. SUPPLEMENTARY NOTES The views, opinions and/or findings contained in this report are those of the author(s) and should not be construed as an official Department of the Army position, policy or decision, unless so designated by other documentation.				
14. ABSTRACT Laser cooling and trapping are central to modern atomic physics. It has been roughly three decades since laser cooling techniques produced ultracold atoms, leading to rapid advances in a vast array of fields and a number of Nobel prizes. Prior to the work presented in this thesis, laser cooling had not yet been extended to molecules because of their complex internal structure. However, this complexity makes molecules potentially useful for a wide range of applications. The first direct laser cooling of a molecule and further results we present here provide a new route to ultracold temperatures				
15. SUBJECT TERMS Laser cooling; laser slowing; ultracold molecules				
16. SECURITY CLASSIFICATION OF:			17. LIMITATION OF ABSTRACT	
a. REPORT UU	b. ABSTRACT UU	c. THIS PAGE UU	UU	
			15. NUMBER OF PAGES	
			19a. NAME OF RESPONSIBLE PERSON David DeMille	
			19b. TELEPHONE NUMBER 203-432-3833	

## Report Title

Laser cooling and slowing of a diatomic molecule

### ABSTRACT

Laser cooling and trapping are central to modern atomic physics. It has been roughly three decades since laser cooling techniques produced ultracold atoms, leading to rapid advances in a vast array of fields and a number of Nobel prizes. Prior to the work presented in this thesis, laser cooling had not yet been extended to molecules because of their complex internal structure. However, this complexity makes molecules potentially useful for a wide range of applications. The first direct laser cooling of a molecule and further results we present here provide a new route to ultracold temperatures for molecules. In particular, these methods bridge the gap between ultracold temperatures and the approximately 1 kelvin temperatures attainable with directly cooled molecules (e.g. with cryogenic buffer gas cooling or decelerated supersonic beams). Using the carefully chosen molecule strontium monofluoride (SrF), decays to unwanted vibrational states are suppressed. Driving a transition with rotational quantum number  $R=1$  to an excited state with  $R_0=0$  eliminates decays to unwanted rotational states. The dark ground-state Zeeman sublevels present in this specific scheme are remixed via a static magnetic field. Using three lasers for this scheme, a given molecule should undergo an average of approximately 100,000 photon absorption/emission cycles before being lost via unwanted decays. This number of cycles should be sufficient to load a magneto-optical trap (MOT) of molecules. In this thesis, we demonstrate transverse cooling of an SrF beam, in both Doppler and a Sisyphus-type cooling regimes. We also realize longitudinal slowing of an SrF beam. Finally, we detail current progress towards trapping SrF in a MOT. Ultimately, this technique should enable the production of large samples of molecules at ultracold temperatures for molecules chemically distinct from competing methods.

# Abstract

## Laser cooling and slowing of a diatomic molecule

John F. Barry

2013

Laser cooling and trapping are central to modern atomic physics. It has been roughly three decades since laser cooling techniques produced ultracold atoms, leading to rapid advances in a vast array of fields and a number of Nobel prizes. Prior to the work presented in this thesis, laser cooling had not yet been extended to molecules because of their complex internal structure. However, this complexity makes molecules potentially useful for a wide range of applications. The first direct laser cooling of a molecule and further results we present here provide a new route to ultracold temperatures for molecules. In particular, these methods bridge the gap between ultracold temperatures and the approximately 1 kelvin temperatures attainable with directly cooled molecules (e.g. with cryogenic buffer gas cooling or decelerated supersonic beams). Using the carefully chosen molecule strontium monofluoride (SrF), decays to unwanted vibrational states are suppressed. Driving a transition with rotational quantum number  $R=1$  to an excited state with  $R'=0$  eliminates decays to unwanted rotational states. The dark ground-state Zeeman sublevels present in this specific scheme are remixed via a static magnetic field. Using three lasers for this scheme, a given molecule should undergo an average of approximately 100,000 photon absorption/emission cycles before being lost via unwanted decays. This number of cycles should be sufficient to load a magneto-optical trap (MOT) of molecules. In this thesis, we demonstrate transverse cooling of an SrF beam, in both Doppler and a Sisyphus-type cooling regimes. We also realize longitudinal slowing of an SrF beam. Finally, we detail current progress towards trapping SrF in a MOT. Ultimately, this technique should enable the production of large samples of molecules at ultracold temperatures for molecules chemically distinct from competing methods.

# Laser cooling and slowing of a diatomic molecule

A Dissertation  
Presented to the Faculty of the Graduate School  
of  
Yale University  
in Candidacy for the Degree of  
Doctor of Philosophy

by  
John F. Barry

Dissertation Director: David DeMille

December 2013

Copyright © 2013 by John F. Barry  
All rights reserved.

# Contents

<b>1</b>	<b>Introduction</b>	<b>6</b>
1.1	Why cold polar molecules? . . . . .	7
1.2	Production methods for cold and ultracold molecules . . . . .	8
1.3	Direct laser cooling of a diatomic molecule . . . . .	11
1.3.1	A cycling transition for a diatomic molecule . . . . .	12
1.4	Thesis organization . . . . .	12
<b>2</b>	<b>Molecules and SrF</b>	<b>14</b>
2.1	Energy level overview . . . . .	15
2.2	Electronic energy levels . . . . .	16
2.3	Vibrational energy levels . . . . .	18
2.4	Rotational energy levels . . . . .	18
2.4.1	The Dunham model . . . . .	19
2.5	Fine structure, hyperfine structure, spin-rotation, and Lambda-doubling energy levels	22
2.5.1	X state spin-rotation and hyperfine structure . . . . .	22
2.5.2	A state spin-orbit and Lambda-doubling structure . . . . .	25
2.6	Labeling of transitions . . . . .	27
2.7	Coupling of angular momenta . . . . .	30
2.8	Franck-Condon factors . . . . .	31
2.9	Branching ratios . . . . .	33
2.9.1	Calculation overview . . . . .	33
2.10	Energy shifts in the presence of an external magnetic field . . . . .	35
2.11	Exact electronic ground state Hamiltonian . . . . .	37

<b>3</b>	<b>SrF and cycling</b>	<b>39</b>
3.1	Quasi-cycling transition . . . . .	39
3.1.1	Vibrational branching . . . . .	39
3.1.2	Rotational branching . . . . .	41
3.1.3	Dark states . . . . .	42
3.1.4	Addressing spin-rotational and hyperfine structure . . . . .	44
3.2	Simplified models of our system . . . . .	46
3.3	Absorption cross section, saturation intensity, etc. . . . .	48
3.3.1	Rabi frequency . . . . .	49
3.3.2	Absorption cross section without broadening . . . . .	51
3.3.3	Multilevel rate equations . . . . .	51
3.3.4	Multilevel rate equation example . . . . .	52
3.3.5	Multilevel rate equations applied to SrF . . . . .	54
3.4	Optical Bloch equations . . . . .	60
3.4.1	Solving the OBEs . . . . .	60
3.4.2	OBE results . . . . .	62
3.4.3	(3,3)+1 system . . . . .	62
3.4.4	(2,4)+2 system . . . . .	64
3.5	Loss mechanisms . . . . .	67
3.6	Benefits of SrF . . . . .	70
3.6.1	Drawbacks of SrF . . . . .	72
<b>4</b>	<b>The laser system</b>	<b>73</b>
4.1	Introduction . . . . .	73
4.2	External cavity diode lasers . . . . .	73
4.2.1	Pivot point calculations . . . . .	76
4.3	Electro-optic modulators . . . . .	78
4.3.1	Simple phase modulation theory . . . . .	78
4.3.2	Construction and components . . . . .	80
4.3.3	Current problems . . . . .	81
4.4	Laser amplifiers . . . . .	82
4.4.1	Injection-seeded slave . . . . .	82

4.4.2	Tapered amplifier . . . . .	84
4.4.3	Tapered amplifier setup and alignment . . . . .	87
4.4.4	Tapered amplifier protection circuit . . . . .	91
4.4.5	Additional TA experiences . . . . .	91
4.5	Fabry-Pérot . . . . .	93
4.6	Frequency reference . . . . .	99
4.7	Software lock . . . . .	100
4.7.1	Scanning . . . . .	101
<b>5</b>	<b>A bright, slow cryogenic molecular beam source for free radicals</b>	<b>105</b>
5.1	Introduction . . . . .	105
5.2	General source properties . . . . .	107
5.2.1	Mean free path . . . . .	108
5.2.2	Thermalization . . . . .	110
5.2.3	Diffusion and extraction . . . . .	111
5.2.4	Beam formation . . . . .	112
5.3	Experimental apparatus . . . . .	113
5.4	Experimental results . . . . .	117
5.4.1	In-cell dynamics and SrF properties . . . . .	117
5.4.2	Molecular beam properties . . . . .	121
5.5	Subsequent source improvements . . . . .	131
<b>6</b>	<b>Radiative force from optical cycling on a diatomic molecule</b>	<b>133</b>
6.1	Introduction . . . . .	133
6.2	Experimental considerations for deflection . . . . .	134
6.3	Experimental apparatus . . . . .	134
6.4	Results . . . . .	137
<b>7</b>	<b>Laser cooling of a diatomic molecule</b>	<b>140</b>
7.1	Experimental apparatus . . . . .	140
7.2	Results overview . . . . .	142
7.3	Quantitative analysis . . . . .	149
7.3.1	Capture velocity and optimum magnetic field for Sisyphus and Doppler forces	149



7.3.2	Estimation of temperature . . . . .	151
7.3.3	Power dependence of Sisyphus and Doppler cooling . . . . .	154
7.4	Chapter conclusion . . . . .	155
<b>8</b>	<b>Laser radiation pressure slowing of a molecular beam</b>	<b>156</b>
8.1	Introduction . . . . .	156
8.2	Experimental apparatus . . . . .	157
8.3	Results . . . . .	160
<b>9</b>	<b>Progress towards a 3-D MOT</b>	<b>165</b>
9.1	An SrF MOT . . . . .	165
9.1.1	Non-traditional MOTS . . . . .	165
9.1.2	MOT polarization . . . . .	166
9.1.3	Unintended excitation . . . . .	166
9.1.4	Preliminary MOT design . . . . .	168
9.2	Frequency distribution of slowing light . . . . .	169
9.3	Vacuum system . . . . .	172
9.3.1	Beam attenuation by room temperature gases . . . . .	172
9.3.2	Calculating gas loads and partial pressures . . . . .	174
9.3.3	Pumping of helium gas . . . . .	175
9.3.4	Revisions to vacuum system . . . . .	176
9.4	Simultaneous cooling and slowing . . . . .	178
9.4.1	Experimental apparatus . . . . .	179
9.4.2	Experimental results . . . . .	180
9.5	MOT detection . . . . .	182
9.5.1	Ion detection . . . . .	184
9.5.2	Blue detection . . . . .	187
9.5.3	Current detection . . . . .	187
9.5.4	Light collection . . . . .	189
9.5.5	Scattered light . . . . .	190
<b>10</b>	<b>Outlook and future directions</b>	<b>194</b>
10.1	Non-radiative slowing . . . . .	194

10.1.1 Transverse confinement methods . . . . .	194
10.2 Collisions and chemical reactions . . . . .	195
10.3 Leaky MOT . . . . .	196
10.4 Cooling beyond MOT temperatures . . . . .	196
10.5 Trapped fluorine . . . . .	197
<b>APPENDICES</b>	<b>198</b>
<b>A Franck-Condon factors</b>	<b>199</b>
A.1 Details of FCF calculation . . . . .	200
<b>B Molecule choosing</b>	<b>203</b>
B.1 Future molecules for laser cooling . . . . .	203
B.1.1 Summary of selection advice . . . . .	204
B.1.2 Estimating Franck-Condon factors . . . . .	204
B.1.3 Singlet Sigma to singlet Pi molecules . . . . .	205
B.1.4 Potential future candidates . . . . .	205
<b>C ECDL further details</b>	<b>208</b>
C.1 Parts and choices for home-built ECDL design . . . . .	208
C.2 ECDL assembly tips . . . . .	209
C.3 Setting up the laser . . . . .	211
C.4 Troubleshooting . . . . .	212
C.5 Miscellaneous ECDL lessons . . . . .	213
C.6 Possible design improvements . . . . .	213
C.7 Setting the correct pivot point . . . . .	213
C.8 Laser diode and grating choices for SrF lasers . . . . .	214
<b>D Tapered amplifier further details</b>	<b>236</b>
D.1 Important precautions . . . . .	236
D.2 Partial assembly instructions . . . . .	238
D.3 TA electrical connections . . . . .	239
D.3.1 Tapered amplifier protection circuit . . . . .	239
D.4 Miscellaneous details . . . . .	240

D.4.1	Tapered amplifier case . . . . .	240
<b>E</b>	<b>Fabry-Pérot further details</b>	<b>251</b>
E.1	Parts list . . . . .	251
E.2	Assembly instructions . . . . .	252
E.3	Cavity alignment tips . . . . .	252
E.3.1	Setting the cavity length . . . . .	252
E.3.2	Fine tuning cavity alignment and mode matching . . . . .	253
E.4	Cavity design principles and comments . . . . .	253
E.5	Outstanding issues . . . . .	253
<b>F</b>	<b>UHV preparation</b>	<b>261</b>
<b>G</b>	<b>Copper blackening</b>	<b>263</b>
G.1	Copper(II) oxide black coating . . . . .	263
G.2	Procedure to grow copper(II) oxide black coating . . . . .	264
<b>H</b>	<b>Homemade windows</b>	<b>266</b>
<b>I</b>	<b>Target making</b>	<b>269</b>
I.1	SrF ablation target making overview . . . . .	269
I.2	Current target making procedure . . . . .	269
I.3	Target composition . . . . .	272
<b>J</b>	<b>PMT light collection</b>	<b>274</b>
J.1	Geometric collection efficiency . . . . .	274
J.2	Filters . . . . .	276
J.3	Scattered light . . . . .	277
J.4	Current PMT collection efficiency . . . . .	279
<b>K</b>	<b>Pictures of experimental apparatus</b>	<b>280</b>

# List of Tables

2.1	Atomic and molecular spectroscopic notation. . . . .	16
2.2	Quantum numbers relevant to SrF. . . . .	16
2.3	Dunham coefficient correspondence. . . . .	19
2.4	Dunham coefficients of the SrF $X^2\Sigma_{1/2}$ electronic ground state. . . . .	20
2.5	Constants for the SrF $A^2\Pi_{1/2}$ state. . . . .	20
2.6	Electronic, vibrational and rotational constants of SrF for electronic states other than $X^2\Sigma_{1/2}$ and $A^2\Pi_{1/2}$ , in $\text{cm}^{-1}$ . . . . .	21
2.7	Parameters used for Dunham expansion of the SR/HF energy levels in the $X^2\Sigma_{1/2}$ state. . . . .	23
2.8	Approximate SR/HF constants for the $X^2\Sigma_{1/2}(v = 0 - 4, N = 1)$ energy levels in MHz. . . . .	23
2.9	Nominal labeling and actual composition of impure spin-rotational and hyperfine sublevels in the $X^2\Sigma_{1/2}$ electronic state. . . . .	24
2.10	SR/HF splittings in MHz for the $X^2\Sigma_{1/2}(v = 0 - 4, N = 1)$ states. . . . .	25
2.11	Good quantum numbers and requirements for Hund's cases (a) and (b). . . . .	30
2.12	Calculated FCFs $q_{v',v''}$ for the $A^2\Pi_{1/2}(v') \rightarrow X^2\Sigma_{1/2}(v'')$ transition. . . . .	32
2.13	Calculated vibrational branching ratios $\mathcal{VBR}_{v',v''}$ for the $A^2\Pi_{1/2}(v') \rightarrow X^2\Sigma_{1/2}(v'')$ transition. . . . .	32
2.14	Calculated values of the equilibrium internuclear separation $r_e$ . . . . .	32
2.15	Approximate R/SR/HF branching ratios for decays from the $A^2\Pi_{1/2}(v' = 0, J' = 1/2^+)$ state to the $X^2\Sigma_{1/2}(v'' = 0, N'' = 1)$ state. . . . .	34
2.16	Branching ratios from a few of the lowest $A^2\Pi_{1/2}$ states to $X^2\Sigma_{1/2}$ states. . . . .	34
2.17	g-factors of the $X^2\Sigma_{1/2}(v = 0, N = 1)$ SR/HF manifolds without and with taking into account the mixing of the states with the same $J$ . . . . .	36
2.18	Equations to construct the full electronic ground state Hamiltonian. . . . .	37

4.1	ECDL design considerations. . . . .	74
4.2	HP/Agilent specifications for 5517B frequency stability. . . . .	99
9.1	Reported values of ionization energies for CaF, SrF and BaF in eV. . . . .	186
A.1	Expanded table of Franck-Condon factors. . . . .	201
C.1	Parts list for home-built ECDL. . . . .	210
D.1	Parts list for home-built TA. . . . .	237
F.1	A sample of UHV compatible materials used during this thesis. . . . .	262
I.1	Partial list of some non-sintered targets we tested. . . . .	272
J.1	Filter transmission at normal incidence. . . . .	276

# List of Figures

2.1	Scale energy level diagram of experimentally observed electronic states of SrF below $40000 \text{ cm}^{-1}$ . . . . .	17
2.2	Rotational, spin-rotational and hyperfine splittings of the $X^2\Sigma_{1/2}(v=0)$ state. . . .	26
2.3	Energy level diagram for the $X^2\Sigma_{1/2} \rightarrow A^2\Pi$ transition. . . . .	29
2.4	Vector coupling diagram for Hund's cases (a) and (b). . . . .	31
2.5	Energy levels of the $X^2\Sigma_{1/2}(v=0, N=1)$ state versus magnetic field. . . . .	38
3.1	Vibrational branching is suppressed in SrF due to the highly diagonal FCFs. . . . .	40
3.2	Rotational branching is eliminated by driving an $R=1 \rightarrow R'=0$ transition. . . . .	41
3.3	Dark state sublevels in a 3+1 system. . . . .	43
3.4	Microwave remixing would require rapidly switching the polarization of microwaves tuned between the $X^2\Sigma_{1/2}(N=0, F=1)$ sublevels and all the $X^2\Sigma_{1/2}(N=1)$ sublevels. . . . .	44
3.5	Matching SrF SR/HF structure with EOM sidebands from a single laser. . . . .	45
3.6	Simplified models of our system. . . . .	47
3.7	Models for determining required laser intensity. . . . .	56
3.8	Predicted values of $n_e$ for a (3,3)+1 system as derived from the OBEs. . . . .	63
3.9	Predicted values of $n_e$ for a (2,4)+2 system for different laser intensities and magnetic field values obtained by solving the OBEs. . . . .	65
3.10	Vibrational lifetimes in the $X^2\Sigma_{1/2}$ state are primarily limited by spontaneous decay from higher vibrational levels. . . . .	69
4.1	Home-built Littrow ECDL design. . . . .	75
4.2	Geometry for derivation of optimal pivot point for Littrow configuration. . . . .	77
4.3	EOM circuit and drive electronics. . . . .	81

4.4	Slave laser injection setup. . . . .	84
4.5	Geometry of a TA chip. . . . .	85
4.6	This tapered amplifier design suffers from poor thermal design. . . . .	86
4.7	Collimation lenses for both the input and output of the TA are attached to a brass part which is translated vertically and horizontally using set screws. . . . .	87
4.8	Picture of a finished TA in use in the experiment. . . . .	88
4.9	Overall setup of input seeding and output coupling of TA. . . . .	90
4.10	TA protection circuit. . . . .	92
4.11	Fabry-Pérot scan showing the occurrence of additional sidebands for large TA injection currents but not for small TA injection currents. . . . .	93
4.12	Example of home-built Fabry-Pérot used to lock lasers and for laser diagnostics. . .	94
4.13	Fabry-Pérot scan resolving the two peaks of a 5517Å frequency-stabilized HeNe. . .	96
4.14	Monitoring Fabry-Pérot drift. . . . .	97
4.15	Software lock interface showing locking of 8 ECDLs on 3 Fabry-Pérots. . . . .	104
5.1	Experimental setup. . . . .	115
5.2	Typical raw absorption traces in the cell and immediately outside at $L_p = 1$ mm for $\mathcal{F} = 5$ sccm and $\mathcal{F} = 50$ sccm. . . . .	116
5.3	Typical in-cell absorption Doppler profile. . . . .	116
5.4	Fractional rotational populations in-cell and at $L_p = 20$ mm downstream, with associated fits to a Boltzmann distribution. . . . .	119
5.5	Relative vibrational populations in-cell and at $L_p = 10$ mm, at $\mathcal{F} = 5$ sccm. . . . .	120
5.6	Number of SrF molecules $N_{SrF}^{cell}$ at $L_p = -1$ mm and $N_{SrF}^{beam}$ at $L_p = +1$ mm, as a function of $\mathcal{F}$ . . . . .	120
5.7	(a) FWHM transverse velocity of the molecular beam $\Delta v_{SrF\perp}$ versus probe distances $L_p$ , for $\mathcal{F} = 5, 15$ , and $30$ sccm. (b) FWHM transverse velocity of the molecular beam versus $\mathcal{F}$ for $L_p = 20$ mm, where the width is no longer increasing with distance from the cell. . . . .	122
5.8	Molecular beam divergence for various flow rates. . . . .	123
5.9	$T_{rot}^{beam}(L_p = 20 \text{ mm})$ versus $\mathcal{F}$ . . . . .	125
5.10	Forward velocity for various flow rates. . . . .	126
5.11	FWHM forward velocity spread for various flow rates. . . . .	127

5.12	Measured forward velocity, measured forward velocity spread, simulated forward velocity and simulated forward velocity spread versus time. . . . .	127
5.13	$\mathcal{B}$ for various flow rates $\mathcal{F}$ measured at $L_p = 1$ mm and $L_p = 135$ mm. . . . .	128
5.14	Normalized $N_{SrF}^{cell}$ as a function of ablation shot number. . . . .	129
6.1	Experimental setup for increased LIF and deflection. . . . .	135
6.2	Signals demonstrating cycling fluorescence in SrF. . . . .	137
6.3	Radiative force deflection of the SrF beam. . . . .	139
7.1	Schematic of the experimental apparatus. . . . .	141
7.2	Laser cooling of SrF. . . . .	144
7.3	Magnetic field and frequency dependence of the cooling forces. . . . .	147
7.4	Schematic illustrating the origin of Sisyphus force in an $F = 1 \rightarrow F' = 0$ system. . .	150
7.5	Results of a Monte Carlo simulation of the SrF beam subjected to Sisyphus type forces.	152
7.6	Molecular beam temperature under Sisyphus and Doppler conditions as the power in the main pump laser is varied. . . . .	155
8.1	Schematic of the experimental apparatus for slowing. . . . .	157
8.2	Relevant energy levels and transitions in SrF used for laser slowing and detection. .	158
8.3	Measured and simulated slowing for different detunings of the main slowing laser. . .	161
8.4	Slowing with no applied magnetic field. . . . .	164
9.1	Proposed polarization scheme for making an SrF MOT. . . . .	167
9.2	Addressing SR/HF structure by the MOT pump laser. . . . .	168
9.3	Increased spontaneous LIF due to extra sidebands for the $\lambda_{00}^s$ laser. . . . .	170
9.4	Spectral profile of the $\lambda_{00}^s$ laser with sidebands created by a fiber EOM. . . . .	171
9.5	Vacuum setup of the current SrF laser cooling experiment. . . . .	177
9.6	Example mounting of 360 mm long transverse cooling mirrors. . . . .	180
9.7	Simultaneous transverse cooling and longitudinal slowing. . . . .	181
9.8	Possibility for Sisyphus-type cooling combined with radiative slowing. . . . .	183
9.9	Diagram for REMPI detection. . . . .	184
9.10	Three photon REMPI signal from the molecular beam. . . . .	186
9.11	Horizontal cross section of the MOT region with an emphasis on methods to reduce scattered light. . . . .	191



A.1	The calculated FCFs $q_{v',v''}$ for decays $A^2\Pi_{1/2}(v') \rightarrow X^2\Sigma_{1/2}(v'')$ . . . . .	202
B.1	For a molecule exhibiting a $X^1\Sigma(R=1) \rightarrow A^1\Pi(R=0)$ cycling transition, only 1/3 of the ground states are dark for $\pi_z$ polarization or $\sigma^+$ polarization. . . . .	206
G.1	2.75" conflat nipple with an OFHC copper insert coated with copper(II) oxide and bare. . . . .	264
H.1	Homemade vacuum windows. . . . .	268
I.1	Testing of multiple ablation targets. . . . .	273
J.1	Light collection setup for collecting LIF at 360 nm. . . . .	275
J.2	An example setup for minimizing scattered light. . . . .	278
K.1	Bottom view of the 3K cryogenic components. . . . .	281
K.2	Back view of the cell. . . . .	282
K.3	View of the 3K bobbin. . . . .	282
K.4	Solidworks picture of experimental apparatus at time of dissertation submission. . .	283

# Chapter 1

## Introduction

Laser cooling and trapping are central to modern atomic physics [1–4]. The ability to trap atomic gases and cool them to ultracold temperatures (about 1 millikelvin or below) has resulted in a number of Nobel prizes [5–9] and led to revolutionary advances across a range of areas including atomic clocks, quantum information processing and simulation of condensed-matter systems. The production of ultracold molecular gases is anticipated to have a similarly broad scientific impact [10].

Compared with atoms, molecules have additional types of internal motion (such as vibration and rotation) that provide new features to study and manipulate. For example, the long-range, strong electric forces between polar molecules make them attractive for use as bits of information in a quantum computer, where conditional logic operations require strong interactions between the constituent bits, or as building blocks for creating exotic phases of matter involving high degrees of quantum entanglement among the particles. Tuning the energy levels of ultracold molecules using electromagnetic fields—which produces particularly significant effects at low temperatures—could allow precise control over chemical reaction rates and enable characterization of molecular interactions with unprecedented precision. Furthermore, minute shifts in molecular energies could be observed at these temperatures; for instance, a small difference in the energies of left- and right-handed chiral molecules has been predicted, owing to the intrinsic handedness of the electroweak force that arises from the exchange of particles ( $Z^0$  bosons) between electrons and nuclei. These applications require molecules to have the low kinetic energy associated with ultracold temperatures; this low energy allows the molecules to be trapped or to be observed for long times, as is typically necessary for precision spectroscopic measurements.

The number of potential applications for ultracold molecular gases has created an intense de-

mand for methods to trap and cool molecules. Unfortunately, standard methods for cooling atoms are not easily extended to molecules because of their more complex internal structure. For example, laser cooling typically requires a particle repeatedly absorb and spontaneously emit about  $10^4$  photons. In practice, achieving a large number of absorption/emission cycles is easiest if each spontaneous emission returns the particle back to the initial quantum state. In contrast to atoms, consistently returning molecules to an initial state is difficult because molecules tend to decay to multiple vibrational and rotational states.

## 1.1 Why cold polar molecules?

We briefly review certain motivations and applications for cold and ultracold polar molecules which exploit the above properties, although we note that comprehensive and detailed discussions can be found in Refs. [10] and [11].

### Quantum information processing

Polar molecules combine the traditional advantages of atomic systems (weak coupling to environment, complete quantum control over states, the ability to be cooled, addressing of individual particles and the ability to manipulate quantum states using microwave radiation) with attractive new features such as strong, tunable and anisotropic coupling between molecules [12–15].

### Precision measurements

The near-degeneracies in the level structure and precise control over the quantum states make cold molecules useful for ultra-precise measurements of physical phenomena. Specifically, cold molecules are useful to improve sensitivity to effects such as electric dipole moments of elementary particles [16–19], parity-violating weak interactions [20–23], and time variation of fundamental constants [24, 25].

### Ultracold chemical reactions

Large samples of ultracold molecules would allow access to new dynamical regimes such as pure quantum tunneling-induced reactions [26], control over collisions via electric fields [27, 28], and other ultracold chemical reaction phenomena [29, 30]. Chemical reaction rates can be enhanced or suppressed by external fields. Cold chemical reactions are central to modern astrophysics and take place during the formation of stars, planets, interstellar clouds, etc. [30].

### Novel many-body quantum systems

Electric dipole-dipole interactions can give rise to strongly-correlated systems with close analogies in the quantum Hall effect [31] and superconductivity [32] as well as new types of quantum phases (e.g., supersolids or lattice spin systems) [33–36].

### Interferometers and sensors

Matter-wave interferometry with polar molecules is expected to exhibit several interesting features and could allow for significant improvements of gyroscopic sensitivity [37, 38]. Moreover, the strong dipolar interactions between molecules may make it possible to produce highly-entangled states (e.g. via dipole blockade techniques [39]), which could lead to interferometers with sensitivity beyond the standard quantum limit [40]. Other possibilities include using molecules as sensors for weak microwave or THz radiation fields.

As a consequence of the abundance of proposed applications, there is substantial interest in developing techniques for producing large samples of cold and ultracold molecules. Additionally, the different proposed applications require a variety of molecular energy-level structures (e.g. unpaired electronic spins [14, 17, 36, 41], omega doublets [19], etc.), and hence a variety of molecular species are desired. Finally, higher phase space densities and larger samples are almost always preferred.

## 1.2 Production methods for cold and ultracold molecules

Methods for cooling and trapping molecules have been of interest for almost two decades now. While many ideas exist, few have been implemented successfully and all that have been implemented have shortcomings. Cold molecule creation methods are broadly classified either as direct or indirect. In direct methods, the molecules are made first and then cooled, while indirect methods achieve cold and ultracold molecules by binding together laser-cooled atoms [10]. We review relevant technologies demonstrated to date.

### Assembly from laser cooled atoms

The most widespread current technique for creating ultracold molecules relies on their assembly from ultracold atoms using either photo-association [42–44] or magneto-association from a Feshbach resonance [45, 46]. Recent experiments have produced ground state polar molecules near quantum degeneracy [45, 46]. Yet, this technology is restricted to molecules composed of atoms that are themselves amenable to laser cooling. Hence, only diatomic molecules composed

of combinations of alkali and alkaline earth atoms<sup>1</sup> have been produced this way, and the number of molecules created is fairly small ( $\sim 10^4$ ) [45].

### **Stark deceleration and other deceleration techniques**

Molecules whose constituent atoms are not amenable to laser cooling require a different approach. If the chosen molecule is not already available as a gas, it is vaporized (by means of an oven, arc discharge, laser ablation, etc.) and thereafter formed into a molecular beam. This molecular beam is frequently altered by the addition of a carrier gas which can produce lower forward velocities or lower rotational temperatures for the seed molecules. Hence, a crucial step to obtaining large samples of ultracold, trapped molecules is developing a means to bridge the gap between typical molecular source velocities ( $\sim 150\text{--}600 \frac{m}{s}$ ) and velocities for which trap loading or confinement is possible ( $\lesssim 5\text{--}20 \frac{m}{s}$ ). Tremendous advances have been made in the deceleration of molecular beams in the past decade. Stark deceleration [47–50], Zeeman deceleration [51–53], counter-rotating nozzles [54, 55], collisional deceleration [56], and photodissociation [57] have all been demonstrated to slow molecular beams. However, only for fairly light species ( $\sim 20$  amu) with substantial vapor pressure at room temperature have these methods been demonstrated to allow slowing to velocities necessary to make trapping possible [58–61]. Optical deceleration has been demonstrated to slow molecular beams to rest [62, 63], but the high laser intensities required in current approaches have thus far limited application to small volumes. Quite recently, near-ultracold OH was obtained using Stark deceleration followed by evaporative cooling [64].

### **Buffer gas cooling**

In this technique, pioneered by the Doyle group [65–67], a molecular species is introduced into a cryogenic buffer gas cell and sympathetically cooled via collisions with a cold buffer gas (usually helium). While this method is widely applicable to a large number of molecules using various injection methods (introduction into the buffer gas cell by an oven, ablation, gas cylinder and arc discharge have all been demonstrated [67–70]), the temperatures reached by buffer gas cooling alone are limited by the vapor pressure of  $^3\text{He}$  to  $\sim 300$  mK [67]. Once sympathetically cooled, these molecules may be loaded into a magnetic trap [66] or evaporatively cooled [71]. However, residual buffer gas generally limits final temperatures if not removed, a task which has proven challenging. Alternatively, the cooled molecules may exit

---

<sup>1</sup>and atoms isoelectronic to the alkaline earth elements, such as Yb

the cell through a small aperture to form a molecular beam [68, 69, 72–75]. Cryogenic buffer gas beam sources of this type produce highly directional beams with large fluxes relative to competitive technologies [76]. This latter technique is used as a preliminary cooling step for the work presented in this thesis.

### Optoelectrical cooling

In optoelectrical cooling, demonstrated by Zeppenfeld *et al.*, a polyatomic molecule is repeatedly subjected to a Sisyphus-type cooling cycle which transfers the molecule in a one-way dissipative process from molecular states with a higher potential energy to states with a lower potential energy all within the confines of an electrostatic trap [77–80]. By carefully engineering the multiple population transfers to occur at different spatial regions within the trap, kinetic energy is converted to potential energy—which is then permanently removed from the system, resulting in cooling. While theoretically generally applicable, the reliance on spontaneous vibrational decay rather than electronic decays causes optoelectrical cooling to be most effective for molecules with short vibrational lifetimes. Furthermore, optoelectrical cooling requires molecules to be already confined within an electrostatic trap [81]. Nevertheless, optoelectrical cooling remains an exciting new method for cooling polyatomic molecules whose complex level structure is expected to prohibit application of other cooling methods.

### Other methods

Other less popular methods of producing cold and ultracold molecules exist but are either very limited, excessively challenging from an experimental point of view, or have not been demonstrated. These include cooling by collision of a molecular beam with an atomic beam [56], sympathetic cooling of molecules by laser-cooled atoms, cavity-assisted laser cooling of molecules [82], photodissociation [57], white-light cooling [83], and chirped, sequential cooling [84].

## 1.3 Direct laser cooling of a diatomic molecule

Direct laser cooling is attractive to avoid the limitations of the above approaches, as is evident by the plethora of atom experiments utilizing laser cooling to create large samples of ultracold atoms. The power of laser cooling arises from the ability of certain particles to repeatedly scatter photons from a laser. Doppler laser cooling relies on small but numerous momentum kicks from the absorption of red-detuned photons counter-propagating to the particle’s direction of motion. Doppler cooling of a particle of mass  $m > 20$  amu with visible light from room temperature to ultracold temperatures

requires  $> 10^4$  photon scatters. To scatter this many photons, a particle must have a closed cycling transition in which each photon absorption is always followed by spontaneous decay back to the initial quantum state.

Unfortunately, there are no completely closed transitions in any real physical systems, and spontaneous decay to other states inevitably occurs, usually before ultracold temperatures are reached. Each additional populated state requires a “repump” laser to return the population back to the main cycle so that photon scattering (and therefore cooling) can continue. Cycling transitions requiring one or two “repump” lasers are common in atomic systems but are quite difficult to find in molecules because of the latter’s vibrational and rotational degrees of freedom. Control over vibrational states is particularly problematic because there is no selection rule to limit electronic decay to only certain vibrational states. Instead, branching to different vibrational states is governed by a molecule’s Franck-Condon factors (FCFs), which describe the overlap of the vibrational wavefunctions for different electronic states. For a typical molecule, the probability to return to the original vibrational state after  $10^4$  photon scatters is extremely small. Furthermore, decay from a single excited state can populate up to three rotational states per vibrational state, since rotational selection rules generally only require  $\Delta R = 0, \pm 1$  where  $R$  is the rotational quantum number. Because each substantially populated state requires an individually tunable “repump” laser, laser cooling of a molecule can easily require so many lasers as to be experimentally unfeasible.

### 1.3.1 A cycling transition for a diatomic molecule

In this work, we demonstrate a scheme for optical cycling in a diatomic molecule, as is necessary for laser cooling. We use the  $X^2\Sigma^+ \rightarrow A^2\Pi_{1/2}$  electronic transition of SrF for cycling. Use of the lowest electronically excited state  $A^2\Pi_{1/2}$  ensures that no other electronic states can be populated by spontaneous decay [85]. The  $A^2\Pi_{1/2}$  state has a large spontaneous decay rate,  $\Gamma = 2\pi \times 6.6$  MHz [86], which enables application of strong optical forces. We have chosen SrF primarily because its favorable FCF’s dictate that only the lowest three vibrational states will be significantly populated after  $10^5$  photon scatters [87], and therefore this cycling scheme requires only three lasers. Rotational branching is eliminated by driving an  $R = 1 \rightarrow R' = 0$  type transition [88], where the prime indicates the excited state. Parity and angular momentum selection rules forbid decays to all but the initial  $R = 1$  state, thereby eliminating rotational branching. Unfortunately, driving an  $R = 1 \rightarrow R' = 0$  transition in SrF optically pumps molecules into dark ground-state Zeeman sublevels regardless of laser polarization [88–90]. We eliminate these dark states by applying a magnetic field oriented at

an angle relative to the fixed linear laser polarization, causing the dark states to Larmor precess into bright states [90]. The  $X(R=1)$  state of SrF is split by both spin-rotation (SR) and hyperfine (HF) interactions into four manifolds. However, use of an electro-optic modulator (EOM) creates radio frequency sidebands on each laser to address all ground state SR/HF substructure. Using three lasers for this scheme, a given molecule should undergo an average of approximately 100,000 photon absorption/emission cycles before being lost via unwanted decay channels. Given that we expect transverse cooling and slowing of our molecular beam to rest to require roughly 20,000 photon absorption/emission cycles, a photon budget of approximately 100,000 cycles should allow us to easily load a magneto-optical trap (MOT) and observe roughly 30 ms MOT lifetimes. Hence, we have proposed a clear path to creating large samples of ultracold molecules.

## 1.4 Thesis organization

The remainder of this thesis is structured as follows: In [chapter 2](#), we document the spectroscopic and energy level structure of SrF. In [chapter 3](#), we detail the selection rationale for SrF and our implementation of the cycling transition. In [chapter 4](#), we document the laser technology which is built up to achieve the results presented in this thesis. In [chapter 5](#), we detail the cryogenic beam source built for this experiment and the measured beam characteristics. In [chapter 6](#), we verify the above cycling method by deflecting an SrF molecular beam using radiative force. In [chapter 7](#), we detail the transverse laser cooling of our SrF molecular beam. In [chapter 8](#), we demonstrate longitudinal slowing of our molecular beam. In [chapter 9](#), we document work completed to date in our attempt to create the first three-dimensional (3-D) molecular MOT. In [chapter 10](#), we discuss ideas for future directions.



## Chapter 2

# Molecules and SrF

A diatomic molecule is composed of two atoms of the same or different atomic species. Diatomic molecules not only possess electronic energy levels similar to atoms but additional degrees of freedom as well, namely those corresponding to vibrations and rotations of the molecule. These additional degrees of freedom cause diatomic molecules to be significantly more complicated than atoms. However, the electronic, vibrational and rotational degrees of freedom are, to zeroth order, decoupled and may be treated separately according to the Born-Oppenheimer approximation. When higher-order cross-coupling exists, such effects can usually be treated perturbatively or evaluated exactly for the state of interest.

Knowing the structure of SrF is important for two reasons: First, so that we can make informed decisions about how to achieve certain results by exploiting the structure of SrF, and second, so that we can find the relevant optical or microwave transitions.<sup>1</sup>

---

<sup>1</sup>Since we are not spectroscopists, we are not overly concerned with finding, understanding, or presenting a general model of the energy levels of our molecule. Even knowing the precise absolute location of a given energy level is not important as long as we can find the transition. We are only concerned with calculating the energy levels well enough to find the appropriate transitions or to make decisions about optimal detunings, etc. For finding optical transitions, knowing frequencies to a few GHz is sufficient, and for deciding detunings, knowing the relative frequencies within an rovibrational manifold to  $\lesssim 1$  MHz is sufficient. Therefore, when looking for optical transitions, we use constants derived from data fit to optical transitions. When calculating and looking for microwave transitions or deciding on relative detunings within a rovibrational sublevel, we use constants derived solely from data pertaining to the microwave transitions. We make no attempt to reconcile the constants from the different methods since they often differ by more than would be expected from associated uncertainties. Finally, we use only as much complexity as is necessary to find our transitions or make decisions about relative detunings.

## 2.1 Energy level overview

In the absence of any external fields, the Hamiltonian for our diatomic molecule is given to good approximation by Ref. [91] Eqn. 7.183 as

$$H = H_e + H_{\text{vib}} + H_{\text{SO}} + H_{\text{rot}} + H_{\text{SR}} + H_{\text{HFS}} + H_{\text{Ad}}, \quad (2.1)$$

where  $H_e$ ,  $H_{\text{vib}}$ ,  $H_{\text{SO}}$ ,  $H_{\text{rot}}$ ,  $H_{\text{SR}}$ ,  $H_{\text{HFS}}$ ,  $H_{\text{Ad}}$  are the electronic, vibrational, spin-orbit, rotational, spin-rotational, hyperfine, and  $\Lambda$ -doubling components of the Hamiltonian, respectively.

In the literature, it is standard to denote electronic energy levels of diatomic molecules by letters, with X always denoting the ground state. Electronically-excited states with the same multiplicity as the ground state are labeled by capital letters (A,B,C,...) while excited states with different multiplicity than the ground state are labeled by lowercase letters (a,b,c,...). The order of the letters in principle corresponds to the energy of the states. When the letter ordering does not follow the energy levels, it is usually because the out-of-order state was found after the other states had been found and labeled. Splittings between different electronic states are typically on the order of 100 THz and are (hopefully) accessible with lasers. Laser sources from  $\sim 400$  nm to  $\sim 1650$  nm are readily available, with sources in the red and near infrared (NIR), being commonly available as diode lasers. Above and below this range, lasers are quite expensive if available at all.

After electronic excitations, the next-largest energy scale corresponds to the molecule's vibrational modes. In each electronic state there is a potential energy curve due to the Coulomb repulsion between the nuclei and the Coulomb attraction between the nuclei and the electrons. The bottom of this potential well can be approximated as quadratic, allowing for the vibrations of the two nuclei to be treated as a harmonic oscillator. Typical spacings between vibrational energy levels are tens of THz. Monochromatic radiation sources in this frequency range are, unfortunately, neither easily nor cheaply available if they exist at all.

The smallest energy scale common to all molecules corresponds to the rotational degree of freedom. The rotational levels are well described by the simple rigid rotor model. Spacings between lower rotational levels are typically  $\sim 10$  GHz. Transitions between rotational levels can often be excited using commercially available microwave sources.

Description	Atomic property		Molecular projection	
	Symbol	Values	Symbol	Values
Electronic spin	$\mathbf{S}$	$0, \frac{1}{2}, 1, \dots$	$\mathbf{\Sigma}$	$0, \frac{1}{2}, 1, \dots$
Electronic orbital angular momentum	$\mathbf{L}$	$s, p, d, \dots$	$\mathbf{\Lambda}$	$\Sigma, \Lambda, \Delta, \dots$
Total angular momentum	$\mathbf{J}$	$0, \frac{1}{2}, 1, \dots$	$\mathbf{\Omega}$	$0, \pm \frac{1}{2}, \pm 1, \dots$

Table 2.1: Atomic and molecular spectroscopic notation. This table is reproduced from Ref. [92].

Angular momenta	Quantum number	Expression
Electronic spin	$\mathbf{S}$	
Nuclear spin	$\mathbf{I}$	
Electronic orbital angular momentum	$\mathbf{L}$	
Total angular momentum	$\mathbf{J}$	
Total angular momentum excluding electronic spin	$\mathbf{N}$	$\mathbf{N} = \mathbf{J} - \mathbf{S}$
Rotational angular momentum of the nuclei	$\mathbf{R}$	$\mathbf{R} = \mathbf{N} - \mathbf{L}$
Grand total angular momentum	$\mathbf{F}$	$\mathbf{F} = \mathbf{I} + \mathbf{J}^*$

Table 2.2: Quantum numbers relevant to SrF. \*This equation is true for all orbitals and cases discussed in this thesis but is not true for diatomic molecules in general. For further information please consult Ref. [91] pgs. 225-233.

## 2.2 Electronic energy levels

The electronic level structure of a diatomic molecule is similar to that of an atom in many ways. Atoms possess electronic spin  $\mathbf{S}$ , electronic orbital angular momentum  $\mathbf{L}$  and total angular momentum  $\mathbf{J}$ . While atoms possess spherical symmetry, diatomic molecules possess axial symmetry about the internuclear axis  $\hat{z}$ . The quantum numbers  $\mathbf{\Sigma}$  and  $\mathbf{\Lambda}$ , respectively, denote the projections of  $\mathbf{S}$  and  $\mathbf{L}$  onto the internuclear axis. Often the quantity  $\mathbf{\Omega} \equiv \mathbf{\Sigma} + \mathbf{\Lambda}$  is used for molecules similar to the way the quantum number  $\mathbf{J}$  is used in atoms. Like  $\mathbf{J}$  in atoms, the quantity  $\mathbf{\Omega}$  does not always have a well-defined value. A simple overview of the connection between atomic and molecular spectroscopic notation is presented in Table 2.1. Similar to atoms, molecules may also possess one or more nuclear spins. For cases relevant to SrF and discussed in this thesis, a single nuclear spin  $\mathbf{I}$  couples to  $\mathbf{J}$  to produce the grand total angular momentum  $\mathbf{F} \equiv \mathbf{I} + \mathbf{J}$ . The rotational degree of freedom is also quantized, with the rotational angular momentum of the nuclei defined as the quantum number  $\mathbf{R}$ . A table reviewing the quantum numbers relevant to SrF is presented in Table 2.2.

The quantum numbers associated with a given electronic state depend on how the molecule's different angular momenta couple together. The number and complexity of these couplings can be quite large, depending on the number of unpaired electronic and nuclear spins. Although most angular momenta are coupled together to some degree, it is helpful to approach this problem in one

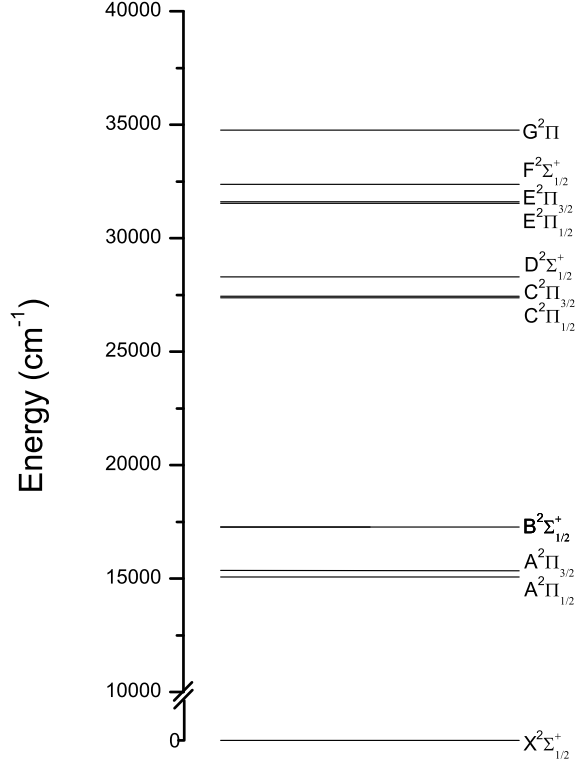


Figure 2.1: Scale energy level diagram of experimentally observed electronic states of SrF below 40000 cm<sup>-1</sup>. A low-lying <sup>2</sup>Δ state is known to exist, but theoretical predications estimate an energy  $\sim 20000$  cm<sup>-1</sup>, well above the A state [85].

of a number of limiting cases (known as Hund's cases) in which the different angular momenta couple together in a prescribed order. In each Hund's case, certain angular momenta are conserved (these angular momenta are the good quantum numbers) and certain angular momenta are not conserved (these angular momenta are not good quantum numbers). The Hund's cases applicable to SrF are discussed in more detail later in this chapter. In addition to being labeled by a letter, electronic energy levels are additionally labeled by their molecular term symbol, given by

$$^{2S+1}\Lambda_{\Omega}^{+/-},$$

where  $+/-$  is the reflection symmetry of the electronic state along an arbitrary plane containing the internuclear axis (and is distinct from the parity). The electronic ground state of SrF is therefore labeled as X<sup>2</sup>Σ<sup>+</sup><sub>1/2</sub> while the lowest electronically-excited state is labeled as A<sup>2</sup>Π<sub>1/2</sub>. A diagram showing observed low-lying electronic energy levels in SrF is shown in Fig. 2.1. The lifetime of the A<sup>2</sup>Π<sub>1/2</sub> state of SrF is measured to be 24.1 ns [86].

## 2.3 Vibrational energy levels

Within a given electronic energy level, the vibrational energy levels of a diatomic molecule can be expanded as a power series given by Ref. [91] Eqn. 6.188

$$G(v) = \omega_e(v + \frac{1}{2}) - \omega_e x_e(v + \frac{1}{2})^2 + \omega_e y_e(v + \frac{1}{2})^3 + \dots, \quad (2.2)$$

where  $\omega_e$  is the vibrational constant,  $\omega_e x_e$  is the harmonic distortion constant, and  $\omega_e y_e$  is another constant. The latter two constants account for the deviations of the vibrational potential curve from that of a harmonic oscillator (anharmonicity). The constants  $\omega_e$ ,  $\omega_e x_e$  and  $\omega_e y_e$  differ for different electronic energy levels. For our purposes,  $\omega_e y_e$  is often negligibly small and can be ignored.

## 2.4 Rotational energy levels

The smallest set of energy levels common to all diatomic molecules are the rotational energy levels which correspond to the energy associated with the rotation of the two nuclei. The rotational energy levels within a given vibrational energy level  $v$  are given by Ref. [91] Eqn. 6.196

$$F_v(J) = B_v J(J+1) - D_v J^2(J+1)^2 + H_v J^3(J+1)^3 + \dots, \quad (2.3)$$

where  $B_v$  is the rotational constant for vibrational level  $v$ . The term proportional to  $D_v$  (the centrifugal distortion term) and the term proportional to  $H_v$  correct for anharmonicities of the electronic potential well, e.g. the stretching of the molecule by centrifugal forces. In some cases,  $B_v$ ,  $D_v$ , and  $H_v$  have been measured for a specific vibrational level. In the general case,  $B_v$ ,  $D_v$ , and  $H_v$  can be expressed in a power series themselves, given by

$$B_v = B_e - \alpha_e(v + \frac{1}{2}) + \gamma_e(v + 1/2)^2 + \dots \quad (2.4)$$

$$D_v = D_e - \beta_e(v + \frac{1}{2})^2 + \dots \quad (2.5)$$

$$H_v = H_e + \dots, \quad (2.6)$$

where  $B_e, \alpha_e, \gamma_e, D_e, \beta_e, H_e$ , etc., are numerical coefficients. We note that  $B_e = \frac{\hbar}{4\pi\mu_r r_e^2} \times 10^{-2}$  cm<sup>-1</sup> where  $\mu_r$  is the reduced mass of the molecule and  $r_e$  is the equilibrium internuclear distance.<sup>2</sup>

---

<sup>2</sup>Different equations for  $B_e$  exist in the literature depending on the units. The use of a single symbol for three separate physical quantities (energy, frequency, and wavenumber) is clearly confusing but is the spectroscopic custom.

The coefficients  $B_e, \alpha_e, \gamma_e, D_e, \beta_e, H_e$ , etc., are closely related to parameters in the Dunham model, discussed below.

### 2.4.1 The Dunham model

Dunham coefficient	Corresponding parameter
$Y_{00}$	$T_e$
$Y_{01}$	$\approx B_e$
$Y_{02}$	$\approx -D_e$
$Y_{03}$	$\approx H_e$
$Y_{10}$	$\approx \omega_e$
$Y_{11}$	$\approx -\alpha_e$
$Y_{12}$	$\approx \beta_e$
$Y_{20}$	$\approx -\omega_e x_e$
$Y_{21}$	$\approx \gamma_e$

Table 2.3: Dunham coefficient correspondence.

It is sometimes helpful to write the rovibrational energies of an electronic state in a more compact fashion. Under these circumstances the energies are given by the Dunham expansion [93] where the energy of a rovibrational level is given by

$$F_{v,N} = \sum_{l,m} Y_{l,m} (v + 1/2)^l [N(N + 1)]^m, \quad (2.7)$$

where  $Y_{l,m}$  are called the Dunham coefficients and are closely related to the constants from the Bohr model. For our purposes we can take the Dunham coefficients to be equal to the constants from the Bohr model,<sup>3</sup> and the correspondence between parameters is shown in Table 2.3. The Dunham coefficients for the  $X^2\Sigma_{1/2}$  state of SrF are shown in Table 2.4. The rovibrational energy levels of the electronic ground state of SrF are, fortunately, well characterized. For any calculation relevant to this thesis, constants for the  $X^2\Sigma_{1/2}$  electronic state are available and have been measured to great precision. Unfortunately the spectroscopy for the  $A^2\Pi_{1/2}$  state is neither as precise nor as complete as the spectroscopy for the  $X^2\Sigma_{1/2}$  state. This is, to some extent, due to the highly diagonal Franck-Condon factors of SrF which make observing high vibrational levels in the  $A^2\Pi$  state challenging, since only the first few vibrational levels of the  $X^2\Sigma_{1/2}$  state are populated for temperatures  $\sim 1000$

<sup>3</sup>Formally, the Dunham coefficients are a power series expansion in  $B_e^2/\omega_e^2$ . For all but the lightest molecules this ratio is on the order of magnitude of  $10^{-6}$  so that the first term in the power series expansion is adequate for our purposes [93]. This small discrepancy arises due to assumptions made within the Born-Oppenheimer approximation [91].

K. Constants for the  $A^2\Pi_{1/2}$  state and their method of calculation are listed in Table 2.5. Table 2.6 presents constants for some of the other electronic states. Spectroscopic knowledge of these other electronic states is useful for certain detection or alternative cycling schemes.

Dunham coefficient	Value ( $\text{cm}^{-1}$ )	
$Y_{00}$	0	
$Y_{01}$	0.250534383(25)	
$Y_{02}$	-2.49586(33)	$\times 10^{-7}$
$Y_{03}$	-3.30(25)	$\times 10^{-14}$
$Y_{10}$	501.96496(13)	
$Y_{11}$	-1.551101(17)	$\times 10^{-3}$
$Y_{12}$	-2.423(17)	$\times 10^{-10}$
$Y_{20}$	-2.204617(37)	
$Y_{21}$	2.1850(58)	$\times 10^{-6}$
$Y_{22}$	1.029(23)	$\times 10^{-11}$
$Y_{30}$	5.2815(28)	$\times 10^{-3}$
$Y_{31}$	1.518(44)	$\times 10^{-8}$

Table 2.4: Dunham coefficients of the SrF  $X^2\Sigma_{1/2}$  electronic ground state. One standard deviation is provided in parentheses. All data come from Ref. [94].

Parameter	2008 value	2013 value	Estimated range
$T_e$	15072.09		
$\omega_e$	509.5406	509.38	509.3-509.7
$\omega_e x_e$	2.2361	2.18	2.15-2.25
$B_e$	0.25359	0.2536135	.25358-.25364
$\alpha_e$	0.00156	0.00156	.0015-.00165

Table 2.5: Constants for the SrF  $A^2\Pi_{1/2}$  state. The 2008 set of constants were calculated by David DeMille from Refs. [95, 96]. In 2013 the constants were updated to reflect additional data made available since 2008. In the 2013 calculation,  $\omega_e$  and  $\omega_e x_e$  are calculated from Refs. [95–97].  $B_e$  is calculated using a recent value of  $B_0$  [98] combined with the original value of  $\alpha_e$  and is consistent with the value presented in Ref. [96]. The estimated range is determined by calculating each parameter with and without different subsets of data that became available since 2008.

Constant	$A^2\Pi_{3/2}$	$B^2\Sigma$	$^2\Delta$	$C^2\Pi$
$T_e$	15216.34287(47) [98]	17267.4465(26) [99]	19830-20553 [85]	27384.67113(93) [98]
$\omega_e$		495.8(7) [100]		
$\omega_e x_e$		2.34(21) [100]		
$B_e$		.24961(9) [100]		
$B_0$	.2528335(37) [98]			0.2462110(39) [98]
$B_1$				
$\alpha_e$		.00175(9) [100]		
$D_e$		$2.53(1) \times 10^{-7}$ [100]		
$D_0$	$2.546(25) \times 10^{-7}$ [98]			$2.897(24) \times 10^{-7}$ [98]
$\gamma$		-.134(6) [100]		
$A$	281.46138(52) [98]			57.9048(14) [98]
$p$	-.133002(28) [98]			$3.712(67) \times 10^{-3}$ [98]
$q$				$-4.16(46) \times 10^{-5}$ [98]

Constant	$D^2\Sigma^+(v=0)$	$D^2\Sigma^+(v=1)$	$E^2\Pi_{1/2}$	$E^2\Pi_{3/2}$
$T_e$	27773.8168(42) [98]	28327.5784(12) [98]	31529.1 [101]	31615 [101]
$\omega_e$			564.4 [101]	
$\omega_e x_e$			3.20 [101]	
$B_e$				
$B_0$	.263677(28) [98]			
$B_1$		0.2627533(42) [98]		
$\alpha_e$				
$D_e$				
$D_0$	$7.07(43) \times 10^{-7}$ [98]	$2.575(25) \times 10^{-7}$ [98]		
$\gamma$	-.016666(82) [98]	.020367(63) [98]		
$A$				
$p$				
$q$				

Constant	$F^2\Sigma^+$	$G^2\Pi(v=0)$
$T_e$	32823.5(4) [102]	34808.9275(18) [102]
$\omega_e$	599.3652(96) [102]	
$\omega_e x_e$	3.4252(19) [102]	
$B_e$	0.270517 [102]	
$B_0$		.2636772(70) [102]
$B_1$		
$\alpha_e$	.0016380(42) [102]	
$D_e$	$0.2210(90) \times 10^{-6}$ [102]	
$D_0$		$2.357(54) \times 10^{-7}$ [102]
$\gamma$	-.04360(29) [102]	
$A$		$1.879 \times 10^{-4}$ [102]
$p$		-.001052(80) [102]
$q$		$-3.43(34) \times 10^{-5}$ [102]

Table 2.6: Electronic, vibrational and rotational constants of SrF for electronic states other than  $X^2\Sigma_{1/2}$  and  $A^2\Pi_{1/2}$ , in  $\text{cm}^{-1}$ . Of the listed electronic transitions, only excitation to the  $D(v=0)$  and  $D(v=1)$  state have been used in our lab at Yale. However, knowledge of constants for other states is useful for possible alternative detection or cycling methods. More constants for the B state can be found in Ref. [100] and are reproduced in Ref. [91] pg. 904. The constant  $A$  is the spin-orbit coupling constant. Constants  $p$  and  $q$  are parameters governing the energy level splitting of  $\Lambda$ -doublets in  $\Pi$  states. All three constants are discussed later in this chapter.



## 2.5 Fine structure, hyperfine structure, spin-rotation, and Lambda-doubling energy levels

Molecules with unpaired spins may demonstrate additional level splittings beyond those discussed above. In particular, molecules with  $I \neq 0$  or  $S \neq 0$  exhibit additional structure arising from the coupling of these angular momenta both to each other and to other angular momenta such as  $N$ ,  $L$ , etc. For our isotope,  $^{88}\text{Sr}^{19}\text{F}$ ,  $I = \frac{1}{2}$  from the  $^{19}\text{F}$  nuclear spin as  $^{88}\text{Sr}$  has no nuclear spin. Similarly, our system has  $S = \frac{1}{2}$  from the lone unpaired electron.

Some terms given in Eqn. 2.1 are zero for certain electronic states. In the  $X^2\Sigma_{1/2}$  electronic ground state,  $L = 0$  and  $\Lambda = 0$ , and hence the spin-orbit and  $\Lambda$ -doubling terms in Eqn. 2.1 are zero. Energy level structure in each  $X^2\Sigma_{1/2}$  rovibrational state is dominated by the  $H_{\text{SR}}$  and  $H_{\text{HFS}}$  contributions. In the  $A^2\Pi$  state, the energy level structure of each rovibrational state is dominated by the  $H_{\text{SO}}$  and the  $\Lambda$ -doubling terms. Splittings due to the spin-orbit interaction in particular are large (on the order of the vibrational energy level splittings).

### 2.5.1 X state spin-rotation and hyperfine structure

The Hamiltonian for the spin-rotation (SR) interaction, denoted  $H_{\text{SR}}$ , and the hyperfine (HF) interaction, denoted  $H_{\text{HFS}}$ , in vibrational level  $v$  and rotational level  $N$  are given respectively by

$$H_{\text{SR}} = \gamma_{vN} \mathbf{S} \cdot \mathbf{N} \quad \text{and} \quad H_{\text{HFS}} = b_{vN} \mathbf{I} \cdot \mathbf{S} + c_{vN} (\mathbf{I} \cdot \hat{\mathbf{z}})(\mathbf{S} \cdot \hat{\mathbf{z}}) + C_{1vN} \mathbf{I} \cdot \mathbf{N}, \quad (2.8)$$

where  $\gamma_{vN}$  is the spin-rotation constant,  $b_{vN}$  is the hyperfine constant,  $c_{vN}$  is the dipole-dipole constant and  $C_{1vN}$  is the nuclear spin-rotation constant. The constant  $C_{1vN}$  is negligibly small for our purposes but is included for completeness. Using Dunham's theory of vibration-rotation energies, these parameters can be represented by a converging series of the form

$$X_{vN} = \sum_{l,j} X_{lj} (v + 1/2)^l [N(N + 1)]^j. \quad (2.9)$$

where the known  $X_{lj}$  coefficients are listed in Table 2.7. As an example, values of the generated constants  $\gamma_{v1}$ ,  $b_{v1}$ ,  $c_{v1}$ ,  $C_{v1}$ ,  $B_v$ , and  $D_v$  are listed for the  $X^2\Sigma_{1/2}(v = 0 - 4, N = 1)$  states in Table 2.8.

In the  $X^2\Sigma_{1/2}(v = 0, N = 1)$  state,  $H_{\text{SR}}$  and  $H_{\text{HFS}}$  are of similar energy scales and thus are treated together. While  $H_{\text{SR}}$  is diagonal in the  $|N, J, F\rangle$  basis,  $H_{\text{HFS}}$  is not. For the ground electronic state,

Parameter	Value (MHz)	Source
$\gamma_{00}$	75.02249(7)	[103]
$\gamma_{01}$	$5.938(6) \times 10^{-5}$	[103]
$\gamma_{02}$	$-6.3(1) \times 10^{-10}$	[103]
$\gamma_{10}$	-0.45528(5)	[103]
$\gamma_{11}$	$-3.37(3) \times 10^{-6}$	[103]
$b_{00}$	97.6670(10)	[103]
$b_{01}$	$-3.300(4) \times 10^{-4}$	[103]
$b_{10}$	-1.1672(8)	[103]
$c_{00}$	29.846(8)	[103]
$c_{10}$	.843(7)	[103]
$C_{I00}$	.00230(1)	[103]

Table 2.7: Parameters used for Dunham expansion of the SR/HF energy levels in the  $X^2\Sigma_{1/2}$  state. The number in parentheses is one standard deviation.

Parameter	$v = 0$	$v = 1$	$v = 2$	$v = 3$	$v = 4$	Source
$\gamma_{v1}$	74.7950	74.3397	73.8844	73.4291	72.9738	[103]
$b_{v1}$	97.0827	95.9155	94.7483	93.5811	92.4139	[103]
$c_{v1}$	30.2675	31.1105	31.9535	32.7965	33.6395	[103]
$C_{v1}$	0.0023	0.0023	0.0023	0.0023	0.0023	[103]
$B_v$	7487.60	7441.23	7395.00	7348.90	7302.95	[94]
$D_v$	0.0075	0.0075	0.0075	0.0075	0.0075	[94]

Table 2.8: Approximate SR/HF constants for the  $X^2\Sigma_{1/2}(v = 0 - 4, N = 1)$  energy levels in MHz. Rotational constants for the  $X^2\Sigma_{1/2}(v = 0 - 4)$  energy levels are shown as well. These constants are used to determine microwave transition frequencies between rotational sublevels and the relative spacing of the SR/HF sublevels within a rovibrational manifold. Although the above SR/HF constants are tabulated for  $N = 1$ , the  $N$  dependence is very small and constants for the  $X^2\Sigma_{1/2}(v = 0 - 4, N \neq 1)$  energy levels differ from those above by  $\sim 10$ 's of Hz [103].

the combined spin-rotation and hyperfine Hamiltonian can be diagonalized analytically to get the energy eigenvalues [104, 105]. The required method is discussed in a later part of this chapter but a portion of the relevant results are presented here in order to elaborate on the SR/HF structure. In the absence of external electric or magnetic fields, the four energy levels, designated by  $E_{N,J,F}$  and shown in Fig. 2.2, are given (in order of highest to lowest energy) by Ref. [103]

$$\begin{aligned}
E_{N,N+1/2,N+1} &= \frac{\gamma_{vN} + C_{vN}}{2} \times N + \frac{b_{vN}}{4} + \frac{c_{vN}}{4(2N+3)} \\
E_{N,N+1/2,N} &= -\frac{\gamma_{vN} + C_{vN} + b_{vN}}{4} \\
&\quad + \frac{1}{4} \sqrt{(2N+1)^2(\gamma_{vN} - C_{vN})^2 - 2(\gamma_{vN} + C_{vN})(2b_{vN} + c_{vN}) + (2b_{vN} + c_{vN})^2 + 4C_{vN}\gamma_{vN}} \\
E_{N,N-1/2,N-1} &= -\frac{\gamma_{vN} + C_{vN}}{2} \times (N+1) + \frac{b_{vN}}{4} - \frac{c_{vN}}{4(2N-1)} \\
E_{N,N-1/2,N} &= -\frac{\gamma_{vN} + C_{vN} + b_{vN}}{4} \\
&\quad - \frac{1}{4} \sqrt{(2N+1)^2(\gamma_{vN} - C_{vN})^2 - 2(\gamma_{vN} + C_{vN})(2b_{vN} + c_{vN}) + (2b_{vN} + c_{vN})^2 + 4C_{vN}\gamma_{vN}}.
\end{aligned} \tag{2.10}$$

For these states,  $N$  and  $F$  have definite values but  $J$  does not (i.e  $J$  is not a good quantum number). Herein, for the purposes of bookkeeping, we will refer to states using the  $|N, J, F\rangle$  notation even though  $J$  is only approximately a good quantum number. We note that the mixing between the  $J$  states decreases rapidly for values of  $N$  beyond the maximal mixing at  $N = 1$  as shown in Table 2.9.

Nominal label	Actual composition	Nominal label	Actual composition
$ N=1, J=3/2, F=1\rangle$	$.8880 J=3/2\rangle + .4598 J=1/2\rangle$	$ N=1, J=1/2, F=1\rangle$	$-.4598 J=3/2\rangle + .8880 J=1/2\rangle$
$ N=2, J=5/2, F=2\rangle$	$.9569 J=5/2\rangle + .2903 J=3/2\rangle$	$ N=2, J=3/2, F=2\rangle$	$-.2903 J=5/2\rangle + .9569 J=3/2\rangle$
$ N=3, J=7/2, F=3\rangle$	$.9776 J=7/2\rangle + .2107 J=5/2\rangle$	$ N=3, J=5/2, F=3\rangle$	$-.2107 J=7/2\rangle + .9776 J=5/2\rangle$
$ N=4, J=9/2, F=4\rangle$	$.9863 J=9/2\rangle + .1650 J=7/2\rangle$	$ N=4, J=7/2, F=4\rangle$	$-.1649 J=9/2\rangle + .9863 J=7/2\rangle$
$ N=5, J=11/2, F=5\rangle$	$.9908 J=11/2\rangle + .1354 J=9/2\rangle$	$ N=5, J=9/2, F=5\rangle$	$-.1354 J=11/2\rangle + .9908 J=9/2\rangle$

Table 2.9: Nominal labeling and actual composition of impure spin-rotational and hyperfine sublevels in the  $X^2\Sigma_{1/2}$  electronic state.  $J$  is good quantum number in the  $|N=0\rangle$  state.

Using Eqns. 2.3 and 2.10 we can calculate the splittings between rotational levels in the  $X^2\Sigma_{1/2}(v=0)$  state and the HF splittings within each rotational manifold of the  $X^2\Sigma_{1/2}(v=0)$  state, which are presented in Fig. 2.2. The calculated values of the HF/SR splittings within each rovibrational sublevel are well characterized and consistent with experimental data from Ref. [103] to within  $\lesssim 20$  kHz. The values presented for the rotational transitions agrees with experimental data presented by Ref. [106] to  $\lesssim 100$  kHz. This accuracy is sufficient for our purposes.

In comparison to an alkali atom (Rb in particular), the small extent of SrF's HF structure in the

SR/HF level	v=0	v=1	v=2	v=3	v=4
$ N = 1, J = 3/2, F = 2\rangle$	63.1827	62.7054	62.2281	61.7508	61.2735
$ N = 1, J = 3/2, F = 1\rangle$	21.8096	21.8028	21.7961	21.7893	21.7825
$ N = 1, J = 1/2, F = 0\rangle$	-58.0935	-58.1407	-58.188	-58.2352	-58.2825
$ N = 1, J = 1/2, F = 1\rangle$	-107.75	-106.932	-106.114	-105.296	-104.478

Table 2.10: SR/HF splittings in MHz for the  $X^2\Sigma_{1/2}(v = 0 - 4, N = 1)$  states.

ground state can be explained as follows: Of strontium's two valence electrons, one fills the valence shell of the fluorine. The paired electronic spins in the fluorine's full valence shell result in no HF shifts from electrons bound to the fluorine. With its extra electron however, the fluorine atom is negatively charged and the lone unpaired electron thus resides predominantly near the strontium atom. In fact, the electron spin density on the fluorine atom is less than 1% for SrF [107]. We note that BaF displays a somewhat smaller HF splittings and CaF displays somewhat larger HF splittings relative to SrF. SrH is expected to exhibit larger HF splittings than SrF.

### 2.5.2 A state spin-orbit and Lambda-doubling structure

In the  $A^2\Pi$  state, we have  $|\Lambda| = 1$ , which gives rise to terms in the Hamiltonian not present in the electronic ground state. The largest of these terms is the spin-orbit coupling which has the Hamiltonian given by

$$H_{SO} = A\mathbf{L} \cdot \mathbf{S}, \quad (2.11)$$

where the parameter  $A$  is the spin-orbit coupling constant. The spin-orbit interaction splits the electronic structure into a multiplet of  $2S+1$  components. For the  $A^2\Pi$  state,  $A = 281.46138 \text{ cm}^{-1}$ , much larger than any hyperfine or rotational energy level spacing. The electronic energy of the multiplet term is therefore given to a first approximation by Ref. [108]

$$T_e = T_0 + A\Lambda\Sigma, \quad (2.12)$$

where  $T_0$  is the term value when the spin is neglected. For the SrF  $A^2\Pi$  state, the two multiplets are the  $A^2\Pi_{1/2}$  and  $A^2\Pi_{3/2}$  states which are separated by  $A$ .

For  $|\Lambda| > 0$  there is a double orbital degeneracy corresponding to the circulation of the single valence electron in either a clockwise or counterclockwise direction. This degeneracy persists for  $|\Omega| > 0$ , and it is customary to use  $|\Omega|$  to represent both values. However the rotation of the molecule lifts this degeneracy in the presence of a perturbing  $\Sigma$  state. For  $^2\Pi$  states in Hund's case

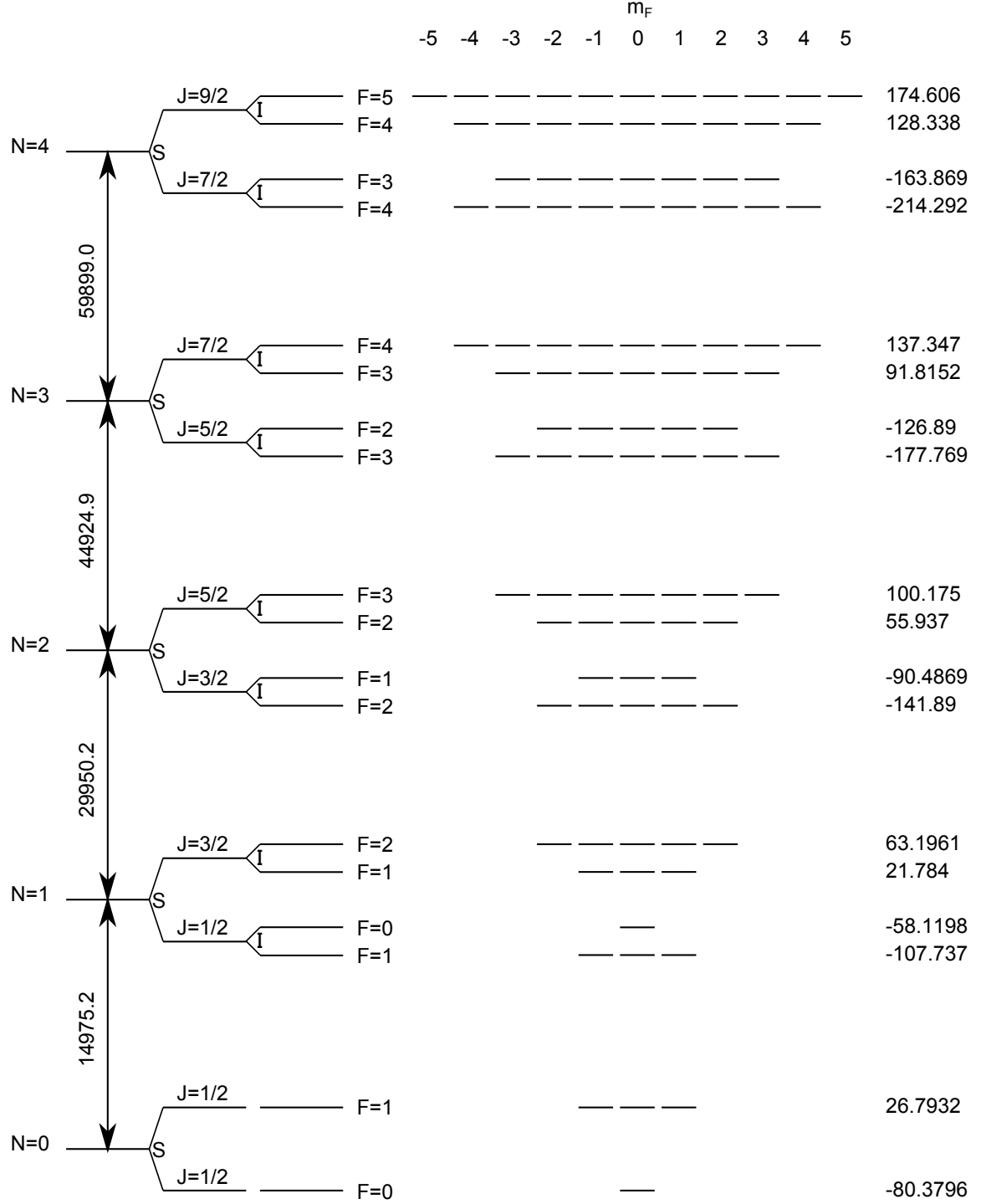


Figure 2.2: Rotational, spin-rotational and hyperfine splittings of the  $X^2\Sigma_{1/2}(v=0)$  state. The calculated values of the HF splittings within each rovibrational sublevel shown are well characterized and consistent with experimental data from Ref. [103] to within  $\lesssim 20$  kHz. The calculated splittings between rotational levels can be verified using a short list of observed microwave transitions given in Ref. [106] and agree with experimental data to  $\lesssim 100$  kHz. We have verified via observation in our own lab that the microwave transition  $|N=0, J=1/2, F=1\rangle \rightarrow |N=1, J=3/2, F=2\rangle$  calculated to be at 15011.6 MHz is observed at that frequency to  $\sim 100$  kHz.

(a), the Hamiltonian describing  $\Lambda$ -doubling is given by Ref. [109]

$$H_{\Lambda d} = -\frac{1}{2}(p+q)(S_+^2 + S_-^2) - \frac{1}{2}(p+2q)(J_+S_+ + J_-S_-) + \frac{1}{2}q(J_+^2 + J_-^2), \quad (2.13)$$

where  $p$  and  $q$  are the  $\Lambda$ -doubling parameters,  $S_{+(-)}^2$  is the spin raising (lowering) operator, and  $J_{+(-)}$  is the total angular momentum raising (lowering) operator. Under the assumption that  $L$  can be attributed to a single electron,  $p$  and  $q$  of a  $^2\Pi$  state can be calculated using the following expressions [108]

$$p = \frac{2A_{\Pi}B_{\Pi}l(l+1)}{\Delta E(T_{\Pi} - T_{\Sigma})} \quad (2.14)$$

$$q = \frac{2B_{\Pi}^2l(l+1)}{\Delta E(T_{\Pi} - T_{\Sigma})}, \quad (2.15)$$

where  $\Delta E(T_{\Pi} - T_{\Sigma})$  is the separation of the  $\Pi$  state from the perturbing  $\Sigma$  state. For Hund's case (a) molecules with  $^2\Pi_{1/2}$  structure, the  $\Lambda$ -doublet splitting is then given by Ref. [109, 110]

$$\Delta E_{\Lambda} = \mp(p+2q)(J+1/2), \quad (2.16)$$

and the - sign applies when  $A$  is positive, the + when  $A$  is negative. However the HF splitting is unresolved and stated to be less than 3 MHz in the  $A^2\Pi$  state [111].

## 2.6 Labeling of transitions

Specific transitions within the  $^2\Sigma \rightarrow ^2\Pi$  electronic transition are identified with a label as

$$M_{ab}, \quad (2.17)$$

where  $M$  is a letter which depends on the  $\Delta J$  of the transition,  $a$  is an indice specifying the excited state of the transition (either the  $^2\Pi_{1/2}$  or  $^2\Pi_{3/2}$  state), and  $b$  is an indice specifying the initial value of  $J$  in the ground state. Transitions with  $\Delta J = -1, 0, 1$  are assigned  $M = P, Q, R$  respectively. For SrF, if the transition is to the  $^2\Pi_{1/2}$  state,  $a = 1$ , and if the transition is to the  $^2\Pi_{3/2}$  state, then  $a = 2$ . For SrF, if the transition originates from the  $J = N + 1/2$  state, then  $b = 1$ , and if the transition originates from the  $J = N - 1/2$  state, then  $b = 2$ . If  $a = b$ , the second subscript is sometimes omitted. Due to additional HF structure in the  $X^2\Sigma_{1/2}$  state, additional weaker transitions called

satellite branches [108] are allowed, but their labeling is not discussed here. Transitions from a  $^2\Sigma_{1/2}$  state to a  $^2\Pi$  state and their labeling are shown in Fig. 2.3. Transitions between the  $A^2\Pi_{3/2}$  and the  $A^2\Pi_{1/2}$  state are forbidden by the selection rule  $\Delta\Sigma = 0$  for transitions in Hund's case (a).

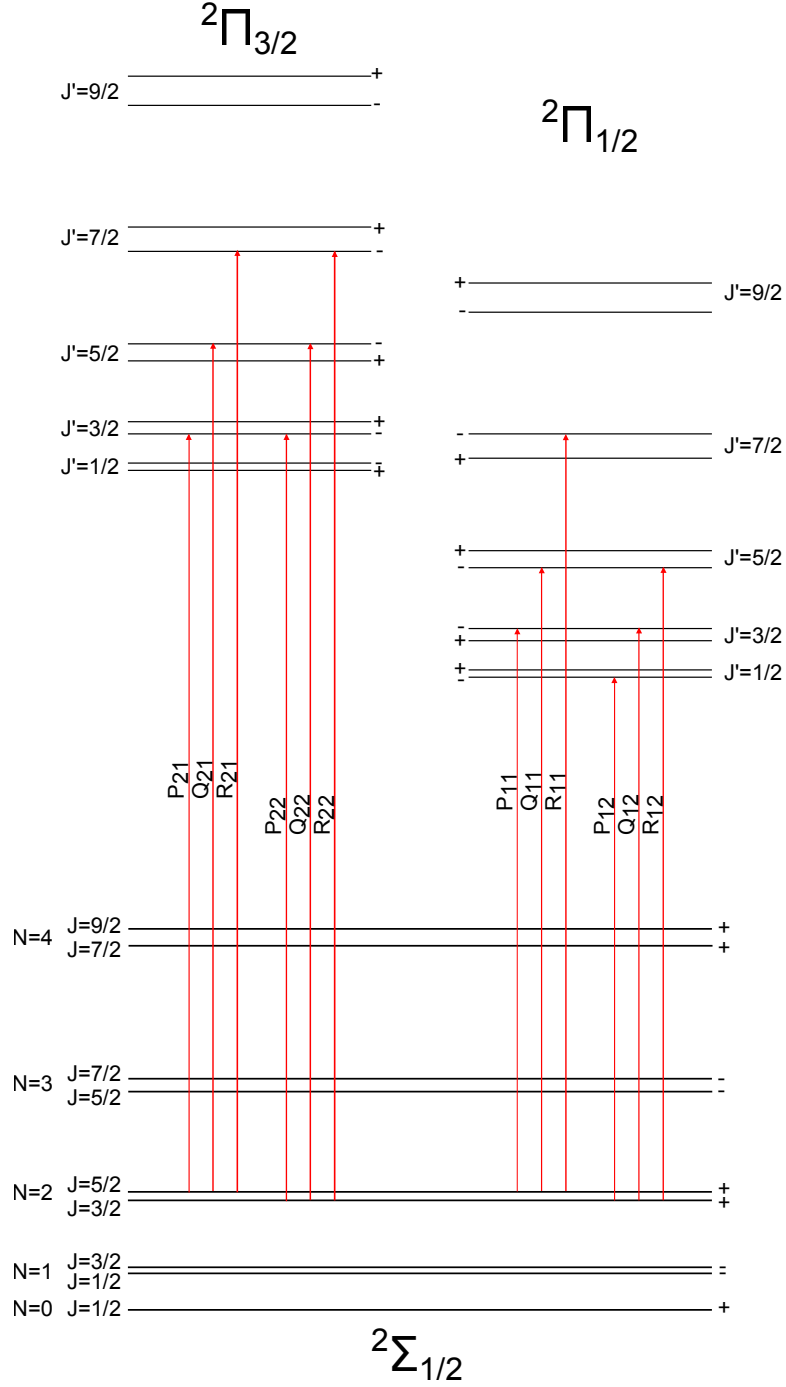


Figure 2.3: Energy level diagram for the  $X^2\Sigma_{1/2} \rightarrow A^2\Pi$  transition. For clarity, only transitions from the  $X^2\Sigma_{1/2}(N = 2)$  state are shown. The  $\pm$  labels indicate the parity quantum numbers of each state. Transition labels, e.g.  $P_{12}$ , are described in the main text.



Coupling case	Good quantum numbers	Requirements
(a)	$\Lambda, S, \Sigma, J, \Omega$	$A\Lambda \gg BJ$
(b)	$\Lambda, N, S, J$	$A\Lambda \ll BJ$

Table 2.11: Good quantum numbers and requirements for Hund’s cases (a) and (b). This table is reproduced from Ref. [91] pg. 226. This table does not include nuclear spin or quantum numbers derived from nuclear spin such as  $F$ .

## 2.7 Coupling of angular momenta

The various angular momenta of diatomic molecules can couple together in a variety of different ways. For different types of these couplings, certain quantities are conserved. These conserved quantities define a basis set of the good quantum numbers. In SrF, the  $X^2\Sigma_{1/2}$  state is well described by Hund’s case (b) while the  $A^2\Pi_{1/2}$  state is best described by Hund’s case (a). We will therefore focus on those two cases. The good quantum numbers for Hund’s case (a) and Hund’s case (b) are shown in Table 2.11.

In Hund’s case (a), shown in Fig. 2.4a,  $\mathbf{L}$  is strongly coupled to the internuclear axis  $\hat{z}$ .  $\mathbf{S}$  is strongly coupled to  $\mathbf{L}$  (and therefore to  $\hat{z}$ ) through spin-orbit coupling. The angular momentum of the rotating nuclei  $\mathbf{R}$  is coupled to  $\mathbf{\Omega}$  to form  $\mathbf{J} = \mathbf{R} + \mathbf{\Omega}$ . The precession of  $\mathbf{L}$  and  $\mathbf{S}$  about the internuclear axis is presumed to be much faster than the rotation of  $\mathbf{\Omega}$  and  $\mathbf{R}$  around  $\mathbf{J}$ .

In Hund’s case (b), illustrated in Fig. 2.4b,  $\mathbf{L}$  is strongly coupled to the internuclear axis.  $\mathbf{\Lambda}$  is coupled to  $\mathbf{R}$  to form  $\mathbf{N}$  and  $\mathbf{N}$  is coupled to  $\mathbf{S}$  to form  $\mathbf{J}$ .  $\mathbf{\Omega}$  is undefined in Hund’s case (b). For molecules with  $^2\Sigma_{1/2}$  ground states (implying  $\mathbf{\Lambda} = \mathbf{L} = 0$ ), the calculation of angular momentum addition parallels that of an atom in that  $\mathbf{L}$  can simply be replaced with  $\mathbf{N}$ .

As stated previously, for all energy levels relevant to this thesis, the single nuclear spin  $\mathbf{I}$  from  $^{19}\text{F}$  couples to  $\mathbf{J}$  so that  $\mathbf{J} + \mathbf{I} = \mathbf{F}$ .

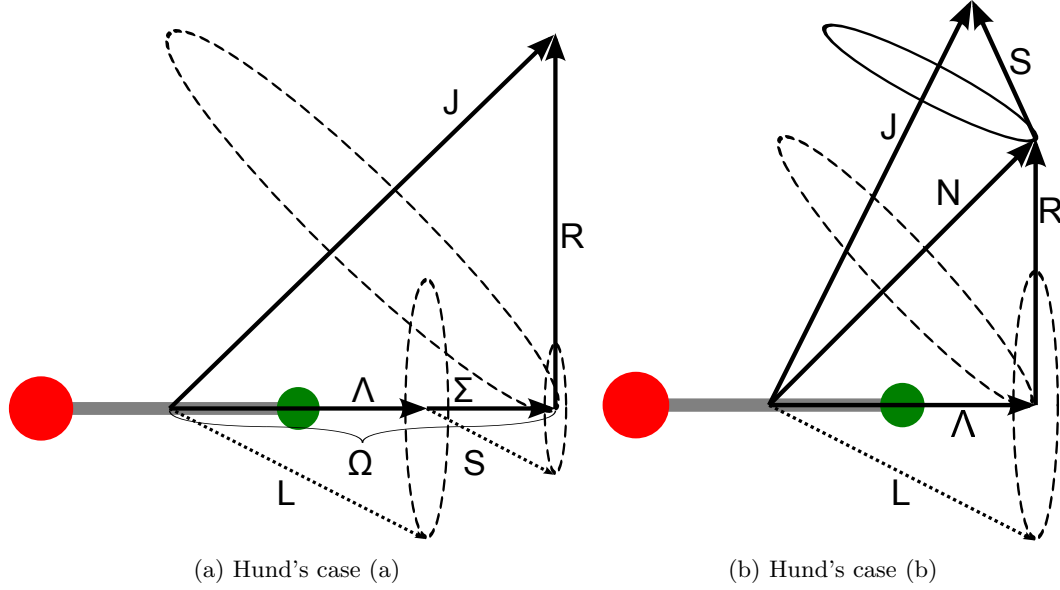


Figure 2.4: Vector coupling diagram for Hund's cases (a) and (b). The  $A^2\Pi_{1/2}$  state of SrF is well described by Hund's case (a) while the  $X^2\Sigma_{1/2}$  state is well described by Hund's case (b). These diagrams are reproduced from Ref. [91] pgs. 225-227.

## 2.8 Franck-Condon factors

The Franck-Condon factors (FCFs) are a multiplicative component of the intensity of electronic transitions between initial and final states of the same or different vibrational number. The FCFs are defined as

$$q_{v',v''} = |\langle \psi_{v'} | \psi_{v''} \rangle|^2, \quad (2.18)$$

where  $\psi_{v'}$  and  $\psi_{v''}$  are the vibrational eigenfunctions of the upper and lower states. For most molecules, the FCFs can easily be measured. For SrF, however, off-diagonal ( $v' \neq v''$ ) FCFs are highly suppressed, which can lead to small signals for such measurements. Table 2.12 shows FCFs for the  $A^2\Pi_{1/2} \rightarrow X^2\Sigma_{1/2}$  transition. The potential energy curves are calculated using the first-order Rydberg-Klein-Rees (RKR) procedure [112–114] using the constants in Table 2.4 for the X state and the constants calculated in 2013 and listed in Table 2.5 for the A state. The FCFs are evaluated using the suite of programs developed by Prof. Robert LeRoy (Waterloo University) [115]. The calculation of the FCFs is checked by performing the same calculation using the X and A state constants listed in Ref. [116] and verifying that the results match the FCFs presented in Ref. [116] under those conditions. For SrF, the FCFs are most sensitive to  $B_e$ , followed by  $\omega_e$ , followed by  $\alpha_e$ , followed by  $\omega_e x_e$ . Given the estimated uncertainty presented in Table 2.5, we do not believe the uncertainty in the A state constants is problematic for calculating the FCFs. Further details of

the FCF calculation are available in [Appendix A](#). Branching ratios to different vibrational states also depend on the energy difference between the two states in addition to depending on  $q_{v',v''}$ . The vibrational branching ratio between different electronic states is

$$\mathcal{VBR}_{v',v''} = \frac{q_{v',v''} \times \omega_{v',v''}^3}{\sum_{k=0}^{\infty} q_{v',k} \times \omega_{v',k}^3}, \quad (2.19)$$

where  $\omega_{v',v''}$  is the energy difference between the initial and final state. Table 2.13 shows calculated vibrational branching ratios for the  $A^2\Pi_{1/2} \rightarrow X^2\Sigma_{1/2}$  transition. In the process of calculating the potential energy curves, we also obtain values for the equilibrium internuclear separation  $r_e$  in both the  $X^2\Sigma_{1/2}$  and  $A^2\Pi_{1/2}$  states, as shown in Table 2.14.

$q_{v',v''}$	$v'' = 0$	$v'' = 1$	$v'' = 2$	$v'' = 3$	$v'' = 4$
$v' = 0$	9.184E-01	1.812E-02	4.303E-04	1.263E-05	4.272E-07
$v' = 1$	1.853E-02	9.451E-01	3.507E-02	1.248E-03	4.841E-05
$v' = 2$	2.718E-05	3.670E-02	9.099E-01	5.085E-02	2.413E-03
$v' = 3$	1.600E-08	8.150E-05	5.445E-02	8.759E-01	6.547E-02
$v' = 4$	2.410E-10	7.834E-08	1.618E-04	7.175E-02	8.431E-01

Table 2.12: Calculated FCFs  $q_{v',v''}$  for the  $A^2\Pi_{1/2}(v') \rightarrow X^2\Sigma_{1/2}(v'')$  transition. For decays from the lowest vibrational state, the first row is applicable.

$\mathcal{VBR}_{v',v''}$	$v'' = 0$	$v'' = 1$	$v'' = 2$	$v'' = 3$	$v'' = 4$
$v' = 0$	9.832E-01	1.641E-02	3.516E-04	9.278E-06	2.815E-07
$v' = 1$	2.046E-02	9.467E-01	3.179E-02	1.022E-03	3.568E-05
$v' = 2$	3.294E-05	4.048E-02	9.114E-01	4.614E-02	1.979E-03
$v' = 3$	2.128E-08	9.892E-05	6.020E-02	8.800E-01	5.965E-02
$v' = 4$	3.770E-10	1.122E-07	2.115E-04	8.553E-02	9.143E-01

Table 2.13: Calculated vibrational branching ratios  $\mathcal{VBR}_{v',v''}$  for the  $A^2\Pi_{1/2}(v') \rightarrow X^2\Sigma_{1/2}(v'')$  transition. For decays from the lowest vibrational state, the first row is applicable.

State	$r_e$ (Å)
$X^2\Sigma_{1/2}$	2.075365702
$A^2\Pi_{1/2}$	2.062729143

Table 2.14: Calculated values of the equilibrium internuclear separation  $r_e$ .

## 2.9 Branching ratios

The branching ratios are a measure of how the total intensity of a transition is distributed among the various rotational / spin-rotational / hyperfine (R/SR/HF) decay paths. The R/SR/HF branching ratios are therefore necessary both for calculating how much laser intensity is needed to drive certain transitions and for using experimentally observed line strengths to determine the molecular distribution among the states.<sup>4</sup> This section outlines the calculation of the R/SR/HF branching ratios for SrF in the field-free limit and follows the procedure presented in Refs. [104, 105]. The complexity of the calculation mainly lies in keeping track of all the states through 3 changes of basis.

### 2.9.1 Calculation overview

The  $A^2\Pi_{1/2}$  state is Hund's case (a) while the  $X^2\Sigma_{1/2}$  state is Hund's case (b). To calculate matrix elements between these two states, we convert all states to the same basis.

1. Write all states in the Hund's case (a) basis ( $|\Lambda, S, \Sigma, \Omega, J, I, F, M_F\rangle$ ).
  - Write mixed  $J$  ground states as a sum of pure  $J$  states. This is done by diagonalizing the Hamiltonians in Eqn. 2.8.
  - Write all ground states in Hund's case (a) basis. The states will then be sums of pure  $J$  and pure  $\Omega$ . Here we use Ref. [117] which dictates how case (b) basis functions may be expressed as linear combinations of case (a) basis functions using the Wigner 3J symbols:

$$|\Lambda; N, S, J\rangle = \sum_{\Omega=-1/2}^{1/2} \sum_{\Sigma=-1/2}^{1/2} (-1)^{J+\Omega} \sqrt{2N+1} \begin{pmatrix} S & N & J \\ \Sigma & \Lambda & -\Omega \end{pmatrix} |\Lambda, S, \Sigma, \Omega, J\rangle. \quad (2.20)$$

Do not use Eqn. 6.149 in Ref. [91] because there is a mistake in the formula.

- Write excited states in terms of basis states of signed  $\Omega$  using Eqn. 6.234 in Ref. [91].
2. Evaluate matrix elements between all states. This will involve 3J and 6J symbols.

The R/SR/HF branching ratios are shown for decays from the  $A^2\Pi_{1/2}(v=0, J=1/2^+)$  state in Table 2.15. A good check of the R/SR/HF branching ratios is that they should sum to 1 for each

---

<sup>4</sup>Knowledge of the population distribution over the molecular states is necessary to determine the temperature of the molecules (only valid if the distribution follows a Boltzmann distribution), to evaluate how best to apply our fixed total laser power, to check for cycling losses, etc.

excited state sublevel. The calculation can also be checked by putting in the coefficients for CaF and comparing to the calculated values to those in Ref. [105]. A table showing branching ratios from the  $A^2\Pi_{1/2}(J = 1/2^+, 3/2^+, 5/2^+, 1/2^-, 3/2^-)$  states is shown in Fig. 2.16 and is calculated in the same way. These branching ratios are useful for alternative cycling or detection methods.

$J''$	$F''$	$m_F''$	$F' = 0$	$F' = 1$		
			$m_F' = 0$	$m_F' = -1$	$m_F' = 0$	$m_F' = 1$
$3/2$	$2$	-2	0	.1667	0	0
		-1	0	.0833	.0833	0
		0	0	.0278	.1111	.0278
		1	0	0	.0833	.0833
		2	0	0	0	.1667
$3/2$	$1$	-1	.0063	.1330	.1330	0
		0	.0063	.1330	0	.1330
		1	.0063	0	.1330	.1330
$1/2$	$0$	$0$	$0$	$0.2222$	$0.2222$	$.2222$
$1/2$	$1$	-1	.3271	.1170	.1170	0
		$0$	.3271	.1170	0	.1170
		$1$	.3271	0	.1170	.1170

Table 2.15: Approximate R/SR/HF branching ratios for decays from the  $A^2\Pi_{1/2}(v' = 0, J' = 1/2^+)$  state to the  $X^2\Sigma_{1/2}(v'' = 0, N'' = 1)$  state.

	$N = 0$	$N = 1$	$N = 2$	$N = 3$
$J = 1/2^+$		1		0
$J = 3/2^+$		7/10		3/10
$J = 5/2^+$		1/5		4/5
$J = 1/2^-$	1/3		2/3	
$J = 3/2^-$	1/6		5/6	

Table 2.16: Branching ratios from a few of the lowest  $A^2\Pi_{1/2}$  states to  $X^2\Sigma_{1/2}$  states.

## 2.10 Energy shifts in the presence of an external magnetic field

For the purpose of remixing dark Zeeman sublevels, trapping molecules, and more, it is often useful to apply an external magnetic field to the molecules. For example, in a MOT, the combination of 3-D Doppler cooling (known as optical molasses) with a quadrupole magnetic field is used to create a position-dependent restoring force that both cools and confines the particles. Each hyperfine manifold with quantum number  $F$  contains  $2F+1$  magnetic sublevels. These Zeeman sublevels are degenerate in the absence of a magnetic field. However when an external magnetic field is applied, the degeneracy is broken. In the presence of an external magnetic field  $\mathbf{B}$ , the Zeeman Hamiltonian is well approximated by

$$H_Z = g_S \mu_B \mathbf{S} \cdot \mathbf{B} + g_L \mu_B \mathbf{L} \cdot \mathbf{B} - g_I \mu_N \mathbf{I} \cdot \mathbf{B} \quad (2.21)$$

$$= \mu_B \left[ g_S S_z + g_L L_z - g_I \left( \frac{\mu_N}{\mu_B} \right) I_z \right] B_z, \quad (2.22)$$

for a magnetic field in the z-direction. Here the electron g-factor is  $g_S \approx 2.002$ , the electron orbital g-factor is  $g_L \approx 1$ , and the nuclear g-factor is  $g_I \approx 5.585$ ;  $\mu_B$  is the Bohr magneton, and  $\mu_N$  is the nuclear magneton. The first two terms are the most important since  $\frac{\mu_N}{\mu_B} \approx \frac{1}{1836}$ . However terms  $\propto g_I$  are hereafter included for completeness. We note that the  $A^2\Pi_{1/2}$  state has  $g \approx 0$ , as do all ideal  $^2\Pi_{1/2}$  states<sup>5</sup>, and experiences no shifts from external magnetic fields. However,  $B$ -fields do shift the levels of the  $X^2\Sigma_{1/2}$  state. When the energy shift due to the magnetic field is small compared to the spin-rotation splittings, we have for the  $X^2\Sigma_{1/2}$  state,

$$H_Z = \mu_B \left[ g_J J_z B_z - g_I \left( \frac{\mu_N}{\mu_B} \right) I_z \right] B_z, \quad (2.23)$$

where the fine structure Landé g-factor  $g_J$  is given by

$$g_J = g_S \frac{J(J+1) - N(N+1) + S(S+1)}{2J(J+1)}. \quad (2.24)$$

Because the above two equations do not take into account the HF structure which may be large compared to the magnetic field splittings, Eqn. 2.24 must be refined further to take the HF structure

---

<sup>5</sup>For such states  $\Omega = |\mathbf{\Lambda} + \mathbf{\Sigma}| = \frac{1}{2}$  but  $\Lambda = 1$ , implying that  $\mathbf{\Sigma}$  and  $\mathbf{\Lambda}$  point in opposite directions. Therefore  $\mathbf{S}$  and  $\mathbf{L}$  point in opposite directions. Since  $g_S \approx 2g_L$ , the total g-factor for the state is  $\approx 0$ .

into account. If the energy shift due to the magnetic field is small compared to the HF structure, then for the  $X^2\Sigma_{1/2}$  state we have

$$H_Z = g_F \mu_B F_z B_z, \quad (2.25)$$

where the Landé g-factor  $g_F$  is given by

$$\begin{aligned} g_F &= g_J \frac{F(F+1) - I(I+1) + J(J+1)}{2F(F+1)} + g_I \left( \frac{\mu_N}{\mu_B} \right) \frac{F(F+1) + I(I+1) - J(J+1)}{2F(F+1)} \\ &\simeq g_J \frac{F(F+1) - I(I+1) + J(J+1)}{2F(F+1)}, \end{aligned} \quad (2.26)$$

where the simplification neglects terms proportional to  $\frac{\mu_N}{\mu_B}$ . Table 2.17 shows values for  $g_F$  calculated using Eqn. 2.26 for the 4 SR/HF manifolds in two cases: first, assuming a small  $B$ -field and that the spin-rotation is large enough so that the states are of pure  $J$ , and second, assuming a small  $B$ -field and solving the Hamiltonian exactly, taking into account that the eigenstates are of mixed and not pure  $J$ . The method for this is discussed in the next section. From the perspective of making a MOT, it is unfortunate that the g-factors do not all share the same sign. This will be discussed later.

Nominal label	$J$ composition	Assuming no $J$ mixing	With $J$ mixing
$ N=1, J=3/2, F=2\rangle$	100% $J=3/2$	0.50	0.5
$ N=1, J=3/2, F=1\rangle$	79% $J=3/2$ , 21% $J=1/2$	0.83	0.97
$ N=1, J=1/2, F=0\rangle$	100% $J=1/2$	0.00	0
$ N=1, J=1/2, F=1\rangle$	79% $J=1/2$ , 21% $J=3/2$	-0.33	-0.47

Table 2.17: g-factors of the  $X^2\Sigma_{1/2}(v=0, N=1)$  SR/HF manifolds without and with taking into account the mixing of the states with the same  $J$ . The g-factors above are valid for  $B$ -fields which produce energy level shifts that are small compared to SR/HF splittings.

spin-rotation	Ref. [91]: Eqn. 9.89
Nuclear spin-rotation	Ref. [91]: Eqn. 8.271
Hyperfine	Ref. [91]: Eqn. 9.90
Dipole-dipole	Ref. [91]: Eqn. 8.259
Electron spin Zeeman	Ref. [91]: Eqn. 8.183
Nuclear spin Zeeman	Ref. [91]: Eqn. 8.185

Table 2.18: Equations to construct the full electronic ground state Hamiltonian.

## 2.11 Exact electronic ground state Hamiltonian

In order to better predict energy shifts in the electronic ground state from external magnetic fields, it is necessary to diagonalize the electronic ground state Hamiltonian exactly. We use the  $|\Lambda, N, S, J, I, F, M_F\rangle$  basis to calculate the energy levels as a function of  $B$ -field for each rovibrational level within the  $X^2\Sigma_{1/2}$  state. Within each rovibrational level, all additional terms in the Hamiltonian (Eqn. 2.21 and Eqn. 2.8) are calculated using the equations listed in Table 2.18. Once the full Hamiltonian is produced and diagonalized, several checks of the limiting cases can help confirm the correctness of the Hamiltonian construction. The energy levels should simplify to Eqn. 2.10 for  $B = 0$ , and the slope of the energy levels should be governed by the g-factors in the case of pure  $J$  states shown in Table 2.17 for small values of  $B$  under the condition  $\gamma \gg b, c, C$ . With the full Hamiltonian, we can now plot the energy level shifts of the  $X^2\Sigma_{1/2}(v = 0, N = 1)$  state versus  $B$ -field as shown in Fig. 2.5.



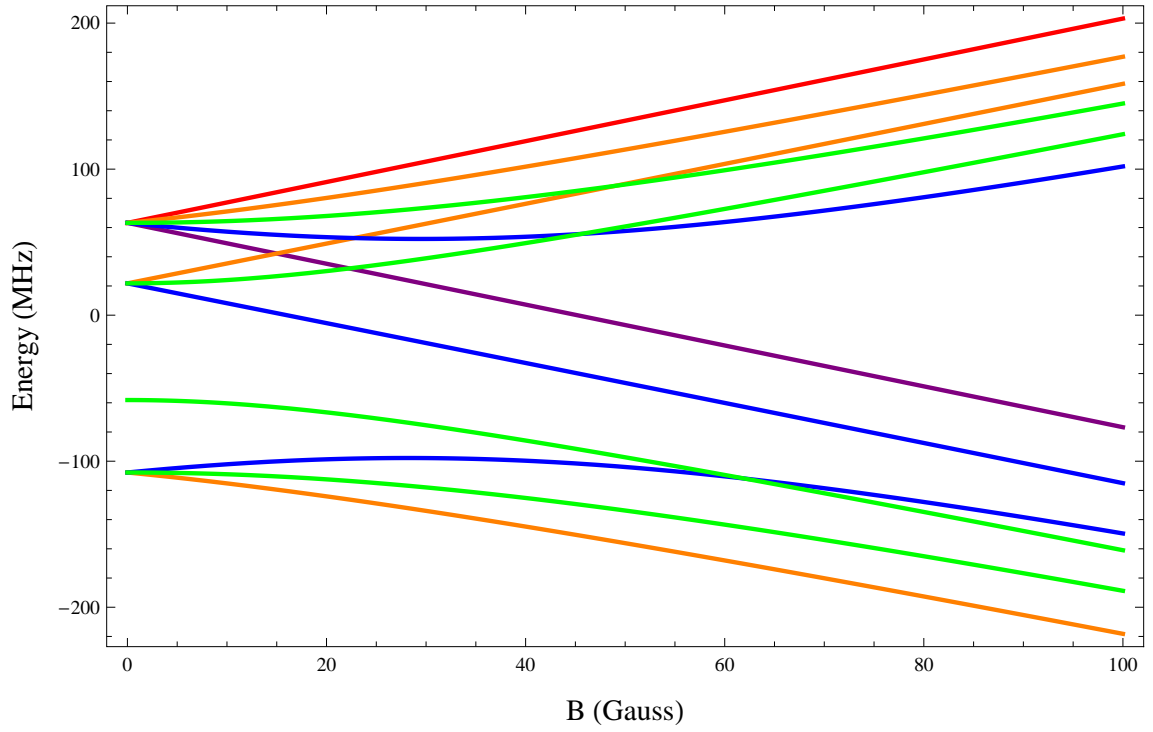


Figure 2.5: Energy levels of the  $X^2\Sigma_{1/2}(v = 0, N = 1)$  state versus magnetic field. The energy levels are labeled by their  $m_F$  value at zero field with  $m_F = 2$  (—),  $m_F = 1$  (—),  $m_F = 0$  (—),  $m_F = -1$  (—),  $m_F = -2$  (—).

## Chapter 3

# SrF and cycling

This chapter details how we create and implement our quasi-cycling transition for SrF. We identify possible loss mechanisms in our quasi-cycling transition and estimate such losses. We also discuss the selection criteria that led us to choose SrF as our species of interest.

### 3.1 Quasi-cycling transition

The creation of a quasi-cycling transition merely requires that all loss mechanisms be addressed. The traditional obstacles to laser cooling a molecule are vibrational branching, characterized by the FCFs, and rotational branching, governed by parity and angular momentum selection rules. Unfortunately, our scheme to address these first two obstacles creates dark states, which must be remixed with the bright states to allow for cycling. Additionally, since SrF has resolved SR/HF structure in the electronic ground state, complications resulting from this structure must be addressed as well.

#### 3.1.1 Vibrational branching

Vibrational branching is addressed by choosing a molecule whose FCFs indicate that spontaneous decay to higher order vibrational levels in the ground electronic state should be well suppressed [87]. Residual vibrational branching can be addressed by a (hopefully) low number of repump lasers. The vibrational repumping scheme for SrF is shown in Figure 3.1. The main cycling laser drives the  $X^2\Sigma_{1/2}(v=0) \rightarrow A^2\Pi_{1/2}(v=0)$  transition at wavelength  $\lambda_{00} = 663.3$  nm. Approximately 98% of all decays from the  $A^2\Pi_{1/2}(v=0)$  state return population to the  $X^2\Sigma_{1/2}(v=0)$  state. However, there is a small probability of decay to the  $X^2\Sigma_{1/2}(v=1)$  state ( $\approx 2\%$ ) and an even smaller

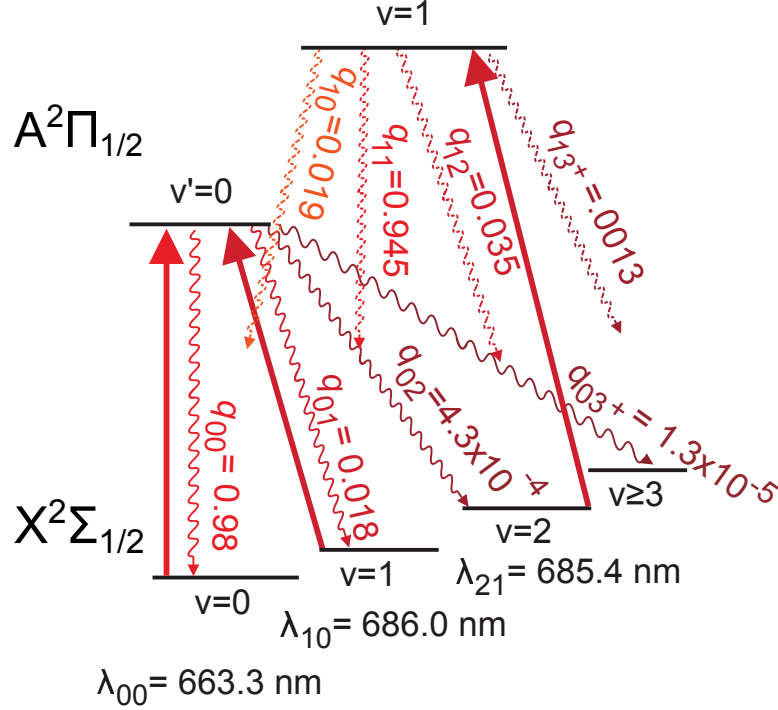


Figure 3.1: Vibrational branching is suppressed in SrF due to the highly diagonal FCFs. Solid upward lines indicate laser-driven transitions in the experiment at wavelengths  $\lambda_{v,v'}$ . Solid wavy lines indicate spontaneous decays from the  $A(v=0)$  state with calculated FCFs  $q_{0v}$  shown. Dashed wavy lines indicate spontaneous decays from the  $A(v=1)$  state populated by the second vibrational repump laser, with calculated FCFs  $q_{1v}$  as shown. Calculated values of the vibrational branching ratios are given in Table 2.13.

probability of decay to the  $X^2\Sigma_{1/2}(v=2)$  state ( $\approx .04\%$ ). Decays to the  $X^2\Sigma_{1/2}(v \geq 3)$  state from the  $A^2\Pi_{1/2}(v=0)$  state occur with probability  $\approx 10^{-5}$ . Calculated values of the vibrational branching ratios are given in Table 2.13. Population accumulating in the  $X^2\Sigma_{1/2}(v=1)$  state is returned directly to the cycling transition by driving the  $X^2\Sigma_{1/2}(v=1) \rightarrow A^2\Pi_{1/2}(v=0)$  transition at wavelength  $\lambda_{10} = 686.0$  nm. Meanwhile, population in the  $v=2$  state is returned indirectly to the main cycling transition by driving the  $X^2\Sigma_{1/2}(v=2) \rightarrow A^2\Pi_{1/2}(v=1)$  transition at  $\lambda_{21} = 685.4$  nm.<sup>1</sup> Molecules decaying to the  $X(v \geq 3)$  state are not returned to the cycling transition and are lost.

<sup>1</sup>The repumping of the  $X^2\Sigma_{1/2}(v=2)$  state through the  $A^2\Pi_{1/2}(v=1)$  state exhibits a number of benefits versus repumping directly to the  $A^2\Pi_{1/2}(v=0)$  state. First, 685 nm diode technology is more developed than that at  $\lambda_{20} \approx 709$  nm, corresponding to the wavelength of the  $X^2\Sigma_{1/2}(v=2) \rightarrow A^2\Pi_{1/2}(v=0)$  transition. Tapered amplifiers exist at 685 nm but not at 709 nm. Second, the power required for the  $\lambda_{21}$  laser is expected to be small compared to that which would be required for a  $\lambda_{20}$  repump laser. The low power requirement results from the fact that the partial linewidth to excite from the  $X^2\Sigma_{1/2}(v=2)$  state to the  $A^2\Pi_{1/2}(v=1)$  state is  $\sim 50\times$  the partial linewidth through which the  $A^2\Pi_{1/2}(v=0)$  state decays into the  $X^2\Sigma_{1/2}(v=2)$  state. Consequently, we find that the  $\lambda_{21}$  laser requires  $\sim 50\times$  less power than either the  $\lambda_{00}$  or  $\lambda_{10}$  lasers. Third, and perhaps most importantly, because the  $\lambda_{21}$  laser does not excite molecules to the  $A^2\Pi_{1/2}(v=0)$  state, there is no possibility of coherent transfer of population to the  $X^2\Sigma_{1/2}(v=2)$  state nor the possibility of coherent dark states between the  $X^2\Sigma_{1/2}(v=2)$  and  $X^2\Sigma_{1/2}(v=0,1)$  states.

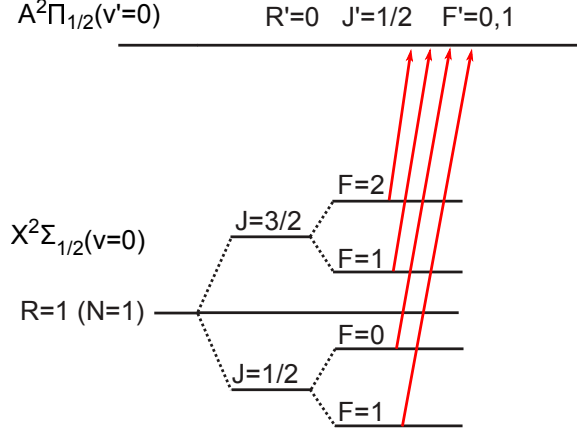


Figure 3.2: Rotational branching is eliminated by driving an  $R = 1 \rightarrow R' = 0$  transition. From the  $A^2\Pi_{1/2}(J = 1/2)$  state, angular momentum and parity selection rules allow decays only back to the  $X^2\Sigma_{1/2}(N = 1)$  state.

### 3.1.2 Rotational branching

In addition to vibrational branching, rotational branching must be eliminated or suppressed as well. In contrast to vibrational branching however, rotational branching for dipole transitions follows strict parity and angular momentum selection rules. Specifically, electric dipole transitions must obey

$$\pi_f = -\pi_i, \quad (3.1)$$

where  $\pi_f$  and  $\pi_i$  are the parity of the initial and final states respectively. Similarly, electric dipole transitions must also obey the angular momentum selection rules

$$\Delta F = 0, \pm 1 \quad (3.2)$$

$$\Delta m_F = 0, \pm 1. \quad (3.3)$$

As pointed out by Stuhl *et al.* [88], rotational branching can be eliminated by choosing a ground state with  $R = 1$  and driving a transition to an excited electronic state where  $R' = 0$ .<sup>2</sup> Then, due to angular momentum and parity selection rules, molecules can only decay back to the  $R = 1$  level of the ground electronic state, thereby eliminating rotational branching. A diagram showing the closing of rotational branching for SrF is shown in Figure 3.2. Because rotational branching is

<sup>2</sup>In the ground  $X^2\Sigma_{1/2}$  state,  $R = N$  and the two quantum numbers can be (and unfortunately are) used interchangeably.

inherently limited by selection rules, other approaches could conceivably be implemented.<sup>3</sup>

### 3.1.3 Dark states

While typical laser cooling and MOTs for atoms operate on a  $F \rightarrow F' = F + 1$  transition, the use of an  $R = 1 \rightarrow R' = 0$  type transition has certain drawbacks, one of which is the creation of dark states.<sup>4</sup> Ignoring SR/HF structure, the main cycling transition reduces to a 3+1 system (3 ground states, 1 excited state). For any given laser polarization, 2/3 of the ground-state sublevels will be dark at any given time. In the absence of a remixing mechanism, population will accumulate in these dark states and cycling will cease.

Dark states can be classified as either stationary or non-stationary depending on whether they evolve in time. Molecules accumulating in stationary dark states will remain there indefinitely. In contrast, molecules initially deposited in a non-stationary dark state will precess between linear superpositions of bright and dark states.

#### 3.1.3.1 Coherent dark states

In a  $\Lambda$ -type system, two ground states may be connected with the appropriate resonant laser frequencies and polarizations to a single excited state. Each ground state individually is bright, and each produces a contribution to the excited state population. However, there exists a particular superposition of these ground states where their contributions to the excited state population cancel, and the probability of exciting to the upper state goes to 0. Dark states produced through this type of interference are known as coherent dark states. Coherent dark states may be either stationary or non-stationary. In order to apply large spontaneous scattering forces, it is desirable that all dark states be non-stationary. It is further desirable that the precession of the non-stationary dark states occurs fast enough so that the precession does not limit the spontaneous scattering rate. However, precession rates approximately equal to or greater than the transition linewidth will broaden the total linewidth of the transition, thereby decreasing the spontaneous scattering rate. We have considered three approaches to remix the dark states with the bright states, all of which are discussed below [89]. As of this writing, have used a magnetic field as the primary remixing mechanism. Although coherent dark states are well characterized for simple systems, research into the pros and cons of different experimental methods for destabilizing coherent dark states in more complicated

---

<sup>3</sup>It is conceivable to laser cool a molecule on an  $R \rightarrow R' = R + 1$  transition [105]. However decays will then populate the  $R'' = R + 2$  rotational state, requiring an additional laser for each vibrational level.

<sup>4</sup>In this work, dark states refer to quantum states in which stimulated absorption of an photon is not possible.

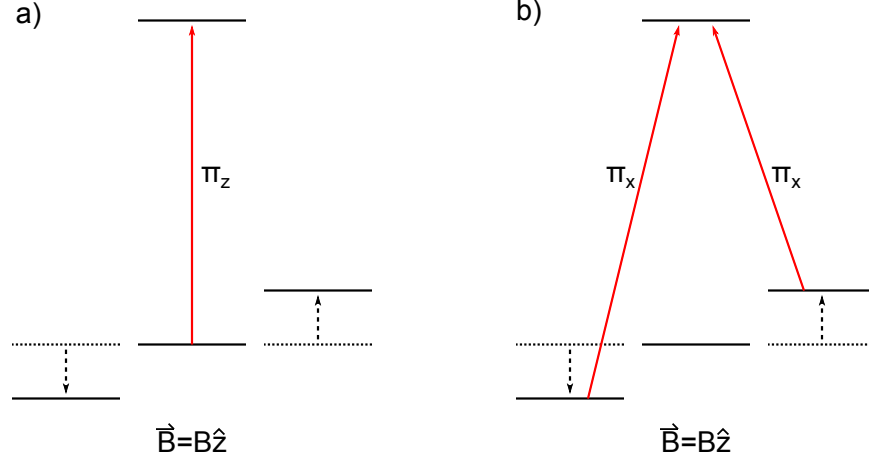


Figure 3.3: Dark state sublevels in a 3+1 system. Dark states are easily illustrated in the Zeeman basis. If the laser polarization and magnetic field are aligned as shown in (a), the  $m_F = \pm 1$  states are stationary dark states. If the laser polarization and magnetic field are orthogonal as shown in (b), the  $m_F = 0$  state is a stationary dark state while a linear combination of the  $m_F = \pm 1$  sublevels is a coherent dark state. The coherent dark state will evolve in time however, and thus is less damaging to cycling than the stationary dark state of  $m_F = 0$ .

systems remains a topic of current interest [89, 118, 119].

### 3.1.3.2 Mechanisms for remixing dark states

#### Magnetic field remixing

Application of a magnetic field with magnitude  $B_0$  at angle  $\theta_B$  relative to the laser polarization will cause Larmor precession of the ground-state Zeeman sublevels. This precession will act to mix the bright states with the dark states so that all molecules will spend some fraction of the total time in the bright states. Precession of the dark states into the bright states will occur at angular frequency

$$\omega_B = \mu_B g_F m_F B_{0\perp} \quad (3.4)$$

where  $\mu_B$  is the Bohr magneton,  $g_F$  is the g-factor of the state of interest with quantum number  $m_F$ , and  $B_{0\perp} = B_0 \sin \theta_B$ . For maximum spontaneous photon scattering, it is desirable that  $\omega_B \sim \Gamma$ . However, there are restrictions on  $\theta_B$ . If  $\theta_B = 0$  or  $\theta_B = \pi/2$ , stationary Zeeman dark states will exist, and the spontaneous scattering will cease (or, in a real experiment, likely be vastly reduced), as shown in Figure 3.3. Berkeland *et al.* [89] predict  $\theta_B \approx 60^\circ$  to be optimal for remixing dark states in a system similar to ours.

#### Microwave remixing

Alternatively, microwave radiation can be applied between the  $X^2\Sigma_{1/2}(N = 1)$  levels and the

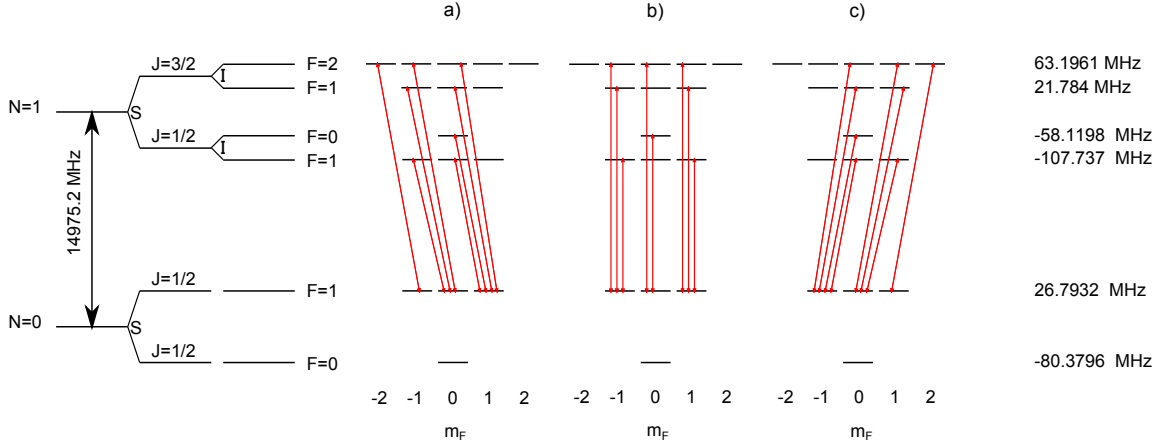


Figure 3.4: Microwave remixing would require rapidly switching the polarization of microwaves tuned between the  $X^2\Sigma_{1/2}(N=0, F=1)$  sublevels and all the  $X^2\Sigma_{1/2}(N=1)$  sublevels. The necessary transitions are shown for microwaves with  $\sigma^-$  (a),  $\pi_z$  (b), or  $\sigma^+$  (c) polarization.

$X^2\Sigma_{1/2}(N=0, F=1)$  levels to remix the dark Zeeman sublevels. This would likely require switching the microwave polarization at a rate  $\sim \Gamma$ . Unfortunately, by introducing additional ground-state sublevels, microwave remixing would likely reduce the maximum scattering rate. However, microwave remixing would have the added benefit that all laser power could be concentrated on the strongest transition from the four SR/HF manifolds to the excited state. If the microwave remixing also includes the  $X^2\Sigma_{1/2}(N=0, F=0)$  level, molecules decaying to states of the opposite parity (a loss mechanism which is discussed below; see [section 3.5](#)) could easily be returned to the cycling transition.<sup>5</sup> A schematic for microwave remixing is shown in [Figure 3.4](#).

### Polarization remixing

Dark Zeeman sublevels can also be remixing by rapidly switching the laser polarization at rate  $\sim \Gamma$  [89, 119]. This approach is employed by Hummon *et al.* to laser cool YO [120].

#### 3.1.4 Addressing spin-rotational and hyperfine structure

As discussed in [chapter 2](#), the SR/HF structure is well resolved in the ground state of the cycling transition. When employing magnetic remixing of the dark Zeeman sublevels, each of the four SR/HF manifolds must be addressed via resonant laser light. Using an electro-optic modulator (EOM) with a modulation frequency of  $f_{mod} \approx 42$  MHz and a modulation depth of  $M_{mod} = 2.63$  radians produces a frequency spectrum that approximately matches the spacing of the four SR/HF

<sup>5</sup>This approach is expected to require a laser to optically excite molecules out of the  $X^2\Sigma_{1/2}(N=2)$  state via the  $A^2\Pi_{1/2}(J=1/2^-)$  state.

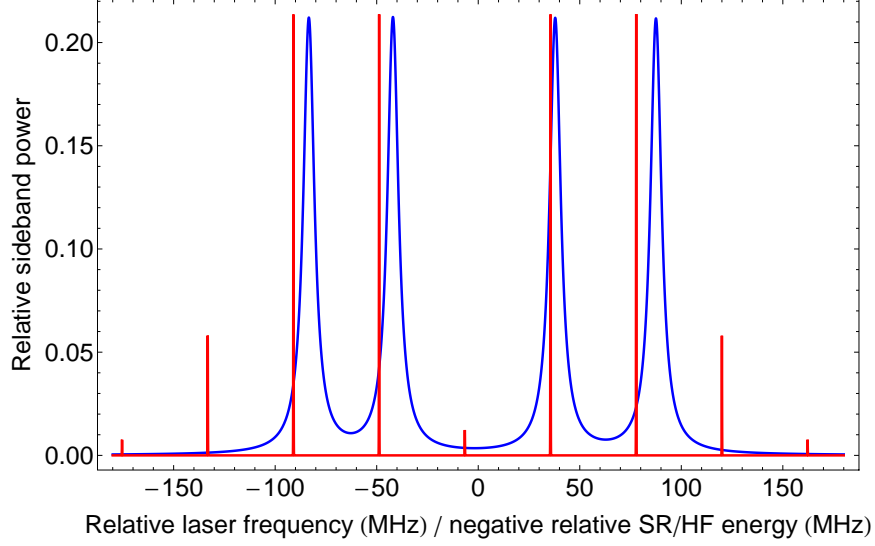


Figure 3.5: Matching SrF SR/HF structure with EOM sidebands from a single laser. Each SR/HF manifold (—) is depicted as a Lorentzian lineshape with a FWHM of  $\frac{\Gamma}{2\pi} = 6.6$  MHz, which should be observed in the limit of low excitation power. The SR/HF levels (in order of decreasing energy) from left to right are  $|N=1, J=3/2, F=2\rangle$ ,  $|N=1, J=3/2, F=1\rangle$ ,  $|N=1, J=1/2, F=0\rangle$ , and  $|N=1, J=1/2, F=1\rangle$ . The EOM sideband profile (—) is simulated for modulation frequency  $f_{\text{mod}} = 42.2$  MHz and modulation depth  $M_{\text{mod}} = 2.63$  radians and is detuned to the red so that the average of the detunings from each SR/HF manifold is equal to  $\frac{\Gamma}{2\pi}$ . (This is approximately the laser frequency profile used in Doppler cooling of SrF.) Using  $f_{\text{mod}} = 42.2$  MHz minimizes the RMS variation of the detuning from each SR/HF manifold. If instead we minimize the RMS variation of the detuning from all 12 SR/HF levels (i.e. we take the degeneracy of the four SR/HF manifolds into account), we find  $f_{\text{mod}} = 42.5$  MHz. With a modulation depth of  $M_{\text{mod}} = 2.63$  radians, approximately 85% of the total laser power resides in the four large sidebands used to address the four SR/HF manifolds.

levels as shown in Fig. 3.5. This avoids using acousto-optic modulators (AOMs) to individually hit all four resonances.<sup>6</sup>

<sup>6</sup>AOMs are chiefly undesirable because the diffracted beam is spatially separated from the fundamental. If the final beam must contain only a single polarization, as is necessary for seeding a tapered amplifier or slave laser, the combination of the fundamental and diffracted beam must be done using a 50/50 beamsplitter, resulting in wasted laser power and extra alignment hassle. However, AOMs do allow for arbitrary distribution of laser power over arbitrary frequencies (although each frequency requires a separate AOM), which is sometimes advantageous.



## 3.2 Simplified models of our system

Incorporating the complexity of our full system makes many calculations undesirably difficult. Hence, it is sometimes useful to employ models of our system in the limit of certain simplifications (e.g., SR structure, HF structure, or higher vibrational levels are ignored) as shown in Fig. 3.6. We refer to different models by listing the number of degeneracies in each resolved ground-state manifold, followed by a “+”, followed by the number of degeneracies in each resolved excited state manifold. States are always listed in order of increasing energy. If we ignore all  $v > 0$  levels and all SR/HF structure, our system reduces to a 3+1 level system as shown in Fig. 3.6a. By symmetry, the branching ratio from the single excited state to each of the three ground states is  $1/3$ . If we include SR structure (but not HF structure) and continue to ignore  $v > 0$  states, we have a (2,4)+2 level system as shown in Fig. 3.6b. The branching ratios to the  $J = 1/2, 3/2$  manifolds in the ground state shown in Fig. 3.6 are obtained by computing Table 2.15 with the HF structure coefficients  $b, c, C$  set to zero and then summing the branching ratios to the  $J = 1/2$  and  $J = 3/2$  manifolds. We find that decays to  $J = 1/2$  are twice as likely as decays to  $J = 3/2$ . Decays within each  $J$  manifold are then determined by Clebsch-Gordan coefficients. The full system (with SR/HF structure) excluding states with  $v > 0$  is shown in Fig. 3.6c and branching ratios are given in Table 2.15. To model the interplay and possible coherent dark states between the  $X(v = 0, N = 1)$  and  $X(v = 1, N = 1)$  states, we employ a (3,3)+1 system as shown in Fig. 3.6d. The total branching ratios for the (3,3)+1 system are obtained by combining the vibrational branching ratios in Table 2.13 and the symmetry arguments presented for the 3+1 system above. This model for the interplay between the  $X(v = 0, N = 1)$  and  $X(v = 1, N = 1)$  states may be extended to include SR/HF structure as well, but this is not shown.

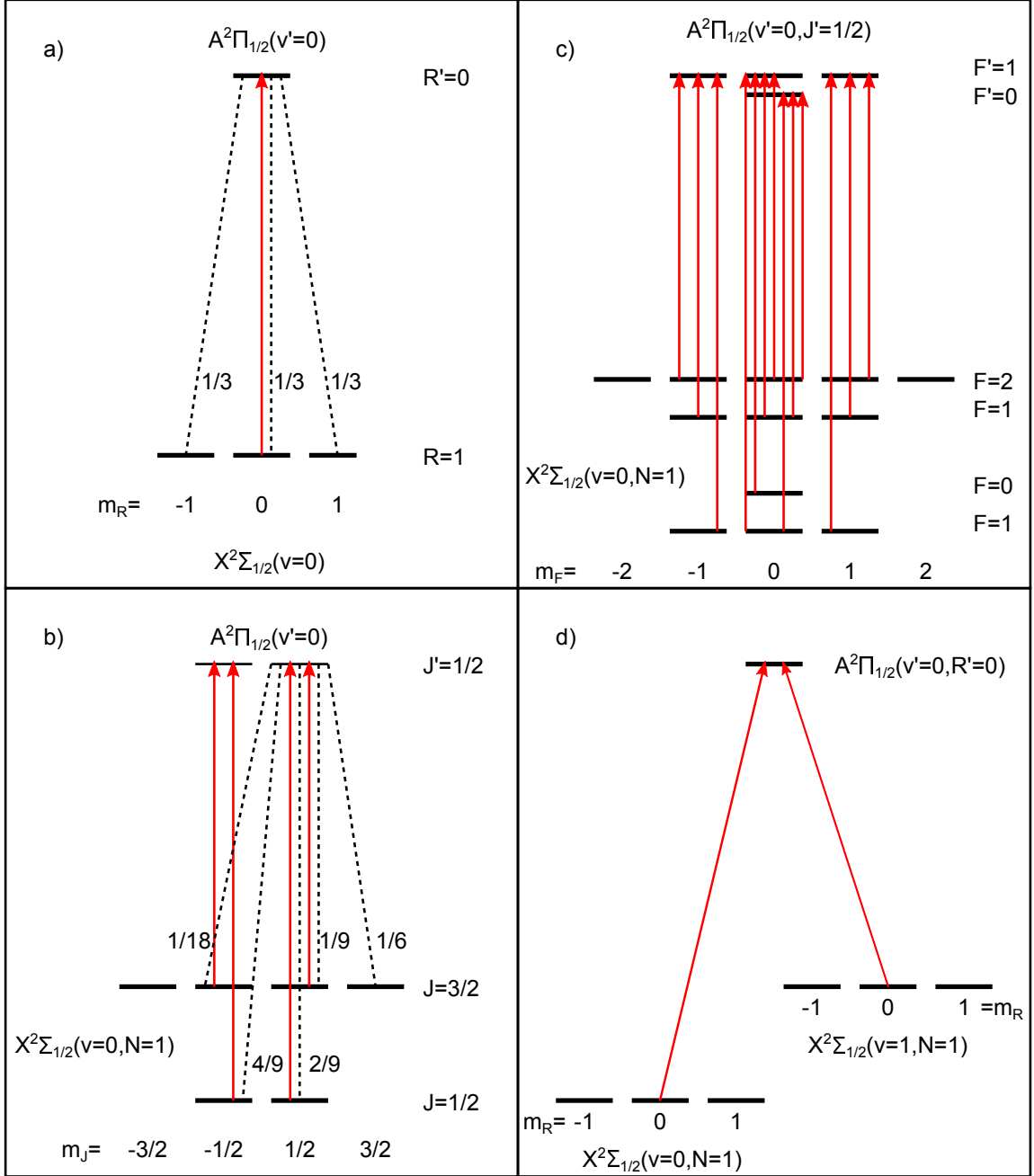


Figure 3.6: Simplified models of our system as discussed in the main text. (a) Ignoring SR/HF structure and all  $v > 0$  levels, our system reduces to a 3+1 system. (b) Ignoring all HF structure and all  $v > 0$  levels, our system reduces to a (2,4)+2 system. (c) The full level structure for our system ignoring all  $v > 0$  levels. (d) Ignoring all SR/HF structure and all  $v > 1$  levels, our system reduces to a (3,3)+1 system. Optical excitation is shown for linearly polarized light (—) for each system and branching ratios (---) are labeled. The branching ratios for (c) are given in Table 2.15 while the branching ratios for (d) can be derived by combining the (angular) branching ratios from (a) with the vibrational branching ratios given in Table 2.13.

### 3.3 Absorption cross section, saturation intensity, etc.

To maximize spontaneous scattering forces it is desirable to maximize the fraction of molecules in the excited state, denoted  $n_e$ .<sup>7</sup> The value of  $n_e$  depends on the intensity, polarization and frequency distribution of the laser light applied to the molecules as well as the strength and orientation of the magnetic field. Of the five parameters listed, the latter four can be varied to almost any arbitrary value (with little or modest experimental effort) necessary to maximize  $n_e$ . However, the laser intensity is limited by the total laser power available and the area over which the laser power must be applied. The maximum laser power is limited by current technology while the latter is generally dictated by the spatial extent of the molecules and is thus fairly inflexible (or rather, applying the same intensity over a smaller area means addressing fewer molecules). For our experiment we wish to answer the following three questions:

- How do our laser intensity requirements compare to that of a two-level system?
- Are the laser intensity requirements for the  $\lambda_{00}$  and  $\lambda_{10}$  lasers approximately the same?
- What is the optimal distribution of laser intensity across the constituent frequencies needed to address the four SR/HF manifolds?

Unfortunately, accurate modeling of our system likely requires solving the optical Bloch equations (OBEs) for the full  $12+12+4=28$  level system<sup>8</sup> involving at least 8 distinct laser frequencies and associated detunings, as well as a magnetic field with magnitude and direction. Use of the OBEs (rather than the multilevel rate equations [121]) is necessary to include the important effects of coherent dark states and their evolution, non-zero laser linewidths, cross-excitation,<sup>9</sup> power broadening, and magnetic field broadening. Unfortunately, solving the OBEs for a system with  $N_{\text{tot}}$  levels involves solving  $N_{\text{tot}}^2$  linear equations for  $N_{\text{tot}}^2$  variables. We have so far been unable to solve the OBEs for our fully system analytically, although a closed-form solution for the steady-state case may be possible [122]. While numerical solutions are valid for a given set of parameters (that is, values of detunings and intensity distribution of the  $\gtrsim 8$  laser frequencies, magnetic field magnitude and direction, etc.), this approach has two drawbacks. First, solving the OBEs numerically for a given set of parameters provides little understanding of the behavior of the system for another set

<sup>7</sup>When there are multiple excited states  $j$  each with population fraction  $n_j$ , we take  $n_e = \sum_j n_j$ .

<sup>8</sup>We neglect leakage to any states outside this system.

<sup>9</sup>Here, cross-excitation refers to non-resonant excitation of a given state by a laser frequency which resonantly addresses a different state.

of parameter values. Since the phase space is very large and there is large interplay between parameters, we achieve little insight into the optimal parameter values. Second, without the ability to easily see how the solutions vary over a range of parameter values (as would be provided by an analytical solution), it becomes hard to check for mistakes in such a complicated system.

Our approach therefore is twofold. First, we employ multilevel rate equations (MLREs) [121] which treat our system semi-classically. Second, we solve the OBEs for our system under certain simplifications (i.e. HF structure is ignored or all  $v = 1$  levels are ignored, etc.). We discuss background necessary for both calculations before presenting results from either the MLRE approach or the OBE approach.

Answering the above questions was, for us, one of the most confusing theoretical problems encountered during this dissertation work. We eventually realized that the entire system, including all lasers, must be treated as a whole. As the entire system is coupled together, examining only subsets of the system individually can give misleading results.<sup>10</sup> For example, the  $\lambda_{00}$  laser intensity necessary to achieve a given value of  $n_e$  depends on the  $\lambda_{10}$  laser intensity. Also, the use of the OBEs is essential to gain some intuition about the system and to guide the application of the MLREs. We find it more productive to focus our models on the degeneracies of the states (i.e. that ignoring SR/HF structure we have a (3,3)+1 system), rather than take a laser-centric viewpoint (i.e. for the  $\lambda_{00}$  transitions we need four laser frequencies so we should treat the system as a 4+1 system); treating the system from a laser-centric viewpoint can again give misleading results.

### 3.3.1 Rabi frequency

The Rabi frequency of a transition between ground state  $i$  and excited state  $j$ , when driven by resonant light of the correct polarization to excite  $i$  to  $j$ , is given by Ref. [123] Eqn. 2.86 to be

$$\Omega_{ij} = E_0 d_{ij} / \hbar, \quad (3.5)$$

where the electric field from the laser is  $\mathbf{E} = \mathbf{E}_0 \cos(\omega_L t)$  and  $d_{ij} = \langle i | -e\mathbf{r} | j \rangle$  is the electric dipole operator (where  $e$  is the absolute value of the electron charge and  $\mathbf{r}$  is the position operator).

There are many definitions of the Rabi frequency in the literature, but this one, used by Cohen-

---

<sup>10</sup>The analysis presented in Ref. [105] is not appropriate in the general case but is appropriate for their system: four open two-level systems which are coupled together through spontaneous decay and which all have the same dipole matrix element for excitation. I suspect their approach would fail for a system where either all the matrix elements of the driven transitions are not the same or where the entire system does not consist of a number of identical two-level systems coupled together through spontaneous decay.

Tannoudji [123], is chosen because it is the real oscillation frequency of the population (assuming the rotating wave approximation (RWA) is made). After the RWA is made, only half the total light acts resonantly on the transition, and for a two-level system each of the two off-diagonal matrix elements of the Hamiltonian corresponding to coherences between  $i$  and  $j$  will have the value  $\Omega_{ij}/2$ .

The resonant absorption cross section for the same transition is given by

$$\sigma_{ij}^0 = 3 \frac{\lambda^2}{2\pi} \frac{\Gamma_{ji}}{\gamma_j}, \quad (3.6)$$

where  $\Gamma_{ji}$  is the partial width of the transition from excited state  $j$  to ground state  $i$  in angular frequency units,  $\gamma_j$  is the total linewidth of the transition (including power broadening, pressure broadening, etc.) in angular frequency units,  $\lambda$  is the wavelength of the resonant light, and the superscript 0 indicates resonant excitation. There are many statements of Eqn. 3.6 in the literature, but all forms can be shown to be equivalent, as demonstrated in Appendix B of Ref. [92].

The total spontaneous emission rate of an excited state  $j$  is given by Ref. [123] Eqn. 6.119 to be

$$\Gamma_j = \frac{1}{3\pi\epsilon_0\hbar c^3} \sum_k \omega_{jk}^3 d_{jk}^2, \quad (3.7)$$

in SI units where the sum runs over all final states  $k$  to which  $j$  may decay. The spontaneous emission rate from excited state  $j$  to a specific ground state  $i$  is then given by

$$\Gamma_{ji} = \frac{1}{3\pi\epsilon_0\hbar c^3} \omega_{ji}^3 d_{ji}^2, \quad (3.8)$$

in SI units. Substitution of Eqn. 3.8 into Eqn. 3.6 yields another useful form of the resonant absorption cross section

$$\sigma_{ij}^0 = \frac{2}{\hbar c \epsilon_0} \frac{\omega_{ji}}{\gamma_j} d_{ij}^2, \quad (3.9)$$

in SI units. If resonant light with photon flux  $\Phi_{ij}$  is applied between states  $i$  to  $j$ , particles will undergo stimulated absorption and stimulated emission at rate

$$R_{ij} = \Phi_{ij} \sigma_{ij}. \quad (3.10)$$

Since laser intensity is given by  $I = \frac{1}{2} \epsilon_0 c E_0^2$  and  $I = \Phi \times \hbar \omega$ , we can rewrite 3.10 using Eqns. 3.5

and 3.9 as

$$R_{ij} = \frac{\Omega_{ij}^2}{\gamma_j}. \quad (3.11)$$

Eqns. 3.5–3.11 are exact and make no approximations or assumptions.

### 3.3.2 Absorption cross section without broadening

In the absence of any broadening mechanisms (time-of-flight broadening, Doppler broadening, power broadening, etc.), we have  $\gamma_j = \Gamma_j$ . Under these conditions, Eqn. 3.6 can be rewritten using Eqns. 3.7 and 3.8 to be

$$\sigma_{ij}^0 = 3 \frac{\lambda^2}{2\pi} \frac{\omega_{ji}^3 d_{ji}^2}{\sum_k \omega_{jk}^3 d_{jk}^2}. \quad (3.12)$$

If  $\omega_{ji} = \omega_{jk}$  for all decays from  $j$ , Eqn. 3.12 can be rewritten as

$$\sigma_{ij}^0 = 3 \frac{\lambda^2}{2\pi} \frac{d_{ji}^2}{\sum_k d_{jk}^2}. \quad (3.13)$$

This form (under the given assumptions) is particularly useful because the last fraction may be replaced by the branching ratios from the excited state  $j$ . Unlike dipole matrix elements, branching ratios are invariant under different systems of units (e.g. cgs vs. SI) and can be checked to sum to 1. Eqn. 3.13 may disagree by factors of order unity with other similar-looking forms for the absorption cross section presented in some textbooks. The discrepancy is almost always due to some set of assumptions regarding the incident light polarization or the population distribution over the degenerate states (and averaging over these states).

If the excitation laser is detuned by  $\Delta \equiv \omega_L - \omega_{ij}$ , Eqn. 3.6 is modified, and the result is given by Ref. [123] Eqn. 2A.51 to be

$$\sigma_{ij}(\Delta) = \sigma_{ij}^0 \times \frac{\Gamma^2/4}{\Delta^2 + \Gamma^2/4}, \quad (3.14)$$

where  $\sigma_{ij}$  may be replaced by Eqn. 3.6 or 3.9 in all cases, or by Eqn. 3.12 or 3.13 if the assumptions given for those formulas are fulfilled.

### 3.3.3 Multilevel rate equations

For a system with  $N_g$  ground states and  $N_e$  excited states where population is transferred between states by time-independent continuous wave (CW) radiation,<sup>11</sup> the fraction of excited state molecules, denoted  $n_e$ , must obey

$$n_e < n_e^{\max} < 1, \quad (3.15)$$

where  $n_e^{\max}$  is the maximum value of  $n_e$ . For systems with spontaneous decay, achieving  $n_e = n_e^{\max}$  under the given assumptions requires infinite laser power. Instead, it is more useful to consider what photon flux  $\Phi$  is required to achieve  $n_e = \frac{1}{2}n_e^{\max}$ , which we denote  $\Phi^{3\text{dB}}$ . The quantity  $\Phi^{3\text{dB}}$  is used as a metric because below this value  $n_e$  increases approximately linearly with  $\Phi$ , while increasing  $\Phi$  in excess of  $\Phi^{3\text{dB}}$  will increase  $n_e$  only marginally and always by less than a factor of two. To gain a qualitative understanding of the power requirements of our system, we employ the MLRE approach. The evolution of all excited states  $j$  and all ground states  $i$  is modeled by

$$\begin{aligned} \frac{\partial n_i}{\partial t} &= \sum_j \Gamma_{ij} n_j - \sum_j R_{ij} (n_i - n_j) - \sum_{k \neq i} M_{ik} (n_i - n_k) \\ \frac{\partial n_j}{\partial t} &= - \sum_i \Gamma_{ij} n_j + \sum_i R_{ij} (n_i - n_j), \end{aligned} \quad (3.16)$$

where  $n_{i(j)}$  is the population fraction in state  $i(j)$ ,  $M_{ik}$  is the remixing rate between ground state  $i$  and ground state  $k$  and the corresponding summation runs over  $k \neq i$ . In the limit of no remixing,  $M_{ik} = 0$ . We do not consider the remixing in the  $n_j$  states because this is not expected to occur in SrF.<sup>12</sup> It is important to understand that the MLREs inherently neglect magnetic field broadening, power broadening, cross-excitation, and coherent dark states. We now work through a simple example.

### 3.3.4 Multilevel rate equation example

We examine the case of a single excited state  $j$  and  $N_g$  ground states  $i$ , and roughly follow the derivation presented in Ref. [124]. For this example, we assume  $M_{ik} = 0$ . The population fractions obey

$$n_j + \sum_{i=1}^{N_g} n_i = 1, \quad (3.17)$$

<sup>11</sup>i.e. no  $\pi$  pulses, stimulated raman adiabatic passage (STIRAP), etc.

<sup>12</sup>The  $A^2\Pi_{1/2}$  state of SrF has no magnetic moment. (See [section 2.10](#).)

and Eqn. 3.16 dictates that the population fractions  $n_i$  will evolve according to

$$\frac{\partial n_i}{\partial t} = \Gamma_{ji}n_j - R_{ij}(n_i - n_j), \quad (3.18)$$

which can be rewritten using Eqn. 3.10 and the property  $\Gamma_{ji}/\sigma_{ij} = \Gamma_j/\sigma_j^{\text{tot}}$  (where  $\sigma_j^{\text{tot}} = \sum_i \sigma_{ij}$ ) as

$$\frac{\partial n_i}{\partial t} = \sigma_{ij} \left[ \frac{\Gamma_j}{\sigma_j^{\text{tot}}} n_j - \Phi_{ij}(n_i - n_j) \right]. \quad (3.19)$$

In the steady state,  $\frac{\partial n_i}{\partial t} = 0$ , and Eqn. 3.19 must be satisfied for all choices of  $i$  and  $j$ . For  $\sigma_{ij} \neq 0$ , this requires

$$0 = \left[ \frac{\Gamma_j}{\sigma_j^{\text{tot}}} n_j - \Phi_{ij}(n_i - n_j) \right]. \quad (3.20)$$

Rearranging gives

$$n_i = \left[ 1 + \frac{\Gamma_j}{\sigma_j^{\text{tot}} \Phi_{ij}} \right] n_j. \quad (3.21)$$

Combining Eqn. 3.21 with Eqn. 3.17 and eliminating all  $n_i$  allows us to write

$$n_j = \frac{1}{1 + \sum_i^{N_g} \left[ 1 + \frac{\Gamma_j}{\sigma_j^{\text{tot}} \Phi_{ij}} \right]} \quad (3.22)$$

$$= \frac{1}{1 + N_g + \frac{\Gamma_j}{\sigma_j^{\text{tot}}} \sum_i^{N_g} \left[ \frac{1}{\Phi_{ij}} \right]}, \quad (3.23)$$

which shows that the value of  $n_j$  depends on  $\Gamma_j$ ,  $\sigma_j^{\text{tot}}$  and  $\Phi_{ij}$  but notably *not* on  $\sigma_{ij}$ . To model the constraint of limited available laser power, we set the total laser photon flux to a constant, i.e.  $\sum_i \Phi_{ij} = \Phi_j^{\text{tot}}$ . Then Eqn. 3.23 shows that maximum  $n_j$  will result from distributing the laser power evenly over all  $N_g$  ground states, i.e.  $\Phi_{ij} = \Phi_j^{\text{tot}}/N_g$  for  $i = 1, 2, \dots, N_g$ , where  $\Phi_j^{\text{tot}}$  is the total photon flux available. It is perhaps surprising that the optimal distribution of  $\Phi_j^{\text{tot}}$  over the different  $\Phi_{ij}$  is independent of  $\sigma_{ij}$ . With respect to SrF, Eqn. 3.23 suggests that the lasers repumping SR/HF levels in the  $X^2\Sigma_{1/2}(v=1)$  state should have the same intensity as the cycling lasers that drive the SR/HF levels in the  $X^2\Sigma_{1/2}(v=0)$  state. By substituting  $\Phi_{ij} = \Phi_j^{\text{tot}}/N_g$  into Eqn. 3.23, we can write the excited state population as

$$n_j = \frac{1}{1 + N_g + \frac{N_g \Gamma_j}{\sigma_j^{\text{tot}} \Phi_j^{\text{tot}}}}. \quad (3.24)$$



From the above equation, we recover that, for infinite photon flux,  $n_j^{\max} = \frac{1}{1+N_g}$ . Similarly, we note that

$$n_j = \frac{n_j^{\max}}{2} \quad \text{when} \quad \Phi_j^{\text{tot}} \equiv \frac{\Gamma_j}{\sigma_j^{\text{tot}}} \left[ \frac{N_g^2}{N_g + 1} \right], \quad (3.25)$$

for this system. This means that the photon flux required to achieve half the maximum spontaneous scattering rate grows with the number of ground states  $N_g$ ; in the limit of  $N_g \gg 1$ , the growth is roughly linear in  $N_g$ . Since it is optimal that  $\Phi_{ij} = \Phi_j^{\text{tot}}/N_g$ , we also have that

$$\Phi_{ij}^{\text{3dB}} \equiv \frac{\Gamma_j}{\sigma_j^{\text{tot}}} \left[ \frac{N_g}{N_g + 1} \right], \quad (3.26)$$

for the photon flux which addresses each ground-state sublevel  $i$ .

In this simple example with  $N_e = 1$  and arbitrary  $N_g$ , we note that  $n_e^{\max}$  obeys

$$n_e^{\max} = \frac{N_e}{N_e + N_g}. \quad (3.27)$$

The above relation is at least approximately true for most systems [124] and holds exactly if  $N_e = 1$  as we have shown. Deviation from Eqn. 3.27 for systems illuminated with CW radiation requires multiple excited states and can occur for systems with asymmetric branching ratios or systems composed of smaller “sub-systems” which are connected only by spontaneous decay.

### 3.3.5 Multilevel rate equations applied to SrF

As stated previously, the MLREs presented here ignore coherent dark states, power broadening, magnetic field broadening and cross-excitation. In this way the MLRE approach is expected to offer a best case scenario as to how much photon flux we require.<sup>13</sup> In the following three MLRE examples, we assume a single excited state  $j$  with decay rate  $\Gamma_j$ . For simplicity, all decay channels are assumed to have the same  $\lambda$ , and therefore from Eqn. 3.13 we have

$$\sigma_j^{\text{tot}} = \sum_i^{N_g} \sigma_{ij} = 3 \frac{\lambda^2}{2\pi}, \quad (3.28)$$

for the single excited state  $j$ .

---

<sup>13</sup>Allowing for cross-excitation might reduce the needed power, but this is likely a small correction as discussed later in this section.

### 3.3.5.1 1+1 system

For the simplest case of a 1+1 system, we consider the  $^{87}\text{Rb}$  stretched-state cycling transition shown in Fig. 3.7a. Solving the MLREs yields

$$\Phi_j^{\text{3dB}} = \frac{\Gamma_j}{2\sigma_j^{\text{tot}}}, \quad (3.29)$$

where we have substituted  $\sigma_j^{\text{tot}} = 3\frac{\lambda^2}{2\pi}$ , which is appropriate for the stretched-state pure 2-level cycling transition in  $^{87}\text{Rb}$ . Equation 3.29 is in agreement with Eqn. 3.25.

### 3.3.5.2 3+1 system

For SrF, the main cycling transition is realized on an  $R = 1 \rightarrow R' = 0$  transition. Ignoring the  $v \geq 1$  states and all SR/HF structure, our system reduces to a 3+1 system as shown in Fig 3.7b. In this system, 2/3 of the ground states are dark at any given time for any given laser polarization. We excite from a single ground-state sublevel to the single excited state and remix the dark ground-state sublevels. Because the total transition linewidth  $\Gamma_j$  is divided over the three ground-state sublevels, we have  $\sigma_{ij} = \sigma_j^{\text{tot}}/3 = \frac{\lambda^2}{2\pi}$  for  $i = 1, 2, 3$ , corresponding to each of the three  $m_R$  sublevels in the  $R = 1$  manifold. We solve the MLREs in the limit of infinitely fast remixing<sup>14</sup> (i.e  $M_{ik} \rightarrow \infty$ ) in the  $R = 1$  state and find

$$\Phi_j^{\text{tot,3dB}} = \frac{3}{4} \frac{\Gamma_j}{\sigma_j^{\text{tot}}/3}, \quad (3.30)$$

for the single bright state. Eqn. 3.30 exactly replicates the result of Eqn. 3.25 for a 3+1 system even though the two equations are derived in entirely different circumstances; the former optically excites from a single ground state to a single excited state and remixes all  $N_g$  ground-state sublevels, while the latter optically excites from each of the  $N_g$  ground-state sublevels and assumes no remixing.

### 3.3.5.3 (3,3)+1 system

We now examine adding the  $v = 1$  state (driven by the  $\lambda_{10}$  laser), which gives us the (3,3)+1 system shown in Fig. 3.7c. We define the branching ratio from the single excited state  $j$  to the  $v = 0$  ground state as  $A_g$  and to the  $v = 1$  ground state as  $1 - A_g$ . The absorption cross sections are  $\sigma_{v=0} =$

<sup>14</sup>Although the limiting case of infinitely fast remixing does not correspond to an experimental reality, using this limit allows remixing effects to be included in the simple MLRE model with only a minimal increase in complexity. Since this section focuses on laser intensity requirements, the assumption of infinitely fast remixing will ensure that  $n_e$  is limited by laser intensity and not remixing.

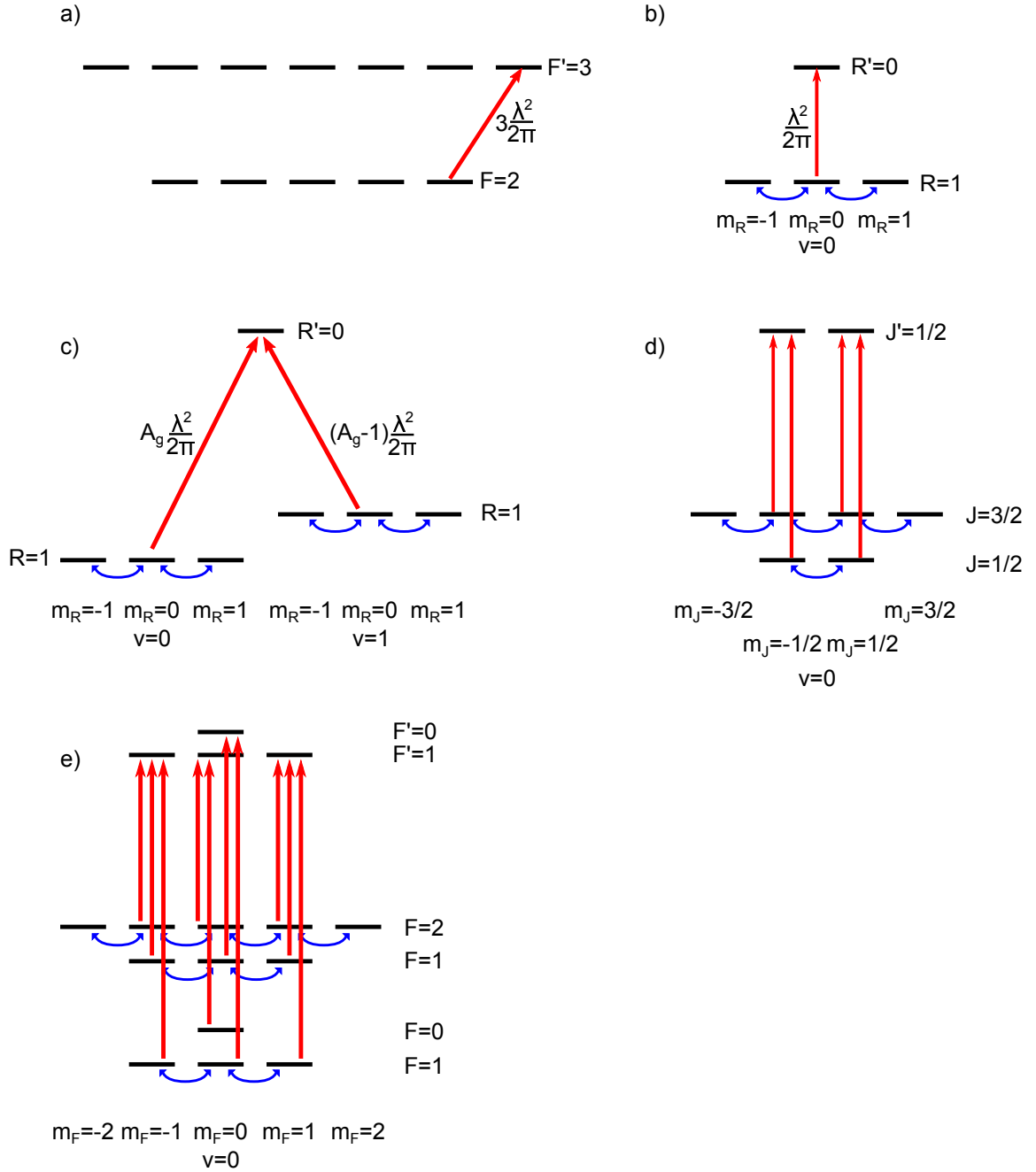


Figure 3.7: Models for determining required laser intensity. (a) A typical cycling transition for a MOT employs a  $F \rightarrow F' = F + 1$  transition. (b) Ignoring SR/HF structure and all  $v > 0$  states, we can model our system as a 3+1 system. (c) If we include the  $v = 1$  state, we can model our system as a (3,3)+1 system. (d) Ignoring HF structure and all  $v > 0$  states, we can model our system as a (2,4)+2 system. (e) All SR/HF levels in the  $v = 0$  ground and excited states are shown. Optical excitations (—) and magnetic remixing (—) are as shown.

$A_g \sigma_j^{\text{tot}}/3 = A_g \frac{\lambda^2}{2\pi}$  for the bright state in the  $v = 0$  manifold and  $\sigma_{v=1} = (1 - A_g) \sigma_j^{\text{tot}}/3 = (1 - A_g) \frac{\lambda^2}{2\pi}$  for the bright state in the  $v = 1$  manifold. For brevity, the usual  $j$  subscript is omitted here when discussing cross sections or photon fluxes involving particular vibrational levels; this should not be problematic since there is only one excited state. Solving Eqns. 3.16, and assuming infinitely fast remixing between ground-state sublevels within the same vibrational state, gives

$$n_j = 1/\left[7 + 3 \frac{\Gamma_j}{\sigma_{v=0} + \sigma_{v=1}} \left[ \frac{1}{\Phi_{v=0}} + \frac{1}{\Phi_{v=1}} \right] \right] \quad (3.31)$$

$$= 1/\left[7 + 3 \frac{\Gamma_j}{\sigma_j^{\text{tot}}} \left[ \frac{1}{\Phi_{v=0}} + \frac{1}{\Phi_{v=1}} \right] \right], \quad (3.32)$$

where  $\Phi_{v=0}$  and  $\Phi_{v=1}$  are the photon fluxes for the bright  $v = 0$  and  $v = 1$  levels in the ground state, respectively. From Eqn. 3.31, we see that for a fixed total photon flux  $\Phi_j^{\text{tot}} = \Phi_{v=0} + \Phi_{v=1}$ , maximum  $n_j$  results when

$$\Phi_{v=0} = \Phi_{v=1} = \Phi_j^{\text{tot}}/2. \quad (3.33)$$

From Eqn. 3.31, we also observe that  $n_e^{\text{max}} = \frac{1}{7}$ . Achieving  $n_j = n_e^{\text{max}}/2$  yields

$$\Phi_j^{\text{tot,3dB}} = 2 \times \frac{6}{7} \frac{\Gamma_j}{\sigma_j^{\text{tot}}/3}, \quad (3.34)$$

so that we have

$$\Phi_{v=0}^{\text{3dB}} = \frac{6}{7} \frac{\Gamma_j}{\sigma_j^{\text{tot}}/3} \quad \text{and} \quad \Phi_{v=1}^{\text{3dB}} = \frac{6}{7} \frac{\Gamma_j}{\sigma_j^{\text{tot}}/3}. \quad (3.35)$$

The value of  $A_g$  does not appear in either Eqn. 3.33 or 3.35, showing that  $\Phi_j^{\text{tot,3dB}}$ ,  $\Phi_{v=0}^{\text{3dB}}$ , and  $\Phi_{v=1}^{\text{3dB}}$  do not depend on the distribution of the total transition strength over all the decay channels. The value of  $\Phi_j^{\text{tot,3dB}}$  in Eqn. 3.34 agrees with Eqn. 3.25, i.e. the value of

$$\Phi_j^{\text{tot,3dB}} = 2 \times \frac{6}{7} \frac{\Gamma_j}{\sigma_j^{\text{tot}}/3} \quad (3.36)$$

for this (3,3)+1 system is exactly the same as for the case of a 6+1 level system where all 6 ground-state sublevels are optically excited. This should not be surprising; in subsection 3.3.5.2 we find that optically exciting all  $N_g$  ground-state sublevels to a single excited state leads to the same value of  $\Phi_j^{\text{tot,3dB}}$  as optically exciting a single ground-state sublevel and remixing all the  $N_g$  ground-state sublevels together infinitely fast. Hence, it is reasonable that combinations of optical excitation and remixing of subsets of ground-state sublevels also lead to the same value of  $\Phi_j^{\text{tot,3dB}}$  if certain symmetry conditions are met. Based on the MLRE model and arguments here, we expect the  $\lambda_{00}$

and  $\lambda_{10}$  lasers to require the same photon flux to achieve  $n_e = n_e^{\max}/2$  in the full experimental system.

Comparison of  $\Phi_j^{\text{tot},3\text{dB}}$  for the 3+1 system (given by Eqn. 3.30) with  $\Phi_j^{\text{tot},3\text{dB}}$  for the (3,3)+1 system (given by Eqn. 3.34) suggests that the addition of the  $v = 1$  state to our model increases the total photon flux required to achieve  $n_e = n_e^{\max}/2$  by a correction factor

$$C_{\text{vib}} = \left(\frac{36}{7}\right)/\left(\frac{9}{4}\right) = \frac{16}{7}. \quad (3.37)$$

#### 3.3.5.4 (2,4)+2 system

Unfortunately, SR/HF structure is resolved in the ground states of the real SrF system. We model SR structure in the  $v = 0$  state using the (2,4)+2 system shown in Fig. 3.7d with angular branching ratios given in Fig. 3.6b, and we ignore HF structure. We apply linearly polarized laser light with photon fluxes  $\Phi_{J=1/2}$  and  $\Phi_{J=3/2}$ , which excite molecules from the  $|J = 1/2, m_J = \pm 1/2\rangle$  and  $|J = 3/2, m_J = \pm 1/2\rangle$  states, respectively. The absorption cross section is  $\sigma_{|\frac{1}{2}, \pm \frac{1}{2}\rangle} = \frac{2}{9}\sigma_j^{\text{tot}}$  for the  $|J = 1/2, m_J = \pm 1/2\rangle$  state and is  $\sigma_{|\frac{3}{2}, \pm \frac{1}{2}\rangle} = \frac{1}{9}\sigma_j^{\text{tot}}$  for the  $|J = 1/2, m_J = \pm 1/2\rangle$  state. We solve Eqns. 3.16 in the limit of infinite remixing between ground-state sublevels with the same value of  $J$  to get

$$n_e = 1/\left[4 + \frac{\Gamma_j}{\sigma_j^{\text{tot}}}\left[\frac{3}{\Phi_{J=1/2}} + \frac{6}{\Phi_{J=3/2}}\right]\right] \quad (3.38)$$

and observe that  $n_e^{\max} = \frac{1}{4}$  for this system, and hence, this system obeys Eqn. 3.27. Under the constraint  $\Phi_{J=1/2} + \Phi_{J=3/2} = \Phi^{\text{tot}}$ , we find  $n_e$  is maximized for

$$\Phi_{J=1/2} = (\sqrt{2} - 1)\Phi^{\text{tot}} \quad (3.39)$$

$$\Phi_{J=3/2} = (2 - \sqrt{2})\Phi^{\text{tot}}. \quad (3.40)$$

Given the optimum allocation of  $\Phi^{\text{tot}}$  above, we find that

$$\Phi^{\text{tot},3\text{dB}} = \frac{3}{4(3 - 2\sqrt{2})} \frac{\Gamma_j}{\sigma_j^{\text{tot}}} \approx 1.46 \frac{\Gamma_j}{\sigma_j^{\text{tot}}/3}, \quad (3.41)$$

which should be compared to Eqn. 3.30. Relative to the 3+1 system, the resolved SR structure of the (2,4)+2 system increases the total photon flux necessary to achieve  $n_e = n_e^{\max}/2$  by the correction factor

$$C_{\text{SR}} \approx (1.46 \times 3)/(9/4) \approx 2. \quad (3.42)$$

Although SR splittings and HF splittings result from different physical mechanisms, both result in a resolved splitting of the  $X^2\Sigma_{1/2}(N=1)$  state sublevels much greater than the natural linewidth of the transition; we therefore believe that accounting for HF in our model should increase the value of  $\Phi^{\text{tot},3\text{dB}}$  necessary to achieve  $n_e = n_e^{\text{max}}/2$  in a manner almost identical to that resulting from adding SR structure to our model. While we do not present any analysis including both HF structure and SR structure together, which would require solving Eqns. 3.16 for the system shown in Fig. 3.7e, we expect for the reason listed above that the additional (resolved) HF structure will further increase the photon flux necessary to achieve  $n_e = n_e^{\text{max}}/2$  by the correction factor

$$C_{\text{HF}} \approx 2. \quad (3.43)$$

### 3.3.5.5 Estimated photon flux requirements for full system

For simplicity, we assume that corrections to  $\Phi^{\text{tot},3\text{dB}}$  are independent of each other. For the full SrF system, with this assumption, we estimate the total photon flux necessary to achieve  $n_e = n_e^{\text{max}}/2$  is

$$\Phi^{\text{tot},3\text{dB}} \approx C_{\text{SR}} \times C_{\text{HF}} \times C_{\text{vib}} \times \frac{3}{4} \frac{\Gamma_j}{\sigma_j^{\text{tot}}/3}, \quad (3.44)$$

where  $\frac{3}{4} \frac{\Gamma_j}{\sigma_j^{\text{tot}}}$  is equal to the value of  $\Phi_j^{\text{tot},3\text{dB}}$  for the 3+1 model of our system and  $C_{\text{SR}}$ ,  $C_{\text{HF}}$ , and  $C_{\text{vib}}$  are the correction factors due to resolved SR structure, resolved HF structure, and vibrational structure, given by Eqns. 3.42, 3.43, and 3.37 respectively. Putting all these factors into Eqn. 3.44, we estimate

$$\Phi^{\text{tot},3\text{dB}} \approx \frac{144}{7} \frac{\Gamma_j}{\sigma_j^{\text{tot}}} \approx 40 \frac{\Gamma_j}{2\sigma_j^{\text{tot}}}, \quad (3.45)$$

which would be equally distributed between the  $\lambda_{00}$  and  $\lambda_{10}$  lasers. Comparison of Eqn. 3.45 and 3.29 suggests that the real SrF system needs  $\approx 40\times$  greater photon flux to achieve  $n_e = n_e^{\text{max}}/2$  than a two-level system of the same wavelength and lifetime. In experimental units, we expect to achieve  $n_e = n_e^{\text{max}}/2$  for a  $\lambda_{00}$  laser intensity of  $\approx 60$  mW/cm<sup>2</sup> and a  $\lambda_{10}$  laser intensity of  $\approx 60$  mW/cm<sup>2</sup> (with each intensity divided over the 4 SR/HF sidebands in the given vibrational level).

### 3.3.5.6 Estimates for necessary laser intensity

Regarding our initial three questions at the beginning of this section, we expect that the  $\lambda_{00}$  and  $\lambda_{10}$  lasers will each require  $\sim \frac{144}{7} \times$  as much laser intensity as would be needed for a single laser driving a two-level system with the same wavelength and lifetime. Coherent dark states, nonzero

laser detunings, power broadening, and magnetic field broadening are expected to cause the system to require more intensity than this simple model predicts while effects from cross-excitation alone might cause this model to overestimate the required intensity. Our simple model suggests that the optimal solution would distribute the laser power evenly over the four SR/HF manifolds within each vibrational level.

### 3.4 Optical Bloch equations

To allow for the contributions of coherences, we employ a density matrix approach. (Here, coherences correspond to off-diagonal elements of the density matrix.) The density matrix approach will also automatically account for power and magnetic field broadening of the transitions as well as correctly handle coherent dark states. Evolution of the density matrix is described by the Kossakowski-Lindblad equation [125],

$$\frac{\partial \rho}{\partial t} = -\frac{i}{\hbar}[H(t), \rho] + \sum_k C_k \rho C_k^\dagger - \frac{1}{2} \sum_k \left[ C_k^\dagger C_k \rho + \rho C_k^\dagger C_k \right], \quad (3.46)$$

where we have explicitly made the Hamiltonian  $H(t)$  time dependent (as would be the case for polarization switching). Non-unitary evolution due to spontaneous decay and other decoherence mechanisms such as non-zero laser linewidths are accounted for by the terms containing the collapse operators  $C_k$ . The collapse operators are of the form  $C_k = \sqrt{\gamma_k}|a\rangle\langle b|$  for a spontaneous decay or decoherence from  $|b\rangle$  to  $|a\rangle$  at rate  $\gamma_k$ . The Kossakowski-Lindblad equation accommodates non-unitary evolution of the density matrix but is trace-preserving and preserves the Hermitian and positive properties of the density matrix [125]. If the non-unitary terms are discarded from Eqn. 3.46 we recover the Liouville equation. Application of Eqn. 3.46 to our system results in a system of coupled linear differential equations commonly referred to as the optical Bloch equations. We note that solving Eqn. 3.46 for a system with  $N_{tot}$  levels involves solving  $N_{tot}^2$  linear equations for  $N_{tot}^2$  variables, which can be computationally intensive for large  $N_{tot}$ . Hence, our approach to solving Eqn. 3.46 is largely driven by computational efficiency since different methods can vary by several orders of magnitude in efficiency and accuracy [126–128] as we quickly found out ourselves.

### 3.4.1 Solving the OBEs

The Hamiltonian  $H(t)$  is made using the AtomicDensityMatrix (ADM) package [129] for Mathematica [130]. Most terms describing incoherent relaxation are also made using the ADM package although certain incoherent relaxation terms such as decoherence due to nonzero laser linewidth must be programmed in manually.<sup>15</sup> One advantage of using the ADM package is that it allows the user to easily switch systems, thereby allowing the code to be checked using fairly simple systems (such as a 3+1 system, which can be solved both analytically and numerically) before transitioning to more complicated systems by changing only a few parameters. While all terms of Eqn. 3.46 are constructed in a  $N_{\text{tot}}$ -dimensional Hilbert space (where the density matrix is represented by an  $N_{\text{tot}}$ -by- $N_{\text{tot}}$  matrix), we thereafter transition to Liouville space (where the density matrix is represented by an  $N_{\text{tot}}^2$ -dimensional vector) to apply certain numerical methods [131]. Equation 3.46 is recast in Liouville space as

$$\frac{d}{dt}|\rho\rangle = -i\frac{\mathcal{L}}{\hbar}(t)|\rho\rangle, \quad (3.47)$$

where  $\mathcal{L}(t)$  is the Liouville operator with dimensions  $N_{\text{tot}}^2 \times N_{\text{tot}}^2$  and  $|\rho\rangle$  is the density matrix in Liouville space with dimensions  $N_{\text{tot}}^2 \times 1$ . We note that the conversion to Liouville space has not added any additional complexity to the problem. In Eqn. 3.46 there are  $N_{\text{tot}}^2$  variables to be solved for, and this remains true for Eqn. 3.47. The solution to Eqn. 3.47 is given by

$$|\rho(t)\rangle = \lim_{\delta t \rightarrow 0} \prod_{k=0}^{t/\delta t} e^{-i\delta t \mathcal{L}(k\delta t)/\hbar} |\rho(0)\rangle \approx \prod_{k=0}^{t/\Delta t} e^{-i\Delta t \mathcal{L}(k\Delta t)/\hbar} |\rho(0)\rangle, \quad (3.48)$$

where  $|\rho(0)\rangle$  is the initial value of  $|\rho\rangle$  at  $t = 0$  and  $\Delta t$  is a small but finite numerical time step. In the case where the Hamiltonian is time-independent,  $\mathcal{L}(t)$  is also time independent and the solution for  $|\rho(t)\rangle$  takes the simple form

$$|\rho(t)\rangle = \exp[-i\frac{\mathcal{L}}{\hbar}t] |\rho(0)\rangle. \quad (3.49)$$

Although all equations are set up using Mathematica, numerical evaluation is done in MATLAB, which is better equipped to handle matrix exponentiation. We use a freely available program called MATLink [132] which allows Mathematica to communicate with and transfer data to and from MATLAB. Using MATLink and MATLAB, Eqn. 3.49 or Eqn. 3.48 is evaluated using the highly efficient Padé approximation [133] to matrix exponentiation. We find this approach far more effective

---

<sup>15</sup>In the following discussion all laser linewidths are assumed to be infinitely narrow unless explicitly stated otherwise.



than Runge-Kutta methods.<sup>16</sup> One useful check of our code is reproducing Figs. 4, 5 and 9 from Ref. [119].

### 3.4.2 OBE results

The exact details of the OBE setup are similar enough to Ref. [119] that only the results are recounted here. We solve the OBEs for two representative systems: a (3,3)+1 system to investigate coherent dark states and related dynamics between the  $X(v=0, N=1)$  and  $X(v=1, N=1)$  states, and a (2,4)+2 system to investigate similar effects within a given ground-state vibrational level.

### 3.4.3 (3,3)+1 system

The interplay between coherent dark states in the  $X(v=0, N=1)$  and  $X(v=1, N=1)$  states and the laser intensity requirements for the  $\lambda_{00}$  and  $\lambda_{10}$  lasers are explored by solving the OBEs for the (3,3)+1 system shown in Fig. 3.7c. Experimentally, we expect to have roughly the same power available for the  $\lambda_{00}$  laser as we have available for the  $\lambda_{10}$  laser. We assume a branching ratio from the single excited state of  $A_g = .98$  to the  $X(v=0, N=1)$  state and a branching ratio of  $(1 - A_g)$  to the  $X(v=1, N=1)$  state. We explore the parameter space around the default values for the Rabi frequencies of

$$\Omega_{v=0} = \sqrt{A_g}\Gamma \quad \text{and} \quad \Omega_{v=1} = \sqrt{1 - A_g}\Gamma \quad (3.50)$$

which correspond to photon fluxes of

$$\Phi_{v=0} = \Phi_{v=1} = \frac{\Gamma}{\sigma_j^{\text{tot}}/3}. \quad (3.51)$$

The magnetic field is defined to lie at 45 degrees relative to the laser polarization and have magnitude  $B = \Omega_L/\mu_B$ , where  $\Omega_L$  is the Larmor frequency. For simplicity, the g-factors are set to 1 for both the  $X(v=0, R=1)$  and  $X(v=1, R=1)$  manifolds. We solve the OBEs for the equilibrium populations using Eqn. 3.49 while varying parameters in three ways: in the first case, we vary  $\Omega_{v=0}$  and  $\Omega_L$  while holding  $\Omega_{v=1}$  at the default value; second, we vary  $\Omega_{v=1}$  and  $\Omega_L$  while holding  $\Omega_{v=0}$  at the default value; and third, we vary  $\Omega_{v=0}$  and  $\Omega_{v=1}$  together in proportion to their default values from Eqn. 3.50 while varying  $\Omega_L$ . This is done for a variety of different detunings  $\Delta_{v=0}$  and  $\Delta_{v=1}$ , which are defined relative to the energy levels with no external magnetic field. Although exploring

<sup>16</sup>In comparison, Runge-Kutta methods displayed problems both preserving the trace of the density matrix and keeping all the diagonal elements of the density matrix positive.

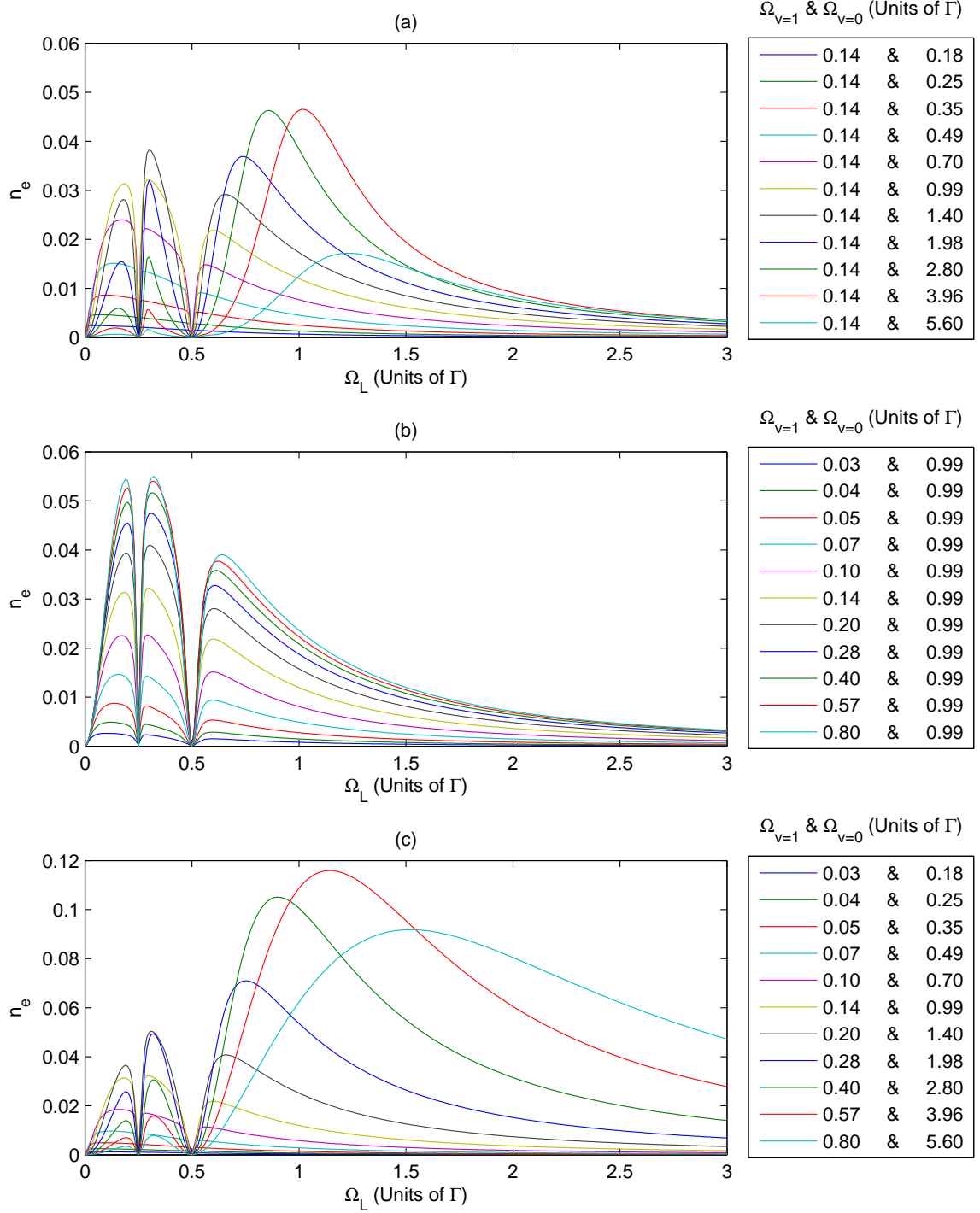


Figure 3.8: Predicted values of  $n_e$  for a (3,3)+1 system as derived from the OBEs. (a) Varying  $\Omega_{v=0}$  and  $\Omega_L$  while holding  $\Omega_{v=1} = \sqrt{.02}\Gamma = .14\Gamma$ . (b) Varying  $\Omega_{v=1}$  and  $\Omega_L$  while holding  $\Omega_{v=0} = \sqrt{.99}\Gamma = .98\Gamma$ . (c) Varying  $\Omega_{v=1}$  and  $\Omega_{v=0}$  with fixed ratio in addition to  $\Omega_L$ . For all plots,  $\Delta_{v=0} = -\Delta_{v=1} = -\Gamma/4$ . Dark resonances are visible for  $\Omega_L = |\Delta_{v=0} - \Delta_{v=1}|$  or  $\Omega_L = \frac{1}{2}|\Delta_{v=0} - \Delta_{v=1}|$ . Note the scale in (c) is larger than in (a) or (b).

the space of the five parameters  $(\Delta_{v=0}, \Delta_{v=1}, \Omega_{v=0}, \Omega_{v=1}, \Omega_L)$  is challenging, we find that a local maximum of  $n_e$  occurs for  $\Delta_{v=0} \sim -\Delta_{v=1} \sim \Gamma/4$  given the conditions of Eqn. 3.50. Under the conditions  $\Delta_{v=0} = -\Delta_{v=1} = \Gamma/4$ , the dependence of  $n_e$  on  $\Omega_{v=0}$ ,  $\Omega_{v=1}$ , and  $\Omega_L$  is shown in Fig. 3.8.

The plots in Fig. 3.8 show narrow dark resonances occur when  $\Omega_L = |\Delta_{v=0} - \Delta_{v=1}|$  or  $\Omega_L = \frac{1}{2}|\Delta_{v=0} - \Delta_{v=1}|$ . However, we observe in our calculations that these dark resonances are destabilized by even very modest laser linewidths  $\sim \Gamma/20$ , and we therefore do not expect to observe such effects in our experiment. The plots also show that, for  $\Omega_L \lesssim .5$ , increasing the value of  $\Omega_{v=0}$  above the default value decreases  $n_e$ , while increasing the value of  $\Omega_{v=1}$  above the default value increases  $n_e$ . We offer a possible explanation for this behavior: even at  $\Omega_{v=0} = \sqrt{A_g}\Gamma$ , the  $\lambda_{00}$  laser may cause some power broadening of the lone excited state. The  $\lambda_{10}$  laser will then suffer a reduction of its Rabi frequency  $\Omega_{v=1}$ , and more power will be required in the  $\lambda_{10}$  laser to again achieve its unperturbed Rabi frequency. Since  $A_g \sim 1$ , the  $\lambda_{10}$  laser is unlikely to ever power broaden the excited state under experimental conditions.

Since the level structure in  $X(v=1, N=1)$  exactly parallels that in  $X(v=0, N=1)$ , which holds for the actual case of SrF where the g-factors are the same to within  $\sim 1\%$  for the  $X(v=0, N=0)$  and  $X(v=1, N=1)$  states, we also observe that the only mechanism for destabilizing dark states in the (3,3)+1 system relies on differences in detuning between the  $\lambda_{00}$  and  $\lambda_{10}$  lasers.<sup>17</sup> Specifically,  $B$ -fields should be ineffective for destabilizing coherent dark states between the  $X(v=0, N=1)$  and  $X(v=0, N=1)$  states in the full experimental system. While the OBEs show that  $n_e$  approaches the  $n_e^{\max} = 1/7$  value predicted from the MLREs for large values of  $\Omega_{v=0}$  and  $\Omega_{v=1}$ , the value of  $n_e \approx .03$  obtained with the OBEs for the default values of  $\Omega_{v=0}$  and  $\Omega_{v=1}$  is lower than the MLRE prediction of  $n_e = \frac{1}{14}$  for a similar photon flux, as can be seen by comparing Eqns. 3.51 and 3.35.

### 3.4.4 (2,4)+2 system

Dynamics and coherent dark states between different  $J$  manifolds within a given ground-state vibrational level are explored by solving the OBEs for the (2,4)+2 system shown in Fig. 3.6b with an added magnetic field for remixing. The magnetic field is defined the same way as in the (3,3)+1 system. In this example, the magnetic field alone is sufficient to destabilize coherent dark states between the  $J = 3/2$  and  $J = 1/2$  states. Hence, except where explicitly noted otherwise, we set  $\Delta_{J=1/2} = 0$  and  $\Delta_{J=3/2} = 0$ , where these detunings are always defined relative to the energy levels

<sup>17</sup>Or, as mentioned above, non-zero laser linewidths.

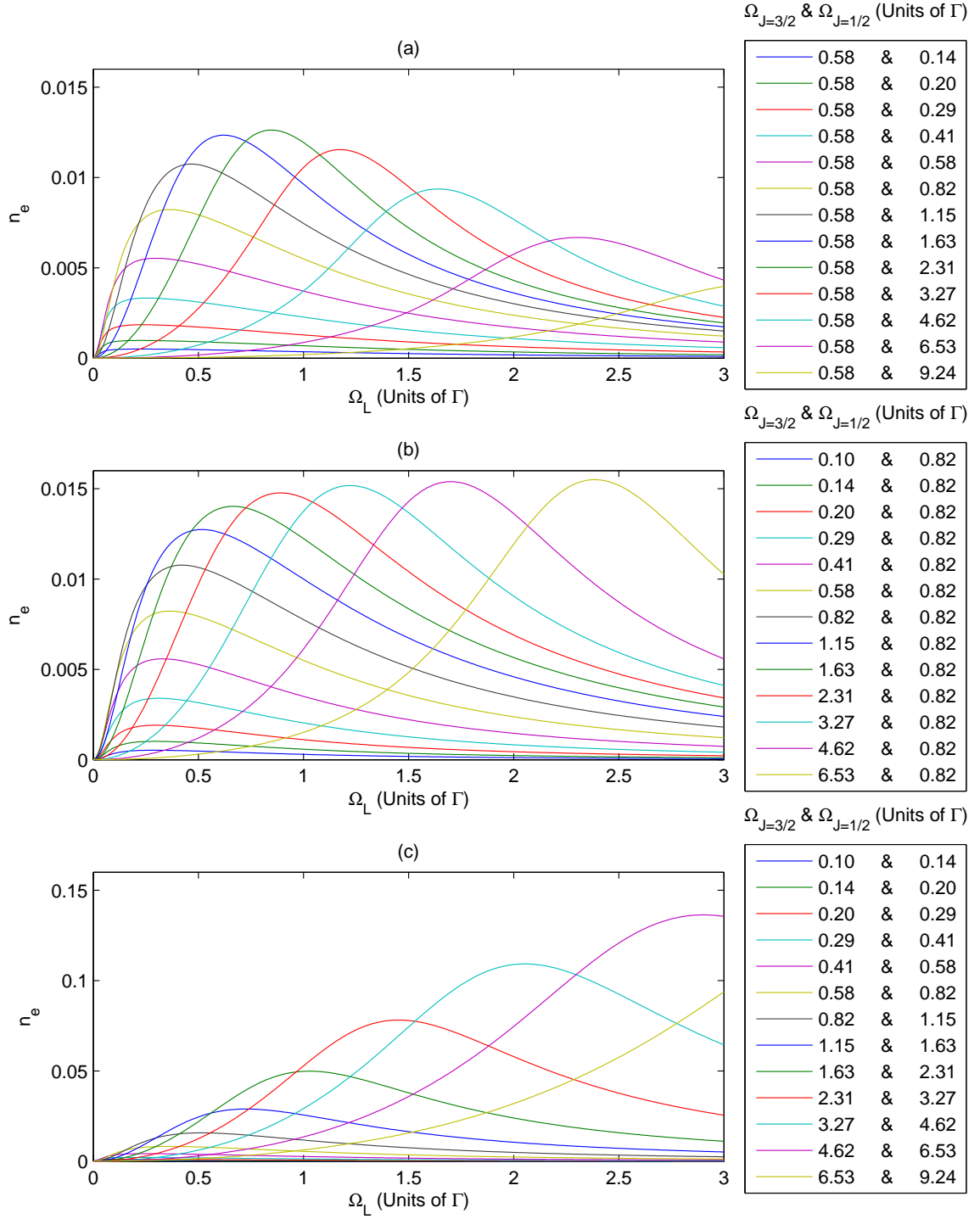


Figure 3.9: Predicted values of  $n_e$  for a (2,4)+2 system for different laser intensities and magnetic field values obtained by solving the OBEs. (a) Varying  $\Omega_{J=1/2}$  and  $\Omega_L$  while holding  $\Omega_{J=3/2} = \sqrt{1/3}\Gamma$ . (b) Varying  $\Omega_{J=3/2}$  and  $\Omega_L$  while holding  $\Omega_{J=1/2} = \sqrt{2/3}\Gamma$ . (c) Varying  $\Omega_{J=3/2}$  and  $\Omega_{J=1/2}$  together at a fixed ratio in addition to  $\Omega_L$ . Note the y-scale in (c) is 10 $\times$  larger than in (a) or (b). All plots here are shown for  $\Delta_{J=1/2} = 0$  and  $\Delta_{J=3/2} = 0$ .

in the absence of a magnetic field. Given these detunings,  $\Omega_L$ ,  $\Omega_{J=3/2}$  and  $\Omega_{J=1/2}$  are the main parameters to vary. Secondary parameters we explore are the branching ratios from each excited state to the  $J = 1/2$  and  $J = 3/2$  states (set to  $A_{J=1/2} = 2/3$  and  $A_{J=3/2} = 1/3$  respectively by default as shown in Fig. 3.6b), the g-factors of the  $J = 3/2$  and  $J = 1/2$  states (set to  $2/3$  and  $-2/3$  respectively by default as in Ref. [134]), and the detunings  $\Delta_{J=1/2}$  and  $\Delta_{J=3/2}$ . Here  $\Omega_L = \mu_B B$ , i.e.  $\Omega_L$  does not include the parameters  $g_J$  or  $m_J$  which are included explicitly in the Hamiltonian.

We explore the parameter space around the default values of

$$\Omega_{J=1/2} = \sqrt{2/3}\Gamma = .82\Gamma \quad \text{and} \quad \Omega_{J=3/2} = \sqrt{1/3}\Gamma = .58\Gamma, \quad (3.52)$$

which correspond to photon fluxes of

$$\Phi_{J=1/2} = \Phi_{J=3/2} = \frac{\Gamma}{\sigma_j^{\text{tot}}/3}, \quad (3.53)$$

and  $\Omega_L$  set to maximize  $n_e$ , as shown in Fig. 3.9. Under these conditions, increasing  $\Omega_{J=3/2}$  is generally more effective to increase  $n_e$  than increasing  $\Omega_{J=1/2}$ . Moreover, large values of  $\Omega_{J=1/2}$  can result in decreased  $n_e$  for any value of  $\Omega_L$  and the default value of  $\Omega_{J=3/2}$ . A decrease in the value of  $n_e$  is not observed when increasing  $\Omega_{J=3/2}$  and holding  $\Omega_{J=1/2}$  at the default value. We do not yet understand either behavior. Both behaviors are also observed when the branching ratios to the two  $J$  manifolds are reversed from their default values. This finding, that the laser intensity requirements of the system may depend on the g-factors or the degeneracy of the levels, is a departure from the MLRE modeling which predicts the optimal solution for a fixed total intensity is to divide the laser intensity evenly over all transitions. Although coherent dark states between  $J = 1/2$  and  $J = 3/2$  should be destabilized by the magnetic field alone, for certain combinations of detunings  $\Delta_{J=1/2}$  and  $\Delta_{J=3/2}$ ,  $n_e$  can be unexpectedly low. For the default g-factors and  $\Delta_{J=1/2} = 0$  and  $\Delta_{J=3/2} = 0$ , this is the case. The strong dependence of  $n_e$  on the g-factors is not yet understood either.

The OBEs show that  $n_e$  approaches the  $n_e^{\text{max}} = 1/4$  value predicted from the MLREs for certain large values of  $\Omega_{v=0}$ ,  $\Omega_{v=1}$ , and  $\Omega_L$ . However, achieving  $n_e \approx n_e^{\text{max}}$  requires  $\Omega_{J=3/2} \gg \Omega_{J=1/2}$ , which we do not currently understand and is not evident from Eqn. 3.38. Further, the value of  $n_e \approx .008$  obtained with the OBEs for the default values of  $\Omega_{v=0}$  and  $\Omega_{v=1}$  is much lower than the MLRE prediction of  $n_e = \frac{1}{8}$  for similar photon fluxes, as can be seen by comparing Eqn. 3.53 with Eqns. 3.39, 3.40, 3.41.

Overall, while the OBEs are useful both by themselves and to guide application of the MLREs,

their results are sometimes hard to interpret even for the simple systems considered here due to the large parameter spaces involved. Hence, while we are able to numerically solve the OBEs for our complete system, these calculations may not provide as much insight into the behavior of the system as we might hope.

### 3.5 Loss mechanisms

While the quasi-cycling transition employed for SrF is highly closed, leakage mechanisms still exist. In this section we discuss mechanisms which cause molecules to permanently exit the quasi-cycling transition. We expect losses from decay to vibrational states which are not currently repumped, losses from off-resonant excitation, losses from level-mixing due to stray electric fields, losses from hyperfine and spin-rotation level-mixing in both the ground and excited states of the cycling transition, losses from stimulated absorption of blackbody photons, losses due to spontaneous vibrational decay, and losses induced by level-mixing from an external magnetic field. Although we expect losses to due light-assisted collisions and quadrupole decays to be negligible, they are included for completeness.

#### Incomplete vibrational repump coverage

The FCFs dictate that molecules will decay from the  $A^2\Pi_{1/2}(v = 0, J = 1/2)$  state to the  $X^2\Sigma_{1/2}(v \geq 3, N = 1)$  state with probability  $\approx q_{03} \times \left(\frac{\lambda_{00}}{\lambda_{03}}\right)^3 \approx 9 \times 10^{-6}$ . Molecules decaying to such states will not be returned to the cycling transition and will be lost. Additional losses arising from repumping the  $X^2\Sigma_{1/2}(v = 2)$  state through the  $A^2\Pi_{1/2}(v = 1)$  state are much smaller, and are estimated to occur with probability  $\approx q_{02} \times \left(\frac{\lambda_{00}}{\lambda_{02}}\right)^3 \times q_{13} \times \left(\frac{\lambda_{11}}{\lambda_{13}}\right)^3 \approx 4 \times 10^{-7}$ . Both loss mechanisms would be addressed by the addition of a third repump laser,  $\lambda_{32}$ , driving the  $X^2\Sigma_{1/2}(v = 3, N = 1) \rightarrow A^2\Pi_{1/2}(v = 2, J = 1/2)$  transition. At present, decay to the  $X^2\Sigma_{1/2}(v = 3)$  state is believed to be the primary cycling loss mechanism.

#### Off-resonant excitation to $A^2\Pi_{1/2}(v = 0, J = 3/2)$

Given that the  $A^2\Pi_{1/2}(v = 0, J = 3/2^+)$  state lies  $\approx 17$  GHz above the excited state of the main cycling transition, the absorption cross section for driving this off-resonant transition is smaller than the absorption cross section for the main cycling transition (when the  $\lambda_{00}$  laser is on resonance) by a factor of  $\sim 2 \times \frac{7}{10} \times \frac{\Gamma^2/4}{(2\pi \cdot 17 \text{ GHz})^2 + \Gamma^2/4} \approx 5 \times 10^{-8}$  (using Eqn. 3.14), where the factor two is the degeneracy ratio between the  $J = 3/2$  and  $J = 1/2$  excited states and the fraction  $\frac{7}{10}$  is the ratio of the partial linewidths and comes from Table 2.16.

However, since 70% of all radiative decays from the  $A^2\Pi_{1/2}(v=0, J=3/2^+)$  state return to the  $X^2\Sigma_{1/2}(v=0, N=1)$  state, molecule loss will instead only happen every  $\sim 1.6 \times 10^{-8}$  stimulated absorption events. The rate of loss from this mechanism is linearly proportional to the  $\lambda_{00}$  laser intensity. For each vibrational level, using a single repump laser driving the  $X^2\Sigma_{1/2}(N=3) \rightarrow A^2\Pi_{1/2}(J=3/2^+)$  transition is expected to eliminate this loss mechanism.<sup>18</sup>

### Stray electric fields

Stray electric fields mix states of opposite parity. Mixing of the positive parity state, ( $A^2\Pi_{1/2}(v=0, J=1/2^+)$ ), with the negative parity state, ( $A^2\Pi_{1/2}(v=0, J=1/2^-)$ ), could lead to population decaying to the  $X^2\Sigma_{1/2}(v=0, N=0, 2)$  states. Population accumulation in these states is quite problematic because such molecules cannot be returned to the cycling transition using an electric dipole transition due to parity selection rules. At least two options exist: driving a non-resonant two-photon transition or remixing the  $X^2\Sigma_{1/2}(v=0, N=0)$  state with the  $X^2\Sigma_{1/2}(v=0, N=1)$  state using microwaves and repumping the  $X^2\Sigma_{1/2}(v=0, N=2)$  state through the  $A^2\Pi_{1/2}(v=0, J=1/2^-)$  state. (See [subsubsection 3.1.3.2.](#)) However, since absorption cross sections for non-resonant two-photon transitions are quite small, the latter option appears more promising (but will likely lead to a reduction in the spontaneous scattering rate by spreading population among more states).

### Hyperfine and spin-rotation mixing in the ground state

Hyperfine mixing between the  $X^2\Sigma_{1/2}(v=0, N=1, J=3/2, F=2)$  and  $X^2\Sigma_{1/2}(v=0, N=3, J=5/2, F=2)$  states could lead to decays from the  $A^2\Pi_{1/2}(v=0, J=1/2^+, F=1)$  state to the  $X^2\Sigma_{1/2}(v=0, N=3, J=5/2, F=2)$  state. However, the hyperfine mixing is expected to be of the order  $\sim \left[\frac{H_{HF}}{\Delta E}\right]^2 = \left[\frac{40 \text{ MHz}}{75.1 \text{ GHz}}\right]^2 = 3 \times 10^{-7}$  where  $\Delta E \approx 75.1$  GHz is the splitting between the two aforementioned ground states. Mixing between the  $X^2\Sigma_{1/2}(v=0, N=1, J=3/2, F=2)$  and  $X^2\Sigma_{1/2}(v=0, N=3, J=5/2, F=2)$  states may also be further suppressed if it requires spin-rotation mixing, expected to be of the order  $\sim \left[\frac{H_{SR}}{\Delta E}\right]^2 = \left[\frac{100 \text{ MHz}}{75.1 \text{ GHz}}\right]^2 = 2 \times 10^{-6}$ . If this is the case, the total mixing should be negligible.

### Hyperfine mixing in the excited state

Hyperfine mixing of the  $A^2\Pi_{1/2}(v=0, J=1/2^+)$  and  $A^2\Pi_{1/2}(v=0, J=3/2^+)$  states could lead to decays to the  $X^2\Sigma(v=0, N=3)$  state. However, since the hyperfine splitting in the  $A^2\Pi_{1/2}$  state is unresolved and stated to be less than 3 MHz [111], this mixing must be less than

---

<sup>18</sup>This loss mechanism occurs  $\approx 50\times$  more often for  $X(v=0)$  than for  $X(v=1)$  due to the FCFs.

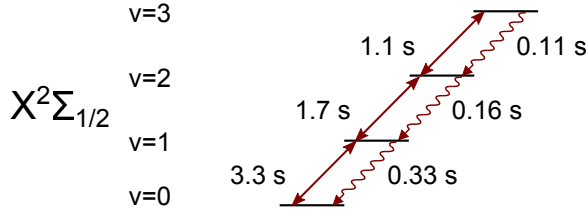


Figure 3.10: Vibrational lifetimes in the  $X^2\Sigma_{1/2}$  state are primarily limited by spontaneous decay from higher vibrational levels. Lifetimes for spontaneous decay ( $\sim$ ) are on the order of 100's of ms. Blackbody radiation at 300 K may also drive stimulated transitions ( $\longrightarrow$ ) between adjacent vibrational levels but such events occur less frequently than  $\sim 1 \text{ s}^{-1}$ .

$\sim \left[ \frac{3 \text{ MHz}}{17 \text{ GHz}} \right]^2 = 3 \times 10^{-8}$  where 17 GHz is the splitting between the  $A^2\Pi_{1/2}(v=0, J=1/2^+)$  and  $A^2\Pi_{1/2}(v=0, J=3/2^+)$  states.

### Stimulated blackbody and spontaneous emission lifetime of vibrational states in X

With the current cycling scheme, electric dipole transitions between vibrational levels will result in molecules ending up in states with the wrong parity, thereby ending cycling. Excited vibrational levels can decay via spontaneous emission. Similarly, 300 K blackbody radiation can stimulate transitions between different vibrational levels. The transition dipole moment between adjacent vibrational levels is given by Ref. [135]

$$\mu_{v+1,v} = \sqrt{\frac{v+1}{2}} \sqrt{\frac{\hbar}{m\omega_e}} \left[ \frac{d\mu}{dR} \right]_{R=R_e}, \quad (3.54)$$

where  $\left[ \frac{d\mu}{dR} \right]_{R=R_e}$  is the first derivative of the electric dipole moment function evaluated at the equilibrium internuclear distance  $R_e$  and  $m$  is the reduced mass of the molecule. Vibrational transitions where  $\Delta v \neq \pm 1$  are suppressed. (See Ref. [91], pg. 266.) Theoretical estimates for the X state of SrF predict  $\left[ \frac{d\mu}{dR} \right]_{R=R_e} \approx 3.17 \frac{\text{debye}}{a_0}$  where  $a_0$  is the Bohr radius [136]. Given  $\mu_{v+1,v}$ , the spontaneous emission lifetime is calculated using Eqn. 3.7 while the expected interval between stimulated absorption/emission events is calculated following the formalism in Ref. [135]. Lifetimes for spontaneous vibrational decay and the expected interval between stimulated events are shown in Figure 3.10. Checks for this calculation for other molecules are available in Refs. [124, 135].

### Light-assisted collisions

This loss mechanism should be negligible until there is sufficient molecular density for collisions.

### Magnetic fields

In the ground state of SrF, a magnetic field of  $\sim 20$  gauss will shift the energy levels by  $\lesssim 20$  MHz. In this case, the mixing in the ground state between the  $N=1$  and  $N=3$  rotational



levels is expected to be  $\sim \frac{20 \text{ MHz}}{75.1 \text{ GHz}} = 7 \times 10^{-8}$  where 75.1 GHz is the spacing between the  $X^2\Sigma_{1/2}(v=0, N=1)$  and  $X^2\Sigma_{1/2}(v=0, N=3)$  states. Mixing due to magnetic fields in the excited state is negligible since the  $A^2\Pi_{1/2}$  state lacks a magnetic moment.

### Electric quadrupole decays

Electric quadrupole moments are typically  $\sim 10^{-8}$  times smaller than equivalent electric dipole moments [108], and therefore loss due to such decays is negligible.

## 3.6 Benefits of SrF

Certain characteristics of a molecule (for example, the molecular yield achieved via ablation in a buffer gas source) can make or break an experiment. Having experienced for two years the severe difficulties encountered with our previous molecule SrO, I can attest that molecule selection is of paramount importance. Once a molecule has been chosen and the experiment built, switching molecules is difficult if not completely unrealistic. Lasers, laser diodes, optics, PMTs, EOMs, AOMs, optical isolators, Fabry-Pérots, photodiodes, fiberports, fibers and more are all tailored to certain wavelengths. Switching molecules (which will likely have a different wavelength for certain excitations) will almost certainly require some if not all of the above be replaced (depending on the proximity of the old wavelength to the new one). Physical dimensions of the vacuum system may also be dependent upon certain molecular attributes (lifetime, mass, excitation wavelength, etc.) as well. Hence, our selection of SrF was done with the utmost care in attempting to avoid as many future problems as possible. SrF was chosen out of roughly a hundred possible candidates. In this section we review some of the benefits of and the selection rationale for SrF.

### Franck-Condon factors

SrF's diagonal FCFs dictate that with only 3 lasers we should be able to scatter  $\gtrsim 10^5$  photons before decaying into a vibrational level for which there is no repump laser as shown in Table 2.13.

### Lifetime

The  $A^2\Pi_{1/2}$  state of SrF has lifetime  $\tau \approx 24.1 \text{ ns}$  [86]. Shorter lifetimes are highly desirable because they allow for faster cycling and therefore for application of larger spontaneous scattering forces, as discussed in Appendix B.

### Transition wavelengths

The transition wavelengths  $\lambda_{00}$ ,  $\lambda_{10}$  and  $\lambda_{21}$  can all be generated by diode lasers with significant power. Because DVD technology employs diode lasers at  $\approx 660$  nm, particularly powerful single mode laser diodes are available for  $\lambda_{00}$ . Tapered amplifiers are commercially available at both 663 nm and 685/686 nm and offer 500 mW and 400 mW output powers respectively. Additionally, the low cost of diode lasers ( $\sim$  \$10k) allows us to employ auxiliary lasers to excite X $\rightarrow$ A transitions other than the cycling transition while simultaneously cycling. This is helpful for normalization and detection.<sup>19</sup>

### Rotational constant

SrF’s electronic ground-state rotational constant results in a  $\approx 15$  GHz splitting between the  $N = 0$  and  $N = 1$  ground-state rotational sublevels and a  $\approx 30$  GHz splitting between the  $N = 1$  and  $N = 2$  ground-state rotational sublevels. Transitions at such frequencies are easily driven by commercially available microwave generators. Microwave amplifiers with powers up to 2 kW are available at 15 GHz and amplifiers with powers  $\gtrsim 100$  Watts are available at 30 GHz.

### Dipole moment

The ground state of SrF is quite polar with a dipole moment of 3.4963 debye [111, 137], and therefore may be manipulated with an electric field.<sup>20</sup>

### Unpaired electron spin and unpaired nuclear spin

Unpaired spins split ground-state sublevels and thus require additional laser frequencies. This significantly increases the complexity of the laser system. However, the presence of an unpaired electron or unpaired nuclear spin allows certain possibilities for quantum information storage [12]. The level structure of SrF also has utility for certain precision measurement applications [124, 138–140]. Moreover, the unpaired electronic spin in the electronic ground state gives SrF a magnetic moment. Hence, SrF may be trapped magnetically while the interactions between trapped molecules are manipulated either optically or electrically.

### Low lying metastable states

Unlike BaF [85], YO [120], and several other candidates for direct molecular cooling experiments, SrF has no low-lying metastable states for molecules to become trapped in. Specifically,

---

<sup>19</sup>The approach is far more expensive for transitions requiring a CW dye laser ( $\sim$  \$200k) or frequency doubled Raman fiber laser ( $\sim$  \$120k) since generating light with the  $\sim 15$  GHz offset needed to hit other rotational levels is challenging using AOMs and EOMs alone.

<sup>20</sup>For completeness, the dipole moment of the A and B states are 2.064 debye and 0.91 debye respectively [111].

the lowest  $\Delta$  state is predicted to lie well above the  $A^2\Pi_{1/2}$  state in SrF [85]. Aside from leading to a reduced scattering rate due to population trapping, the presence of such metastable states is particularly deleterious because decays from such states will populate ground-state sublevels with parity opposite to that required for cycling. As discussed in [section 3.5](#), returning molecules to the cycling transition from such states is either challenging or produces unwanted side-effects.

### Miscellaneous benefits

Less importantly, all four SR/HF manifolds can be excited using a single laser and a single EOM, the SrF<sub>2</sub> precursor appears to ablate well with little dust, and the spectroscopy of SrF is well established. Finally, SrF<sub>2</sub> is neither toxic, hazardous, radioactive nor reacts with atmospheric gases such as H<sub>2</sub>O. In comparison to other candidate molecules, SrF’s molecular mass of 107 amu is moderate and the main cycling transition wavelength is in the red, which decreases the number of photon scattering events necessary for a given change in velocity compared to heavier molecules or compared to molecules requiring longer excitation wavelengths.

#### 3.6.1 Drawbacks of SrF

While potentially useful for quantum simulation and other future applications, the unpaired nuclear and electronic spins in SrF create otherwise undesirable complications. For example, almost every laser in the experiment must have an associated EOM to generate the optical frequencies necessary to address the four SR/HF manifolds. Because the saturation intensity with our current approach may scale linearly with the number of resolved discrete ground-state levels as discussed in [section 3.3](#), more laser power may also be required to address the resolved SR/HF manifolds than would be required in the absence of this structure. As of this writing, saturation of the SrF cycling transition requires even more power than we would naively have predicted. Although this is not yet understood, the apparently large laser power requirements are quite disadvantageous. Further, there exists the possibility of coherent dark states between different SR/HF manifolds. The resolved SR/HF structure is also expected to complicate the realization of an SrF MOT as discussed in [chapter 9](#).

Some relevant considerations for choosing molecules for future laser cooling experiments are discussed in [Appendix B](#).

## Chapter 4

# The laser system

The vast majority of atomic physics labs use lasers for atom/molecule manipulation. The creation of stable lasers adequate for atomic physics research can be broken down into three tasks: making the lasers, creating a frequency reference, and locking the lasers (the act of stabilizing the lasers' frequency to the frequency reference). This chapter details our solution to all three problems. Auxiliary laser components such as EOMs and laser amplifiers are discussed as well.

### 4.1 Introduction

As an experiment attempting to laser cool a molecule, we knew we would require a large number of lasers. The current version of the experiment involves eleven master external cavity diode lasers (ECDLs), seven slave lasers and three tapered amplifiers (TAs). Given the large number of lasers, it is important that each individual component of the laser system be robust. In this endeavor we have been partially successful. For example, one of our ECDLs stayed locked continuously for a period of 45 days. However, more typical performance for most of our ECDLs is to remain locked for several days to a week before suffering an abrupt change in frequency (termed a mode-hop; see below).

### 4.2 External cavity diode lasers

ECDLs generate the single-frequency, tunable, coherent light for the experiment. A variety of ECDL designs are available in the literature, each of which may be optimized for one or more characteristics of either the desired light output or operation of the laser itself. Table 4.2 gives an overview of some considerations when choosing an ECDL design.

Property	Consideration	Examples
Mode-hop-free tuning range	Hitting multiple spectral lines easily	[141–147]
Laser linewidth	Hitting narrow lines	[148, 149]
Power	Driving transitions strongly	[150]
Ease of assembly		[151, 152]
Ease of setup and alignment		[151, 153–155]
Cost		[151, 153]
Size		[151–153, 156, 157]

Table 4.1: ECDL design considerations.

Given the large number of diode lasers in use in our experiment and in the DeMille group as a whole, we set out to design and build our own ECDLs.<sup>1</sup> The goal of the home-built laser is to build a laser to satisfy 90% of likely applications within the DeMille group. Cost, ease of use and assembly, mode-hop-free tuning range (MHFTR), size and long-term stability are all primary design considerations. Laser linewidth is a property that is deemed acceptable to compromise on.

We now review some important points of our ECDL design, shown in Fig. 4.1: We exclusively employ Littrow-Hänsch [153, 156, 158] style ECDLs (hereafter referred to as Littrow) due to the design’s higher output power and better ability to tolerate cheap, non-anti-reflection- (non-AR-) coated diodes versus the Littman-Metcalf [159–161] style ECDLs. The increased linewidth of Littrow versus Littman-Metcalf is currently unimportant since all SrF linewidths are  $\approx 6.6$  MHz, and therefore ECDL linewidths  $\lesssim 1$  MHz are acceptable. No significant effort is made to protect the laser from acoustic noise other than using a .5” thick acrylic housing for the top and sides of the laser. All our ECDLs feature beam steering mirrors to maintain the angle of the laser output as the laser frequency is varied [152]. All necessary machining is wavelength-independent. The lasers employ relatively cheap electronics: a single stage of temperature control (Thorlabs, TEC200C) and a cheap current controller (Thorlabs, LDC202C or similar) which we find is adequate for our linewidth needs. Aside from the laser diodes and the machining (performed in-house), all laser parts are available from Thorlabs, Edmund Optics and Digikey. The laser is constructed from Alloy 360 brass which offers a good combination of cost, machinability, yield strength, elasticity, thermal conductivity, and thermal expansion.<sup>2</sup> For applications where better thermal stability is desired, our design should be compatible with Invar, but this has not been tested.

General principles of ECDL operation are reviewed in Ref. [153]. The ECDL frequency  $f_{\text{DL}}$  is

<sup>1</sup>The motivation is mainly driven by cost since the home-built ECDLs cost  $\sim \$3500$  while commercial ECDLs are  $\sim \$15\text{k}–\$20\text{k}$ .

<sup>2</sup>We use an energy dispersive spectrometer (EDS) to do a chemical composition analysis on a commercial ECDL and find the material to be closest to “Navy G” bronze. We are not aware of any particular reason why such an odd alloy is chosen by this commercial vendor.

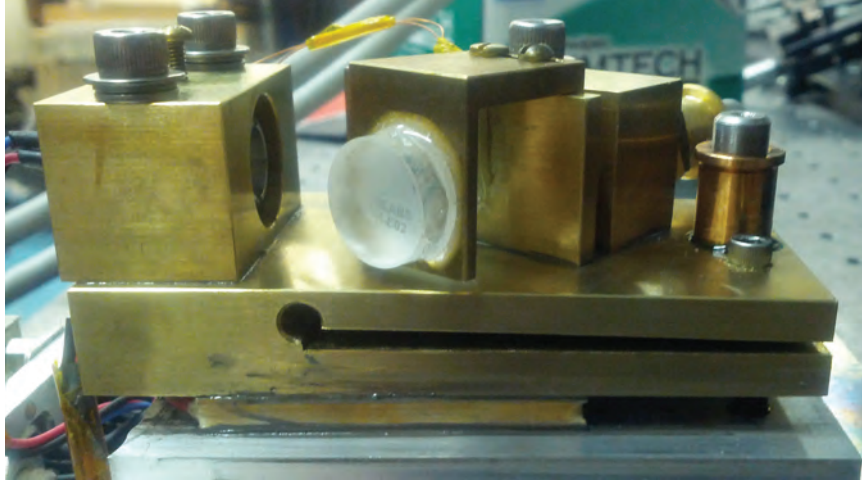


Figure 4.1: Home-built Littrow ECDL design.

controlled in three ways. A physical knob allows coarse variation of  $f_{\text{DL}}$  by varying the angle of the diffraction grating. A piezo provides finer control of  $f_{\text{DL}}$  in the same fashion but with a low bandwidth  $\sim 700$  Hz [162]. Finally,  $f_{\text{DL}}$  may be adjusted by varying the current injected into the laser diode (small dynamic range and  $\gtrsim$  GHz bandwidth). For daily operation, the piezo actuator is the primary means used to vary  $f_{\text{DL}}$  in a smooth monotonic fashion.<sup>3</sup>

A single stage of temperature control stabilizes the laser temperature at  $T_{\text{laser}}$  to minimize variation of  $f_{\text{DL}}$  due to thermal drift of the laser cavity. Because the stability rather than the value of  $T_{\text{laser}}$  is important for this purpose, the actual value of  $T_{\text{laser}}$  can be used to shift the gain profile of the laser diode (width  $\sim 1$  THz) to coincide with  $f_{\text{DL}}$ . Temperature is never used to directly vary  $f_{\text{DL}}$ . (See [Appendix C](#).)

For finding spectral lines, it is desirable that  $f_{\text{DL}}$  vary smoothly. However under certain conditions,  $f_{\text{DL}}$  may abruptly change to a different value, an event termed a mode-hop. In part, mode-hops occur because the angular feedback profile of the grating does not match the wavelengths supported by the changing length of the laser cavity. The bandwidth over which the laser can be tuned without a mode-hop is called the mode-hop free tuning range (MHFTR) and is dependent upon laser geometry. The analysis is different for ECDLs using AR-coated laser diodes and non-AR-coated laser diodes. We treat the former case first before expanding analysis to the latter.

<sup>3</sup>The injection current is also used as a supplementary means to change  $f_{\text{DL}}$ , but generally it cannot be used alone to vary  $f_{\text{DL}}$  smoothly over a frequency range  $\gtrsim 1$  GHz. Coarse physical adjustment of the diffraction grating is used only when the laser frequency must be adjusted by  $\gtrsim 20$  GHz and is not used daily.

### 4.2.1 Pivot point calculations

The ECDL wavelength is determined both by the standing-wave condition, i.e that the round trip length of the cavity, denoted  $L_{\text{cavity}}$ , equal an integer number of wavelengths, and by the spatial profile of light diffracted from the grating. These two conditions are described by

$$\lambda = L_{\text{cavity}}/N_{\lambda} \quad (4.1)$$

$$\lambda = 2d \sin \Theta, \quad (4.2)$$

respectively, where  $\lambda$  is the lasing wavelength,  $N_{\lambda}$  is an integer,  $\Theta$  is the angle between the back facet of the laser diode and the grating plane, and  $d$  is the line spacing of the grating. To achieve continuous tuning without mode-hops (i.e. maximize the MHFTR), both  $\Theta$  and  $L_{\text{cavity}}$  must change synchronously. This can be accomplished by rotating the grating about a carefully chosen pivot point.<sup>4</sup> Much has been written about design considerations to increase the MHFTR of an ECDL [141–147, 160, 161].

The geometry considered is shown in Fig. 4.2 and is applicable to Littrow ECDLs. The plane of the grating pivots around a point  $P$  and is laterally displaced from  $P$  by  $x_1$ , while the plane containing the back facet of the laser diode is laterally displaced from  $P$  by  $x_0$ . The accrued phase of the light, denoted  $\psi$ , after one round trip inside the cavity can be shown to be (to within an additive constant) [161]

$$\psi = 2k [x_0 + x_1 \cos \Theta], \quad (4.3)$$

where  $k = 2\pi/\lambda$ . Substituting Eqn. 4.2 into Eqn. 4.3 and differentiating in terms of  $\Theta$  yields

$$\frac{d\psi}{d\Theta} = \frac{2\pi}{d} \left[ -\frac{\cos \Theta}{\sin^2 \Theta} x_0 - \frac{1}{\sin^2 \Theta} x_1 \right]. \quad (4.4)$$

To maximize the MHFTR, we desire the round trip phase to remain constant as  $\Theta$  is varied and we therefore set  $\frac{d\psi}{d\Theta} = 0$ . Simplifying then suggests that Littrow configurations satisfying

$$x_0 \cos \Theta + x_1 = 0, \quad (4.5)$$

will result in maximal MHFTR. An effectively infinite range will result if  $x_1 = x_0 = 0$  [160]. Since the grating and grating arm have non-zero, finite thickness, Littrow designs satisfying Eqn. 4.5 for

---

<sup>4</sup>Other methods to achieve the same result exist, as demonstrated in the Toptica Photonics Inc. DL Pro, which employs a virtual pivot point [163].

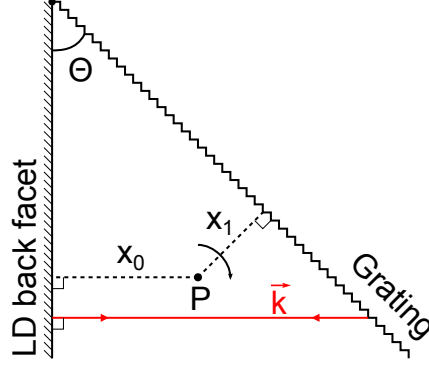


Figure 4.2: Geometry for derivation of optimal pivot point for Littrow configuration. The back facet of the laser diode is held fixed a distance  $x_0$  from the pivot point  $P$ . The grating rotates about  $P$  but is displaced from  $P$  by distance  $x_1$ . The angle between the back facet of the laser diode and the grating plane is  $\Theta$ . The wavevector  $k$  denotes the intra-cavity path of the laser light (—).

all  $\Theta$  can sometimes have fairly large or odd geometries [148]. For size and machining considerations, however, it is often preferable that  $x_1 \neq 0$ . Hence, we wish to determine how nonzero values of  $x_1$  limit the maximal MHFTR. We follow the procedure outlined in Ref. [164] to estimate the MHFTR for a given geometry and to determine the dependence of the MHFTR upon the value of  $x_1$ . We find that for  $x_1 \approx 1$  cm, the tolerance on the value of  $x_0$  needed to satisfy Eqn. 4.5 will require the back facet of the laser diode to be located within a  $\approx 3.4$  mm range relative to  $P$  for a 100 GHz MHFTR and to be located within a 300  $\mu\text{m}$  range to allow for a 1 THz MHFTR. Overall, we find the tolerance required to achieve a given MHFTR  $\lesssim 1$  THz is largely independent of the value of  $x_1$  and therefore nonzero  $x_1 \sim 1$  cm are not expected to significantly impact the MHFTR.

To reduce fragmentation, minimize design overhead, and allow for interchangeable parts, it is preferable that the ECDL design be wavelength-independent. Commercially available diffraction gratings restrict  $d$  to certain values, and therefore a wavelength-independent laser design must be able to satisfy Eqn. 4.5 for a continuous range  $30^\circ \lesssim \Theta \lesssim 60^\circ$ . In our physical laser design,  $x_1$  and  $P$  are fixed,<sup>5</sup> and Eqn. 4.5 is satisfied by varying  $x_0$ , achieved by manual translation of the cylindrical collimation tube (Thorlabs, LT230-B) holding the laser diode.

For ECDLs employing non-AR-coated diodes, the above analysis of the MHFTR's dependence upon geometry is further complicated by the significant reflectivity of the laser diode output facet, which divides the main ECDL cavity into two cavities. The first cavity consists of the laser diode back facet and the laser diode output facet (typical reflectivity  $\sim 30\%$  for  $\approx 660$  nm laser diodes) while the second cavity consists of the laser diode output facet and the grating. Synchronous scanning of both cavities is necessary to avoid mode-hops in addition to the conditions described by Eqns. 4.1 and 4.2. Since the length of the cavity internal to the laser diode cannot be easily changed physically, its effective length is varied instead by changing the index of refraction of the gain medium using

<sup>5</sup> $x_1$  is fixed by the thickness of the grating and grating arm while  $P$  is fixed because the grating holder must be rotated to satisfy Eqn. 4.2.



the injection current. The process of changing the injection current simultaneously with the piezo to prevent mode-hops is called a feed forward [142]. With a feed forward, the design presented here can achieve  $\gtrsim 20$  GHz MHFTR for non-AR-coated diodes. 40 GHz has been observed using non-AR-coated diodes in a similar, older design which is schematically the same as the current design. The feed forward results in intensity variation when scanning the laser which can be undesirable for some applications. In principle, it is possible to use the feed forward alone to achieve large MHFTRs using a Littrow ECDL with an AR-coated diode regardless of geometry [146, 165]. The optimal feed forward is not necessarily linear and performance may be improved with an additional quadratic term [155]. Without feed forward, our lasers with non-AR-coated diodes scan  $\sim 2$ -4 GHz. Additional details of the design, construction, operation, setting of the feed forward, troubleshooting, and observations on ECDLs similar to the one presented here are available in [Appendix C](#).

### 4.3 Electro-optic modulators

Because all but two lasers in the experiment are used to drive transitions from multiple SR/HF levels simultaneously (and thus require multiple frequencies), we build our own EOMs using LiTaO<sub>3</sub> crystals and use phase modulation to create the necessary sidebands. The general EOM design is based on [166], and the first EOMs were built by David Glenn [167] and have subsequently been built by Eric Norrgard. We briefly review the theory (Ref. [168]) and construction principles (Refs. [166, 167]) of EOMs, with the suggested references available for further reading. We then discuss specific issues with and possible improvements to the current design. We note that all commercial free-space EOMs we have seen display the problems identified, and we demonstrate at least fair progress in resolving these problems.

#### 4.3.1 Simple phase modulation theory

Application of a voltage difference  $V_0$  across a crystal of length  $l$ , with electrode spacing equal to the crystal thickness  $d$ , creates an electric field  $E_0 = V_0/d$  inside the crystal. The change in the index of refraction due to the electric field is given by

$$\Delta n = n_0^3 r \frac{E_0}{2}, \quad (4.6)$$

where  $n_0$  is the unperturbed index of refraction of the crystal and  $r$  is the appropriate element in the electro-optic tensor for the specific orientation of the crystal and polarization of incident light [169]. Light of wavelength  $\lambda$  passing through the crystal experiences an additional phase shift, which we denote as  $M_{\text{mod}}$ , given by Ref. [168]

$$M_{\text{mod}} = \frac{2\pi}{\lambda} l \Delta n \quad (4.7)$$

$$= \frac{\pi n_0^3 r V_0}{\lambda} \frac{l}{d}, \quad (4.8)$$

where we have substituted in Eqn. 4.6.  $M_{\text{mod}}$  is commonly referred to as the modulation index. A commonly-used specification for EOMs is the half-wave voltage

$$V_\pi = \frac{\lambda}{n_0^3 r} \frac{l}{d}, \quad (4.9)$$

which results in  $M_{\text{mod}} = \pi/2$  (from Eqn. 4.7). We now consider the case where the applied voltage varies in time. Prior to passing through the crystal, the electric field of the unmodulated light is given by

$$E(t) = E_0 e^{i\omega_c t}, \quad (4.10)$$

where  $\omega_c = 2\pi c/\lambda$  is the carrier frequency. This light is then sent through the crystal with the polarization aligned along the axis perpendicular to the surface electrodes. For a sinusoidally varying voltage  $V(t) = V_0 \sin \omega_m t$  applied across the crystal electrodes, the output light is described by

$$E_{\text{pm}}(t) = E_0 e^{i\omega_c t + iM_{\text{mod}} \sin \omega_m t}, \quad (4.11)$$

where the subscript pm denotes phase modulation (PM). Equation 4.11 can be rewritten using the Jacobi-Anger expansion as

$$E_{\text{pm}}(t) = E_0 e^{i\omega_c t} \left[ J_0(M_{\text{mod}}) + \sum_{k=1}^{\infty} J_k(M_{\text{mod}}) e^{ik\omega_m t} + \sum_{k=1}^{\infty} (-1)^k J_k(M_{\text{mod}}) e^{-ik\omega_m t} \right], \quad (4.12)$$

where  $J_k$  is the  $k^{\text{th}}$  order Bessel function of the first kind. Eqn. 4.12 gives the amplitudes and relative phases of all the sidebands. The intensity of the light is then given by  $I(t) = \frac{1}{2} \epsilon_0 c |E_{\text{pm}}(t)|^2$ . It is worth noting that although it is not obvious from Eqn. 4.12,  $I(t)$  is constant in time which is easily seen from Eqn. 4.11.

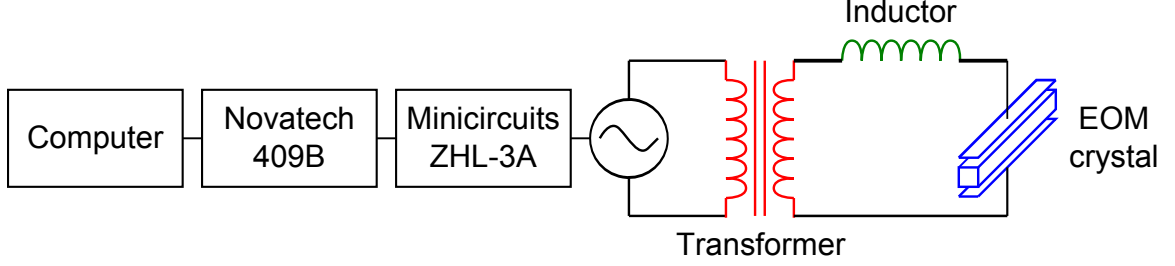


Figure 4.3: EOM circuit and drive electronics.

### 4.3.2 Construction and components

The EOM crystal is supplied by Almaz Optics and is a Y-cut (as needed for phase modulation)  $3.0 \times 3.0 \times 40.0$  mm LiTaO<sub>3</sub> crystal with both ends AR-coated for 600-1100 nm and Cr+Au electrodes on the two Z sides of the crystal. The EOM circuit and drive components are shown in Fig. 4.3. A computer controls a 4-channel direct digital synthesizer (Novatech, 409B) which is amplified (Minicircuits, ZHL-3A) and impedance matched using a transformer to the rest of the EOM circuit shown in Fig. 4.3. Components in the circuit are selected as follows: the resonant frequency of the EOM is given by

$$\omega_{\text{res}} = \frac{1}{\sqrt{LC}}, \quad (4.13)$$

where  $L$  and  $C$  are the inductance and capacitance in the EOM circuit. The DC capacitance of the crystal is approximately 15 pF. Thus for a given target  $\omega_{\text{res}}$ , the known value of  $C$  and Eqn. 4.13 determine the needed  $L$ . The  $L$  and  $C$  will have a characteristic impedance, denoted  $Z_{LC}$ , of a few Ohms which can be measured with a network analyzer. The approximate desired transformer will have turn ratio  $\approx 50/Z_{LC}$  for optimal impedance matching to 50Ω. Sometimes a commercial transformer is used; other times the transformer is wrapped manually ourselves. Addition of the transformer usually changes the inductance of the circuit, thereby shifting  $\omega_{\text{res}}$ , but this can usually be accounted for by adjusting the number of turns around the inductor (either actually changing the number of turns or just pushing the wire around). Optimal selection of transformer and inductor to achieve maximum  $M_{\text{mod}}$  for a given  $f_{\text{mod}}$  is quite complicated,<sup>6</sup> and we are not qualified to offer advice on this matter and instead refer the reader to Ref. [170] for the general case. However for making EOMs with  $f_{\text{mod}} \approx 40$  MHz, a 16:1 commercial transformer (Minicircuits, XFA-0101-16UH) and a 1/8 inch diameter Teflon core inductor with  $\sim 30$  turns works reasonably well. We do not know how far this solution is from optimal.

<sup>6</sup>The phase space of choices is quite large. Transformer choices include material, size, winding method, wire insulation choice, etc. Inductor choices are similar.

### 4.3.3 Current problems

The current EOM design has several shortcomings. To create large order sidebands ( $M_{\text{mod}} \gtrsim 5$  radians) the EOM must be driven with a large amount of RF power ( $\sim 1 - 2$  watts typically). Empirically, a good fraction of this power is dissipated over the LiTaO<sub>3</sub> crystal. The dissipation of heat has two main unwanted effects: The output beam is angularly (and possibly spatially) shifted and the EOM resonance and modulation index (both of which display significant hysteresis) are sometimes shifted as well.<sup>7</sup> These effects are highly undesirable because the EOM sidebands cannot be repeatedly chopped from on to off or from off to on, as is sometimes desirable to do between successive molecular pulses.

To combat both of these problems, a prototype EOM design is fabricated where the EOM crystal is sandwiched between two large pieces of OFHC copper and good thermal and electrical contact is ensured by using strips of 75  $\mu\text{m}$  thick 99.995% pure indium between the crystal electrodes and the OFHC copper. While this construction does not address the thermal conductivity of the crystal itself, it should vastly improve the thermal-related stability of the EOM relative to the same crystal mounted on either stainless steel (as in Thorlabs EO-PM-NR-C1), directly on a PCB (as in Ref. [167]), or on a thin 1/8" aluminum plate (as in the current design). In practice, the OFHC/indium construction is only partially successful; it merely extends the time constant of the beam shift upon applying or removing RF power from several seconds to a time on the order of 10 minutes. However, this design is likely sufficient to enable stable performance in a scheme where EOM sidebands are chopped on and off at a rate  $\sim 1$  Hz.

The beam shift is likely not due solely to the changing index of refraction of the crystal as the crystal heats up. Were this the case, we would expect a laser aligned exactly normal to the crystal surface to experience no spatial or angular shift. To test this hypothesis, a laser is aligned into a fiber. The EOM with no RF frequency is then inserted into the beam path before the fiber and, using a tip-tilt stage, is positioned so that maximal coupling into the fiber is again achieved. This alignment should ensure that the laser is completely normal to the EOM surface. However when the RF is turned on, the fiber coupling efficiency slowly decreases over  $\sim 10$  minutes. We speculate that this effect could arise from a thermal gradient and hence an index gradient, and we are continuing

---

<sup>7</sup>Often we wish to maximize the value of  $M_{\text{mod}}$  to create a large number of sidebands but are insensitive to the exact value of the EOM frequency  $f_{\text{mod}}$ . To achieve the largest value of  $M_{\text{mod}}$ , the value of  $f_{\text{mod}}$  is tuned to the resonant frequency of the EOM circuit. In practice with the current design, changing  $f_{\text{mod}}$  alters the heat load dissipated in the EOM crystal (and possibly in other components of the circuit) and causes the circuit resonance to shift. Due to the empirically long time constant ( $\sim 5$  minutes for the current EOM design) for thermal equilibration of the circuit,  $f_{\text{mod}}$  must be slowly adjusted in time to achieve maximum values of  $M_{\text{mod}}$ . If the EOM is subsequently turned off, the crystal will cool and turning the RF back on can sometimes result in a very different value of  $M_{\text{mod}}$  for the same value of  $f_{\text{mod}}$  and applied RF power.

to work to understand this behavior.

Hopefully in the future these issues with the home-built EOMs will be solved. Fiber EOMs made by companies such as Jenoptik avoid many of the above issues and offer high values of  $M_{\text{mod}}$  for a large range of frequencies, but at  $\sim \$6,000$  per fiber EOM, this option is cost-prohibitive to include on all of our ECDLs.

## 4.4 Laser amplifiers

In some cases, more laser power may be desired than can be produced by a single ECDL alone. This section details the two kinds of amplifiers used in our lab: injection-seeded slave laser diodes (hereafter referred to as injection-seeded slaves) and tapered amplifiers.

### 4.4.1 Injection-seeded slave

The use of an injection-seeded slave is an effective way to increase the optical power delivered to the experiment. For an injection-seeded slave and an ECDL using the same laser diode, the slave is expected to provide more laser power since there is no need to divert a fraction of the output light for feedback, locking, or wavelength measurement as is required with an ECDL.

The slave laser diode is held in a mount (Thorlabs, TCLDM9) epoxied to a steel block affixed to the optics table. The Thorlabs mount includes a thermoelectric cooler (TEC) for temperature control. The output of the slave laser is collimated with a collimating lens (typically Thorlabs, C330TME-B) which screws into an adapter (Thorlabs, S1TM09) which screws into the faceplate of the slave mount. The procedure for collimating the slave is not substantially different than for collimating a laser diode in an ECDL.<sup>8</sup> A typical slave laser setup is shown in Fig. 4.4. After the collimation lens, light from the slave travels through a half ( $\lambda/2$ ) waveplate and then a Glan-type polarizer mounted at an angle of 45 degrees to vertical. The light then passes through a Faraday rotator oriented to rotate the light so that it leaves the Faraday rotator vertically polarized. The waveplate is rotated to maximize the power exiting the Faraday rotator. The slave light then impinges upon a polarizing beam splitter (PBS) where, since it is vertically polarized,  $\sim 99.5\%$  is reflected. From there, the slave light is aligned into a single-mode polarization-maintaining (PM)

---

<sup>8</sup>The TCLDM9 mount is epoxied to the steel base in such a way that the TCLDM9 faceplate can be translated slightly (subject to the screw / clearance hole tolerance) in both directions perpendicular to the light emission. The collimation lens is screwed entirely into the S1TM09 adapter. The x and y position are adjusted by loosening the faceplate screws and prodding the faceplate. The use of washers on the faceplate screws can increase the translation range if needed (by elevating the screw heads above the counterbores of the faceplate). The z position of the lens is adjusted by rotating the S1TM09 adapter.

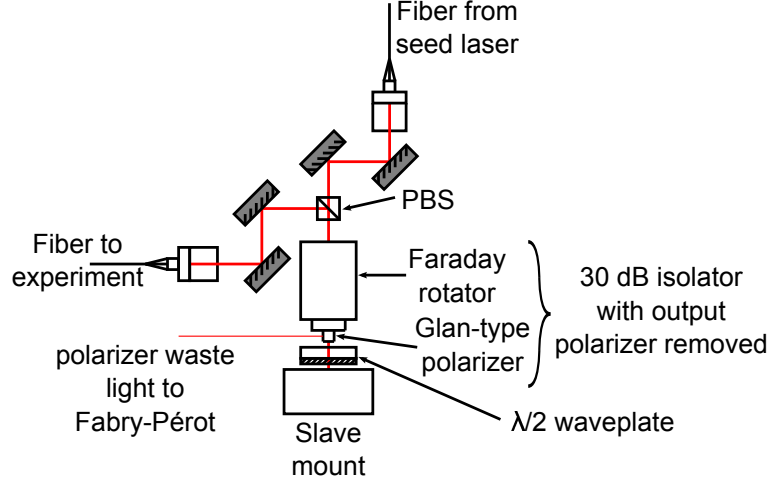


Figure 4.4: Slave laser injection setup. The fiber from the seed laser is oriented so that a half ( $\lambda/2$ ) waveplate is not needed for seed light transmission through the PBS.

fiber to be sent to the experiment. We have achieved up to 77% coupling efficiency of an injection-seeded slave into a single-mode PM fiber with this setup. In this case the slave diode collimation lens was a Thorlabs C330TME-B lens, and there were no additional beam shaping optics. In some cases an additional telescope is used to improve the coupling efficiency of the slave light into the fiber.

The slave is ideally seeded from a single-mode PM fiber which delivers  $\approx 5$  mW to the slave. Power significantly below this generally results in the slave laser coming unlocked often. The seed fiber polarization axis is oriented in the fiberport to avoid using a half waveplate. The seed light is then aligned to pass straight through the PBS in order to inject the slave. The seed alignment of a slave diode is simple if the setup matches that shown in Fig. 4.4. Some of the output light from the slave will leak through the PBS and be incident on the seed fiberport (typically Thorlabs, PAF-X-11-B). To optimize the seeding of the slave, we simply optimize the coupling of this “waste” light backwards through the fiber. Sometimes a telescope is used to increase the coupling of seed light into the slave laser. In some cases, alignment of the seed light is done with no mirrors, using only the fiberport degrees of freedom for alignment.

In general, the desired properties of a slave are that it produce the desired output power and remain locked to the master laser at all times. Each slave is continuously monitored by sending the waste light from the Glan-type polarizer to a Fabry-Pérot. Empirically we find the slaves stay locked longest when the temperature is tuned so that the slave’s free running wavelength (wavelength when the seed light is blocked) matches the seed laser’s wavelength as closely as possible ( $\lesssim 10$  GHz).

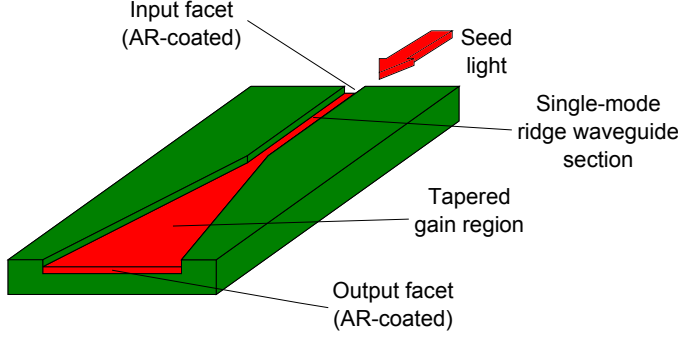


Figure 4.5: Geometry of a TA chip. Seed light is coupled into the TA chip via a single-mode ridge waveguide section before entering the tapered gain region where the light is amplified. The geometry of the tapered gain region is engineered to approximately match the diffraction of the seed laser. Both input and output facets are AR-coated to prevent parasitic lasing.

It is conceivable that the additional heat load from the seed light could shift the optimal slave temperature, but this is ignored. The current to the slave laser diode is then tuned to the middle of the range where the slave locks to the seed. For some slaves this range is as high as  $\sim 4$  mA and for others it is  $< 1$  mA. If the slave comes unlocked, its current is adjusted to the middle of the range where it achieves seeding again. When the experiment only had 5 slaves, there were days when no slave came unlocked. If the unlocking of slaves becomes more problematic in the future, potential solutions exist [165].

The slave lasers are turned off at the end of every day. If possible, the slave diode is wavelength selected so that its operating temperature at the desired wavelength is  $\sim 15$  °C. We believe this to be a good temperature to balance the increased risk of condensation at lower temperatures with the increased longevity of the slave diode when operated at lower temperatures. The injection current supplied to each slave laser is very aggressive and almost always in excess of factory specified standard conditions. For example, one slave laser<sup>9</sup> we have is specified to be injected with 75 mA (and produce 50 mW). In our implementation however the slave temperature is set to  $\sim 15$  degrees Celsius, and the diode is injected with a current of 120 mA and produces  $\sim 100$  mW. This laser has lasted  $\approx 2$  years under these circumstances. We believe the key is to run the laser at a low temperature and to turn it off when it is not in use, i.e. at the end of every day. Each slave laser takes  $\sim 10$  minutes to warm up every day. During this time the laser will quickly hop around in frequency as the laser diode reaches thermal equilibrium. We have not seen any evidence of problems due to insufficient optical isolation in our slave lasers.

#### 4.4.2 Tapered amplifier

The output power of single-mode laser diodes is typically limited by thermal damage induced by the heat-load of the laser beam on the input/output facets. By increasing the size of the output

<sup>9</sup>This slave uses a Opnext HL6750MG laser diode.

facet, larger powers may be obtained, but the quality of the resulting spatial mode will be poor. One solution to this problem is a type of diode laser called a tapered amplifier (TA) which is schematically shown in Fig. 4.5. Seed light is coupled into a ridge waveguide (RW) section of the TA that acts as a spatial mode filter (similar to a single-mode fiber). Following the RW section, light then enters a tapered gain section whose geometry is engineered<sup>10</sup> to approximately match the spatial diffraction of the seed laser. The light is amplified in a single pass through the tapered region and exits through a large AR-coated output facet. In this way high output powers can be achieved without a reduction in beam quality. As an example, for 663 nm laser diodes, the highest power single-mode diodes currently available are specified to produce 130-150 mW. However, a TA (Eagleyard Photonics EYP-TPA-0670-00500-2003-CMT02-0000) at that wavelength can produce 500 mW.

Unfortunately, commercially available TA systems are fairly expensive ( $\sim$  \$20k-\$30k, depending on options). For most popular wavelengths, including 663 nm, TA chips are available alone for  $\approx$  \$2k. (However, TA chips at  $\sim$  690 nm currently cost  $\approx$  \$8k.) Since our experiment will likely need a fair number of TAs in the future (as of this writing we have 2), it was deemed best to design our own. The two existing TA designs within the DeMille lab had each suffered from at least one fairly serious issue. The first design has no easy way to adjust the x or y position of the input or output collimation lenses. In practice any adjustment was done by shimming the lens holder with little strips of aluminum foil (vertical alignment) or by manually screwing and unscrewing the lens holder in the hopes that one could luckily get the horizontal alignment just right. This made any sort of alignment extremely tedious and time intensive. The second design, illustrated in Fig. 4.6, suffered from a different flaw. As shown, the collimation lenses are connected to the heat sink or “exhaust” side of the TEC. Given that our 663 nm TAs are specified to draw a maximum of 1 amp with a voltage drop of  $\sim$  2.5 volts while producing  $\approx$  500 mW of laser power, this indicates that  $\approx$  2 watts is dissipated as heat. When this TA is turned on, the extra heat generated by the TA is deposited on the “exhaust” side of the TEC. Since the collimation lenses are attached to this side of the TEC, thermal expansion will cause the lenses to shift in position. The thermal conductivity through this path is quite low due to both the materials used (some steel) and due to the necessarily low cross sectional area of part of the flexure mount on which the collimation lenses are mounted. Therefore if the temperature setpoint of the TA is changed or the TA is turned on after being off, it takes a long time (typically  $\sim$  3 hours) for the entire system to reach thermal equilibrium. Only then will the pointing of the TA become stable. Due to this fatal flaw, this TA could not be turned

---

<sup>10</sup>The authors of Refs. [171, 172] fabricated TAs with a variety of tapered angles and empirically determined which tapered angle worked best based on the quality of the output beam.



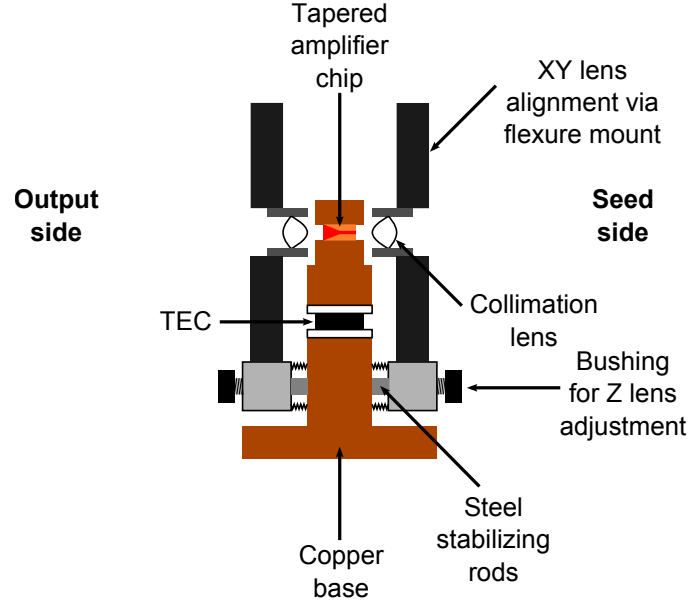


Figure 4.6: This tapered amplifier design suffers from poor thermal design. Not only are the collimation lenses not thermally stabilized, but varying thermal loads when the TA is turned on and off cause the position of the lenses to change since they are connected to the “exhaust” side of the TEC.

off, and this likely led to its eventual failure.

Based on these experiences, we designed a third-generation TA. The considerations for a TA design are similar to that of an ECDL although some points bear emphasizing. If the TA is turned on and off daily (as suggested to prolong the life of the TA), the thermal cycling can cause consistent misalignment of a laser beam. Hence the mechanical stability of the TA upon thermal cycling (given our experience with the aforementioned design) is paramount. The core difficulty is that allowing the positions of two objects to be adjusted relative to each other often requires minimizing their mechanical contact, which minimizes the thermal contact between the two parts (as can be seen, e.g., in the design of a mirror mount).

Our solution to this problem, shown in Fig. 4.7, forms the basis of our TA design. A movable brass part holding a collimation lens is attached to a fixed brass bracket via four large screws with two washers on each screw. Thermal paste (Arctic Silver 5) is applied between the two brass parts. The movable brass part may be translated in the  $x$  and  $y$  directions (the directions perpendicular to the laser propagation) via pushing forces from several setscrews. The four large screws with washers are tightened as much as permitted without impeding smooth translation of the movable brass part. Due in part to the layer of thermal paste between the two brass parts which acts as a lubricant, the screws can be made tight enough for good mechanical and thermal contact while still allowing

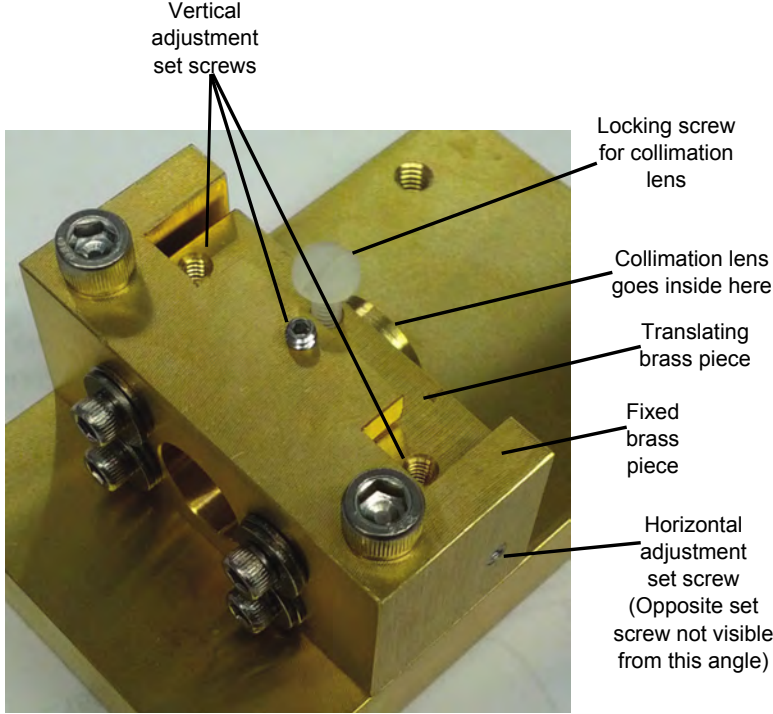


Figure 4.7: Collimation lenses for both the input and output of the TA are attached to a brass part which is translated vertically and horizontally using set screws. This part is attached to a fixed brass part using four larger screws. The screws are tightened as much as possible while still allowing for smooth translation of the movable brass part. Thermal paste between the two brass parts ensures good thermal contact and facilitates easier translation as well. Overall, this design allows good thermal contact and mechanical stability while allowing for translation of the collimation lens.

for smooth translation. The collimation adjustment of the lens is done with a spanner wrench. Empirically, this setup is thermally and mechanically stable, and we have been very satisfied with this design. Fig. 4.8 shows a picture of the finished TA.

#### 4.4.3 Tapered amplifier setup and alignment

Optimal alignment of certain TAs is the hardest alignment task in our lab.<sup>11</sup> The fundamental issue is that TAs do not operate as true single-mode devices, i.e. they support more than a single transverse mode.<sup>12</sup> Consequently, the spatial mode structure of the TA output depends upon the spatial mode structure and alignment of the seed beam. Thus, optimizing the input beam alignment and shape for maximum TA output power is unproductive if the light is to be eventually coupled into a single-mode fiber. This is expanded upon later in this section.

Input seeding and output coupling of the TA are shown in Fig. 4.9. Fiber-coupled seed light passes through a 2:1 telescope and a 4X anamorphic prism pair (APP) before coupling into the

<sup>11</sup>This section is based on our experience with three different 663 nm TA chips. Preliminary evidence suggests that the TA difficulties described in the following section may be specific to the 663 nm tapered amplifiers we have been using. All three 663 nm TAs we have used have displayed the difficulties with alignment described in this section. Interestingly, a 690 nm TA from the same vendor which we recently set up displays none of these complications.

<sup>12</sup>We do not fully understand the reason for this behavior. The multi-mode behavior may be caused by the fact that the input ridge waveguide section of the device is not long enough to fully extinguish all but the lowest order mode. Alternatively, the input facet might not be quite narrow enough to ensure single spatial mode operation. The ridge waveguide section is likely 750  $\mu\text{m}$  long and 7.5  $\mu\text{m}$  wide [171] while the ridge waveguide section of high power single-mode ridge waveguide laser diodes in this wavelength regime are typically 2.0-2.5  $\mu\text{m}$  wide [173].

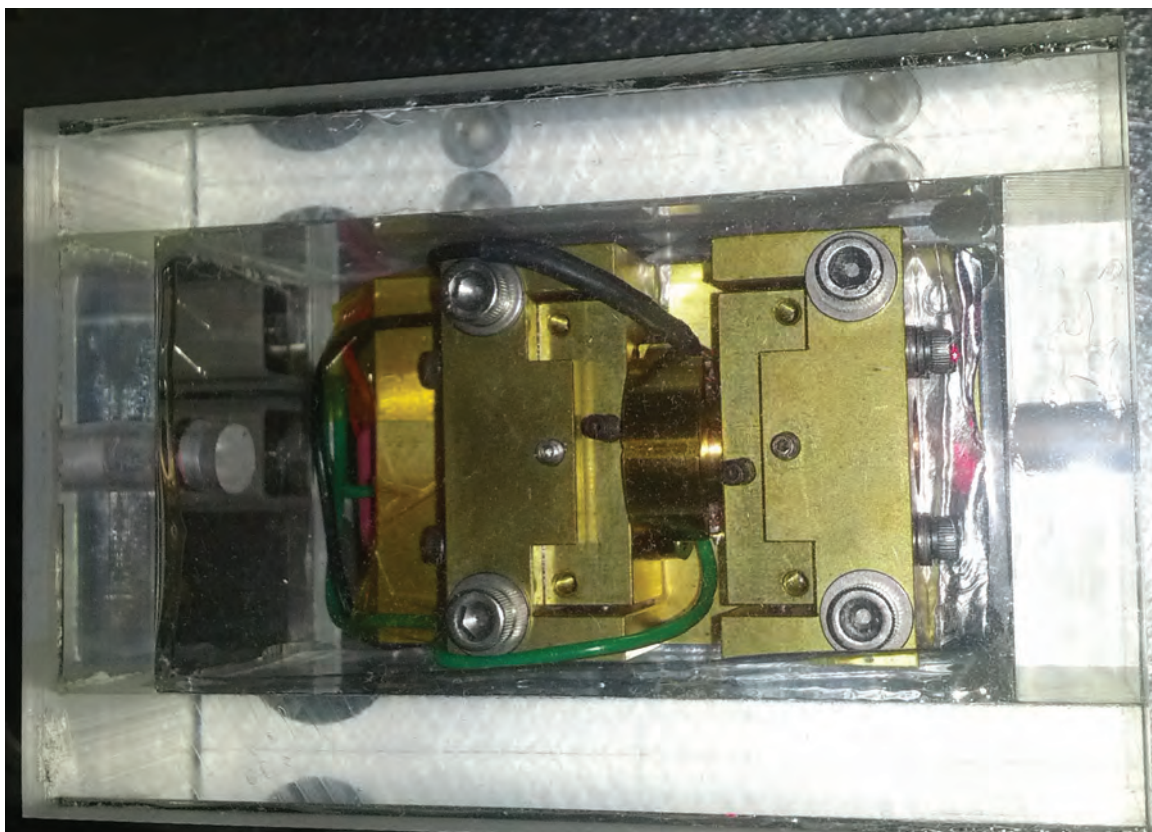


Figure 4.8: Picture of a finished TA in use in the experiment.

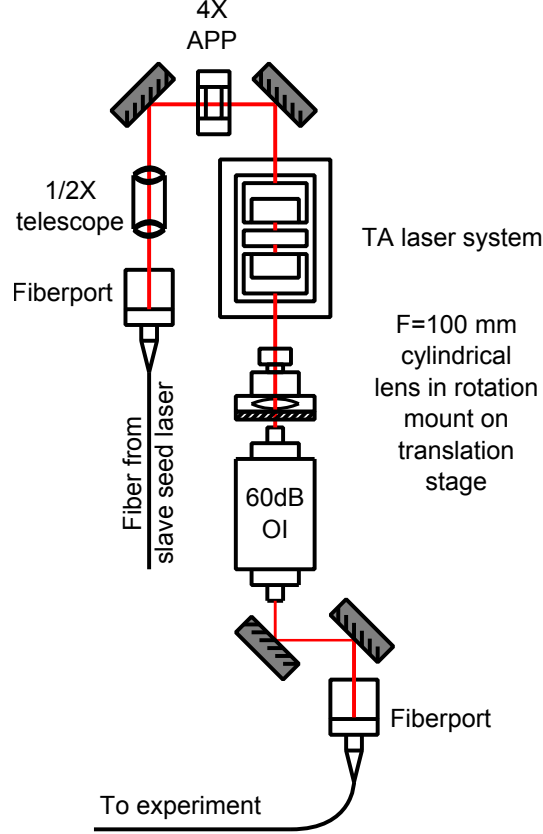


Figure 4.9: Overall setup of input seeding and output coupling of TA.

input RW section of the TA via an aspheric lens (Thorlabs, C230TME-B). The output of the TA is collimated by a similar aspheric lens (Thorlabs, C330TME-B). Due to the high aspect ratio of the TA output facet, the beam divergence is greater in the horizontal direction than the vertical. This is corrected by placing a cylindrical lens downstream at the point where the full width half maximum (FWHM) of the beam is the same for the vertical and horizontal directions. The focal length of this lens should be approximately equal to its distance from the initial collimation lens of the TA. We have found that TAs from the same batch can have different output mode structures and therefore the correct focal length of this cylindrical lens can vary. We have used focal lengths of 100 mm and 250 mm. To facilitate easier positioning, this lens is placed in a rotation mount on a small translation stage. Isolation is provided by a 60 dB optical isolator (Conoptics 716) which is placed either before or after the cylindrical lens. Lastly, the light is coupled into a single-mode PM fiber using a fiberport (Thorlabs, PAF-X-11-B). It is conceivable that an additional telescope could increase the coupling efficiency. With the latest TA, we have achieved 68% coupling efficiency into the single-mode PM fiber, although achieving this is quite time consuming, as described next.

The  $M^2$  of the TA output beam strongly affects the coupling efficiency of the TA light into a single-mode PM fiber through which the light is delivered to the experiment. The beam profile (and therefore the  $M^2$ ) of the TA output beam is affected not only by the x and y position of the output collimation lens and the cylindrical lens (as expected) but also by the parameters of the input beam (size, aspect ratio, collimation, angular alignment) as well. Because effective seeding of the TA requires both a telescope and an anamorphic prism pair, the number of parameters affecting the profile of the output beam is very large. More unfortunate is that certain parameters (input telescope, input anamorphic prism pair, focal length of cylindrical lens on the output) are not continuously variable, at least not easily so,<sup>13</sup> and therefore varying these discrete parameters typically requires realignment of some of the other elements. Ultimately, the entire system is coupled together and alignment is achieved not by a deterministic approach, but rather by iteratively varying all parameters.<sup>14</sup> The lack of a completely deterministic approach to seeding the TA is the main reason why TA alignment is so tedious and time consuming.

Unlike infrared (IR) wavelength TAs, red wavelength TAs like ours have a gain of typically 10. Thus to achieve the specified output power of 500 mW, 50 mW must be delivered to the TA. We seed the TA using a single-mode PM fiber from the master laser. This cleans up the mode and isolates the two systems.<sup>15</sup> However this approach then requires an ECDL master laser to produce enough power so that after the 60 dB isolator (90% transmission), EOM (90% transmission), fiber coupling losses ( $\sim 60 - 70\%$  efficiency), etc., 60 mW is be delivered out of the fiber to the TA. This ultimately required master ECDL outputs of  $\sim 140$  mW and drive currents of  $\sim 230 - 250$  mA. As we found out empirically several times, neither the ML101J27 nor the ML101U29 laser diodes would last much longer than a month or so when driven at these high currents ( $\gtrsim 220$  mA) in an ECDL configuration. Ultimately a slave laser was inserted in between the master ECDL and each TA.

#### 4.4.4 Tapered amplifier protection circuit

The high cost of TA chips makes using a protection circuit prudent. The protection circuit employed for our TAs is diagrammed in Fig. 4.10 and is derived from the design presented in Ref. [174] but

<sup>13</sup>Our experience with zoom beam expanders is that they can display significant hysteresis and therefore are a poor choice for this application.

<sup>14</sup>Maximizing the coupling of the backwards emitted amplified spontaneous emission (ASE) from the TA into the seed fiber did not result in either the highest TA output powers or the highest powers coupled from the output beam into a single-mode fiber. However, turning the TA off and coupling the seed laser light (through the TA) into the output fiberport was more helpful. Coupling light from the output fiberport backwards through the TA (off in this case) into the input seed fiberport also appeared to be somewhat helpful. We experienced the difficulty described with three different 663 nm TAs.

<sup>15</sup>This is particularly useful so that should the master laser fail, realignment of the TA beamline is not necessary.

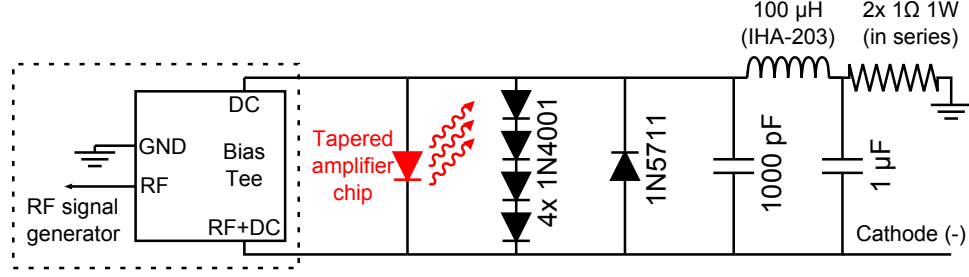


Figure 4.10: TA protection circuit as described in the main text. The optional bias tee is generally not employed.

modified for larger currents. The two  $1\ \Omega$  1 watt resistors are chosen so that the circuit will hit the current controller's compliance voltage at the maximum recommended current for the TA chip. These resistors, along with a  $1\ \mu\text{F}$  capacitor, form a low-pass filter. Another low-pass filter is formed by a  $100\ \mu\text{H}$  inductor (Vishay, IHA-203) and a  $1000\ \text{pF}$  capacitor. The TA is protected from reverse biasing by a 1N5711 diode and from excessive forward voltage by four 1N4001 diodes. Four diodes are used so that the cumulative turn-on voltage of the 1N4001 diodes is slightly greater than the TA's voltage at the maximum recommended current.

#### 4.4.5 Additional TA experiences

At one point we seeded a TA with two frequencies separated by  $\delta \approx 40\ \text{MHz}$ . Light from a master ECDL was sent through a  $40\ \text{MHz}$  AOM. The fundamental and diffracted beams were then combined on a 50/50 beam splitter and sent through a single-mode PM fiber before seeding the TA. As shown in Fig. 4.11, the output spectrum shows that for low injection currents, only the two injected frequencies are amplified. As the injection current is increased however, additional sidebands appear with spacing  $\delta$ . At  $900\ \text{mA}$  injection current, the additional sidebands are  $\sim 40\%$  the total intensity. Similar additional sidebands were observed elsewhere in a comparable setup for frequencies  $\delta \leq 2\ \text{GHz}$  [175]. These additional sidebands are likely due to beating between the two injection frequencies which in turn modulates the injected seed light intensity with frequency  $\delta$ . This effect is not observed for a TA seeded with light from an EOM. The difference is that the amplitudes of the different frequencies present in light which is phase modulated conspire to produce a total intensity that does not vary in time. (See subsection 4.3.1.)

We also attempted to modulate the TA injection current in order to phase modulate the output light. It was hoped that changing the current density in the TA would result in a large enough change in the refractive index that we could eliminate the use of a resonant EOM in favor of



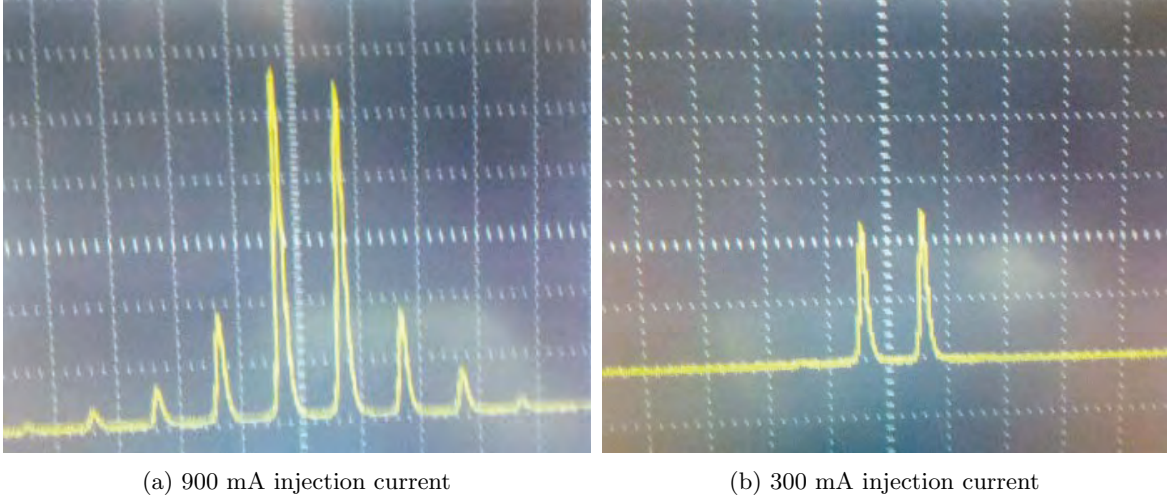


Figure 4.11: Fabry-Pérot scan showing the occurrence of additional sidebands for large TA injection currents (a) but not for small TA injection currents (b) when the TA is seeded with two frequencies separated by  $\delta \approx 40$  MHz which are generated using a single master laser and an AOM. In both panels, the spacing between the two central peaks is  $\delta$ . Additional sidebands in panel (a) are also spaced by  $\delta$ .

direct modulation of the TA current instead. The latter appeared favorable because direct current modulation would not be limited to a single frequency, as is the case with a resonant EOM. The TA injection current modulation was achieved by inserting a bias tee (Universal Microwave Components Corporation, BT-0500-LS) into the circuit shown in 4.10 and applying RF to the RF port of the bias tee. Unfortunately, even RF drive powers large enough to produce  $\sim 20\%$  peak-to-peak modulation of the total TA output power resulted in sidebands with a few percent of the total output power for modulation frequencies 2–20 MHz. The relatively small amount of modulation observed is consistent with amplitude modulation rather than phase modulation. Another group produced sidebands with  $\approx .3\%$  relative amplitude at 6.6 GHz with an RF drive power of 35.1 dBm [176]. They believe the low efficiency results from extremely poor impedance matching between the  $50\ \Omega$  bias tee and the TA chip ( $\sim 3\ \Omega$  impedance). It is not yet fully understood why no phase modulation was observed.<sup>16</sup>

## 4.5 Fabry-Pérot

In the absence of a frequency comb, strong iodine lines,<sup>17</sup> or a vapor cell [177], an alternative method must be used to frequency stabilize the ECDLs. Initially we considered stabilizing our ECDLs to

<sup>16</sup>In contrast, even modest modulation of the injection current of an ECDL produces sidebands with a modulation index  $\gtrsim 10$ .

<sup>17</sup>An iodine-based saturated absorption lock was created using an ECDL at 663 nm, but due to the small partial linewidths of iodine transitions at wavelengths  $\sim 663$  nm, the lock required  $\gtrsim 50$  mW of laser power and a lock-in amplifier and thus was deemed unsuitable for our experiment.

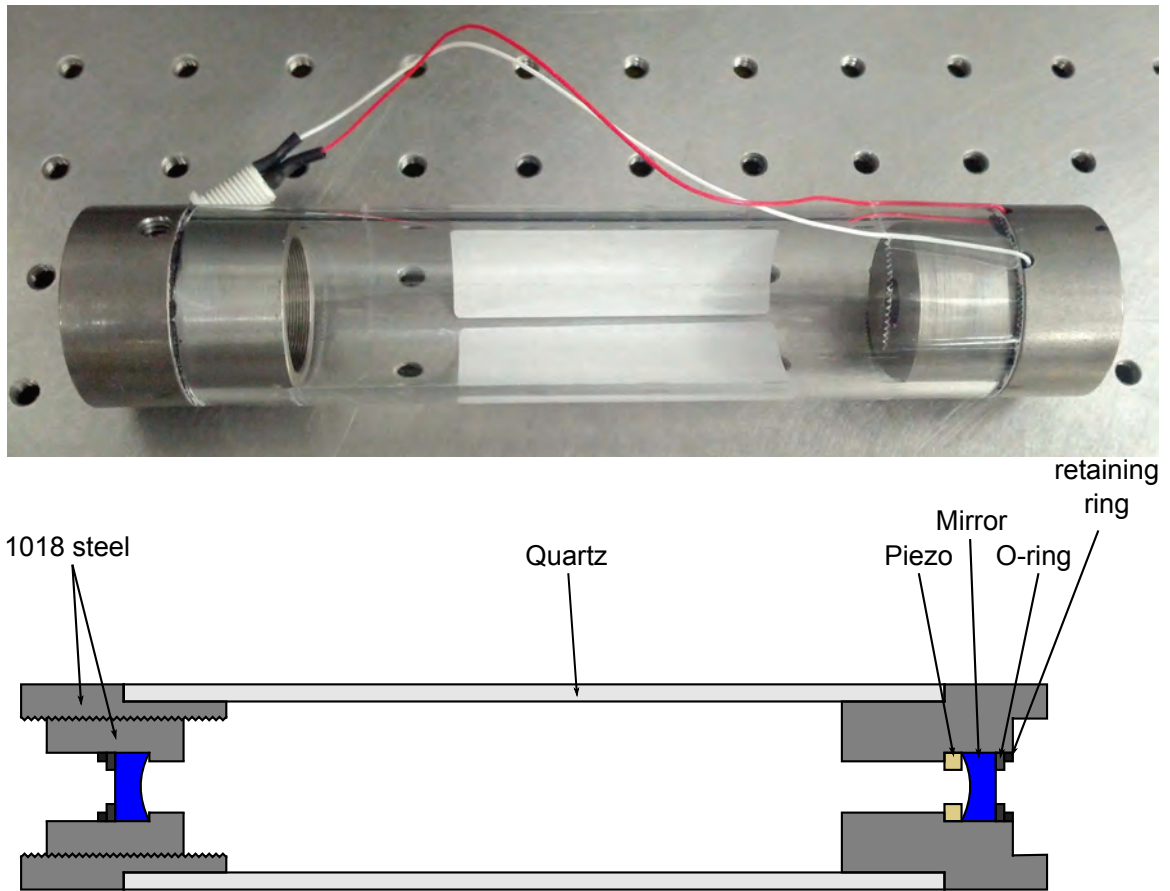


Figure 4.12: Example of home-built Fabry-Pérot used to lock lasers and for laser diagnostics. The top panel shows an actual picture of a 500 MHz FSR Fabry-Pérot while the bottom panel depicts a conceptual schematic of the same Fabry-Pérot.



Fabry-Pérots alone and engineering the necessary Fabry-Pérots to have resonances stable to a 1 MHz range. While this is commonly done with ULE and Zerodur cavities costing  $\gtrsim$  \$5000 and housed in UHV vacuum chambers pumped on with ion pumps, achieving the same performance with cheaper materials is challenging. Two main sources of Fabry-Pérot drift are thermal expansion of components and pressure variation which changes the index of refraction. We therefore settled upon the current solution for our experiment, where Fabry-Pérots are instead used to transfer the frequency stability of a frequency-stabilized HeNe laser (discussed in a later section) to the ECDLs. For this purpose, a Fabry-Pérot should have a finesse  $\gtrsim 1000$  to accurately resolve the position of the laser resonances (peaks), should have minimal drift,<sup>18</sup> and should be cheap. Fabry-Pérots are also used for general laser diagnostics, but this application is far less demanding than locking.

Although the frequency-stabilized HeNe provides the absolute frequency reference in our current setup, drift of the Fabry-Pérot is still undesirable. When used for locking, if the Fabry-Pérot drifts one or more free spectral ranges (FSRs), the position of the ECDL peaks relative to the HeNe's will change since  $\lambda_{\text{HeNe}} \neq \lambda_{\text{ECDL}}$ . In principle, if the Fabry-Pérot has drifted a known number of FSRs, it is possible to calculate the new positions of the ECDL peaks based on their old positions. In practice, ECDL resonances differed from the expected value by  $\sim 5$  MHz between adjacent FSRs. While the origins of this effect are currently being investigated, we theorize this effect is caused by a non-linearity of the piezo itself or its integration into the Fabry-Pérot system. Furthermore, it is fairly easy to experimentally determine whether or not the Fabry-Pérot is on the same FSR as before, but the determination of how many FSRs the Fabry-Pérot has drifted is more involved. Finally, because the piezo has a finite range, only a finite amount of drift can be corrected for by the piezo; hence, even when the piezo scan range is actively locked (by referencing the HeNe transmission peaks) to a particular FSR of the cavity,<sup>19</sup> long-term drift may eventually make it impossible to maintain scanning across this FSR. Thus, for multiple reasons, it is highly desirable that the Fabry-Pérot does not drift even though it is not used as a frequency reference itself.

---

<sup>18</sup>While the Fabry-Pérot is not relied upon in the current scheme as the frequency reference, there are significant benefits to employing a Fabry-Pérot whose drift is small enough to employ the same free spectral range of the Fabry-Pérot over several months or even years. This is discussed later in this section.

<sup>19</sup>Typically, when we refer to a particular FSR of the cavity, we are referring to the range of frequencies between two adjacent HeNe transmission peaks. As long as these peaks are continuously locked in a given location by feeding back on the offset of the piezo scan, we can ensure that these transmission peaks correspond to an integer number of HeNe wavelengths that is constant in time. Hence, if the desired position of an ECDL is located once relative to these particular HeNe transmission peaks, that position will remain constant (relative to the HeNe peaks) as long as the cavity is maintained on this FSR. In practice, an Agilent/HP 86120B wavemeter is used to determine laser frequencies to within  $\sim \pm 300$  MHz; once a laser is within this range of its desired frequency, the peak location of the laser on the Fabry-Pérot cavity may be used to locate the desired laser frequency to within  $\sim 1$  MHz. Due to uncertainty and drift in the wavemeter reading, the desired laser frequency may be one FSR above or below where it is initially locked; however, which of these frequencies is correct can usually be quickly determined using the molecules in the experiment as a frequency reference.

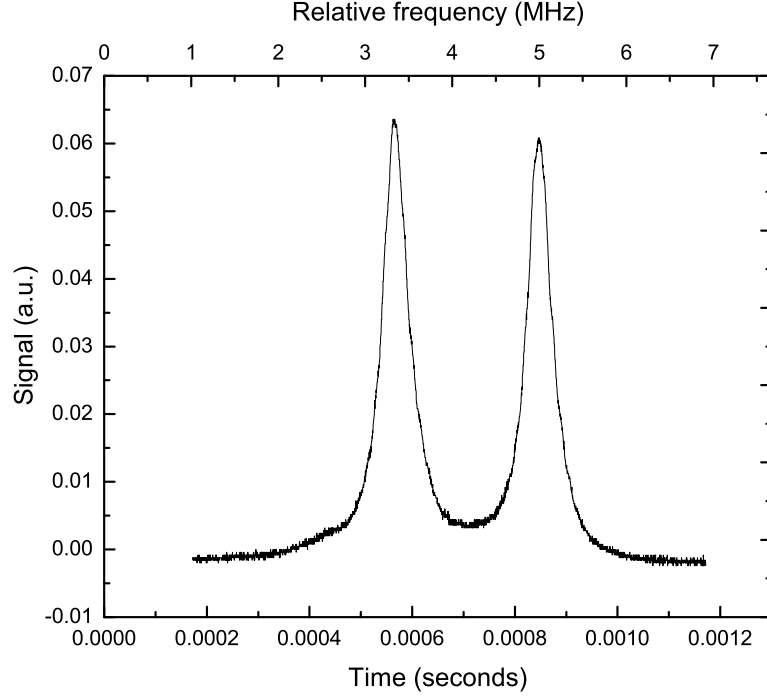


Figure 4.13: Fabry-Pérot scan resolving the two peaks of a 5517Å frequency-stabilized HeNe. The two resolved peaks are known to be 1.65 MHz apart. Since the FSR of this Fabry-Pérot is 500 MHz, this Fabry-Pérot has an estimated finesse of  $\sim 1500$ .

Our Fabry-Pérot design is theoretically athermal, i.e. it is designed so that the spacing between the cavity mirrors should be invariant under changes in the temperature of the cavity. This is accomplished by constructing the cavity of multiple materials in a geometry such that the thermal expansion of the various components cancel out. Fig. 4.13a shows a picture of a home-built 500 MHz FSR Fabry-Pérot. The cavity is a simple confocal<sup>20</sup> design consisting of a quartz tube, two 1018 steel endcaps, a piezo and two mirrors as shown in 4.13b. Fabry-Pérots of different lengths only require different lengths of quartz and no changes to the machined endcaps.<sup>21</sup> Rough adjustments of cavity length are done with a spanner wrench while a piezo allows for fine adjustment and/or scanning. (See Appendix E for alignment tips.) Fig. 4.13 shows a Fabry-Pérot trace of the two peaks from a frequency-stabilized HeNe (HP/Agilent 5517A) and displays a finesse of  $\sim 1500$ .

Fabry-Pérots used for locking are housed in a vacuum-tight container made from a KF50 tee, home-made windows, and a BNC feedthrough; however, the container is not evacuated. This keeps

<sup>20</sup>All of our cavities are operated in the confocal configuration to aid in ease of alignment. Half-confocal configurations display the unfortunate property that light which is not transmitted through the cavity is reflected directly towards the source which may cause feedback problems. Half-confocal cavities offer no advantage over confocal cavities in the ratio of FSR/finesse, and we therefore choose the confocal configuration.

<sup>21</sup>The endcap on one side of the cavity is adjustable. Hence, by varying both the cavity length added by this steel endcap (adjusted in-situ) and the quartz length (calculated prior to cavity construction), both the athermal condition and the confocal condition can simultaneously be fulfilled.

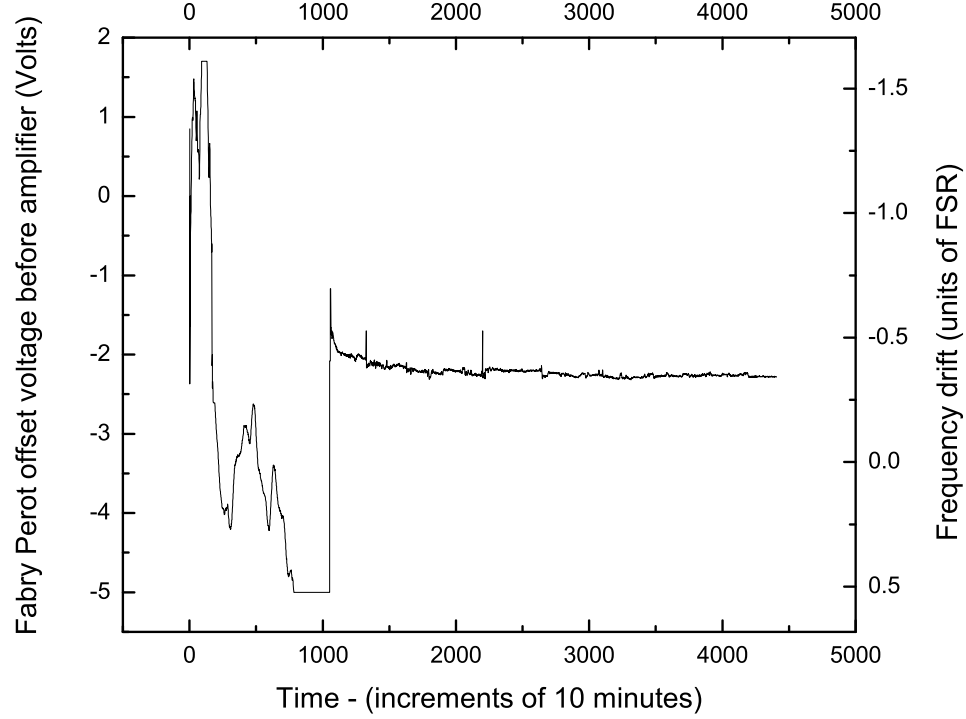


Figure 4.14: Monitoring Fabry-Pérot drift. The data show the output voltage necessary to lock a Fabry-Pérot to a frequency-stabilized HeNe over the time period beginning November 11th, 2012 and ending December 31st 2012. On November 26th, a leaky feedthrough on the Fabry-Pérot vacuum housing was replaced. The data show that complete vacuum-tight sealing of the Fabry-Pérot is important to reduce long-term drift. The FSR of this Fabry-Pérot is 750 MHz.

the pressure of the cavity constant even as atmospheric pressure varies by several tens of Torr, a typical pressure variation in New Haven over a year. Otherwise a 500 MHz cavity will drift about 2.7 FSRs per Torr for resonant light at 663 nm. The offset voltage of the Fabry-Pérot piezo is recorded by the software lock (discussed later in this chapter) every 10 minutes. In this way we can identify if a cavity is drifting consistently in one direction or if the housing is not vacuum-tight. The long-term recording of the cavity drift is important. Without it, manual checks are required to determine that the cavity is still on the same FSR as before. In the rare case that a cavity has drifted far enough that it can no longer be locked to the same FSR, the desired location of each laser peak relative to the HeNe transmission peaks on this new FSR must be empirically determined anew.

Fig. 4.14 shows the long-term drift of a Fabry-Pérot with  $\text{FSR} = 750 \text{ MHz}$  before and after a leaky feed-through was replaced. With the proper sealing, the Fabry-Pérot is stable to  $\sim 50 \text{ MHz}$  over a period of more than a month. If a cavity of the same length were instead constructed of Invar or quartz, we would expect a drift of  $\approx 550 \text{ MHz}$  or  $185 \text{ MHz per } ^\circ\text{C}$  respectively. Since at the time the data was taken, our lab was only stabilized to a temperature range of  $\sim \pm 2^\circ\text{C}$ , we can conclude

that the athermal cavity design results in a much lower drift than a uni-material cavity of Invar or quartz.

Since the Fabry-Pérot has gone through six iterations, we point out several features of the current Fabry-Pérot design which were implemented after the first-generation design. The latest version of the Fabry-Pérot uses the Thorlabs SM1 tap and therefore mates directly with Thorlabs photodiodes and lens tubes. Such mating is only useful for cavities used for diagnostics and monitoring; cavities used for laser-locking (see [section 4.7](#)) are set up with the necessary lenses and photodiodes external to the vacuum-tight housing. The latest version also uses Thorlabs retaining rings to secure the mirrors, and the cavity length can be changed with a commonly available spanner wrench (Thorlabs, SPW602). Finally, the quartz on the current version is 3 mm thick, which we found substantially reduced vibrations relative to the original cavity which used 1.5 mm thick quartz.

The Fabry-Pérot mirrors are typically high reflectivity (HR) mirrors from Layertec. We have used Layertec part numbers 102966 and 103951 for 500 MHz cavities and Layertec 105738 for all 750 MHz cavities. Since these mirrors are not specified for transmission, occasionally the transmission of a given Fabry-Pérot will be poor. Sets of bad mirrors are relegated to Fabry-Pérots used for diagnostics where signal-to-noise (SNR) is relatively unimportant. Usually Layertec will agree to measure the radius of curvature (ROC) of each mirror to .01 mm so the quartz can be cut to the exact right length (although at least once they have refused). We couple into each Fabry-Pérot cavity with a spherical singlet lens. The lens helps to mode match more power into the  $\text{TEM}_{00}$  mode, resulting in overall narrower resonances than without the lens. We find that using a lens with focal length equal to the length of the cavity works well for the laser beam sizes typical in our lab, keeping the setup compact. This may not be the optimal lens for mode matching, but it works well enough.

The parts list for the Fabry-Pérot, machine drawings and construction tips are available in [Appendix E](#). Approximately 20 of these Fabry-Pérots have been built and are in use in our experiment and in  $\sim 10$  other groups. Each Fabry-Pérot itself costs  $\approx$  \$800 with the plurality of that cost typically being the mirrors and the balance primarily consisting of the piezo and machining costs.

## 4.6 Frequency reference

Currently we use HP/Agilent 5517B lasers as frequency references. The 5517B is a type of axial Zeeman-split frequency-stabilized HeNe laser [178]. The general operating principle is as follows: Application of an axial magnetic field along the bore of the HeNe causes Zeeman splitting of the Ne atoms, resulting in the creation of two separate gain curves. While the exact details of the physical mechanisms involved are quite complicated [179–181] and likely arise from both mode pulling [182, 183] and magnetically-induced birefringence [184] and possibly other effects, the end result is the creation of left- and right-circularly-polarized modes that oscillate at different frequencies with a typical frequency separation of up to a few MHz. The beat frequency (and intensity ratio) between the two polarizations is dependent, among other factors, on the cavity length which controls the position of each polarization within the Zeeman-split gain profile. Stabilizing either the frequency difference [184] or the intensity ratio [185] between the two polarizations will therefore stabilize the cavity length and hold the frequency of each polarization constant (at least over the short term<sup>22</sup>). On the 5517B, the two intensities are stabilized by using a single photodiode, a liquid crystal device (LCD) polarization selector, and a polarizer to alternatively sample the intensity of each polarization with a period of approximately 2-3 seconds. The cavity length is then controlled using a resistive heater wrapped around a “mirror spacing rod” inside an internal-mirror hard-sealed HeNe tube. Extensive details on the 5517B and similar lasers are available from Ref. [186].

Of central importance for our application is the long-term frequency stability of the 5517B lasers. Since the linewidth of the SrF cycling transition is  $\approx 6.6$  MHz, we would ideally like our frequency reference to be stable to within a 1-2 MHz window. The manufacturer specifications for the frequency stability of 5517B lasers are shown in Table 4.2.

Specification	ppm units	frequency units
Vacuum wavelength stability (one hour):	$\pm .002$ ppm typical	$\pm .947$ MHz
Vacuum wavelength stability (lifetime):	$\pm .02$ ppm typical	$\pm 9.47$ MHz

Table 4.2: HP/Agilent specifications for 5517B frequency stability.

The specifications for the one hour stability are supported by a test conducted in Ref. [187] in which, among other things, the frequency stability of 28 5517A lasers<sup>23</sup> was evaluated, each for a period of 24 hours after allowing for a 1 hour warm-up period. The data from the test show that 26 of the 28 lasers stayed within a 2.05 MHz window during each laser’s 24 hour test period. This is

<sup>22</sup>Aging effects and possibly variations in ambient temperature can affect mid- and long-term stability. This is discussed later in this section.

<sup>23</sup>The HP/Agilent 5517A and 5517B lasers are extremely similar and can be treated as identical for our purposes.

consistent with Agilent’s specifications.

Multiple groups find that lasers which are left locked exhibit no frequency shift due to laboratory-type temperature fluctuations [188, 189]. This is consistent with temperature fluctuations causing a shift of the neon gain curve (for typical He:Ne isotopic fill ratios) of only  $\sim 200$  KHz/ $^{\circ}$ C [189], which is further mitigated by the fact that the vast majority of the laser tube is held at a constant temperature in order to maintain a fixed distance between the cavity mirrors. However, the 5517B design departs from standard designs in the literature in ways likely to increase frequency drift due to changes in ambient temperature.<sup>24</sup> Further, if the 5517B lasers are turned off, they are not guaranteed to lock to the same cavity fringe of the HeNe tube, and the chosen fringe will likely vary with ambient temperature [187, 190] and thereby hurt frequency reproducibility. Similarly, turning off these lasers makes it impossible to ensure that each Fabry-Pérot cavity remains locked to the same FSR over time. For these reasons and others, the 5517B lasers are only turned off when the apparatus is not expected to be used for long periods.

Over long periods of time different mechanisms (cathode aging, gain aging, a change in the He:Ne ratio including isotopic composition, etc.) can cause frequency drift of the 5517B lasers. This drift is typically  $\sim 3$  MHz/year [184, 189, 191] for Zeeman-stabilized HeNes and is likely no different for other frequency-stabilized HeNes [192]. It remains to be seen whether the 5517B laser stability will prove adequate for this experiment in the future. Possible alternatives include a frequency-doubled non-planar ring oscillator (NPRO) laser locked to an iodine transition as in Ref. [193] or a distributed feedback (DFB) laser locked to a potassium or rubidium transition using a saturated absorption lock.

## 4.7 Software lock

ECDLs typically have linewidths of 1 MHz or better but can drift tens of MHz or more per hour depending on ambient conditions. Since many atomic and molecular transitions have linewidths  $< 10$  MHz, long-term stabilization of an ECDL’s frequency to a stable frequency reference is often required. A common solution uses an analog PID feedback loop to lock the ECDL to certain spectral features in a vapor cell using saturated absorption. Stabilization to the fringe of a low-drift reference cavity (typically made of ULE or Zerodur) or to a frequency comb are viable methods too. A plethora

---

<sup>24</sup>The 5517B uses a mirror spacing rod (which is heated using a bifilar-wound heater coil *inside* the mirror spacing rod) internal to a hard sealed mirror tube. This stands in contrast to designs in the literature where a resistive heater is wrapped around a standard HeNe tube and the end mirrors create the seal [184]. In the latter, holding the distance between the mirrors constant will effectively keep the temperature of the entire tube roughly constant. In the former, the temperature of the mirror spacing rod will vary over the length of the tube.

of other methods exist as well.

For reasons discussed previously, we choose to lock our lasers to a frequency-stabilized HeNe laser (HP/Agilent 5517B typically) and use a low-drift Fabry-Pérot as a transfer cavity. A Labview program scans the Fabry-Pérot and records the positions of the reference HeNe peaks and all present ECDL peaks.<sup>25</sup> By comparing peak positions relative to the peaks of the 5517B laser, the computer generates an error signal, which is used to apply a feedback voltage to the piezo of the ECDL. We also find it useful to lock the Fabry-Pérot to the HeNe using the same method. Implementation of the entire system is digital. This offers advantages in scalability, cost, flexibility and ease of setup. Additionally it is easy to consolidate complete control of all ECDL lasers into one place. Although several systems similar to this one have been demonstrated in the literature [194–201], we recount the main details here.

#### 4.7.1 Scanning

The Labview program produces a reverse sawtooth waveform<sup>26</sup> ( $\sim 3$  volt amplitude,  $\sim 400$  Hz frequency) which is output using a DAQ (National Instruments PCI-6259 or similar) to a high voltage amplifier (Thorlabs, MDT693A typically, gain =  $15\times$ ) which directly drives the piezo of the Fabry-Pérot. The resulting waveform is recorded, and the positions of the peaks of the HeNe and all present ECDLs are determined using the Labview peak-finding algorithm. The cavity is locked to the HeNe by using a PID algorithm to adjust the offset voltage of the sawtooth waveform output so that the first HeNe peak occurs at the same time in each scan. Typically the Fabry-Pérot can be locked to the HeNe with an RMS linewidth of  $\lesssim 40$  kHz. This linewidth is likely limited by the precision with which the software can identify the HeNe peak location (limited by the DAQ sampling rate) or the discrete set of output voltages (limited by the DAQ’s 16-bit digital-to-analog converter) available for feedback control.<sup>27</sup>

Simultaneously, the difference in time between the first and second HeNe peaks on the Fabry-Pérot trace is converted to a frequency scale using the known FSR of the Fabry-Pérot. The positions of the ECDL peaks in time are converted to a frequency offset<sup>28</sup> from the first HeNe peak which is arbitrarily defined to be 0 MHz. The measured frequency of each ECDL is compared to the desired

<sup>25</sup>After transmission through the cavity, light from the various lasers being monitored on a given cavity is separated using a combination of polarization (PBS) and wavelength (dichroic filters). After separation, the light from each laser is aligned onto a dedicated photodiode, each of which occupies a dedicated channel on the DAQ. In this way, several lasers can share a single cavity, and the peak locations of each laser can be independently monitored and controlled.

<sup>26</sup>The convention is that a sawtooth waveform ramps upward and then sharply drops. However, in a “reverse sawtooth waveform,” the wave ramps downward and then sharply rises.

<sup>27</sup>The 16-bit DAQ is set to output in the range -5 Volts to 5 Volts.

<sup>28</sup>This frequency conversion requires some scaling since  $\lambda_{\text{HeNe}} \neq \lambda_{\text{ECDL}}$ .

setpoint to generate an error signal. We find the software lock works best using a maximally-asymmetric reverse sawtooth waveform to drive the Fabry-Pérot. A small section (typically  $\sim 10\%$  of the beginning of the scan) is discarded. This portion corresponds to the Fabry-Pérot being driven by the near-vertical portion of the reverse sawtooth waveform and causes the Fabry-Pérot to quickly scan through all the peaks during this time. This disturbance lasts significantly longer than the near discontinuity in the waveform would indicate, presumably due to the non-zero capacitance of the piezo.

For each ECDL, only the position of the first peak is used to calculate the ECDL's measured offset frequency, denoted  $\nu_{\text{measured}}$ . The desired frequency offset  $\nu_{\text{input}}$  for each ECDL is entered in MHz. However, the software uses a different setpoint

$$\nu_{\text{setpoint}} \equiv \nu_{\text{input}} \bmod \text{FSR}. \quad (4.14)$$

This allows the user (or computer) to incrementally scan the laser over a frequency range greater than one FSR. In practice there is usually a slight discontinuity (a few MHz) when the software switches which ECDL peak is used to determine  $\nu_{\text{measured}}$  as the laser is scanned over a FSR. For our experiment this discontinuity is of little consequence. There is no fundamental limit to the frequency range over which the software lock can scan an ECDL. In practice, the scan range is limited either by the output voltage range of the high voltage amplifier or by the mode-hop-free tuning range of the laser, both of which can be as high as 40 GHz. The software is set so that no output voltage (to either the Fabry-Pérot cavity or to any ECDL) is modified if two distinct HeNe peaks (separated by a FSR) are not present. The software also does not modify the output voltage for an ECDL if the peaks for that ECDL are not found. This prevents either the ECDLs or the Fabry-Pérot cavity from coming unlocked if any laser beams are momentarily blocked (inadvertently or otherwise).

There are numerous other benefits of the software lock. For example, the capture range of the lock is very large (approximately equal to the Fabry-Pérot FSR), and therefore acoustic noise does not unlock the lasers under normal conditions. Setting up the software lock requires no soldering, and therefore installation, replication and upgrades are all fairly painless. The digital control of all setpoints also allows easy archiving and historical recording of laser frequencies over time.

Our software lock exhibits some unforeseen advantages as well. Since fast frequency scanning of the lasers is not desirable at this point in our experiment, there is an option to limit the voltage



correction per unit time. This allows a laser to be frequency chirped (assuming the duty cycle of the chirp is low) via directly modulating the diode current while its long-term frequency remains locked. Further, because the software lock uses only the first peak of each ECDL resonance to determine frequency position, a laser with resolved sidebands created via current modulation can still be locked. Lasers which are purposely broadened via current modulation can also be locked provided the broadening is much less than the FSR of the Fabry-Pérot.

There are however some drawbacks to the software lock. Most importantly, the locking results in little if any narrowing of the ECDL linewidth beyond the natural linewidth of the laser. Also, it is not possible to use the software lock to precisely ramp the laser frequency in a given pattern that includes variations over short timescales (e.g., typically, ms).<sup>29</sup>

In practice, the software lock is highly successful. In the days when the experiment had 8 ECDLs, there were several times when all lasers stayed locked for 12+ hours. The system presented here provides a robust and versatile solution for locking ECDLs for applications in atomic physics which do not require linewidth-narrowing of lasers. The solution is practical in spectral regions where references lines are unavailable or where Pound-Drever-Hall-style locks [202] to individual stabilized cavities are not feasible. I would like to thank in particular Stephan Falke, Mattias Gustavsson, Jeff Ammon and Matthew Steinecker who all made significant contributions to the software lock.

---

<sup>29</sup>With the software lock, it is possible to vary the laser frequency over  $\lesssim 10$  ms time scales (as might be desired for chirped slowing of our pulsed molecular beam) by directly varying the ECDL injection current. However, this method requires both that the period of the frequency deviation from  $\nu_{\text{setpoint}}$  be short enough that the software lock cannot correct for this deviation, and (so far) requires frequency deviations from  $\nu_{\text{setpoint}}$  to occur with a fairly small duty cycle ( $\lesssim 10\%$ ). Because the laser is not strictly locked during each frequency deviation, precise reproducibility of this method is not guaranteed. In contrast, locks with sufficiently high lock-loop bandwidths such as Pound-Drever-Hall-style locks [202] or locks based on phase-locked loops are often fast enough that desired frequency deviations can be inserted directly into  $\nu_{\text{setpoint}}$ .

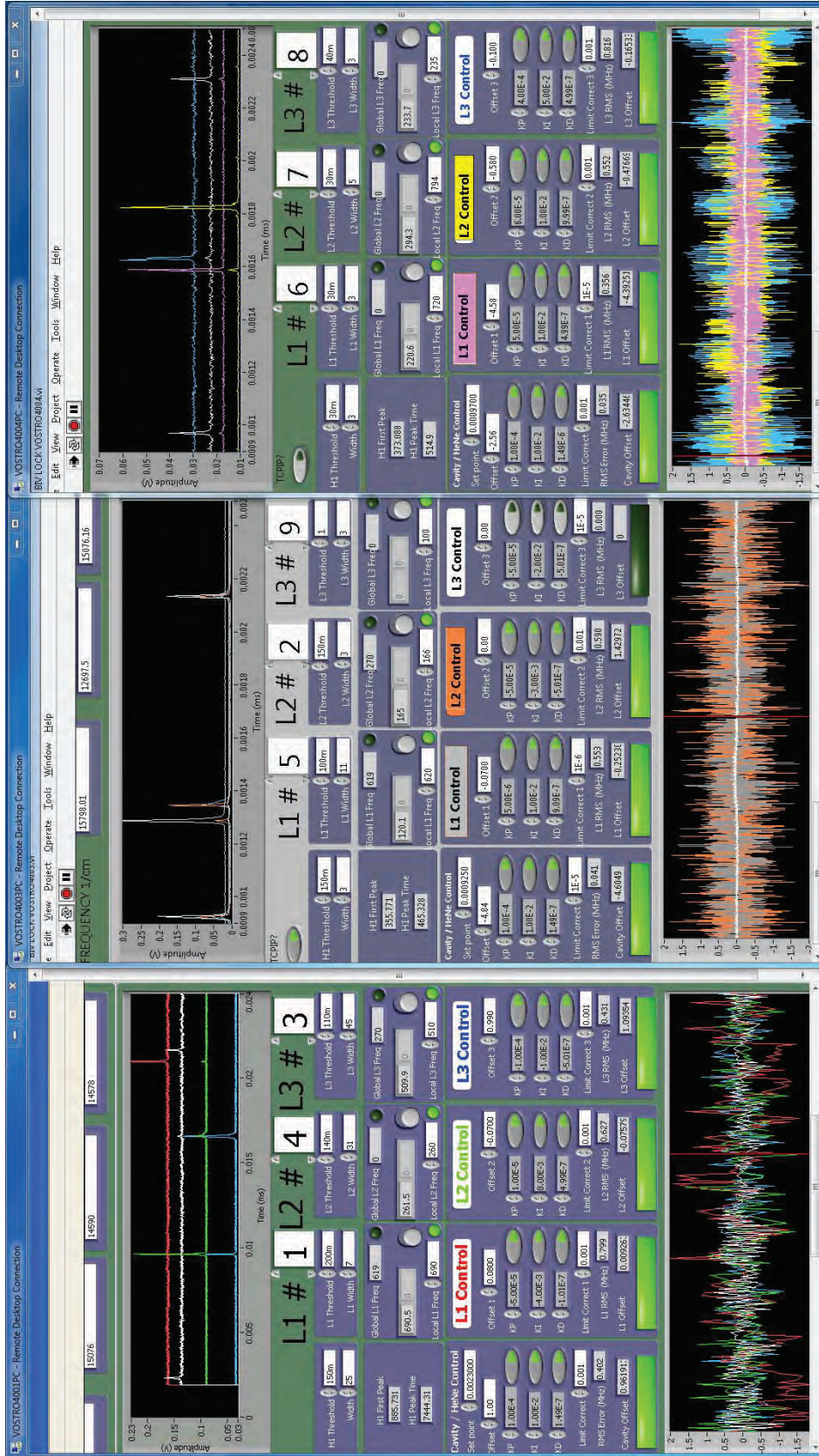


Figure 4.15: Software lock interface showing locking of 8 ECDLs on 3 Fabry-Pérots. Each of the three panels corresponds to a single Fabry-Pérot. The top of each panel shows a single trace of a Fabry-Pérot scan. HeNe peaks are always shown in white while each ECDL peak is displayed in a different color. The middle section of each panel contains all of the controls. For example, the user can set options to control the peak finding algorithm. The user can also toggle control of the laser frequency between local or global control, locally set the laser frequency, set the offset voltage of each ECDL, view the DAQ output voltage to the high voltage amplifier and view the RMS error frequency of the lock for each ECDL. The bottom graph on each of the three panels depicts the error signal in MHz as a function of time with the entire x axis corresponding to a timespan of several seconds. In the middle and left panels, the Fabry-Pérot is locked to the HeNe with an RMS error  $\approx 40$  kHz. The ECDLs in the middle and left panels are locked to the Fabry-Pérot with an RMS error  $\approx 500$  kHz.

## Chapter 5

# A bright, slow cryogenic molecular beam source for free radicals

This chapter mainly includes the theory and experimental results presented in Ref. [73]. We add updated references relevant to on-going work in this field, add comments relevant to the design details and document further changes and data taken since publication of Ref. [73]. In this chapter, we demonstrate and characterize a cryogenic buffer gas-cooled molecular beam source capable of producing bright beams of free radicals and refractory species. Details of the beam properties (brightness, forward velocity distribution, transverse velocity spread, rotational and vibrational temperatures) are measured under varying conditions for the molecular species SrF. Under typical conditions we produce a beam of brightness  $1.2 \times 10^{11}$  molecules/sr/pulse in the  $X^2\Sigma_{1/2}(v=0, N_{rot}=0)$  state,<sup>1</sup> with  $140 \frac{m}{s}$  forward velocity and a rotational temperature of  $\approx 1$  K. This source compares favorably to other methods for producing beams of free radicals and refractory species for many types of experiments. We provide details of construction that may be helpful for others attempting to use this method.

### 5.1 Introduction

A general technique for trapping molecules is to directly load them into a trap from a molecular beam [203]. In this case the number of molecules trapped is directly tied to the flux, translational and internal (rotational and vibrational) temperatures, and forward velocity of the beam. Specifically,

---

<sup>1</sup>In this chapter we explicitly use  $N_{rot}$  instead of  $N$  to denote the rotational quantum number.

slow, cold molecular beams with high flux are ideal for loading traps. Such beams of molecules are also useful for high precision spectroscopy [24].

Unfortunately, traditional supersonic and effusive molecular beams are not ideally suited to these requirements. Thermal effusive sources can produce translationally slow molecules, but the finite rovibrational temperatures of the molecules vastly reduce the effective flux of these beams. On the other hand, supersonic beam sources are quite efficient at cooling both internal and external molecular degrees of freedom, but the resultant molecular beam velocity is quite high, which prohibits direct molecular trapping.

The development of general methods for directly producing slow, cold molecules applicable to a variety of molecular species remains an active area of research. Tremendous advances have been made in the deceleration of supersonic beams in the past decade. Stark deceleration [48, 49], Zeeman deceleration [51, 52], optical deceleration [62], collisional deceleration [56], and rotating nozzles [54, 55] have all been developed to slow supersonic beams to velocities of a few m/s, where molecules can be loaded into a trap. Although this is a highly general technique for producing beams of slow, cold molecules, it becomes significantly more challenging for unstable molecules (e.g. free radicals) or molecules that do not have substantial vapor pressure at room temperature. The high forward velocity in supersonic beams also makes slowing heavy molecules much more challenging, and thus far the slowing techniques have primarily been limited to light molecules [59]. Furthermore, these slowing techniques have so far resulted in molecular beams with relatively low flux.

Another promising technique is cryogenic buffer gas cooling. Typically in these experiments, the target molecules and the buffer gas are enclosed in a cell. Collisions with the buffer gas cool both the internal and external degrees of freedom to the temperature of the cell. This technique has been demonstrated for a wide variety of molecular species [204], with resulting molecular temperatures as low as 100 mK and the ability to trap molecules demonstrated in situ [66]. The primary disadvantage of buffer gas cooling is that the cold molecules remain in the cell where collisions prohibit most further measurements and manipulation of the molecules. It remains a significant challenge to separate the buffer gas from the molecules of interest.

Cryogenic buffer gas cooling has also served as the basis for molecular beams [68, 69, 72, 205]. In these experiments, the cell has an exit aperture through which the molecules can escape and form a beam. These sources can be operated both in an effusive regime and a “hydrodynamically enhanced” regime, depending on the buffer gas density. For low buffer gas densities, there are relatively few collisions near the exit aperture, and the beam exits effusively from the cell. Effusive beams are



characterized by thermal molecular beam velocities and low flux due to poor extraction of molecules from the cell. For higher buffer gas densities, hydrodynamic effects inside the cell lead to nearly complete extraction of molecules from the cell. However, in the hydrodynamic regime, collisions between molecules and buffer gas near the exit aperture can result in a boosted forward velocity.

Here we report on the development and characterization of an ablation-loaded, cryogenic buffer gas beam source of a diatomic free radical. The source is designed to produce a beam of molecules which will subsequently be laser cooled [90, 206], and ultimately loaded into a trap. We operate the source at intermediate buffer gas densities, where the extraction efficiency of molecules into the beam is high, while the forward velocity of the beam is significantly lower than the full supersonic speed of the buffer gas. Previous studies on such beams have focused on only a few of the properties under a limited range of conditions [68, 69, 72, 205]. The characterization given here provides a more complete description of a cryogenic buffer gas beam source, including measurement of the beam brightness, forward velocity distribution, transverse velocity spread, and rotational and vibrational temperatures over a wide range of buffer gas densities. We also characterize the molecular beam flux into a room-temperature apparatus, bluea first at the time.. We find that the brightness of the cryogenic beam source compares very favorably with other sources capable of producing beams of similar refractory species. Although the measurements presented here were all conducted using strontium monofluoride (SrF), we expect similar performance from other species which can be vaporized by ablation of solid precursors.

The remainder of this chapter is structured as follows: In [section 5.2](#) we detail basic theory and properties of buffer gas beams. In [section 5.3](#) we describe the experimental construction and design principles. In [section 5.4](#) we present detailed measurements of the beam properties, make additional observations regarding source operation and present a comparison to existing sources based on other technologies. In [section 5.5](#) we discuss subsequent improvements to the beam source since publication of Ref. [73].

## 5.2 General source properties

The basic principles of a buffer gas beam source are simple. A cold cell is held at temperature  $T_0$  while gaseous buffer gas atoms  $b$ , also at  $T_0$ , are continuously flowed through the cell at a rate  $\mathcal{F}$ . The value of  $\mathcal{F}$  can typically be continuously varied over a wide range of values, which allows control over the density of  $b$  inside the cell. The target molecules  $a$  are injected into the cell at an

initial temperature  $T_a(t = 0) \gg T_0$ , in our case by laser ablation of a solid precursor inside the cell. These initially hot molecules undergo many collisions with the buffer gas, which cool both the translational and rotational degrees of freedom to near  $T_0$ . During and after this thermalization, the target molecules diffuse through the buffer gas to the cell walls, where they stick and are lost. Simultaneously, both the target molecules and the buffer gas are extracted into a beam through a hole in the cell. The ratio of the time scales for these competing processes determines the efficiency of molecule extraction from the cell. Meanwhile the number of collisions between the buffer gas atoms and the molecules around the exit aperture determines the divergence, forward velocity distribution, and internal temperatures of the molecules in the beam. Although these basic principles of buffer gas beam sources are simple, the actual dynamics in and around the cell can be quite complex for ablation-loaded sources such as ours. In the remainder of this section we describe relevant characteristics of the cell conditions and the resulting molecular beam. The description given here is meant to provide a qualitative description of a few of the relevant parameters of these sources. More sophisticated models would be necessary to give a complete quantitative description.

### 5.2.1 Mean free path

The basic properties of the buffer gas beam are primarily determined by the mean free paths  $\lambda_a$  and  $\lambda_b$  of particles  $a$  and  $b$  inside the cell. Under typical operating conditions, the density  $n_b$  of the buffer gas far exceeds that of the target molecules  $n_a$ . This allows two simplifying assumptions to be made. First, collisions involving two  $a$  particles are rare and therefore may be ignored; thus  $\lambda_a$  then depends only on  $n_b$ . Similarly, collisions between two  $b$  particles are much more likely than between  $a$  and  $b$  particles, so  $\lambda_b$  also depends only on  $n_b$ . Under these conditions the mean free paths are

$$\lambda_a = \frac{1}{n_b \sigma_{ab} \sqrt{m_a/m_b + 1}} \quad \text{and} \quad \lambda_b = \frac{1}{\sqrt{2} n_b \sigma_{bb}}, \quad (5.1)$$

where  $\sigma_{ab}$  is the elastic collision cross section between species  $a$  and  $b$ ,  $\sigma_{bb}$  is the elastic collision cross section between  $b$  particles, and  $m_a$  and  $m_b$  are the masses of  $a$  and  $b$ , respectively.

In practice  $b$  is usually a noble gas, so  $n_b$  is not easy to measure using laser absorption or fluorescence techniques. Instead the value of  $n_b$  in our experiments is inferred from simple cell dynamics described here. Under steady state conditions, the flow rate of  $b$  into the cell,  $\mathcal{F}$ , will equal the rate of  $b$  out. The rate at which particles of  $a(b)$  are emitted out of the source exit

aperture (with area  $A$ ) into solid angle  $d\omega$  at angle  $\theta$  is

$$dQ_{a(b)} = \frac{d\omega}{4\pi} n_{a(b)} v_{a(b)}^{exit} A \cos \theta, \quad (5.2)$$

where  $v_{a(b)}^{exit}$  is the mean velocity at the exit aperture of species  $a(b)$  [207].

The values of  $v_a^{exit}$  and  $v_b^{exit}$  can vary significantly depending on the number of collisions particles of the given species experience near the exit aperture. The Reynolds number for  $a$  and  $b$ , defined as  $Re_a = \frac{d}{\lambda_a}$  and  $Re_b = \frac{d}{\lambda_b}$  where  $d$  is the cell aperture diameter, characterizes the number of collisions each species experiences while exiting the cell aperture. Typically  $m_a > m_b$  and  $\sigma_{ab} \approx \sigma_{bb}$ , so we assume hereon that  $Re_a > Re_b$ . For  $1 \gg Re_a > Re_b$ , the molecules exit the hole effusively. For  $Re_a > Re_b \gg 1$ , the particles undergo many collisions around the exit aperture, resulting in supersonic velocities as the beam escapes the source.

We relate  $n_b$  to the flow rate  $\mathcal{F}$  via the following reasoning. Under effusive conditions,  $v_b^{exit}$  is the same as the mean velocity of  $b$  inside the cell:  $v_b^{exit} = \bar{v}_b = (2/\sqrt{\pi})\beta$ . Here  $\beta \equiv \sqrt{2k_B T_b/m_b}$ , where  $T_b$  is the translational temperature of  $b$ . Integration of Eqn. 5.2 over all angles leads to a total rate of  $Q_b^e = \frac{n_b A \beta}{2\sqrt{\pi}}$ , in the effusive regime. In the fully supersonic regime, the value of  $v_b^{exit}$  is less clear. Collisions in and around the aperture boost the forward velocity of the buffer gas atoms from  $\bar{v}_b$  up to a maximum value given by the fully supersonic velocity [208, 209]

$$v_{b\parallel}^s = \sqrt{\gamma/(\gamma-1)}\beta, \quad (5.3)$$

where for a noble gas the heat capacity ratio is  $\gamma = 5/3$ . We can obtain an upper limit on the total rate in the supersonic regime by assuming that all particles of  $b$  exit the cell along the beam line at  $v_{b\parallel}^s$ . Under these assumptions Eqn. 5.2 yields an upper limit on the total rate  $Q_b^s = \sqrt{5/2} n_b A \beta$ . By equating  $\mathcal{F}$  to  $Q_b$  we arrive at the density of  $n_b$  for the two cases given by

$$n_b = \frac{\kappa \mathcal{F}}{A \beta}, \quad (5.4)$$

where  $\kappa = \kappa^e = 2\sqrt{\pi}$  for fully effusive and  $\kappa = \kappa^s = 1/\sqrt{\gamma/(\gamma-1)}$  for fully supersonic; hence  $\frac{\kappa^e \mathcal{F}}{A \beta} > n_b > \frac{\kappa^s \mathcal{F}}{A \beta}$ .

### 5.2.2 Thermalization

The extraction of target molecules into the beam depends critically on their thermalization with the buffer gas. If the molecules do not thermalize before they make contact with the cell walls, they will stick and be lost. Thermalization of initially hot molecules inside a cold buffer gas cell can be described by a simple kinematic model [67]. At time  $t = 0$ , ablation creates  $N_a^{cell}$  particles of species  $a$  at initial high translational temperature  $T_a(0)$ . The particles cool via collisions with the buffer gas; the translational temperature  $T_a(\mathcal{N})$  of species  $a$  after  $\mathcal{N}$  collisions can be written as a differential equation:

$$\frac{dT_a(\mathcal{N})}{d\mathcal{N}} = -\frac{T_a(\mathcal{N}) - T_b}{C}, \quad (5.5)$$

where  $C \equiv (m_a + m_b)^2 / (2m_a m_b)$ . This simple model assumes  $T_b = T_0$  at all times. Integration of Eqn. 5.5 yields

$$T_a(\mathcal{N}) = T_b + (T_a(0) - T_b)e^{-\mathcal{N}/C}. \quad (5.6)$$

The temperature of species  $a$  then asymptotically approaches  $T_b$ . We define a nominal number of collisions necessary to thermalize species  $a$ ,  $\mathcal{N}_{Th}$ , as the number of collisions such that  $T_a(\mathcal{N}_{Th}) = 2T_b$ . This yields  $\mathcal{N}_{Th} \equiv C \ln \left( \frac{T_a(0) - T_b}{T_b} \right) \sim C \ln \left( \frac{T_a(0)}{T_b} \right)$  since  $T_a(0) \gg T_b$ . The resulting thermalization time  $\tau_{Th}$  is then given by

$$\tau_{Th} = \frac{\mathcal{N}_{Th}}{R_a}. \quad (5.7)$$

where  $R_a \approx n_b \sigma_{ab} \bar{v}_b \sqrt{1 + m_b/m_a}$  is the approximate collision rate for species  $a$ .

The value of  $\mathcal{N}_{Th}$  allows us to estimate the minimum density  $n_b$  necessary to achieve thermalization. After  $\mathcal{N}_{Th}$  collisions, each particle  $a$  has traveled a total distance  $\mathcal{N}_{Th} \lambda_a$ . However the net distance, defined as  $X_{Th}$ , must range between the distance traveled by a diffusive random walk and purely ballistic flow, or  $\sqrt{\mathcal{N}_{Th}} \lambda_a \leq X_{Th} \leq \mathcal{N}_{Th} \lambda_a$ . The heavy and initially hot molecules have much more momentum than the light and cold buffer gas, so we take the ballistic limit  $X_{Th} = \mathcal{N}_{Th} \lambda_a$ . For ablation in the middle of a cubic cell of side length  $L_c$ , the particles of  $a$  exiting through the aperture will be efficiently thermalized only if  $X_{Th} \lesssim L_c/2$ . Using Eqn. 5.1 leads to a density requirement for thermalization given by

$$n_{Th} \gtrsim \frac{2C}{\sigma_{ab} L_c \sqrt{m_a/m_b + 1}} \ln \left( \frac{T_a(0) - T_b}{T_b} \right). \quad (5.8)$$

For most species  $\sigma_{ab}$  is unknown; however,  $\sigma_{ab}$  typically shows little variation among target species  $a$



for a given buffer gas  $b$  [70, 210–213], and for noble gases  $\sigma_{ab} \approx \sigma_{bb}$  [214, 215]. Furthermore, the exact value of  $T_a(0)$  is unknown, and must be estimated (typical estimates for ablation temperatures are  $T_a(0) \sim 10^4$  K [216]). Nonetheless, we expect that Eqn. 5.8 provides the correct order of magnitude for the density required for thermalization.

Similar arguments are applicable to the internal (vibrational and rotational) temperatures of  $a$ , provided that the appropriate collisional cross sections are used. In general the collision cross sections for vibrational, rotational and translational relaxation obey [208, 209]

$$\sigma_{ab}^{vib} \ll \sigma_{ab}^{rot} < \sigma_{ab}, \quad (5.9)$$

where  $\sigma_{ab}^{vib}$ ,  $\sigma_{ab}^{rot}$ , and  $\sigma_{ab}$  are the respective vibrational, rotational and translational collisional cross sections between species  $a$  and buffer gas  $b$ . In this case we expect similar thermalization behavior for rotational and translational degrees of freedom, while vibrational thermalization may occur over much longer time scales.

### 5.2.3 Diffusion and extraction

After thermalization, particles of both species  $a$  and  $b$  are extracted from the cell through the cell aperture and into the beam. The efficiency of extraction of  $a$  through the hole is primarily limited by the diffusion of these particles to the cell walls where they stick and are lost. The diffusion of species  $a$  into species  $b$  at temperature  $T$  is governed by the diffusion equation,  $\frac{dn_a}{dt} = \nabla^2(Dn_a)$  [217]. Here  $D$  is the diffusion constant, given to good approximation by  $D = 3/(16\sigma_{ab}n_b) \times \sqrt{2\pi k_B T/\mu}$  [217], where  $\mu = (m_a m_b)/(m_a + m_b)$  is the reduced mass. We can therefore approximate the time for species  $a$  to be lost to the cell walls via diffusion,  $\tau_{diff}$ , by the time constant of the lowest-order diffusion mode [217], giving

$$\tau_{diff} \approx \frac{L_c^2}{4\pi^2 D}. \quad (5.10)$$

We approximate  $\tau_{pump}^b$ , the time constant governing the extraction of  $b$  through the cell aperture, by the typical time for the cell volume to be emptied by flow out of the exit aperture:

$$\tau_{pump}^b \approx \frac{L_c^3 n_b}{\mathcal{F}} = \frac{\kappa L_c^3}{A\beta}. \quad (5.11)$$

In the remainder of the chapter we assume that species  $a$  is fully entrained in the flow of species  $b$  inside the cell. With this assumption, species  $a$  also will exit the cell with the same time constant.

The cell extraction efficiency  $\epsilon$  is the fraction of  $a$ , which, once produced and thermalized inside the cell, is extracted into a beam. The quantity

$$\xi \equiv \frac{\tau_{diff}}{\tau_{pump}^b} \propto \frac{\mathcal{F}}{L_c} \quad (5.12)$$

has been found to be strongly correlated with  $\epsilon$  [68]. Eqn. 5.12 suggests that small cells operated at high flow rates are ideal for maximal extraction efficiency. For  $\xi \gg 1$  we expect particles of  $a$  to exit the cell before they diffuse to the cell walls; therefore in this “hydrodynamic” regime we expect to observe  $\epsilon_{hyd} \sim 1$ . Values of  $\epsilon > 0.4$  have been reported [68] for  $\xi \gtrsim 1$ . For  $\xi \ll 1$  we expect purely diffusive in-cell behavior, with  $\epsilon$  determined by the geometric extraction efficiency  $\sim A/(\pi L_c^2)$  for molecules produced in the center of the cell. In this regime values of  $\epsilon \sim 0.001$  have been reported [72].

#### 5.2.4 Beam formation

As the molecules pass through the exit aperture, the number of collisions that particles of  $a$  and  $b$  experience determines to a large extent the properties of the beam. For  $1 \gg Re_a > Re_b$  (effusive regime), there are no collisions for either species in the vicinity of the aperture and the extracted beam is purely effusive. In this regime the mean forward velocities of  $a$  and  $b$  in the beam, denoted by  $v_{a\parallel}$  and  $v_{b\parallel}$  respectively, are given by Ref. [207]

$$v_{a\parallel} = v_{a\parallel}^e = \frac{3}{4}\sqrt{\pi}\alpha \quad \text{and} \quad v_{b\parallel} = v_{b\parallel}^e = \frac{3}{4}\sqrt{\pi}\beta, \quad (5.13)$$

where  $\alpha \equiv \sqrt{2k_B T_a/m_a}$ . We also expect the translational temperatures of  $a$  and  $b$  in the beam obey  $T_a^{beam} = T_b^{beam} = T_0$ .

For  $Re_a > Re_b \gg 1$  (supersonic regime), all particles experience many collisions as they exit the aperture and expand into vacuum. Because  $n_b \gg n_a$  the buffer gas species  $b$  drives the expansion, and the properties of  $b$  in the beam determine to a large extent the beam properties of  $a$ . During the isentropic expansion,  $v_{b\parallel}$  increases while  $T_b^{beam}$  cools, resulting in a boosted but narrow velocity distribution. Using a simple hard-sphere scattering model to describe the cooling during the expansion [209], we can estimate  $T_b^{beam}$  to be

$$T_b^{beam} \lesssim 3.12(\sigma_{bb}n_b d)^{-\frac{4}{5}}T_0. \quad (5.14)$$

This value of  $T_b^{beam}$  represents an upper bound on the beam temperature because it neglects quantum mechanical effects which become more important for low values of  $T_b^{beam}$  [218, 219], particularly for  $b = \text{He}$ . In the supersonic regime we expect  $T_a^{beam}$  to approach  $T_b^{beam}$ . We also expect  $v_{a\parallel}$  to approach  $v_{b\parallel}$  and  $v_{b\parallel}$  to approach  $v_{b\parallel}^s$ .

### 5.3 Experimental apparatus

In this experiment, SrF is the molecule of interest  $a$ , and the buffer gas species  $b$  is He. The apparatus is built around a 2-stage closed cycle pulse tube refrigerator (Cryomech, PT415). A vacuum chamber contains the pulse tube head, with vacuum ports providing access for temperature sensor and helium gas feedthroughs as well as for various vacuum connections and gauges. A radiation shield attached to the first stage of the pulse tube (at  $\approx 30$  K) reduces the heat load on the colder second stage (at  $\approx 3$  K). Rectangular windows on both sides of the 30K shield allow optical access to the cell and along the beam line. A 1" hole at the front of the 30K shield allows extraction of the molecular beam.

The cell is attached to a 3K cold plate bolted to the second stage of the pulse tube. A 3K shield reduces the blackbody heat load on the cell. Windowless holes in the shield allow optical access to the cell and along the beam line, while a hole in the front enables beam extraction. The inside of the shield is covered with coconut charcoal (PCB 12 $\times$ 30 mesh Calgon Charcoal), which acts as a cryopump for helium gas [220, 221]; the charcoal is affixed to the shield with epoxy (Arctic Silver Thermal Adhesive).

Room temperature helium gas (99.999% purity) flows into the cell through a series of stainless steel and OFHC copper tubes. The flow rate  $\mathcal{F}$  is monitored outside the vacuum chamber (using an MKS 246 Flowmeter). The helium gas first thermalizes to 30 K and then to 3 K via copper bobbins on the two cryogenic stages. Thin-walled stainless steel tubes thermally isolate the bobbin stages from each other and from room temperature. High-purity helium is used to reduce the risk of clogging the flow tubes through condensation of impurities in the gas. The cooled helium enters the back of the cell through a 3.2 mm OD copper tube. The cell is formed by drilling two perpendicular holes (22.9 mm diameter) into a copper block, giving the cell an interior volume of  $\approx 15 \text{ cm}^3$  with characteristic size  $L_c \approx 2.5 \text{ cm}$ . The size of the cell was chosen to be small such that large extraction of molecules into the beam could be achieved (see Eqn. 5.12). The ablation target is mounted at 45 degrees relative to the molecular beam axis on a copper holder near the helium gas inlet. Cell

windows are uncoated sapphire for maximum thermal conductivity and are sealed to the cell with indium for good thermal contact. AR coated windows are avoided since they tend to become opaque, presumably from reacting with products of the ablation.

A mixture of helium, SrF, and other particles created via ablation exit the cell through a  $d = 3$  mm diameter hole in a 0.5 mm thick copper plate at the front of the cell to form a beam. The beam passes through a 6 mm diameter hole in a coconut charcoal-covered 3K copper plate, typically placed 34 mm from the cell. This plate acts to reduce the helium gas load into the rest of the apparatus. 73 and 86 mm from the cell, the beam passes through holes in the 3K and 30K shields respectively, and propagates into a room temperature vacuum apparatus.

We optically probe the SrF molecules at various distances  $L_p$  from the exit aperture to measure the characteristics of the molecular beam. We have optical access to the molecular beam for  $1 \text{ mm} < L_p < 65 \text{ mm}$  through rectangular holes in the vacuum chamber and the radiation shields. All measurements for  $L_p > 65 \text{ mm}$  occur in the room-temperature beam region. This region consists of either a small cross or an octagonal structure. The cross has two viewports perpendicular to the molecular beam, and allows optical access to the beam at  $L_p = 135 \text{ mm}$ . The octagon has 6 viewports, two perpendicular to the molecular beam and four oriented at  $\pm 45^\circ$ , and allows measurements at  $L_p = 305 \text{ mm}$ . Fig. 5.1 depicts the apparatus.

A Nd:YAG laser (Big Sky Laser, CFR200) produces 25 mJ pulses of 1064 nm light with  $\approx 10 \text{ ns}$  pulse duration for ablation of the molecular precursor target. The laser beam is expanded through a telescope to a diameter of  $\sim 15 \text{ mm}$  before being tightly focused onto the ablation target by a lens of focal length  $f = 20 \text{ cm}$ . We note that the optimal conditions for focusing are observed to differ between species and targets; this configuration represents the optimum for production of SrF from our SrF<sub>2</sub> targets. Ablation targets are typically made by subjecting anhydrous SrF<sub>2</sub> powder (Sigma-Aldrich, 450030) to a pressure of 600 MPa using a die (Carver, 3619) and a hydraulic press.

The continuous operation time of the beam is limited in part by saturation of the charcoal cryopump. We use  $\approx 400 \text{ cm}^2$  of charcoal and find that it is adequate to allow run times of  $> 20$  hours at  $\mathcal{F} = 5 \text{ sccm}$ . At this flow rate we estimate the vacuum to be  $\sim 4 \times 10^{-8}$  Torr inside the cryogenic region based on measured pumping speeds for coconut charcoal [220, 221]. Once the charcoal is saturated, it must be warmed to  $\gtrsim 20 \text{ K}$  to allow the He to desorb and then be removed by the room-temperature vacuum pumps. The regeneration process for the charcoal cryopump (including the subsequent cooldown) takes  $\sim 1$  hour. Outside the cryogenic region, a 70 L/s turbo pump maintains the vacuum at  $\sim 5 \times 10^{-7}$  Torr for a flow rate of  $\mathcal{F} = 5 \text{ sccm}$ .

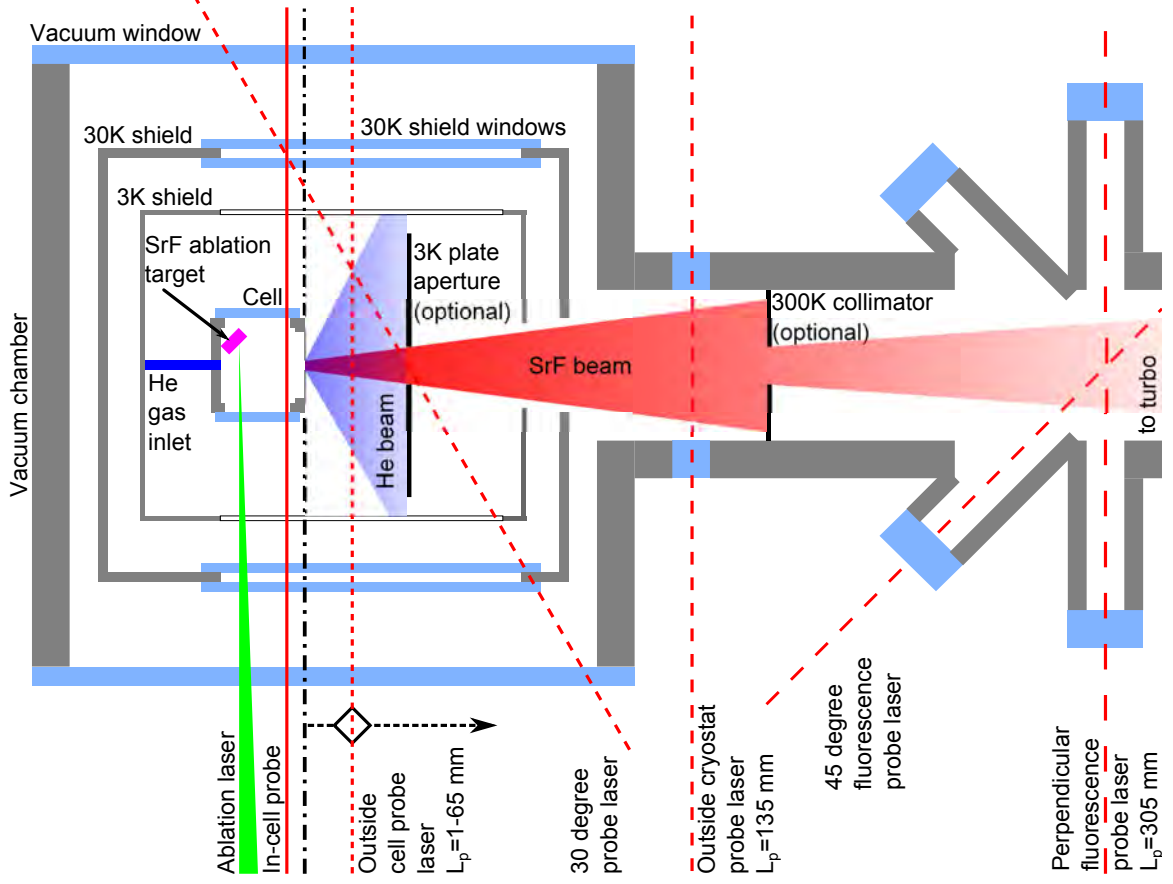


Figure 5.1: Experimental setup. Absorption measurements were made in-cell, perpendicular to the beam with  $1 \text{ mm} < L_p < 65 \text{ mm}$ , at 30 degrees to the beam at  $L_p = 20 \text{ mm}$ , and perpendicular to the beam outside the cryostat at  $L_p = 135 \text{ mm}$ . Fluorescence measurements were made perpendicular to and at 45 degrees to the beam at  $L_p = 305 \text{ mm}$  using the octagonal room-temperature apparatus.

We probe the number, temperature, and velocities of SrF in the cell and in the beam with resonant laser light from an external cavity diode laser using either absorption or laser-induced fluorescence (LIF). Unless explicitly noted otherwise, the laser drives  $Q_{11}(1/2)$  transitions from the ground state,  $X^2\Sigma_{1/2}^+(v=0, N_{rot}=0, J=1/2)$ , to the electronically excited state,  $A^2\Pi_{1/2}(v'=0, J'=1/2^-)$ , at 663 nm as defined in Ref. [90].

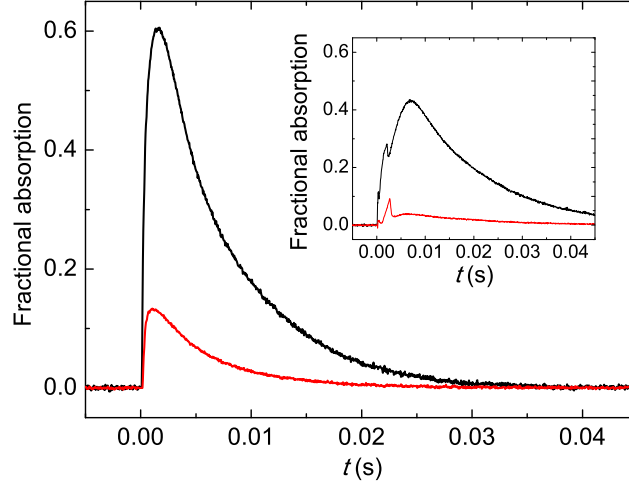


Figure 5.2: Typical raw absorption traces in the cell (—) and immediately outside at  $L_p = 1$  mm (—) for  $\mathcal{F} = 5$  sccm (main figure) and  $\mathcal{F} = 50$  sccm (inset). The in-cell and beam time traces are very similar to each other for each flow rate.

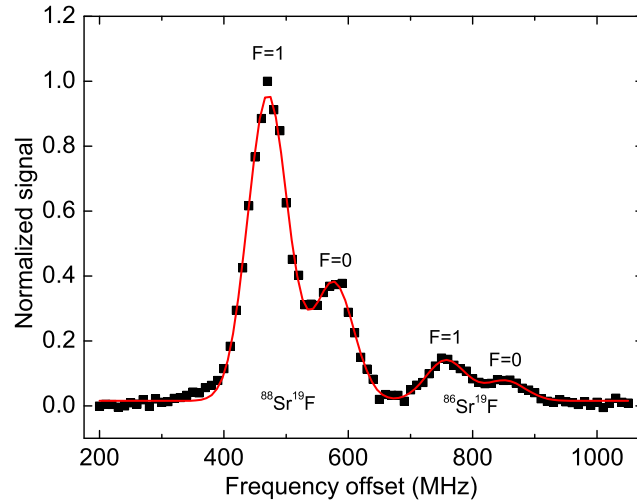


Figure 5.3: Typical in-cell absorption Doppler profile. This spectrum was recorded by scanning a probe laser located inside the cell over the  $X (v = 0, N_{rot} = 0) \rightarrow A (v' = 0, J' = 3/2^-)$  transition. This plot shows the total time-integrated absorption (traces similar to those shown in Fig. 5.2) for each laser frequency. The four peaks correspond to the two  $F = 0, 1$  HF levels for the two  $^{88}\text{Sr}^{19}\text{F}$  and  $^{86}\text{Sr}^{19}\text{F}$  isotopes as labeled. The HF levels exhibit the expected 3:1 signal height ratios due to their Zeeman degeneracy, while the isotopes exhibit the expected 8.5:1 height ratio based on their natural abundance. The solid line indicates the Doppler fit as described in the main text.

## 5.4 Experimental results

### 5.4.1 In-cell dynamics and SrF properties

#### 5.4.1.1 Thermalization

In Fig. 5.2 we show typical in-cell absorption time traces. At time  $t = 0$  the ablation laser pulse fires. For the first  $\sim 500 \mu\text{s}$  after the ablation pulse, the number of molecules in the X ( $N_{\text{rot}} = 0$ ) state rapidly increases as SrF molecules thermalize with the 3K helium gas and pass through the probe laser. This process causes the initial sharp increase in the absorption shown in Fig. 5.2. At long times the absorption signal decreases as molecules are lost from the cell through the exit aperture, and through collisions with the cell walls. Although we did not study in-cell thermalization in detail, we can compare the thermalization time to that predicted by Eqn. 5.7. There are no measurements of  $\sigma_{\text{SrF-He}}$ , so we assume that  $\sigma_{\text{SrF-He}} \approx \sigma_{\text{He-He}} = 1.05 \times 10^{-14} \text{ cm}^2$  [222]. The calculated value of  $\tau_{Th}$  also depends on the value of  $n_{\text{He}}$ . Here and for the remainder of this chapter,  $\kappa$  is estimated to be the geometric mean of the completely effusive and completely supersonic limiting cases, which yields  $\kappa = 1.5$ . For  $\mathcal{F} = 5 \text{ sccm}$  this corresponds to a density  $n_{\text{He}} = 3.5 \times 10^{15} \text{ cm}^{-3}$ . We also estimate here and throughout that the initial translational temperature of the SrF molecules is  $T_{\text{SrF}}(0) = 10^4 \text{ K}$  [216]. However we note the thermalization characteristics of this model depend only weakly on  $T_{\text{SrF}}(0)$ . Under these assumptions we obtain  $\tau_{Th} \approx 250 \mu\text{s}$ , which is in reasonable agreement with our observations.

After the initial thermalization time, the absorption signal peaks and then decays as the molecules diffuse throughout the cell to the walls, and are pumped out the exit aperture. By fitting this decay to an exponential, we can determine the molecule removal time constant  $\tau_{rmvl}$ . For example, we find  $\tau_{rmvl} = 7 \text{ ms}$  for the in-cell data with  $\mathcal{F} = 5 \text{ sccm}$  shown in Fig. 5.2. We find that  $\tau_{rmvl}$  depends critically on ablation parameters. Under only nominally different ablation locations on the target, or slightly different YAG focusing conditions, we observe that  $\tau_{rmvl}$  can vary by a factor of 2 or more. This indicates that the simple model of diffusion and extraction is heavily perturbed by the ablation process. We also find that for high flow rates,  $\mathcal{F} \gtrsim 30 \text{ sccm}$ , the temporal shape of the absorption signal changes significantly as shown in the inset of Fig. 5.2, indicating more complicated in-cell processes than just simple diffusion. Nonetheless, by fitting the decay at long times to an exponential, we find that  $\tau_{rmvl}$  is of the same order of magnitude as either  $\tau_{\text{pump}}^{\text{He}}$  or  $\tau_{\text{diff}}$  for all flow rates investigated. For example, at  $\mathcal{F} = 5 \text{ sccm}$ ,  $\tau_{\text{diff}} = 1.2 \text{ ms}$ ,  $\tau_{rmvl} = 7 \text{ ms}$ , and  $\tau_{\text{pump}}^{\text{He}} = 25 \text{ ms}$ .

### 5.4.1.2 In-cell translational, rotational and vibrational temperature

During thermalization, collisions with  $b$  cause the in-cell translational temperature of SrF,  $T_{SrF}^{cell}$ , to cool. We obtain  $T_{SrF}^{cell}$  and in-cell velocity distributions for the molecules by incrementally scanning the probe laser frequency and recording a signal trace in time for each discrete frequency. The raw signals are integrated in time, starting 300  $\mu$ s after the ablation for a duration of 20 ms unless explicitly noted otherwise. A typical in-cell absorption spectrum is shown in Fig. 5.3. The four peaks correspond to the two  $F = 0, 1$  HF levels for  $^{86}\text{Sr}^{19}\text{F}$  and  $^{88}\text{Sr}^{19}\text{F}$ . The integrated signal versus frequency lineshape is then fit to a sum of four Gaussians. The relative amplitudes of the Gaussians are constrained by the known abundance of the Sr isotopes and the degeneracies for the HF levels. The widths of the Gaussians are constrained to be the same for each peak. From the fitted width we extract a translational Doppler temperature and a velocity distribution.

We find  $T_{SrF}^{cell} \approx 5$  K over the full range of flow rates investigated. The value of  $T_{SrF}^{cell} \approx 5$  K we observe is larger than the temperature of the cell,  $T_0 \approx 3$  K. This is believed to be due to the initial heating of the buffer gas by the ablation of the target. In support of this claim, we have measured the in-cell translational Doppler width in 1 ms time increments after ablation and found that the translational width decreases at longer times ( $t \gtrsim 2$  ms), despite the fact that these observation times are very long compared to  $\tau_{Th}$ . This type of behavior has also been observed in other similar experiments [213].

Thermalization also cools the in-cell rotational temperature,  $T_{rot}^{cell}$ . For temperatures  $\sim 4$  K, typically  $\sigma_{SrF-He}/\sigma_{SrF-He}^{rot} \sim 10-100$  [204, 223]. However, due to the large mass mismatch between SrF and He, overall we expect both translational and rotational thermalization to occur with similar efficiency. We determine  $T_{rot}^{cell}$  by comparing the relative populations in the X ( $N_{rot} = 0-4$ ) states using the  $X^2\Sigma_{1/2}^+(v=0, N_{rot}=0-4) \rightarrow A^2\Pi_{1/2}(v'=0, J'=1/2^- - 9/2^-)$  transitions. We then fit the relative populations to a Boltzmann distribution. As shown in Fig. 5.4, inside the cell we find  $T_{rot}^{cell} = 5.3$  K, comparable to results obtained with a similar apparatus and another molecular species [210]. We note  $T_{SrF}^{cell} \approx T_{rot}^{cell}$  as expected.

Vibrational temperatures are expected to thermalize much more slowly than the rotational and translational temperatures because  $\sigma_{SrF-He}^{vib} \ll \sigma_{SrF-He}$ . In Fig. 5.5 we plot the relative populations of the first four vibrational levels ( $v = 0, 1, 2, 3$ ) inside the cell obtained by probing the  $X^2\Sigma_{1/2}^+(v=0-3, N_{rot}=0) \rightarrow A^2\Pi_{1/2}(v'=0-3, J'=1/2^-)$  transitions. As shown in Fig. 5.5, the data cannot be described by a Boltzmann distribution. Nonetheless, we can roughly characterize the distribution by fitting the relative populations of the first two vibrational levels to a Boltzmann dis-



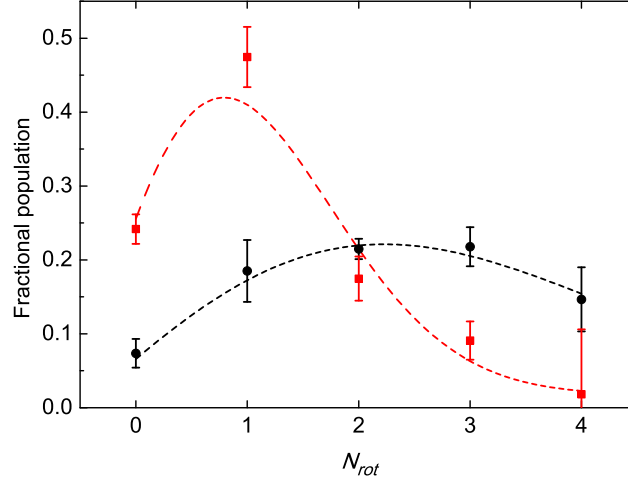


Figure 5.4: Fractional rotational populations in-cell (●) and at  $L_p = 20$  mm downstream (■), with associated fits to a Boltzmann distribution. This data was taken at  $\mathcal{F} = 5$  sccm. The fits indicate  $T_{rot}^{cell} = 5.3$  K and  $T_{rot}^{beam}(L_p = 20 \text{ mm}) = 1.2$  K; this shows substantial rotational cooling as the beam leaves the cell. Error bars in this and in all figures hereon represent the standard deviation of a set of several (typically 3-10) data points taken under nominally identical conditions.

tribution to yield the in-cell vibrational temperature,  $T_{vib}^{cell} \sim 300$  K. We find that  $T_{vib}^{cell} \gg T_0$  which indicates that the vibrational degree of freedom has not completely thermalized with the helium buffer gas. Nevertheless,  $T_{vib}^{cell}$  is still far lower than would be expected for that of unthermalized ablation products.

#### 5.4.1.3 SrF yield

In Fig. 5.6 we show the number of molecules in the  $N_{rot} = 0$  state created in the cell,  $N_{SrF}^{cell}$ , for various flow rates and approximate values of  $n_{He}$ . The number of molecules is determined through the direct absorption of an in-cell probe laser with a diameter of 2 mm located at  $L_p = -1$  mm (1 mm before the exit aperture). For a resonant probe laser sampling species  $a$  over a path length  $L_s$ , the ratio of the transmitted power  $P_T$  to the initial power  $P_0$  will vary as

$$\frac{P_T}{P_0} = e^{-n_a L_s \sigma_D}. \quad (5.15)$$

Here  $\sigma_D$  is the Doppler broadened absorption cross section [224], which is calculated from the lifetime of the  $A^2\Pi_{1/2}$  state and the Hönl-London factors [105] for SrF. We use the peak absorption signal to calculate the in-cell number. Using Eqn. 5.15 and assuming a uniform  $n_{SrF}$  within the entire volume of the cell, we obtain  $N_{SrF}^{cell}$ .

As shown in Fig. 5.6,  $N_{SrF}^{cell}$  increases with  $\mathcal{F}$  for flows up to  $\mathcal{F} \sim 5$  sccm, then reaches a maximum

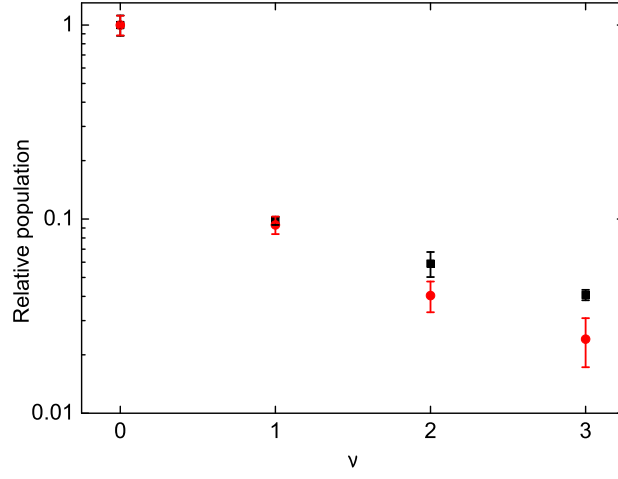


Figure 5.5: Relative vibrational populations in-cell (■) and at  $L_p = 10$  mm (●), at  $\mathcal{F} = 5$  sccm. Both datasets are normalized to 1 at  $v = 0$ .

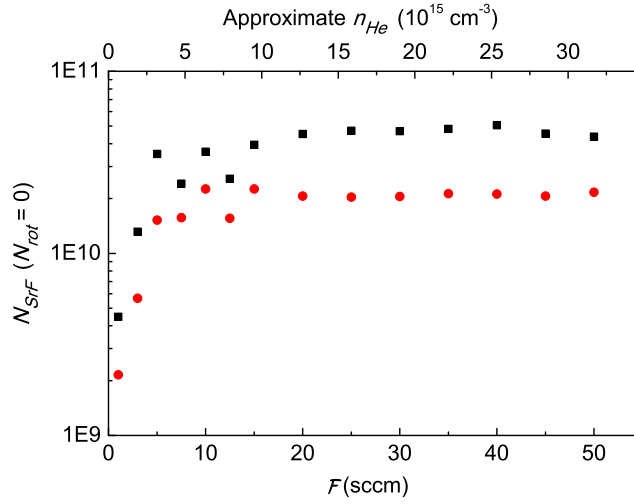


Figure 5.6: Number of SrF molecules  $N_{SrF}^{cell}$  at  $L_p = -1$  mm (■) and  $N_{SrF}^{beam}$  at  $L_p = +1$  mm (●), as a function of  $\mathcal{F}$ . Although the parameter  $\xi$  in Eqn. 5.12 varies between 0.01 and 0.5 over the flow rates examined here, the data indicate an extraction efficiency of  $\epsilon \approx 0.5$  independent of  $\mathcal{F}$ .

value of  $N_{SrF}^{cell} \approx 4 \times 10^{10}$  and remains constant for higher flow rates. We attribute the decrease in  $N_{SrF}^{cell}$  at low flow rates to insufficient helium density to completely thermalize all the molecules. The helium density at  $\mathcal{F} = 5$  sccm is  $n_{He} \approx 3.5 \times 10^{15} \text{ cm}^{-3}$ , which is in reasonable agreement with the minimum density required for thermalization as predicted by Eqn. 5.8,  $n_{Th} \approx 1.5 \times 10^{15} \text{ cm}^{-3}$ .

### 5.4.2 Molecular beam properties

In Fig. 5.2 we show a typical absorption time trace taken for  $\mathcal{F} = 5$  sccm with the probe laser located at  $L_p = 1$  mm (just outside the cell exit aperture). The molecules that exit the cell exhibit a similar temporal profile as molecules in the cell. As the SrF molecules exit the cell, the number of collisions between SrF and helium in and around the exit aperture largely determines the properties of the molecular beam far downstream. We expect  $Re_{SrF} > Re_{He}$  as discussed previously, but since we do not have an accurate value for  $\sigma_{SrF-He}$ , we solely use  $Re_{He}$  to provide a qualitative indicator of whether the molecular beam should exhibit supersonic or effusive characteristics. Values of  $Re_{He}$  are estimated using Eqns. 5.1 and 5.4.

#### 5.4.2.1 Extraction from cell

We determine the number of molecules in the X ( $N_{rot} = 0$ ) state which exit the cell by measuring the absorption of a resonant probe laser with diameter small compared to  $d$  and located at  $L_p = 1$  mm. We then time-integrate the resonant absorption traces (similar to the one shown in Fig. 5.2). We also assume a uniform  $n_{SrF}$  over the same area as the exit aperture and the measured Doppler spread ( $\approx 5$  K). The number of molecules in the beam at distance  $L_p$  from the aperture,  $N_a^{beam}$ , can then be found using

$$N_a^{beam} = \frac{A_d v_{a\parallel}}{L_s \sigma_D} \int \ln \left[ \frac{P_0}{P_T} \right] dt, \quad (5.16)$$

where  $P_0/P_T$  is the ratio of incident to transmitted power of the probe laser and  $A_d$  is the cross sectional area of the molecular beam at  $L_p$ , determined either by geometric constraints after any collimators or by the measured divergence of the beam prior to any collimators. In Fig. 5.6 we plot  $N_{SrF}^{cell}$  (at  $L_p = -1$  mm) and  $N_{SrF}^{beam}$  immediately outside the cell (at  $L_p = 1$  mm) for various flow rates. By comparing the number of molecules inside and just outside the cell, we can determine the extraction efficiency  $\epsilon$  for the cell. Over the range of flows examined, the ratio of the estimated diffusion time to the estimated pumpout time,  $\xi$ , varies between 0.01 and 0.5. Based on the extraction model presented earlier, we would crudely expect  $\epsilon$  to vary between  $\epsilon_{eff} \sim 0.003$  and  $\epsilon_{hyd} \sim 1$  over

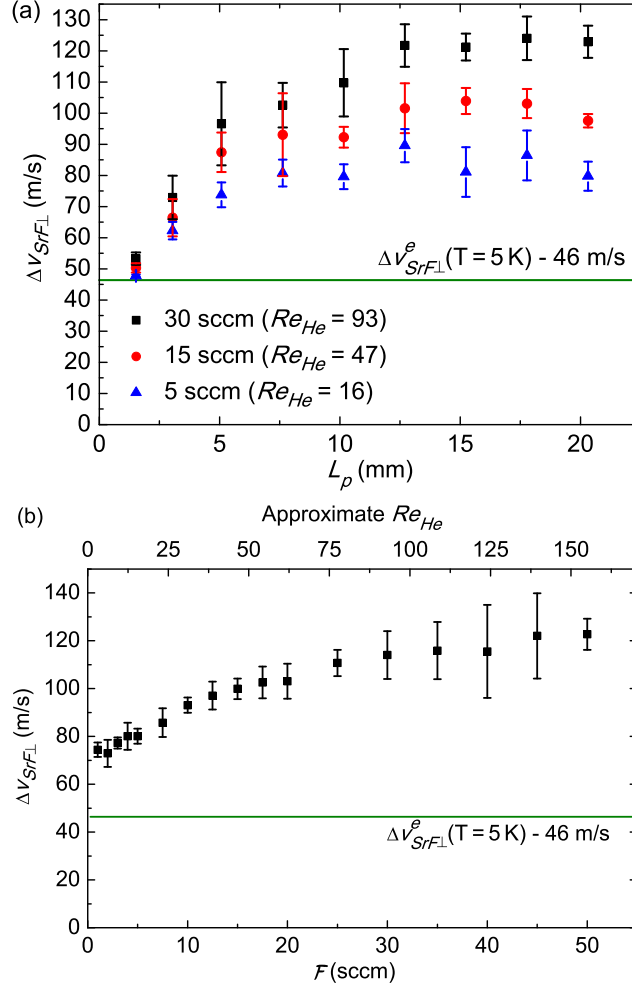


Figure 5.7: (a) FWHM transverse velocity of the molecular beam  $\Delta v_{SrF\perp}$  versus probe distances  $L_p$ , for  $F = 5$  (▲), 15 (●), and 30 (■) sccm respectively. The value of  $\Delta v_{SrF\perp}^e$  is calculated from Ref. [207]. (b) FWHM transverse velocity of the molecular beam versus  $F$  for  $L_p = 20\text{ mm}$ , where the width is no longer increasing with distance from the cell.

this range. Instead, we find that  $\epsilon \sim 0.5$ , independent of  $F$  over this range. This suggests that the extraction model presented earlier is too simplistic to fully capture the dynamics inside the cell.

#### 5.4.2.2 Beam transverse measurements

As the SrF molecules propagate from the cell, they experience fewer collisions with the helium buffer gas, as its density falls as  $1/L_p^2$ . However, the expansion of the helium gas into the vacuum outside the cell and ongoing helium-SrF collisions dramatically change the characteristics of the beam. An example of this behavior is shown in Fig. 5.7(a). Here we plot the FWHM transverse velocity spread,  $\Delta v_{SrF\perp}$ , of the molecular beam as a function of  $L_p$  for a few different values of  $F$ . Within one hole radius of the aperture,  $\Delta v_{SrF\perp}$  was measured to be consistent with a  $\sim 5\text{ K}$  Boltzmann distribution

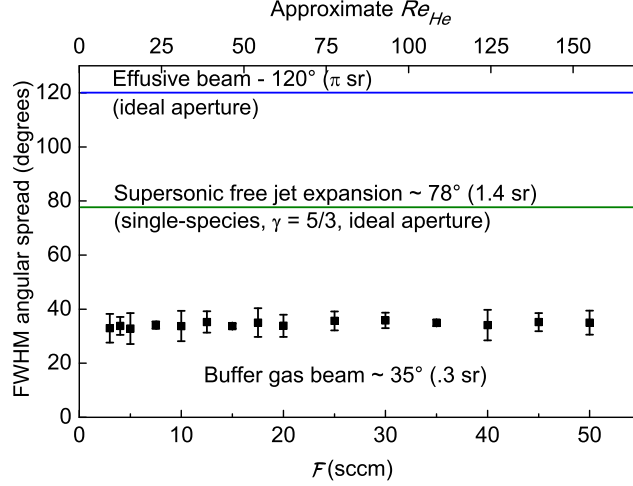


Figure 5.8: Molecular beam divergence for various flow rates. The final beam divergence demonstrates little dependence on  $\mathcal{F}$ . Included is a comparison of beam divergences for different types of beams. The divergence of an effusive beam is calculated from Ref. [207] while the divergence of a single-species supersonic free jet expansion from an ideal aperture is calculated from Ref. [225], in agreement with measurements [226].

for SrF, independent of  $\mathcal{F}$ . This value is very similar to  $T_{SrF}^{cell} \approx 5$  K. However,  $\Delta v_{SrF\perp}$  increases at further distances downstream before leveling off for  $L_p \gtrsim 10$  mm, as shown in Fig. 5.7(a), with larger  $\mathcal{F}$  resulting in larger final values of  $\Delta v_{SrF\perp}$ . The broadening of  $\Delta v_{SrF\perp}$  outside the aperture nozzle is in qualitative agreement with the presence of a He pressure gradient transverse to the molecular beam outside the cell [227–229]. This would cause the greatest rate of broadening closest to the cell aperture where pressure gradients are strongest. Larger values of  $\mathcal{F}$  would also produce larger pressure gradients, resulting in greater broadening of  $\Delta v_{SrF\perp}$ . Additional broadening beyond  $L_p \gtrsim 10$  mm is not observed, as shown in Fig. 5.7(a), indicating that collisions with helium no longer affect the characteristics of the SrF beam beyond this distance. Fig. 5.7(b) depicts  $\Delta v_{SrF\perp}$  for  $L_p = 20$  mm for a variety of flow rates  $\mathcal{F}$ . Combining this data with the beam forward velocities measured in the next section, we determine the beam divergence to be nominally independent of  $\mathcal{F}$  as shown in Fig. 5.8. Compared to both an effusive beam and a single-species supersonic free jet expansion beam from an ideal aperture, the beam in this work is significantly more directional. This increased directionality has been observed for binary mixtures of gases of disparate masses using similar geometries and Reynolds numbers and is likely a result of aerodynamic focusing [230, 231]. We did not thoroughly investigate the effects of specific aperture geometries on the beam. However while all other data presented in this chapter employed a 3 mm diameter exit hole in the cell, a 1 mm  $\times$  7 mm slit was also employed. This slit produced beams slower by 7% on average at  $\mathcal{F} = 5$

sccm and with  $\sim 10\%$  lower final transverse velocities as measured along the long dimension of the slit.

#### 5.4.2.3 Beam rotational and vibrational temperature

The remainder of the measurements are made for  $L_p > 10$  mm, where collisions within the beam have largely ceased, and the characteristics of the beam are expected to be static. In Fig. 5.4 we show the relative rotational populations measured at  $L_p = 10$  mm for  $\mathcal{F} = 5$  sccm. This distribution is consistent with a beam rotational temperature of  $T_{rot}^{beam} = 1.2$  K and is significantly colder than the measured in-cell rotational temperature of  $T_{rot}^{cell} = 5.3$  K. The observation of  $T_{rot}^{cell} > T_{rot}^{beam}$  is attributed to cooling of rotational degrees of freedom via collisions near the aperture, as is typically observed in standard free jet expansions [208, 209].

In a separate measurement at  $L_p = 20$  mm downstream, similar rotational cooling was observed for a variety of  $\mathcal{F}$ , as shown in Fig. 5.9. We find that  $T_{rot}^{beam} \approx 1$  K for all flow rates investigated. Since the number of collisions outside the aperture is expected to scale linearly with  $\mathcal{F}$ , it is interesting that there is little change in  $T_{rot}^{beam}$  over the range  $\mathcal{F} = 5$ -30 sccm. The measured values of  $T_{rot}^{beam}$  may be compared to the conservative upper limit on the ultimate downstream He temperature at these flow rates using Eqn. 5.14. In this limit we find  $T_{He}^{beam} < 2.38$  K, 0.99 K and 0.57 K for  $\mathcal{F} = 5, 15$  and 30 sccm respectively. Similar results demonstrating  $T_{rot}^{beam}$  largely independent of backing pressure have been observed for CO seeded in room-temperature He [232].

In Fig. 5.5 we plot the relative vibrational populations in the beam at  $L_p = 10$  mm. We observe little or no cooling of the vibrational degree of freedom in the beam. This is consistent with the notion that many more collisions are required to thermalize the vibrational degree of freedom [204] than the rotational or translational degrees of freedom.

#### 5.4.2.4 Beam forward velocity and temperature

In Fig. 5.10 we show the measured dependence of the beam forward velocity,  $v_{SrF\parallel}$ , on the helium flow rate  $\mathcal{F}$  taken at two different places downstream from the cell. For  $L_p = 15$  mm, we determine  $v_{SrF\parallel}$  by comparing the Doppler shifts of direct absorption profiles of two probe lasers, one normal to the molecular beam and one at 30 degrees relative to normal. For  $L_p = 305$  mm, the same technique is employed but using LIF instead.

For all values of  $\mathcal{F}$ , we observe  $v_{SrF\parallel} > v_{SrF\parallel}^e$ , indicating that there are still sufficient collisions near the aperture to cause significant increase in  $v_{SrF\parallel}$  even at the lowest flow rates where  $Re_{He} \sim 1$ .

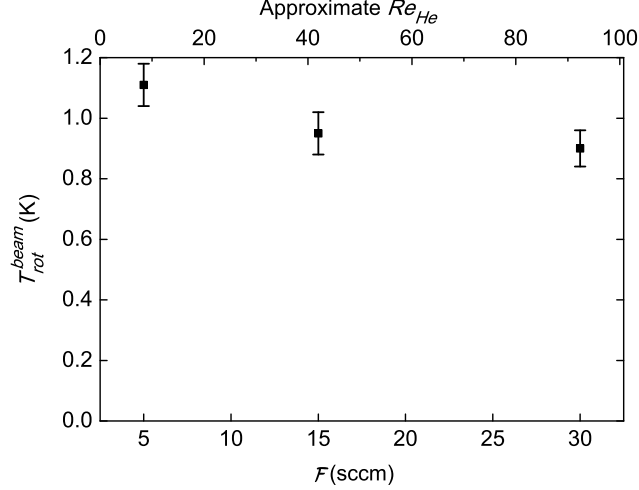


Figure 5.9:  $T_{rot}^{beam}(L_p = 20 \text{ mm})$  versus  $\mathcal{F}$ . For the range of  $\mathcal{F}$  investigated, rotational temperatures in the beam are  $\approx 1 \text{ K}$ . While we expect  $T_{rot}^{beam}$  to decrease with increasing  $\mathcal{F}$ , these observations are consistent with other free jet sources that show a termination of rotational cooling. These temperatures were determined by a fit to data similar to those shown in Fig. 5.4.

At the highest  $\mathcal{F}$  where  $Re_{He} \gg 1$ , we expect that  $v_{SrF\parallel}$  should approach  $v_{He\parallel}^s$ , in agreement with our observations. However even at the highest  $\mathcal{F}$ ,  $v_{SrF\parallel} < v_{He\parallel}^s$ . Since we cannot measure the forward velocity of the helium in the beam,  $v_{He\parallel}$ , this observation may simply result from  $v_{He\parallel} < v_{He\parallel}^s$  with  $v_{SrF\parallel} = v_{He\parallel}$ . It may also be due to the phenomenon known as velocity slip, where the speed of the seeded species does not get fully boosted to the speed of the carrier [208, 209, 233–235].

In Fig. 5.11 we show the FWHM of the forward velocity,  $\Delta v_{SrF\parallel}$ , for various values of  $\mathcal{F}$ .  $\Delta v_{SrF\parallel}$  was measured in LIF by varying the frequency of a  $45^\circ$  probe laser 305 mm downstream and integrating over the entire duration of the molecular beam pulse. An aperture collimates the molecular beam so that the transverse Doppler width is reduced to near the natural linewidth of the X-A probe transition ( $\approx 6.6 \text{ MHz}$ ). The Doppler broadening from the forward velocity of the beam is substantially larger than this ( $\sim 100 \text{ MHz}$ ); thus, fitting these distributions to a Gaussian enables extraction of the forward temperatures of the molecular beam. For the range of  $\mathcal{F}$  explored, the typical measured values of  $\Delta v_{SrF\parallel} \approx 75 \frac{m}{s}$  (corresponding to  $T_{SrF\parallel} \approx 13 \text{ K}$ ) are well above  $\Delta v_{SrF\parallel}^e$ . This is in contrast to the behavior of typical seeded free jet expansions where  $\Delta v_{SrF\parallel} < \Delta v_{SrF\parallel}^e$  due to cooling during the isentropic expansion. We note as well that for fixed  $\mathcal{F}$ , the measured values of  $\Delta v_{SrF\parallel}$  varied appreciably ( $\sim 40\%$ ) under nominally identical conditions. These observations are not compatible with the simple thermalization model presented in the text, and suggest that the ablation significantly perturbs the in-cell thermalization process.

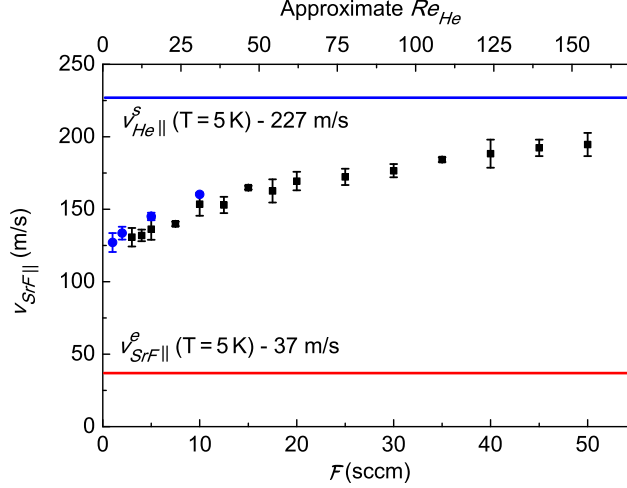


Figure 5.10: Forward velocity for various flow rates. The data were taken at  $L_p = 15$  mm in absorption (■) and at  $L_p = 305$  mm using LIF (●). Measurements at different values of  $L_p$  are in good agreement.

A number of observations regarding the forward velocity suggest that the simplistic thermalization model described previously may not be adequate to describe this system. For example, we find that the measured values of  $v_{SrF||}$  and  $\Delta v_{SrF||}$  vary by  $\sim 15\%$  under nominally similar ablation conditions, depending on the location ablated on the target. Specifically, ablating closest to the He gas inlet and furthest from the exit aperture tended to produce the lowest  $v_{SrF||}$  and  $\Delta v_{SrF||}$ . We also find that the characteristics of the ablation laser also change  $v_{SrF||}$  and  $\Delta v_{SrF||}$ . In particular, the focus and the power of the ablation laser can alter  $v_{SrF||}$  and  $\Delta v_{SrF||}$  by  $\sim 15\%$ . Finally, we observe very fast molecules ( $\gtrsim 225$  m/s) with large  $\Delta v_{SrF||}$  at early times ( $t \lesssim 2$  ms) in the molecular pulse, as shown in Fig. 5.12. The observed time variation in  $v_{SrF||}$  and  $\Delta v_{SrF||}$  cannot be fully explained by time of flight effects, which suggests that molecules leaving the cell at different times thermalize to different temperatures. These observations are difficult to explain using the simple models outlined earlier, and suggest more complicated in-cell dynamics.

#### 5.4.2.5 Beam brightness

Finally, we have measured  $\mathcal{B}$ , the brightness of the molecular beam in the X ( $N_{rot} = 0$ ) state, both just outside the cell (at  $L_p = 1$  mm) and at  $L_p = 135$  mm in a room-temperature environment, as shown in Fig. 5.13. Inside the cryostat, geometrical constraints make further slowing, trapping, or precision spectroscopy of the molecular beam quite challenging, so  $\mathcal{B}(L_p = 135$  mm) is representative of the useful beam brightness for most experiments. To calculate  $\mathcal{B}$  downstream we use Eqn. 5.16. A collimating aperture constrains the molecular beam to  $\sim 0.03$  sr, so we assume a uniform  $n_{SrF}$  over



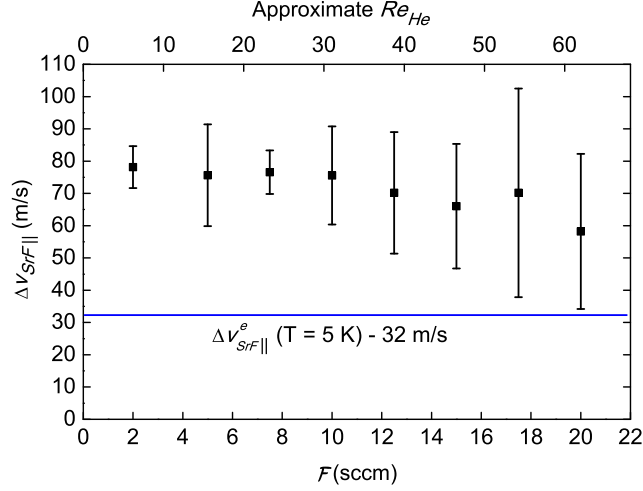


Figure 5.11: FWHM forward velocity spread for various flow rates. The typical measured value of  $\Delta v_{SrF||} \approx 75 \frac{m}{s}$  is roughly constant across the range of  $\mathcal{F}$  explored. The value of  $\Delta v_{SrF||}$  is well above the maximum expected value of  $\Delta v_{SrF||}^e$  (—), calculated from Ref [207].

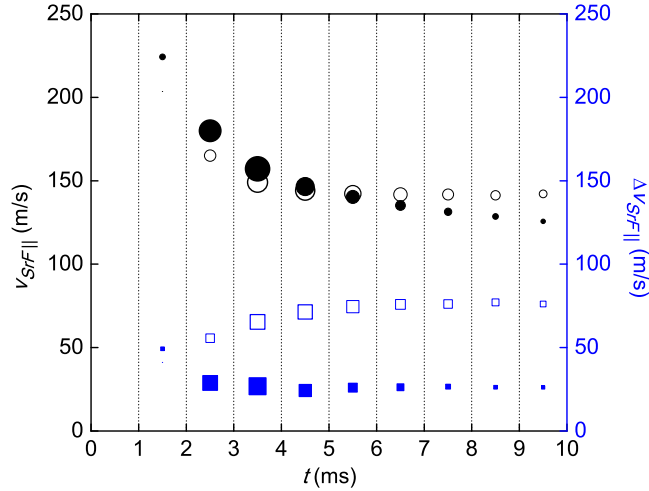


Figure 5.12: Measured forward velocity (●), measured forward velocity spread (■), simulated forward velocity (○) and simulated forward velocity spread (□) versus time. The data were taken at  $L_p = 305$  mm in LIF using 1 ms time bins for a flow rate of  $\mathcal{F} = 5$  sccm. The size of the points indicate relative molecule number. The measured data indicate that both  $v_{SrF||}$  and  $\Delta v_{SrF||}$  vary significantly over the time the beam persists; molecules detected earliest have the largest  $v_{SrF||}$  and  $\Delta v_{SrF||}$ , and both decrease with time. The simulated data assume a time-invariant Gaussian velocity distribution at the exit aperture with  $v_{SrF||} = 145$  m/s and  $\Delta v_{SrF||} = 75$  m/s; thus, the time dependence of the simulated data downstream is solely due to time of flight effects. Although the simulated data exhibit similar time variation in  $v_{SrF||}$ , the magnitude of the effect is not sufficient to completely describe the measurements. Furthermore the simulation is in qualitative disagreement with the measured time variation in  $\Delta v_{SrF||}$ . These observations are consistent with initial heating of the buffer gas at early times, as described previously.

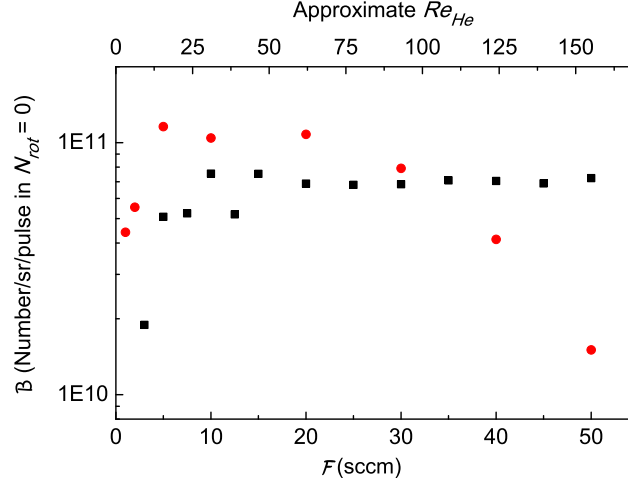


Figure 5.13:  $\mathcal{B}$  for various flow rates  $\mathcal{F}$  measured at  $L_p = 1$  mm (■) and  $L_p = 135$  mm (●). The data indicate the beam is attenuated over long distances, when the cell is operated at flow rates  $\mathcal{F} \gtrsim 20$  sccm. The increased  $\mathcal{B}$  downstream versus upstream at low flow rates is likely due to rotational cooling in the beam. Downstream data were taken with the plate at  $L_d = 34$  mm.

this solid angle and the Doppler spread associated with this geometry. Nominally, we expect  $\mathcal{B}$  to remain constant as the beam propagates. However, we observe  $\mathcal{B}(L_p = 135 \text{ mm})/\mathcal{B}(L_p = 1 \text{ mm}) > 1$  for low  $\mathcal{F}$ . We attribute this increase in observed downstream brightness to rotational cooling during the first  $\sim 10$  mm of beam propagation. For high  $\mathcal{F}$ ,  $\mathcal{B}(L_p = 135 \text{ mm})/\mathcal{B}(L_p = 1 \text{ mm}) < 1$ , indicating a loss of molecules during beam propagation. Because this loss increases with larger  $\mathcal{F}$ , we believe that the cause is a higher helium gas load, which can lead to a larger background density of helium and hence collisional attenuation of the SrF beam.

In our initial experiments, the ratio  $\mathcal{B}(L_p = 135 \text{ mm})/\mathcal{B}(L_p = 1 \text{ mm})$  was significantly worse at high flow rates. We found that placing a charcoal-covered plate (2.5 mm thick, with a 6.35 mm diameter hole) in the beam line substantially reduced this problem. We suspect that the plate provides strong pumping of He gas near the beam axis, creating a differentially-pumped region behind the plate through which the beam can travel through without undergoing collisions with background helium. This plate was tested in two separate positions, at  $L_d = 21$  mm and  $L_d = 34$  mm downstream from the cell aperture; both placements largely eliminated beam brightness decreases for  $\mathcal{F} \lesssim 20$  sccm. Ultimately we find that  $L_d = 34$  mm results in the highest brightness at  $L_p = 135$  mm for  $\mathcal{F} \lesssim 20$  sccm. For  $\mathcal{F} \gtrsim 20$  sccm, we still observe a significant reduction in  $\mathcal{B}$ . We did not investigate this further because we plan to primarily operate the apparatus in the low flow ( $\mathcal{F} \lesssim 20$  sccm) regime where the forward speeds are the lowest. We speculate that the use of a true molecular beam skimmer might help alleviate this problem.

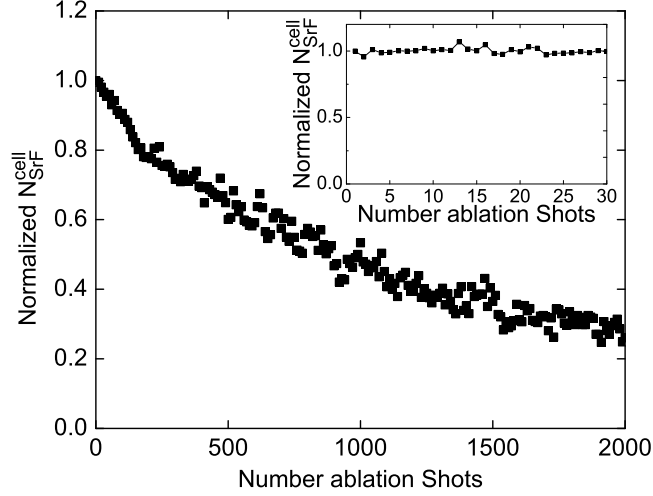


Figure 5.14: Normalized  $N_{SrF}^{cell}$  (which is well-correlated with  $N_{SrF}^{beam}$ ) as a function of ablation shot number. In the main figure, each data point represents the average of 10 ablation shots. The inset shows  $N_{SrF}^{cell}$  for 30 consecutive shots to illustrate the shot-to-shot fluctuations in  $N_{SrF}^{cell}$ . The variation shown here ( $< 10\%$ ) is typical for this system. For the data shown in the inset, the pulse tube refrigerator was turned off, to distinguish ablation variation from the 1.4 Hz pulse tube temperature variation.

#### 5.4.2.6 Ablation, noise and variation

We typically ablate the  $SrF_2$  target at  $R_{YAG} = 1$  Hz repetition rate. We observe that operation at  $R_{YAG} > 1$  Hz sometimes decreases  $N_{SrF}^{cell}$  by a factor of 2 or more. Other times  $N_{SrF}^{cell}$  is nominally independent of  $R_{YAG}$ , up to  $R_{YAG} \sim 15$  Hz. This dependence on  $R_{YAG}$  varies from target to target, and from spot to spot on the same target.

For consecutive shots on the same spot on the target,  $N_{SrF}^{cell}$  typically varies by  $\sim 5\%$  from shot to shot. Thus to produce consistent data, the ablation spot was changed only when necessary. Ablation yield from a single spot on the target was found to decrease after many shots. Typically  $N_{SrF}^{cell}$  decreased by a factor of 2 after 500-1000 shots on the same spot (although this could vary by a factor of 2 or more). The steady decrease in  $N_{SrF}^{cell}$  versus shot number for a single ablation spot, depicted in Fig. 5.14, is typical.

The in-cell ablation yields are observed to vary significantly (a factor of 2 or more) for different nearby spots on the target. However, in the absence of significant visible damage to the window, an ablation spot can generally be found which will yield very nearly the maximum  $N_{SrF}^{cell}$  from that target. Finding such optimal spots typically requires sampling of a dozen or so different ablation spots.

In an effort to improve yield, durability, or allow consistent operation at higher  $R_{YAG}$ , we in-

investigated different ablation targets: an  $\text{SrF}_2$  single crystal, a commercial isostatically hot-pressed  $\text{SrF}_2$  target, and eight cold-pressed targets made in-house with the same procedure but using different precursor materials. The in-house targets used pure powders of anhydrous  $\text{SrF}_2$ , precipitated  $\text{SrF}_2$ ,  $1\ \mu\text{m}$   $\text{SrF}_2$  and crushed macroscopic crystals of  $\text{SrF}_2$ , as well as the same powders mixed with powdered boron metal in a 1/9 molar ratio. While the yield from all targets was the same to within a factor of  $\sim 2$ , ultimately the anhydrous  $\text{SrF}_2$  with powdered boron metal offered the greatest yield and allowed repetition rates up to 15 Hz, equal to the best repetition rates of the group. All targets lasted for the same number of shots to within a factor of  $\sim 2$ .

Ablation of  $\text{SrF}_2$  produced macroscopic amounts of dust inside the cell. However, this dust did not create any known problems. After more than  $10^6$  total ablation shots, both cell windows were visibly covered with dust (resulting in less than 10% transmission of a cw probe laser through each cell window), but  $N_{\text{SrF}}^{\text{cell}}$  was not significantly affected. Thus  $10^6$  can be taken as a lower bound on the number of ablation shots possible before the apparatus must be opened and the target replaced. The ablation laser appears to remove any dust from the window in its path.

In addition to variation due to ablation, the periodic temperature oscillation of the pulse tube refrigerator’s second stage (1.4 Hz period,  $T_{\min} = 2.85\ \text{K}$ ,  $T_{\max} = 3.15\ \text{K}$ ) was observed to affect both  $N_{\text{SrF}}^{\text{cell}}$  and  $N_{\text{SrF}}^{\text{beam}}$ . This oscillation correlates with a  $\sim 10\%$  peak to peak variation of  $N_{\text{SrF}}^{\text{cell}}$  and a  $\sim 25\%$  peak to peak variation of  $N_{\text{SrF}}^{\text{beam}}$ . While temperature-induced variation in the rotational population may explain the variation of  $N_{\text{SrF}}^{\text{cell}}$ , it cannot account for the larger variation in  $N_{\text{SrF}}^{\text{beam}}$ . We speculate that the background He pressure outside the cell is changing at the 1.4 Hz frequency due to temperature-dependent pumping and/or outgassing rates from the charcoal cryosorb. We have seen that in a similar apparatus cooled with liquid helium rather than a pulse tube, both  $N_{\text{SrF}}^{\text{cell}}$  and  $N_{\text{SrF}}^{\text{beam}}$  vary by 5% or less shot to shot.

#### 5.4.2.7 Source comparison

For the production of bright, slow, and cold beams of free radicals and refractory molecular species, this source compares favorably in many respects to competing technologies. In particular, the brightness  $\mathcal{B} = 1.2 \times 10^{11}\ N_{\text{rot}} = 0$  molecules/sr/pulse in this work is approximately 100 times that produced by the brightest [76] design based on a pulsed Smalley-type laser ablation supersonic expansion source [236–238] we are aware of. Furthermore, that free jet expansion beam has a mean forward velocity of  $280\ \frac{\text{m}}{\text{s}}$ , roughly twice that of the cryogenic buffer gas beam characterized in this paper. Another group created a beam of SrF by heating  $\text{SrF}_2$  and boron metal to 1550 K [239].

While the total brightness (over all states) of  $2.1 \times 10^{15}$  molecules/sr/s of that source is quite high, the brightness in the rovibrational ground state is  $\mathcal{B} = 5 \times 10^{11}$  molecules/sr/s, comparable to the source presented here for  $R_{\text{YAG}} = 4$  Hz. However, the high-temperature source can only be operated for a short time before the oven must be refilled. Moreover, the forward (effusive) velocity is  $v_{\text{SrF}}^e \sim 650 \frac{\text{m}}{\text{s}}$  at that temperature, undesirable for many experiments.

While the measurements in this work were performed using only SrF, our beam source can be readily adapted by changing the target to create a wide variety of species. Within our group beams of BaF [240] and ThO [74] have been realized using similar techniques, with similar brightness and overall performance. Similar cryogenic beam sources are also currently in use in other groups as well [74, 75, 241, 242].

## 5.5 Subsequent source improvements

Subsequent to publication of Ref. [73], several improvements are made to the beam source. The original Nd:YAG laser used for ablation is replaced by a different Nd:YAG laser (Continuum, Minilite II) which displays less variation in pulse energy shot to shot, thereby decreasing the downstream variation in molecule number by  $\sim 2\times$ . At the suggestion of Markus Greiner, the ablation laser is synced to fire a single laser pulse at the coldest point of the  $\approx 1.4$  Hz temperature cycle of the pulse tube. This is observed to decrease the downstream variation in molecule number by  $\sim 2\times$ . Installation of a “snorkel” on the cell allows the ablation window to be moved further from the ablation target, thereby decreasing problems with dust contaminating the ablation window without significantly changing the cell volume. The OFHC copper snorkel has a .332 inch ID, a  $\sim .3$  inch wall thickness, a 1 inch length and is centered on the cell. Smaller snorkel IDs and longer lengths are desirable to decrease the number of SrF molecules diffusing to the cell window but increase ablation laser alignment difficulty. The snorkel ID and length chosen are a compromise between these two considerations. The original 1” diameter hole on the front of the 30K shield is replaced with a differential pumping tube (2.75” long with 7.35 mm diameter) to decrease the He gas load on the room temperature turbo pumps. For further discussion of this change which occurred in parallel with other vacuum-related changes, see [section 9.3](#). The target-making procedure is changed to include sintering of the targets, thereby increasing the number of shots after which the ablation spot has to be moved (from  $\sim 500$  shots to  $\sim 2000$ -4000 shots on average). The target-making procedure in use at the time of this writing is detailed in [Appendix I](#). A few pictures of the current apparatus

are included in [Appendix K](#).

We acknowledge the contributions of Nick Hutzler, Elizabeth Petrik, Dave Patterson, John Doyle, Amar Vutha, Peter Orth, Matthew Steinecker, Chris Yale, and Colin Bruzewicz to the work detailed in this chapter.

## Chapter 6

# Radiative force from optical cycling on a diatomic molecule

This chapter outlines the set of experiments where we verify the feasibility of creating a cycling transition for SrF. Specifically, we employ this cycling transition to exert a transverse radiative force on the molecules within our molecular beam. The data presented in this chapter parallel that of Ref. [90].

### 6.1 Introduction

Given the proposed scheme to create a cycling transition for SrF outlined in [chapter 3](#), we seek to experimentally verify the feasibility of our proposal. Verification is broken down into two phases. The first phase aims to demonstrate an increase in laser induced fluorescence (LIF) from spontaneously scattered photons by sequentially adding the conditions for cycling to a control setup. Relative to illumination of the molecules by the  $\lambda_{00}$  laser alone, the addition of either a magnetic field or the  $\lambda_{10}$  laser is expected to increase the number of states taking part in the cycling and thus increase the resulting LIF. However, while an increase in LIF is an indicator of cycling, other mechanisms could conceivably result in the same effect. For example, increased LIF could result instead from liberating molecules trapped in coherent or Zeeman dark states or from a high-lying metastable state slowly repopulating one of the states involved in our cycling transition.

Hence, deflection of our molecular beam by radiative force is more definitive test of our technique. Applying the  $\lambda_{00}$  and  $\lambda_{10}$  lasers in only a single direction perpendicular to the molecular beam at a

point upstream (the interaction region) should result in a spatial deflection of the molecular beam further downstream (the probe region). In contrast to an increase in LIF, observation of deflection requires the same molecules scatter  $\sim 100$  photons, a good test of the robustness of our proposed cycling transition. The  $\lambda_{00}$  and  $\lambda_{10}$  lasers applied in the interaction region are referred to as the pump and repump lasers respectively to distinguish them from lasers driving the same transition in the detection region.

## 6.2 Experimental considerations for deflection

We briefly review considerations to optimize the observed deflection. The recoil velocity for SrF is given by

$$v_r = \frac{\hbar k}{m_{\text{SrF}}} = 5.62 \text{ mm/s}, \quad (6.1)$$

where  $k = 2\pi/\lambda_{00}$  and  $m_{\text{SrF}}$  is the mass of SrF. The downstream deflection  $d$  of the molecular beam should obey

$$d = \frac{N_{\text{sc}} v_r D}{v_{\parallel}}, \quad (6.2)$$

where  $N_{\text{sc}}$  is the number of photons scattered in the interaction region,  $D$  is the distance between the interaction and the probe region, and  $v_{\parallel}$  is the molecular beam forward velocity. The value of  $N_{\text{sc}}$  can be increased both by using more laser power (although this saturates) or by using a longer interaction region. Rather than expanding the  $\lambda_{00}$  and  $\lambda_{10}$  laser beams (and correspondingly decreasing the intensity), we reflect the laser beams around the interaction region so that the beams make a number of passes through the interaction region, each in the same direction. While the observed deflection may also increase by decreasing the value of  $v_{\parallel}$ , this quantity is not easily decreased. Finally, increasing the propagation length should result in increased observed deflection. In our experiment, the value of  $D$  is limited by both space constraints and the desire to image our molecular beam using a 1:1 imaging ratio. Ultimately, the final apparatus is constructed as a compromise between expediency and the desire to maximize the observed deflection  $d$ .

## 6.3 Experimental apparatus

The molecular beam source used in these experiments is similar to that detailed in [chapter 5](#). After exiting the cryostat, the molecular beam passes through a 1.5 mm tall  $\times$  3 mm wide slit which collimates the beam transversely to  $\Delta v_{\perp} \simeq 3 \text{ m/s}$  for the direction along the slit width as shown in



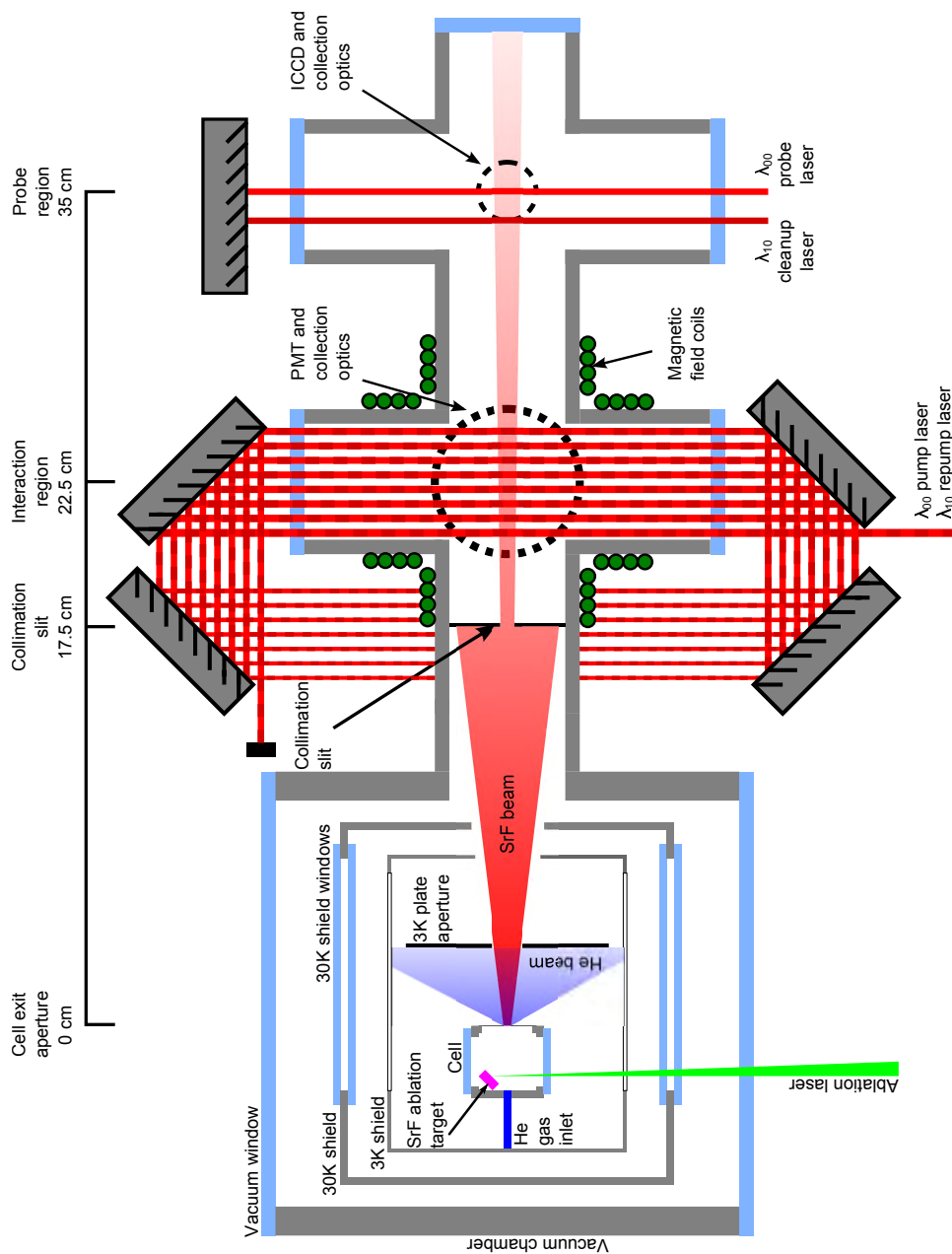


Figure 6.1: Experimental setup for increased LIF and deflection. A collimating aperture limits the transverse velocity spread of the molecular beam. Further downstream in the interaction region, the molecules are excited via repeated passes of the  $\lambda_{00}$  pump and  $\lambda_{10}$  repump lasers which are overlapped on a dichroic mirror (not shown). In the interaction region, a magnetic field provides remixing of the dark Zeeman sublevels and the resulting LIF is recorded using a PMT. The molecular beam then propagates further downstream to the probe region where first the  $\lambda_{10}$  cleanup laser returns all molecules to the  $X(v=0)$  state. Next, the molecules are excited by the  $\lambda_{00}$  probe laser. The spatial intensity profile is then determined by imaging the resulting LIF onto an ICCD camera. The turbopump is not shown in the above diagram. The cleanup and probe lasers are retroreflected to eliminate artificial Doppler shifts.

Fig. 6.1. The slit height ensures all molecules traverse the  $\approx 2$  mm laser beams while the slit width ensures that the entire spatial extent of the molecular beam can be imaged onto the camera.

The vacuum region downstream of the slit consists of an interaction region and a probe region, separated by  $D = 12.5$  cm. This part of the apparatus is constructed entirely from commercial KF40 components except for the home-made Brewster windows allowing optical access to the interaction region. The choice of KF components instead of conflat components is unfortunate; the former have a tendency to move during vacuum pump-down of the apparatus. The positional reproducibility of the KF components is also poor, which results in alignment problems whenever the apparatus is disassembled and reassembled. Ultimately, a series of clamps is used to partially alleviate problems related to movement of the vacuum apparatus.

The interaction region is defined by two pairs of orthogonal 4 cm diameter Helmholtz coils used to add a magnetic field  $\mathbf{B}$ , and a 3 cm clear aperture which gives optical access to the SrF beam. The  $\lambda_{00}$  pump laser and the  $\lambda_{10}$  repump laser have linear polarization, sidebands with modulation frequency  $f_{\text{mod}} = 42.5$  MHz and modulation index  $M_{\text{mod}} = 2.6$ , beam diameters of 1.9 mm ( $\frac{1}{e^2}$  full width intensity waist), and powers of  $\sim 60$  and  $\sim 50$  mW respectively. They are spatially overlapped using a dichroic mirror (Semrock, FF669-Di01) before passing through the interaction region along the 3 mm axis of the slit. Windows are home-made Brewster windows (See Appendix H). The laser beams are reflected around a circular path for a total of 8 passes through the molecular beam, all originating from the same direction. This results in an interaction length  $l_0 = 0.9$  cm and an interaction time  $t_0 = v_{\parallel}/l_0 = 44$   $\mu\text{s}$ . LIF from the  $\lambda_{00}$  transition is monitored in the interaction region using a PMT (See Appendix J for details on PMT light collection). The interior of the interaction region is lined with black electrostatic foam to minimize the amount of scattered laser light and room light incident on the PMT. It is determined empirically that outgassing from the black foam is insufficient to attenuate the molecular beam in this experiment. The spatial intensity profile of the SrF beam in the probe region is determined by imaging LIF, created by a “probe”  $\lambda_{00}$  laser driving the  $X(v = 0, N = 1) \rightarrow A(v = 0, J = 1/2)$  transition, onto the photocathode of an intensified CCD camera (Princeton Instruments PI-MAX2 with Unigen II image intensifier). A “cleanup”  $\lambda_{10}$  laser is introduced between interaction and probe regions, to return residual population in the  $X(v = 1, N = 1)$  state back to the  $X(v = 0, N = 1)$  state. Both probe and cleanup lasers have sidebands with modulation frequency  $f_{\text{mod}} = 42.5$  MHz and modulation index  $M_{\text{mod}} = 2.6$  in order to maximize the LIF, are retroreflected to eliminate artificial Doppler shifts, and are linearly polarized. The room temperature apparatus beyond the  $1.5 \times 3$  mm collimation slit is held at  $\lesssim 10^{-6}$

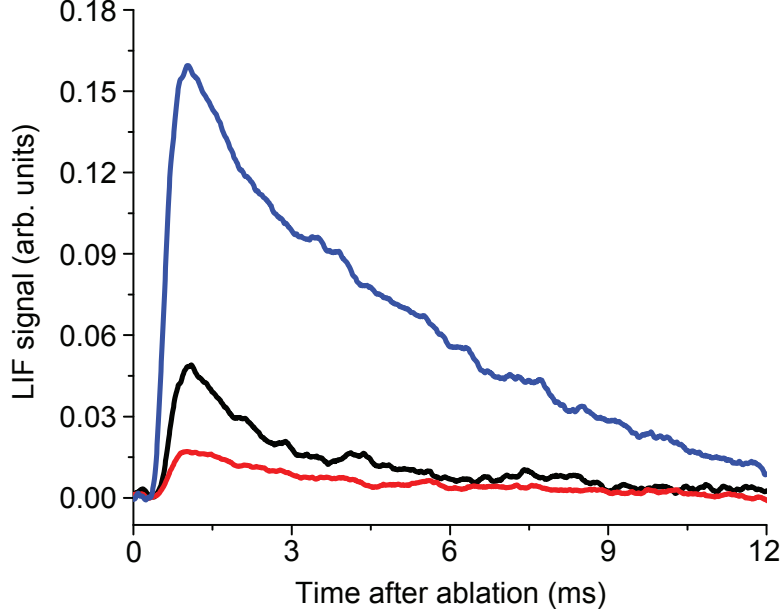


Figure 6.2: Signals demonstrating cycling fluorescence in SrF. LIF signal from the  $\lambda_{00}$  pump laser in the interaction region with  $B = 0$  Gauss (—), with  $B = 7$  Gauss (—), and with both the  $\lambda_{10}$  repump and  $B = 7$  Gauss (—). The addition of the magnetic field  $B$  results in a  $\sim 3.5\times$  enhancement in signal due to remixing from dark Zeeman sublevels. The addition of the  $\lambda_{10}$  repump results in another  $\sim 3.5\times$  enhancement, indicating pumping to and from the X ( $v = 1, N = 1$ ) state as a result of optical cycling.

Torr by a 60 L/s turbomolecular pump (Pfeiffer, TMU 071 P).

## 6.4 Results

In Fig. 6.2 we show LIF from the  $\lambda_{00}$  laser in the interaction region. The addition of  $B = 7$  Gauss (oriented at angle  $\theta_B = 30^\circ$  relative to the linear laser polarization) increases the resulting LIF by a factor of 3.5. We find that the magnitude of the LIF signal does not depend strongly on the magnitude or direction of  $\mathbf{B}$ , as long as  $B \gtrsim 3$  Gauss and  $\theta_B \neq 0, 90^\circ$ . Assuming complete remixing of the dark Zeeman states and sufficient interaction time, each molecule should scatter  $N_{00} \sim \frac{1}{q_{00}}$  photons. In a separate experiment, we determined the  $q_{01}$  FCF from absorption spectroscopy on the X( $v = 1, N = 1$ )  $\rightarrow$  A ( $v' = 0, J' = 1/2$ ) transitions in the buffer cell. From the ratio of observed transition strengths, and using the calculated value  $q_{11} = 0.95$ , we determined  $q_{01} = 0.021 \pm .005$  and correspondingly,  $N_{00} = 48$ , in good agreement with our calculations. The LIF enhancement due to application of  $\mathbf{B}$  indicates that  $\sim 48/3.5 = 14$  photons are scattered when  $\mathbf{B} = 0$ . Although for  $B = 0$  we expect only 3 photon scatters before pumping into a dark Zeeman sublevel, the earth's  $B$ -field (not canceled in our measurements) is sufficient to account for our observations.

The addition of the  $\lambda_{10}$  repump laser further increases the LIF by a factor of 3.5, indicating a total of number of photons scattered:  $N_{\text{sc}} \approx 170$ . This represents a significant radiative force on the molecules and, as shown in Fig. 6.3, results in a substantial deflection of the SrF beam. The unperturbed SrF beam is approximately 6 mm wide in the probe region as the result of the collimating slit. The addition of the  $\lambda_{00}$  pump and  $\lambda_{10}$  repump lasers causes a shift in position by  $\sim 0.5$  mm while the width remains  $\sim 6$  mm. We also show the LIF signal in the probe region without the  $\lambda_{10}$  repump or  $\lambda_{10}$  cleanup lasers. Here only 5% of the molecules remain in the  $X(v = 0, N = 1)$  state. The addition of both  $\lambda_{10}$  lasers recovers 90% of the original LIF signal, indicating nearly complete pumping to and repumping from the  $X(v = 1, N = 1)$  state. The remaining 10% loss is in reasonable agreement with the expected loss of  $\sim 6\%$  of the population to the  $X(v = 2, N = 1)$  state (not repumped in this experiment) after 170 photons are scattered.

We independently determine  $N_{\text{sc}}$  from the observed deflection using Eqn. 6.2. The observed deflection  $d = 0.5$  mm corresponds to  $N_{\text{sc}} = 140$  which is in reasonable agreement with the number estimated from the LIF increase. This number of photon scatters induces Doppler shifts much smaller than the natural linewidth of the transition.

We also measure  $N_{\text{sc}}$  (as determined from beam deflection) as a function of  $t_0$  (see Fig. 4 inset). By varying the number of passes in the interaction region, we vary  $t_0$  from 0 to 44  $\mu\text{s}$  in eight 5.5  $\mu\text{s}$  increments. These data clearly show a linear increase for  $N_{\text{sc}}$  versus  $t_0$ . Fitting the linear dependence yields a spontaneous scattering rate  $S_{\text{sc}} = 3 \times 10^6 \text{ s}^{-1}$ . We can compare this to the scattering rate expected assuming full saturation of the  $X(v = 0, 1; N = 1) \rightarrow A(v = 0, J = 1/2)$  transitions and complete  $B$ -field remixing of ground state sublevels. Here the molecule spends an equal amount of time in the 24  $X(v = 0, 1; N = 1)$  sublevels and the 4  $A(v = 0, J = 1/2)$  sublevels. Spontaneous emission requires one lifetime  $\tau$  in the excited states, so the maximum spontaneous scattering rate is  $S_{\text{sc}}^{\text{max}} = \frac{4}{24+4} \times 1/\tau = 6 \times 10^6 \text{ s}^{-1}$ . We find  $S_{\text{sc}} \simeq S_{\text{sc}}^{\text{max}}/2$ , indicating that either all transitions are not saturated or that  $S_{\text{sc}}$  is limited by remixing of dark states.

In conclusion, we demonstrate optical cycling resulting in radiative force on a diatomic molecule. Our results are consistent with  $N_{\text{sc}} \sim 150$  photons, limited only by the interaction time with the lasers. These results suggest a clear path to direct laser cooling of SrF or other species with similar structure.

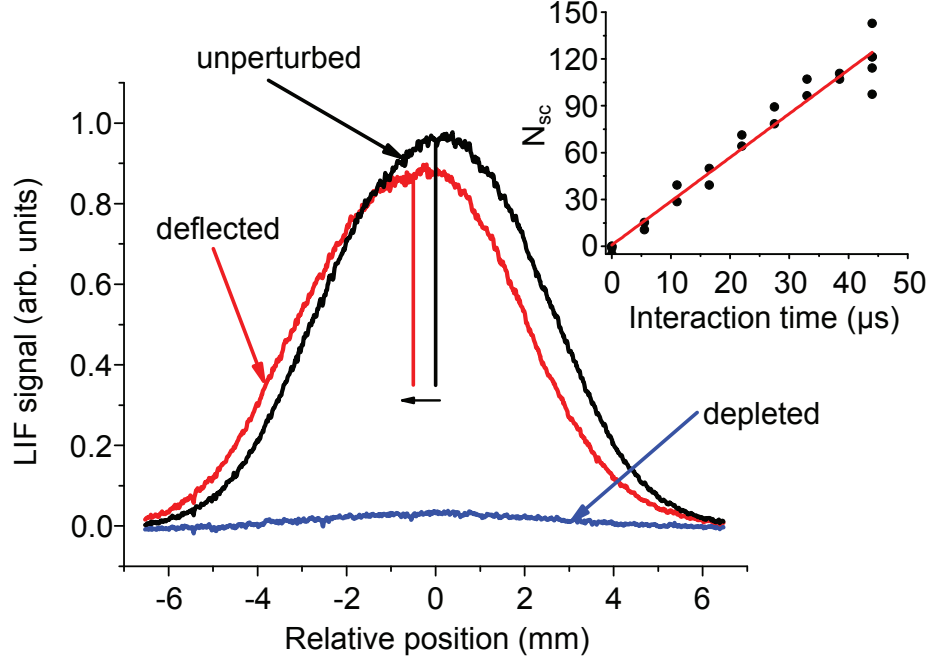


Figure 6.3: Radiative force deflection of the SrF beam. Positional LIF from the  $\lambda_{00}$  probe laser with no lasers in the interaction region ( $\blacksquare$ ), with  $\lambda_{00}$  pump and  $\lambda_{10}$  repump lasers in the interaction region ( $\blacksquare$ ), and with  $\lambda_{00}$  pump laser but no  $\lambda_{10}$  repump or  $\lambda_{10}$  cleanup laser ( $\blacksquare$ ). Without the  $\lambda_{10}$  repump and  $\lambda_{10}$  cleanup lasers, nearly complete depletion of the  $X(v=0, N=1)$  state is observed. Addition of both  $\lambda_{10}$  lasers results in nearly full recovery of the LIF signal amplitude, indicating optical pumping to and repumping from the  $X(v=1, N=1)$  state. The  $\lambda_{00}$  pump and  $\lambda_{10}$  repump lasers also cause deflection of the SrF beam due to radiative force. This plot shows raw data, with no rescaling applied. Inset: Dependence of the number of scattered photons on the interaction time in the interaction region. Points are data and the line is a fit, showing that  $N_{sc}$  increases linearly with interaction time.

## Chapter 7

# Laser cooling of a diatomic molecule

This chapter outlines the set of experiments where we transversely laser cool our SrF molecular beam in one dimension. The data presented in this chapter parallel that of Ref. [206].

### 7.1 Experimental apparatus

Use of an  $R = 1 \rightarrow R' = 0$  type transition leads to a lower photon scattering rate than a traditional two-level atomic cycling transition [88, 90]. To overcome the relatively low scattering rate, we use an elongated transverse cooling region. A schematic showing the experimental apparatus is shown in Fig. 7.1. The molecular beam used for the experiments outlined in this chapter is similar to the one described in chapter 5. A distance  $z = 34$  mm downstream from the  $\approx 3$  mm diameter cell exit aperture, the molecular beam passes through a 6.35 mm diameter hole which collimates the SrF beam while also limiting the flow of helium into the rest of the apparatus. At  $z = 11$  cm the molecular beam is collimated by a  $1.5 \times 1.5$  mm<sup>2</sup> aperture. 3 cm after the collimating aperture, the molecular beam enters the cooling region, which is defined by 15 cm long windows. Spatial measurements of the molecular beam (discussed in the next paragraph) indicate the unperturbed beam has a FWHM transverse velocity of  $v_{\perp}^{\text{FWHM}} \approx 4$  m/s.<sup>1</sup>

The SrF beam is intersected by the three cooling laser beams, denoted  $\lambda_{00}^t$ ,  $\lambda_{10}^t$  and  $\lambda_{21}^t$ , at nearly

---

<sup>1</sup>This value is estimated from a measured 5.7 mm FWHM molecular beam intensity profile for the geometry shown in Fig. 7.1 treating the  $1.5 \times 1.5$  mm collimation slit as a point source and assuming  $v_{\parallel} \approx 200$  m/s, correct for the beam source at the time [90].

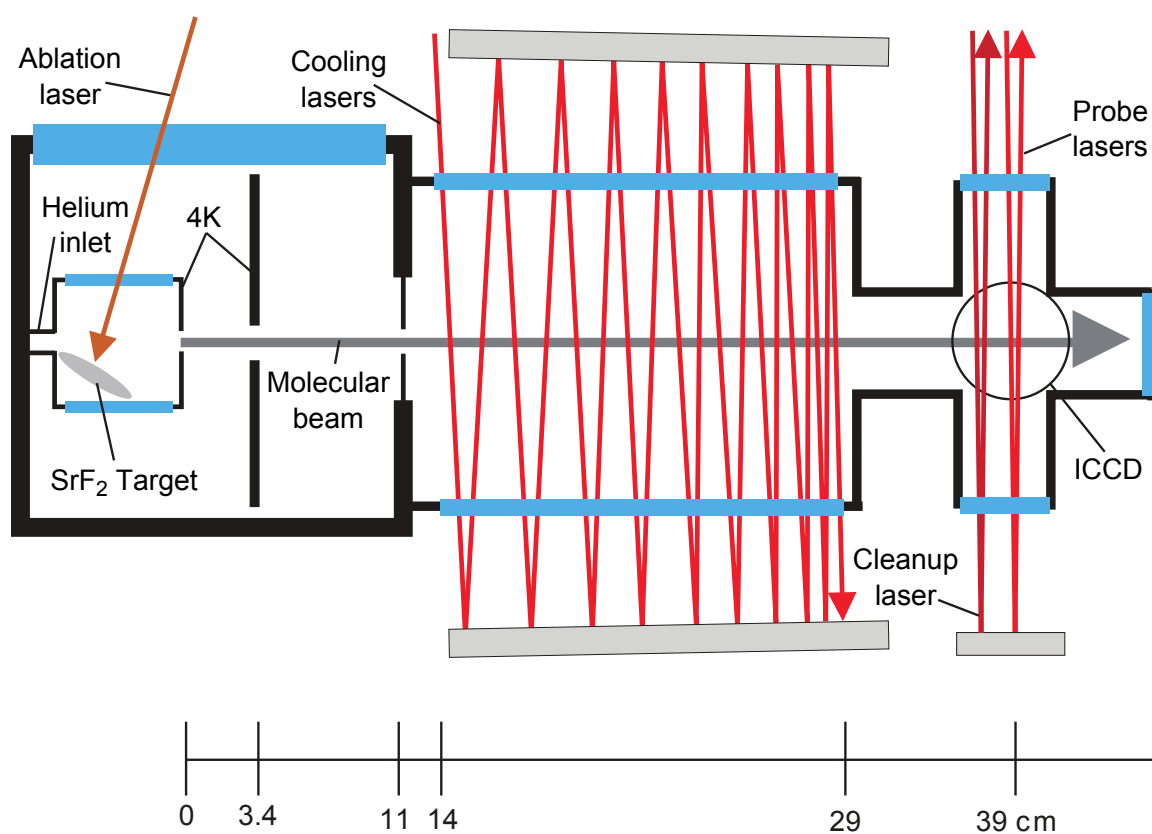


Figure 7.1: Schematic of the experimental apparatus. Black represents aluminum, red represents the laser paths, which can pass through glass/windows (blue) and reflects off mirrors outside the vacuum chamber (gray).

right angles. We use the superscript ‘t’ to denote that the cycling lasers are applied transverse to the molecular beam. The linearly polarized laser beams are reflected back and forth using 20 cm long mirrors located outside the vacuum chamber. The windows are mounted at Brewster’s angle to allow the laser beams to pass multiple times through the cooling region with minimal attenuation. We apply  $B$  fields at angle  $\theta_B$  to the linear laser polarization using two pairs of rectangular coils mounted outside the cooling region (not shown). LIF can be monitored at any position in the cooling region using a red-sensitive PMT (Thorlabs PMM02). The laser beams are reflected back and forth at a slight angle so that they intersect the SrF beam  $\sim 75$  times in the 15 cm long cooling region. At the end of the cooling region the beams are nearly retroreflected, resulting in the formation of standing waves. The combination of magnetic field remixing of Zeeman sublevels and standing waves can lead to Sisyphus forces in addition to Doppler forces as has been observed in atomic systems [243–245]. 10 cm after the end of the cooling region, the SrF beam enters the probe region where LIF from the  $X(v=0, N=1) \rightarrow A(v'=0, J'=1/2)$  transition is imaged with a 1:1 imaging ratio onto an intensified CCD camera (Princeton Instruments PI-MAX2 with Unigen II image intensifier). A “cleanup”  $\lambda_{10}$  laser beam intersects the SrF beam between the cooling and probe regions to return any residual population in the  $X(v=1)$  state back to the  $X(v=0)$  state. Both probe and “cleanup” beams are retroreflected to eliminate artificial Doppler shifts. This spatial distribution maps onto the velocity distribution of the molecules with a resolution of  $\sim 1$  m/s, so from such images we can extract information about the velocity-dependent forces applied to the molecules, as well as the beam’s transverse temperature  $T$ .

## 7.2 Results overview

We find there are two cooling regimes with qualitatively different features that depend critically on the magnitude of the applied  $B$  field. In Figs. 7.2a and 7.2b we show data with  $B = 5$  G and 0.6 G respectively that are characteristic of these regimes. In both regimes we find that  $\theta_B$  is unimportant if  $\theta_B \neq 0, 90^\circ$ . In all cases we observe that the total integrated LIF signal in the probe region is constant to within the experimental reproducibility ( $\sim 5\%$ ), and so changes in the spatial distribution of the LIF accurately reflect changes in the velocity distribution of the molecular beam. The top and bottom panels of Fig. 7.2a and 7.2b are representative molecular beam images for two different main pump laser detunings,  $\Delta\omega_{00}^t = \pm 1.5\Gamma$ . In this system there is not a single well-defined value of the detuning for the pump and repump lasers because each laser contains several sideband



frequencies that each interact with multiple transitions between ground and excited states. We define the detunings  $\Delta\omega_{00}^t = 0$ ,  $\Delta\omega_{10}^t = 0$  and  $\Delta\omega_{21}^t = 0$  experimentally by determining the laser carrier frequency which produces maximal LIF. For  $\Delta\omega_{00}^t = -(+)1.5\Gamma$  the detuning of the nearest sideband from each transition ranges from 0 to  $\sim -(+)1.5\Gamma$ , indicating that the sign of  $\Delta\omega_{00}^t$  corresponds to net average red (blue) detuning. Here and throughout the rest of the paper both vibrational repump lasers have modulation frequencies  $f_{\text{mod}}^r = 43$  MHz and  $\Delta\omega_{10}^t = 0$  and  $\Delta\omega_{21}^t = 0$ . The main pump laser has modulation frequency  $f_{\text{mod}}^p$  as listed in the captions.

For a red detuned main pump laser,  $\Delta\omega_{00}^t = -1.5\Gamma$ , and  $B = 5$  G we observe significant narrowing of the molecular beam and enhancement of molecules with low transverse velocity,  $v_\perp$ , as shown in the bottom panel of Fig. 7.2a. This corresponds to a reduction in the spread of  $v_\perp$ , and is a clear signature of Doppler cooling. Also, it is evident that the entire molecular beam experiences cooling forces, indicating that the cooling force is significant for all  $v_\perp$  in the molecular beam. The molecular beam is constrained by collimating apertures to have  $v_\perp < v_{\text{Dop}}^{\text{Beam}} \simeq 4$  m/s. For a blue detuned main pump laser,  $\Delta\omega_{00}^t = +1.5\Gamma$ , and  $B = 5$  G we observe depletion of low  $v_\perp$  molecules and broadening of the molecular beam as shown in the top panel of Fig. 7.2a, as expected for Doppler heating. Under these conditions, there is also a small but noticeable sharp feature in the center of the molecular beam, indicating some residual cooling of the remaining molecules with low  $v_\perp$ .

In Fig. 7.2b we show data characteristic of a small applied  $B$  field of 0.6 G, which are strikingly different from the data in Fig. 7.2a. The most significant difference between Figs. 7.2a and 7.2b is that cooling occurs for detunings of opposite sign. For a red detuned main pump laser,  $\Delta\omega_{00}^t = -1.5\Gamma$ , we observe (Fig. 7.2b, lower panel) two relatively sharp peaks, neither of which is centered around  $v_\perp = 0$ . This indicates the heating of molecules with low  $|v_\perp|$  and accumulation around two stable velocity points with  $v_\perp \neq 0$ . For a blue detuned main pump laser,  $\Delta\omega_{00}^t > -1.5\Gamma$ , we observe (Fig. 7.2b, lower panel) a sharp central spike and a large enhancement of low  $v_\perp$  molecules. This feature results from the strong cooling of molecules over a small range of  $v_\perp$  around zero. Meanwhile molecules with larger  $|v_\perp|$  experience small heating forces, resulting in a very slight enhancement at large  $|v_\perp|$ .

A complete characterization of the detailed cooling forces responsible for these observations would require the solution of the OBEs for this system. All relevant quantities (detunings, Larmor frequencies, Rabi frequencies,  $\Gamma$ ) are the same within factors of order unity, so the full 44 level system, driven by twelve laser frequencies, each interacting with multiple levels, must be solved. Such a calculation is beyond the scope of this work; however, the main features we have observed

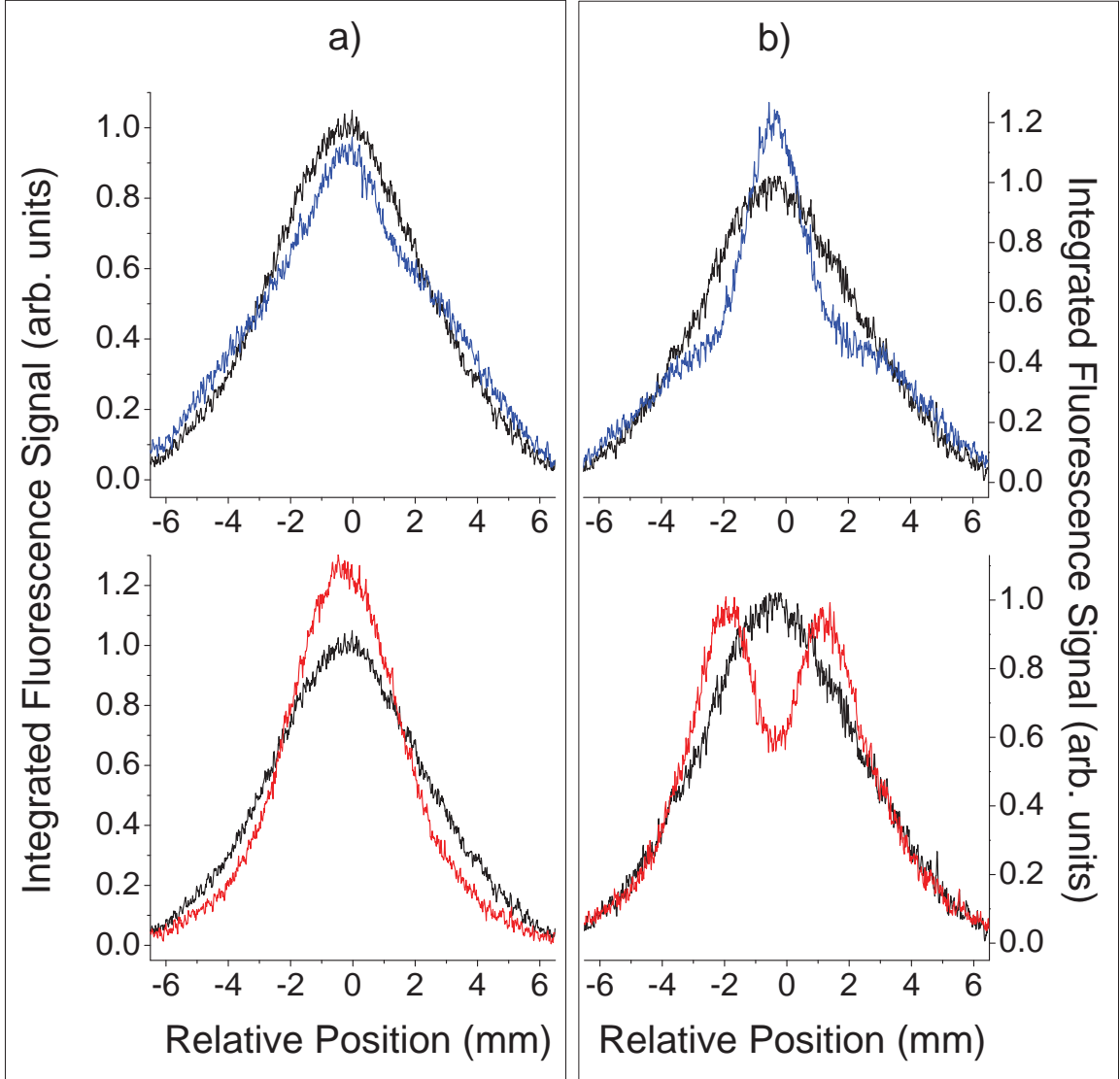


Figure 7.2: Laser cooling of SrF. LIF in the probe region without cooling lasers in the interaction region (black curves), with cooling lasers and main pump laser red-detuned by  $\Delta\omega_{00}^t = -1.5\Gamma$  (red), and with cooling lasers and main pump laser blue-detuned by  $\Delta\omega_{00}^t = +1.5\Gamma$  (blue) for (a)  $f_{\text{mod}}^p = 46.4$ ,  $B = 5$  G,  $\theta_B = 60^\circ$ , and (b)  $f_{\text{mod}}^p = 43.2$  MHz,  $B = 0.6$  G,  $\theta_B = 30^\circ$ . In (a) cooling (heating) of the beam is observed for red (blue) detuning; both are in accordance with expectations for Doppler forces. In (b) cooling (heating) is observed for blue (red) detuning, as is expected for Sisyphus forces. In all cases the total integrated signal is the same to within 5%. The blue-detuned curves systematically have the lowest total integrated signal, likely because some molecules have been pushed outside the imaging region by the Doppler heating force. We observe qualitatively similar behavior in both cases for pump laser modulation frequencies  $42 < f_{\text{mod}}^p < 47$  MHz. However the  $f_{\text{mod}}^p$  values shown here were chosen because they produced the clearest Doppler and Sisyphus effects. This plot shows raw data, with no rescaling applied.

are common to any system with magnetically remixed dark sublevels driven by a standing wave [243–245]. The simplest such system is an  $F = 1 \rightarrow F' = 0$  transition driven by a single laser frequency, and it provides substantial insight into our observations. A linearly polarized, blue (red) detuned laser of wavelength  $\lambda$  produces an AC Stark shift which attracts (repels) the  $F' = 0, M = 0$  and  $F' = 1, M' = 0$  levels, while the  $F = 1, M = \pm 1$  levels are unperturbed by the light field, to first order, as shown schematically in Fig. 7.4. In a standing wave, the  $F = 1, M = 0$  level undergoes a spatially periodic AC Stark shift with period  $\lambda/2$ . For blue (red) detuning, molecules ride up a potential hill in this level, losing (gaining) kinetic energy, before they are optically pumped at a rate  $R_{\text{op}} < \Gamma$  into the  $F = 1, M = \pm 1$  sublevels which are dark. If a  $B$ -field is applied at  $\theta_B \neq 0^\circ, 90^\circ$  then the molecules precess from the dark  $M = \pm 1$  sublevels back into  $M = 0$  at the nodes of the standing wave at a rate  $\omega_B$ . The Sisyphus force is maximized when  $v_\perp = v_{\text{Sis}}^{\text{Max}} \sim \frac{\lambda}{4} R_{\text{op}}$ , and  $\omega_B^{\text{Sis}} \sim R_{\text{op}}$  (See subsection 7.3.1).  $v_{\text{Sis}}^{\text{Max}}$  defines the effective velocity range of the Sisyphus force. Larger values of  $\omega_B$  produce a much smaller Sisyphus force because the molecules are pumped back and forth between bright and dark states at random points in the standing wave. Because the molecules spend more time in the bright states the photon scattering rate is higher, and the Doppler force is larger. Simple arguments suggest that  $\omega_B^{\text{Dop}} \sim \Gamma$  for maximum Doppler cooling forces, and that Doppler forces occur over a larger range of velocities  $v_\perp = v_{\text{Dop}}^{\text{Max}} = \frac{\lambda\Gamma}{2\pi} = 4 \text{ m/s}$  (See subsection 7.3.1).

This qualitative discussion provides substantial insight into our observations. At low  $B$  fields we expect to observe Sisyphus forces, which are characterized by cooling (heating) for blue (red) detuning for molecules with low  $v_\perp$  as observed in Fig. 7.2b. At higher  $B$  fields we expect to observe Doppler forces, characterized by cooling (heating) for red (blue) detuning. Since  $v_{\text{Dop}}^{\text{Beam}} \simeq v_{\text{Dop}}^{\text{Max}}$ , Doppler cooling forces should affect the entire molecular beam as observed in the bottom panel of Fig. 7.2a. In subsection 7.3.1, we provide the argument for the estimate  $R_{\text{op}} \sim \frac{\Gamma}{21}$ , which yields  $v_{\text{Sis}}^{\text{Max}} \sim 0.3 \text{ m/s}$ . This is much smaller than  $v_{\text{Dop}}^{\text{Beam}} \simeq v_{\text{Dop}}^{\text{Max}} \simeq 4 \text{ m/s}$ , and is consistent with our observations.

Of course neither regime can be characterized purely by either Sisyphus or Doppler forces. In the moderate  $B$  regime residual Sisyphus forces lead to a slight additional broadening (narrowing) in the low-velocity part of the distribution for red (blue) detuning. This residual narrowing is clear in the top panel of Fig. 7.2a, while the broadening is too small to observe in the bottom panel of Fig. 7.2a. In the low  $B$  regime residual Doppler forces result in small heating (cooling) over a large range of velocities for blue (red) detuning. This gives rise to non-zero unstable (stable) velocities  $v_\perp = \pm v_0$ , where the net force is zero and population is depleted (accumulates). These stable points

$v_{\perp} = \pm v_0$  are clear in the bottom panel of Fig. 7.2b. In the top panel of Fig. 7.2b the unstable velocities are clearly depleted, and there is some residual Doppler broadening in the wings of the molecular beam. Although the arguments presented here derive from an  $F = 1 \rightarrow F' = 0$  example system, they are common to any  $F \rightarrow F' < F$  system and to  $F \rightarrow F' = F$  systems with dark ground state sublevels. Furthermore the effects described here have been observed in several such atomic systems [243–245].

To clearly illustrate the  $B$ -field dependence of the cooling force, we show the magnetic field dependence of the cooling force for a red detuned pump laser,  $\Delta\omega_{00}^t = -1.5\Gamma$ , in Fig. 7.3a. As shown for very small  $B$  fields, the width of the molecular beam increases due to Sisyphus heating effects. This increase is followed by a sharp decrease in the molecular beam width corresponding to Doppler cooling. The width of the molecular beam is quite insensitive to the magnetic field over a range of intermediate magnetic field amplitudes between 2 and 6 G. Finally at magnetic fields higher than 6 G the Doppler forces are reduced because the magnetic field artificially broadens the transitions, resulting in lower scattering rates, and lower Doppler forces. We estimate values for  $\omega_B$  in subsection 7.3.1 which yield  $B_{\text{Dop}} \approx 5$  G and  $B_{\text{Sis}} \sim 0.7$  G for the maximum Sisyphus and Doppler forces, in reasonable agreement with our observations. Once again, detailed comparison would require the full solution of the OBEs for our system.

As an example of the complex features present in this system, we show the frequency dependence of the width of the SrF beam under Doppler force-dominated conditions of  $B = 5$  G, for various pump laser detunings  $\Delta\omega_{00}^t$  in Fig. 7.3b. The frequency dependence of the width is substantially more complicated than that of a typical 2-level system. As shown the force oscillates many times between heating and cooling for  $-250 \text{ MHz} < \Delta\omega_{00}^t < 250 \text{ MHz}$ . However, this complicated structure is amenable to a simple interpretation. As the pump laser frequency is varied, the nearest laser frequency to each molecular transition oscillates between red-detuned (cooling) and blue-detuned (heating) with a variation that is nearly periodic in the sideband frequency. The frequency dependence in the Sisyphus regime, shown in Fig. 7.3c, is somewhat more complicated, but for small detunings  $-50 \text{ MHz} < \Delta\omega_{00}^t < 50 \text{ MHz}$  the Sisyphus force has the opposite sign as the Doppler force as expected. In subsection 7.3.3, we also show the power dependence of the Sisyphus and Doppler cooling force, both of which are in reasonable agreement with expectations.

Finally, we discuss our determination of the transverse motional temperature  $T$  of the molecules after they are cooled. The unperturbed beam is constrained by collimating apertures to have  $T = T_0 = 50$  mK. The long interaction region prevents a precise determination of  $T$  for the cooled beam,

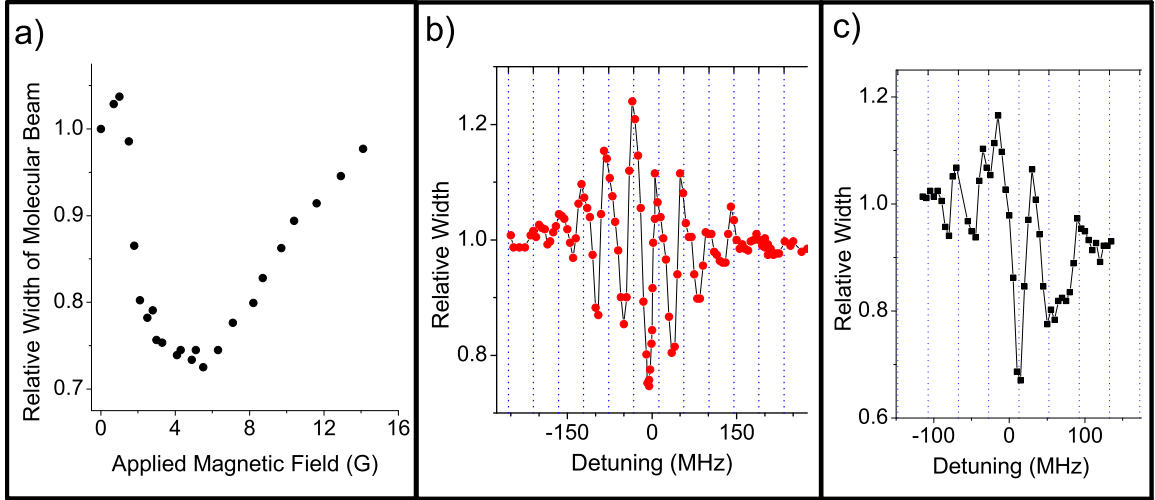


Figure 7.3: Magnetic field and frequency dependence of the cooling forces. a) Magnetic field dependence of the cooling force. The width of the molecular beam is plotted for  $f_{\text{mod}}^p = 46.4$  MHz,  $\Delta\omega_{00}^t = -1.5\Gamma$ , and various  $B$  fields at  $\theta_B = 30^\circ$ . For  $B < 2$  G the beam is broader due to Sisyphus forces. At approximately  $B = 2$  G we see a sharp transition between Sisyphus dominated heating forces, and Doppler dominated cooling forces. For  $B > 6$  G the width increases as described in [section 7.2](#). Frequency dependence of the cooling forces under b) Doppler ( $B = 5$  G) and c) Sisyphus ( $B = 0.6$  G) dominated conditions. The solid lines between data points are drawn as a guide to the eye. The vertical dashed lines are spaced by the sideband frequency of a) 46.4 MHz and b) 43.2 MHz, and illustrate the dependence of the oscillations on sideband frequency. Describing the molecular beam simply by a width is potentially problematic in the Sisyphus dominated regime where more than one velocity class are present. Nonetheless the total width of the beam for the red (blue) detuned pump laser is larger (smaller) than the unperturbed beam width, and thus the width provides a reasonable description of the molecular beam. The asymmetry around  $\Delta\omega_{00}^t = 0$  in b) and c) underscores the complex nature of this system and is likely representative of the fact that every sideband does not have the same detuning from the nearest transition. Therefore, the detuning of each sideband from the nearest transition is not zero for  $\Delta\omega_{00}^t = 0$ . Furthermore, the absolute values of the individual sideband detunings are not the same for  $+\Delta\omega_{00}^t$  and  $-\Delta\omega_{00}^t$ .

because the beam continues to expand as it experiences an imperfectly known distribution of cooling forces throughout the interaction region. To estimate  $T$ , we calculate the molecular beam profile using a Monte Carlo simulation of classical particles subjected to the qualitatively expected force vs. velocity profile (See [subsection 7.3.2](#)). Using these simulations we find  $T \simeq T_{\text{Sis}} = 300 \mu\text{K}$  for the Sisyphus regime in the top panel of Fig. 7.2b. We also estimate a conservative upper limit on the temperature of  $T < T_{\text{Sis}}^{\text{Max}} = 5 \text{ mK}$ .

For the Doppler regime, we find that  $T \simeq T_{\text{Dop}} = 5 \text{ mK}$ , and  $T < T_{\text{Dop}}^{\text{Max}} = 15 \text{ mK}$ . These values of  $T$  for the Doppler regime are consistent with the final temperature expected if the molecules are subjected to  $N_{\text{sc}} \approx 500 - 1000$  photon scatters. This value of  $N_{\text{sc}}$  agrees with expectations based on the previously observed scattering rate for this system and roughly known interaction time [90]. Importantly, the total integrated signal of the Doppler-cooled beam and the unperturbed beam are the same to within the level of experimental reproducibility ( $\approx 5\%$ ), indicating that our cycling scheme is highly closed.

## 7.3 Quantitative analysis

### 7.3.1 Capture velocity and optimum magnetic field for Sisyphus and Doppler forces

In this section we provide estimations of the capture velocities and optimum magnetic fields for Sisyphus and Doppler forces, which should be accurate within a factor of  $\sim 2$ . Once optical cycling is achieved in a system, the application of laser beams in opposite directions can lead to substantial cooling forces. The simplest of these is the Doppler force, where the Doppler shift of a moving molecule brings it closer to or further from resonance with the laser. Molecules closer to resonance scatter more photons, leading to a velocity-dependent force,  $F_{\text{Dop}} \propto v_{\perp}$ . The Doppler force affects molecules with velocities such that the Doppler shift,  $\omega_D = kv_{\perp}$ , is not greater than the transition linewidth  $\Gamma$  in angular frequency units, where  $k = 2\pi/\lambda_{00}$ . This leads to an effective velocity range for the Doppler force given by:  $|v_{\perp}| \lesssim v_{\text{Dop}}^{\text{Max}} = \Gamma/k = 4 \text{ m/s}$ . Molecules with larger velocities than  $v_{\text{Dop}}^{\text{Max}}$  experience a reduced force.

Both Sisyphus and Doppler forces depend on the optical excitation rate  $R_{\text{ex}}$ , the optical pumping rate  $R_{\text{op}}$ , and the spontaneous scattering rate  $S_{\text{sc}}$ . In the limit of low laser intensity  $R_{\text{ex}} \approx S_{\text{sc}}$  since almost every excitation will be followed by a spontaneous decay. In the opposite limit, where all transitions are completely saturated, the molecules spend equal time in the 24  $v = 1$  and  $v = 0$  ground states, and the 4 excited states.<sup>2</sup> The maximum spontaneous photon scattering rate is then  $S_{\text{sc}}^{\text{Max}} = \frac{4}{24+4} \times \Gamma = \frac{\Gamma}{7}$ . The time-averaged optical pumping rate is given by  $R_{\text{op}} = S_{\text{sc}} \times C_{\text{dark}}$  where  $C_{\text{dark}}$  is the branching ratio to dark states. For a  $F = 1 \rightarrow F' = 0$  system,  $C_{\text{dark}} = 2/3$ . Due to the plethora of magnetic remixing rates and Rabi frequencies in our system,  $S_{\text{sc}}$  is ideally determined experimentally. From the deflection experiments (which used similar laser intensities) we observed  $S_{\text{sc}}^{\text{Obs}} \approx \frac{1}{2} S_{\text{sc}}^{\text{Max}} \approx 3 \times 10^6 \text{ s}^{-1}$  which suggests  $R_{\text{op}} \approx 2 \times 10^6 \text{ s}^{-1}$ .

In systems with dark Zeeman sublevels, such as SrF and any  $F = 1 \rightarrow F' = 0$  system, optical cycling ceases as soon as the molecules are pumped into these dark states. If a magnetic field is applied, then the dark states can Larmor precess into bright states and optical cycling can continue. The applied magnetic field should be large enough that dark state precession does not limit  $R_{\text{ex}}$ . However, if the applied magnetic field is too large, it will needlessly broaden the transition. An estimate for the optimal  $B$  field for Doppler cooling,  $B_{\text{Dop}}$ , can be made by equating the Larmor precession frequency,  $\omega_B \sim B\mu_B g_F$ , and the linewidth of the transitions  $\Gamma$ . In SrF,  $g_F \sim 1$  for the

<sup>2</sup>This assumes the magnetic field is sufficient to remix the dark states but not large enough to broaden the transition.

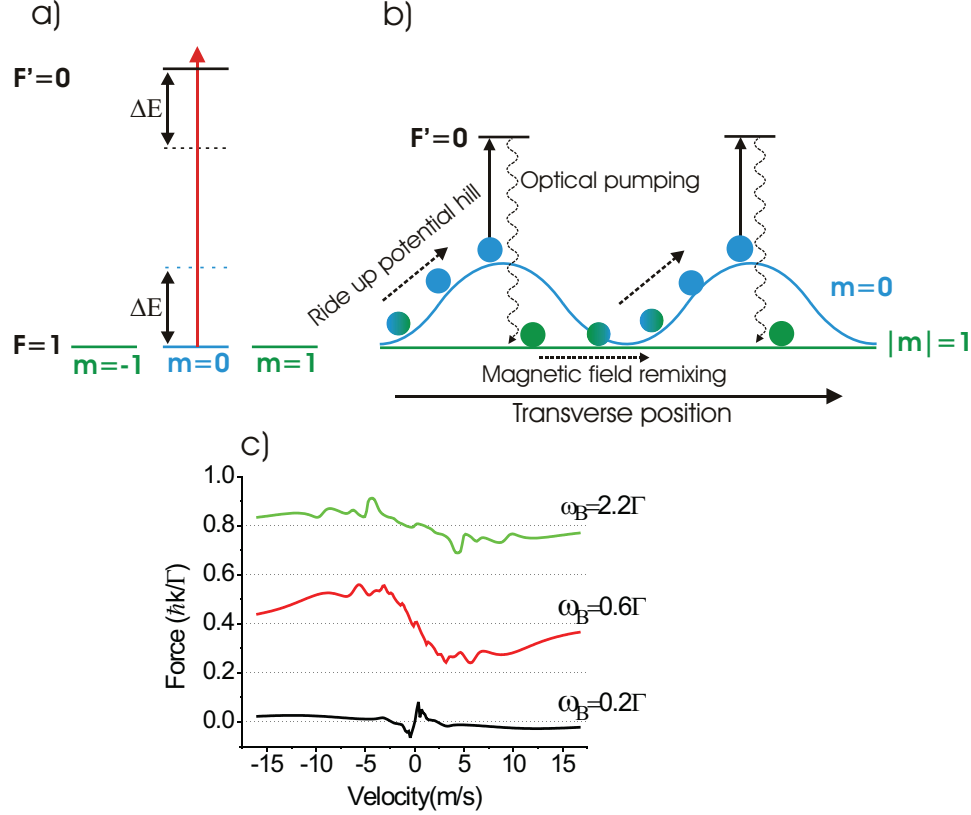


Figure 7.4: Schematic illustrating the origin of Sisyphus force in an  $F = 1 \rightarrow F' = 0$  system. (a) Zero field energy levels (solid) and AC Stark shifts (dashed) in the presence of a blue detuned, linearly polarized laser field. (b) Energy levels and motion of molecules in a blue detuned standing wave. As explained in the text, the molecules effectively ride continuously up potential hills, losing kinetic energy. For red detuning the picture is reversed, with molecules gaining kinetic energy as they ride down potential hills. For optimum Sisyphus forces, the molecules must traverse from node to antinode in the optical pumping time,  $1/R_{\text{op}}$ , and the molecules must traverse from antinode to antinode in the magnetic field remixing time,  $2\pi/\omega_B$ . (c) Results of a semi-classical calculation of the average force on a molecule in a standing wave with Rabi frequency  $\Omega_R = \Gamma$ , and red detuning  $\Delta = -\Gamma$  for low (bottom), intermediate (middle), and high (top) field remixing rates  $\omega_B$ . The curves are offset by  $0.4 \hbar k/\Gamma$  for clarity. For small  $\omega_B$  we observe Sisyphus heating at small velocities and small Doppler cooling at large velocities, with two stable points at  $v_{\perp} \simeq \pm 2.5$  m/s. For higher  $\omega_B$  we observe almost pure Doppler cooling forces for all velocities. For the highest  $\omega_B$  the Doppler force decreases because the  $B$ -field broadens the transitions resulting in lower photon scattering rates. For a blue detuning of  $\Delta = +\Gamma$ , the force is the same magnitude, but reversed in sign. The calculation then predicts Sisyphus cooling for small  $\omega_B$  and Doppler heating for higher  $\omega_B$ .



hyperfine levels. We then have  $B_{\text{Dop}} \sim \frac{\Gamma}{\mu_B} = 5$  G. This estimate is in good agreement with the data shown in Fig. 7.2 which show maximum Doppler forces occur over the range 2-6 Gauss.

As described in section 7.2, these types of systems also give rise to Sisyphus forces if they are subjected to a standing wave. The basic mechanism responsible for the Sisyphus effects is shown schematically in Fig. 7.4. Sisyphus forces are maximal for molecules that travel a distance of  $\lambda/4$  in the time it takes for the molecules to be pumped into the dark states,  $\frac{1}{R_{\text{op}}}$ . In this case the laser field extracts the maximum kinetic energy from the molecules as they ride up the entire potential hill. This leads to an effective velocity range of  $v_{\perp} = v_{\text{Sis}}^{\text{Max}} \sim \frac{\lambda}{4} R_{\text{op}}$  for Sisyphus forces. We then find that  $v_{\text{Sis}}^{\text{Max}} \approx 0.3$  m/s.

The previous discussion gives the optimal  $v_{\perp}$  for Sisyphus forces; however, the maximum force can only be achieved over a small range of  $B$  fields. If  $B$  is too small or too large, then the molecules precess back and forth between bright and dark states at random points in the standing wave. The net result is that after several Sisyphus cycles, the molecules have neither gained nor lost a significant amount of energy. If on the other hand  $\frac{\omega_B}{2\pi} \simeq \frac{1}{2} R_{\text{op}}$  then molecules with  $v_{\perp} \simeq v_{\text{Sis}}^{\text{Max}}$  travel  $\lambda/4$  in the time it takes to precess out of the dark states. At this point the molecules can repeat the Sisyphus process shown in Fig. 7.4b. Using the value of  $R_{\text{op}}$  estimated in the previous paragraph, we obtain  $B = 0.7$  Gauss for optimal Sisyphus cooling.

### 7.3.2 Estimation of temperature

As mentioned in section 7.2, we use a Monte Carlo simulation of classical particles subjected to the qualitatively expected Sisyphus and Doppler force versus velocity curves. To obtain qualitative estimates of these force curves we have solved the OBEs for an  $F = 1 \rightarrow F' = 0$  system in a standing wave and magnetic field. We then compute the average force over one wavelength. Typical results of such calculations are shown in Fig. 7.4c, and show good agreement with the qualitative discussion in section 7.2. Specifically, in the calculation we see that there are three distinct magnetic field regimes. At low  $B$  fields the calculation shows strong Sisyphus forces. For low  $B$  fields, blue (red) detuning produces cooling (heating) forces for  $|v_{\perp}| < v_{\text{Sis}}^{\text{Max}} \simeq 0.4$  m/s. We also see that for  $|v_{\perp}| > 2$  m/s there are residual Doppler forces that are of opposite sign as the Sisyphus force. This gives rise to non-zero unstable (stable) velocities  $v_{\perp} = \pm 2$  m/s, where the net force is zero and the population is diminished (accumulates). We also see that Sisyphus forces are not substantial for  $|v_{\perp}| > v_{\text{Sis}}^{\text{Max}}$ , so  $v_{\text{Sis}}^{\text{Max}}$  indicates the velocity extent of the Sisyphus force.

At intermediate  $B$  fields the Sisyphus forces are substantially reduced, and instead the force

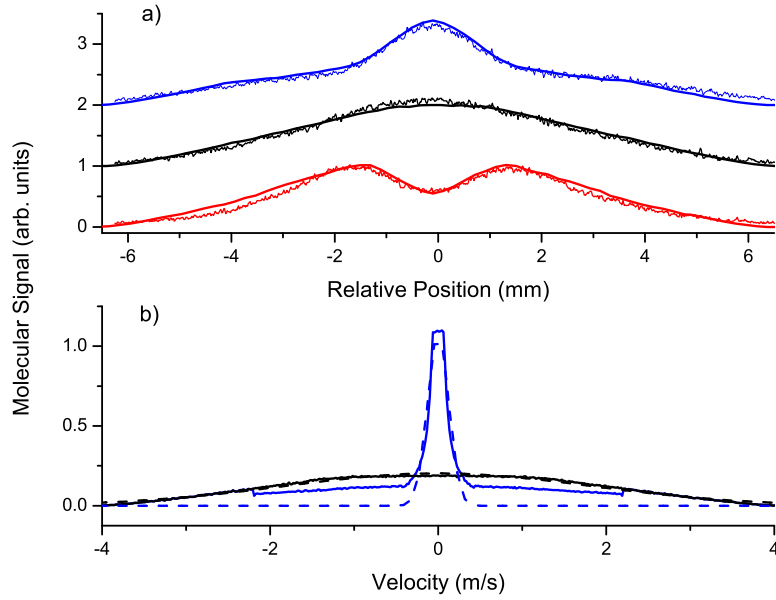


Figure 7.5: Results of a Monte Carlo simulation of the SrF beam subjected to Sisyphus type forces. a) Experimental (noisy) and Monte Carlo simulation (clean) molecular signal for the unperturbed (black), Sisyphus cooled (blue), and Sisyphus heated (red) molecular beam. The curves are offset by one unit for clarity. The total area of the simulated molecular beam curves are normalized to their respective experimental curve. The difference in area between the experimental Sisyphus cooled beam and the unperturbed beam is  $\sim 5\%$ . b) Velocity distribution (solid) and Gaussian fit (dashed) for the unperturbed (black) and Sisyphus-cooled (blue) molecular beam resulting from the Monte Carlo simulation of the molecular beam. From the Gaussian fit we extract the transverse temperature  $T$  of the molecular beam.

curve is indicative of Doppler forces. In contrast to the Sisyphus mechanism, red detuning produces Doppler cooling, while blue detuning produces Doppler heating. Furthermore, the Doppler cooling/heating forces extend over much larger transverse velocities than the Sisyphus forces. The Doppler forces have a broad maximum value around  $v_{\perp} \sim 4$  m/s, indicating that  $v_{\text{Dop}}^{\text{Max}} \sim 4$  m/s as expected. At this intermediate  $B$  field, there still remains a small residual Sisyphus force for small  $v_{\perp}$  that has opposite sign to the Doppler force. At the highest  $B$ -fields shown in Fig. 7.4c the calculation shows reduced Doppler force because the magnetic field artificially broadens the transitions, resulting in lower scattering rates, and lower Doppler force.

We have used the general shape of the force curve derived from the calculation in our simulations of the molecular beam after exposure to Sisyphus and Doppler type cooling conditions. In these simulations we have used the value of  $v_{\text{Sis}}^{\text{Max}}$  obtained from the  $F = 1 \rightarrow F' = 0$  calculation. In the real system, Rabi frequencies and  $g$  factors vary between the different SR/HF manifolds; hence we take the value of  $v_{\text{Sis}}^{\text{Max}}$  observed in the calculations as an upper limit on the value in our experimental system. To estimate the temperature of the Sisyphus cooled beam, we assume that the Sisyphus cooling occurs only over the last third of the cooling region (where the standing waves are most pronounced). We then adjust the magnitude of the force by an overall factor  $\beta$  until the simulation matches the experimental LIF profile.

Examples of these simulations are shown in Fig. 7.5a under Sisyphus conditions, and show good agreement with the experimental results. The final temperature estimated in the case of Sisyphus cooling is primarily dependent on  $v_{\text{Sis}}^{\text{Max}}$ .  $v_{\text{Sis}}^{\text{Max}}$  is proportional to  $R_{\text{op}}$ , and the temperature extracted is higher for larger values of this velocity. To obtain a conservative estimate of  $T$  we have used the value of  $v_{\text{Sis}}^{\text{Max}}$  from the  $F = 1 \rightarrow F' = 0$  calculation. This value is likely larger than in the actual SrF system as shown by our estimation, so we expect that this calculation tends to overestimate  $T$ . Using this simulation we find  $T \simeq T_{\text{Sis}} = 300$   $\mu\text{K}$ . However, because the full SrF system was not used to calculate the force used in the simulation, we derive a bound for the maximum value of  $T$  by making two overly conservative assumptions. First, we assume that the cooling force only occurs over a 1 cm length at the beginning of the interaction region. Second, we allow  $v_{\text{Sis}}^{\text{cap}}$  to be larger than the value found from either the  $F = 1 \rightarrow F' = 0$  calculation or our estimation. We then find the largest value of  $v_{\text{Sis}}^{\text{cap}}$  which still replicates the experimental data under variation of  $\beta$ . Under these very conservative assumptions we estimate  $T_{\text{Sis}}^{\text{Max}} = 5$  mK for  $v_{\text{Sis}}^{\text{cap}} = 0.8$  m/s. This value is significantly larger than either  $v_{\text{Sis}}^{\text{cap}} \approx 0.3$  m/s from our estimation, or  $v_{\text{Sis}}^{\text{cap}} = 0.4$  m/s from the  $F = 1 \rightarrow F' = 0$  calculation.

In the Doppler regime, we assume a uniform cooling force  $F = -\alpha v$  over the whole interaction region and molecular beam velocity distribution. The overall magnitude of the force is adjusted until the simulated molecular beam width matches the width of the experimental LIF profile. With this method we find  $T \simeq T_{\text{Dop}} = 5$  mK. We also estimate a conservative upper limit by assuming this cooling force is only applied over a 1 cm length in the beginning of the cooling region; from this we find  $T < T_{\text{Dop}}^{\text{Max}} = 15$  mK. If we use the more realistic force vs. velocity curve shown in Fig. 7.4c rather than  $F = -\alpha v$  we obtain similar temperature estimates, and slightly better agreement between the simulation and the data. Specifically, inclusion of the residual Sisyphus force in the Doppler force curve reproduces the small, sharp feature in the center of the molecular beam in Fig. 7.2a.

We have also performed calculations for a system with lower states  $J = 3/2$  and  $J = 1/2$  excited to a single  $J' = 1/2$  upper state driven by two laser frequencies. In this calculation we assume that each laser only drives population from the nearest  $J$  level. This calculation produced a very similar  $B$ -field dependence and temperature estimate as the calculation based on the simpler system shown here.

### 7.3.3 Power dependence of Sisyphus and Doppler cooling

In this section we present additional data illustrating the dependence of the cooling forces on the laser power. In Fig. 7.6 we have plotted the pump laser power dependence under both Sisyphus and Doppler cooling conditions with  $\Delta\omega_{00}^t = +1.5\Gamma$  (Sisyphus cooling) and  $\Delta\omega_{00}^t = -1.5\Gamma$  (Doppler cooling). As shown in Fig. 7.6b, the Doppler cooling force increases linearly with power until it becomes saturated. This type of behavior is expected for Doppler cooling because at low powers the Doppler force varies as the photon scattering rate which is linear with power. At higher powers, the photon scattering rate saturates because it is limited by the spontaneous emission rate, and larger excitation rates do not lead to larger photon scattering rates.

The Sisyphus cooling force, as shown in Fig. 7.6a, however, does not appear to saturate. The energy extracted on each Sisyphus cycle is proportional to the AC Stark shift of the ground state. For Rabi frequencies smaller than the detuning, the AC Stark shift varies as the intensity of the laser, while for Rabi frequencies larger than the detuning the AC Stark shift varies as the electric field of the laser. The data shown here are not sufficient to draw firm conclusions regarding a linear or quadratic power dependence; however, it is apparent that Sisyphus cooling requires more power than Doppler cooling.

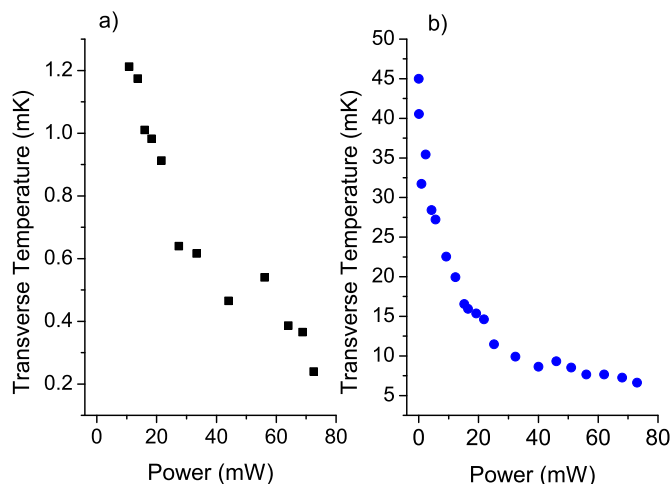


Figure 7.6: Molecular beam temperature under a) Sisyphus and b) Doppler conditions as the power in the main pump laser is varied. Doppler cooling saturates at a main laser power of approximately 30 mW, while the Sisyphus cooling continues to increase as the power is raised. At powers below 10 mW, Sisyphus cooling is no longer observed.

## 7.4 Chapter conclusion

Our results have immediate implications for a number of future experiments. For example, the 1D cooling and optical cycling demonstrated here could dramatically improve the statistical sensitivity of searches for electron electric dipole and nuclear anapole moments [17, 41], by providing more collimated molecular beams and enhanced detection efficiency in these experiments. In addition, the combination of 1D cooling and a highly closed cycling transition opens the door to laser cooling of molecules in 3D. Given the calculated FCF's, a large fraction of molecules should scatter the  $\sim 40,000$  photons necessary to bring a beam of SrF to a stop, and subsequently load the molecules into a trap. Furthermore the experimentally determined loss rate of molecules in this system is  $< 5\%$  for  $N_{sc} \sim 1000$ , implying that  $> 10\%$  can be brought to rest, given sufficient interaction time. The laser cooling techniques presented here are limited, from a practical standpoint, to those molecules which have closed electronic transitions with diagonal FCFs and therefore require relatively few lasers. For this reason these techniques are applicable only to a small fraction of diatomic molecules. However because the set of diatomic molecules is very large, this subset contains a significant number of molecules [87]. We are aware of at least a dozen diatomic molecules with a wide range of internal structures that appear amenable to laser cooling with similar methods. (See [Appendix B](#)). Laser cooling such molecules to ultracold temperatures would open the door to the study of a wide variety of new physical phenomena.

## Chapter 8

# Laser radiation pressure slowing of a molecular beam

This chapter details the deceleration of our SrF beam using radiative forces. There is no simultaneous transverse cooling. The results presented here parallel those presented in Ref. [246].

### 8.1 Introduction

A crucial step to obtaining large samples of ultracold, trapped molecules is developing a means to bridge the gap between typical molecular source velocities ( $\sim 150 - 600 \frac{m}{s}$ ) and velocities for which trap loading or confinement is possible ( $\lesssim 5 - 20 \frac{m}{s}$ ). Tremendous advances have been made in the deceleration of molecular beams in the past decade. Stark deceleration [47–50], Zeeman deceleration [51–53], counter-rotating nozzles [54, 55], collisional deceleration [56], and photodissociation [57] have all been demonstrated to slow molecular beams. However, only for fairly light species ( $\sim 20$  amu) with substantial vapor pressure at room temperature have these methods been demonstrated to allow slowing to velocities necessary to make trapping possible [58–61]. Optical deceleration has been demonstrated to slow molecular beams to rest [62, 63], but the high laser intensities required limit application to small volumes.

While these slowing methods are useful, all of them conserve phase-space density and hence slow without cooling. Assuming a given species (such as SrF) is amenable to laser cooling, the same radiative forces can be used for slowing. As is well known from atoms [1, 247], laser slowing can be effective over broad velocity ranges and is insensitive to position, so that it can work on a large

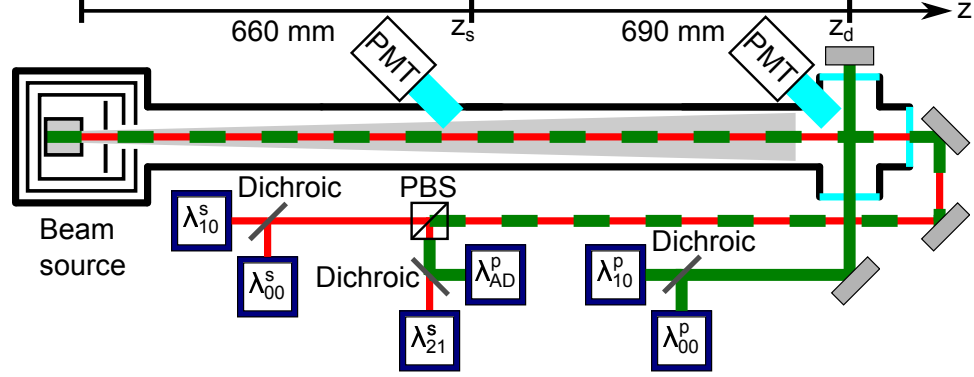


Figure 8.1: Schematic of the experimental apparatus for slowing. Red lines (—) indicate slowing laser beams while green lines (—) indicate probe laser beams. PMT locations are marked on the  $z$  axis.

phase-space volume of molecules. Laser slowing can also lead to simultaneous longitudinal velocity compression, which is advantageous for loading traps. Once trapped, these molecules may be further laser-cooled to increase the phase-space density.

Here we experimentally demonstrate deceleration of our SrF molecular beam by radiative forces. The crucial enabling feature for radiative slowing is the ability to scatter  $\gtrsim 10^4$  photons without heating the internal degrees of freedom of the molecules. Under certain conditions, the deceleration results in a substantial flux of detected molecules with velocities  $\lesssim 50 \frac{m}{s}$ . Simulations and other data indicate that the detection of molecules below this velocity is greatly diminished by transverse divergence from the beam. The observed slowing, from  $\sim 140 \frac{m}{s}$ , corresponds to scattering  $\gtrsim 10^4$  photons. We also observe longitudinal velocity compression under different conditions.

## 8.2 Experimental apparatus

We use the ablation-loaded cryogenic buffer gas beam source detailed previously, which provides relatively low initial forward velocities, low internal temperatures, and high brightness. To mitigate variations of the molecular beam flux due to changing ablation yields, data are taken by chopping the slowing lasers on or off between successive ablation shots. Chopping vastly increases data quality by controlling for long term drift of the ablation yield, previously the dominant systemic noise source. Due to concerns about residual helium atoms attenuating our molecular beam, data in this chapter are taken with a flow rate of 1 sccm. A home-made skimmer (6.35 mm diameter) followed by a short differential pumping tube (19 mm long and 12.7 mm diameter) also reduces the conductance out of the 30K shield, thereby reducing the helium gas load on the room temperature pumps. At a flow

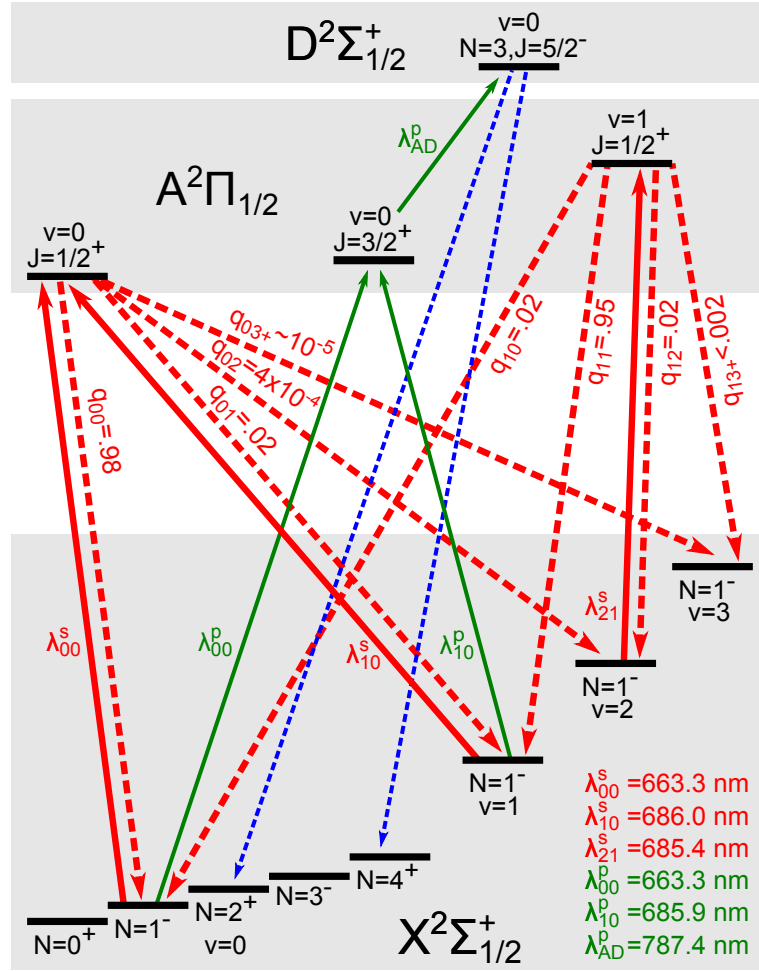


Figure 8.2: Relevant energy levels and transitions in SrF used for laser slowing and detection. Solid thick red lines (—) denote slowing lasers, while solid thin green lines (—) denote probe lasers. Dashed thick red lines (---) denote spontaneous decay channels from the A state and corresponding FCFs ( $q_{v'v''}$ ) are labeled. Dashed thin blue lines (---) indicate decay fluorescence channels used to determine the beam Doppler profile.



rate of  $\mathcal{F} = 1$  sccm, the background pressure in the beam propagation region is held to  $\sim 2 \times 10^{-7}$  Torr by two turbos (both Pfeiffer TMU 071 P). Of the total background pressure, approximately half is due to helium and the remainder is almost entirely due to water vapor.

With the slowing lasers and slowing repump lasers, denoted  $\lambda_{00}^s$ ,  $\lambda_{10}^s$ , and  $\lambda_{21}^s$  respectively, applied counter-propagating to the molecular beam as shown in Fig. 8.1, molecules cycle over the three bright ground states:  $X(v = 0, 1, 2; N = 1)$  as shown in Fig. 8.2. The  $X(v = 0, 1; N = 1)$  populations are expected to be comparable, while the  $X(v = 2, N = 1)$  population should be significantly less since the FCFs dictate that decays to this latter state are rare compared to the rate at which population in this state is pumped out via the  $A(v = 1, J = 1/2)$  intermediate state. We hence employ a scheme shown in Fig. 8.2 to detect population in both  $X(v = 0, 1; N = 1)$  states (including all SR/HF structure). Molecules in these states are excited to the  $A(v = 0, J = 3/2)$  state (unresolved HF) via two perpendicular probe lasers, denoted  $\lambda_{00}^p$  and  $\lambda_{10}^p$ , which are spatially overlapped and intersect the molecular beam at  $z = z_d$ , 1350 mm downstream from the source, as shown in Fig. 8.1. A longitudinally propagating probe laser, denoted  $\lambda_{AD}^p$ , then excites to the  $D(v = 0, N = 3, J = 5/2)$  state (unresolved HF structure), and the resulting laser-induced fluorescence (LIF), predominantly at 360 nm, is filtered and measured by a photon-counting PMT (Sens-Tech, P25USB) at  $z = z_d$ . Monitoring the  $D \rightarrow X$  LIF as a function of the  $\lambda_{AD}^p$  laser frequency yields a Doppler-shifted longitudinal velocity profile (LVP) free of SR/HF structure, at a wavelength easily filtered from all laser light. Both the  $\lambda_{00}^p$  and  $\lambda_{10}^p$  lasers have frequency-modulated (FM) sidebands with modulation frequency  $f_{\text{mod}} = 42$  MHz and modulation index  $M_{\text{mod}} = 2.6$  to excite all SR/HF levels of the  $X(v = 0, 1; N = 1)$  states [90]; since they intersect the collimated molecular beam transversely, they are subject to negligible Doppler shift and broadening. The  $\lambda_{00}^p$  and  $\lambda_{10}^p$  laser powers are set so that the excitation rate is the same for both transitions. We verified that the detection efficiency and measured LVP are independent of whether the molecule is detected from  $X(v = 0, N = 1)$  or  $X(v = 1, N = 1)$ . Power broadening from the  $\lambda_{AD}^p$  laser ( $\sim 23$  MHz FWHM) and magnetic field broadening ( $\sim 18$  MHz FWHM) lead to a measured broadening of 42 MHz FWHM for the  $\lambda_{AD}^p$  detection profile, equivalent to all velocity profiles being convolved with a detection profile of 34 m/s FWHM. The  $\lambda_{00}^s$ ,  $\lambda_{10}^s$ ,  $\lambda_{21}^s$ , and  $v_{AD}^p$  lasers are spatially overlapped using a combination of dichroic mirrors (Semrock FF669-Di01 and Semrock FF741-Di01) and a polarizing beam splitter (PBS) to produce a single beam with  $\frac{1}{e^2}$  full width intensity waist  $d = 3.4$  mm (except for the  $\lambda_{AD}^p$  laser with  $d = 4.4$  mm) counter-propagating to the molecular beam. To address all SR/HF levels over a wide velocity range, the  $\lambda_{00}^s$ ,  $\lambda_{10}^s$ , and  $\lambda_{21}^s$  lasers have FM sidebands

with  $41 \text{ MHz} < f_{\text{mod}} < 44 \text{ MHz}$  and  $M_{\text{mod}} = 3.1$  unless noted otherwise. Due to the large frequency extent of the sidebands, we do not expect longitudinal velocity compression [248]. We note that the dark magnetic sublevels of the  $X(N = 1)$  state unfortunately prevent use of a Zeeman slower. The slowing lasers are not chirped [249] due to the temporal extent of the molecular beam pulse ( $\sim 10 \text{ ms}$ ). A supplementary light detector at  $z = z_s$ , 660 mm downstream from the source, allows monitoring of the LIF from spontaneously emitted photons during cycling. The  $\lambda_{00}^s$ ,  $\lambda_{10}^s$ ,  $\lambda_{21}^s$  and  $v_{AD}^p$  laser powers are 140 mW, 73 mW, 45 mW, and 70 mW respectively. The  $\lambda_{00}^s$ ,  $\lambda_{10}^s$ , and  $\lambda_{21}^s$  laser detunings from resonance, denoted  $\Delta\nu_{00}^s$ ,  $\Delta\nu_{10}^s$ , and  $\Delta\nu_{21}^s$  respectively, are first varied iteratively to maximize LIF at  $z = z_s$ . For finer tuning, the  $v_{AD}^p$  laser detuning from resonance, denoted  $\Delta\nu_{AD}^p$ , is set to resonantly excite SrF molecules with  $v_f \approx 50 \frac{\text{m}}{\text{s}}$ , and  $\Delta\nu_{00}^s$ ,  $\Delta\nu_{10}^s$ , and  $\Delta\nu_{21}^s$  are varied iteratively to maximize the number of molecules detected in that Doppler class. Unless explicitly noted,  $\Delta\nu_{10}^s$  and  $\Delta\nu_{21}^s$  remain at these empirically determined values, denoted  $\Delta\nu_{10}^{s, \text{opt}}$  and  $\Delta\nu_{21}^{s, \text{opt}}$  respectively. Magnetic field coils create an approximately uniform field  $B = 9 \text{ G}$  at an angle  $\theta_B = 45^\circ$  relative to the  $\lambda_{00}^s$  linear polarization over the length  $120 \text{ mm} \lesssim z \lesssim 1350 \text{ mm}$ .

### 8.3 Results

Application of the slowing lasers shifts the molecular beam LVP, as shown in Fig. 8.3a for various  $\Delta\nu_{00}^s$ . As  $\Delta\nu_{00}^s$  is tuned towards  $\langle v_f \rangle / \lambda_{00}^s$  from the red (where  $\langle v_f \rangle$  is the mean forward velocity), the LVP is shifted to lower velocities, until  $\Delta\nu_{00}^s \approx \langle v_f \rangle / \lambda_{00}^s$  (i.e., when the slowing laser is tuned to the maximum of the Doppler-shifted peak); then, when tuned further to the blue, the LVP gradually returns to its unperturbed state. However, the shift to lower velocities is accompanied by a decrease in the number of detected molecules, which is most severe when  $\Delta\nu_{00}^s \approx \langle v_f \rangle / \lambda_{00}^s$ .

We use the quantity  $\Delta_{HM}$ , defined as the shift of the half-maximum point on the leading edge of the observed slowed LVP (versus that of the control LVP), as one simple measure to evaluate the effectiveness of our slowing for different experimental parameters. Because slowed molecules are less likely to be detected (due to increased divergence, etc.),  $\Delta_{HM}$  likely provides an underestimate of the actual slowing. With  $\Delta\nu_{00}^s = -260 \text{ MHz}$ , providing resonant excitation for molecules with  $v_f = 175 \frac{\text{m}}{\text{s}}$ , we routinely achieve  $\Delta_{HM} \approx 45 - 60 \frac{\text{m}}{\text{s}}$ . Since the SrF recoil velocity is  $v_r = 5.6 \frac{\text{mm}}{\text{s}}$ , we interpret this as a mean number of photons scattered per molecule  $\langle N_{sc} \rangle \approx 10^4$ , roughly an order of magnitude greater than that demonstrated in our transverse cooling experiment [206].

We argue that the decrease in the number of detected molecules is due primarily to increased

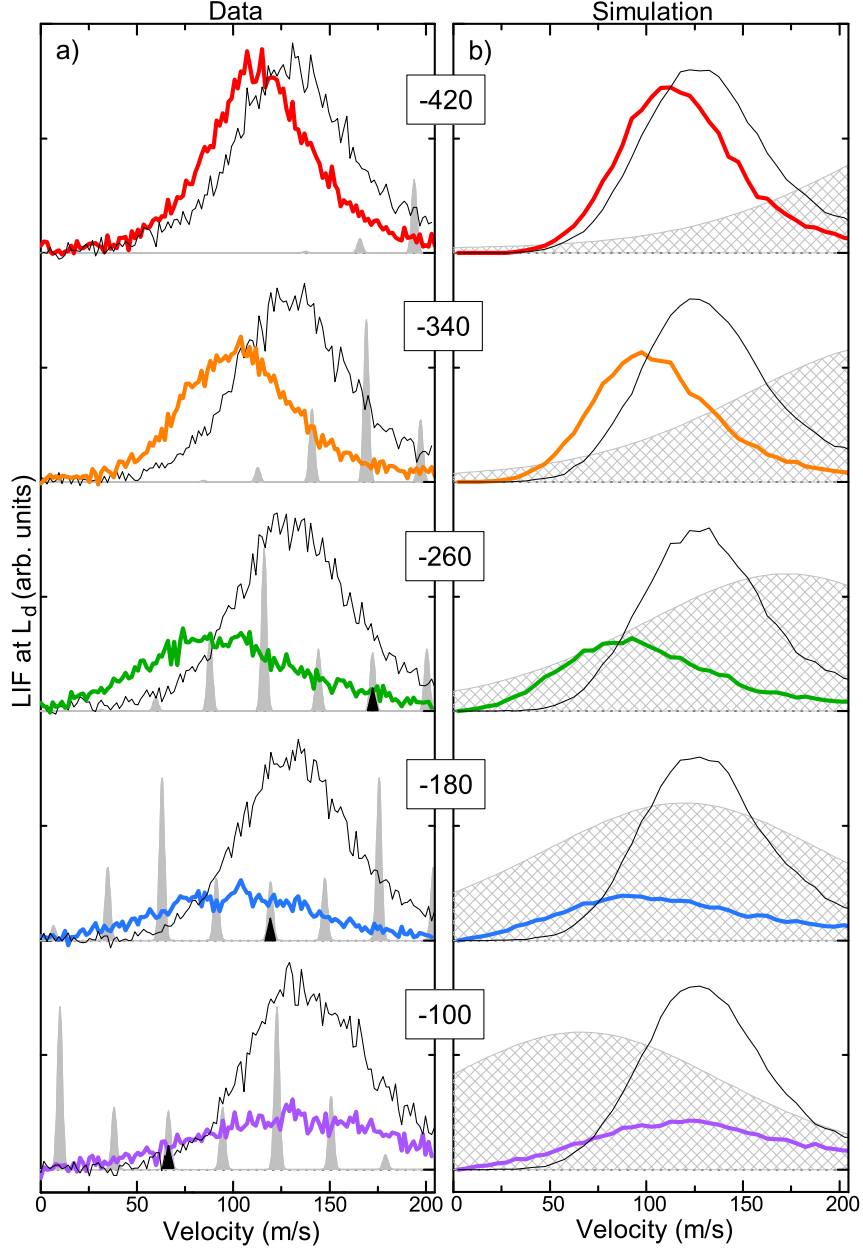


Figure 8.3: Measured and simulated slowing for different detunings of the main slowing laser. a) Measured slowed LVP (solid thick color), control LVP (—), and velocities corresponding to the  $\lambda_{00}^s$  FM sideband spectrum (gray, with center  $\blacktriangle$ ). The panels are scaled so that all controls have equal heights. b) Simulated slowed LVP (solid thick color) and simulated control LVP (—). The gray shaded area indicates the assumed force versus velocity profile used in the simulation. The  $\Delta\nu_{00}^s$  detuning (in MHz) is shown in the centered box for each panel set. The simulation indicates that nearly all of the decrease in the number of detected molecules can be attributed to increased divergence and transverse heating.

divergence and transverse heating as the beam is slowed. Several other loss mechanisms were ruled out as the dominant cause after investigation. Increasing the background gas pressure (primarily helium) by  $5\times$  changed the slowed LVPs little, indicating that background gas collisions are not a dominant loss mechanism. We investigated possible loss to other rovibrational states which could arise from various mechanisms. For example, off-resonant excitation to the  $A(v = 0, J = \frac{3}{2})$  state by the  $\lambda_{00}^s$  laser or HF mixing in the  $A(v = 0, J = \frac{1}{2})$  state could transfer population to the dark  $X(v = 0, N = 3)$  state; stray electric fields could lead to decays from the  $A(v = 0, J = \frac{1}{2})$  state to the dark  $X(v = 0; N = 0, 2)$  states; or the  $\lambda_{AD}^p$  laser could off-resonantly excite molecules from the  $A(v = 0, J = \frac{1}{2})$  state to the  $D(v = 0, N = 1)$  state before they reach  $z = z_d$ . To investigate such mechanisms, we explicitly probed the populations of the  $X(v = 0; N = 0, 2, 3)$  and  $X(v = 1, N = 0)$  states and determined that  $< 10\%$  combined total loss could be attributed to such processes. Loss to the  $X(v = 3, N = 1)$  state was not directly measured, but was estimated from the observed increase in spontaneous scattering LIF at  $z = z_s$  by adding the  $\lambda_{21}^s$  repump laser; this indicated that molecules cycled through the  $X(v = 2, N = 1)$  state  $\sim 3\times$  before reaching  $z = z_d$ . Together with the estimated FCFs [90], this yields an estimated  $\sim 6\%$  loss to the  $X(v = 3, N = 1)$  state. Over all, the lack of observed population accumulation in states outside those involved in the cycling transition is preliminary evidence that our cycling transition is nearly closed for up to  $\sim 10^4$  scattered photons.

The decrease in the number of detected molecules due to increased divergence and transverse heating is modeled via a Monte Carlo simulation. In the simulation, particles are created at the source with randomized velocity distribution matching the measured forward and transverse velocity distributions of our source [73]. We assume equal detection efficiency over the  $\lambda_{AD}^p \frac{1}{e^2}$  beam waist at  $z = z_d$ . We estimate the force profile using a 4+1 level model of our system, which consists of one excited state and four ground states (to match the four SR/HF levels). The degeneracy of the SR/HF levels and the accompanying level shifts and remixing within each SR/HF level due to the applied  $B$ -field are not included in the simulation. The saturation parameter  $s$  is calculated for each of the four SR/HF levels assuming an estimated saturation intensity of  $6 \text{ mW/cm}^2$  and the known  $\lambda_{00}^s$  laser FM sideband spectrum. Using  $\tau$  and  $s$ , classical rate equations are solved to determine the equilibrium excited state population fraction,  $\rho_{ee}$ , as a function of the laser detuning from the center of the Doppler shifted SR/HF spectrum,  $\Delta$ . The dependence of  $\rho_{ee}$  is then fit to a Voigt profile. This process is repeated for the range of powers dictated by the  $\lambda_{00}^s$  laser's Gaussian intensity profile. Using the peak values of  $\rho_{ee}$  for each intensity, we derive an estimate of how the maximum scattering rate varies with the distance from the center of the slowing beams,  $r$ . We finally model

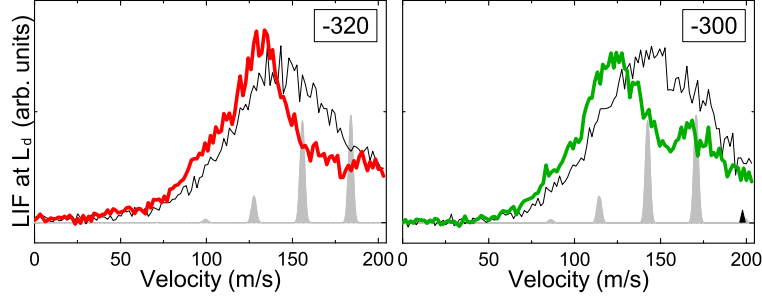


Figure 8.4: Slowing with no applied magnetic field. The  $\Delta\nu_{00}^s$  detuning (in MHz) is shown in the upper right. Otherwise the representation is the same as in Fig. 8.3. Note the sharp features, in particular the increase in the ratio of peak height to width of the LVP; these indicate longitudinal velocity compression within part of the distribution. This should be contrasted with the smooth LVPs obtained at large  $B$  (Fig. 8.3). Here  $M_{\text{mod}} = 2.6$  for the  $\lambda_{00}^s$  laser, where the sharp features were generally more pronounced than at the typical  $M_{\text{mod}} = 3.1$  used for most of the slowing data.

the scattering rate  $R$  as the analytic function

$$R(\Delta, r) = R_{\text{max}} \left[ \frac{1}{1 + (r/r_0)^a} \right] \left[ N_1 \int_{-\infty}^{\infty} \frac{e^{-t^2/(2w_G^2)}}{(w_L/2)^2 + (\Delta - t)^2} dt \right],$$

where the normalization  $N_1$  is chosen so that  $R(0, 0) = R_{\text{max}}$ . The parameter values  $r_0 = 1.3$  mm,  $a = 3.75$ ,  $w_L = 99$  MHz and  $w_G = 95$  MHz are derived from these fits, without reference to the LVP data. The first two parameters control how the scattering rate varies with the beam intensity, while the latter two characterize the functional dependence of  $R$  on  $\Delta$ . Finally, the free parameter  $R_{\text{max}}$  is varied manually to fit the LVP data for a variety of  $\Delta$ . We achieve good agreement with  $R_{\text{max}} = 2.8 \times 10^6 \text{ s}^{-1}$ , consistent with our previous observations from deflection [90]. Typical simulation results, shown in Fig. 8.3b, indicate that nearly all of the decrease in the number of detected molecules can be attributed to increased divergence and transverse heating. Several other pieces of evidence (e.g., dependence of the slowed LVP on laser power for various detunings) suggest that larger scattering rates may result in greater slowing but that this additional slowing may not be apparent in the data due to increased divergence and therefore decreased detection probability for the slowest molecules. We note some interesting behavior the simulation alerted us to. The simulation results do not match the data until the laser beams' Gaussian profiles (and therefore the spatially dependent power broadening) are taken into account. The simulation also does not reproduce the data until we account for the spatial broadening of the beam source due to collisions with helium near the cell exit aperture.

Most data was taken with an ambient magnetic field of  $B \approx 4 - 9$  G and  $\theta_B = 45^\circ$ . Over

this range, the slowed LVPs and LIF at  $z = z_s$  were fairly insensitive to the value of  $B$ . However, we observed that Earth's magnetic field,  $B_E \approx .5$  G with  $\theta_B \approx 102^\circ$ , on its own allows some remixing of the dark Zeeman sublevels. Under certain conditions when  $B = B_E$ , qualitatively different behavior was observed; namely, sharp features appeared in the LVP, as shown in Fig. 8.4. Moreover, under these conditions there is clear evidence for longitudinal velocity compression: the ratio of peak height to width of the LVP increases under these conditions for certain detunings  $\Delta\nu_{00}^s$ . We have been unable to find a simple explanation for these features, and full modeling of the system (including all  $\sim 33$  slowing laser frequencies, 44 molecular sublevels,  $B$ -field remixing, coherent dark states [89], spatially varying laser intensity profiles, etc.) is challenging. However, this behavior could potentially be used to compress the molecular beam LVP. Ideally this would be done after slowing had already removed most of the kinetic energy from the beam, e.g., by using an initial region of large  $B$  for broadband slowing, followed by a second region of small  $B$  for longitudinal velocity compression and further slowing. A slow and nearly monoenergetic beam would be ideal for trap loading.

In summary, we have demonstrated radiation pressure slowing of an SrF molecular beam. Under certain conditions, we detect  $\sim 6\%$  of the initial detected flux at velocities  $< 50 \frac{m}{s}$ . The dominant loss mechanism at present is the increased divergence and transverse heating of the beam due to the slowing. It may be possible to use a low  $B$ -field section to compress the velocity distribution following the initial slowing. A slow molecular beam could be directly loaded into either a magneto-optical trap (MOT) [88] or a sufficiently deep conservative trap, using optical pumping as a dissipative loading mechanism [77, 203, 250–254]. Furthermore, the preliminary evidence of little loss during cycling, even after  $\gtrsim 10^4$  photons have been scattered, invites the possibility of moderately long lifetimes for SrF in a MOT.

## Chapter 9

# Progress towards a 3-D MOT

All work presented in this chapter is geared towards realizing the first 3-D MOT. Many changes are implemented relative to the experimental setups in [chapter 7](#) and [chapter 8](#). Small sections of this chapter are taken from Ref. [\[134\]](#).

### 9.1 An SrF MOT

Traditional alkali MOTs operate on a  $F \rightarrow F' = F + 1$  transition. There are no dark Zeeman sublevels in the ground state. For the  $R = 1 \rightarrow R' = 0$  cycling transition in SrF, 2/3 of the ground states are dark at any given time for a given laser polarization. There are substantial questions regarding the viability of creating a MOT on a transition with dark Zeeman sublevels, as discussed next.

#### 9.1.1 Non-traditional MOTS

A variety of non-traditional MOTs have been demonstrated to work in the presence of dark Zeeman sublevels. For example, MOTs have been shown to work on a  $F \rightarrow F' = F - 1$  transition for  $^{85}\text{Rb}$  [\[255\]](#) and Na [\[256, 257\]](#). A “type II” MOT with  $F \rightarrow F' = F$  has also been demonstrated for Na [\[258, 259\]](#). None of the above are necessarily analogous to a hypothetical SrF MOT since the small hyperfine splitting of these atoms’ excited states may help to provide confinement [\[256\]](#). We believe the closest analogy to a hypothetical SrF MOT are MOTs for alkali atoms operating on a D1 ( $F \rightarrow F' = F$ ) transition, which has been demonstrated only for Na [\[260\]](#). A D1 MOT for K was not observed in Ref. [\[261\]](#). It is possible that both the magnetic field [\[262\]](#) and the 3-D nature

of the light<sup>1</sup> play a role in remixing the dark Zeeman sublevels and allow the D1 MOT to work. All of the above non-traditional MOTs report larger diameter clouds of atoms and higher temperatures than standard D2 MOTs.

### 9.1.2 MOT polarization

For making an SrF MOT, it is unfortunate that the g-factors of the four SR/HF manifolds do not all share the same sign as shown in Table 2.17 and in Fig. 2.5. Hence, for MOT pump light with a single polarization (albeit with four frequencies), at least one level will experience a scattering force which is damping but anti-restoring from the MOT center. MOTs have been demonstrated on transitions where certain states experience no trapping force [264, 265], but MOT lifetimes are reduced under these conditions. Hence, we desire that all (non-dark) states feel a restoring force from the light. Our solution combines laser light from a TA with  $f_{\text{mod}} = 40.4$  MHz and  $M_{\text{mod}} = 2.6$  with single frequency light from a slave laser on a PBS to create the MOT trapping light. As shown in Fig. 9.1, the TA light addresses the  $|N = 1, J = 3/2, F = 2\rangle$ ,  $|N = 1, J = 3/2, F = 1\rangle$ , and  $|N = 1, J = 1/2, F = 0\rangle$  states primarily while the single frequency light (with polarization opposite to the TA light) addresses the  $|N = 1, J = 1/2, F = 1\rangle$  state. The value of  $f_{\text{mod}}$  for the TA light is chosen to minimize the RMS value of the detuning for the upper three SR/HF levels for  $B = 0$  Gauss. The single frequency slave laser is tuned 9.0 MHz to the blue of one of the 2nd order TA sidebands. This polarization scheme is not implemented for the MOT repump lasers since the forces derived from these lasers should be relatively small.

### 9.1.3 Unintended excitation

Ideally, each of the four laser frequencies would be near-resonant with only a single SR/HF manifold. Unfortunately, the different  $m_F$  sublevels cross at various values of  $B$ , with the first crossing occurring at  $B \approx 15$  Gauss as shown in Fig. 9.2. Assuming the excitation scheme shown in Fig. 9.2, when  $B \approx 15$  Gauss, molecules in the  $|J = 3/2, F = 2, m_F = -2\rangle$  level will start to scatter photons from the laser sideband intended to address the  $|J = 3/2, F = 1\rangle$  SR/HF manifold. However, the  $|J = 3/2, F = 2, m_F = -2\rangle$  state will be dark to photons which oppose molecule motion and light to photons aligned to the molecule motion, resulting in a net anti-restoring force. It is not *a*

---

<sup>1</sup>Absorption and emission of photons polarized with respect to an axis orthogonal to the magnetic field at a given particle's location act to randomize the particle's state over all ground state sublevels. This effect is rarely discussed in standard MOT discussions found in most textbooks since it cannot be applied to MOT mechanics which treat only one dimension [263].



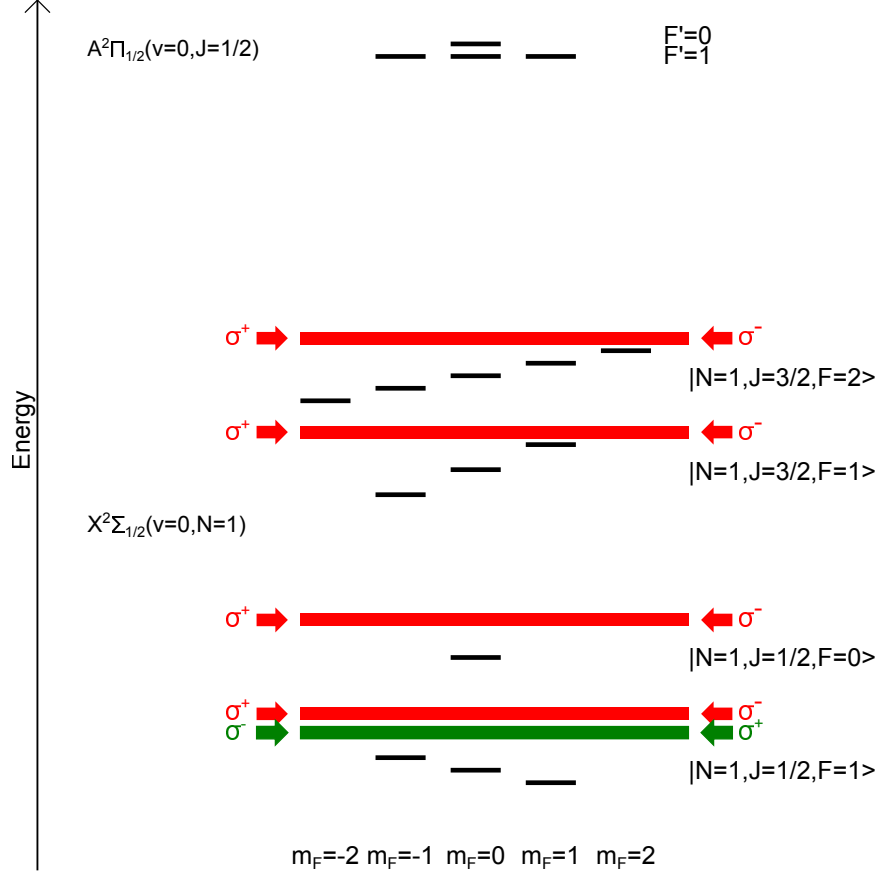


Figure 9.1: Proposed polarization scheme for making an SrF MOT as discussed in the main text. The energy levels are shown for a positive  $B$ -field. The TA light (■) primarily addresses the  $|N = 1, J = 3/2, F = 2\rangle$ ,  $|N = 1, J = 3/2, F = 1\rangle$ , and  $|N = 1, J = 1/2, F = 0\rangle$  states while the single frequency light with opposite polarization (■) addresses the  $|N = 1, J = 1/2, F = 1\rangle$  state. Addressing each SR/HF manifold with the proper polarization (for the sign of that manifold's  $g$ -factor) ensures that molecules in bright states always feel a restoring force. The energy scale increases towards the top of the figure so that all laser frequencies are red-detuned to the primary SR/HF manifold they address. This polarization scheme is only employed for the main cycling transition and not for the repump lasers.

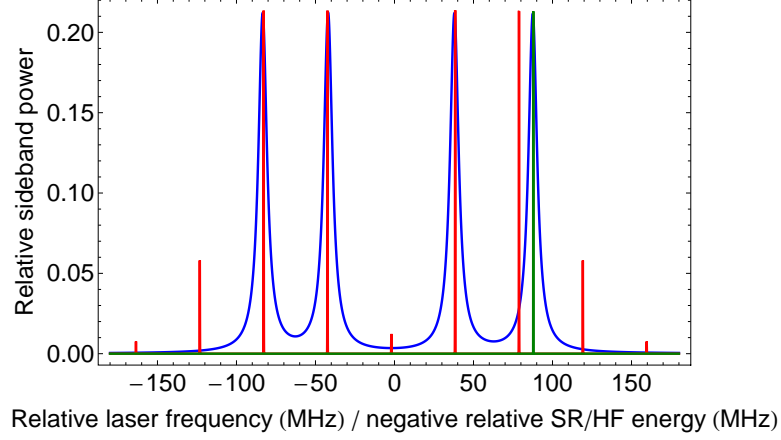


Figure 9.2: Addressing SR/HF structure by the MOT pump laser as discussed in the main text. Each SR/HF manifold is shown (—) as a Lorentzian profile of width  $= \frac{\Gamma}{2\pi}$ . MOT TA light on the main cycling transition is shown (—) for  $f_{\text{mod}} = 40.4$  MHz and  $M_{\text{mod}} = 2.6$ . A single slave laser (—) addresses the  $|J = 1/2, F = 1\rangle$  state. This scheme is only employed for the main cycling transition.

*priori* clear how detrimental this effect will be. This crossing may limit us to small magnetic fields, potentially problematic in light of the relatively large  $B$ -field gradients employed in the D1 MOT of Ref. [260]. On the other hand, it is conceivable to create an SrF MOT using a single laser frequency red-detuned to all SR/HF substructure. Among other necessary changes, this would likely require broadening the MOT lasers by  $\gtrsim 100$  MHz unless remixing of the dark Zeeman sublevels is provided by microwaves resonant with the  $R = 1 \rightarrow R' = 0$  transition in the ground state as discussed in subsection 3.1.3.

#### 9.1.4 Preliminary MOT design

Currently all MOT light is aligned into a single-mode PM fiber. Due to the multiple polarizations present as shown in Fig. 9.1, the MOT light is first split by a 70/30 non-polarizing beam splitter followed by a 50/50 non-polarizing beam splitter into 3 beams. MOT beams are large to increase the capture velocity. The current MOT beams are limited to sizes less than 23 mm by optical apertures outside the vacuum chamber. MOT beam alignment is typically done by minimizing scattered light generated as the MOT beams pass through apertures in vacuum chamber. (See subsection 9.5.5.) For power considerations, each of the three MOT beams is retro-reflected. Water-cooled MOT coils designed by Eric Norrgard provide a quadrupole  $B$ -field with gradients up to  $\sim 140$  Gauss/cm. Preliminary searches for an SrF MOT have so far have focused on increasing the LIF of slow molecules in the MOT region. For a spatial LIF region of fixed size, slow molecules should undergo more LIF cycles than fast molecules.

However, prior to attempting to realize a 3-D SrF MOT, a number of changes were implemented relative to the experimental setups detailed in [chapter 7](#) and [chapter 8](#), in an effort to increase the number of slow molecules delivered to the MOT region. Specifically, we attempted to increase the spontaneous scattering force of the slowing lasers, we redesigned the vacuum system to allow for much lower pressures, and we attempted to add transverse cooling simultaneous with the slowing. We discuss such work and other MOT-related work completed to date in the remainder of this chapter.

## 9.2 Frequency distribution of slowing light

In [chapter 8](#) each slowing laser has RF sidebands with  $f_{\text{mod}} \approx 42$  MHz and  $M_{\text{mod}} \approx 2.6$ . Molecules whose Doppler-shifted resonant excitation frequency lies between two RF sidebands presumably depend on power broadening and  $B$ -field shifting/broadening for excitation. This approach has two drawbacks. First, a laser intensity distribution more uniform in frequency (e.g. a top-hat profile) should lead to larger values of  $S_{\text{sc}}$  for the same slowing laser beam diameter (or to the same value of  $S_{\text{sc}}$  for larger slowing laser beam diameters). Either might result in more slow molecules delivered to the downstream detection region. Second, if a top-hat profile allows for decreased laser intensity, there should be less power broadening and molecules might accumulate at a single low velocity [266], particularly in the presence of a weak co-propagating laser [248, 267]. This analysis is complicated by the presence of the four well-resolved SR/HF sublevels.

We investigate varying the  $\lambda_{00}^{\text{s}}$  laser’s frequency distribution using the setup described in [chapter 8](#) and add an additional EOM, which can be turned on and off, to the  $\lambda_{00}^{\text{s}}$  laser with  $f_{\text{mod}} \approx 9$  MHz and  $M_{\text{mod}} \sim 5$ . LIF from the X→A transition  $\approx 6$  cm downstream from the cell is monitored by a PMT. As shown in [Fig. 9.3](#), additional 9 MHz sidebands on the  $\lambda_{00}^{\text{s}}$  laser increase both the peak height and area of the LIF profile by  $\approx 30\%$ . Later, similar EOMs are added to the  $\lambda_{10}^{\text{s}}$  and  $\lambda_{21}^{\text{s}}$  lasers as well. Ultimately, this approach allows us to increase the diameters of the slowing lasers from that in [chapter 8](#) by  $\sim 30\%$  while maintaining qualitatively similar slowing performance.

In a later revision, a fiber EOM (Jenoptik, PM660) driven by an amplifier (Minicircuits, LZY-22+) creates RF sidebands with  $f_{\text{mod}} = 4.5$  MHz and  $M_{\text{mod}} \approx 40$  on the  $\lambda_{00}^{\text{s}}$  laser and results in an approximate flat-top profile for the  $\lambda_{00}^{\text{s}}$  laser as shown in [Fig. 9.4](#). Even with this profile, we do not observe velocity compression at low velocities. We attempt several other techniques to compress the LVP, including “shelving” molecules reaching a certain low velocity into another state

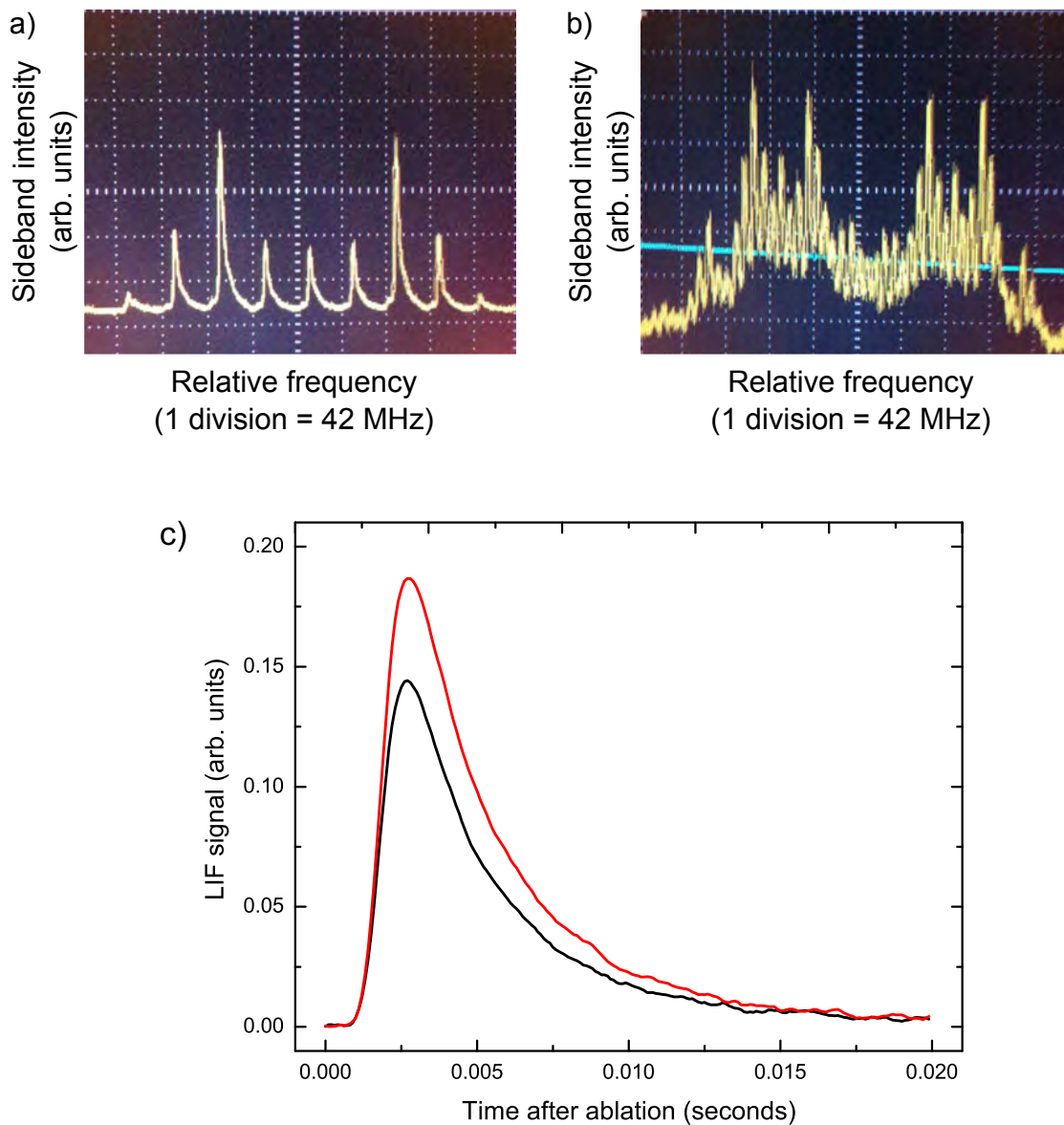


Figure 9.3: Increased spontaneous LIF due to extra sidebands for the  $\lambda_{00}^s$  laser. A single resonant EOM with  $f_{\text{mod}} \approx 42$  MHz and  $M_{\text{mod}} \approx 2.6$  produces the  $\lambda_{00}^s$  laser frequency profile shown in (a) and the resulting spontaneous LIF from the molecular beam at a point  $\approx 6$  cm downstream from the cell exit aperture is shown by (—) in (c). Adding an additional EOM with  $f_{\text{mod}} = 9$  MHz creates the frequency spectrum shown in (b) and results in a  $\approx 30\%$  increase in LIF (both in peak height and area) as shown (—) in (c).

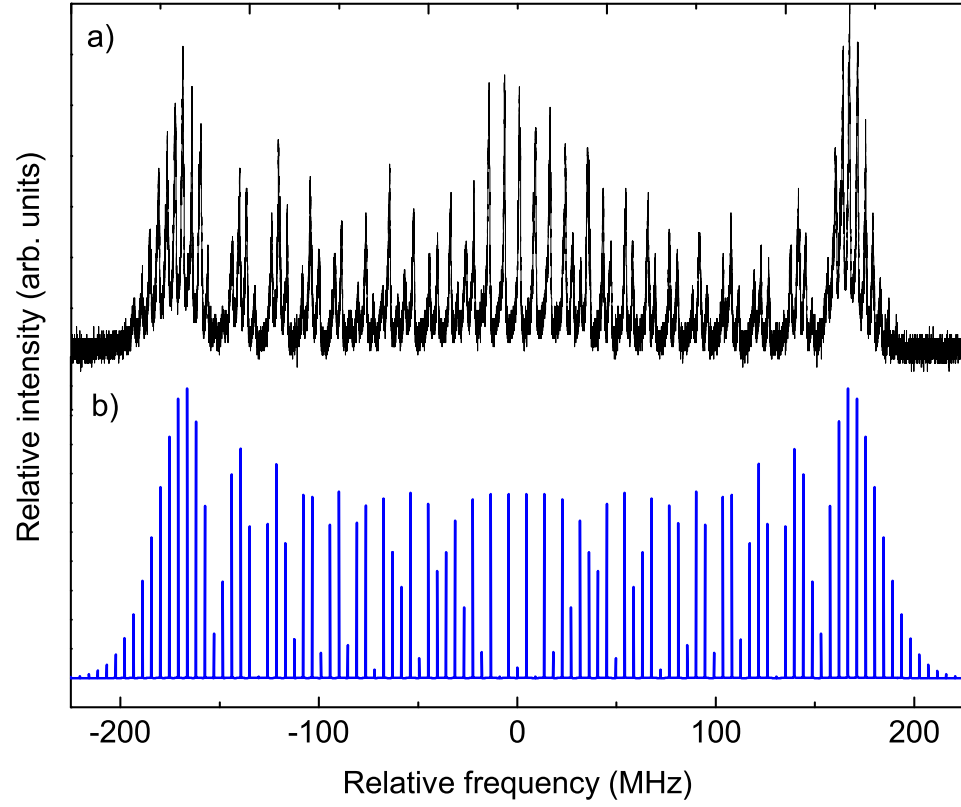


Figure 9.4: Spectral profile of the  $\lambda_{00}^s$  laser with sidebands created by a fiber EOM. (a) Measured sideband spectral profile when  $f_{\text{mod}} = 4.5$  MHz and  $M_{\text{mod}} \approx 40$  (—) and (b) simulated profile for  $f_{\text{mod}} = 4.5$  MHz and  $M_{\text{mod}} = 40$  (—).

and a co-propagating laser (which can be thought of as similar to a moving molasses [248, 266–268]). Although we observe compression for velocities  $\gtrsim 50$  m/s for each technique, we are so far unable to increase the number of molecules at any velocity  $\lesssim 50$  m/s using either of these two methods relative to radiative slowing alone.

### 9.3 Vacuum system

The pressure inside the vacuum region needs to be low enough that attenuation of the molecular beam is minimal.<sup>2</sup> Additionally, trap lifetimes  $\gtrsim 1$  s require a pressure in the trapping region  $\lesssim 10^{-9}$  Torr. Since the beam source emits  $\mathcal{F} = 5$  sccm of He, achieving this is not automatic. In our current vacuum system, the dominant gases are He, N<sub>2</sub> and H<sub>2</sub>O. He is produced from the cryogenic buffer gas cell, while H<sub>2</sub>O and N<sub>2</sub> result from outgassing of non-cryogenic surfaces. Unlike most MOT vacuum systems, there is a large active gas load distinct from the species to be trapped. Thus, we review our approach.

#### 9.3.1 Beam attenuation by room temperature gases

The SrF molecular beam has forward velocity  $v_{\text{SrF}\parallel} \approx 125$  m/s, much lower than the mean thermal velocities of He, N<sub>2</sub> or H<sub>2</sub>O at 293 K, which are  $\approx 1250$ , 590 and 470 m/s respectively. Conceptually, the slow SrF molecules can be thought of as approximately stationary relative to the faster background gases, and there is an expected mean free time between SrF collisions with background gas particles. Hence, the mean free path of an SrF molecule is dependent on that molecule’s velocity.

We treat the general case of a molecular beam of particles of species  $a$  and attenuation by background gas  $b$ . We define  $\beta = \sqrt{2k_B T_b / m_b}$  as in subsection 5.2.1. The mean free path of particle  $a$  depends on its velocity  $v_a$ , and the general solution is given in Ref. [207] II. 4.2 by

$$\lambda_a(v_a) = \frac{\sqrt{\pi}(v_a/\beta)^2}{n_b \sigma_{ab}} \times \frac{1}{\psi(v_a/\beta)} \quad (9.1)$$

$$\text{where } \psi(x) = x \exp(-x^2) + (2x^2 + 1) \int_0^x \exp(-y^2) dy. \quad (9.2)$$

We note that even for unsloved molecules, the quantity  $(v_a/\beta) \sim \frac{1}{10} \ll 1$  for  $b = \text{He}$  and  $v_a \sim v_{\text{SrF}\parallel}$ . Taylor expanding Eqn. 9.1 about  $v_a/\beta = 0$  and throwing away terms of order  $(v_a/\beta)^3$  and higher

---

<sup>2</sup>In chapter 8, low pumping speeds and high He gas loads on the room temperature pumps require  $\mathcal{F} = 1$  sccm of He to minimize molecular beam attenuation.

yields

$$\lambda_a = \frac{\sqrt{\pi}(v_a/\beta)}{2n_b\sigma_{ab}}. \quad (9.3)$$

This can be rearranged to give a mean free time between collisions,

$$\tau_{\text{coll}} = \frac{\sqrt{\pi}}{2n_b\sigma_{ab}\beta}, \quad (9.4)$$

which holds for both molecules in the molecular beam and for trapped molecules. Because molecules are detected a fixed distance downstream at  $z = L_d$ , slower molecules take longer to traverse this distance and are therefore more likely to be attenuated by collisions with background gas. The slowest molecules (most important for trapping) are, unfortunately, attenuated the most. This velocity-dependent attenuation complicates the interpretation of a measured velocity profile at  $z = L_d$ , since the attenuation factor may vary drastically over the range of velocities measured. Measured values of  $\sigma_{ab}$  for  $a = \text{SrF}$  and  $b = \text{He}$  do not exist but can be estimated from data in Refs. [207, 269, 270]. Eqn. 9.4 predicts  $\tau_{\text{coll}} \approx 130$  ms at  $10^{-7}$  Torr of He if we take  $\sigma_{\text{SrF/He}} = 1.6 \times 10^{-14}$  cm<sup>2</sup> based on He collision cross sections with other atoms and molecules from Refs. [269–271].

We test this model by alternating the rotation speed of the turbopump  $R_{\text{turbo}}$  between its maximum value  $R_{\text{turbo}}^{\text{max}}$  and a lesser value  $AR_{\text{turbo}}^{\text{max}}$ , where  $A < 1$  is a constant, and recording the LIF signal size  $N_{\text{LIF}}$  at a point  $z = L_d$  downstream with no slowing applied. We then have from Eqn. 9.4

$$N_{\text{LIF}}(R_{\text{turbo}}^{\text{max}}) = N_0 \exp\left[\frac{-L_d}{v_a \tau_{\text{coll}}(R_{\text{turbo}}^{\text{max}})}\right] \quad (9.5)$$

$$N_{\text{LIF}}(AR_{\text{turbo}}^{\text{max}}) = N_0 \exp\left[\frac{-L_d}{v_a \tau_{\text{coll}}(AR_{\text{turbo}}^{\text{max}})}\right], \quad (9.6)$$

where  $N_0$  is the LIF signal at  $z = L_d$  in the absence of collisions (i.e. perfect vacuum) and  $\tau_{\text{coll}}(R_{\text{turbo}})$  is the mean free time between collisions for the SrF molecules as a function of the turbopump rotation speed  $R_{\text{turbo}}$ . If we make the assumption<sup>3</sup> that  $\tau_{\text{coll}}(R_{\text{turbo}}) \propto R_{\text{turbo}}$ , combining the two above equations yields the lifetime

$$\tau_{\text{coll}}(R_{\text{turbo}}^{\text{max}}) = \frac{L_d(A-1)}{Av_a \log\left[\frac{N_{\text{LIF}}(AR_{\text{turbo}}^{\text{max}})}{N_{\text{LIF}}(R_{\text{turbo}}^{\text{max}})}\right]}. \quad (9.7)$$

---

<sup>3</sup>Although varying  $R_{\text{turbo}}$  alters both the compression ratio  $K_0$  (which varies exponentially with  $R_{\text{turbo}}$ ) and the pumping speed  $S_{\text{turbo}}$  of the turbo, it is safe to assume that  $S_{\text{turbo}} \leq S_{\text{turbo}}^{\text{max}} \times R_{\text{turbo}}/R_{\text{turbo}}^{\text{max}}$ . The assumption that the pumping speed is linear with the rotation speed of the turbo requires the pressure be limited by the pumping speed of the turbo and not by conductance, which is valid for our apparatus.

The measurement described here avoids relying on ion gauges and estimated values of  $\sigma_{\text{SrF/He}}$ . Eqn. 9.7 is a lower bound on  $\tau_{\text{coll}}(R_{\text{turbo}}^{\text{max}})$  since, due to compression ratio considerations, the lifetime may increase faster than linearly with  $R_{\text{turbo}}$ . In February of 2012, we measured  $\tau_{\text{coll}} = 160$  ms in the beam propagation region. Since then, the partial pressure of He has been further decreased by better sealing the 30K shield. (See subsection 9.3.4.)

### 9.3.2 Calculating gas loads and partial pressures

Design of the current vacuum system employs modeling of the various gas loads, discussed here. The vacuum system consists of several consecutive regions, labeled by  $k = 1, 2, 3$ , etc., separated by apertures. The partial pressure of gas  $i$  in region  $k$  is given by

$$P_{k,i} = Q_{k,i}/S_{k,i} \quad (9.8)$$

where  $Q_{k,i}$  is the gas load on region  $k$  from species  $i$  in Torr·L/s and  $S_{k,i}$  is the pumping speed in region  $k$  for species  $i$  in L/s. For all regions  $k$  at  $\approx 293$  K, we typically observe  $\sum_{i \neq \text{He}} P_{k,i} \sim P_{k,\text{H}_2\text{O}} \sim 10P_{k,\text{N}_2}$ . Since several factors limit bake temperatures to  $\sim 70$  °C,<sup>4</sup> this ratio does not change significantly after baking. We treat all non-helium background gases as a single gas with partial pressure  $P_{k,\text{BG}}$ .<sup>5</sup> Given that  $\mathcal{F} = 5$  sccm of He currently, the value of  $P_{k,\text{He}}$  can be quite large. For non-cryogenic regions, if  $P_{k,\text{BG}} > P_{k,\text{He}}$ , baking will reduce  $P_{k,\text{BG}}$  so that  $P_{k,\text{BG}} < P_{k,\text{He}}$ . For cryogenic regions  $P_{k,\text{BG}} \approx 0$ . Hence, we proceed assuming that  $P_{k,\text{BG}} < P_{k,\text{He}}$ .

We treat  $Q_{k,\text{He}}$  as the sum of a diffuse helium gas load  $Q_{k,\text{He}}^{\text{diff}}$  and a ballistic helium gas load  $Q_{k,\text{He}}^{\text{ball}}$ . All He originates from the cryogenic buffer gas cell; He from other sources is negligible. Diffuse He may be dealt with effectively by differential pumping. Ballistic He follows the path of the molecules and can be cut down by reducing the solid angle, but doing so will also cut out the species of interest (here, SrF). The spatial distribution of the He emitted from the cryogenic buffer gas cell is given by Eqn. 5.2. If the units of Eqn. 5.2 are converted to Torr·L/s, we have

$$Q_{k,\text{He}}^{\text{ball}} = \int_{d\Omega_k} dQ_{\text{He}} - \int_{d\Omega_{k+1}} dQ_{\text{He}}, \quad (9.9)$$

where  $d\Omega_k$  is the solid angle from the cell exit aperture subtended by the entrance aperture of region

<sup>4</sup>Temperatures above 325 K void the pulse tube warranty, so the source region can never be baked at all. Some of the turbopumps in use limit bake temperatures to  $\sim 70$  °C.

<sup>5</sup>Relative to He, the dominant background gasses H<sub>2</sub>O and N<sub>2</sub> all have similar thermal velocities and collision cross sections.



$k$  and  $d\Omega_{k+1}$  is the solid angle subtended by the exit aperture of region  $k$ , typically equal to the solid angle subtended by the entrance aperture of region  $k + 1$ . The cell exit aperture is treated as a point source since  $d\Omega_k$  varies negligibly for helium emitted from different points within the cell aperture for all regions  $k$  at 293 °C. The diffuse helium gas load on region  $k$  is

$$Q_{k,\text{He}}^{\text{diff}} = C_{k,k-1,\text{He}}(P_{k-1,\text{He}} - P_{k,\text{He}}) + C_{k,k+1,\text{He}}(P_{k+1,\text{He}} - P_{k,\text{He}}), \quad (9.10)$$

where  $C_{x,y,\text{He}}$  is the conductance between adjacent regions  $x$  and  $y$  in Torr·L/s for He. Conductance formulas for tubes and cones are calculated using Ref. [272]. Since thermal He is  $\approx 2.65\times$  faster than thermal air/N<sub>2</sub>, calculated conductances for He should be increased by this factor if the conductance is calculated with equations for air/N<sub>2</sub>. The pressure of He,  $P_{k,\text{He}}$  in region  $k$  will be

$$P_{k,\text{He}} = \frac{1}{S_{k,\text{He}}} \times [Q_{k,\text{He}}^{\text{ball}} + Q_{k,\text{He}}^{\text{diff}}] \quad (9.11)$$

$$P_{k,\text{He}} = \frac{1}{S_{k,\text{He}}} \times [Q_{k,\text{He}}^{\text{ball}} + C_{k,k-1,\text{He}}(P_{k-1,\text{He}} - P_{k,\text{He}}) + C_{k,k+1,\text{He}}(P_{k+1,\text{He}} - P_{k,\text{He}})]. \quad (9.12)$$

Solving the coupled equations for all  $k$  yields numerical values for all  $P_{k,\text{He}}$ . The above treatment is appropriate for gases other than He with the modification that there is no ballistic gas load but there is an additional term in Eqn. 9.10 due entirely to outgassing.<sup>6</sup> Changes made to our vacuum system in subsection 9.3.4 are based on the above modeling.

### 9.3.3 Pumping of helium gas

Most pumps are less effective at pumping helium than pumping most other gases. For instance, liquid nitrogen cryopumps and titanium sublimation pumps do not pump He. Ion pumps pump He at a fraction ( $\lesssim 30\%$ ) of their nominal pumping speed. Diffusion pumps with diffusion pump oil rated to  $10^{-10}$  Torr can pump He but present the possibility of coating the vacuum chamber or the cryogenic charcoal sorbs with oil. Turbopumps are an effective (but expensive) solution, and this is the solution we have chosen. It is important to ensure  $P_{k,\text{He}}$  will be limited by the turbo's pumping speed rather than its compression ratio. For light gases such as helium, this is not guaranteed, especially with older turbo pumps or turbopumps which do not incorporate a molecular drag/Holweck stage.

---

<sup>6</sup>Virtual leaks may also contribute for a poorly designed vacuum system. There is also some real leak rate into the vacuum system, but for our system this rate is negligible.

### 9.3.4 Revisions to vacuum system

Given the analysis in [subsection 9.3.2](#), we designed and built the current vacuum setup for the experiment shown in [Fig. 9.5](#). Herein, we drop the  $k$  subscript and refer to regions by the titles given in [Fig. 9.5](#). To decrease  $P_{\text{He}}$  in the beam propagation region, the conductance from inside to outside the 30K shield is reduced by taping (3M, #56f “yellow” tape or McMaster, 7631A41 aluminum tape) over all holes, cracks, etc. in the 30K shield, leaving only the molecular beam exit aperture. The 30K exit aperture is a 1” hole in [chapter 5](#) and in [Ref. \[73\]](#). In [chapter 8](#) and in [Ref. \[246\]](#), this 1” hole is replaced with a home-made skimmer (6.35 mm diameter) followed by a short differential pumping tube ( $\sim 19$  mm long and 12.7 mm diameter). Following the work in [chapter 8](#), the 30K exit aperture is further revised, and the current exit aperture is a 2.75” long 7.35 mm diameter differential pumping tube. We measure that taping the holes in the 30K shield and putting in place the current long differential pumping tube reduces the total He gas load on the room temperature pumps by a factor of  $\approx 5\times$  relative to the short differential pumping tube described in [chapter 8](#). We also replace the two small turbopumps (Pfeiffer, TMU 071 P, 55 L/s He) used in [chapter 8](#) with a single larger turbopump (Pfeiffer, HiPace 700, 655 L/s He) and increase the conductance to the single large turbopump by increasing the cross sectional area of the beam propagation region (from a  $\approx 3.8$ ” ID circular tube to a square tube with inner side length of 5.5”). We measure that the larger turbopump and increased conductance decreases  $P_{\text{He}}$  by a factor  $\approx 6\times$ . At present,  $P_{\text{BG}} \approx 9 \times 10^{-9}$  Torr while  $P_{\text{He}} \approx 3 \times 10^{-8}$  Torr for  $\mathcal{F} = 5$  sccm in the beam propagation region. In total, the changes described in this paragraph reduce  $P_{\text{He}}$  in the beam propagation region by  $\gtrsim 30\times$  (for equal values of  $\mathcal{F}$ ) relative to [chapter 8](#) and by an even greater amount relative to [chapter 5](#).

The UHV region is separated from the beam propagation region by a differential pumping tube (5” long, 12.7 mm diameter, OFHC copper). The UHV region is pumped on by a large turbopump (Pfeiffer, HiPace 700, 655 L/s He). In the UHV region,  $P_{\text{BG}} \approx 4 \times 10^{-10}$  Torr and  $P_{\text{He}} \approx 1.75 \times 10^{-9}$  Torr for  $\mathcal{F} = 5$  sccm. Calculations indicate that the gas load from ballistic helium is  $\sim 3\times$  that from diffuse helium in the UHV region. Further reduction of  $P_{\text{He}}$  in the UHV region would likely require decreasing the ballistic helium gas load by decreasing the diameter of the differential pumping tube between the UHV and beam propagation regions.<sup>7</sup> A pump with a higher pumping speed could also be placed in the chamber of interest, but given the large turbopump already present, a larger pump

<sup>7</sup>For ease of aligning apertures, smaller diameters for this differential pumping tube are undesirable. All apertures in the system are aligned with a theodolite (Topcon, DT-209), used industrially in surveying.

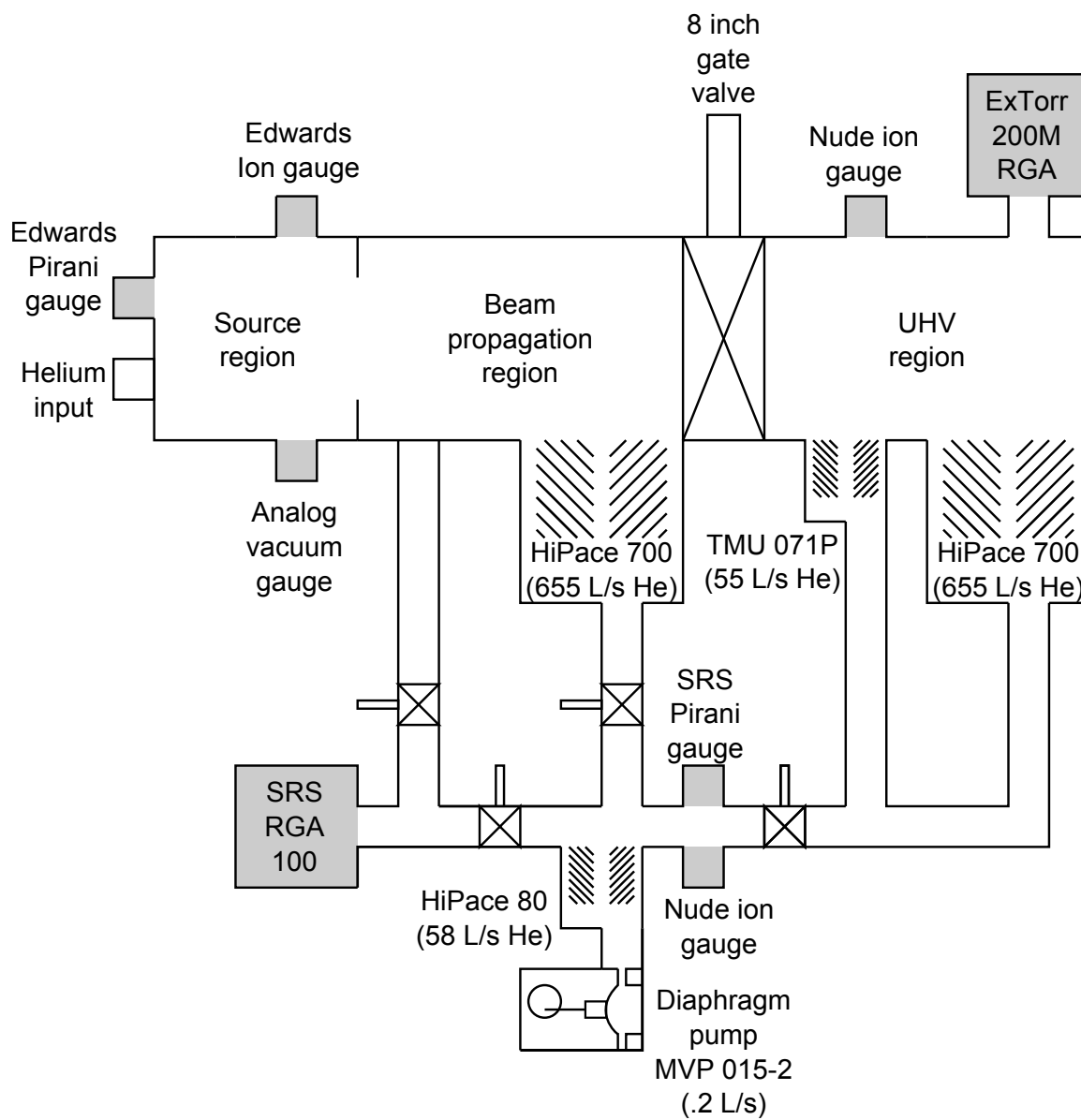


Figure 9.5: Vacuum setup of the current SrF laser cooling experiment.

is not entirely realistic. (The average gas load on the UHV region could also be reduced by placing a shutter before this region [273] or by implementing a pulsed He source.)

Because the compression ratio of all turbopumps in the experiment is  $\sim 10^7$  for He, turbopumps attached directly to the main experimental regions are backed by a single pumping station (Pfeiffer, HiCube Eco) consisting of a turbopump (Pfeiffer, HiPace 80) backed by a diaphragm pump (Pfeiffer, MVP 015-2) as shown in Fig. 9.5. This ensures that  $P_{k,\text{He}}$  is limited by  $S_{k,\text{He}}$  and not by compression ratio for all regions  $k$  at 293 K.<sup>8</sup> Although pump-down time is limited by the slow diaphragm pump and other factors<sup>9</sup> to  $\gtrsim 15$  minutes, the system is oil-free, quiet and low maintenance. This is deemed an acceptable trade-off.

A residual gas analyzer (RGA) (Stanford Research Systems, RGA-100) positioned between two valves, as shown in Fig. 9.5, allows connection to either the beam propagation region or to the pumping station for use in leak checking. Connecting the RGA to the pumping station is particularly effective for leak checking with He; all He entering the apparatus will eventually pass through the pumping station. This makes leak checking with the RGA in this position roughly an order of magnitude more sensitive than with the RGA connected to the main vacuum region. (A good indication of the presence of a leak somewhere in the system is that  $P_{N_2} \approx 4P_{O_2}$ ; He can then be used to locate the leak on the apparatus.)

An analog vacuum gauge is useful to monitor the pressure of the source region when He is desorbed since the Pirani gauges cannot read He above a few Torr. Nude ion gauges are Varian 971-5007 or equivalent with dual  $\text{ThO}_2/\text{Ir}$  filaments. The UHV region is also equipped with an RGA (ExTorr, 200M).

## 9.4 Simultaneous cooling and slowing

Having demonstrated transverse cooling [206] and longitudinal slowing [246] separately, a natural approach is to combine both to increase the downstream flux of slow molecules. However, this method poses more difficulty than might be expected.

---

<sup>8</sup>It is important that pressure not be limited by the conductance between the primary turbopumps and the pumping station which backs the primary turbopumps. We ensure this is the case by using bellows with the necessary diameter to connect the primary turbopumps and the pumping station.

<sup>9</sup>The purposely low conductance from inside to outside the 30K shield extends the pump-down time by  $>2\times$ .

### 9.4.1 Experimental apparatus

Whereas in [chapter 7](#) the molecular beam is apertured and collimated by a  $1.5 \text{ mm} \times 1.5 \text{ mm}$  slit, in this chapter we wish to maximize the number of slow molecules delivered to the MOT region and thus wish to cool all molecules emerging from a 7.35 mm diameter tube. (See [section 9.3](#).) The enlarged diameter roughly doubles the maximum perpendicular velocity  $v_{\perp}$  versus that in [chapter 7](#). Hence, relative to our previous work in [chapter 7](#), we wish to achieve the same cooling over a larger area and for larger transverse velocities. Because the available laser power is roughly the same as before, our solution uses a longer transverse cooling region. Ultimately, we use 360 mm long mirrors (Casix, custom) and 400 mm long Brewster windows of 10-5 scratch-dig BK7 (Casix, custom). These mirrors are  $\approx 2.5\times$  longer than those used in [chapter 7](#). Due to vacuum considerations, the spacing between the mirrors is about 16", approximately  $2\times$  that in [chapter 7](#). The  $\lambda_{00}^t$  laser passes through the cooling region  $\approx 60$  times ( $\approx 30$  reflections from each mirror), giving a total path length of  $\approx 25 \text{ m}$ .

Given the long path length, mirror stability is critical. For protection, each mirror is encased in an aluminum holder mounted on a large gimbal mirror mount (Newport, SL15ABM) which provides good short- and long-term pointing stability as shown in [Fig. 9.6](#). The transverse cooling mirrors generally do not require daily adjustment. The stability requirements for the transverse cooling mirrors are not dissimilar to that of a flat-flat Fabry-Pérot with finesse equal to the number of round trip passes.

Stress-induced birefringence both from internal stresses and from atmospheric pressure leads to polarization rotation during the large number of passes. As the laser bounces back and forth through the Brewster windows between the mirrors, the polarization is rotated ( $\sim 5^\circ$  per pass). At certain locations the polarization is optimal for transmission through the Brewster windows whereas elsewhere the polarization is optimal for reflection ( $\approx 20\%$ ), and therefore much laser intensity is needlessly lost. Further, atmospheric pressure causes the glass Brewster windows to bow, leading to displacement of the laser beam,<sup>10</sup> particularly near the beginning and ends of the Brewster windows. Future approaches, if any, will likely employ AR-coated windows instead. AR-coated windows allow for various  $\lambda_{00}^t$  laser polarizations as would be required for 2-D magneto-optic compression [[120](#)].

A single  $\lambda_{00}^t$  laser is applied transverse to the molecular beam as in [chapter 8](#), and the  $\lambda_{00}^s, \lambda_{10}^s$ , and  $\lambda_{20}^s$  lasers are applied counter-propagating to the molecular beam but with the sideband profiles described in [section 9.2](#). This approach assumes the  $\lambda_{10}^s$  and  $\lambda_{21}^s$  lasers are sufficient for repumping

---

<sup>10</sup>Pointing however is not affected by this issue.

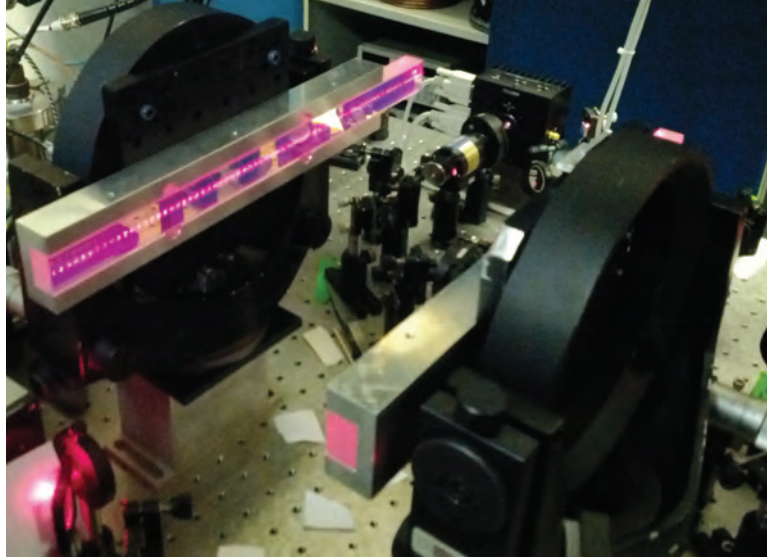


Figure 9.6: Example mounting of 360 mm long transverse cooling mirrors. Shown here for  $\gtrsim 120$  passes (60 reflections off each mirror) with a small laser beam. In the actual experiment, the laser beam is expanded by a 4:1 telescope and there are fewer reflections as a result. The unanodized aluminum pieces are later extended to protect the entire length of the transverse cooling mirrors.

and the  $\lambda_{10}^t$  and  $\lambda_{21}^t$  lasers are therefore unnecessary, greatly simplifying this setup. Since little force is derived from the repump lasers directly, elimination of the  $\lambda_{10}^t$  and  $\lambda_{21}^t$  lasers is valid.

When the  $\lambda_{00}^t$  laser is applied in 1-D (with the  $\lambda_{10}^s$  and  $\lambda_{21}^s$  lasers but not the  $\lambda_{00}^s$  laser), the addition of a 300-mm-focal-length cylindrical lens placed immediately prior to the  $\lambda_{00}^t$  laser bouncing back and forth between the transverse cooling mirrors increases the downstream flux of unslowed molecules by  $\sim 30\%$  relative to the flux of transversely cooled unslowed molecules without using the cylindrical lens. We speculate that this lens helps to fill in the spatial gaps between the retro-reflected laser beams. The increased angular spread of the transverse cooling light, perhaps surprisingly, does not appear to be a problem.

#### 9.4.2 Experimental results

Both cooling and slowing methods employed here depend on scattering photons. Because the maximum spontaneous scattering rate of SrF is fixed at  $S_{sc}^{\max} = \frac{\Gamma}{7}$ , slowing and cooling forces compete if either is sufficient to achieve  $S_{sc} \sim S_{sc}^{\max}$  alone. This effect is seen in our own data for simultaneous longitudinal slowing and 1-D transverse cooling shown in 9.7 and in Ref. [120] for two-dimensional (2-D) transverse cooling.

Hence, when simultaneously applying longitudinal slowing and 2-D transverse cooling, the cooling

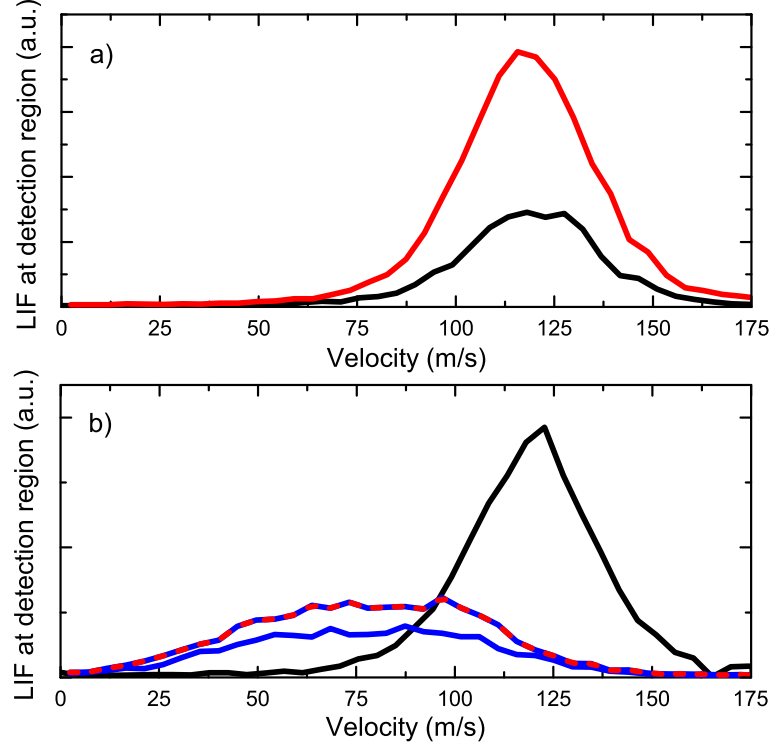


Figure 9.7: Simultaneous transverse cooling and longitudinal slowing. For this data, we use a 1-D transverse cooling region of length  $\approx 36$  cm (that begins  $\approx 14$  cm from the beam source and uses  $\approx 60$  passes of the transverse cooling laser beams to nearly fill the region) and detect the velocity profile downstream at  $L_d = 1.1$  m. Control velocity distributions with no slowing or cooling are as shown (—). (a) Applying one-dimensional transverse cooling near the source (—) increases the number of molecules detected at  $z = L_d$  by  $\approx 2.6\times$  versus the control profile. This is in fair agreement with a Monte Carlo simulation (similar to that described in Refs. [73, 206]), which predicts the increase in number due to the transverse cooling to be  $\approx 3.6\times$  for this geometry. (b) Relative to the profile achieved using longitudinal slowing alone (—), adding the same 1-D transverse cooling simultaneously (—) merely increases the number of molecules at the detection region by  $\approx 1.4\times$ . The decrease in gain from transverse cooling in the presence of longitudinal slowing is attributed to competition for spontaneous photon scattering between the transverse and longitudinal lasers.

rate in each transverse direction will be  $\leq 1/3$  of the maximum rate for 1-D cooling alone.<sup>11</sup> In addition, the slowing will proceed at less than the maximum rate while the transverse cooling is applied, requiring an increase in the slowing distance  $L$ . Overall, it appears difficult to obtain a very large increase in useful slow flux simply by adding transverse laser cooling without extending the total length. However, note that transverse cooling would again become extremely useful if it could be applied to molecules that already have been slowed and which were transversely confined during the slowing. In this case, the reduced forward velocity results in a longer interaction time for a given interaction distance, meaning that transverse cooling to sufficiently low temperature for delivery to the trap volume could be done with a realistic size of the cooling region.

The above discussion applies to radiative Doppler forces only. In [chapter 7](#) the  $\lambda_{00}^t$  laser alone provides both the spatially varying potential and the optical excitation, both of which are necessary for Sisyphus cooling. However, we speculate that this need not be the case. For example, the molecular beam could be radiatively slowed and transversely cooled simultaneously by an intense blue-detuned laser whose only function is to create a spatially varying potential. Presumably due to the larger  $\lambda_{00}^t$  laser beam diameters ( $\frac{1}{e^2}$  intensity full width  $\approx 9$  mm) necessary to cool the spatially larger molecular beam relative to that in [chapter 7](#), we did not observe Sisyphus cooling with the above setup, as expected from [Fig. 7.6](#). However, we observed a possibly similar effect for large ( $\sim 200$  MHz) blue detunings of the  $\lambda_{00}^t$  laser from resonance, but only in the presence of the slowing laser. This effect is shown in [Fig. 9.8](#). Preliminary results show that the effect is diminished for lower-velocity molecules, and thus this behavior has not yet been investigated. One possible issue with radiative slowing and simultaneous transverse Sisyphus cooling is that Sisyphus cooling requires a lower remixing rate, and hence smaller  $B$ -fields, than radiative slowing (or Doppler cooling). We believe that by careful  $B$ -field orientation and choice of laser polarizations, the conditions required optimal Sisyphus cooling in both transverse dimensions and radiative slowing and can be achieved simultaneously.

## 9.5 MOT detection

We attempted a number of methods for MOT detection which are discussed here. The minimum number of molecules that must be trapped in order to allow detection is an important figure of merit for the various detection schemes.

---

<sup>11</sup>This assumes that  $S_{sc}$  from the slowing lasers alone is equal to or greater than  $S_{sc}$  of the transverse cooling lasers, which is generally true for our experiment.



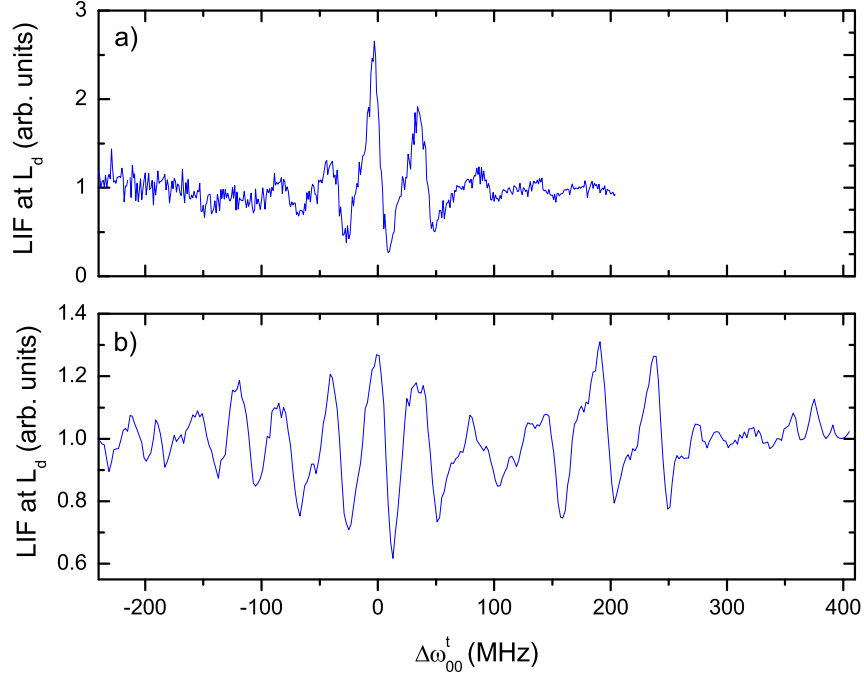


Figure 9.8: Possibility for Siyphus-type cooling combined with radiative slowing. In (a) we record LIF at  $L_d = 1.1$  m for molecules with  $v_{\parallel} \sim 125$  m/s and vary  $\Delta\omega_{00}^t$  with no slowing applied. When  $\Delta\omega_{00}^t \sim -\Gamma$ , we see the LIF at  $L_d$  increase by  $\sim 2.6\times$ , consistent with data from Fig. 9.7. In (b) we record LIF at  $L_d$  for molecules with  $v_{\parallel} \sim 75$  m/s ( $\approx$  the modal forward velocity for the slowed beam at  $L_d$ ) with radiative slowing applied and vary  $\Delta\omega_{00}^t$ . In addition to observing an increase in LIF at  $L_d$  for  $v_{\parallel} \sim 75$  m/s molecules when  $\Delta\omega_{00}^t \sim -\Gamma$ , we also observe increased LIF when  $\Delta\omega_{00}^t \approx 190$  MHz or  $\Delta\omega_{00}^t \approx 240$  MHz. Note the difference in the LIF axis scales for the two panels. The  $\sim 40$  MHz periodicity observed in both panels is due to the interaction of the four  $\lambda_{00}^t$  frequencies with the four SR/HF manifolds. (See Fig. 7.3.) Plots are normalized to 1 at the given velocity in the absence of the  $\lambda_{00}^t$  laser. Unless otherwise specified, the experimental setup for the data here is the same as for Fig. 9.7.

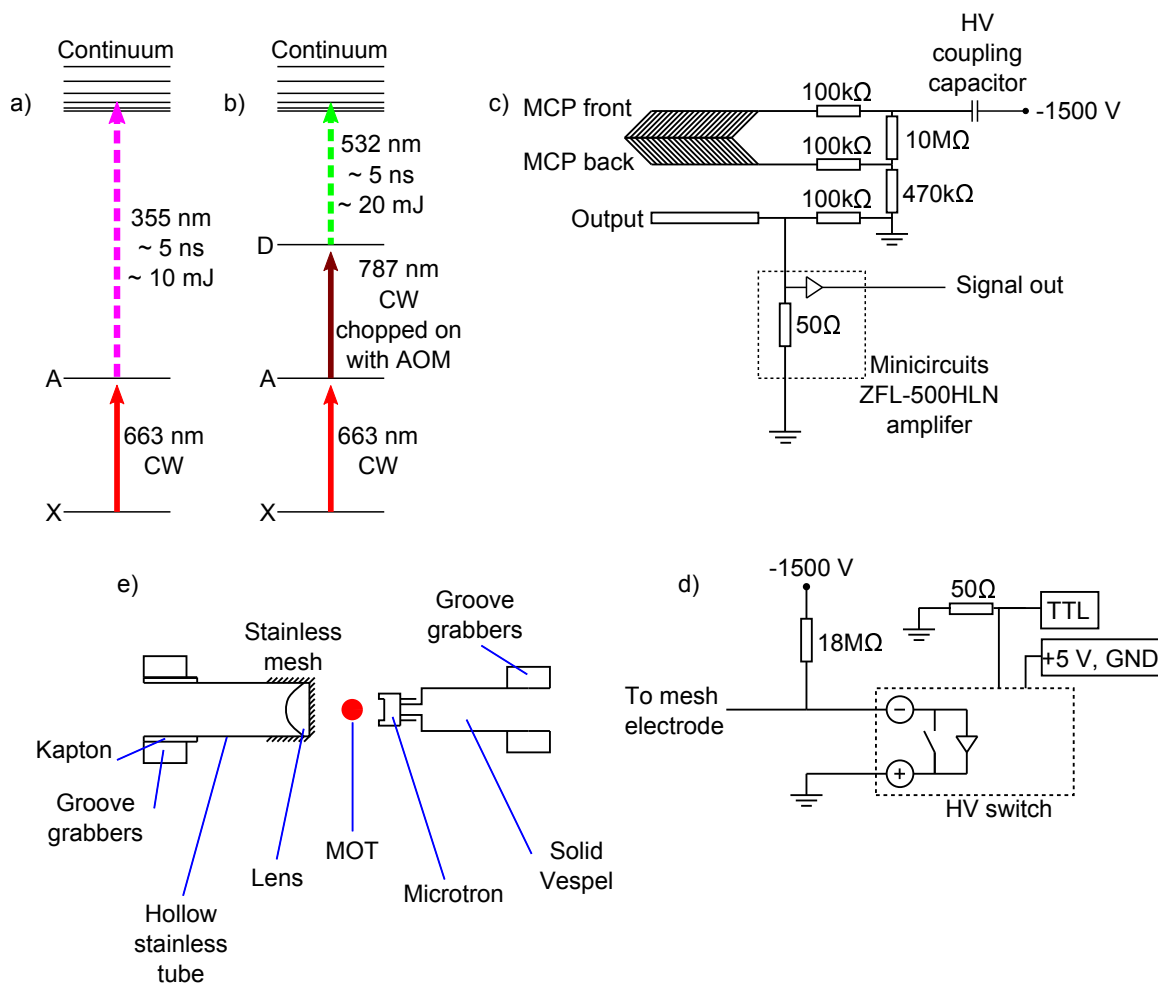


Figure 9.9: Diagram for REMPI detection as described in the main text.

### 9.5.1 Ion detection

The original plan for MOT detection employed resonantly enhanced multiphoton ionization (REMPI) and an ion detector (Photonis USA Inc., Microtron detector, 30042).<sup>12</sup> REMPI can detect single molecules and does not suffer from background scattered light. Molecules in the MOT cycling on the  $X \rightarrow A$  transition would be excited from A to the continuum via a  $\sim 10$  mJ pulse of 355 nm light as shown in Fig. 9.9a.

Mounting of the Microtron was tricky, and one Microtron was broken in the process. Ultimately the leads were spot welded to 22 AWG Kapton-coated copper wire (Accuglass Inc, 100680) and attached to a Vespel rod mounted inside the MOT region using groove grabbers (Kimball Physics,

<sup>12</sup>Compared to other microchannel plates (MCPs), this product is cheap (\$1150) and small (.56" OD). Unlike most MCPs, the Microtron is supposedly not susceptible to water damage, although Photonis suggests storage at  $10^{-4}$  Torr or better anyway. Calculations suggest the low-gain chevron model is more than sufficient to detect single ions. This is confirmed experimentally.

MCF275-GrvGrb-CYL1000) as shown in Fig. 9.9e. Due to concerns about gating high voltage to the Microtron directly, the Microtron was always biased to negative high voltage (-1.5kV to -2kV) as shown in Fig. 9.9c. Because a DC electric field will cause decays to states of the wrong parity during cycling, an opposing electrode was held at a negative high voltage in order to null the electric field in the MOT region. Immediately prior to the 355 nm pulse, this electrode was grounded using a high voltage switch (Williamette High Voltage, MHVSW-005V) and the circuit shown in Fig. 9.9d. The opposing electrode was stainless steel mesh (TWP Inc, 100X100T0011W48T) with 88% transparency and was positioned over a lens which allowed for backup optical detection of the MOT using a camera. (See subsection 9.5.2.) The Microtron signal exited the vacuum chamber through a UHV feedthrough and was immediately amplified (Minicircuits, ZFL-500HLN) with no intervening cables. We found the ion gauge in the MOT region created ions which were useful to test the Microtron without the molecular beam. The Microtron output signal displayed significant reflections. We speculate this occurred due to the non-50 $\Omega$  impedance of the UHV feedthrough or because the in-vacuum wiring did not use 50 $\Omega$  coaxial cable. Further, the lack of in-vacuum coaxial shielding caused the Microtron output signal to display large voltage spikes when the opposing electrode was grounded.

When ionizing molecules using the scheme shown in Fig. 9.9a, we detected large signals with a time-of-flight consistent with SrF's mass of 107 amu. Such signals occurred even in the absence of the X $\rightarrow$ A excitation laser. We speculate that this background arises from the 355 nm laser breaking apart large molecules present in the beam, some fraction of which produces SrF ions. Because the MOT should persist long after the molecular beam pulse has subsided, the above alone was not enough to warrant abandoning this approach. However, we also determined that the presence of the X $\rightarrow$ A laser did not create any additional signal during application of the 355 nm pulsed light. At the time, we could not say why the 663+355 REMPI approach failed with any certainty. We hypothesized that either the SrF was predissociating or that the published value of the  $5.21 \pm .06$  eV for the SrF ionization energy was wrong [274]. Both appeared unlikely.

Subsequently, we attempted the three photon REMPI detection scheme shown in Fig. 9.9b to isolate Microtron problems from ionization problems. Molecules in the molecular beam were continuously excited at a given point in front of the Microtron from X to A using 663 nm CW light. Another laser driving the A $\rightarrow$ D transition at 787 nm was then chopped on using an AOM and followed by a 532 nm pulse of  $\sim 20$  mJ. This 663+787+532 REMPI detection required both the X $\rightarrow$ A laser and the A $\rightarrow$ D laser to be resonant to achieve a signal. In contrast to the 663+355

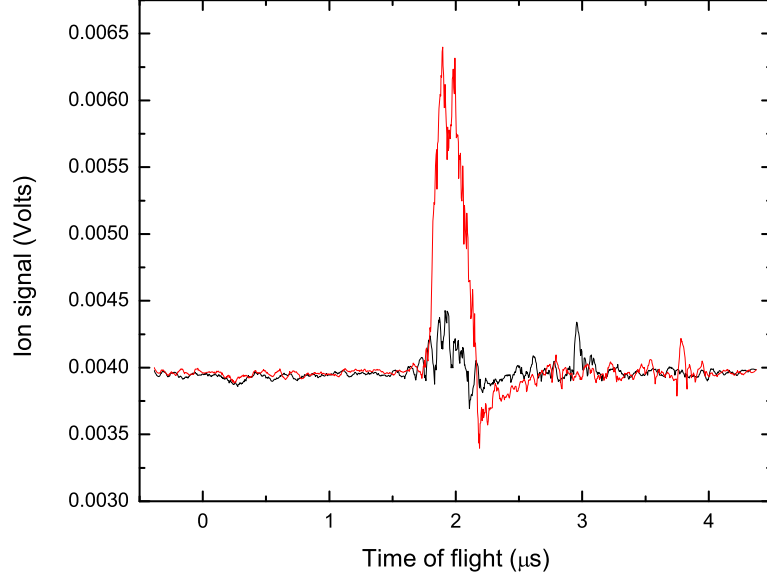


Figure 9.10: Three photon REMPI signal from the molecular beam. The signal with the SrF beam present (—) corresponds to about 10 ions detected while the signal with the SrF beam absent (—) shows the background ion signal which corresponds to a single ion on average.

REMPI detection, the background signal from non-resonant ionization of SrF or anything else was extremely small using this 663+787+532 REMPI detection and averaged less than 1 molecule per pulse as shown in Fig. 9.10. We detected  $\sim 10$  SrF ions per pulse with this inefficient method, far less than the  $\sim 300$  ions expected or the  $\sim 4000$  molecules hit by the 532 nm pulsed light. Subsequent investigation showed that the 787 nm laser intensity of  $\sim 100$  mW applied over  $\sim 10$  mm<sup>2</sup> was inadequate to saturate, which may explain the small signal of SrF ions. Although ion detection was abandoned in favor of alternative detection methods, it offered certain insight into the experiment; we observed no ions in the MOT region due to ablation alone, encouraging since stray electric fields cause loss from our cycling transition.<sup>13</sup> We also learned that fast switching of high voltages is to be avoided if possible.

	Belyaev <i>et al.</i> [274]	Jakebek <i>et al.</i> [275]
CaF	$5.51 \pm .07$	$5.8270 \pm .0006$
SrF	$5.21 \pm .06$	
BaF	$4.59 \pm .06$	$4.8034 \pm .0004$

Table 9.1: Reported values of ionization energies for CaF, SrF and BaF in eV. The discrepancy between the two sources for CaF and BaF, when combined with the results outlined in the main text, suggest the SrF ionization energy listed in Ref. [274] is too low by  $> .15$  eV. A 663, 787, and 532 nm photon correspond to 5.61 eV while a 663 and a 355 nm photon correspond to 5.36 eV.

<sup>13</sup>An ion signal due to ions created during ablation in the cell making it to the MOT region would be discouraging since accumulation of these ions on non-conductive surfaces might cause stray electric fields in the MOT region.

Later, we noticed data (summarized in Table 9.1) which suggest that the published value of  $5.21 \pm .06$  eV for the SrF ionization energy [274] is likely too low. This is consistent with the failure of the 663+355 REMPI and the success of the 663+787+532 REMPI. Based on these two data points, we can say that

$$5.36 \text{ eV} < E_{\text{ionize}}^{\text{SrF}} < 5.61 \text{ eV}, \quad (9.13)$$

where  $E_{\text{ionize}}^{\text{SrF}}$  is the ionization energy for SrF.

### 9.5.2 Blue detection

MOT detection can conceivably be done with LIF at 360 nm, similar to the detection scheme employed in chapter 8. Advantages of this detection method are zero background from scattered light and zero read noise assuming use of an ICCD camera bought for another purpose (Princeton Instruments, PIMAX2 with Filmless Gen III Unigen 2 intensifier) or a PMT. However, the sensitivity of this method is low, since each molecule emits only a single blue photon during detection. For example, given a geometric collection efficiency of  $\eta_{\text{geo}} = 1\%$ , a quantum efficiency of  $\eta_{\text{qe}} = 8\%$  at 360 nm and the small but non-negligible noise sources (dark counts from the photocathode on an ICCD or dark counts and spurious noise on an EMCCD), sensitivities are likely limited to MOTs with  $\gtrsim 1000$  molecules or more. This method was investigated but abandoned due to low sensitivity.

### 9.5.3 Current detection

Current detection uses spontaneous LIF from the  $X \rightarrow A$  cycling transition at 663 nm to detect the presence of a MOT. Since the sensitivity of imaging LIF from the  $X \rightarrow A$  transition is likely to be limited by scattered laser light from the MOT lasers, it is not obvious that this approach can improve on the blue detection sensitivity (e.g. be sensitive to  $\lesssim 1000$  molecules) since the amount of scattered light is, in our experience, hard to predict. A MOT of 1000 molecules scattering spontaneous photons at  $S_{\text{sc}} = 3 \times 10^6 \text{ s}^{-1}$  will result in an ideal detector recording  $9 \times 10^4$  photons assuming  $\eta_{\text{geo}} = 1\%$  and an integration time of 30 ms. Alternatively, 300 mW of 663 nm light corresponds to  $\approx 10^{18}$  photons/second. If  $3 \times 10^{-11}$  of this MOT light inadvertently scatters into the detector, the number of signal photons will equal the number of background photons. Given less than ideal surface qualities, dust, and other imperfections on windows, waveplates, and mirrors, stray light is practically unavoidable.

It is not useful, however, to minimize scattered light to a level far below that of other noise

sources. On a CCD with quantum efficiency  $\eta_{\text{qe}}$ , electron readout noise  $N_r$  (RMS  $e^-/\text{pixel}$ ), and dark current  $D$  ( $e^-/\text{pixel}/\text{second}$ ), the signal to noise ratio (SNR) after an observation time  $t$  for  $M_{\text{bin}}$  pixels that have been binned together is given by Ref. [276]

$$\text{SNR} = \frac{M_{\text{bin}} P_{\text{sig}} \eta_{\text{qe}} t}{\sqrt{M_{\text{bin}} (P_{\text{sig}} + B_{\text{sl}}) \eta_{\text{qe}} t + M_{\text{bin}} D t + N_r^2}}, \quad (9.14)$$

where  $P_{\text{sig}}$  is the incident signal photon flux (photons/pixel/second) and  $B_{\text{sl}}$  is the incident background flux (photons/pixel/second) due to stray/scattered light. The value of  $P_{\text{sig}}$  is given by

$$P_{\text{sig}} = N_{\text{MOT}} \times \eta_{\text{geo}} \times S_{\text{sc}} \times \eta_{\text{trans}}, \quad (9.15)$$

where  $N_{\text{MOT}}$  is the number of molecules in the MOT and  $\eta_{\text{trans}}$  accounts for small losses due to reflections, absorption etc., of the optical elements. We measure  $\eta_{\text{trans}} \approx .84$ . We also expect roughly that  $B_{\text{sl}} \propto \eta_{\text{geo}}$ , which applies exactly if the scattered light is uniformly distributed. To increase the SNR, we integrate only over pixels inside a certain region of interest (ROI) where we expect the MOT. Conceptually, this method of MOT detection can be thought of as roughly equivalent to using a PMT and spatial filter to eliminate background scattered light. The values of  $N_r$  and  $D$  in Eqn. 9.14 are camera-dependent and can be solved by buying a better camera. (We do not use the ICCD due to risk of damage.<sup>14</sup>) For a state of the art EMCCD (Andor iXon Ultra 897,  $\sim \$41\text{k}$ ) cooled to  $-100^\circ\text{C}$ , the read noise is effectively zero and the dark current + spurious background is  $\sim .002 e^-/\text{pixel}/\text{s}$ . We show we can obtain similar sensitivities using a much cheaper camera, the Apogee Ascent A285 ( $\sim \$3200$ ), which is typically used for astronomy applications. The A285 is cooled via a single-stage TEC to  $\sim -15^\circ\text{C}$  and offers reasonably low dark current ( $D = .007 e^-/\text{pixel}/\text{s}$  at  $-9^\circ\text{C}$  from the camera test datasheet provided by the manufacturer). The camera read noise ( $N_r = 4.5 e^-$  RMS) can effectively be made arbitrarily small (for our purposes) by hardware binning up to  $M_{\text{bin}}^{\text{max}} = 10 \times 1024 = 10240$  pixels together. Hardware binning on this scale is not typical for current scientific CCDs. Such binning comes at the expense of image pixelation but, given the integration method over the ROI, is a desirable trade-off. The value of  $M_{\text{bin}}$  is typically set so that the SNR is

---

<sup>14</sup>Unlike EMCCDs, ICCDs (including the PIMAX2) can be permanently damaged by overexposure even to small levels of light. Hence, lasers present a serious danger to the ICCD. For detection in the blue with excitation lasers at 663 nm and 787 nm, filters to eliminate background light from the lasers will also protect the camera. However, for MOT imaging using LIF from the main cycling laser with hundreds of mW of 663 nm light, filters cannot be used to protect the camera, making such an approach risky. It is worth noting that EMCCDs have surpassed or are comparable to ICCDs in performance for all but a small number of niche applications. One notable exception is that ICCDs can be gated on/off or even chopped with a time resolution  $\lesssim 500$  ps. EMCCDs however are not susceptible from damage from excess light exposure.

almost entirely limited by the value of  $B_{\text{sl}}$ . Currently, a value of  $M_{\text{bin}} = 10 \times 10 = 100$  yields values of  $\text{SNR} \approx 80\%$  of that achieved with  $M_{\text{bin}} = M_{\text{bin}}^{\text{max}}$  and produces images of  $104 \times 139$  pixels, fine for our purposes. With the above detection method and camera, the SNR should be limited entirely by scattered light for the foreseeable future.<sup>15</sup> Several steps are taken to minimize the scattered light. (See subsection 9.5.5.)

#### 9.5.4 Light collection

If detection sensitivity is limited by scattered light, the SNR will vary as  $\sqrt{\eta_{\text{geo}}}$ , since the noise due to scattered light grows as the square root of the scattered light collected. (See Eqns. 9.14 and 9.15.) LIF is collected from a single 2.75" conflat viewport. The collection optics consist of a 150-mm-focal-length spherical-singlet lens (flat side facing experiment) followed by a large camera lens (Senko, 50mm F/0.95) as shown in Fig. 9.11. The spherical singlet approximately collimates the LIF since the minimum focal length of the camera lens is 600 mm. This camera lens is selected to collect as much light as possible while also imaging the MOT LIF on as few pixels as possible, thereby reducing read noise and dark current noise. Behind the camera lens is a single interference filter (Semrock, FF01-650/60, 24 mm diameter) chosen to maximize transmission of 663 nm light while blocking repump light at 685 nm for all geometrically relevant angles of incidence (AOI).

We measure  $\eta_{\text{geo}}$  of the LIF collection setup in the presence of the interference filter.<sup>16</sup> A MOT "simulant" is created at the appropriate distance from the collection optics by back-illuminating a 1/4" thick piece of white Delrin with 663 nm light. The front surface of the Delrin is covered with aluminum tape except for a 5 mm hole to simulate the MOT. This method gives approximately uniform LIF at 663 nm over the range of angles we are interested in. With the interference filter in, the total number of photons hitting the CCD is measured with all collection optics and again with the interference filter and bare CCD alone. This ratio is then compared to the solid angle subtended by the collection optics versus the CCD sensor alone. Accounting for the transmission of the collection optics at 663 nm (measured  $\approx 90\%$ ) we find  $\eta_{\text{geo}} = 0.82 \times \eta_{\text{geo}}^{\text{max}}$  in the presence of the interference filter where  $\eta_{\text{geo}}^{\text{max}} = 0.0111$  is the geometric collection efficiency in the limit that all light exiting the viewport is incident on the camera CCD. The remaining 18% is presumably

<sup>15</sup>And, depending on when the camera is triggered to begin its exposure, possibly by LIF from non-trapped molecules passing through the MOT region.

<sup>16</sup>Angular effects from the filter must be included in  $\eta_{\text{geo}}$  because the filter transmission depends on the light's AOI. However all other filter loss mechanisms are included in  $\eta_{\text{trans}}$ . Although the angular dependence of the filter transmission can be calculated using standard formulas, I recommend a tool from the Semrock website [277], which will do this for you and can even calculate average transmission for light emitted uniformly over a cone with a user-specified half angle.

blocked by the interference filter whose transmission decreases as the light's AOI is varied from 90 degrees.<sup>17</sup> With this setup, the CCD image is  $M_{\text{mag}} = 0.45\times$  the real image size. The value of  $M_{\text{mag}}$  is measured empirically using a grid of 1-mm-side-length black squares with center-to-center spacing of 2 mm on a white background which is back-illuminated with 663 nm light. This allows  $M_{\text{mag}}$  to be measured in the final experimental configuration, with all filters in place. Calculating  $M_{\text{mag}}$  theoretically proves challenging since the multi-element camera lens cannot be treated as a single thin lens.

### 9.5.5 Scattered light

General methods for reducing scattered light are discussed in [Appendix G](#). However, due to the importance of minimizing scattered light for MOT detection, the specific methods used in the MOT region are discussed here. For LIF detection at 663 nm, background scattered light must be physically blocked or absorbed. We use a process to blacken OFHC copper by growing a dense microstructure of copper(II) oxide (CuO) dendrites on the surface. The procedure is described in [Appendix G](#). This process produces a remarkably black surface that is UHV compatible. These sheets of OFHC copper can be formed prior to blackening to fit over almost any surface that needs to be black inside the vacuum region. We also use aluminum foil coated with a UHV-compatible black coating (Acktar, Spectral Black) in the few instances where the blackened OFHC copper is inconvenient.

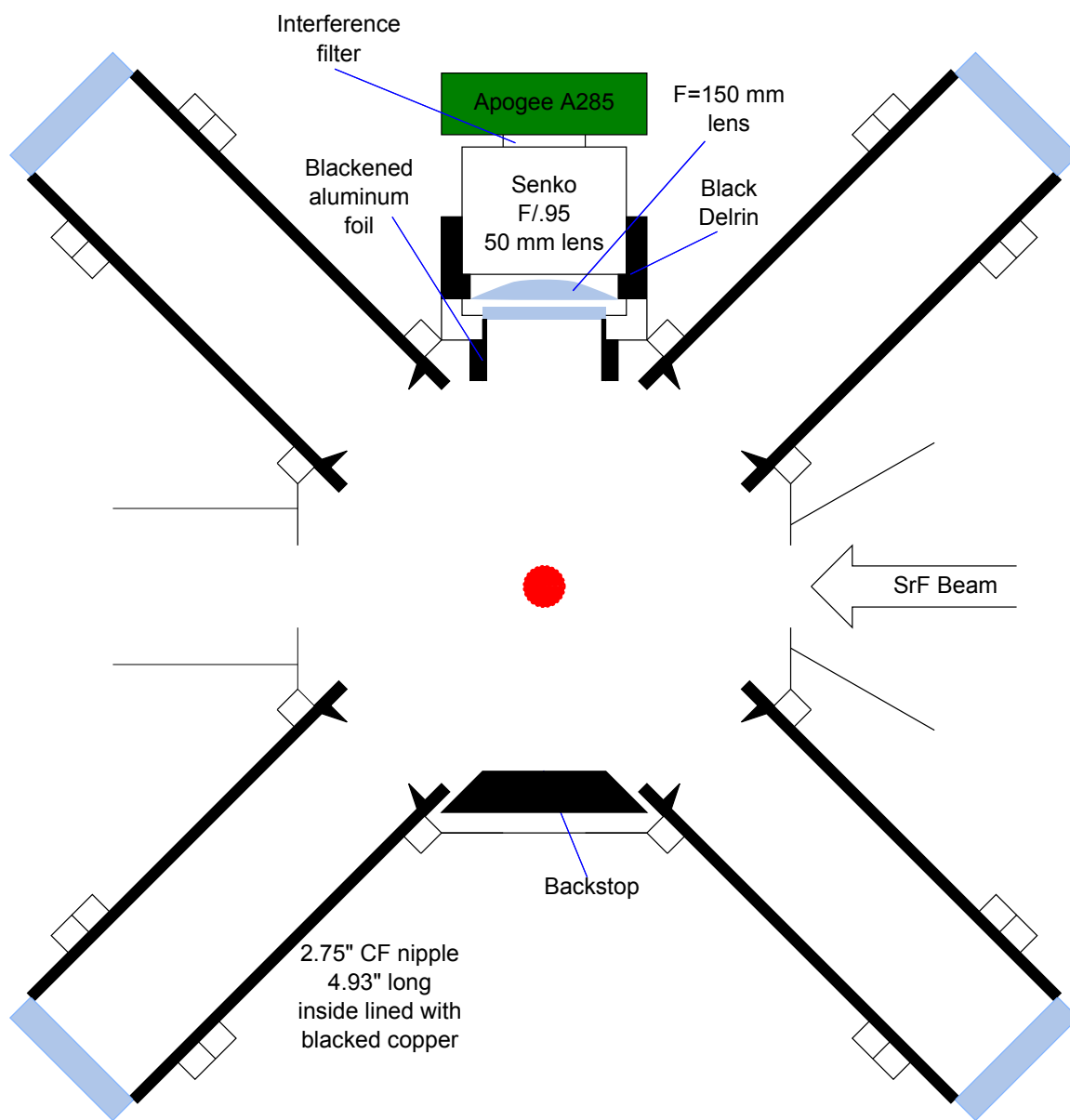
The MOT region was originally designed to use ion detection or blue detection, and therefore no initial design consideration was given to minimizing scattered light. Not only is the MOT chamber (Kimball Physics, MCF600-SphOct-F2C8) electropolished (order unity spectral reflectivity at 663 nm), but the curved walls of the region act as concave mirrors which image diffuse scattered light from certain viewports onto a region either directly behind the MOT or directly onto the viewport where the camera is located.

Figure 9.11 depicts the MOT chamber. MOT windows are 10-5 scratch-dig fused silica windows (CVI, PW1-2037-UV) AR-coated with a V-coating for 663 nm (Thin Film Labs) and epoxied with UHV compatible epoxy (Epotek, 302-3M) onto the KF40 side of a KF40 to 2.75" CF adapter. (See [Appendix H](#).) These windows are offset from the MOT region by 4.93" long nipples (Lesker, FN-0275S) to minimize scattered light from the windows reaching the camera. The inside of the nipples and the adapters are lined with .02" thick blackened OFHC copper. While the OFHC copper

---

<sup>17</sup>Given the unknown and multi-element nature of the camera lens, predicting the angular spread of the light at the camera lens back aperture is difficult. Assuming a worse case scenario in that the back aperture of the camera lens is perfectly sized to pass all the light, we estimate  $\eta_{\text{geo}} = 0.63 \times \eta_{\text{geo}}^{\text{max}}$  including the interference filter.





10-5 scratch-dig AR V-coat for 663 nm  
custom-made windows on a  
KF40 to 2.75" CF adapter

Figure 9.11: Horizontal cross section of the MOT region with an emphasis on methods to reduce scattered light. Surfaces which are shown as thick black lines are covered with blackened OFHC copper unless noted otherwise.

gaskets sealing the 2.75" nipples to the MOT chamber are left unaltered,<sup>18</sup> a blackened OFHC copper “collar” sits inside each uncoated gasket. Each collar has a 26 mm open bore and sharp edges. The MOT is imaged directly in front of a contoured sheet of blackened OFHC copper referred to as the “backstop.” The bottom and top parts of the region are similarly covered in blackened OFHC copper or, sparingly, blackened aluminum foil.

The configuration described above is arrived at iteratively. The general approach to minimizing scattered light is to make changes in a systematic way. Typically, all parts are removed (windows, nipples, apertures, etc.) and sequentially added, and the resultant increase or decrease in scattered light for each part is tabulated. Efforts to reduce scattered light then focus on reducing scattered light from the dominant source. The minimization of scattered light in the MOT region becomes difficult beyond a certain point where scattered light is dominated by an unknown mechanism (speculated to be water, microscopic dust, etc.) which scatters light from the MOT lasers propagating in free space at atmospheric pressure. When scattered light is limited by this mechanism, checking for additional sources of scattered light becomes significantly more time intensive since the region must be pumped out to eliminate this “atmospherically-induced” scattered light. Purging with Ar or N<sub>2</sub> instead of pumping out might partially alleviate this problem but was not tried.

Given the measured values of  $\eta_{\text{geo}} = .82 \times .011 = .009$ ,  $\eta_{\text{trans}} = .84$  and an assumed  $S_{\text{sc}} = 3 \times 10^6 \text{ s}^{-1}$ , we have  $P_{\text{sig}} \approx 23000$  photons/second/molecule divided over the illuminated pixels from Eqn. 9.15. Each pixel is  $6.45 \mu\text{m} \times 6.45 \mu\text{m}$  in size. Assuming the MOT diameter to be 5 mm, the MOT image on the CCD will correspond to  $\approx 95000$  pixels since  $M_{\text{mag}} = .45$ , and hence  $P_{\text{sig}} \approx .24$  photons/pixel/second/molecule. After scattered light minimization, we achieve  $B_{\text{sl}} = 39$  photons/pixel/second with 280 mW total of 663 nm MOT light divided into 3 beams, each of which is retro-reflected. If we use  $M_{\text{bin}} = 10 \times 10 = 100$ ,  $\eta_{\text{qe}} = .53$ , and  $t = 25$  ms, we find from Eqn. 9.14 that a single super-pixel of  $M_{\text{bin}} = 10 \times 10 = 100$  pixels will have a SNR of  $\approx .037$ /molecule. Since the total signal is distributed over  $\approx 950$  super-pixels, integration over a ROI consisting of only these super-pixels will increase the SNR to  $\approx .037 \times \sqrt{950} \approx 1.1$ /molecule.

Because the SNR is primarily limited by the value of  $B_{\text{sl}}$ , this calculation is relatively insensitive to the values of  $\eta_{\text{geo}}$ ,  $\eta_{\text{trans}}$ ,  $\eta_{\text{qe}}$ ,  $B_{\text{sl}}$  and  $t$  (e.g. the SNR varies as the square root of these quantities). It is reasonable to ask whether we can know in advance the MOT size and location. We assume the MOT will be centered near the  $B$ -field zero, which we determine by imaging beam LIF on the  $X \rightarrow A$  transition in the MOT region with large  $B$ -field gradients. Regions of high  $B$ -field exhibit

---

<sup>18</sup>We found empirically that OFHC copper gaskets do not easily seal if they are blackened.

reduced LIF due to the Zeeman shift of the SR/HF sublevels out of resonance. The SrF MOT size is estimated based on the D1 MOT size in Ref. [260]. The most concerning assumption is probably  $S_{\text{sc}} = 3 \times 10^6 \text{ s}^{-1}$ . However, this value is likely only off by a factor of a few [278]. The SNR estimated here neglects background from untrapped molecules passing through the MOT region from the long temporal tail of the molecular beam. This background can likely be eliminated by optically pumping such molecules into non-cycling states immediately upstream of the MOT location. Hopefully the sensitivity of the detection method here will enable us to realize and detect the first 3-D molecular MOT.

## Chapter 10

# Outlook and future directions

In this short chapter we review preliminary ideas for the mid- to far-future. Some focus on increasing the flux of slow molecules delivered to the trapping region while others discuss issues beyond MOT trapping, such as sub-Doppler cooling. Small sections of this chapter are taken from Ref. [134] although new ideas are presented as well.

### 10.1 Non-radiative slowing

The small forces provided by spontaneous photon scattering are particularly inconvenient for slowing, where a large amount of energy ( $\sim 100$  K) must be removed from each molecule to allow for trapping. For forward beam velocities similar to ours ( $\sim 125$  m/s) this can require fairly long slowing lengths  $\gtrsim 1$  meter, which are experimentally inconvenient. This has led to the development and use of slower beam sources even though brightness is vastly reduced [68, 241]. Consequently, alternative methods of slowing are currently being investigated which apply stronger, non-radiative forces for slowing. One approach is to employ a moving optical lattice [62, 279]. Another approach builds on the success of bichromatic force slowing for atoms [280], which is intrinsically attractive and has already been proposed to slow molecules similar to SrF [281]. Non-radiative slowing methods will be covered in Eustace Edward's thesis.

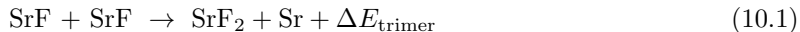
#### 10.1.1 Transverse confinement methods

Employing guiding techniques in conjunction with radiative or other slowing methods should greatly increase the flux of slow molecules delivered to the MOT region. Magnetic guiding [68], electrostatic

guiding [167, 282], and microwave guiding [283] have all been demonstrated for molecular beams. Prior to the SrF experiment discussed in this thesis, we demonstrated guiding of SrO using an electrostatic guide, documented in Ref. [167]. Unfortunately, both magnetic and electrostatic guiding are not inherently compatible with the SrF cycling transition. In both guiding methods, certain ground state sublevels are guided while others are anti-guided, as described in Ref. [134]. Since SrF lacks a “stretched state” cycling transition, molecules would decay to guided and unguided states with equal probability. This shortcoming may be overcome by continuous transfer of molecules to guided states using microwaves or optical pumping but such schemes are likely complex [134]. In contrast, microwave guiding [283] can offer confinement for all  $X^2\Sigma_{1/2}(N = 1)$  states simultaneously, and is therefore compatible with the SrF cycling transition, as detailed in Ref. [134]. In practice, short periods of radiative slowing and microwave guiding would be alternatively applied to the molecules. Stimulated slowing methods would also benefit from microwave confinement. The temporally and spatially long molecular beam could first be loaded into a long microwave guide, after which the guide is turned off and the stimulated slowing applied, followed by continued guiding of the slowed molecules to the trapping region. We fabricated a  $\sim .5$  meter long microwave cavity with an unloaded  $Q \sim 18,000$ , close to the theoretical maximum limited by the resistance of OFHC copper. With 20 Watts of input power, we estimate trap depths of  $\approx 8$  mK, offering confinement for molecules with transverse velocities below  $\approx 1.1$  m/s. The cavity has not yet been tested with a molecular beam. Microwave guiding will be detailed in the thesis of Eustace Edwards.

## 10.2 Collisions and chemical reactions

Thermodynamically, SrF is expected to chemically react with itself even at ultralow temperatures through the reaction [254]



which is barrierless. However this reaction can only occur in the singlet channel, i.e the reaction can only take place on the potential energy surface with total electronic spin  $S = 0$  [254]. Hence, chemical reactions are expected to occur at high rates for unpolarized SrF molecules, but are expected to be suppressed at least to some degree for spin-polarized SrF, which scatter primarily on the triplet surface [254]. Spin-rotation couplings however will prevent total suppression of these chemical reactions [284] and thus the outlook for evaporative cooling of SrF remains uncertain.

### 10.3 Leaky MOT

Using only three lasers, the trap lifetime of an SrF MOT should be on the order 30 ms, limited by one of the loss mechanisms discussed in [section 3.5](#). This lifetime may possibly be extended by additional repump lasers (to lessen vibrational branching), using microwave remixing (decays to states of opposite parity do not automatically result in molecule loss), or other methods depending on the principal loss mechanism. (See [section 3.5](#).) However, transfer of molecules to an auxiliary trap is likely to be necessary for experiments requiring observation times  $\gtrsim 1$  s or rovibrational ground state molecules. The molecules could be transferred in place to a magnetic trap, a microwave trap [[167](#), [203](#)], or an electrostatic trap [[285](#)]. Cold SrF molecules could also be transported using a magnetic transport scheme [[286](#)] to a science chamber and trapped there. If the molecules are not transported elsewhere, a shutter will likely be required to block ballistic helium incident upon the trapping region. However, there are good reasons to avoid use of physical shutters inside UHV vacuum chambers [[273](#)]. Another interesting idea is to apply a static DC electric field during MOT operation, purposely causing molecule decay to the  $X(v=0, N=0, 2)$  levels, some of which would be trapped by the quadrupole magnetic field. Molecules in untrapped states could be transferred to trapped states using microwaves or optical pumping. Should MOT operation prove hard, the slow molecular beam could be loaded into a deep magnetic trap [[287](#)] or a microwave trap using dissipative forces [[167](#), [203](#)].

### 10.4 Cooling beyond MOT temperatures

For molecules created from laser cooled atoms, cooling of translational motion is difficult due to the lack of a dissipation mechanism [[79](#)]. Evaporation could conceivably be used [[64](#)], but such molecules are usually created in low numbers, which is problematic given the additional loss during evaporation. Further, many molecular species composed of laser-cooled atoms are chemically reactive, which complicates evaporative cooling. Generally, molecules created from laser-cooled atoms are limited to approximately the translational temperature of the constituent atoms from which they are made. This is a partial reason why quantum degeneracy has not been reached for a heteronuclear molecule composed of two different atomic species. The cooling of SrF is more comparable to that of an atom; by combining non-lossy cooling techniques (both Doppler and sub-Doppler) with further source improvements, large molecular samples with temperatures below the recoil limit can likely be achieved. However, evaporative cooling, used by every atomic BEC to date except for one [[288](#)],

is expected to fail for SrF. Even if chemical reactions can be heavily suppressed by spin polarization [254], “sticky collisions” leading to 3-body losses are expected to create an additional loss mechanism [289].

Based on operation of the D1 MOT for Na [260], we do not expect molecules in an SrF MOT to be particularly cold (we expected temperatures  $\sim 1$  mK) and hence, further cooling will likely be required. One possibility is to employ a Sisyphus cooling scheme similar to that observed in chapter 7. This method has recently been demonstrated for cooling  $^{40}\text{K}$  [290] and  $^7\text{Li}$  [291] atoms using a D1 transition.<sup>1</sup> It is hard to predict whether a uniform magnetic field alone would allow for 3-D Sisyphus cooling in SrF although Refs. [290, 291] achieve such cooling with no applied magnetic field. Alternatively, we could control the remixing of the dark Zeeman sublevels with the bright sublevels using microwave remixing. SrF’s rich structure may allow for further unseen sub-Doppler cooling mechanisms which exploit the rotational or vibrational degrees of freedom in addition to utilizing the optical cycling transition. One similar example is the optoelectrical cooling in Ref. [79] which uses a (quasi-closed) vibrational transition.

## 10.5 Trapped fluorine

The production of trapped, cold halogen atoms remains a daunting task in atomic physics. In particular, laser cooling of fluorine appears nearly impossible with current technology since the lowest electric-dipole spin-allowed transition in fluorine ( $2p^4\ ^2P_{3/2} \rightarrow 3s^2P_{3/2}$ ) requires an  $\approx 96$  nm laser, prohibitively short for current CW laser technology [292]. Laser cooling from a metastable transition also appears unlikely [293]. Further, fluorine is experimentally difficult because it reacts even with glass and other UHV materials due to its large electronegativity. Hence, dissociation of trapped ultracold SrF may provide a realistic route to obtaining trapped samples of ultracold fluorine. Efficient population transfer to the dissociated state may be complicated by SrF’s diagonal FCFs [292]. The notion of laser cooling a molecule to obtain trapped atoms may appear convoluted, but offers the possibility to trap atoms which are not amenable to laser cooling themselves with current technology. Although outside the likely direction of this experiment, direct laser cooling of molecules to obtain trapped oxides [120] and carbides [294] appears viable as well.

---

<sup>1</sup>The closely spaced HF structure of the excited state of the  $^{40}\text{K}$  and  $^7\text{Li}$  D2 transitions greatly reduces the effectiveness of polarization gradient cooling [263] for these species.

## Appendix A

# Franck-Condon factors



## A.1 Details of FCF calculation

As stated in the main text, the calculation of the FCFs for the  $A^2\Pi_{1/2} \rightarrow X^2\Sigma_{1/2}$  transition employs the suite of programs developed by Prof. Robert LeRoy (Waterloo University) [115]. Here we list a few observations about the calculation and use of the program.

One subtle issue that was initially confusing is that only certain Dunham coefficients (only  $Y_{10}$ ,  $Y_{11}$ ,  $Y_{12}$ , etc., and  $Y_{01}$ ,  $Y_{02}$ ,  $Y_{03}$ , etc., but not  $Y_{20}$ ,  $Y_{21}$ ,  $Y_{22}$ , etc., or  $Y_{30}$ ,  $Y_{31}$ ,  $Y_{32}$ , etc., or  $Y_{40}$ ,  $Y_{41}$ ,  $Y_{42}$ , etc., etc.) need to be entered into the program. This is explained as follows: The  $Y_{2x}$  series of Dunham coefficients, the  $Y_{3x}$  series of Dunham coefficients, the  $Y_{4x}$  series of Dunham coefficients, etc., where  $x = 0, 1, 2$ , etc., are not independent of the  $Y_{0x}$  and  $Y_{1x}$  series of Dunham coefficients, as discussed in Ref. [91] pg. 340. Therefore, there is purposely no way to input the non-independent Dunham coefficient series. One can check using the RKR1 and LEVEL8.0 programs, when given only the  $Y_{0x}$  and  $Y_{1x}$  series of Dunham coefficients, the program can calculate the higher order series of Dunham coefficients and the results of the calculation can be compared with existing data.

A full table of the FCFs  $q_{v',v''}$  for decays  $A^2\Pi_{1/2}(v') \rightarrow X^2\Sigma_{1/2}(v'')$  is given in Table A.1 and may be compared to the large table presented in Ref. [116]. We found the large table useful to verify the absence of even very small inconsistencies between the FCF calculation in Ref. [116] and ours.

Having verified our calculation method by comparison, we next investigated the sensitivity of the FCF calculation to the input parameters. For SrF, the FCFs  $q_{v',v''}$  for decays  $A^2\Pi_{1/2}(v') \rightarrow X^2\Sigma_{1/2}(v'')$  are most sensitive to  $B_e$ , followed by  $\omega_e$ , followed by  $\alpha_e$ , followed by  $\omega_e x_e$ . These results are summarized in Figure A.1.

	$v''=0$	$v''=1$	$v''=2$	$v''=3$	$v''=4$	$v''=5$	$v''=6$	$v''=7$
$v'=0$	9.8144E-01	1.8118E-02	4.3031E-04	1.2625E-05	4.2717E-07	1.4083E-08	3.4433E-10	2.0994E-12
$v'=1$	1.8534E-02	9.4510E-01	3.5067E-02	1.2483E-03	4.8414E-05	2.0375E-06	8.1119E-08	2.3927E-09
$v'=2$	2.7176E-05	3.6701E-02	9.0989E-01	5.0851E-02	2.4133E-03	1.1604E-04	5.8311E-06	2.7247E-07
$v'=3$	1.6000E-08	8.1496E-05	5.4454E-02	8.7587E-01	6.5472E-02	3.8862E-03	2.2249E-04	1.2980E-05
$v'=4$	2.4098E-10	7.8339E-08	1.6177E-04	7.1753E-02	8.4312E-01	7.8939E-02	5.6297E-03	3.7327E-04
$v'=5$	1.0019E-10	8.3559E-10	2.3934E-07	2.6564E-04	8.8557E-02	8.1169E-01	9.1259E-02	7.6077E-03
$v'=6$	4.2034E-12	5.4530E-10	1.6297E-09	5.8325E-07	3.8958E-04	1.0483E-01	7.8165E-01	1.0244E-01
$v'=7$	5.8381E-14	2.7772E-11	1.7228E-09	2.2512E-09	1.2388E-06	5.2901E-04	1.2055E-01	7.5305E-01
$v'=8$	6.2714E-16	4.4783E-13	1.0479E-10	4.1229E-09	2.2970E-09	2.3945E-06	6.7831E-04	1.3568E-01
$v'=9$	1.2083E-15	5.1729E-15	1.9254E-12	2.9634E-10	8.2665E-09	1.5976E-09	4.3165E-06	8.3102E-04
$v'=10$	3.7002E-16	1.1559E-14	2.4097E-14	6.1124E-12	6.9774E-10	1.4610E-08	4.9276E-10	7.3690E-06
$v'=11$	8.4348E-17	3.9510E-15	6.1014E-14	8.3627E-14	1.5963E-11	1.4441E-09	2.3434E-08	3.8607E-11
$v'=12$	1.8499E-17	9.8990E-16	2.3020E-14	2.3491E-13	2.4120E-13	3.6287E-11	2.7132E-09	3.4725E-08
$v'=13$	4.2156E-18	2.3478E-16	6.2841E-15	9.6955E-14	7.3699E-13	6.1210E-13	7.4305E-11	4.7250E-09
$v'=14$	1.0313E-18	5.7181E-17	1.6043E-15	2.8641E-14	3.3013E-13	1.9978E-12	1.4134E-12	1.4018E-10
$v'=15$	2.4665E-19	1.4661E-17	4.1638E-16	7.8283E-15	1.0491E-13	9.6418E-13	4.8490E-12	3.0348E-12
	$v''=8$	$v''=9$	$v''=10$	$v''=11$	$v''=12$	$v''=13$	$v''=14$	$v''=15$
$v'=0$	3.4682E-13	1.7543E-13	2.9029E-14	2.5094E-15	4.6353E-17	2.3141E-17	3.4655E-17	1.9678E-17
$v'=1$	2.0869E-11	2.1370E-12	1.4060E-12	2.6258E-13	2.4657E-14	4.4778E-16	3.0213E-16	4.6202E-16
$v'=2$	9.4826E-09	1.1262E-10	6.9007E-12	6.1158E-12	1.2834E-12	1.2986E-13	2.2484E-15	2.1320E-15
$v'=3$	6.9703E-07	2.8133E-08	4.3774E-10	1.5017E-11	1.9048E-11	4.4824E-12	4.8496E-13	7.6726E-15
$v'=4$	2.4764E-05	1.5039E-06	6.9424E-08	1.3723E-09	2.3389E-11	4.7315E-11	1.2490E-11	1.4344E-12
$v'=5$	5.7246E-04	4.2520E-05	2.8831E-06	1.5048E-07	3.6845E-09	2.4680E-11	9.9008E-11	2.9405E-11
$v'=6$	9.7855E-03	8.2292E-04	6.7594E-05	5.0642E-06	2.9599E-07	8.7904E-09	1.2625E-11	1.7991E-10
$v'=7$	1.1251E-01	1.2129E-02	1.1263E-03	1.0130E-04	8.3140E-06	5.3967E-07	1.9098E-08	8.9510E-14
$v'=8$	7.2593E-01	1.2146E-01	1.4607E-02	1.4833E-03	1.4489E-04	1.2932E-05	9.2556E-07	3.8441E-08
$v'=9$	1.5019E-01	7.0034E-01	1.2933E-01	1.7188E-02	1.8935E-03	1.9952E-04	1.9247E-05	1.5092E-06
$v'=10$	9.8000E-04	1.6406E-01	6.7632E-01	1.3614E-01	1.9841E-02	2.3555E-03	2.6623E-04	2.7607E-05
$v'=11$	1.2037E-05	1.1176E-03	1.7728E-01	6.5390E-01	1.4190E-01	2.2540E-02	2.8673E-03	3.4592E-04
$v'=12$	2.0647E-09	1.8949E-05	1.2361E-03	1.8981E-01	6.3312E-01	1.4664E-01	2.5256E-02	3.4257E-03
$v'=13$	4.8071E-08	9.0032E-09	2.8900E-05	1.3278E-03	2.0165E-01	6.1399E-01	1.5039E-01	2.7966E-02
$v'=14$	7.7357E-09	6.2577E-08	2.3430E-08	4.2875E-05	1.3855E-03	2.1277E-01	5.9654E-01	1.5317E-01
$v'=15$	2.4751E-10	1.2026E-08	7.6843E-08	4.7293E-08	6.2062E-05	1.4031E-03	2.2316E-01	5.8081E-01

Table A.1: Expanded table of Franck-Condon factors. The FCFs shown here are calculated using LEVEL8.0 [115] with the constants in Table 2.4 for the  $X^2\Sigma_{1/2}$  state and the constants calculated in 2013 listed in Table 2.5 for the  $A^2\Pi_{1/2}$  state.

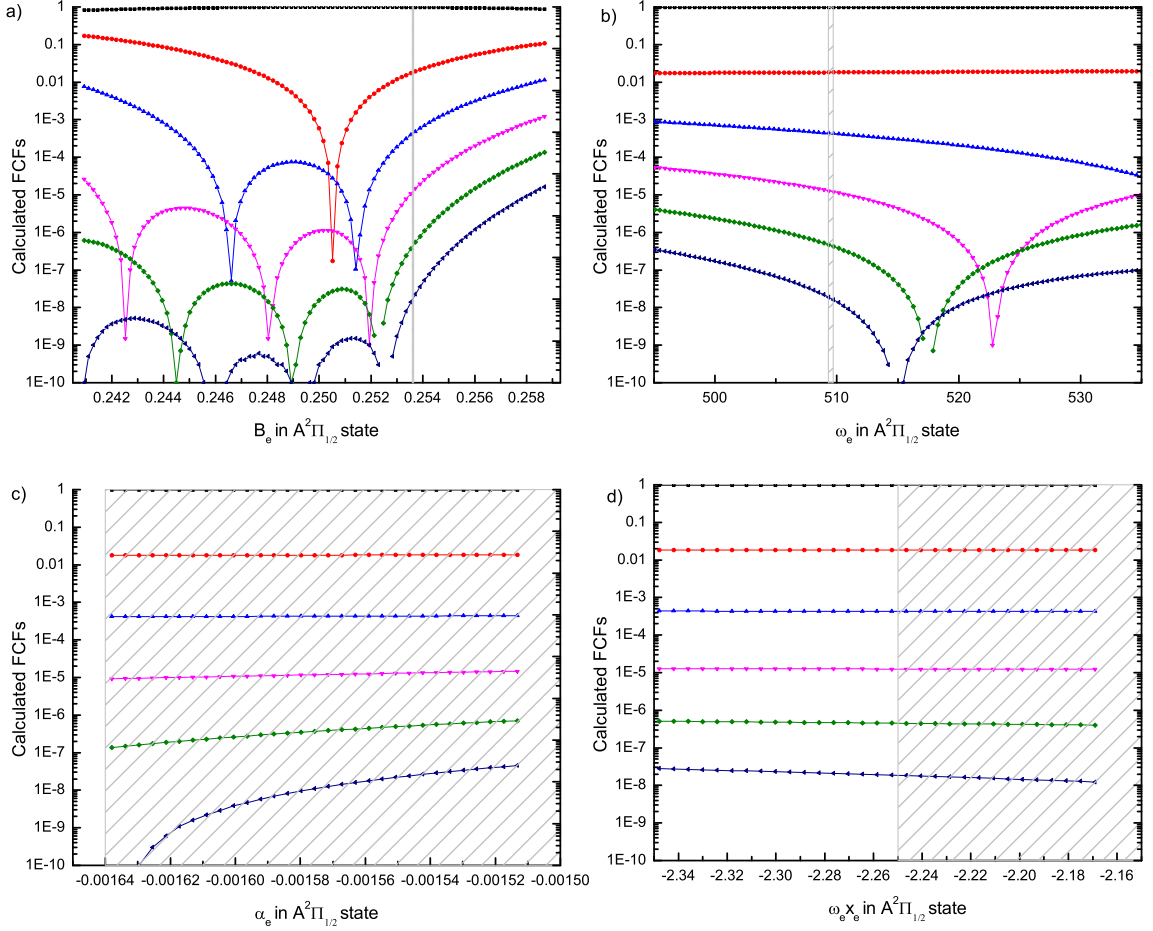


Figure A.1: The calculated FCFs  $q_{v',v''}$  for decays  $A^2\Pi_{1/2}(v') \rightarrow X^2\Sigma_{1/2}(v'')$ . The FCFs for  $q_{00}$  (■),  $q_{01}$  (●),  $q_{02}$  (▲),  $q_{03}$  (▼),  $q_{04}$  (◆), and  $q_{05}$  (◄) are plotted while individually varying the values of  $B_e$  (a),  $\omega_e$  (b),  $\alpha_e$  (c), and  $\omega_e x_e$  (d) over a  $\sim 10\%$  range near their calculated value. The estimated experimental uncertainty in each parameter is depicted by the gray box. The lines are only to guide the eye. The sharp negative peak for  $q_{01}$  occurs when  $B_e$  in the  $A^2\Pi_{1/2}$  state approaches  $B_e$  in the  $X^2\Sigma_{1/2}$  state.

## Appendix B

# Molecule choosing

### B.1 Future molecules for laser cooling

The present difficulty with laser cooling, slowing and magneto-optically trapping molecules relative to atoms arises in large part from the smaller spontaneous forces that have so far been applied to molecules [90, 120, 206, 246]. Relative to atoms, capture velocities are therefore smaller, and experiments often require sources based on cryogenic buffer gas beams, etc. Other obstacles include higher laser power requirements relative to atoms, but this is related to the former problem. Surprisingly, the large number of lasers required for molecular cooling experiments is only a secondary complication.

To examine spontaneous force limitations further, we compare SrF to Rb since the lifetime, excitation wavelength and mass are all the same to  $\approx 20\%$ . In the limit of infinite laser power, the maximum possible spontaneous force will vary for most systems as

$$F_{sp}^{\max} = \frac{h}{\lambda_{00}} \frac{N_e}{N_{tot}} \frac{1}{\tau}, \quad (\text{B.1})$$

where  $h$  is Planck's constant,  $\lambda_{00}$  is the excitation wavelength,  $N_e$  is the number of excited states in the main cycling transition and  $N_{tot}$  is the number of ground states connected to the excited state of the main cycling transition plus  $N_e$ . For SrF,  $N_e = 4$  and  $N_{tot} = 12 + 12 + 4 = 28$ , resulting in  $N_e/N_{tot} = \frac{1}{7}$ . For the cycling transition in Rb (or any alkali or alkaline earth atom),  $N_e/N_{tot} = \frac{1}{2}$ . So relative to an atom with the same  $\lambda_{00}$  and  $\tau$ , even with infinite laser power,  $F_{sp}^{\max}$  will be  $3.5\times$

smaller for SrF. From the kinematic equation

$$v_f^2 = v_i^2 - 2ad, \quad (\text{B.2})$$

where  $v_{f(i)}$  is the final (initial) velocity,  $a$  is the acceleration, and  $d$  is the distance, it may be seen that for slowing via spontaneous radiation pressure forces, the distance required is proportional to the applied force and thus the factor of 3.5 is a major disadvantage. Further, the cycling transition employed on SrF prohibits the use of a Zeeman slower for two reasons: first, because the ground state g-factors of the different SR/HF levels are all different; second, because the  $^2\Sigma_{1/2}(N=1) \rightarrow ^2\Pi_{1/2}(J=1/2)$  transition prevents the use of a stretched state to create an effective two-level system.

### B.1.1 Summary of selection advice

Laser cooling of molecules will continue to grow in the future. Given my experience, I can offer some limited advice on choosing a molecule. Molecules requiring only diode laser excitation wavelengths will result in a cheaper laser setup with more flexibility. Molecules with low-lying metastable states may be problematic [120] due to population trapping. To apply large spontaneous accelerations for cooling, slowing and trapping considerations, it is desirable to have a low mass, a short  $\lambda_{00}$  and a short  $\tau$ . Unpaired spins which result in resolved splittings are generally undesirable because they require AOMs or EOMs to generate the necessary frequencies and increase the total laser power required. While molecules with more diagonal FCFs are desirable to limit the number of lasers, the power of vibrational repump lasers beyond  $\lambda_{10}$  will be reduced by  $\sim \frac{q_{01}}{q_{00}}$  relative to the  $\lambda_{00}$  and  $\lambda_{10}$  lasers. Further, since little force is derived from such lasers, their polarization is flexible. Multiple repump lasers could be combined to seed a single slave laser or a single TA.

### B.1.2 Estimating Franck-Condon factors

When searching for molecular laser cooling candidates, a quick estimation of  $q_{00}$  is helpful. If  $q_{00} \gtrsim .8$ , laser cooling may be feasible with a reasonable number of lasers. We employ the crude estimation outlined in Ref. [295] which states that

$$q_{00} \approx \text{Exp} \left[ -\frac{\mu\tilde{\omega}(\Delta r_e)^2}{2 * 5.807^2} \right], \quad (\text{B.3})$$

where  $\mu$  is the reduced mass of the diatomic molecule (in units of amu),  $\tilde{\omega} \equiv \omega_1\omega_2/(\frac{\omega_1+\omega_2}{2})$  is an “average” of  $\omega_e$  in the ground and electronic excited states (in  $\text{cm}^{-1}$ ) and  $\Delta r_e$  is the difference between the equilibrium internuclear separation  $r_e$  in the ground and excited state (in Ångstroms). The numerical constant 5.807 is equal to the value of  $\sqrt{h/(4\pi^2ca)}$  in Ångstroms where  $h$  is Planck’s constant (in J·s),  $c$  is the speed of light (in cm/s), and  $a = 1$  amu (in kg). Similar estimations can be made for higher order FCFs [295]. However we are mostly interested in  $q_{00}$ . For SrF the estimation is quite accurate and yields  $q_{00}^{\text{est}} = .98146$  using the  $r_e$  values in Table 2.14 while an RKR calculation yields  $q_{00}^{\text{RKR}} = .98144$ .

### B.1.3 Singlet Sigma to singlet Pi molecules

Although SrF has a  $^2\Sigma \rightarrow ^2\Pi$  quasi-cycling transition, there are benefits to choosing a molecule with a  $^1\Sigma \rightarrow ^1\Pi$  quasi-cycling transition instead.

- As shown in Fig. B.1a and B.1b, only 1/3 of the ground states will be dark for any given laser polarization. However, since the magnetic moment of the ground state is small, microwave or polarization remixing would be required. For the  $X^2\Sigma \rightarrow A^2\Pi$  quasi-cycling transition in SrF, 2/3 of the ground states are dark.
- Because  $S=0$  for  $^1\Sigma$  states, there is no SR structure and HF splittings are small and maybe even unresolved. Hence one laser frequency is likely sufficient to repump each vibrational level. Since the amount of laser power required varies approximately linearly with the number of laser frequencies, this is highly desirable.
- The  $^1\Sigma$  ground state will have a very small magnetic moment while the excited state should exhibit a sizable magnetic moment. This allows for the possibility of a Zeeman slower, shown in Fig. B.1c. This is in contrast to a  $X^2\Sigma \rightarrow A^2\Pi$  transition for which a Zeeman slower does not appear to be possible.

Unfortunately, most molecules with  $X^1\Sigma$  ground states and  $A^1\Pi$  excited states are either not diagonal (MgO, BeO, CaO, SrO, BaO), require  $\lambda_{00}$  to be in the UV, or have low-lying states. Molecules with this energy level structure with diagonal FCFs are discussed in the next section.

### B.1.4 Potential future candidates

Many potential candidates exist for molecular laser cooling. Perhaps the only firm requirement is that the FCFs limit vibrational branching to a reasonable number of lasers. However, molecular

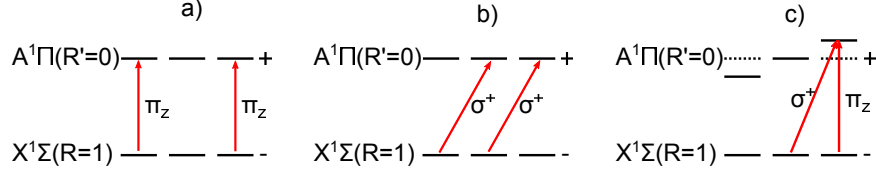


Figure B.1: For a molecule exhibiting a  $X^1\Sigma(R=1) \rightarrow A^1\Pi(R=0)$  cycling transition, only 1/3 of the ground states are dark for  $\pi_z$  polarization (a) or  $\sigma^+$  polarization (b). Microwave or polarization switching would be required for remixing since the ground state experiences little or no shift in a magnetic field. The excited state however experiences a large Zeeman shift. By polarization switching between  $\sigma^+$  and  $\pi_z$  light a Zeeman slower appears viable (c).

laser cooling is made substantially harder by certain undesirable traits: excitation at wavelengths requiring lasers  $\gtrsim$  \$100k–\$200k per laser, low-lying metastable states, long excited state lifetimes, and large hyperfine splittings between a large number of levels all create additional experimental challenges. However, no single one of these traits is by itself a fatal flaw. We now discuss some future candidate molecules.

The alkaline earth monohydrides (BeH, MgH, CaH, SrH, BaH) are good candidates and generally have diagonal FCFs. For some applications, hydrides are undesirable because of the  $\gtrsim$  100 GHz rotational transitions. While CaH, SrH and BaH require diode laser excitation wavelengths in the red or IR, BeH has  $\lambda_{00} \sim 500$  nm while MgH  $\lambda_{00} \sim 520$  nm. Laser diodes at 520 nm have become available in the last year.

The alkaline earth monofluorides all have diagonal FCFs and are in principle amenable to laser cooling. Although the wavelengths for BeF ( $\lambda_{00} \sim 300$  nm), MgF ( $\lambda_{00} \sim 360$  nm), and CaF ( $\lambda_{00} \sim 606$  nm) are not currently accessible by diode laser, those for SrF and BaF are. CaF has recently been laser cooled and slowed [242]. BaF unfortunately has a low-lying  $^2\Delta$  state, which acts as leak from the cycling transition and a trap for population. The chief drawback to these molecules beyond some of the excitation wavelengths is the presence of resolved SR/HF structure and the fact that, as demonstrated above, a  $^1\Sigma \rightarrow ^1\Pi$  transition is likely preferable to the  $^2\Sigma \rightarrow ^2\Pi$  transitions of the alkaline earth monofluorides. Attempts to laser cool similar molecules such as YbF are under way as well [124].

The alkaline earth monochlorides all display diagonal FCFs but aside from chemical diversity, offer little obvious benefit over the alkaline earth monofluorides. To some extent, the wavelengths are slightly longer and therefore offer better laser accessibility: BeCl ( $\lambda_{00} \sim 357$  nm), MgCl ( $\lambda_{00} \sim 378$  nm), CaCl ( $\lambda_{00} \sim 621$  nm), SrCl ( $\lambda_{00} \sim 675$  nm), BaCl ( $\lambda_{00} \sim 966$  nm). However lifetimes are longer and the FCFs are slightly less diagonal. Unfortunately, the  $I = 3/2$  nuclear spin of both

$^{35}\text{Cl}$  and  $^{37}\text{Cl}$  results in a larger splitting and number of ground state SR/HF sublevels relative to an analogous alkaline earth monofluoride.<sup>1</sup> The larger mass of Cl versus F is also somewhat disadvantageous. For similar reasons, the alkaline earth monobromides and monoiodides are likely slightly more technically challenging to laser cool than the alkaline earth monofluorides as well.

The group 3 monoxides (and monosulfides, etc.) all display diagonal FCFs with short lifetimes. ScO ( $\lambda_{00} \sim 606$  nm), LaO ( $\lambda_{00} \sim 791$  nm) and LuO ( $\lambda_{00} \sim 507$  nm) appear challenging because the combination of their  $I = 7/2$  nuclear spin and strong Fermi contact interaction results in extensive SR/HF structure spread out over a few GHz. YO is problematic both because it requires a CW dye laser for  $\lambda_{00}$  and has a low-lying metastable state. Nevertheless these problems for YO are not fatal and laser cooling of YO has been demonstrated [120].

The group 4 monoxides (TiO, TiS, etc.) and similar molecules display somewhat diagonal FCFs and a proposal (the impetus for this thesis work) was made to laser cool TiO [88]. While the 5  $\mu\text{s}$  lifetime of TiO is likely problematic, the TiS lifetime is 249 ns.

The boron group monohalides and monohydrides generally possess highly diagonal FCFs, display the desirable  $^1\Sigma \rightarrow ^1\Pi$  cycling transition, have extremely short excited state lifetimes,<sup>2</sup> have no SR structure, and display small or unresolved HF due to their closed electron shells. Unfortunately, these elements typically have  $\lambda_{00} \lesssim 300$  nm (except for BH where  $\lambda_{00} = 433$  nm) and many (BH, BF, AlH, AlF, GaH, GaF, InF, InBr, InCl) if not all display low-lying metastable states. However because excited state decays to some of these states are spin-forbidden and therefore highly suppressed, their presence may not be problematic. AlF is particularly interesting since calculations [296] indicate  $q_{00} = .99992$  (so that  $> 10000$  photons could be scattered with a single laser), the excited state lifetime is extremely short at 1.8 ns, and HF structure is unresolved. Unfortunately,  $\lambda_{00} = 227$  nm for AlF and there is a low-lying triplet state. Laser cooling of TlF has been proposed for high-precision searches for the Schiff moment and the proton electric dipole moment (EDM) [297]. The group of Ed Hinds is currently working to laser cool BH.

Laser cooling molecules from metastable states should also be possible and the species FeC, ZrO, HfO, ThO, and SeO look promising in this application. Due to the large number of diatomic molecules, there are many more candidates as well. It is likely if not inevitable that the number of laser cooled molecular species will exceed the number of laser cooled atoms simply due to the much larger number of diatomic molecules.

---

<sup>1</sup>This effect arises because the spin density of the unpaired electron in the  $\sigma$  orbital is less centered on the alkaline earth atom.

<sup>2</sup>Electronic structure in these molecules is analogous to that of alkaline earth atoms which display short lifetimes as well.



## Appendix C

# ECDL further details

This section elaborates on our fairly extensive experience with ECDLs. The drawings may have to be rescaled so that the sheet scale is correct. The version of this thesis posted on the DeMille group website [298] has the appropriate scale listed on the drawing sheets<sup>1</sup> if the pdf pages are printed with no rescaling (confirm that this option is off during printing). The official version of this thesis submitted to Yale University however has margin restrictions, requiring the drawings to be shrunk and therefore the sheet scale is not valid for the official Yale version of this thesis. Updates to this design and any relevant additional material will be posted on the DeMille group website.

### C.1 Parts and choices for home-built ECDL design

1. **Grating choice:** When choosing a grating there are at least three important choices: The grating type (holographic or ruled), the grating lines/mm, and for holographic gratings, whether the grating is VIS or UV optimized. We exclusively use holographic gratings since holographic gratings create far less stray light than ruled gratings. The appropriate grating lines/mm can be calculated from the laser geometry using the grating formula from Eqn. 4.2 which is reproduced here:

$$\lambda = 2d \sin \theta. \quad (\text{C.1})$$

The last (and really the only non-trivial grating related selection) is whether the grating is optimized for UV light or for visible light. This selection depends on how much feedback the laser diode requires to get to the desired wavelength, denoted  $\lambda_{\text{desired}}$ . For a non-AR-coated wavelength-selected laser diode whose free-running wavelength, denoted  $\lambda_{\text{free}}$ , is already close to  $\lambda_{\text{desired}}$ , the grating which gives the least feedback is generally chosen.

As an example of feedback diffraction efficiency, a 2400 lines/mm grating optimized for the UV (Thorlabs, GH13-24U) has a diffraction efficiency of  $\approx 2\%$  at 660 nm while a 2400 lines/mm grating optimized for the visible (Thorlabs, GH13-24V) has a diffraction efficiency of  $\approx 12\%$  at 660 nm. The given values for diffraction efficiency are for light polarized parallel to the lines of the diffraction grating, as is typically the case for our 663 nm ECDLs which employ laser diodes with TM polarization.

We have observed the following

**Less feedback offers:**

- Single-mode behavior over a greater fraction of diode drive currents

---

<sup>1</sup>e.g. 1 inch on the drawing sheet corresponds to 2 inches on the part if the sheet scale is labeled as 1:2.

- More output power
- Greater suppression of spurious sidebands (more common in red lasers)
- Laser possibly lasts longer due to less feedback

**More feedback offers:**

- Laser can operate with  $\lambda_{\text{desired}}$  farther from  $\lambda_{\text{free}}$
- Temperature range over which laser can lase at  $\lambda_{\text{desired}}$  is larger
- Initial alignment of cavity is easier

We speculate that for non-AR-coated diodes, there is already a feedback mechanism present due to the non-zero reflectivity of the diode front facet. In such cases, even slight amounts of external feedback from the grating is enough to cause preferential selection of a given longitudinal laser mode. We have observed that for gratings with higher feedback, multiple modes are more likely to be excited, resulting in non-single-mode behavior.

2. **Diode choice:** Typically, the diode chosen is the one which is specified to have the most power available at  $\lambda_{\text{desired}}$ . If possible, getting the diode wavelength selected is advised. Ideally the diode should be wavelength selected so that

$$\lambda_{\text{free}} = \lambda_{\text{desired}} \text{ at } 15 \text{ Celcius} \quad (\text{C.2})$$

where  $\lambda_{\text{free}}$  is evaluated at the laser's expected injection current  $I_{LD}$  when operational. This is an effort to extend the diode lifetime since diodes last longer at lower temperatures. A measure of the parameter  $\frac{d\lambda}{dT_{LD}}$  where  $T_{LD}$  is the temperature of the laser diode is often available in the diode spec sheet. For ML101U29 laser diodes we measured that  $d\lambda/dT_{LD} = .18 \text{ nm/Celcius}$  and  $d\lambda/dI_{LD} = .018 \text{ nm/mA}$ .

A list of the parts required for the home-made ECDL (excluding screws, washers, DB9 connectors, DB9 cables, wire, etc.,) is listed in Table C.1.

## C.2 ECDL assembly tips

1. If using parts from a design older than the current, make the necessary modifications if desired.
2. When you put the thermistor in, use the Arctic Silver Thermal Epoxy. This epoxy is kept in a refrigerator to make it last longer. The darker compound flows much more freely when it isn't cold though. The darker compound can be warmed up by putting it in the microwave until it sparks, which usually takes  $\sim 3$  seconds.
3. Sand all mating surfaces. I usually do this up to at least 1000 grit sandpaper. Then ultrasonically clean everything in Citronix. That should be clean enough for our purposes.
4. Use a few washers for the grating holder so the screw doesn't hit the bottom. I used four 8-32 washers.
5. The push screws for the grating should be steel socket cap screw 1/2 inch long. Screws that are only 3/8 probably do not have enough thread. The way that thing works is you loosen the push screws before turning the bushing clockwise and vice versa. In the final position the pull screws should be tight. There is some hysteresis as you might imagine so there is an art to this.
6. It may be useful to calculate where the diode collimation tube should go to satisfy the pivot point position. To do this you will have to know what collimation tube you have and the position of the active emitter of the laser diode relative to its housing. With my mathematica file and the solidworks assembly you can probably get this done although I imagine it will take a few hours. The time is probably worth it.

Item	Part Number	Supplier	Quant.	Unit Cost	Total Cost
Channel piezo controller	MDT693A*	Thorlabs	1	1580	527
Alt Piezo controller	MDT694A*	Tholabs	0	527	
Current controller	LDC202C or similar	Thorlabs	1	950	950
Alt low cost temp controller	MPL250	Wavelength Elect.	0	309	
Temperature controller	TED200C	Thorlabs	1	768	768
Alt low cost temp controller	PTC2.5K-CH	Wavelength Elect.	0	259	
Collimation tube	LT230P-B	Thorlabs	1	111	111
Bushings	P25SB075V	Thorlabs	2	23	46
Sapphire plates	NT45-567	Edmund	3	20	60
Bushing glue	Loctite 680	McMaster			
Thermal paste	Arctic Silver 5 (AS5)	Arctic Silver			
Thermal adhesive	Thermal adhesive (ASTA-7G)	Arctic Silver			
DB9 Male connector	L717SDE09P-ND	Digikey	1	1	1
DB9 Female connector	L77SDE09S-ND	Digikey	1	1	1
DB9 Jackscrews	1195-2600-ND	Digikey	4	.48	1.92
BNC Connector	93F7577	Newark	1	2.24	2.24
Piezo	PSt 150/4/5 sph**	Piezomechanik	1	210	210
Thermistor	TH10K	Thorlabs	1	15	15
TEC	102-1678-ND	Digikey	1	13.45	13.45
Aluminum blank for base	9057K78	McMaster	1	87.66	87.66
2" wide acrylic for case sides	1227T439	McMaster	1	22.08	22.08
3" wide acrylic for case top	1227T459	McMaster	1	16.36	16.36
360 brass laser parts (4 tot.)					345
Laser diode					
Holographic grating		Thorlabs			
Beam steering mirror	BB05-E02 or similar	Thorlabs	1	49.40	49.40
Laser diode socket	S7060R or similar	Thorlabs	1	5.35	5.35

Table C.1: Parts list for home-built ECDL. This list excludes screws, washers, wire, etc. Unit cost is in dollars. \*The MDT693A has three high voltage outputs and thus can be used for three lasers while the MDT694A has a single high voltage output. \*\*This piezo replaces the previously used piezo which had a much smaller free stroke (Noliac, NAC2121). Unfortunately, we have not changed the drawings yet to reflect this change and have instead machined cylindrical adapters for the newer piezos. Updated drawings when this change is fully tested will be posted on the DeMille group website [298].

7. The design will work well for 663, 780 and 850 nm lasers and many others. For certain wavelengths the brass part holding the grating may need to be modified so as not to clip the output beam or the brass part holding the beam steering mirror might need to be modified so that everything fits inside the plexiglass housing. I recommend using the grinder but have not tried this myself.
8. I recommend using thermal paste (Arctic Silver Inc., Arctic Silver 5) in these areas:
  - Aluminum base/TEC junction
  - TEC/brass base junction
  - Brass collimation tube holder / brass base
  - Brass grating holder / brass base

I have traditionally not used thermal paste between the collimation tube and the collimation tube holder. Wipe away any visible thermal paste afterwards.
9. I recommend 5 minute epoxy to put the grating on. However you need to know where the grating goes first. Usually I use double sided sticky tape to position the grating the first time in order to make the laser lase (you also need to know the angle at which the grating goes). This can be calculated with Eqn. C.1. After I know where the grating goes I epoxy it. You will probably have to take the grating holder off the laser when you epoxy it.
10. The Loctite glue is for the bushings.

### C.3 Setting up the laser

1. **Laser diode collimation:** The laser diode is collimated by minimizing the spot size beyond the maximum location of the beam waist. Send the laser as far away as possible (generally  $\gtrsim 3$  m) and try to minimize the spot size and make the beam spot look round at this distance. Due to the rectangular symmetry of the diode active region, the output in the near field will be cigar-shaped. Diodes with TE modes have their polarization along the cigar. Diodes with TM modes have their polarization perpendicular to the cigar. For either TE or TM diodes, the spot should ideally have two symmetry axes. If the beam shape does not look 2-fold symmetric, try poking the collimation lens. Once you are happy with the beam shape, use 5 minute epoxy to fix the collimation lens in place permanently. Proper diode collimation is critical to achieve high fiber coupling efficiency. For certain laser diodes (notably Opnext HL6750MG), we were unable to achieve a symmetrical output in the far field. The reasons for this are unknown.
2. **Laser temperature.** The laser diode temperature is important for two main reasons: First, the temperature affects the diode's free running wavelength. Typically the ECDL will be tune and perform most reliably when the temperature (and current) of the free-running diode are set so that  $\lambda_{\text{free}} = \lambda_{\text{desired}}$ ; Second, the lifetime of the laser diode is strongly dependent on temperature. Diodes operated at lower temperatures will last longer. As stated in Ref. [299], for almost all common laser diodes from 600-1200 nm, a good rule of thumb is that for every  $10^\circ$  C marginal increase in operating temperature, the diode lifetime will decrease by  $2.5\times$ . However, predictions from Ref. [299] specifying diode lifetime as a function of drive current do not match our empirical data; we find that diode lifetime decreases faster than in proportion to the inverse square of the drive current. This makes sense since a diode run at  $3\times$  its rated current is very unlikely to last  $1/9$  as long as when the diode is run at its rated current.

Therefore put the diode in and couple the light into a fiber or use the Ocean Optics spectrometer or a wavemeter. The wavemeter will still read occasionally even if the diode is not getting feedback from the grating. Depending on the relative humidity, temperatures below  $13^\circ$  C may cause condensation. I cringe when diodes have to be run above  $35^\circ$  C.

3. **Cavity alignment:** To make the laser lase, turn the laser diode current down to about the lasing threshold. Then try to align the negative first order diffraction beam back into the diode. If the shape of the output beam is horizontal (cigar-like), I usually try to misalign the negative-first order diffraction vertically so it is separated from the diode output. This will allow you to see the position of the negative first order diffraction. Now try to align the negative first order diffraction and the diode output horizontally. Once that is done, simply move the negative first order beam downwards. I do this because I am pretty sure that (due to the grating), the ECDL will laser from feedback for a larger range of horizontal angles than vertical angles. I usually have a white notecard placed immediately after the grating (i.e. not in the laser cavity). If you ever see a very weak spot of light somewhere on the card, try to align it to overlap it with the main outgoing laser beam. The vast majority of times, this will make the laser lase. I am not sure what the weak spot is. Maybe it is a reflection off the front facet or collimating lens from light going back from the grating to the laser diode.
4. **Pivot point / diode collimation tube location:** The diode collimation tube location is the single adjustable element by which the user can ensure that the laser geometry satisfies the pivot point criteria described by Eqn. 4.5. The optimal location of the diode collimation tube can be calculated from the laser geometry and the method for this is detailed later in this section. In practice the tube is initially placed at the theoretical optimum position and the position is varied empirically. If the laser tunes poorly or erratically (cannot tune even  $\sim 2$  GHz without a mode hop with no feed forward) the diode can be moved a small fraction of a mm. In practice we do not have a deterministic method to tell whether the collimation tube is too far forward or too far behind the optimal position. However for unknown reasons we have circumstantial evidence that tuning characteristics are far worse when  $x_0$  is too small rather than when  $x_0$  is too large.
5. **Avoid back reflections:** The laser is sensitive to back reflections. Do not send the beam exactly back into the laser with a mirror, the head of a power meter or any highly reflective surface. Under such conditions, all light generated by the laser diode will eventually be dissipated by heat inside the laser diode and will likely kill the diode. This is called catastrophic optical damage (COD) and is to be avoided.

## C.4 Troubleshooting

Here we list advice for some common problems with ECDLs.

1. **Poor tuning:** If the tuning is better at different diode currents (there are many cases of lasers performing well at low currents but less well when the current is turned up), typically the temperature needs to be changed. If the tuning is systematically poor, the likely culprit could be the feed forward or the location of the diode collimation tube. There have been cases (although such cases are rare) where a certain diode will not tune satisfactorily at any temperature or current. The few times this has been observed, an identical diode has been put into the laser and performed well.
2. **Optical feedback:** A good test for problems of optical feedback is to insert an ND filter (typically ND1) prior to the optical element suspected of generating the feedback. If doing this makes a difference, there is likely a feedback problem.
3. **Noise from piezo:** Unplug the piezo and see if the laser looks better
4. **Current noise:** Measure the current noise using a resistor commensurate with the diodes current/voltage curve on a high impedance scope.
5. **Setting feed forward:** There are multiple ways to do this. I typically follow the method suggested in the Toptica manual in which the piezo is fed a sawtooth and the feed forward is adjusted to maximize the number of consecutive peaks on the Fabry-Pérot.

6. **Other:** Some of the other issues I have encountered include noisy DAQs (fixed with a low-pass filter on the DAQ output), ground loops, improper diode collimation tube placement, and acoustic pickup.

## C.5 Miscellaneous ECDL lessons

We now quickly recount a few miscellaneous lessons we have learned the hard way. To ensure good pointing stability, lasers are clamped directly to the optical table rather than mounted on top of alternating layers of vibration isolation and metal plates. The addition of a bias tee should be inside the laser head and allows for easy, direct modulation of the injection current. While automated feed forward is convenient to achieve mode hop free tuning ranges of  $\gtrsim 5$  GHz for non-AR-coated diodes, the feed forward can also be easily applied manually by the user to get the laser to the right wavelength when long automated laser scanning is not necessary.

## C.6 Possible design improvements

1. Making the lens adjustment on the ECDL similar to the lens adjustment on TA might eliminate the need for mirrors between the isolator and the ECDL. However such modifications would make it harder to vary  $x_0$  and therefore to satisfy Eqn. 4.5 for arbitrary  $\lambda$ .
2. Employing a DL Pro-type design [163] would minimize acoustic pickup. A design similar to this was not pursued in part due to the lack of wire electrical discharge machining at Yale and in part because narrow linewidth lasers were not needed for this experiment.

## C.7 Setting the correct pivot point

In our design, the machining is independent of the wavelength/grating/ $\Theta$  combination. The MHFTR may be maximized by varying the position of the laser collimation tube (which houses the laser diode) inside its housing until Eqn. 4.5 is satisfied. The placement of otherwise identical AR-coated and non-AR-coated diodes should be different. For an AR-coated diode, the cavity should extend to the back facet of the laser diode. For the non-AR-coated diode, the cavity only extends to the laser diode output facet. The estimation of where to properly position the collimation tube is outlined as follows:

1. Use Eqn. 4.2 to determine  $\Theta$  for a given grating period  $d$  and desired  $\lambda$ . Using the Solidworks assembly, set the grating angle. Note: Because the brass grating holder pivots around its mounting point it is easier to let Solidworks take care of this aspect of the geometry.
2. Use Eqn. 4.5 and recall that for a Thorlabs grating (.243" thickness) paired with the given laser pivot arm thickness (distance from pivot = .17"), we have  $x_1 = -.413$ " and solve for  $x_0$ .
3. After initial placement, the diode collimation tube is manually moved forwards and backwards until the laser tunes sufficiently well.

For example, using the ML101J27, the emitting surface is located 2.27 mm in front of the diode mounting surface. Using the drawings for the collimation tube and the collimation lens we estimate that the C230TME-B lens tube should protrude from the brass housing by .87 mm. This analysis takes the index of refraction of the collimation lens into account.

## C.8 Laser diode and grating choices for SrF lasers

We have the most experience with lasers at 663 nm and 685 nm. The latest 663 nm laser was set up with a ML101J27 laser diode and a 2400 lines/mm holographic grating optimized for the UV (Thorlabs GH13-24U) which has a diffraction efficiency of 2%. While the ML101U29 diodes

supposedly offer more power, they tend to die when placed in ECDL configurations even when run well below their specified current. Curiously, when tested in a free-running configuration, these diodes have proved far more robust. The latest 685 nm laser was set up with a HL6750MG laser diode and the above diffraction grating, which has a diffraction efficiency of 2% at 685 nm. Both lasers tune very well.

John Barry  
john.barry@yale.edu  
203 561 6060 (cell)  
203 432 3834 (lab phone)  
DeMille Group

Charging =

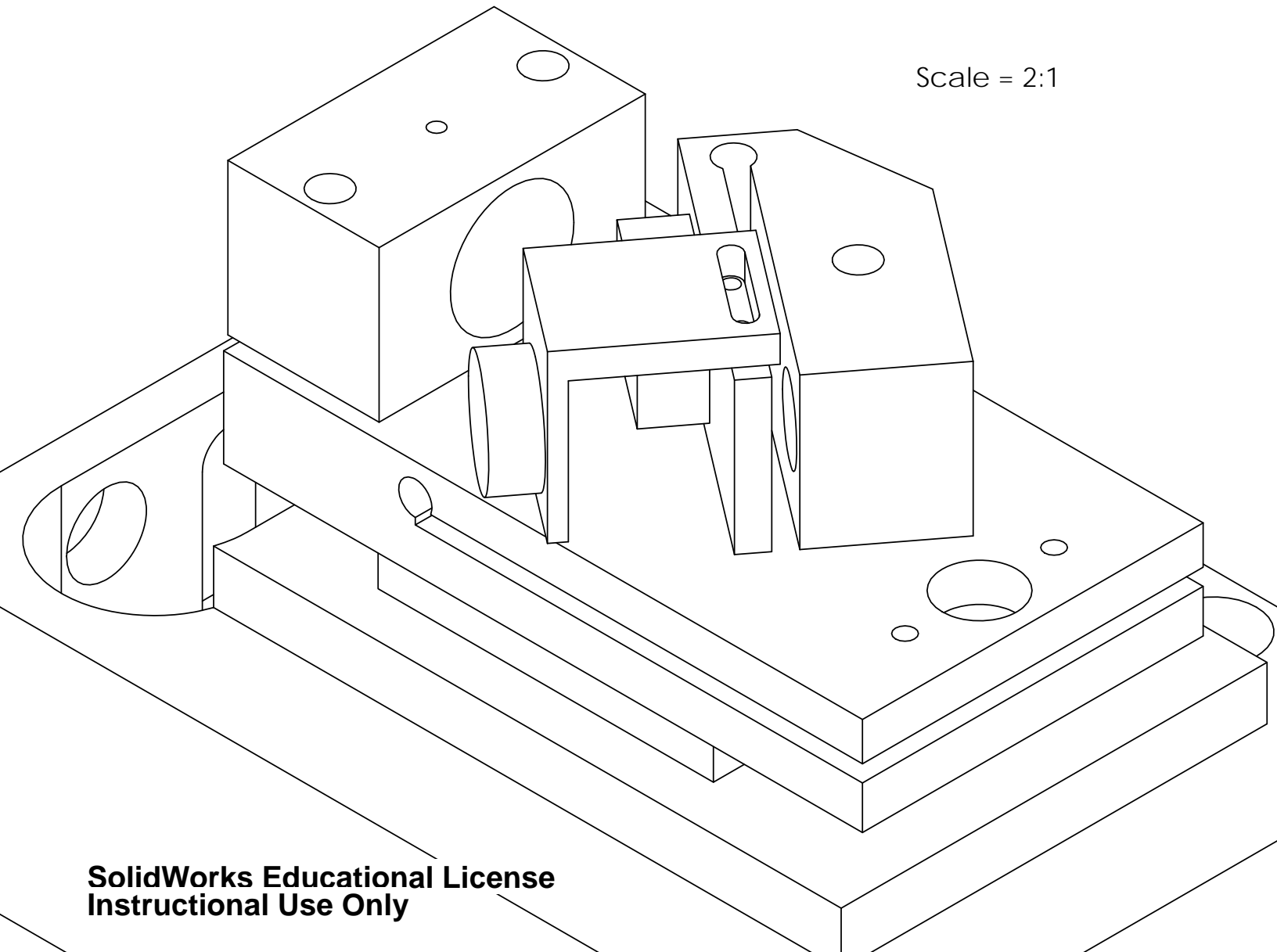
Material = 360 Brass

Quantity 2 of each of the following parts

Diode Housing  
Base Flexure  
Grating Flexure  
Beam Steering Mirror Mount

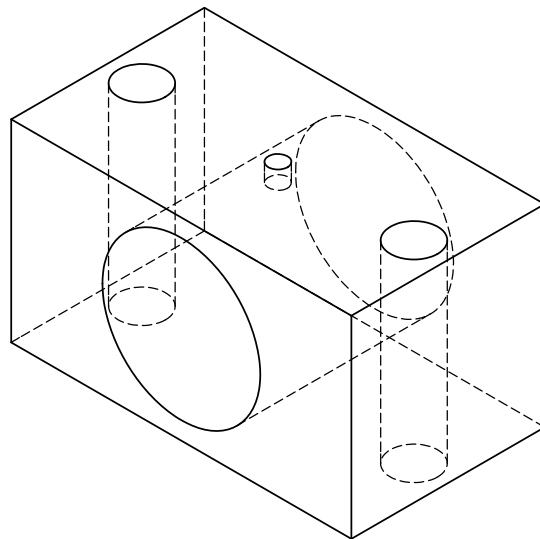
- All cuts may be rough cuts except when marked otherwise. When a specific surface finish is needed it will be marked.
- All dimensions are +/- .01 unless otherwise noted. This is written on every page that has dimensions
- The scale of the drawings to the actual parts is 2:1. This is written on every page as well

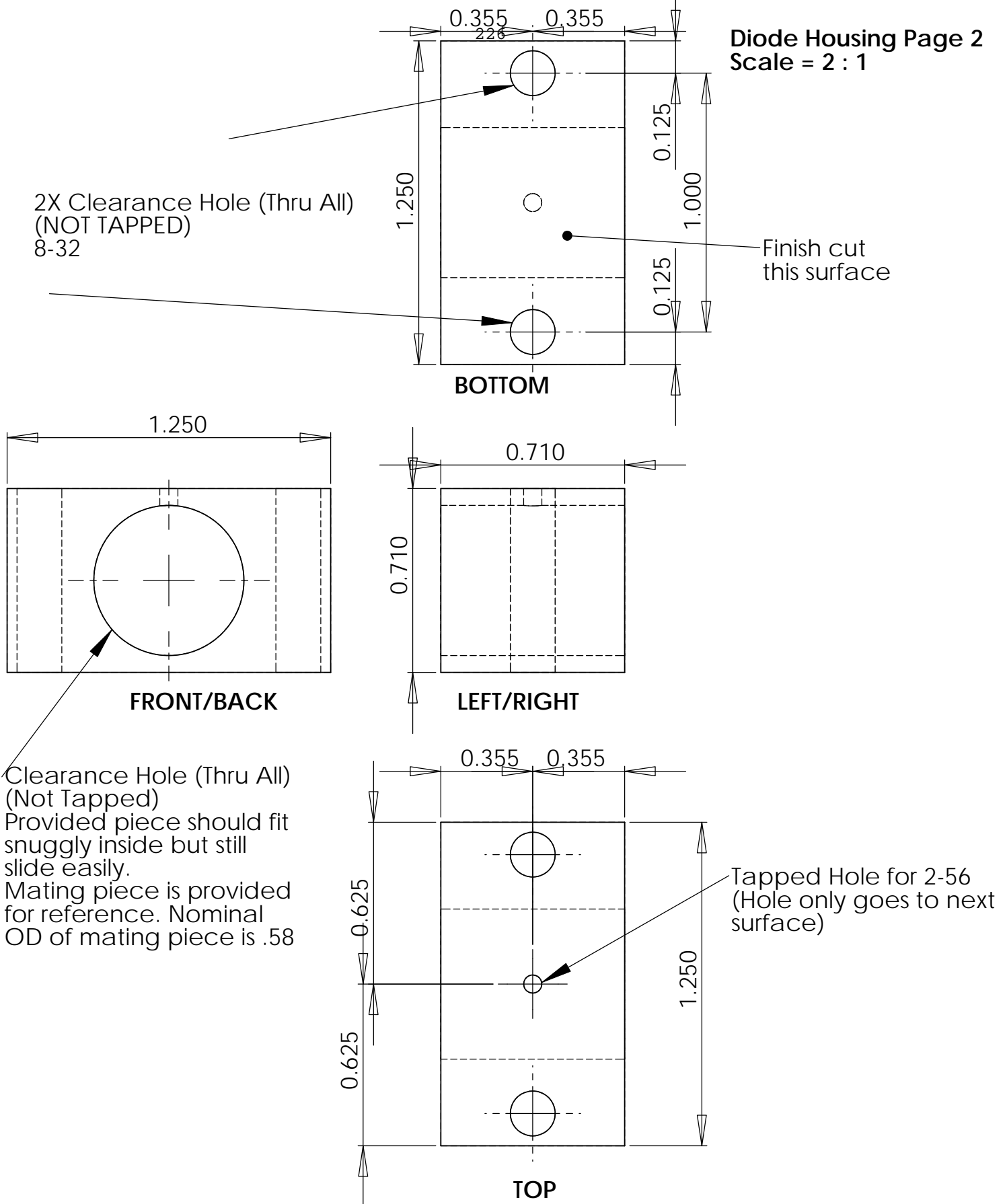
Scale = 2:1





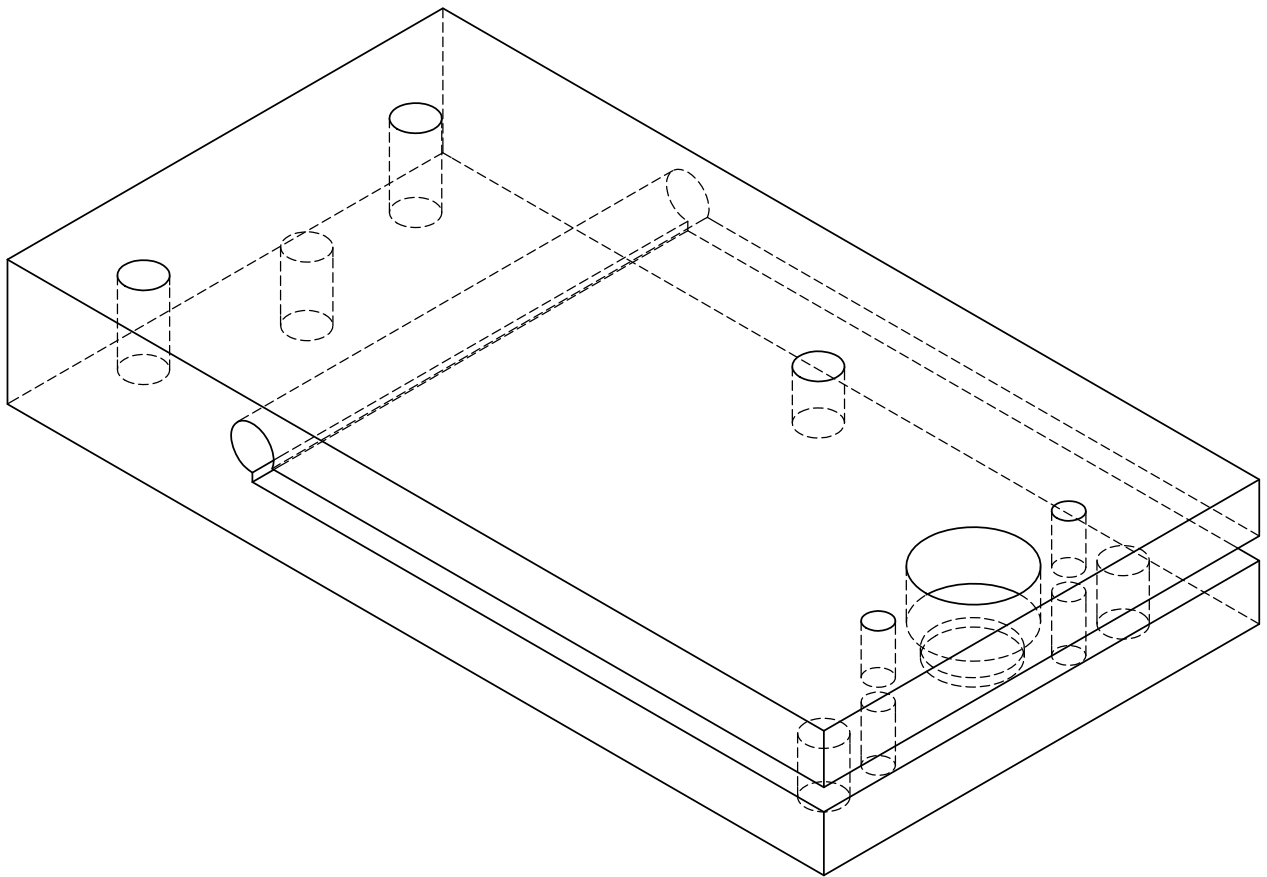
Diode Housing Page 1  
Scale = 2 : 1



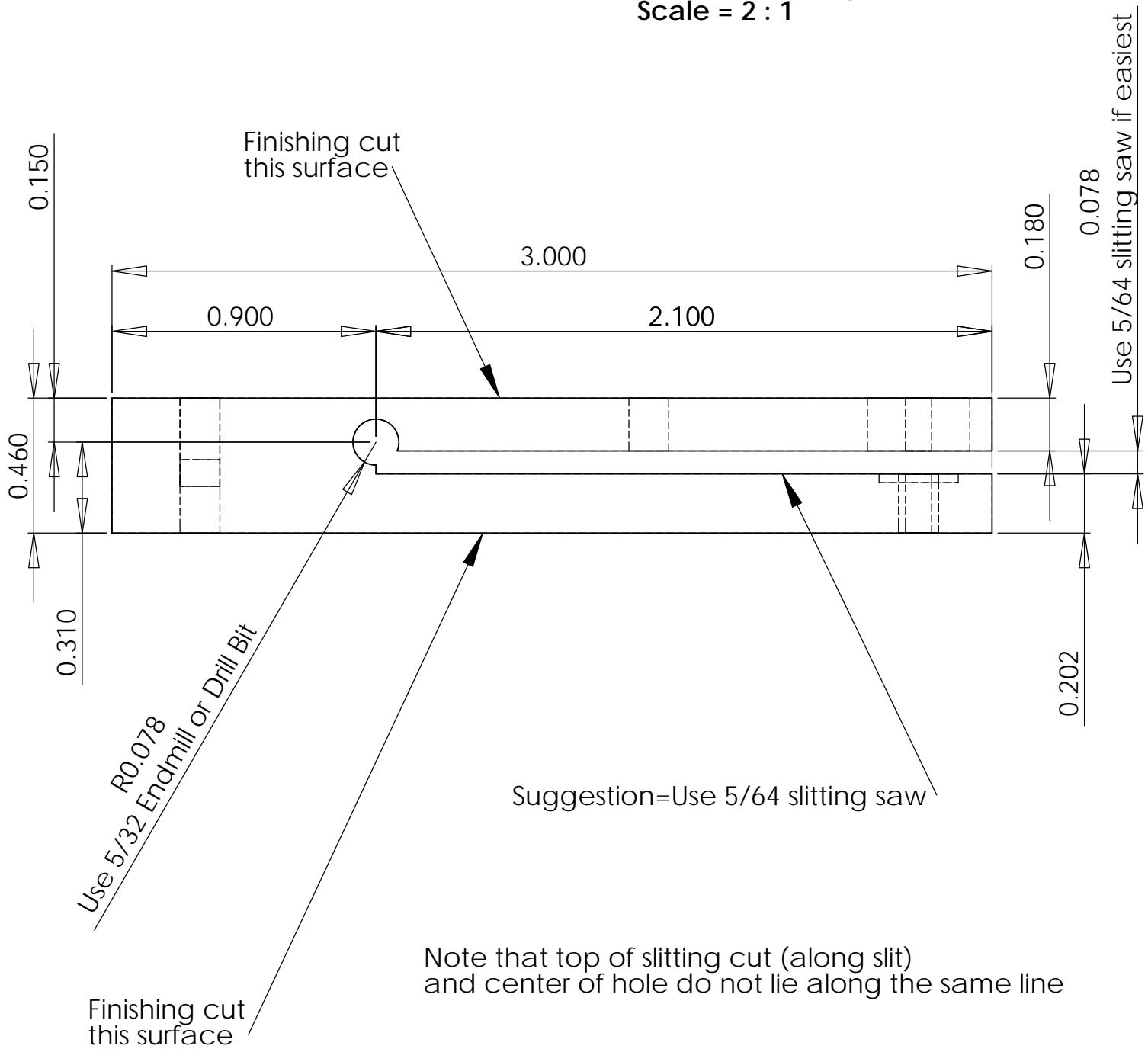


All dimensions are +/- .01  
unless otherwise noted

Base Flexure Page 1  
Scale = 2 : 1



Base Flexure Page 2  
Scale = 2 : 1

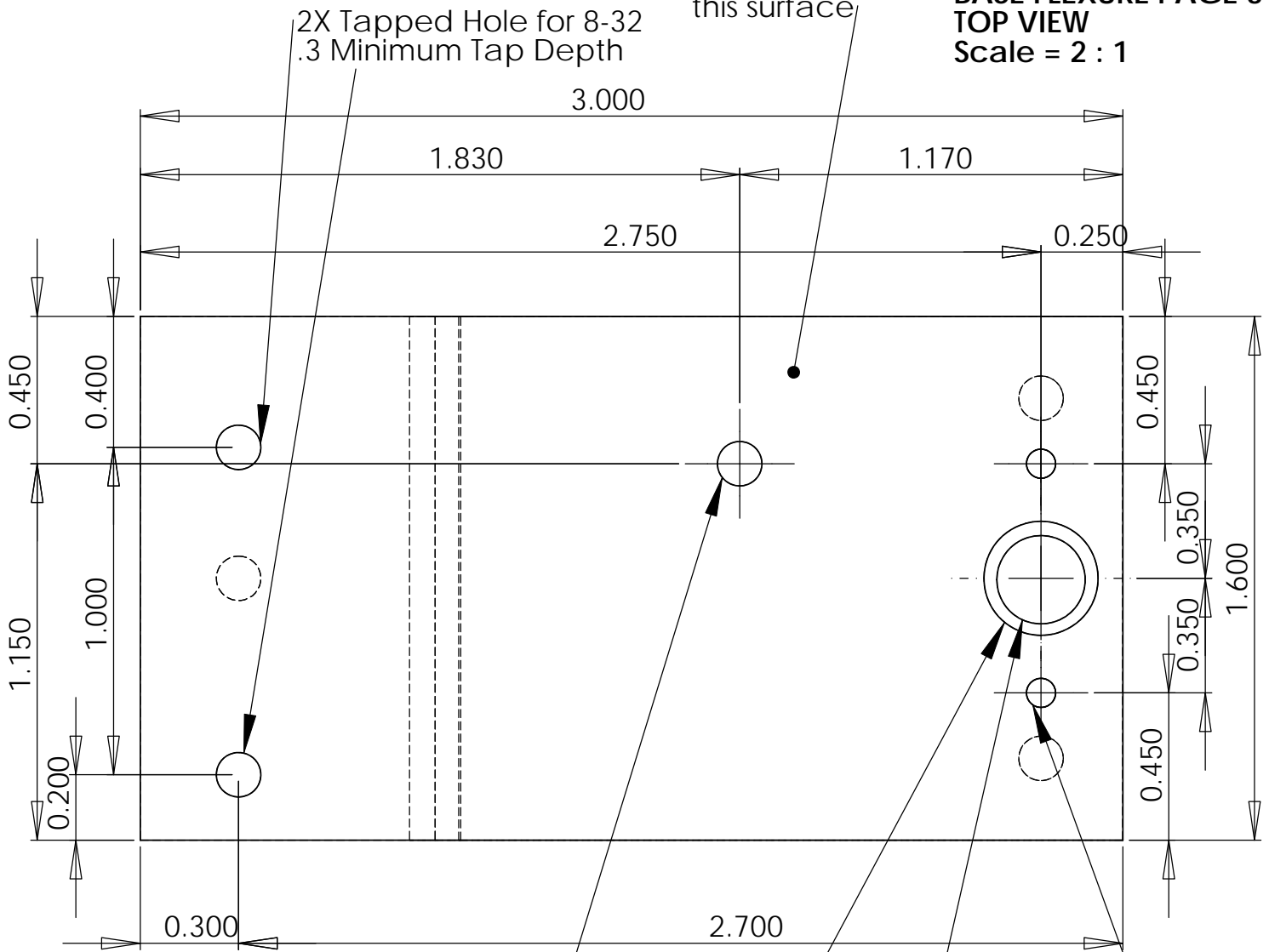


All dimensions are +/- .01  
unless otherwise noted

229

Finishing cut  
this surface

**BASE FLEXURE PAGE 3**  
**TOP VIEW**  
**Scale = 2 : 1**



Tapped Hole (To next surface)  
8-32

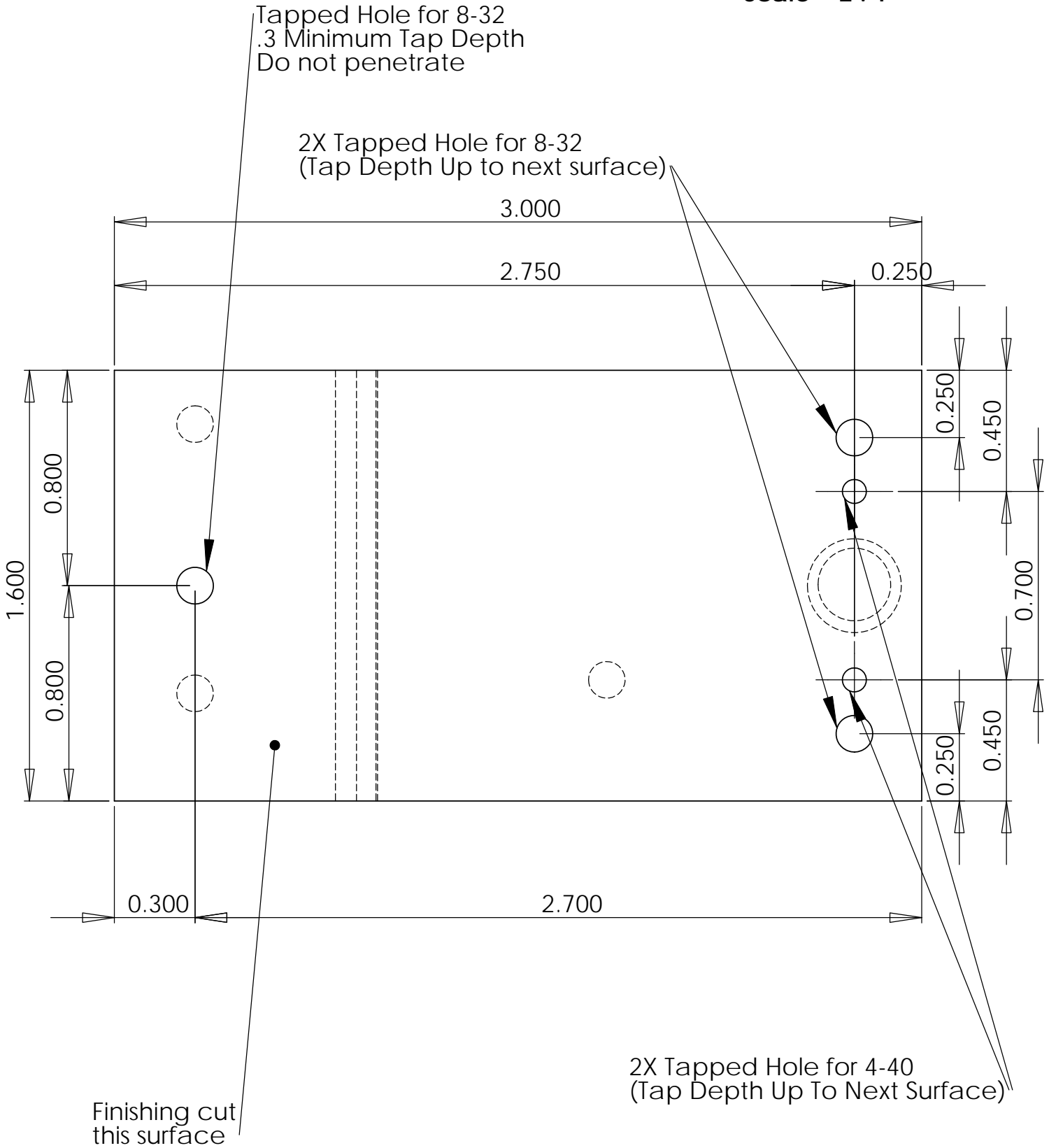
Clearance Hole (To next surface)  
(NOT TAPPED)  
Hole should have .002 of clearance  
on all sizes of bushing. This is the ideal  
clearance for the desired adhesive  
(Nominal hole size is .353 since  
part is spec'd at .349)  
Part is provided for reference

.27 diameter pocket  
.03 deep

2X Clearance Hole (To next surface)  
(NOT TAPPED)  
4-40

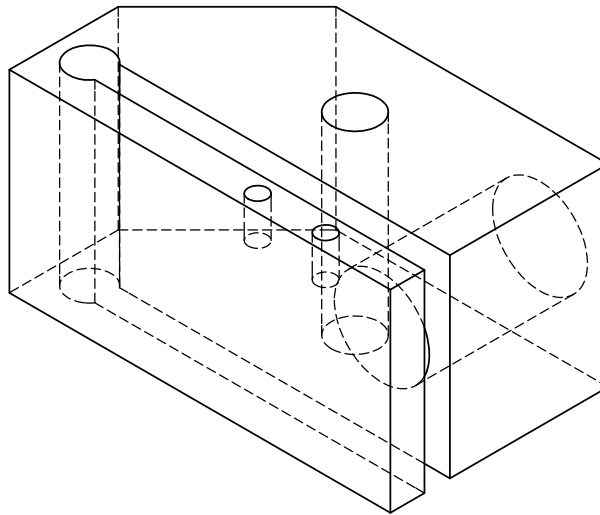
**All dimensions are +/- .01  
unless otherwise noted**

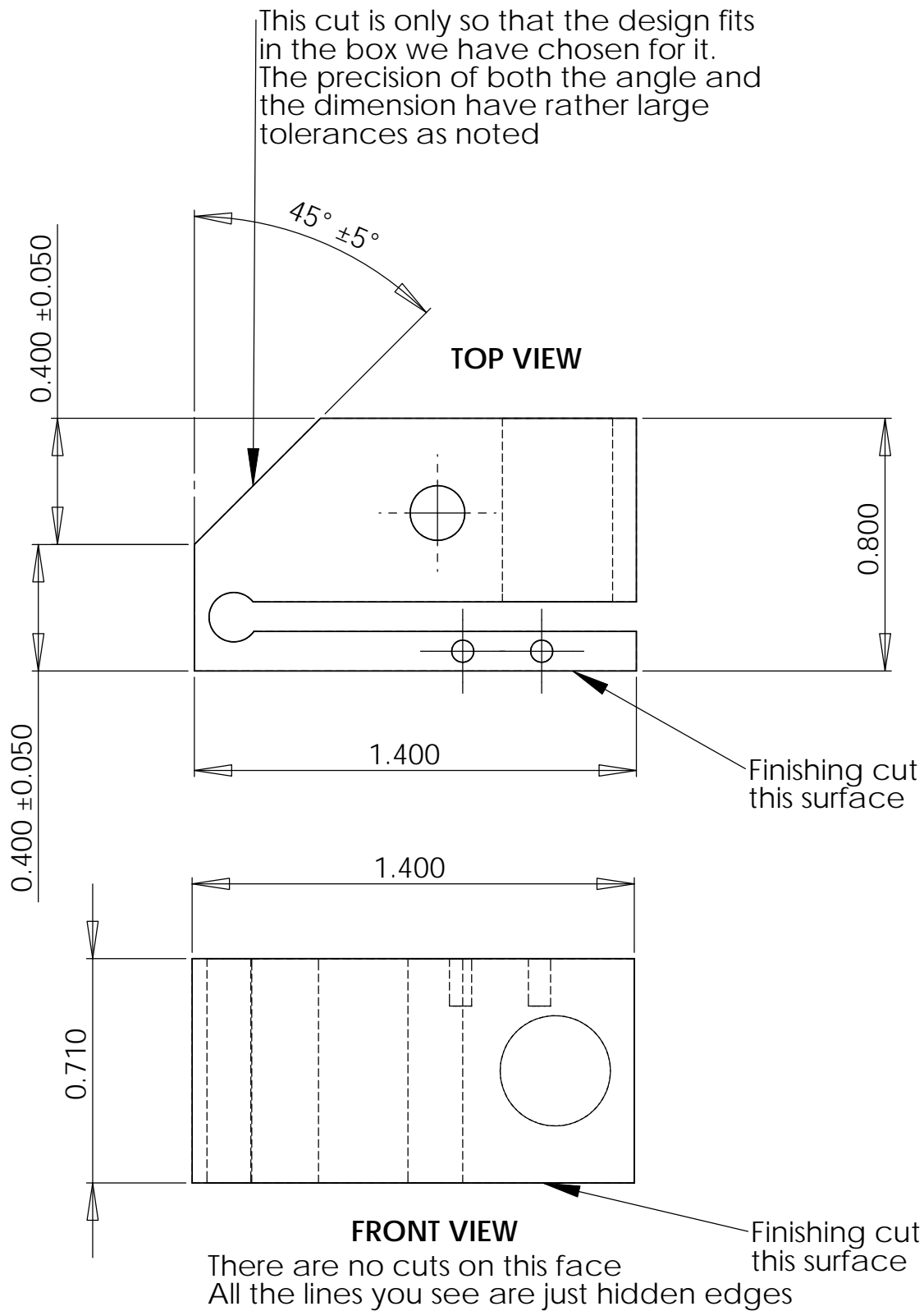
**Base Flexure Page 4**  
**Bottom View**  
**Scale = 2 : 1**



**All dimensions are +/- .01  
unless otherwise noted**

Grating Flexure Page 1  
Scale = 2 : 1





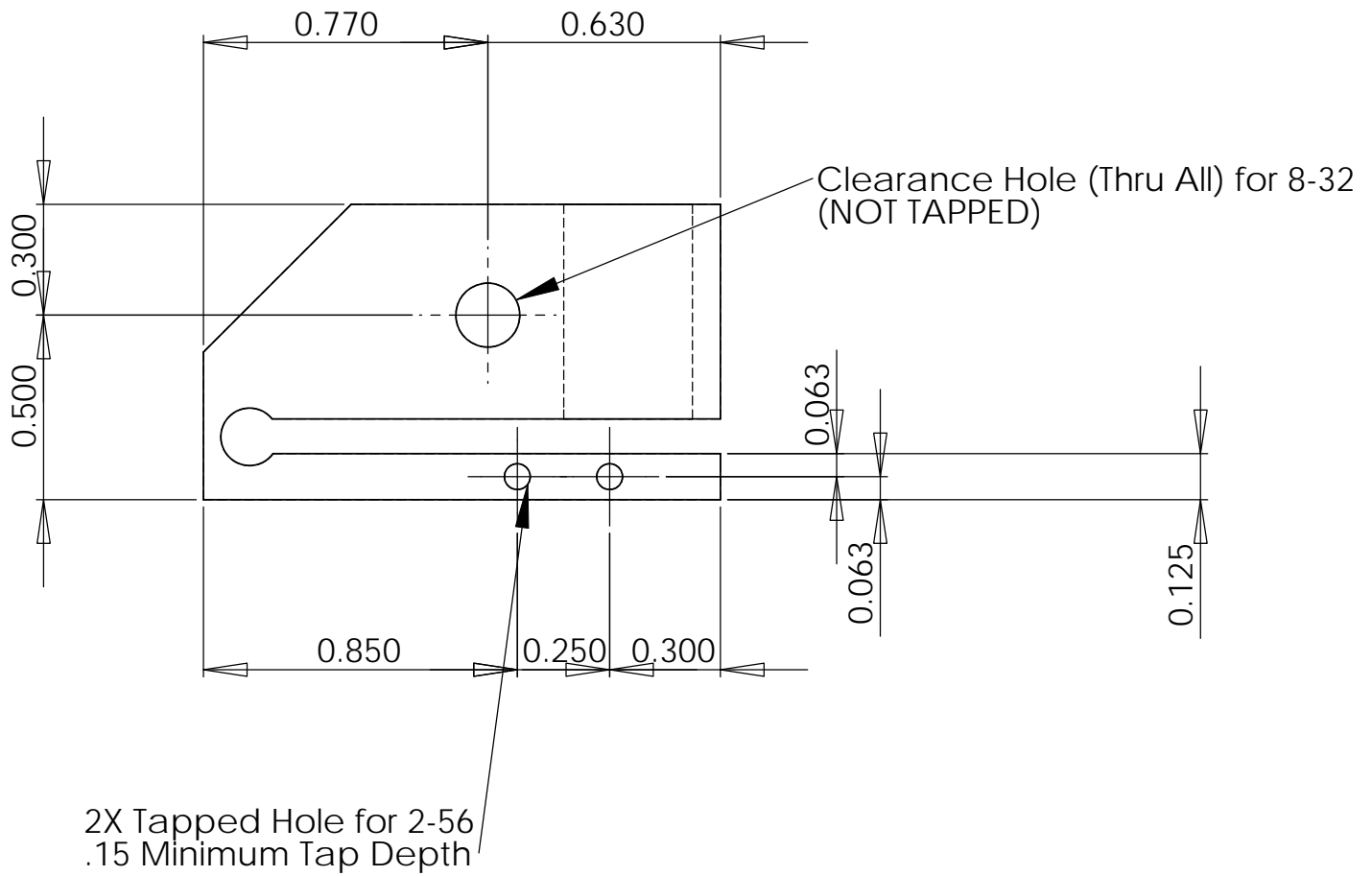
**All dimensions are +/- .01  
 unless otherwise noted**





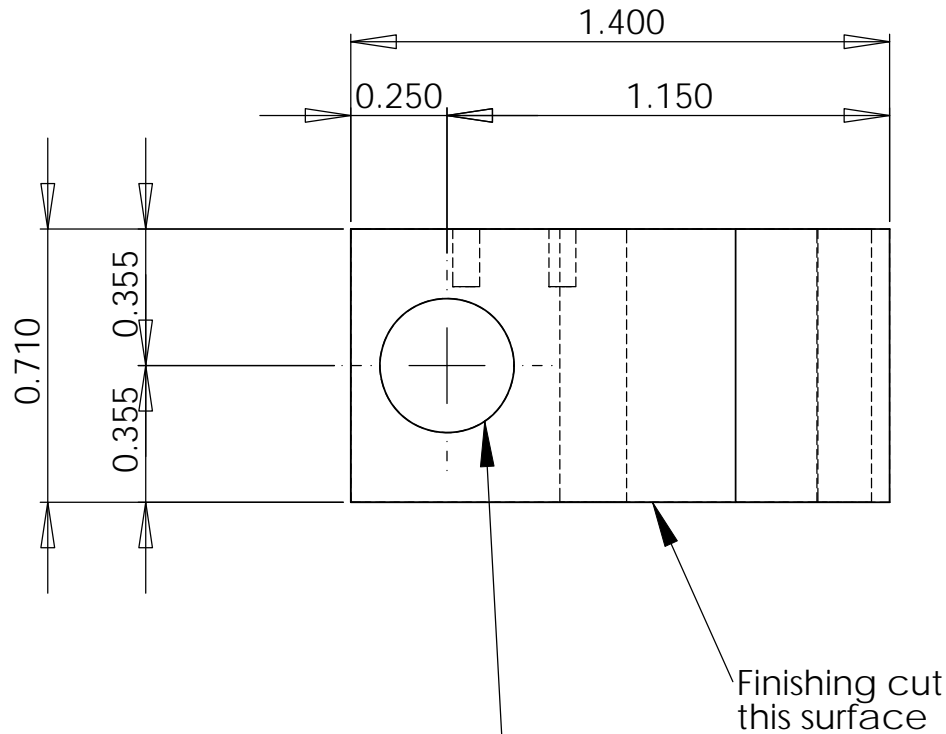
Use 5/32 Endmill or Drill Bit  
if this is easiest

Grating Flexure Page 4  
Top View  
Scale = 2 : 1



All dimensions are +/- .01  
unless otherwise noted

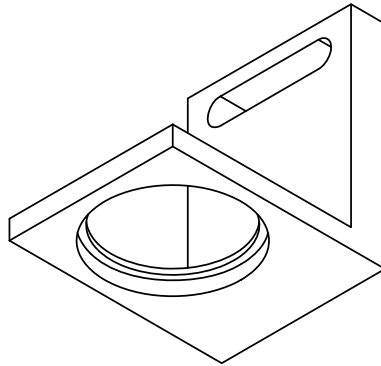
Grating Flexure Page 5  
Back View  
Scale = 2 : 1

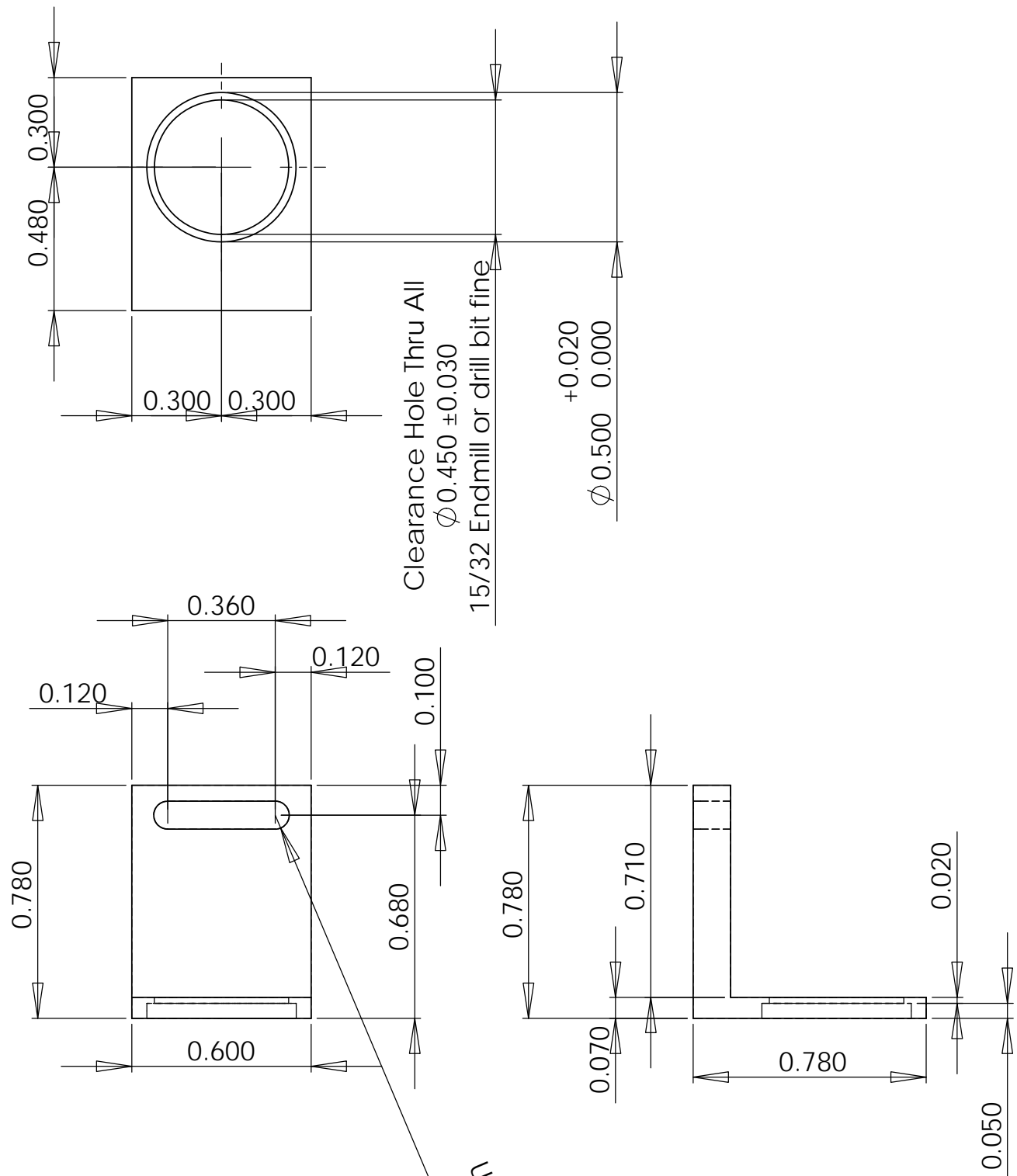


Clearance Hole (To next surface)  
(NOT TAPPED)  
Hole should have .002 of clearance  
on all sizes of bushing. This is the ideal  
clearance for the desired adhesive  
(Nominal hole size is .353 since  
part is spec'd at .349)  
Part is provided for reference

All dimensions are +/- .01  
unless otherwise noted

Beam Steering Mirror Mount Page 1  
Scale = 2 : 1





All dimensions are +/- .01  
unless otherwise noted

Part = Laser Base Version 2

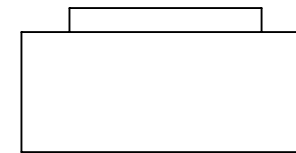
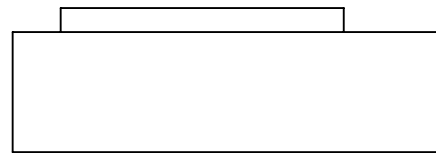
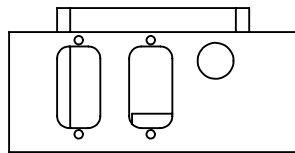
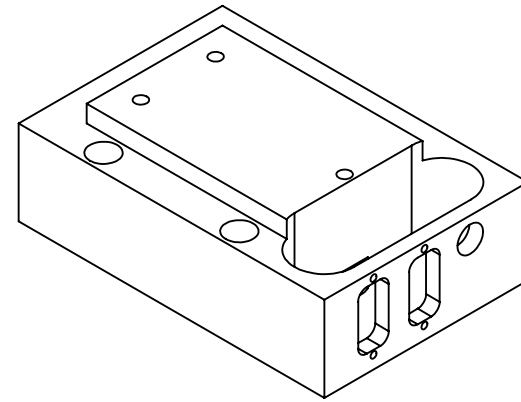
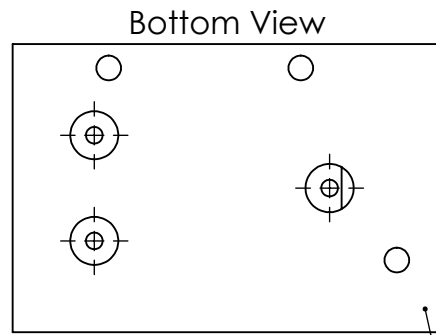
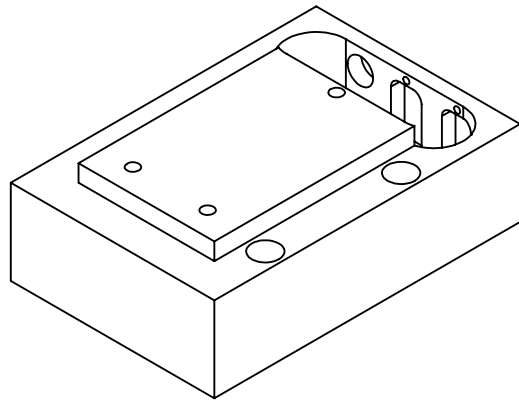
John Barry  
john.barry@yale.edu  
203 561 6060 (cell)  
203 432 3834 (lab phone)  
DeMille Group

Charging = Buffer Lab MURI

Material = Aluminum (Any)

Quantity = 3 of the following part

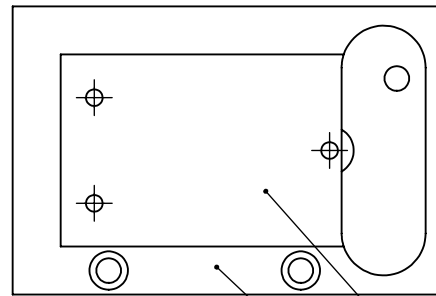
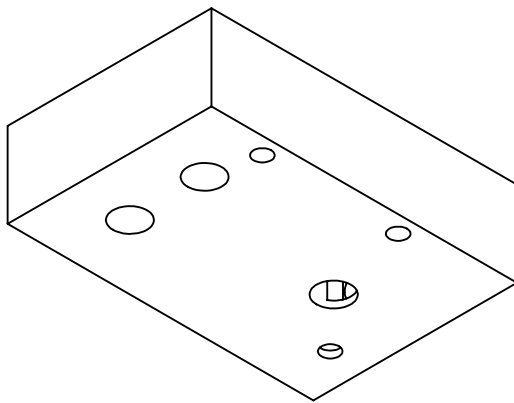
- All cuts may be rough cuts except when marked otherwise. When a specific surface finish is needed it will be marked.
- All dimensions are +/- .01 unless otherwise noted. This is written on every page that has dimensions.
- The scale on any page with dimensions is 1:1. This is written on every page as well.



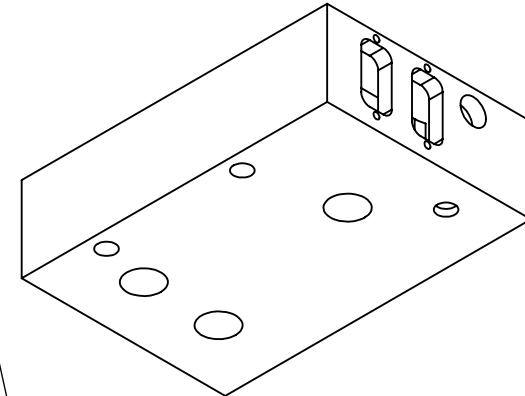
Back View

Right Side View

Front View



Top View

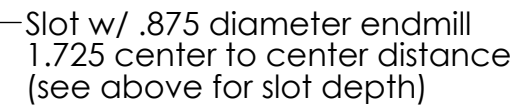


Machine Finish

Machine Finish

Machine Finish

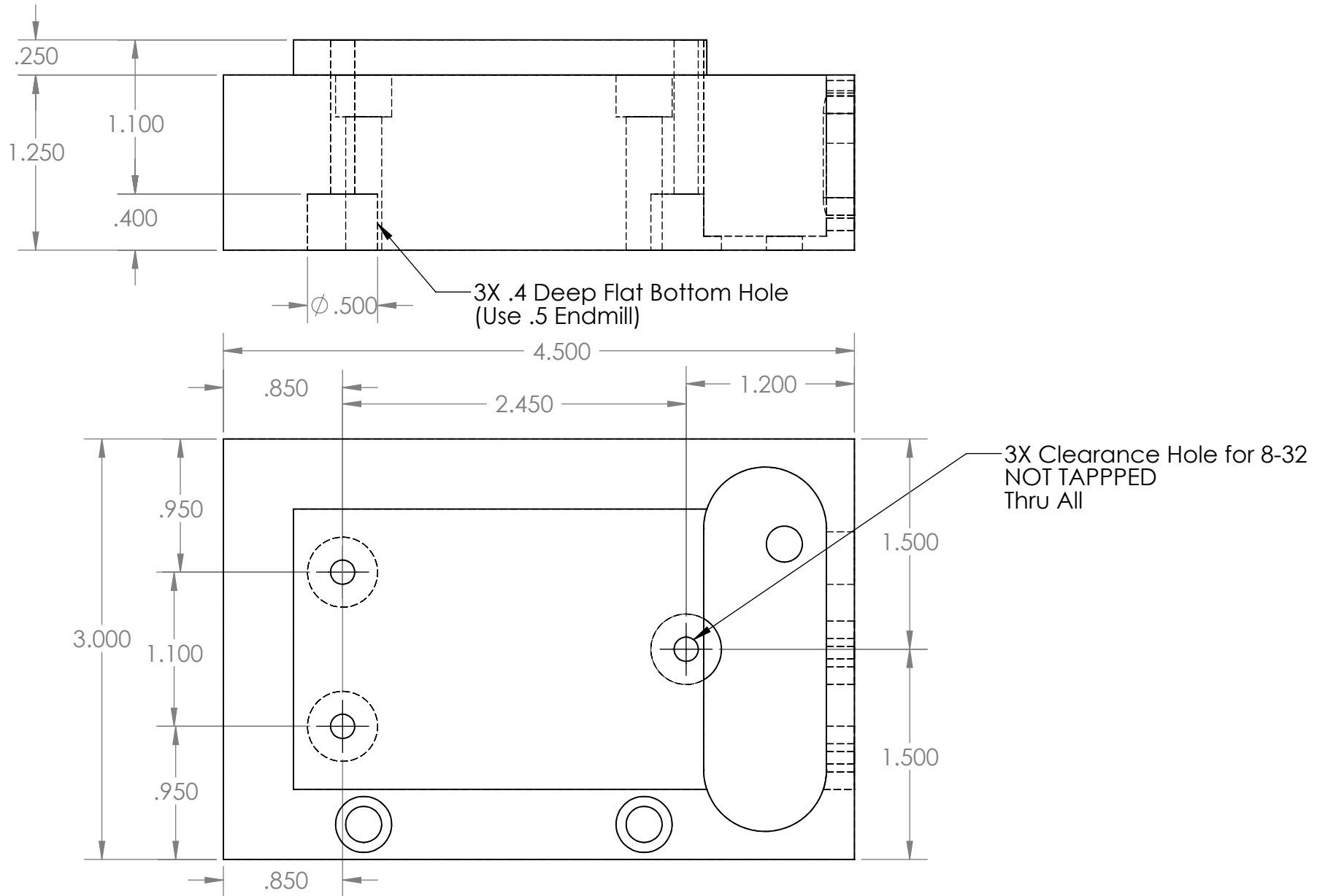
Rough finish on all other surfaces

Machine Finish-  
Machine Finish-

All dimensions are +/- .01 unless marked otherwise

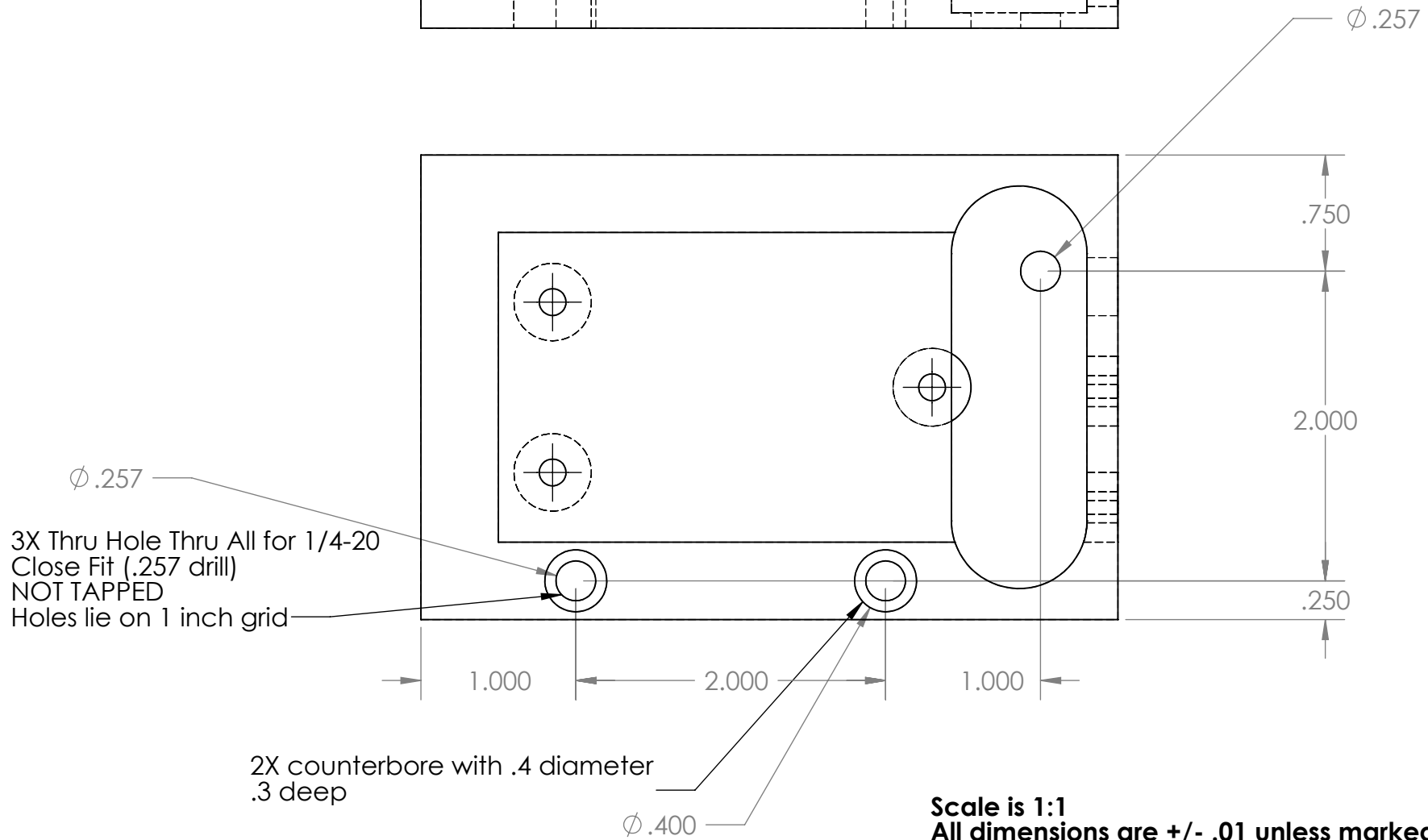
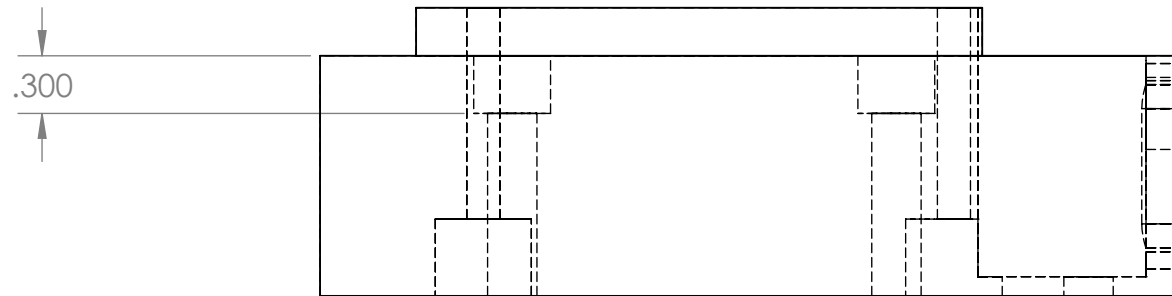


# TOP AND SIDE VIEW 2/3



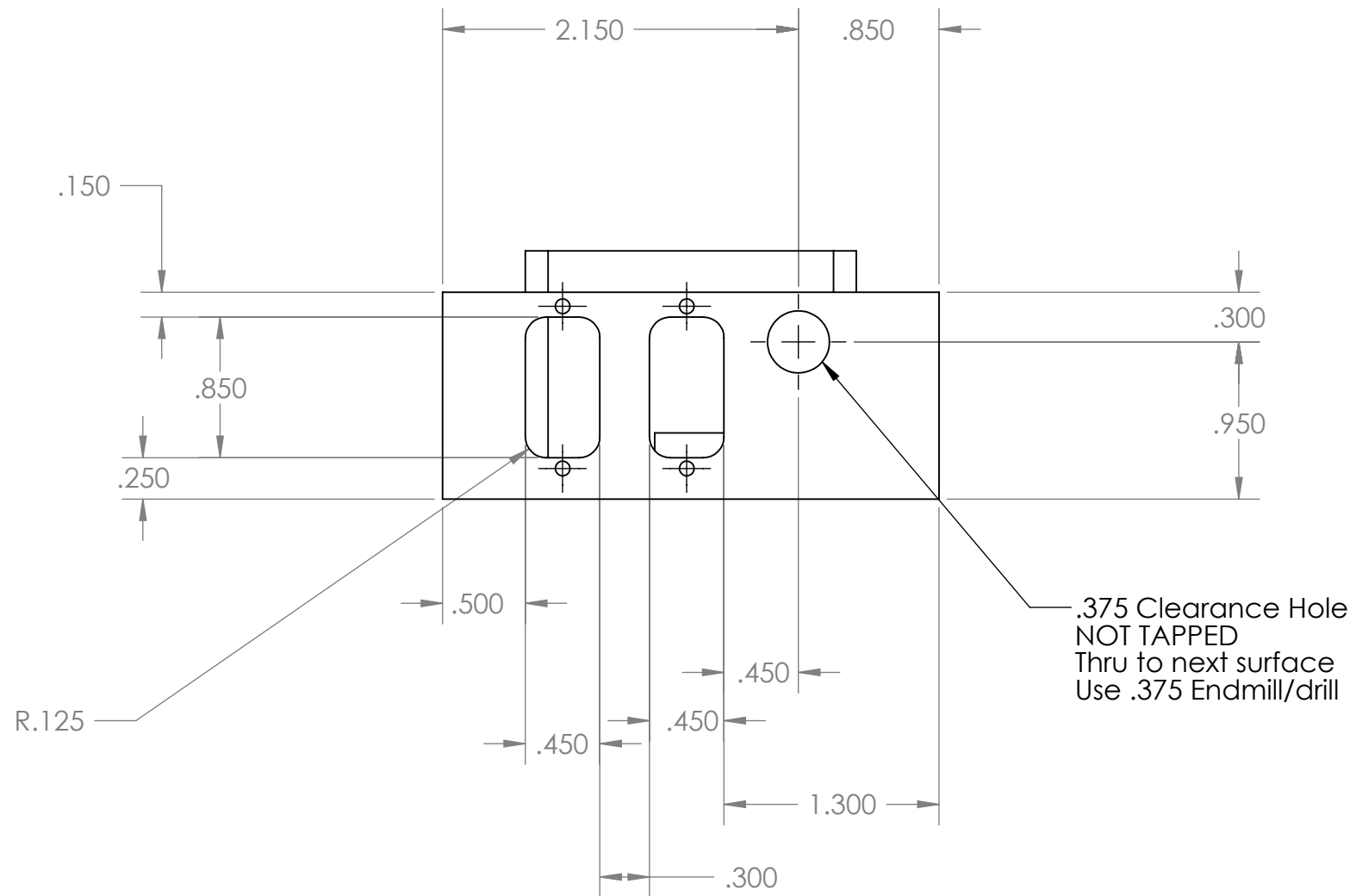
Scale is 1:1  
All dimensions are +/- .01 unless marked otherwise

# TOP AND SIDE VIEW 3/3



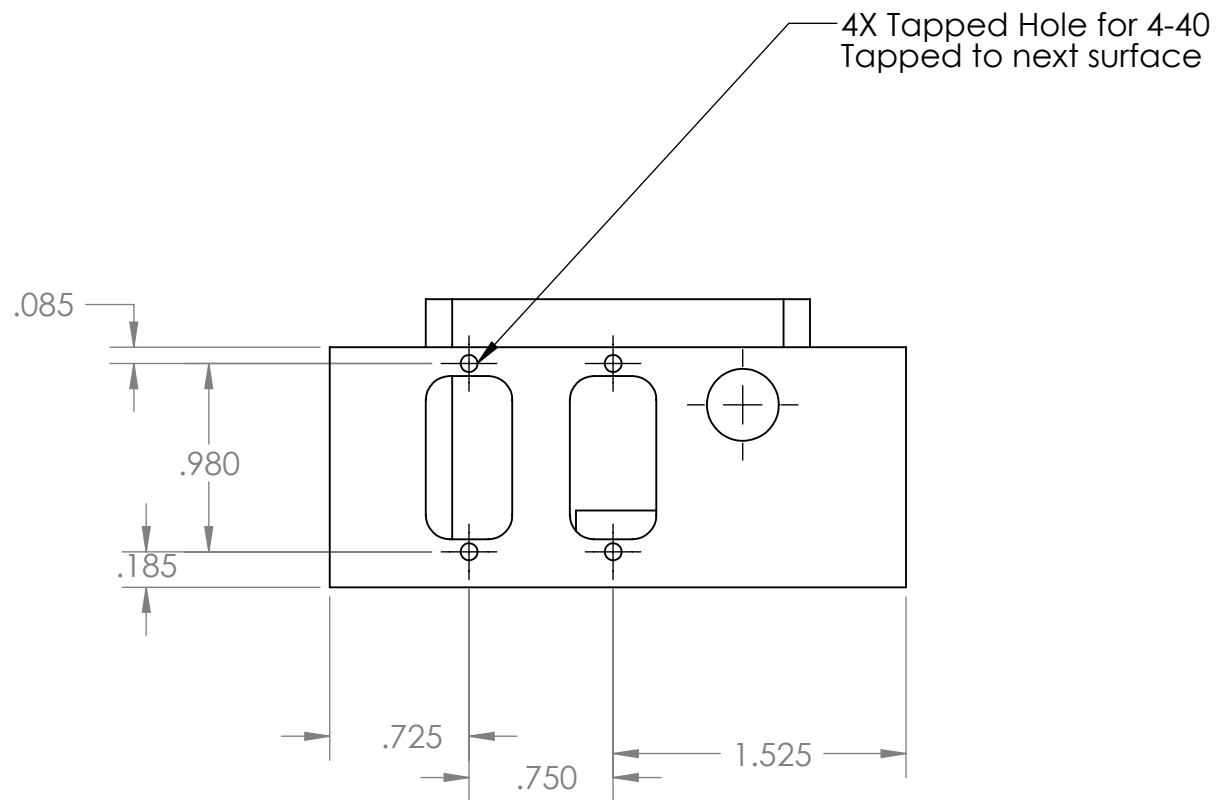
**Scale is 1:1**  
**All dimensions are +/- .01 unless marked otherwise**

## BACK VIEW 1/2



**Scale is 1:1**  
**All dimensions are +/- .01 unless marked otherwise**

**BACK VIEW 2/2**



**Scale is 1:1**  
**All dimensions are +/- .01 unless marked otherwise**

## Appendix D

# Tapered amplifier further details

This guide is not all-encompassing. You should be thinking for yourself. At least two people have built this design given only the machined brass and aluminum parts and no instructions. Those TA systems work fine. However, this guide should make building a TA system easier, faster, or hopefully both. An example datasheet for a TA from Eagleyard Photonics is given in Ref. [300].

The attached drawings are for a TA chip with a 2 mm long active region. If the active region of your TA chip is of a different length, the two tapped holes on the brass “plank” for the brass bracket used to mount the brass output collimation lens holder will have to be moved. The aluminum base for the TA is the exact same as the aluminum laser base for the ECDL.

The drawings may have to be rescaled so that the sheet scale is correct. The version of this thesis posted on the DeMille group website [298] has the appropriate scale listed on the drawing sheets<sup>1</sup> if the pdf pages are printed with no rescaling (confirm that this option is off during printing). The official version of this thesis submitted to Yale University however has margin restrictions, requiring the drawings to be shrunk and therefore the sheet scale is not valid for the official Yale version of this thesis. Updates to this design and any relevant additional material will be posted on the DeMille group website.

### D.1 Important precautions

- Do NOT run the tapered amplifier for long times without seed power. This advice comes from a Toptica TA datasheet. Although Toptica does not specify what constitutes a long time, I don’t block the input/seed light for the TA for  $\gtrsim 10$  seconds when the TA is at its full current.
- Do NOT connect the current to the tapered amplifier wrong (i.e. with the wrong polarity). Please check and recheck the polarity of the current (both the wiring and the output polarity, if any, of the current driver) with a resistor before driving current through the TA.
- Use a static wrist band.
- It is advisable not to run the TA for long periods of time without the case. Dust is attracted to the high-power output facet of the TA and keeping the case on when the TA is on should drastically reduce exposure of the TA chip to dust. Failure of this output facet is a common degradation mechanism of high-power laser diodes in general. Typically, the case is off only during the few hours when the TA is being initially set up, aligned, and injected. Afterwards, the case is always on.

---

<sup>1</sup>e.g. 1 inch on the drawing sheet corresponds to 2 inches on the part if the sheet scale is labeled as 1:2.

- TAs are turned off at the end of every day to maximize their lifetime.
- In general, both the anode and the cathode of the TA should probably be shorted together (preferably both to ground) during periods of the set-up process where the possibility of electrostatic discharge exists.

Item	Part Number	Supplier	Quant.	Unit cost	Total cost
Output coupling lens	C330TME-B	Thorlabs	1	87	87
Input coupling lens	C230TME-B	Tholabs	1	87	87
Current/temp. controller	ITC4001*	Thorlabs	1	2950	2950
Indium foil - we use 75 $\mu$ m thickness					
Thermal paste	Arctic Silver 5 (AS5)	Arctic Silver			
Thermal adhesive	Thermal adhesive (ASTA-7G)	Arctic Silver			
DB9 Male connector	L717SDE09P-ND	Digikey	1	1	1
DB9 Female connector	L77SDE09S-ND	Digikey	1	1	1
DB9 Jackscrews	1195-2600-ND	Digikey	4	.48	1.92
Thermistor	TH10K	Thorlabs	1	15	15
TEC	102-1678-ND	Digikey	1	13.45	13.45
5 or 6 360 brass machined parts					
Tapered amplifier chip					
Aluminum blank for laser base	9057K78	McMaster	1	87.66	87.66
2" wide acrylic for case sides	1227T439	McMaster	1	22.08	22.08
3" wide acrylic for case top	1227T459	McMaster	1	16.36	16.36
3/32" diameter 0.25" long brass pin	97325A115	McMaster	1		
Shoulder washer	97325A115	McMaster	1		
4-40 .75" screws	92185A112	McMaster	8		
8-32 1.0" screws	92185A199	McMaster	4		
4-40 washers	96659A101	McMaster	16		
4-40 3/16" set screw w/ nylon tip	90291A105	McMaster	2		
4-40 3/16" set screw w/ metal tip	92158A121	McMaster	10		
8-32 1.25" plastic screws	95868A201	McMaster	3		
M2.5 6 mm long screws	92290A056	McMaster	2		
8-32 button cap screw	92949A187	McMaster	1		
M2 screw for TA chip	91613A031	McMaster	1		

Table D.1: Parts list for home-built TA. Unit cost is in dollars. \*There are multiple options from Thorlabs for this part. Although no longer sold, we have used Thorlabs ITC510 or a combination of Thorlabs TED350 and Thorlabs LDC340 as well.

## D.2 Partial assembly instructions

1. Sand all surfaces so they are smooth and flat. I sand the surfaces with up to 2000 grit sandpaper. Clean all mating surfaces with acetone. Good thermal contact between parts is critical to turn the TA on and off with minimal shift of the output beam.
2. Arctic Silver thermal epoxy should be used to put the thermistor in the thermistor mounting hole on the side of the brass plank. Care should be taken to avoid air bubbles in this hole, as air bubbles will increase the thermistor response time. Make sure the thermistor wires do not stick out too much. Otherwise it will be hard to put the case on. After installation, check that the thermistor is neither shorted nor open and that the case can easily be put on and off.
3. Arctic Silver thermal paste (not epoxy) should be applied in a thin layer between certain parts. I usually apply this thermal paste using a razor blade and then rub the parts together in a circular fashion. If you do this correctly, the two parts will stick together with surprising force. It is important to remember that the thermal conductivity of thermal paste is generally much better than air, but much worse than brass (and most common metals). Hence, a thin layer of thermal paste with no air bubbles is ideal. The Arctic Silver thermal paste should be applied in the following places:
  - Between the aluminum base and the TEC.
  - Between the TEC and the brass plank.
  - Between the rectangular brass bracket that holds collimation lens holders and the collimation lens holders themselves. Both of these pieces must be put on after the TA chip and round TA mounting bracket are fully installed and wired.
4. Once the Arctic Silver thermal paste is applied, clean up any visible thermal paste. If you can see the thermal paste, it isn't doing anything anyway. You do not want thermal paste getting on your gloves or any exposed surfaces, since it can then get on optics or even worse, the TA input/output facet. I typically use a combination of Q-tips, Kimwipes, and methanol to remove excess thermal paste.
5. The brass plank, TEC and aluminum laser base are held together by three nylon 8-32 screws. The screws are nylon so that the ground of the TA is not electrically connected to the aluminum base and is therefore isolated from the optics table. Unfortunately, the plastic screws are often not as rigid as desired. For further stability without electrical contact, little "drips" or "pyramids" of 5- minute epoxy mechanically connect the corners of the brass plank to the aluminum laser base.
6. Indium should be used to increase the thermal contact between the following:
  - Between the brass plank and the round TA mounting bracket. The round TA mounting bracket must go on the brass plank before any of the collimation optic holders or related parts.
  - Between the brass plank and the rectangular brass brackets that hold the brass collimation lens holders. The rectangular brass brackets and the brass collimation lens holders must be put on only after the TA is mounted and wired.
7. When viewed from the side of the seed light, the temperature/TEC control DB9 should go on the right-hand side of the laser base. The current driver DB9 goes on the left-hand side. Tape over the BNC hole with aluminum tape since it is typically not used for the TA. Label each connector. Follow the male/female convention of the Thorlabs TCLDM9 mount, i.e. the TA current driver receptacle on the laser base is female while the TA temperature/TEC receptacle on the laser base is male.
8. The TA is held to the round TA mounting bracket by an M2 screw. This screw needs to be short. Thin indium increases thermal contact between the C-Mount TA chip and the round TA mounting bracket.

### D.2.0.1 Temperature protection

It is helpful for the TA current driver to employ a temperature protection interlock. This turns off the TA current if the temperature of the TA goes outside a pre-defined temperature window, which offers protection in case the temperature stabilization fails. You don't want water condensating on your TA.

## D.3 TA electrical connections

### D.3.1 Tapered amplifier protection circuit

It is prudent to test the TA electronics and protection circuit (see [subsection 4.4.4](#)) prior to installing the TA chip. Our 663 nm TA can be simulated by a  $3\Omega$  resistor. The 663 nm TA takes a maximum of 1 amp and has a voltage drop of  $\sim 2.5$  volts, equivalent to 2.5 watts. If a  $3\Omega$  2.5 watt resistor is not available, you can make one from several higher resistance, lower-wattage resistors combined in parallel. Use this  $3\Omega$  2.5 watt resistor to test the TA protection circuit. In our implementation, the TA protection circuit is housed in a small plastic box ( $\sim 2'' \times 1.5'' \times .25''$ ) to prevent shorting of the TA protection circuit with any metal on the laser base or elsewhere.

The design presented here works both if the user buys the individual C-Mount TA chip alone or buys a TA chip which is mounted on a specific commercial mount (Eagleyard Photonics, EYP-MNT-0000-00000-0000-CRM14-0001 [301]). Buying the TA chip pre-installed on the Eagleyard CRM mount eliminates machining of a custom part, allows the manufacturer to install the chip on the mount with the proper indium and screw force, and reduces overall user handling of the TA chip. Procedures differ slightly depending on which of the two options are chosen. I prefer Eagleyard to mount the TA chip on their CRM mount, although there is at least one complication related to this mount discussed shortly.

#### D.3.1.1 TA pre-mounted by Eagleyard

The original design assumes (incorrectly) M2 thru holes in the Eagleyard CRM mount. When the mount arrived, the holes were instead tapped for M2-threaded screws. We therefore wished to slightly enlarge the M2 tapped holes to M2 thru holes. Initially, we hoped to remove the TA chip from the mount to perform this modification. The TA chip is mechanically affixed to the CRM mount by a screw (easily removed) and also by solder which connects the TA flag to a pin on the CRM mount. According to Eagleyard, unsoldering this connection is possible. They recommend applying  $300^\circ\text{C}$  for 10 seconds to the TA flag. However, higher soldering temperatures may cause the tiny wires which attach the strain-relieved flag to the active region of the TA to become unsoldered. Soldering may also contaminate the TA input/output facets. While attempting to unsolder this connection, I blew ultra-high-purity He gas over the face of the TA chip which was also protected from contamination using Kapton tape. However,  $300^\circ\text{C}$  for 10 seconds was not enough to melt the solder on the TA flag contacted with the mounting pin. In an effort not to damage the TA chip, we did not investigate desoldering further. Ultimately, I carefully enlarged the two tapped M2 holes to M2 thru holes with a manual (human-powered) hand drill. I used drill numbers #40, #38, #36 successively. The above operation was performed with the TA chip still affixed to the CRM mount, which made this a very delicate operation. The next generation design might have smaller tapped holes in the brass plank instead.

For the TAs which come on the CRM mounts, the cathode pin was connected using the metal inside of a jumper (Digikey S9001-ND or similar). This worked pretty well.

#### D.3.1.2 TA chip alone on home-made mount

If the TA chip is obtained from a vendor other than Eagleyard, a homemade version of the Eagleyard CRM mount must be machined and used since Eagleyard does not sell the CRM mount without a TA chip. Caution: I do not recommend the following solution, although it has been implemented successfully several times by other people in our lab although it has failed at least once. Cut the



3/32" diameter brass bar to the appropriate length. Solder the black anode wire to this pin. Insert the pin into the round homemade TA mounting bracket using the plastic shoulder washer. Check to make sure the brass pin is insulated from the brass TA mounting bracket. It may be helpful to add a little 5-minute epoxy to ensure that the pin remains in place. Once the TA chip is subsequently mounted on the round TA mounting bracket, slightly bend the TA flag so that the flag slightly pushes against the brass pin. Epoxy the flag to the pin with electrically conductive epoxy.

#### D.3.1.3 Wiring

As with all C-Mounts, the TA chip is almost certainly anode grounded (although this should definitely be checked). The (anode) grounding wire should be green. It is probably best to attach the anode wire to the round TA mounting bracket. For the homemade mount, this is done with the 8-32 button head screw (which can be screwed into the .157" hole opposite the hole for the TA flag) and a ring terminal. For the Eagleyard CRM round TA mounting bracket, this is done by clamping the anode wire under a washer under one of the screws that affixes the round CRM TA mounting bracket to the brass plank (I use the screw on the side opposite the TA flag). Both anode and cathode wires are strain-relieved with epoxy.

## D.4 Miscellaneous details

The brass brackets are attached to the brass collimation lens holders with 4-40 screws. If the screws are too tight, the brass collimation lens holder will not be able to translate. If the screws are too loose, thermal conductivity may suffer. Two washers are always used for these 8 screws.

### D.4.1 Tapered amplifier case

The case for the TA is the same as that for the ECDL and consists of two long sides (2X 4.5" × 2" × .5", cut from a 2" × .5" acrylic bar), two short sides (2X 2" × 2" × .5", cut from a 2" × .5" acrylic bar), and a top (3" × 4.5" × .5", cut from a 3" × .5" acrylic bar) which are held together with 5-minute epoxy. Historically, we have not used windows on the TA case and have instead drilled ~ 7 mm holes in the plastic case for both the seed light and the output light. After the TA is wired, tested and the case is made, the TA is turned on at low current and the spots where the amplified spontaneous emission (ASE) hits the case are marked and subsequently drilled out. If one desires the TA to have windows (to protect from dust for example), Thorlabs WG11050-B or a similar window is probably a good choice. These windows can likely be epoxied onto the acrylic case described above. Brewster windows are another option.

A nylon-tipped set screw holds the collimation lenses in place. However, this screw tends to distort the angle of the lens, causing the input and output beams to not be exactly horizontal. For the input (seeding) lens this wasn't a problem (that I felt obviously affected me) since the input mirrors can compensate for any slight deviation from horizontal. However for the output lens, this could limit the ability to align the TA light through an optical isolator without using mirrors (the elimination of unnecessary mirrors between the TA and the isolator is highly desirable to reduce thermal drift). I folded some thin indium up and put it under the brass bracket that holds the brass collimation lens holder. This worked fairly well but a more elegant solution would be welcome for future iterations.

## **Part = Brass Tapered Amplifier**

John Barry  
203 561 6060  
john.barry@yale.edu  
DeMille Group

Charging = ARO

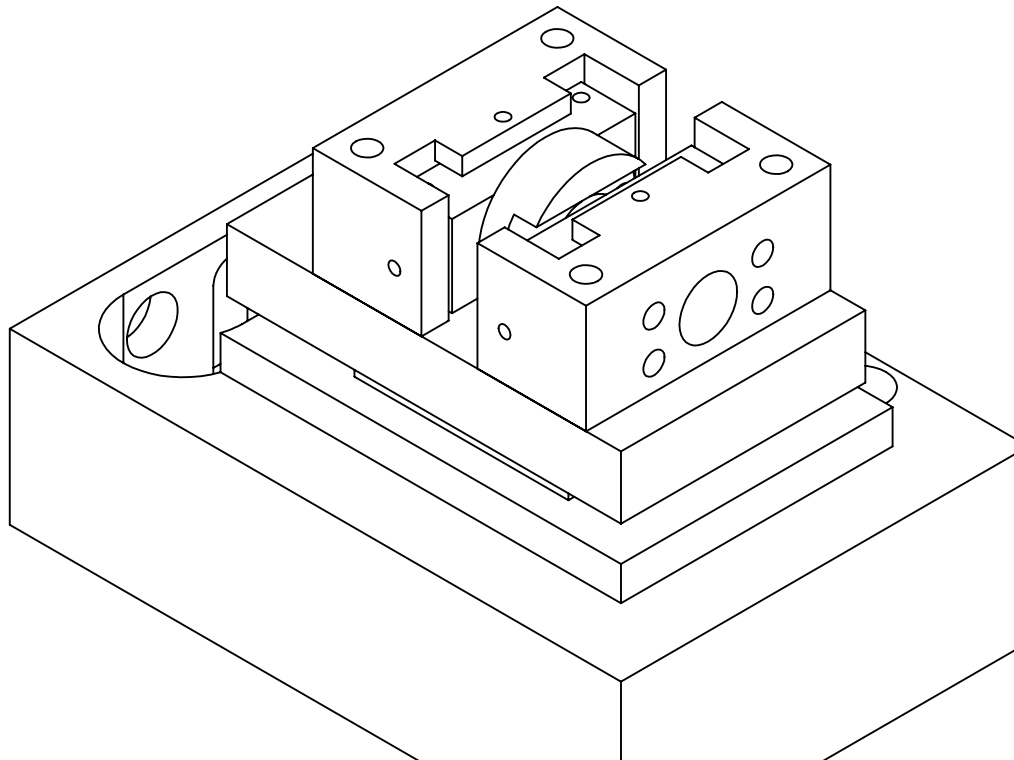
**Matrial = 360 Brass**

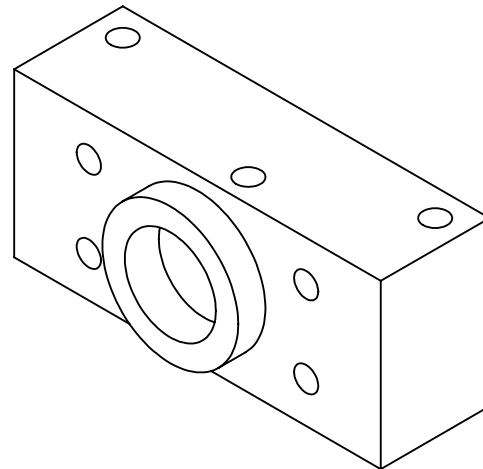
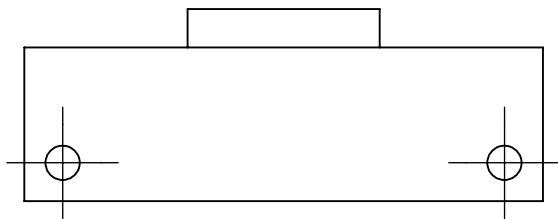
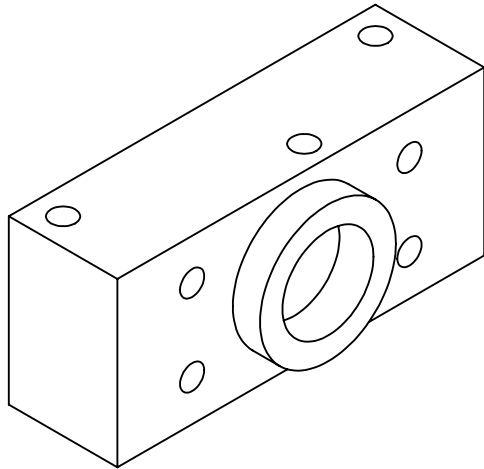
**Thermalized Base ==> Quantity = 1**

**Fixed Collimation Lens Part ==> Quantity = 2**

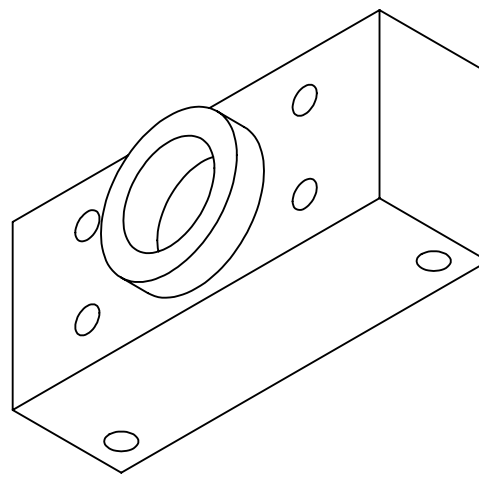
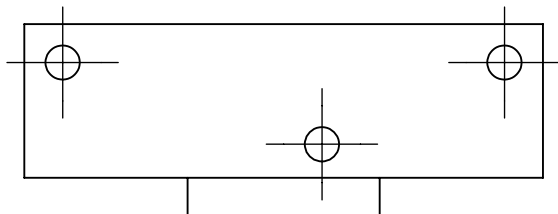
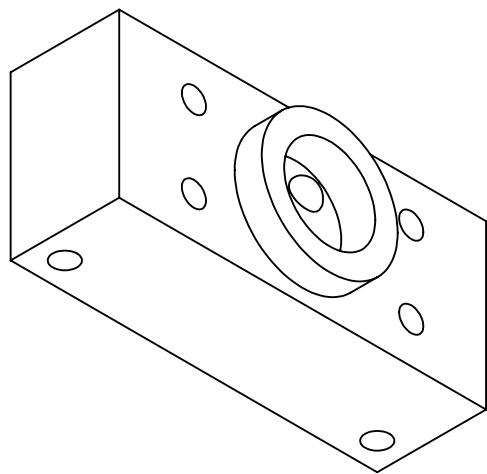
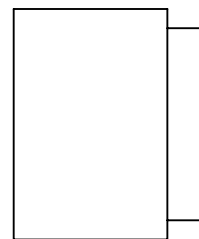
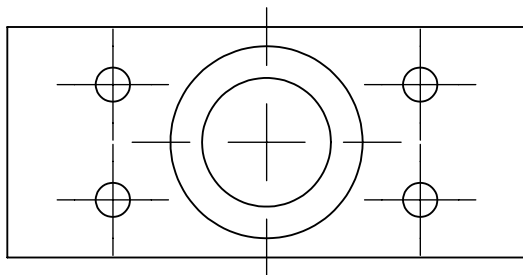
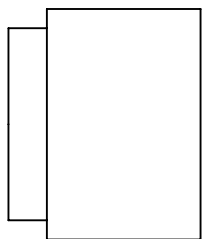
**Movable Collimation Lens Part ==> Quantity = 2**

- The scaling of each part is written on the drawing page for the part
- Any surface mating with another surface needs a machine finish. These are marked
- Regarding the M9x0.5 mm thread for the lens==> Ideally the lens will both be held well and will turn smoothly.



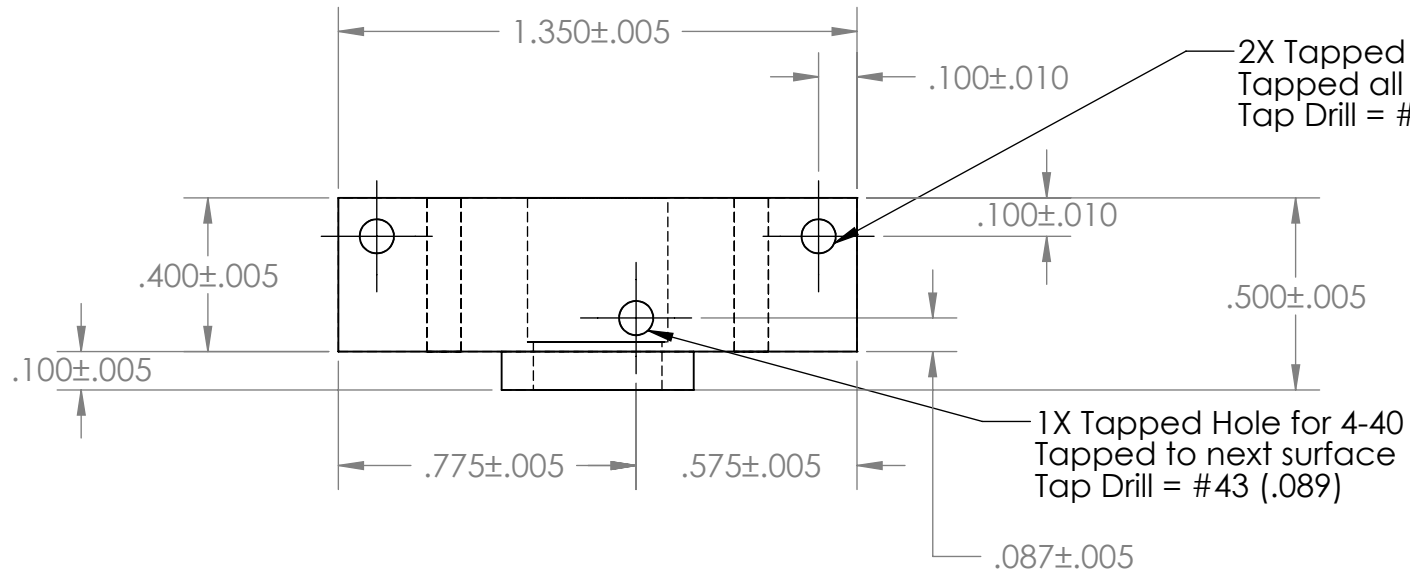


**Movable Collimation Lens Part**

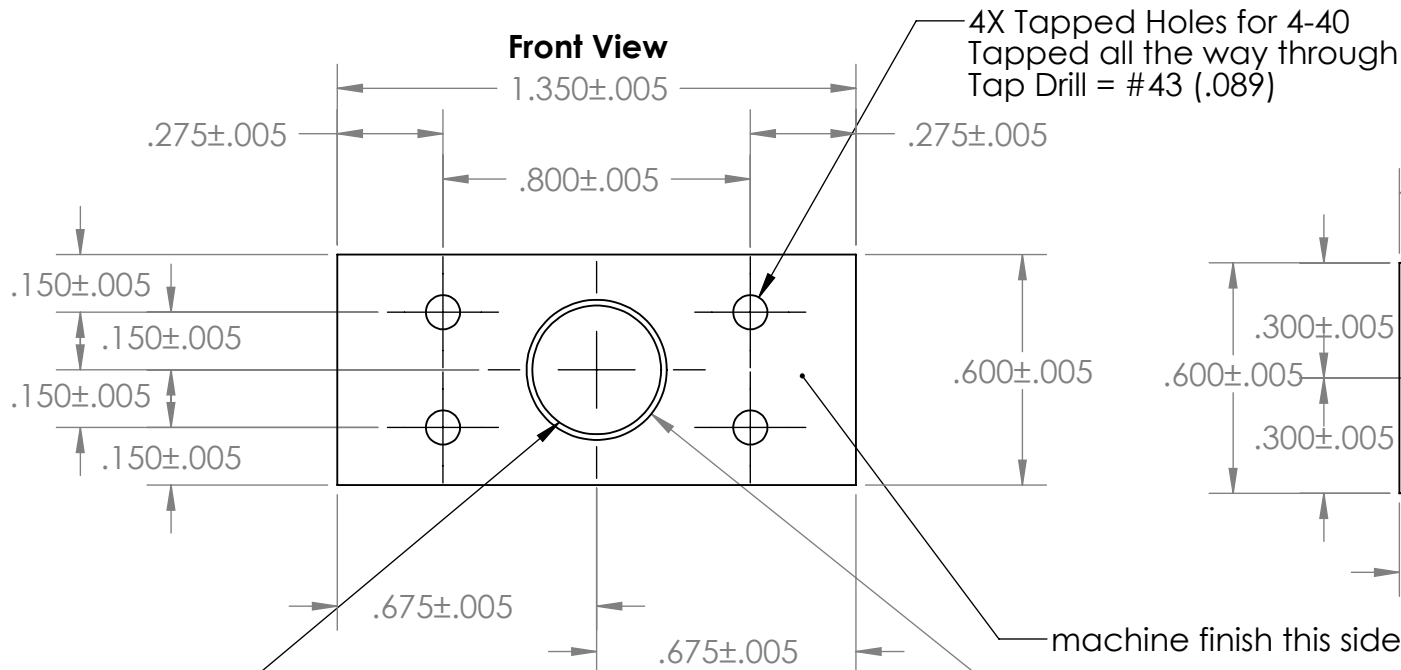


### Top View

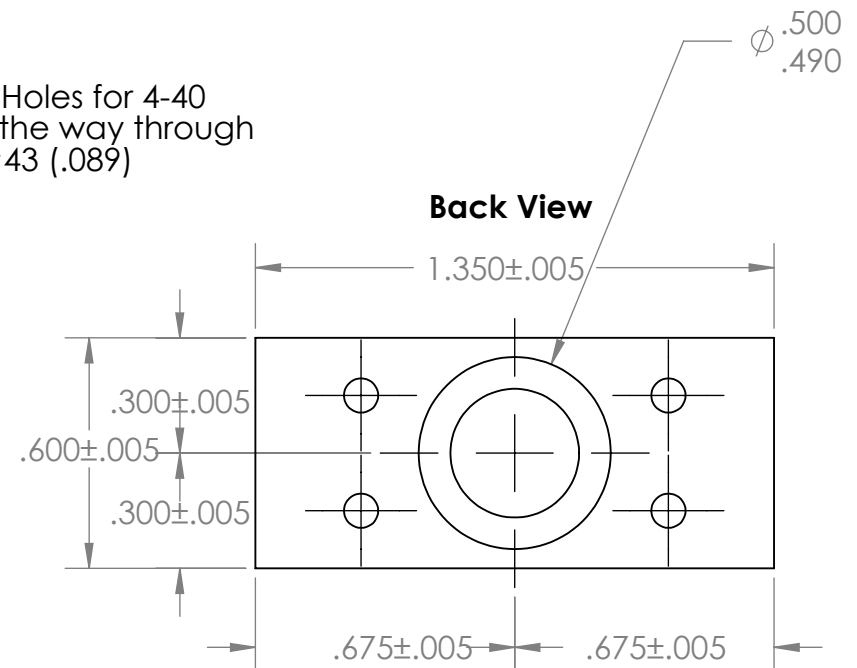
**Scale = 2:1**



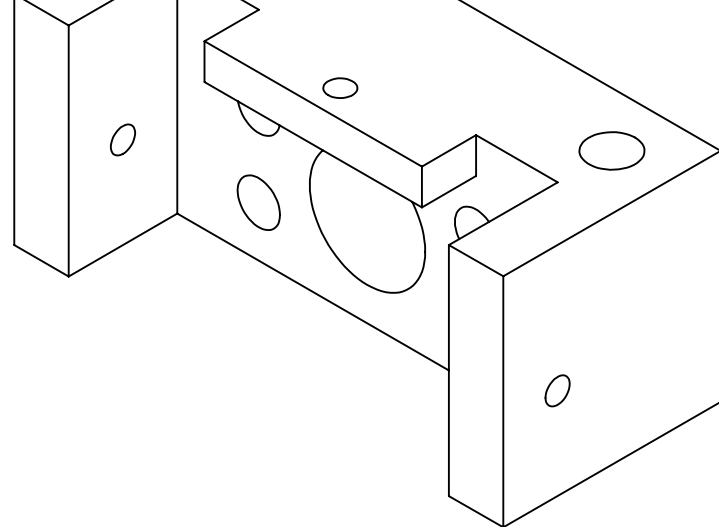
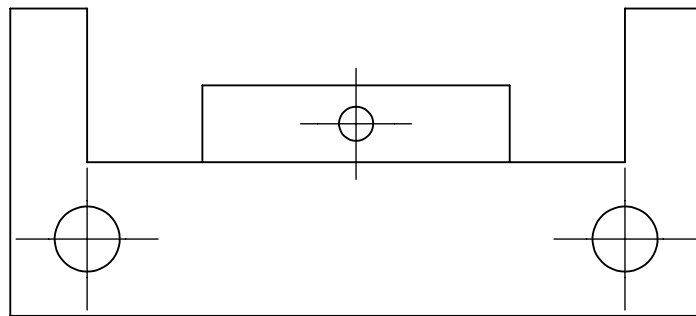
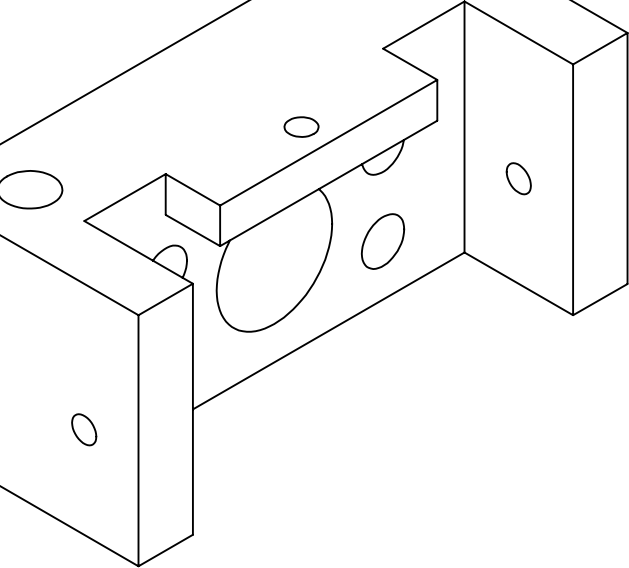
**Except for single off axis 4-40 tapped hole, the part is left/right and up/down symmetric**



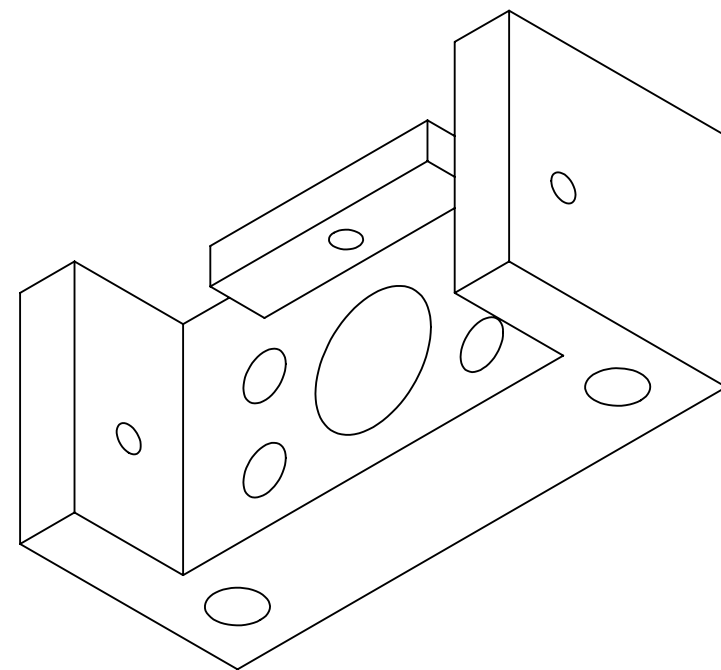
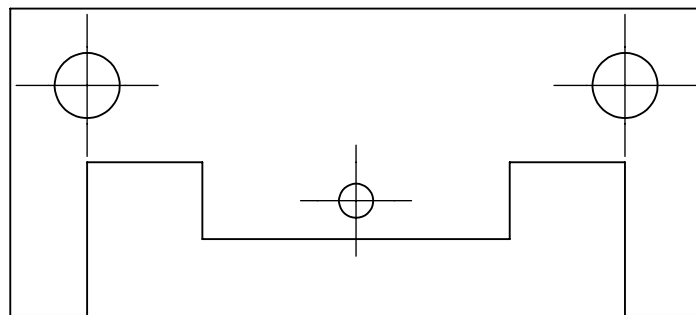
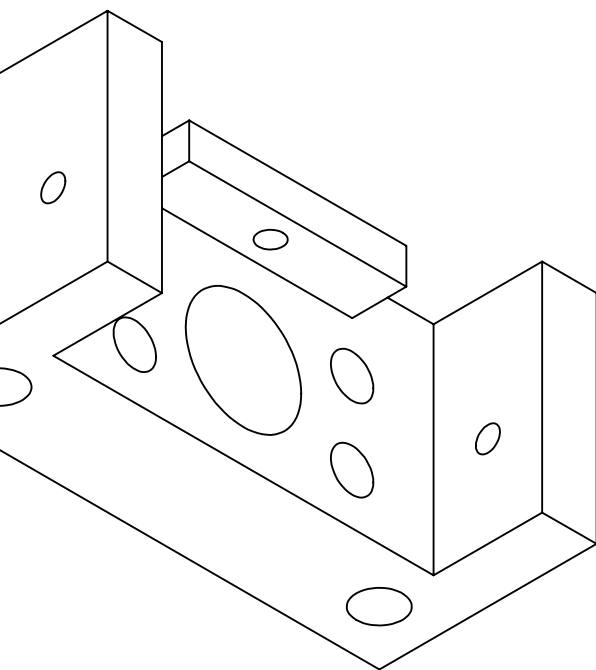
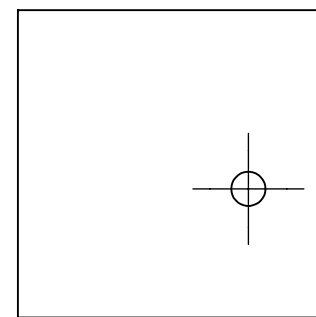
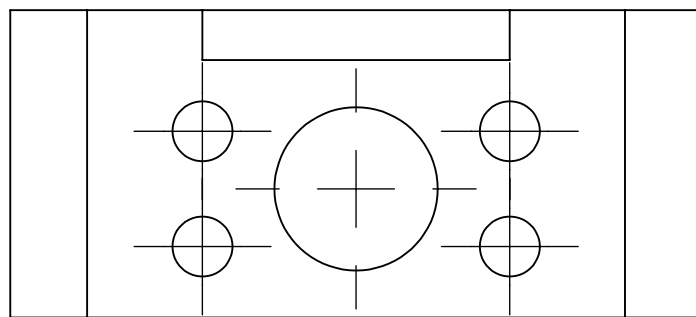
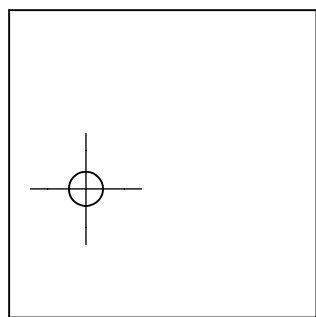
- Tapped for M9x0.5  
Tap Drill Size = 8.5 mm = .335 inches diameter  
Tap needs to be straight  
(hand tapping probably not ok here)  
lens holder, tap and spanner wrench are provided



$\phi$  .370  
 $\phi$  .365  
 Counterbore .375 +/- .005 deep  
 Lens holder and spanner wrench are provided

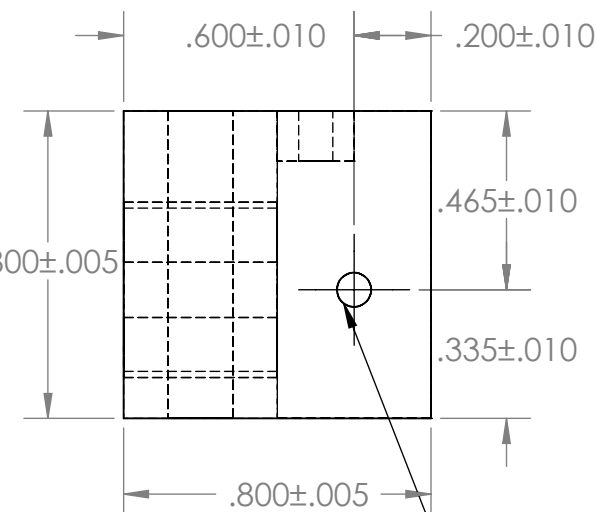


**Fixed Collimation Lens Part**



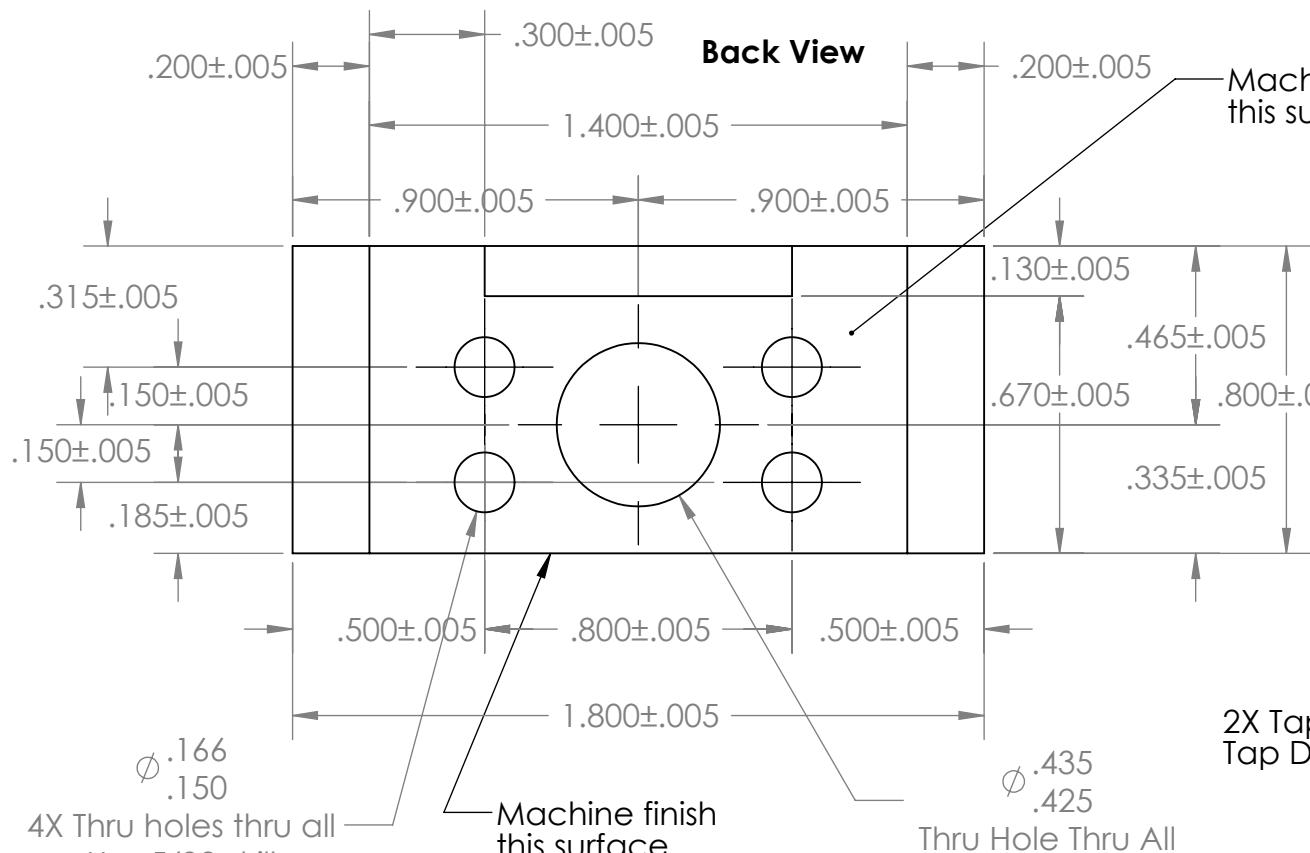
**Fixed Collimation Lens Part**  
**Scale = 2:1**

**Side View**



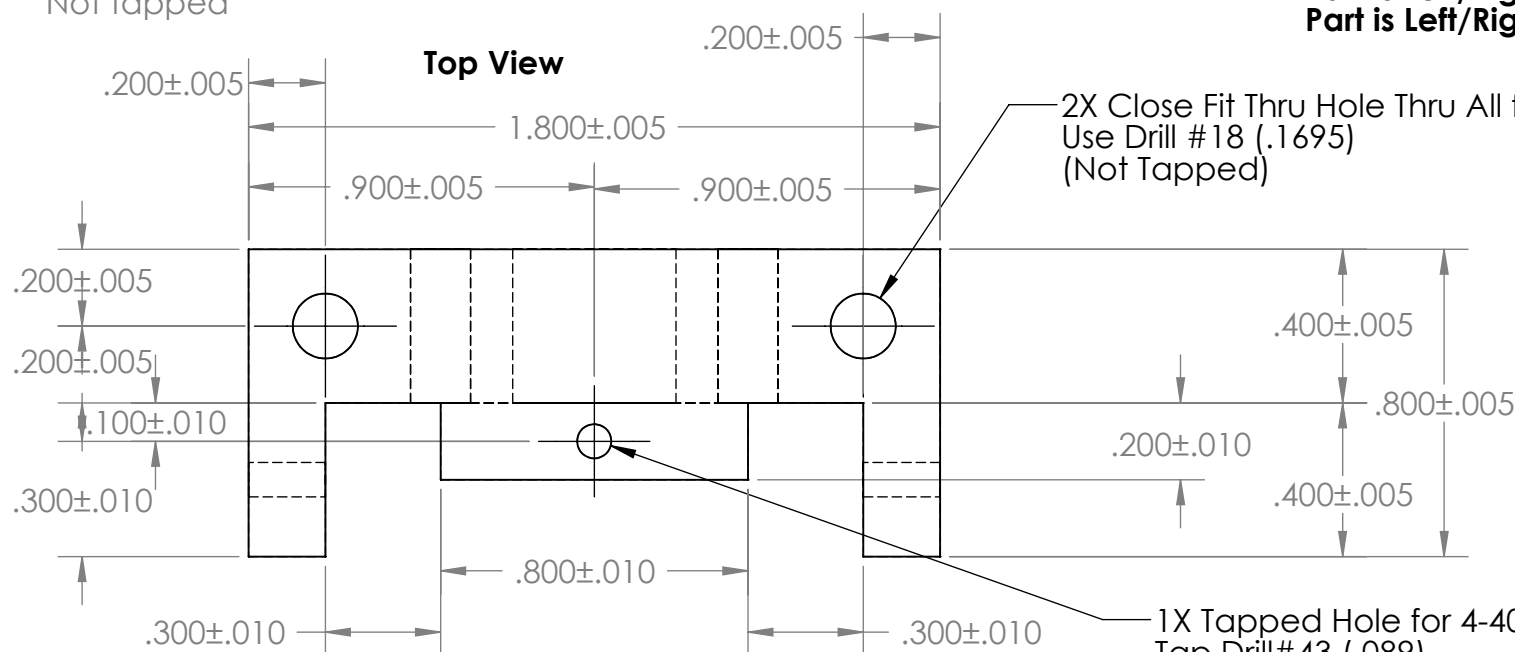
2X Tapped Hole for 4-40 to next surface  
Tap Drill #43 (.089)

**Back View**



4X Thru holes thru all  
Use 5/32 drill  
Not tapped

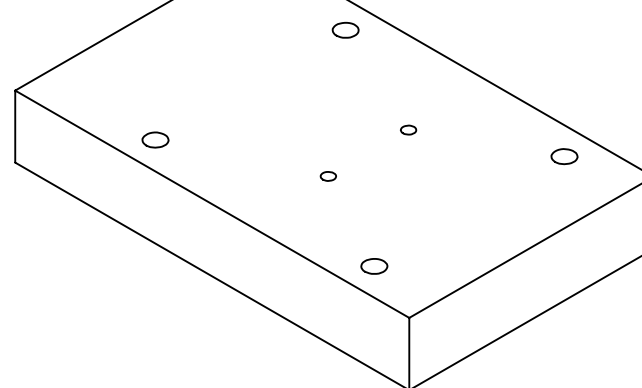
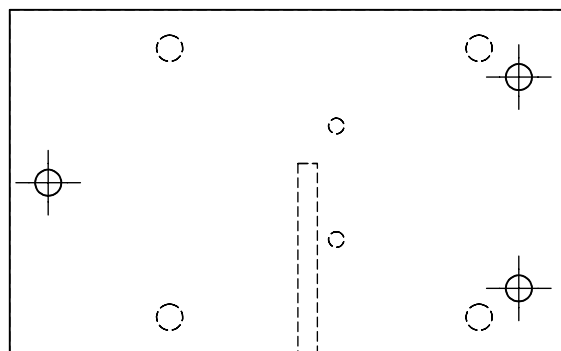
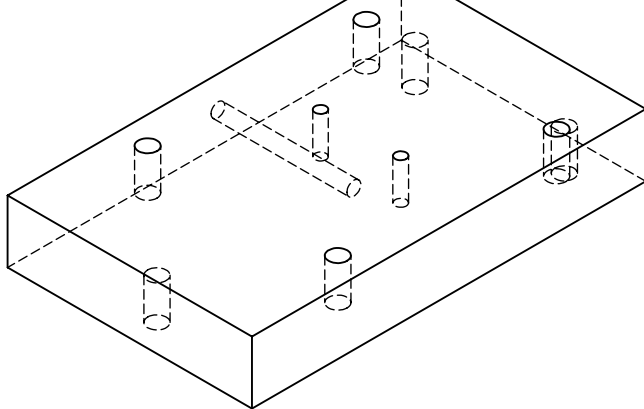
**Top View**



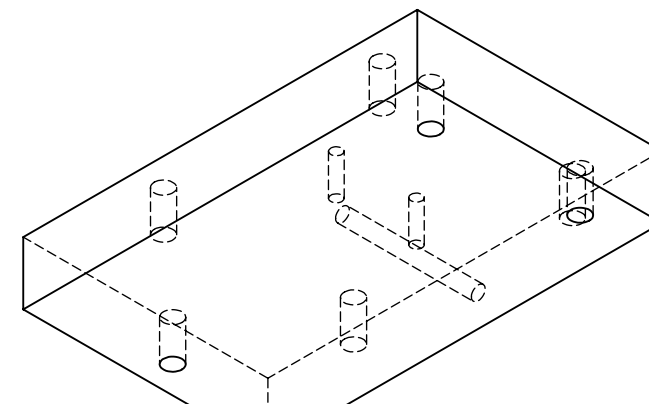
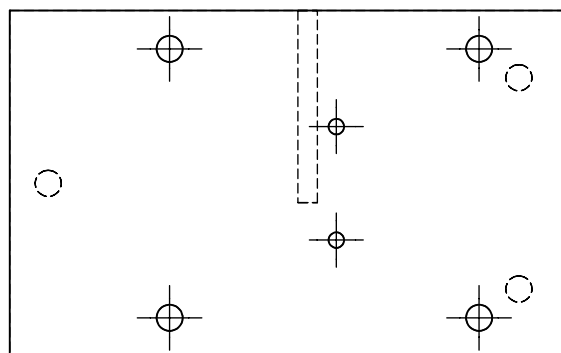
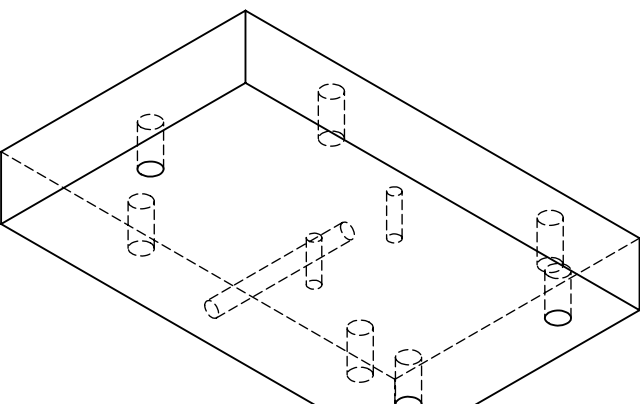
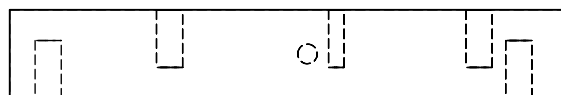
2X Close Fit Thru Hole Thru All for 8-32  
Use Drill #18 (.1695)  
(Not Tapped)

1X Tapped Hole for 4-40 to next surface  
Tap Drill #43 (.089)

**Part is Left/Right symmetric from the back**  
**Part is Left/Right symmetric from the top**



### Thermalized Base



**Thermalized Base**

**Scale = 1:1**

**Bottom View**

**Side View**

**Top View**

**Part is Left/Right symmetric  
(although drawings here  
are rotated 90 degrees)  
(except for single hole in the  
side of the part)**

1X Hole with #38 Drill  
(.1015 diameter)  
1 Inch deep  
(Not tapped)  
Bottom of hole does  
not need to be flat  
Hole line is dashed because  
from this view hole is on other side

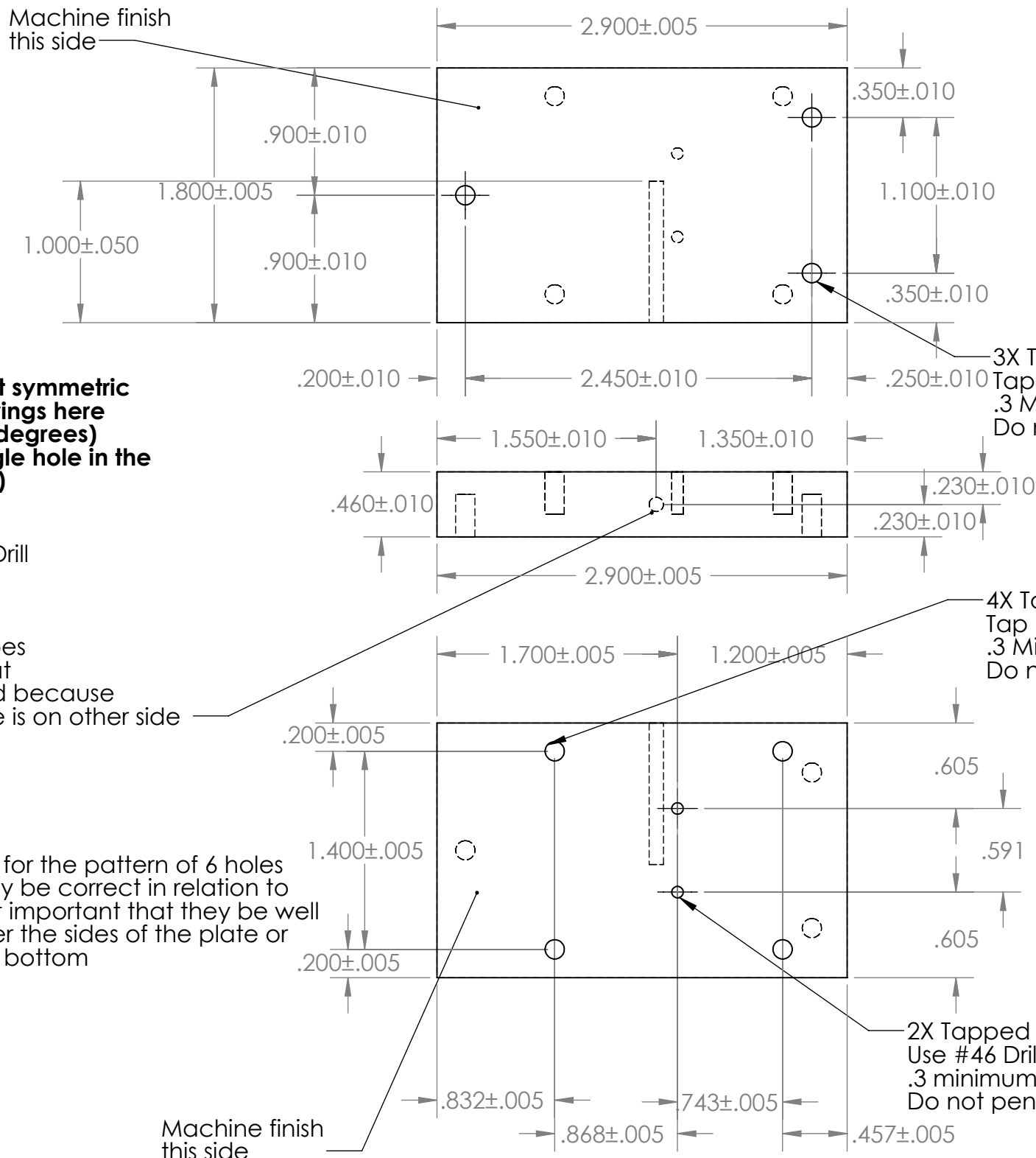
It is most important for the pattern of 6 holes  
on the top that they be correct in relation to  
each other. It is not important that they be well  
referenced to either the sides of the plate or  
to the holes on the bottom

Machine finish  
this side

3X Tapped Holes for 8-32  
Tap Drill = #29 (.136)  
.3 Minimum Tap Depth  
Do not penetrate

4X Tapped Holes for 8-32  
Tap Drill = #29 (.136)  
.3 Minimum Tap Depth  
Do not penetrate

2X Tapped Hole for M2.5x.45  
Use #46 Drill (.081)  
.3 minimum Tap Depth  
Do not penetrate





Part = Tapered Amplifier Mounting Part

John Barry  
DeMille Lab  
203 561 6060  
203 432 2824  
john.barry@yale.edu

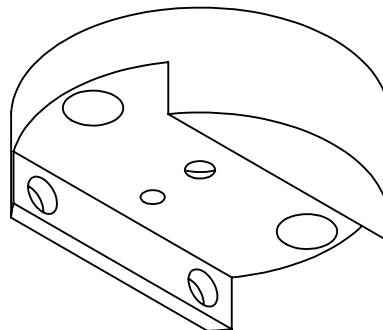
Charging = NSF ARO

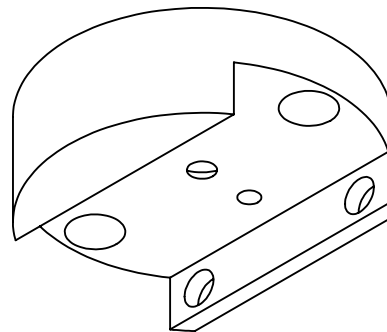
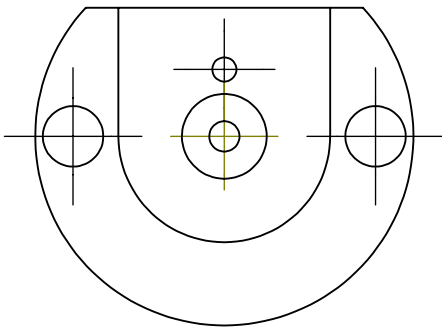
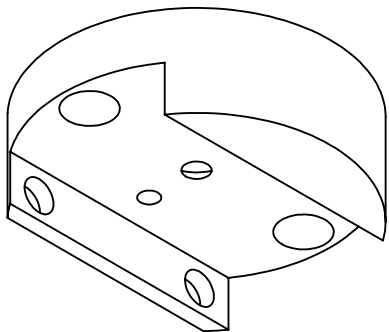
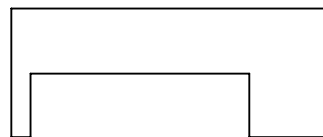
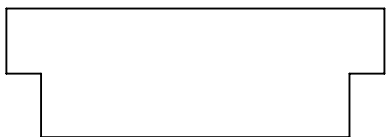
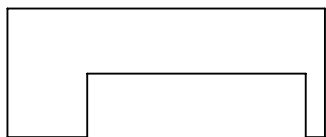
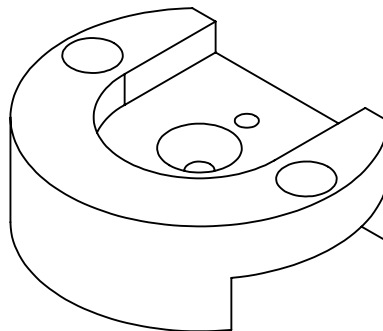
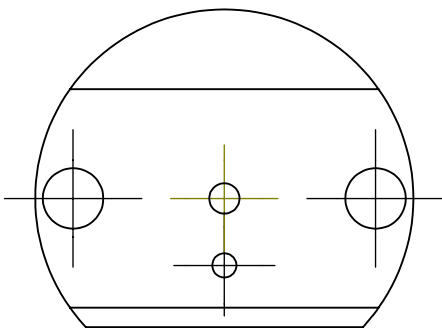
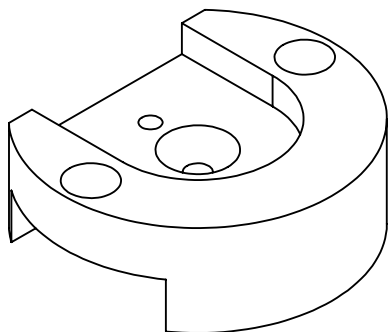
**Quantity = 1**  
**Material = 360 Brass**

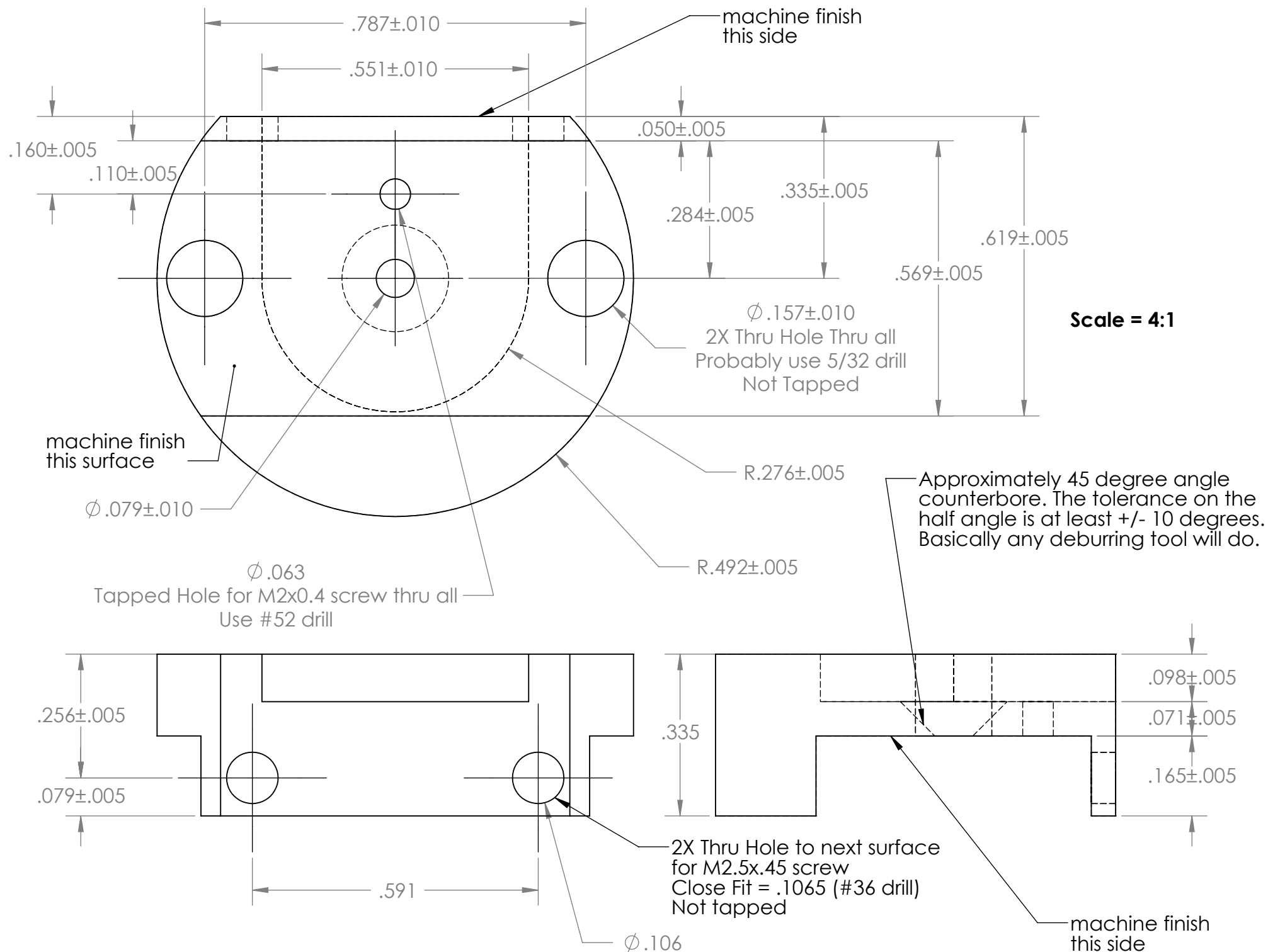
#### **NOTES**

- All dimensions and tolerances as are given.
- This part is supposed to be as close a copy of an existing commercial part as possible. The drawings for the existing commercial part are included

Sides that need to be smooth (machine finish) are noted. All other sides a standard or rough finish is fine.







## Appendix E

# Fabry-Pérot further details

This section details our current Fabry-Pérot design. The drawings may have to be rescaled so that the sheet scale is correct. The version of this thesis posted on the DeMille group website [298] has the appropriate scale listed on the drawing sheets<sup>1</sup> if the pdf pages are printed with no rescaling (confirm that this option is off during printing). The official version of this thesis submitted to Yale University however has margin restrictions, requiring the drawings to be shrunk and therefore the sheet scale is not valid for the official Yale version of this thesis. Updates to this design and any relevant additional material will be posted on the DeMille group website.

### E.1 Parts list

1. **National Scientific Company, 32.00 x 38.00 GE Type 214 quartz tubing.** This is for the quartz spacer. It will need to be cut to the right length, ideally with .001 inch accuracy. The phone number for the vendor is 215.536.2577. We usually buy it in four foot lengths and cut it in-house as needed.
2. **Noliac NAC2123.** This is the piezo. The old part number is CMAR03. It is approximately \$135. Tell them you need the leads attached and tell them specifically not to damage the wire when they strip the rubber. The leads should lie flat in the plane of the piezo. The red wire is positive and the white wire is ground. Required quantity = 1.
3. **McMaster 90291A529.** This is an optional setscrew to lock the length of the cavity. I don't use this setscrew but it could prove useful for applications where the cavity is subject to transport or vibrations. Required quantity = 1.
4. **McMaster 4061T155.** These o-rings act as a cushion between the retaining ring and the mirror. Required quantity = 2.
5. **Nailpolish.** Any brand is fine but I personally prefer the quick-drying variety. Under certain circumstances it may be advisable to use a low-outgassing substance in place of nailpolish as discussed later in this section.
6. **Mirrors.** The cavity is designed for 1/2 inch diameter mirrors. The Fabry-Pérot mirrors are typically high reflectivity (HR) mirrors from Layertec. I have used Layertec part number 102966 and 103951 with a nominal 150 mm radius of curvature (ROC) for the 500 MHz FSR cavities and Layertec part number 105738 with a nominal 100 mm ROC for the 750 MHz FSR

---

<sup>1</sup>e.g. 1 inch on the drawing sheet corresponds to 2 inches on the part if the sheet scale is labeled as 1:2.

cavities personally. Since none of these mirrors are specified for transmission, occasionally the transmission of the Fabry-Pérot will be poor. Sets of bad mirrors are relegated to Fabry-Pérots used for diagnostics where SNR is relatively unimportant. I usually have the Fabry-Pérot in confocal configuration but other configurations should not be a problem.

7. **Thorlabs SM05RR.** This is just a standard .5 inch retaining ring for the Thorlabs SM05 lens tube series. It is used to hold the mirrors in place. Required quantity = 2.
8. **Thorlabs 97355.** This is a 1.035-40 tap and will allow the Fabry-Pérot to mate with Thorlabs photodiodes and SM1 lens tubes.
9. **Thorlabs 83373.** This is a .535-40 tap and is used to tap the approximately 1/2 inch holes where the mirrors sit. Thorlabs suggests using a .508 inch tap drill.
10. **Tapco 86748A.** This is a 1.035-40 specialty die. This is available from [www.tapcotaps.com](http://www.tapcotaps.com) and will cost approximately \$250.
11. **Epoxy or glue.** Historically we have used a single component glue (McMaster 74555A44). However in the future we will likely use a two component epoxy with a high glass transition temperature such as Epotek 353ND. This change should lead to less outgassing and hopefully less creep.

## E.2 Assembly instructions

1. Using my Mathematica file and the known mirror ROCs, calculate the optimal length for the quartz tube and get that cut to length.
2. Glue or epoxy the steel endcaps onto the quartz tube while trying to center the pieces as well as possible.
3. Put nailpolish on the exposed piezo solder joints so that nothing shorts. Scrape the excess nailpolish off the flat sides of the piezo with a razor blade so that everything will lie flat. Obviously nail polish between cavity elements will probably lead to unknown relaxation or other undesirable effects. I recommend this step although some people have had success without it. My experience is that if you skip this step, the piezo will not short the vast majority of the time but not always. For cavities with nice mirrors, it may be advisable to use a two component epoxy or other means to prevent shorting rather than nailpolish to prevent contamination of the mirrors. Put the piezo in.
4. Put the mirrors in. Behind each mirror put a rubber o-ring. Behind each rubber o-ring, put in the Thorlabs retaining ring to clamp the mirrors in.

## E.3 Cavity alignment tips

### E.3.1 Setting the cavity length

The approximately correct position of the mirror held by the adjustable endcap can be calculated given the length of the quartz, the ROC of the mirrors and the dimensions of the adjustable endcap. The cavity is first adjusted to this length. After, a laser is aligned roughly into the cavity. Typically, we use a narrow, single frequency laser such as the HP/Agilent 5517B for this purpose. This avoids missing cavity resonances because the laser is running multi-mode.

### E.3.2 Fine tuning cavity alignment and mode matching

Once the cavity is near the confocal condition, we optimize the alignment to increase the finesse. First, we iteratively adjust the laser alignment into the cavity and the cavity length. Once this has been done, a mode matching lens will usually further increase the realized finesse. Again, use of a narrow, single frequency laser is helpful since all resonance linewidths can then be attributed to the cavity.

## E.4 Cavity design principles and comments

The cavity is designed to be athermal. For this to work the ROC of the mirrors should be known to  $\sim .01$  mm. Typically I ask Layertec to measure the ROC and sometimes they do and sometimes they don't. The length of the cavity does not affect the machining of the metal parts (the design of those is independent of cavity length), only the length of the quartz tube. I have attached my calculations for the length of the quartz tube. In practice most of the drift likely comes from variations in atmospheric pressure or from some other unknown source as opposed thermal expansion of the cavity. To date I use thermal expansion coefficients from MATWEB. The specific brand of quartz and steel recommended were chosen because of abundant data on their thermal expansion.

If you are unable to get Layertec to measure the actual ROC for the mirrors you order, I have the following data: For the nine nominal 150 mm ROC mirrors they have measured for me so far, the mean ROC was 149.97 mm and the standard deviation of the ROCs was .03 mm. This would then require a piece of quartz cut to a 152.823 mm length. For the two nominal 100 mm ROC mirrors they have measured for me, the mean ROC was 99.91 mm. This would then require a piece of quartz cut to a 100.827 mm length. The tolerance on the length of the quartz should (ideally) be .025 mm.

Ideally the Fabry-Pérot should be housed in a vacuum tight container to limit drift due to atmospheric pressure variation. Historically I have used KF vacuum parts although in retrospect conflat probably would have been a better choice. My containers are generally not evacuated but are vacuum tight. The vacuum tight container is most important to reduce drift. Atmospheric pressure can vary as much as  $\sim 3\%$  which corresponds to a drift of many, many free spectral ranges.

## E.5 Outstanding issues

1. According to the piezo specifications listed on the Noliac website, a voltage of  $\sim 15 - 20$  Volts should change the cavity length by  $\approx 1$  FSR. In practice 1 FSR typically requires a voltage change of 40 - 50 Volts. The origin of this discrepancy remains unknown for now.
2. Effects causing and/or resulting from the non-linearity of the piezo remain an unsolved issue. How to achieve best linearity? Does it depend on the clamping force? How does it vary with the frequency of the triangle wave the piezo is driven at?
3. Some cavities appear to slowly relax over a period of months or years. Is this due to relaxation of the glue/epoxy or the quartz or possibly due to an inadvertent layer of nailpolish?
4. In retrospect, the initial choice of the single-component Loctite glue was perhaps poor. Not only might the glue outgas but it could also cause creep. The glue was initially chosen because it was soluble in acetone which would allow for the cavity to be taken apart and re-glued if the initial gluing was not satisfactory. This glue is used by Coherent on their commercial Fabry-Pérots. Nevertheless, I imagine a better choice would be a low creep epoxy. Several groups have utilized a UV curing epoxy (Epotek 353ND) for their high-finesse Zerodur or ULE cavities [302–304].

Quartz Fabry Perot Version 6

Charging:

John Barry  
DeMille Group  
203 561 6060  
[John.barry@yale.edu](mailto:John.barry@yale.edu)

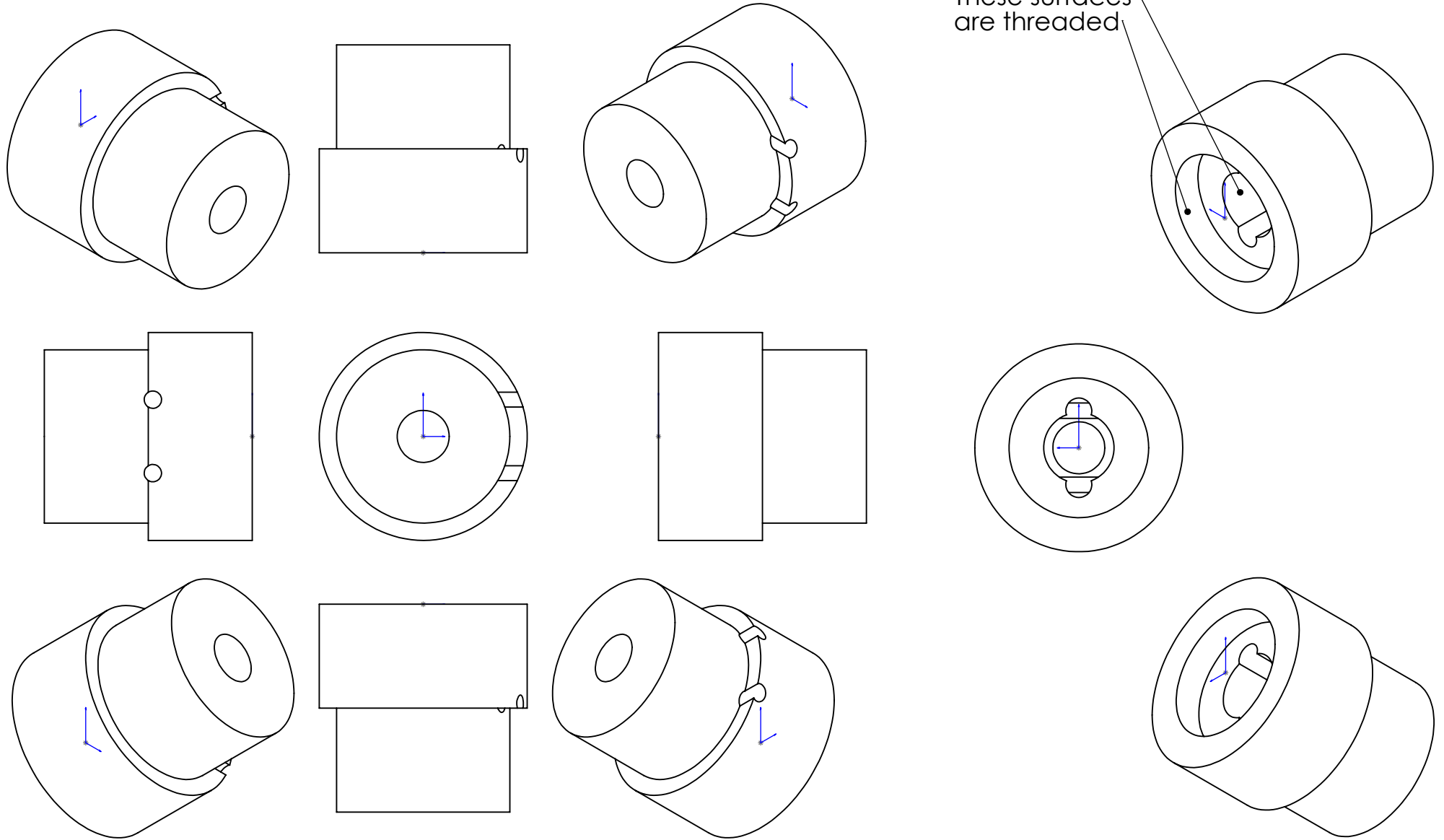
Material: 1018 Steel for all parts (available from McMaster in 1.500 diameter)

Quantity: 5 each of the following three parts

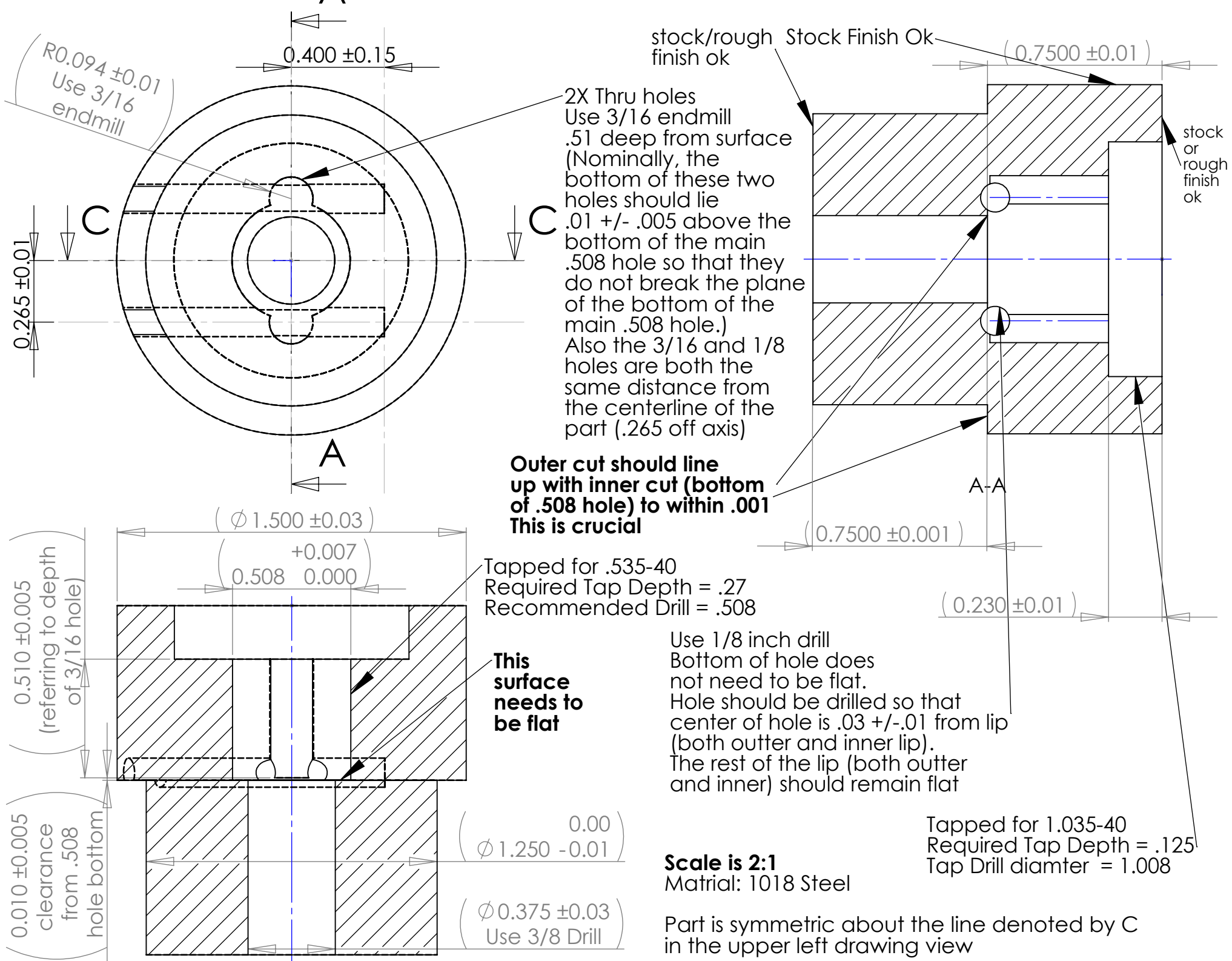
Notes:

We would prefer a tight fit between the two parts with the 1.035-40 threads. We do not want the inner part to be loose.

# Part = Fixed End

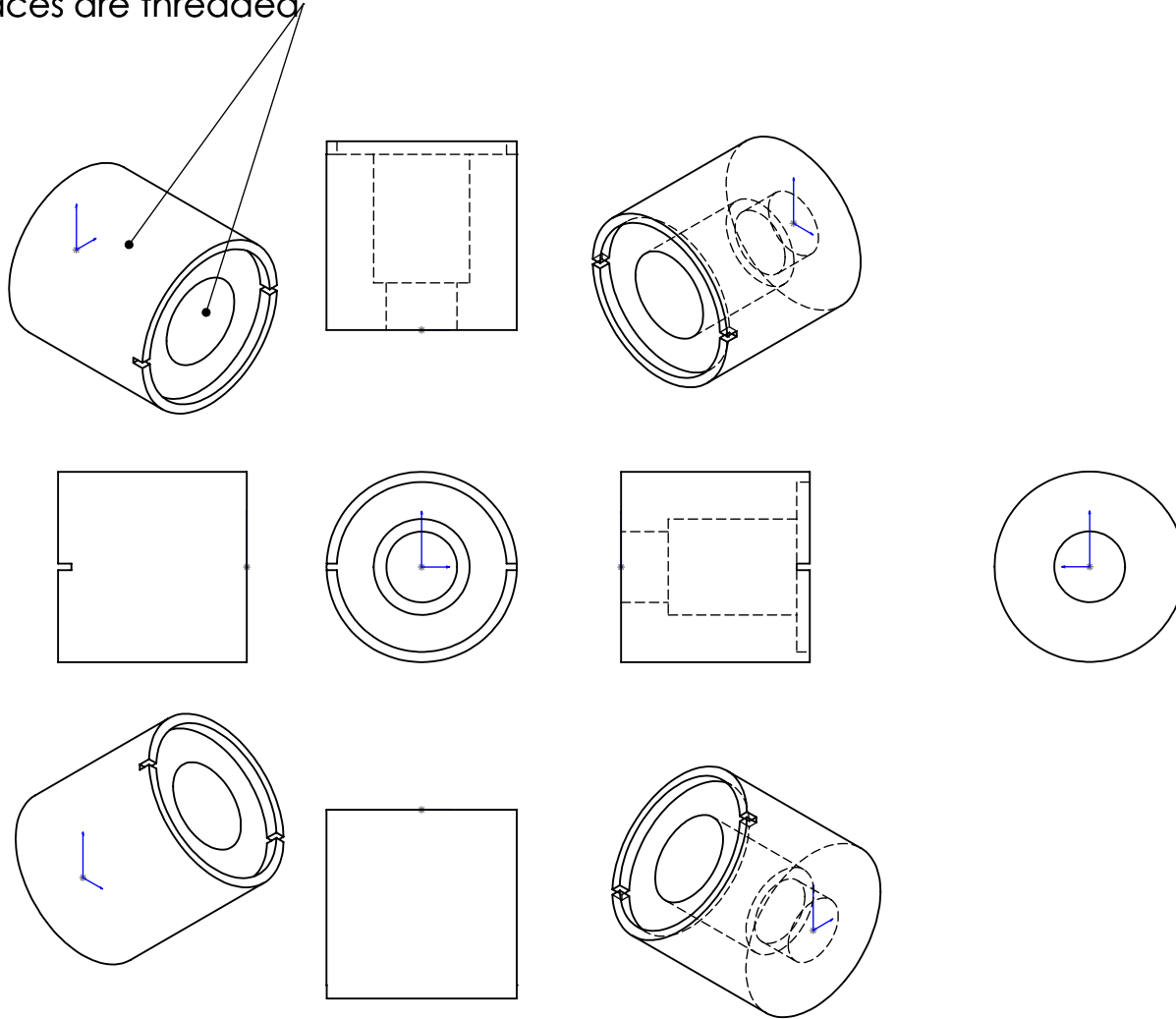






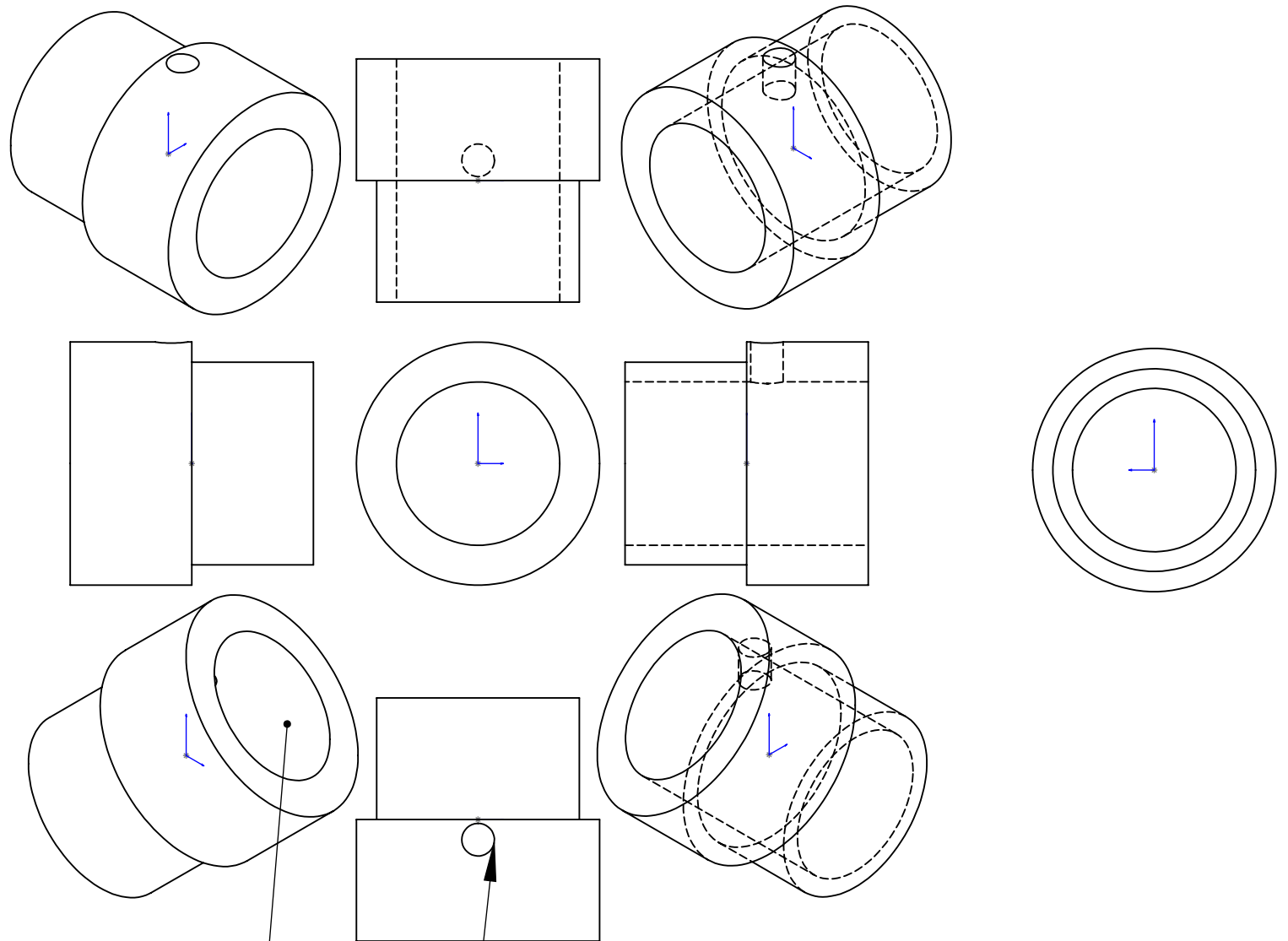
## Steel Threaded Inner Ring

These surfaces are threaded





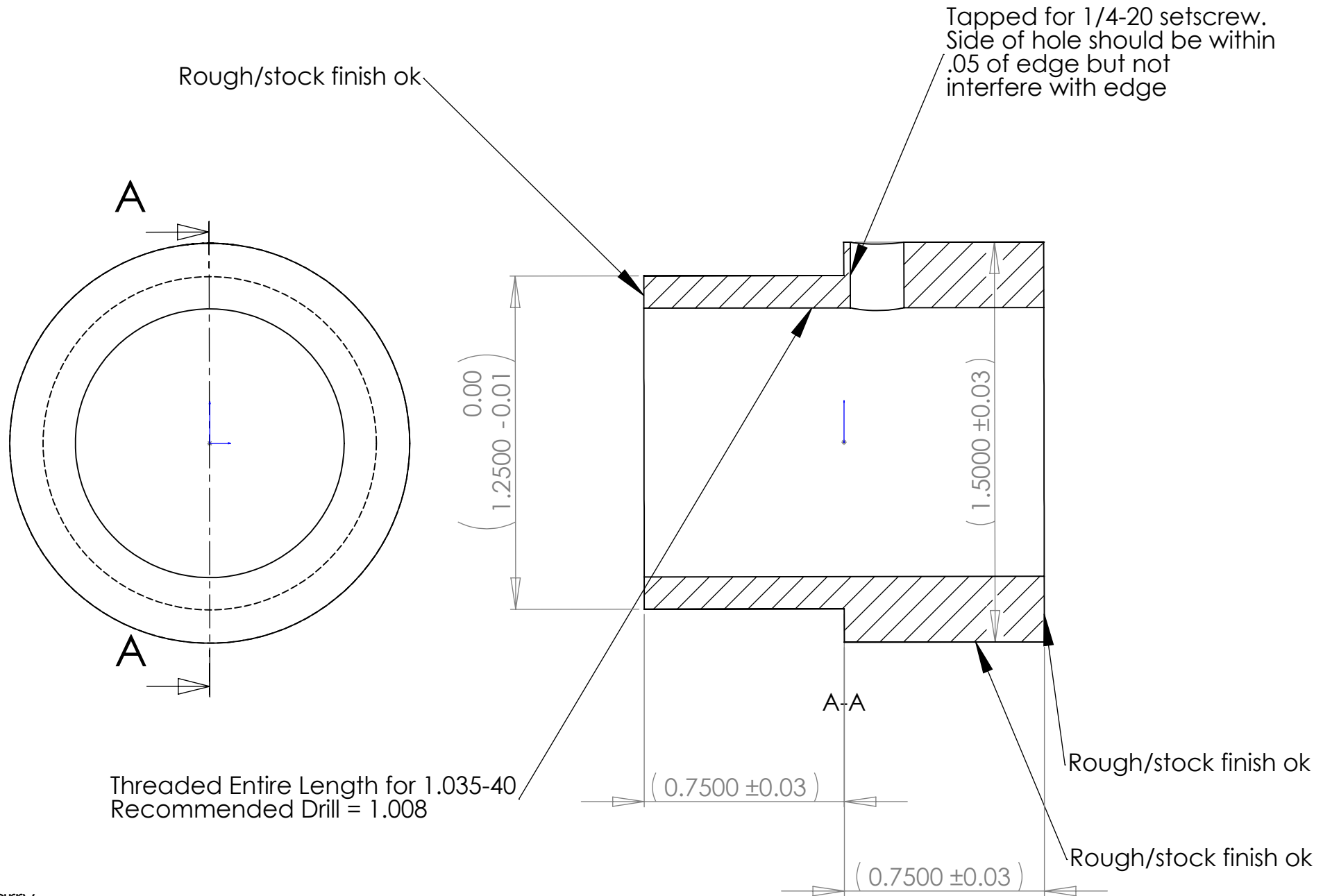
**Part = Steel Threaded Outer Ring**



This surface is threaded

This is a tapped hole

# Part = Steel Threaded Outer Ring



## Appendix F

# UHV preparation

For the UHV region of the experiment, only certain materials are allowed. A partial list of acceptable materials is given in Table F.1 while a more complete list is given by Ref. [305]. Other helpful resources include a guide to UHV procedures by an atomic physicist in Ref. [306], and outgassing data from NASA [307]. The Kurt J. Lesker company will also answer any vacuum-related question for free. For UHV compatible small parts, feedthroughs etc., Accuglass is a good supplier.

Most UHV experiments are ultimately limited by the partial pressure of hydrogen which slowly diffuses out of the walls of the stainless steel vacuum chamber. For experiments employing stainless steel (as opposed to glass cells), removing/blocking this hydrogen is paramount for achieving long vacuum lifetimes. Hydrogen removal can be accomplished by heating the steel to increase the diffusion constant of hydrogen  $D_{\text{diff}}$ . As shown in Ref. [308],  $D_{\text{diff}}$  varies approximately exponentially with temperature. For example,  $D_{\text{diff}}$  increases by  $\sim 6\times$  from 400 °C to 450 °C. From random walk considerations, the rate at which hydrogen diffuses out of the steel varies as the square root of the bake time. Thus, baking at high temperature is essential and bake-time is at most a minor correction. Because in-situ bakes at temperatures sufficient to remove hydrogen ( $\sim 400\text{-}450$  °C) are experimentally difficult, an alternative solution uses a large vacuum oven to pre-bake the parts at high temperature first. A low-temperature in-situ bake can be used to remove water after assembly of the vacuum chamber if needed.

We modified a fairly large (16"×13"×14", 53 Liter) vacuum oven (MTI Corporation, EQ-DZF-6050-HT) for this purpose. Initially, the oven could only reach 100 mTorr, but after replacing certain vacuum fittings with welds, the vacuum oven reached pressures below  $10^{-4}$  Torr at room temperature, which we deemed sufficient for our purposes. Additionally, we replaced the stock

---

OFHC copper
316L, 316LN, 304L and 304LN stainless steel
Kapton/Vespel
Quartz and fused silica
Macor
Sapphire
Beryllium copper

---

Table F.1: A sample of UHV compatible materials used during this thesis. Brass is not allowed due to the presence of Zn, which has a fairly high vapor pressure. During a bake, Zn will come out of the brass and coat the chamber walls. Most aluminum is technically UHV compatible, but aluminum tends to have a thick oxide layer which absorbs water and other contaminants and thus, ideally, requires special surface treatment for UHV use. The plastics Ultem and PEEK are not strictly UHV compatible but are low-outgassing nonetheless.

thermal insulation with better insulation and made a new heat shield from 4 layers of stainless steel for the oven door.

Above 450 °C, stainless steel may become brittle so we generally limit maximum pre-bake temperatures to  $\approx 450$  °C. Air baking has been shown in some cases to be equally effective at removing/limiting/blocking diffusion of hydrogen from the chamber walls but the additional layer of iron oxide increases the surface area of the chamber.

The following is our UHV cleaning procedure which is based on that of Emil Kirilov in Ref. [309].

1. Parts are inspected for large particles of dirt or grease and these are removed manually.
2. Most parts (all steel and stainless steel parts) are vacuum baked at 450 °C for 1 week or at their otherwise highest rated temperature. The parts are wrapped in two layers of UHV foil during the vacuum bake.
3. Copper and aluminum parts are ultrasonically cleaned in Citronox while steel and stainless steel parts are ultrasonically cleaned in Alconox, all for 10 minutes.
4. All parts are ultrasonically cleaned in acetone for 10 minutes.
5. All parts are ultrasonically cleaning in de-ionized water for 10 minutes.
6. All parts are then rinsed in de-ionized water and blown dry with dry nitrogen.

## Appendix G

# Copper blackening

### G.1 Copper(II) oxide black coating

For the reduction of scattered light, it is often preferable to create black parts with a UHV compatible coating. Over the years many different approaches were tried to solve this problem including commercial black UHV compatible paint, cheap commercial spray paint (Krylon, Ultraflat Black - 1602), black anti-static foam, charcoal, etc. No approach offered both excellent blackness and strict UHV compatibility. However, we have recently reproduced a UHV compatible blackening process for OFHC copper that creates a deep black velvet coating<sup>1</sup> which is visually blacker than anything we have seen for angles from normal incidence ( $90^\circ$ ) to approximately  $15^\circ$ . Although this coating must be grown on copper, OFHC copper is an ideal candidate for small in-vacuum UHV parts because it is widely available, easily machined, cheap for small quantities, and has low rates of hydrogen outgassing and therefore does not strictly require pre-baking like stainless steel. Similar to all good black coatings, there are two mechanisms at work. First, the copper(II) oxide itself has a high emissivity. Second, the coating consists of a dense fibrous micro-structure of copper(II) oxide dendrite crystals. The dendrites act to trap light far more effectively than a flat surface. These dendrites are extremely fragile and, once touched, are visibly less black. Fig. G.1 shows two CF nipples, one with a blackened OFHC copper insert and the other without. The process for creating this black coating for OFHC copper parts is given next.

---

<sup>1</sup>We followed instructions from Ref. [310].





Figure G.1: 2.75" conflat nipple with an OFHC copper insert coated with copper(II) oxide (left) and bare (right).

## G.2 Procedure to grow copper(II) oxide black coating

1. Clean copper surface to expose bare copper using sandpaper or steel wool. The bare (non-oxidized) copper must be exposed.
2. Copper parts should then be cleaned in a Citronox solution ultrasonically for 10 minutes. We do not perform additional cleaning steps beyond this because the alkaline solution should be sufficient.
3. Prepare a solution in a glass beaker composed of equal parts NaOH (75 g/L) and NaClO<sub>2</sub> (75 g/L) and de-ionized water.
4. Using goggles and the fume hood, heat the solution to 99-102 C° on a hotplate. Use an in-solution glass thermometer to monitor the temperature of the solution. The solution should simultaneously be mixed with a magnetic stir bar. Slightly hotter temperatures will work, but too hot and the solution will boil away. Water that boils away however can be replaced simply by adding more deionized water. Boil-off can be minimized by covering the beaker with a steel plate.

5. Place copper parts in heated bath for 10 minutes. The blackening is very delicate so mounting of the parts in the bath is important to consider so as not to crush the dendrites. Stainless steel is compatible with the bath solution.
6. Remove parts from the bath and sonicate in deionized water for 10 minutes. Then blow dry with dry nitrogen.
7. After all parts are coated, titrate the remaining bath solution with glacial acetic acid to bring the pH to 7 before disposal.

Treatment times greater than 10 minutes do not visually increase the light-absorptive properties of the surface. If something goes wrong with the coating process, the coating can be removed with sandpaper or steel wool and the process repeated. Because the rate of blackening is quite sensitive to temperature, it is sometimes a successful strategy to have the solution boiling and periodically add small amount of de-ionized water to replace the boil-off.

## Appendix H

# Homemade windows

Commercially available vacuum windows are expensive, particularly if AR coatings are desired and commercial parts are generally limited to standard conflat (CF) sizes. The heat of the braze may also distort or dirty the window. Further, AR coatings may be limited and lead times for custom coated parts are generally long. Hence the popularity of home-made window techniques such as the “Kasevich method” [311]. Here we document our own homemade solution for vacuum windows. The technique is UHV compatible.

1. Mix the epoxy (Epotek 302-3M).<sup>1</sup> It is important to mix the epoxy well. The directions specify 60 seconds of clockwise mixing followed by 60 seconds of counterclockwise mixing.
2. The next step is to degas the epoxy. Put the epoxy in some sort of vacuum ( $\lesssim 10$  Torr is fine, oil-free vacuum preferred) for  $\sim 10$  minutes. The bubbles should expand and come out of the solution. Remove the epoxy from the vacuum. Repeat this process once more.
3. Prepare the surfaces. If the surface is not glass, it should ideally be roughed up with sandpaper (lower grits such as 60 are ideal) to increase the surface area for the adhesion. Both surfaces should then be cleaned if necessary using UHV compatible cleaning techniques. Sometimes AR-coated optics are left as shipped by the manufacturer. However, there is no reason not to clean metal or uncoated optics.
4. Apply the epoxy to the surface and put the parts together. Since the epoxy has very low viscosity, parts tend to slide. Holding the parts in place is therefore advised.

---

<sup>1</sup>This epoxy is on the NASA list of low outgassing materials [307]. According to the manufacturer, heating the epoxy will help what little outgassing there might be to occur faster. The epoxy can be removed if necessary but doing so is time and labor intensive. In the future, we may use Epotek 353ND epoxy instead due to its higher operating temperature.

For 2.75" conflat windows, we use a 2" optic (e.g. Edmund Optics, #47-523) and a 2.75" CF to KF40 adapter (Lesker, F0275XQF40) as shown in Fig. [H.1a](#). For KF50 and similar windows we typically use a 2" optical window and an aluminum or stainless steel unbored stub blank (eg. LDS Vacuum, NW50-200-UA) and we drill the window hole ourselves as shown in Fig. [H.1b](#). It is important to offset the window sealing surface from surfaces which experience mechanical strain when the vacuum seal is tightened, hence the above solutions. We have also applied this method to make custom Brewster windows as shown in Fig. [H.1c](#).

For windows at room temperature made with this method, we have never observed a seal failure for any window whose largest dimension is less than 8". We have observed failures only for extremely large windows ( $\sim 400$  mm long) at room temperature. Although the exact cause of the failure is unknown, temperature cycling has been observed to exacerbate this problem for these large windows.

Maximum bake temperature remains an open question for  $\sim 2$ " and smaller windows using this method. Based on data from other groups for Epotek 302-3M [\[303\]](#), we expect the seal to fail somewhere between the glass transition temperature of 70 °C and the max continuous operating temperature 175 °C. Multiple groups report successful bakes at 200 °C using a similar epoxy (Epotek, 353ND) rated for slightly higher temperatures to make vacuum seals [\[303, 312\]](#). For us, every seal failure which has occurred to date (only on very large windows) is visually evident. This is perhaps because the index of refraction of the epoxy is different from that of air. To investigate window seal failure with temperature, a window using Epotek 302-3M epoxy identical to the one shown in Fig. [H.1a](#) is heated up to a temperatures  $T$  for a period of 4 hours and the seal is afterwards visually investigated for compromise. We observe no seal compromise at  $T=150$  °C but compromise at  $T=175$  °C and above. Danny McCarron performed the seal failure testing described above.

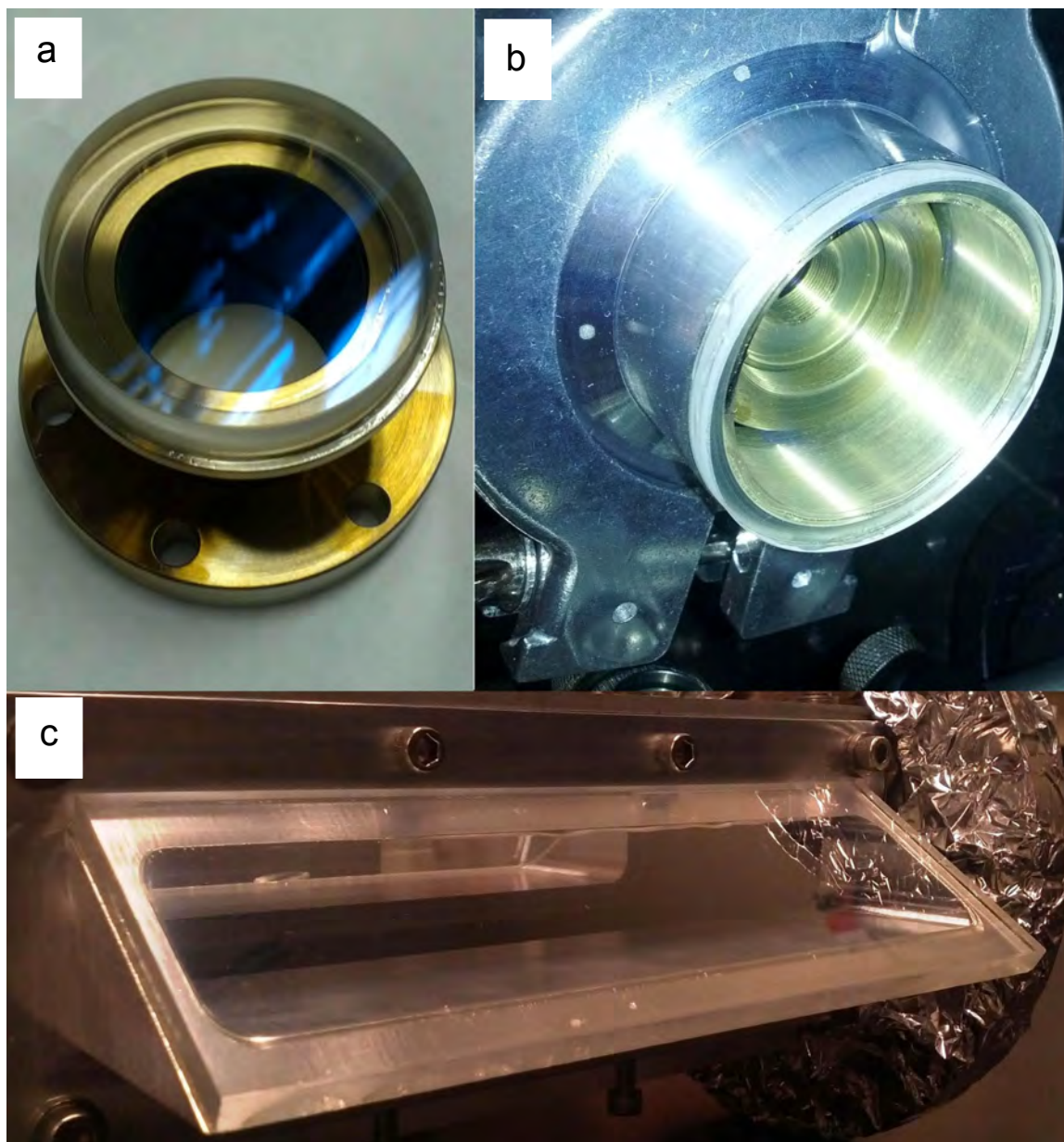


Figure H.1: Homemade vacuum windows. (a) A homemade 2.75" CF window with a 2" optic on a 2.75" CF to KF40 adapter. (b) A homemade KF50 window with a 2" optic on a bored aluminum KF50 stub flange. (c) A homemade Brewster window on a custom aluminum flange.

# Appendix I

## Target making

### I.1 SrF ablation target making overview

This section describes our current target making procedure and associated reasoning. Desirable measurable target properties are: high ablation yield (creating more SrF is better), good target durability (ablation laser removes material from target slowly), and high half-life (number of shots before yield decreases by  $2\times$ ). Although in one example, inspired by Ref. [239], an additive (boron) increased the ablation yield of SrF in our experiment, additives were almost always detrimental to one or more of the above desirable properties when used. However, we found that increasing target relative density improved all of the above properties. The target density is set by unknown properties of the precursor material but can generally be improved by sintering. Thus, in order to improve target performance, improving the relative density of the target is a measurable property that has been correlated with better target performance. One exception to this rule is a pure single crystal of  $\text{SrF}_2$  whose ablation properties are quite poor.

### I.2 Current target making procedure

Current targets are made by compressing 99.99% pure anhydrous strontium difluoride (Sigma Aldrich, 450030<sup>1</sup>) using a pellet die (Carver, 3619) and a benchtop hydraulic press (Carver, 4350.L) which allows application of up to 18000 pounds of force over a 13 mm diameter area ( $\sim 630$  MPa).

---

<sup>1</sup>We do not know the grain size.

### I.2.0.1 Calcination and target making instructions

1. Heat raw powder on an alumina plate at 550° C for 2 hours in 1 atm argon in the tube furnace. This is done in theory to drive off impurities from the target. At this temperature the SrF will not contract and form crystals, which we only desire to happen later during sintering [].
2. Put powder in Carver die. The order of pieces (from bottom to top) is: 6.35 mm metal piece with sharp side facing powder, powder, long plunger with sharp side facing powder and rounded side facing up. If you fill powder to  $\sim 4$  mm below top of die before any compression, final target will be  $\sim 4$  mm thick, which is a fairly desirable thickness.
3. Turn on the vacuum pump (preferably use a dry backing pump to avoid pump oil contamination) connected to the pellet pressing die. This is supposed to suck out any water vapor that might otherwise get turned into ice inside the target. This may not be necessary.
4. To begin pressing, tighten the black knob until it stops using only your thumb and forefinger. Now begin pumping the hydraulic handle. It is important not to tighten the black knob too much or it becomes very hard to release the pressure of the hydraulic press in a smooth, controlled manner. This is discussed later.
5. Slowly increase hydraulic press pressure up to 18000 lbs. Take about 1 minute to do this.
6. Keep the pellet under maximum pressure for at least 10 minutes. If the hydraulic press pressure decreases over time, increase the pressure back to 18000 lbs. Unless the black knob is too tight, the pressure should slowly decrease.
7. Very carefully release the pressure on the hydraulic press so that the pressure decreases slowly ( $\sim 1000$  lbs/second). On the Carver 4350.L, this can be done by pushing very hard on the black knob as the pressure is released. Sudden decreases in pressure tend to cause the back of that target to fall off when the target is removed from the press.
8. Once the pressure has been reduced to zero, the pellet die can be removed from the hydraulic press.
9. Use the accessory to press the target out of the top of the Carver die. Therefore the target should be pressed out of the top of the die. Do this pressing fairly slowly as well. You are done with making the target.

### I.2.0.2 Target sintering instructions

1. Put newly made targets on an high density non-porous alumina plate and place in the center of the vacuum furnace.
2. Ramp the temperature up to the maximum vacuum furnace temperature possible ( $\sim 1100^\circ\text{C}$  for our current furnace) at  $5^\circ\text{C}$  per minute. Have a dwell time of 4 hours. Then ramp down at  $5^\circ\text{C}$  per minute. This is the sintering step. This step is done in vacuum.
3. Repeat sintering steps 3 times.
4. Take the target out of the vacuum furnace. You are done with sintering the target.

In theory, after pressing, the target should display a uniformly dense consistency (similar to chalk) and there should be no problems with crumbling. After sintering, the targets should be much more ceramic-like (similar to a coffee mug) and should (in theory) “clink” when dropped on a hard surface. Do not test this theory by dropping the targets. For the latest batch of targets I made, the relative density (compared to the density of a pure  $\text{SrF}_2$  crystal) was  $81.5\% \pm .5\%$  after pressing. After sintering for one hour at  $1100^\circ\text{C}$ , they achieved relative densities of  $\approx 94\%$ . After three further sinterings of the target, the relative densities increased slightly further to  $95.7\% \pm .5\%$ . While sintering improves the yield only mildly ( $\sim 10\text{-}40\%$ ), it has several other highly desirable benefits

- Physical durability is increased (less material is removed for a fixed number of ablation shots)
- The yield of the target drops much more slowly (half-life of  $\sim 2000\text{-}4000$  shots for sintered targets vs.  $\sim 500$  shots for non-sintered targets).
- The sintered targets appear to produce less “dust” inside the cell.

Given the hassle to create these targets, it is possibly worth looking into an alternate supplier or method to achieve the same desired result: a high relative density target (that is not a single crystal). Commercial companies that supply such an item are American Elements (can promise 90% relative density), Lesker, and Sophisticated Alloys (tested and under-performs in-house made targets). Alternatively, the Hudson group at UCLA has had success making targets for a similar analogous molecule ( $\text{BaCl}$ ) simply by heating the precursor powder to just below the melting point. For  $\text{SrF}_2$  this would require heating to just below  $1750^\circ\text{C}$ , and we do not have a vacuum furnace



---

99.99% anhydrous $\text{SrF}_2$ (control)
99.99% anhydrous $\text{SrF}_2$ with $\text{AlF}_3$ additive
99.99% anhydrous $\text{SrF}_2$ with boron additive
99.99% anhydrous $\text{SrF}_2$ with strontium additive
Single crystal of $\text{SrF}_2$
Crushed single crystal $\text{SrF}_2$
Crushed single crystal $\text{SrF}_2$ with strontium additive
Crushed single crystal $\text{SrF}_2$ with boron additive
Crushed single crystal $\text{SrF}_2$ with $\text{AlF}_3$ additive
99.995% precipitated $\text{SrF}_2$
$<1 \mu\text{m}$ $\text{SrF}_2$ power
$\text{AlF}_3$ with strontium

---

Table I.1: Partial list of some non-sintered targets we tested.

for that. Finally, when heating and pressing simultaneously, one group achieved a relative density of 99% [313].

### I.3 Target composition

It is worth detailing how we arrived at the above procedure for anyone looking to improve the current targets. Before we tried sintering, we varied the composition of the targets, trying a variety of targets, listed in Table I.1. Of the unsintered targets listed, the only targets producing a higher yield than the control (unsintered anhydrous) were the targets with added boron, which increased the yield ( $\gtrsim 10\text{-}40\%$ ) versus the unsintered anhydrous target. The boron was added to the  $\text{SrF}_2$  in the stoichiastically correct ratio and the two components were ball-milled together. However, when combined with sintering, the added boron caused large holes  $\sim 1 \text{ mm}$  and warping of the targets. Thus the sintered target of boron and anhydrous  $\text{SrF}$  was not tried. Of the different targets pressed from pure  $\text{SrF}$ , the anhydrous target had the highest relative density before sintering. It also produced the highest yields and held up the best, which prompted us to investigate improving target density, accomplished by sintering. Interestingly enough, the single crystal of  $\text{SrF}_2$  was one of the worst targets we tested: Its yield was  $\sim 60\%$  compared to any target made with pure pressed unsintered power, and its durability worse and its half life was worse. Making targets with pure strontium outside a glove box was found to be challenging if not impossible. Also, even were we able to make such a target, the time to install it is such that it might completely react with the water in the air.

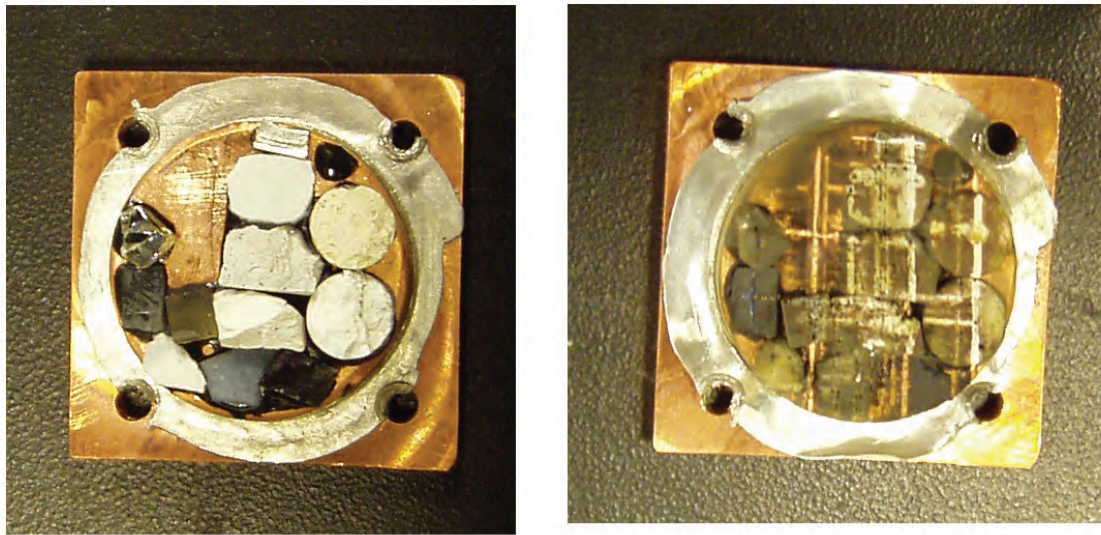


Figure I.1: Testing of multiple ablation targets. Before ablation the targets are in good condition (left). Ablation can sometimes remove large amounts of material from the targets and is prone to creating dust and “drilling” deep holes drilled into the targets (right). The vertical and horizontal lines in the right image correspond to the path of the ablation laser.

## Appendix J

# PMT light collection

This section outlines accumulated knowledge regarding LIF collection and minimization of background/stray/scattered light. Generally the goal of most light collection setups is the same: To collect as much LIF as possible while minimizing the amount of other light (background) hitting the detector. Collecting LIF is a matter of maximizing the geometric collection efficiency  $\eta_{\text{geo}}$ . Minimizing background is accomplished by both physically blocking unwanted light (using an iris for example), absorbing unwanted light (using black surfaces), and using interference filters. This section focuses on LIF collection setups for out molecular beam using a PMT. While better solutions for LIF collection admittedly exist [240], the solution presented here uses only off-the-shelf parts and requires no custom machining.

### J.1 Geometric collection efficiency

The most recent PMT setup to collect LIF at 360 nm is shown in Fig. J.1. LIF can enter the light pipe (quartz, 1" diameter x 12" length)<sup>1</sup> either directly or after first being reflected from a 10 mm focal length aluminum concave mirror (Edmund Optics, #43-464) mounted opposite the light pipe on an OFHC copper pedestal. The spacing between the light pipe and concave mirror is estimated to be  $\approx 6$ -10 mm and we therefore take this value to be 8 mm. Light is confined via internal reflection as it travels through the light pipe to the PMT (Sens-Tech, P25USB with 22 mm diameter photocathode and  $\eta_{\text{qe}} = 28\%$  at 360 nm). Upon exiting the light pipe, the light strongly

---

<sup>1</sup>While quartz light pipes are used in this example for light at 360 nm, acrylic light pipes may be suitable for light at higher wavelengths and can be made on the lathe and polished with regular sandpaper up to 2000 grit followed by Thorlabs sandpaper (Thorlabs LFG03P = 300 nm grit). Using plastic from Modern Plastic in Bridgeport, CT, USA, this technique produces light pipes with transmissions approaching that of quartz for 663 nm light. Empirically, acrylic from McMaster is not as good as that from Modern Plastic.

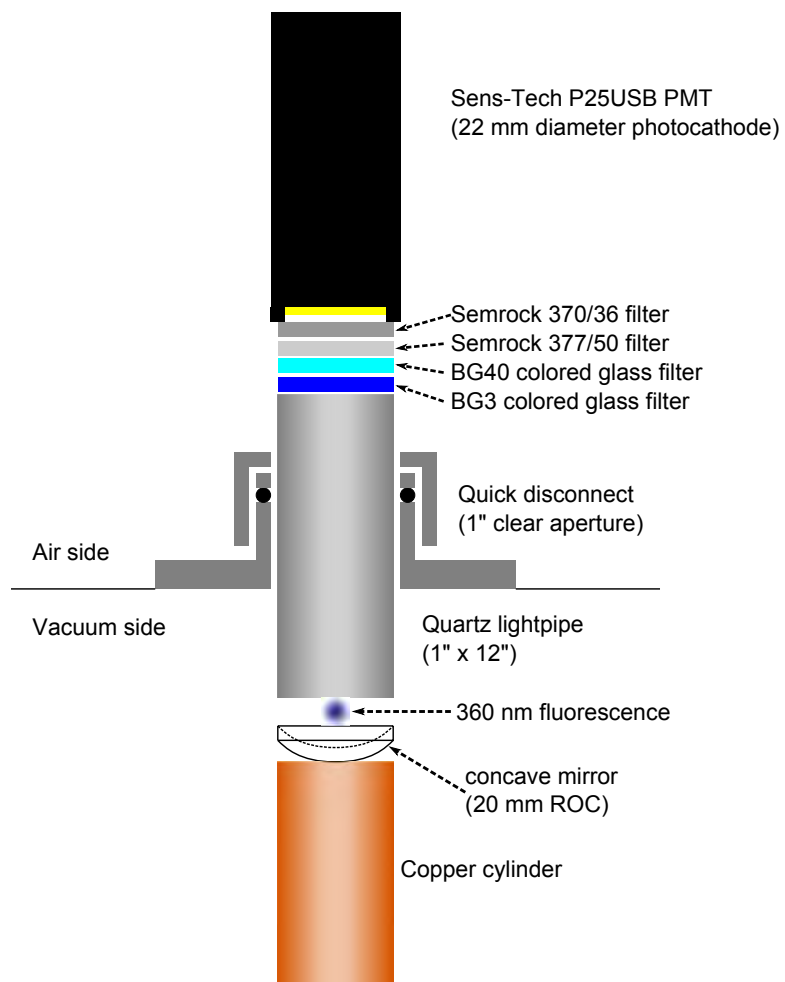


Figure J.1: Light collection setup for collecting LIF at 360 nm.

diverges and only some passes through a combination of filters and reaches the PMT photocathode located 15 mm beyond the light pipe exit.

Using ray tracing software (Optical Research Associates, LightTools) we estimate that  $\sim 63\%$  of emitted LIF is coupled into the light pipe and that  $\sim 31\%$  of the emitted LIF reaches the PMT photocathode. The ray tracing simulation alerts us to a few subtleties of this setup. For example, photons hitting the concave mirror and photons entering the light pipe first are present in equal numbers inside the light pipe. However, of the photons reaching the PMT photocathode, the simulation estimates  $\sim 71\%$  originally bounced off the concave mirror. We speculate this effect arises because the concave mirror helps to collimate the light going into the light pipe and these photons are better aligned to hit the detector upon exiting the light pipe.

While we have simulated  $\eta_{\text{geo}}$  here, the value is ideally measured if possible. One difficulty with such measurements is creating a truly isotropic light source. In the past we have used a Ruby sphere (Edmund Optics, #43-645) illuminated with 532 nm light to create LIF at 694 nm. However, we find the spatial LIF emission only moderately isotropic and that this emission varies with the 532 nm pump light alignment. It may also be possible to use a white Delrin sphere glued to the tip of a multimode fiber. For LIF collection over a small angle, a 1/4" thick piece of white Delrin back-illuminated with light of the LIF wavelength works well. The front of the Delrin is covered in aluminum tape except for a small hole.

## J.2 Filters

Filter	Type	360 nm	663 nm	685 nm	710 nm	787 nm
Semrock 370/36	Interference	0.92	6.60E-10	8.40E-08	6.30E-10	2.90E-08
Semrock 377/50	Interference	0.91	5.40E-06	6.60E-06	1.50E-05	1.00E-03
Thorlabs FGB37	BG40 colored glass	0.78	0.35	0.15	0.1	0.005
Thorlabs FGB25	BG3 colored glass	0.89	4.70E-05	0.03	0.5	0.99
Total		0.581184	5.86E-20	2.49E-15	4.73E-16	1.44E-13

Table J.1: Filter transmission at normal incidence. Transmission for 360 nm includes losses due to reflections while the transmission for the other wavelengths do not. The 710 nm wavelength approximately corresponds to a hypothetical laser to drive the  $X(v = 2) \rightarrow A(v = 0)$  transition, although it does not appear likely that such a laser will be used in the future.

For LIF emitted at a wavelength  $\lambda_{\text{LIF}}$  significantly different than the excitation light wavelength  $\lambda_{\text{excite}}$ , scattered light can be eliminated entirely using filters, particularly if  $\lambda_{\text{LIF}} < \lambda_{\text{excite}}$ .<sup>2</sup> Interfer-

<sup>2</sup>Some filters have the unfortunate property that light with wavelength  $\lambda_{\text{excite}}$  may cause fluorescence in the filter itself at another wavelength  $> \lambda_{\text{excite}}$ . Filter fluorescence for wavelengths  $< \lambda_{\text{excite}}$  is prohibited by energy conservation assuming non-linear optical effects are not present in the filter.

ence filters exhibit high transmission in the passband and high attenuation elsewhere but the spectral features depend on the light's angle of incidence  $\theta$ . A spectral feature occurring at wavelength  $\lambda_0$  for light at normal incidence will then occur at

$$\lambda(\theta) = \lambda_0 \sqrt{1 - \left( \frac{\sin \theta}{n_{\text{eff}}} \right)^2}, \quad (\text{J.1})$$

for light incident at angle  $\theta$  where  $n_{\text{eff}}$  is the effective index of refraction, which varies with both  $\theta$  and the light polarization. For the Semrock filters we use (RazorEdge series) it is appropriate to use  $n_{\text{eff}} = 2.08(1.62)$  for s(p) polarized light according to the manufacturer's website [277]. Alternatively, you can use the tool available from the Semrock website [277], which will calculate such spectral feature shifts for you and can even calculate average filter transmission for light emitted uniformly over a cone (with a user-specified half angle). In contrast to interference filters, colored glass filters operate via absorption and thus have no intrinsic angular dependence (aside from reflection coefficients and path length through the colored glass, which both vary moderately with  $\theta$ ) but offer only modest attenuation.

For our setup to collect 360 nm fluorescence, we use two interference filters and two colored glass filters, detailed in Table J.1. Also depicted is each filter's transmission at several wavelengths of interest. Overall, we see that for 360 nm light at normal incidence, the transmission is  $\approx 58\%$ . The high attenuation at laser wavelengths is necessary; otherwise increased counts from excitation laser light can mimic signal during optical alignment. As expected from the data in Table J.1, we do not observe an increase in photon counts above the dark count rate of the PMT ( $\sim 50$  counts/s) even when the four longitudinal lasers ( $\lambda_{00}^s$ ,  $\lambda_{10}^s$ ,  $\lambda_{21}^s$ , and  $\lambda_{AD}^p$  with typically 450 mW total power) are aligned to directly hit the concave mirror or the light pipe. To achieve this performance, it is necessary to wrap the filters snugly with black electrical tape before inserting them into their lens tube housing, in order to ensure light does not travel around the filters. When choosing interference filters, it is valuable to evaluate transmission for all  $\theta$  present in the experiment using Eqn. J.2 or the tool in Ref. [277]. This is always done but is not discussed here.

### J.3 Scattered light

It is sometimes necessary that  $\lambda_{\text{LIF}} = \lambda_{\text{excite}}$ . In these cases, scattered/stray light must be physically prevented from entering the detector. Physical methods can be broken down into two groups: Light

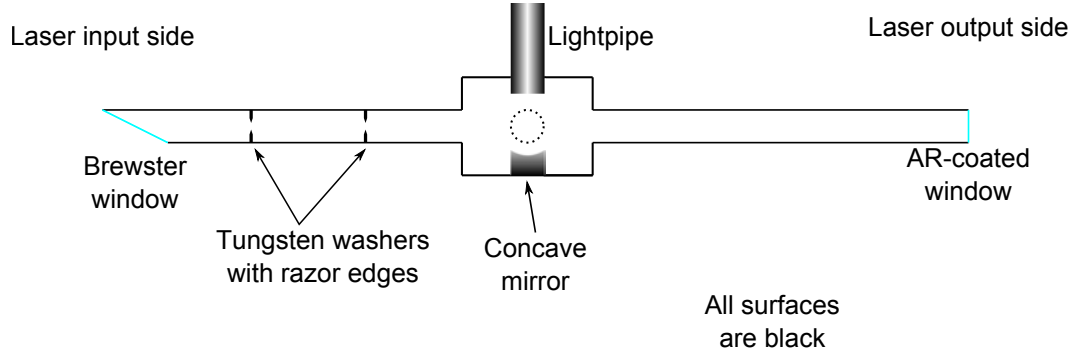


Figure J.2: An example setup for minimizing scattered light.

absorption and light blocking.

**Light absorption:** Black velvet (McMaster, 88015k1), black electrostatic foam, and black spray paint (Krylon, Ultra-Flat Black) have all been used to absorb scattered light. The first two are both fairly black and share the property that they are fairly porous and therefore incident light sometimes gets trapped in the nooks and crannies and absorbed before the light can leave. The latter is found empirically to be the blackest of standard commercial-variety spray paints but fails to benefit from any geometric effects assisting in light absorption. Qualitatively, black velvet is slightly better than the black electrostatic foam and both are much better than a flat test piece coated with the black spray paint. While both the black electrostatic foam and the black spray paint were employed in vacuum at times with no documented detrimental effects, I cannot advise this. We believe the best black for light at normal and near-normal angles of incidence is that detailed in [Appendix G](#).

**Light blocking:** Large amounts of scattered light can be generated if the non-Gaussian wings of a laser beam are clipped in the LIF collection region. A successful method for minimizing such scattered light is to send the excitation laser beams through apertures situated before the LIF region. In multiple experiments we employ tungsten washers made by Jeff Ammon with chemically-sharpened inner edges as apertures. The washers are painted black (Krylon, Ultra-Flat Black) except for the sharp, inner edges and function to not only block the Gaussian wings of the laser but also to decrease the solid angle for scattered light or room light (if any) present elsewhere to enter the LIF collection region. We find a good setup to consist of a Brewster input window, followed by two tungsten washers spaced many inches apart, followed by the light collection region, followed by a long tube ending in an AR-coated window as shown in Fig. [J.2](#). Empirically, an AR coated window is better for the output window than a Brewster window but the opposite was true on the input window. We believe this is because any reflections on the output Brewster window are

reflected back into the vacuum chamber whereas any reflections off the input Brewster window do not enter the vacuum chamber. It is also helpful to minimize surfaces and objects close to the light collection, make sure the mirrors in use outside the vacuum chamber do not have excess dust on them, and to terminate the excitation laser beam into a piece of black velvet or a proper beam dump located away from the experiment. Checking for scattered light should be done under as close to final experimental conditions as possible before the vacuum is closed (and maybe after if necessary) and definitely always before any cryogens are used.

## J.4 Current PMT collection efficiency

Combining the geometric collection efficiency  $\eta_{\text{geo}} \approx 33\%$ , the filter transmission  $\eta_{\text{filters}} \approx 58\%$ , and the PMT quantum efficiency at 360 nm, given by  $\eta_{\text{qe}} \approx 28\%$ , the total collection efficiency  $\eta_{\text{total}}$  is given by

$$\eta_{\text{total}} = \eta_{\text{geo}} \times \eta_{\text{filters}} \times \eta_{\text{qe}}, \quad (\text{J.2})$$

to be  $\approx 5.0\%$  for collection of 360 nm LIF for the setup shown in Fig. [J.1](#).



## Appendix K

# Pictures of experimental apparatus

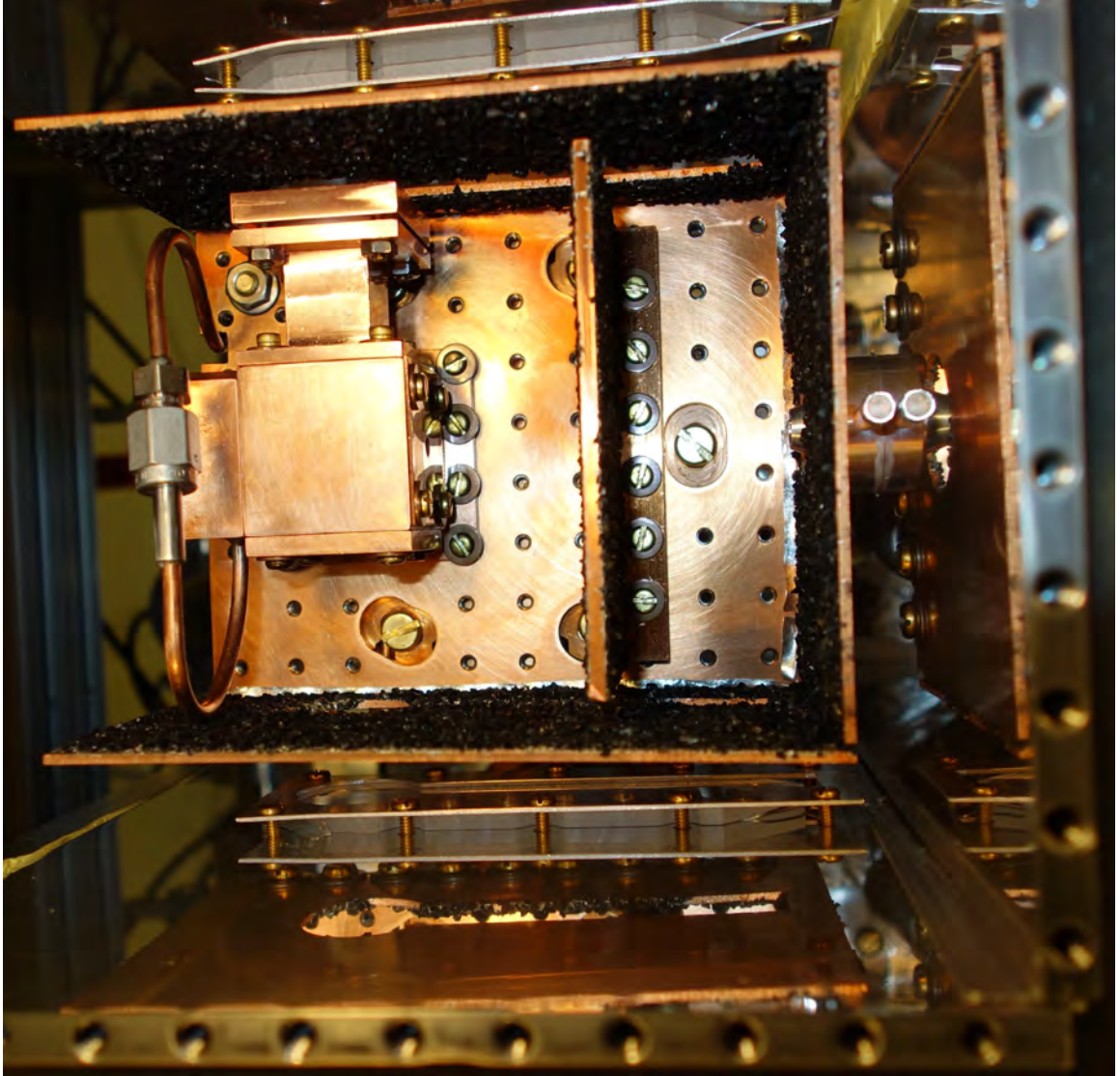


Figure K.1: Bottom view of the 3K cryogenic components.

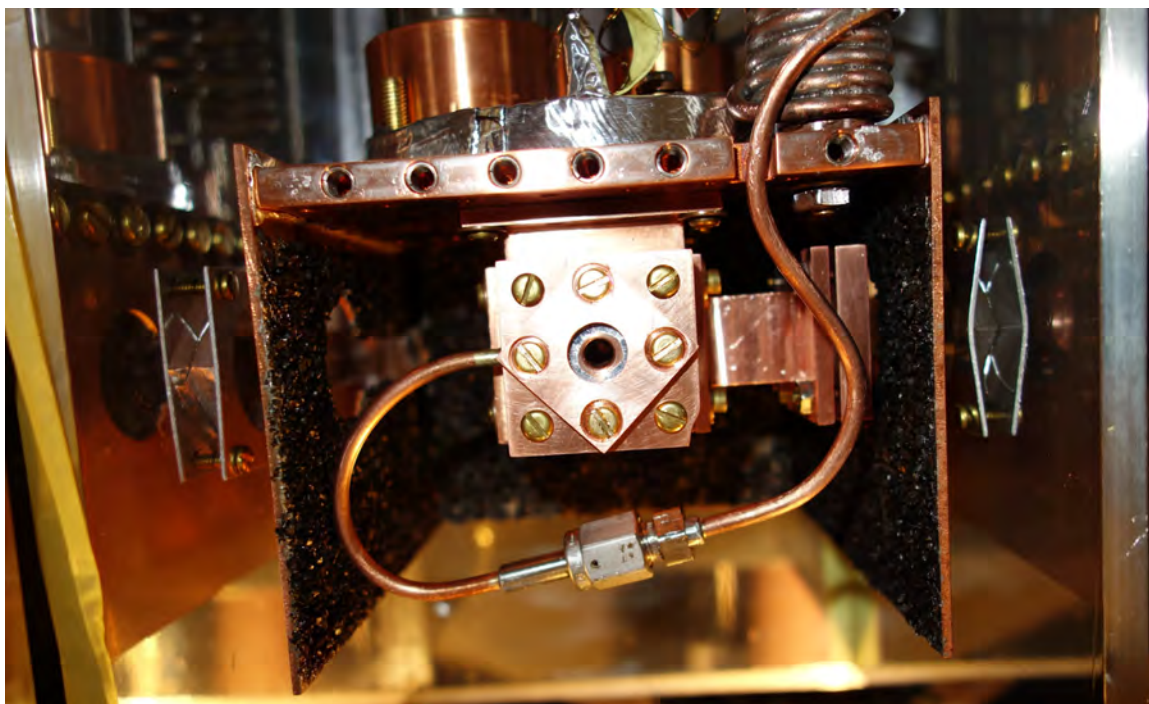


Figure K.2: Back view of the cell.

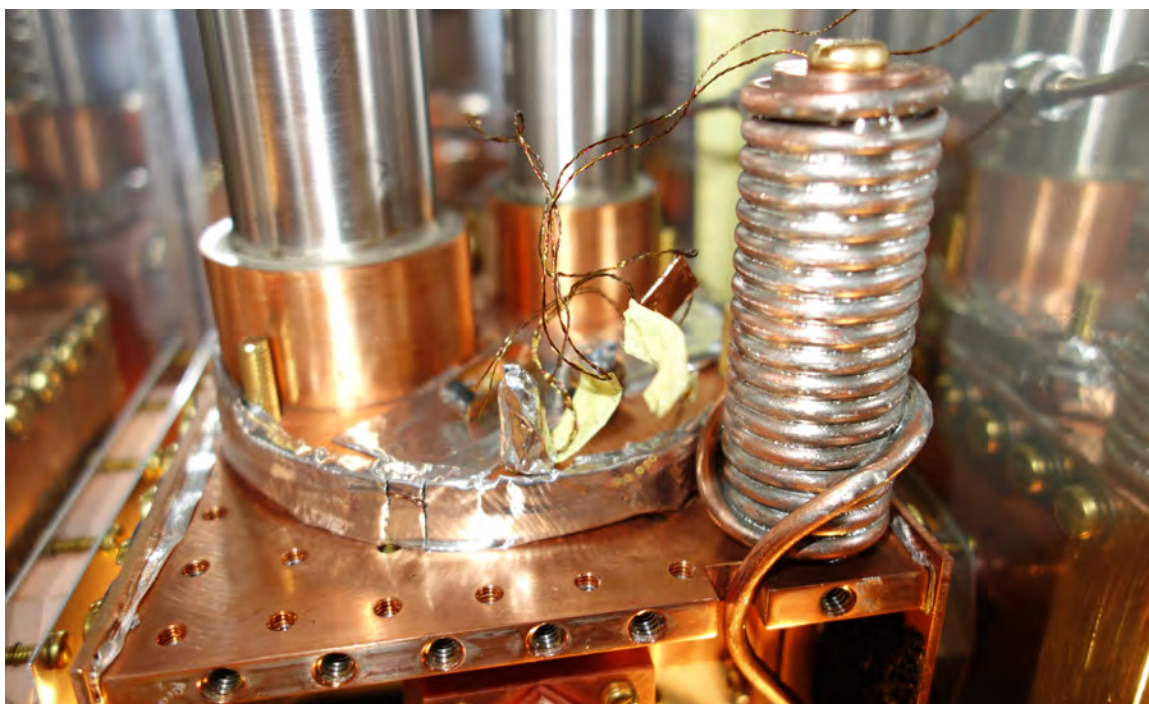


Figure K.3: View of the 3K bobbin.



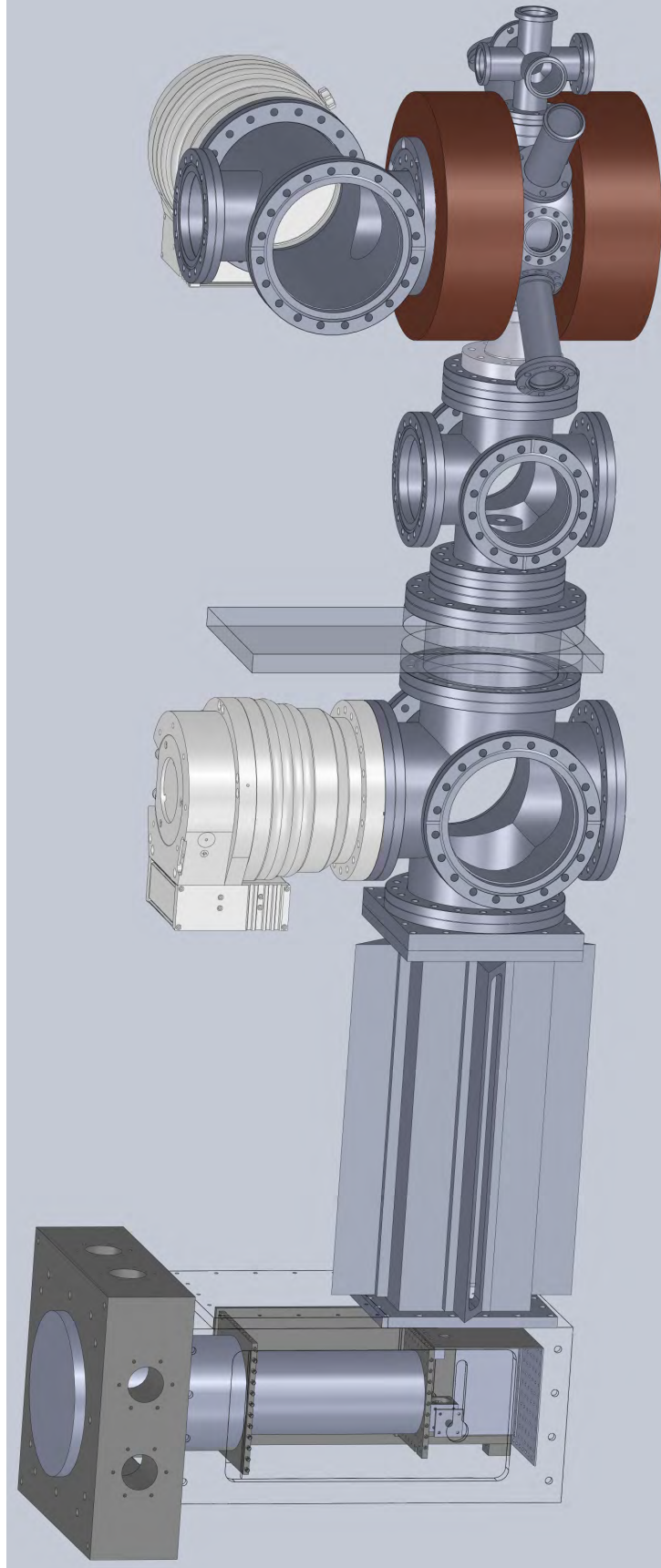


Figure K.4: Solidworks picture of experimental apparatus at time of dissertation submission. Many parts are not shown.

# Bibliography

1. Phillips, W. D. & Metcalf, H. “Laser deceleration of an Atomic Beam”. *Phys. Rev. Lett.* **48**, 596–599 (1982).
2. Migdall, A. L., Prodan, J. V., Phillips, W. D., Bergeman, T. H. & Metcalf, H. J. “First Observation of Magnetically Trapped Neutral Atoms”. *Phys. Rev. Lett.* **54**, 2596–2599 (1985).
3. Chu, S., Bjorkholm, J. E., Ashkin, A. & Cable, A. “Experimental Observation of Optically Trapped Atoms”. *Phys. Rev. Lett.* **57**, 314–317 (1986).
4. Raab, E. L., Prentiss, M., Cable, A., Chu, S. & Pritchard, D. E. “Trapping of Neutral Sodium Atoms with Radiation Pressure”. *Phys. Rev. Lett.* **59**, 2631–2634 (1987).
5. Chu, S. “Nobel Lecture: The manipulation of neutral particles”. *Rev. Mod. Phys.* **70**, 685–706 (1998).
6. Cohen-Tannoudji, C. N. “Nobel Lecture: Manipulating atoms with photons”. *Rev. Mod. Phys.* **70**, 707–719 (1998).
7. Phillips, W. D. “Nobel Lecture: Laser cooling and trapping of neutral atoms”. *Rev. Mod. Phys.* **70**, 721–741 (1998).
8. Ketterle, W. “Nobel lecture: When atoms behave as waves: Bose-Einstein condensation and the atom laser”. *Reviews of Modern Physics* **74**, 1131–1151 (2002).
9. Cornell, E. A. & Wieman, C. E. “Nobel Lecture: Bose-Einstein condensation in a dilute gas, the first 70 years and some recent experiments”. *Reviews of Modern Physics* **74**, 875–893 (2002).
10. Carr, L., DeMille, D., Krems, R. & Ye, J. “Cold and ultracold molecules: science, technology and applications”. *New J. Phys.* **11**, 055049 (2009).
11. Doyle, J., Friedrich, B., Krems, R. V. & Masnou-Seeuws, F. “Editorial: Quo vadis, cold molecules?” *European Physical Journal D* **31**, 149–164 (2004).
12. DeMille, D. “Quantum Computation with Trapped Polar Molecules”. *Phys. Rev. Lett.* **88**, 067901 (2002).
13. Rabl, P. *et al.* “Hybrid Quantum Processors: Molecular Ensembles as Quantum Memory for Solid State Circuits”. *Phys. Rev. Lett.* **97**, 033003 (2006).
14. André, A. *et al.* “A coherent all-electrical interface between polar molecules and mesoscopic superconducting resonators”. *Nature Phys.* **2**, 636–642 (2006).
15. Micheli, A., Brennen, G. K. & Zoller, P. “A toolbox for lattice-spin models with polar molecules”. *Nature Physics* **2**, 341–347 (2006).
16. Kozlov, M. G. & Labzovsky, L. N. “Parity violation effects in diatomics”. *J. Phys. B: At. Mol. Opt. Phys.* **28**, 1933 (1995).
17. Tarbutt, M., Hudson, J., Sauer, B. & Hinds, E. “Prospects for measuring the electric dipole moment of the electron using electrically trapped polar molecules”. *Faraday Discuss.* **142**, 37 (2009).
18. Hudson, J. J. *et al.* “Improved measurement of the shape of the electron”. *Nature* **473**, 493–496 (2011).

19. Vutha, A. C. *et al.* “Search for the electric dipole moment of the electron with thorium monoxide”. *Journal of Physics B Atomic Molecular Physics* **43**, 074007 (2010).
20. DeMille, D. *et al.* “Enhanced Sensitivity to Variation of  $m_e/m_p$  in Molecular Spectra”. *Phys. Rev. Lett.* **100**, 043202 (2008).
21. Zelevinsky, T., Kotochigova, S. & Ye, J. “Precision Test of Mass-Ratio Variations with Lattice-Confined Ultracold Molecules”. *Phys. Rev. Lett.* **100**, 043201 (2008).
22. Hudson, E. R., Lewandowski, H. J., Sawyer, B. C. & Ye, J. “Cold molecule spectroscopy for constraining the evolution of the fine structure constant”. *Phys. Rev. Lett.* **96**, 143004 (2006).
23. Schiller, S. & Korobov, V. “Tests of time independence of the electron and nuclear masses with ultracold molecules”. *Phys. Rev. A* **71**, 032505 (2005).
24. Flambaum, V. V. & Kozlov, M. G. “Enhanced Sensitivity to the Time Variation of the Fine-Structure Constant and  $m_p/m_e$  in Diatomic Molecules”. *Phys. Rev. Lett.* **99**, 150801 (2007).
25. Chin, C., Flambaum, V. V. & Kozlov, M. G. “Ultracold molecules: new probes on the variation of fundamental constants”. *New Journal of Physics* **11**, 055048 (2009).
26. Bodo, E., Gianturco, F. A. & Dalgarno, A. “F+D<sub>2</sub> reaction at ultracold temperatures”. *J. Chem. Phys.* **116**, 9222 (2002).
27. Avdeenkov, A. V. & Bohn, J. L. “Linking ultracold polar molecules”. *Phys. Rev. Lett.* **90**, 043006 (2003).
28. Avdeenkov, A. V., Bortolotti, D. C. E. & Bohn, J. L. “Field-linked states of ultracold polar molecules”. *Phys. Rev. A* **69**, 2710 (2004).
29. Balakrishnan, N. & Dalgarno, A. “Chemistry at Ultracold Temperatures”. *Chem. Phys. Lett.* **341**, 652 (2001).
30. Krems, R. V. “Cold controlled chemistry”. *Phys. Chem. Chem. Phys.* **10**, 4079–4092 (2008).
31. Baranov, M. A., Osterloh, K. & Lewenstein, M. “Fractional Quantum Hall States in Ultracold Rapidly Rotating Dipolar Fermi Gases”. *Phys. Rev. Lett.* **94**, 070404 (2005).
32. Petrov, D. S., Baranov, M. A. & Shlyapnikov, G. V. “Superfluid transition in quasi-two-dimensional Fermi gases”. *Phys. Rev. A* **67**, 031601 (2003).
33. Góral, K. and Santos, L. and Lewenstein, M. “Quantum Phases of Dipolar Bosons in Optical Lattices”. *Phys. Rev. Lett.* **88**, 170406 (2002).
34. Baranov, M. A., Mar’enko, M. S., Rychkov, V. S. & Shlyapnikov, G. V. “Superfluid pairing in a polarized dipolar Fermi gas”. *Phys. Rev. A* **66**, 013606 (2002).
35. Barnett, R., Petrov, D., Lukin, M. & Demler, E. “Quantum Magnetism with Multicomponent Dipolar Molecules in an Optical Lattice”. *Phys. Rev. Lett.* **96**, 190401 (2006).
36. Pupillo, G., Micheli, A., Büchler, H. P. & Zoller, P. in *Cold Molecules: Theory, Experiment, Applications* (eds Krems, R. V., Stwalley, W. C. & Friedrich, B.) (CRC Press, 2009).
37. Dutta, O., Jääskeläinen, M. & Meystre, P. “Polarizing beam splitter for dipolar molecules”. *Phys. Rev. A* **71**, 051601 (2005).
38. Dutta, O., Jääskeläinen, M. & Meystre, P. “Single-mode acceleration of matter waves in circular waveguides”. *Phys. Rev. A* **74**, 023609 (2006).
39. Lukin, M. D. *et al.* “Dipole Blockade and Quantum Information Processing in Mesoscopic Atomic Ensembles”. *Phys. Rev. Lett.* **87**, 037901 (2001).
40. Bouyer, P. & Kasevich, M. A. “Heisenberg-limited spectroscopy with degenerate Bose-Einstein gases”. *Phys. Rev. A* **56**, 1083 (1997).
41. DeMille, D., Cahn, S. B., Murphree, D., Rahmlow, D. A. & Kozlov, M. G. “Using Molecules to Measure Nuclear Spin-Dependent Parity Violation”. *Phys. Rev. Lett.* **100**, 023003 (2008).
42. Sage, J. M., Sainis, S., Bergeman, T. & DeMille, D. “Optical Production of Ultracold Polar Molecules”. *Phys. Rev. Lett.* **94**, 203001 (2005).

43. Kerman, A. J., Sage, J. M., Sainis, S., Bergeman, T. & DeMille, D. “[Production of Ultracold, Polar RbCs\\* Molecules via Photoassociation](#)”. *Phys. Rev. Lett.* **92**, 033004 (2004).
44. Kerman, A. J., Sage, J. M., Sainis, S., Bergeman, T. & DeMille, D. “[Production and State-Selective Detection of Ultracold RbCs Molecules](#)”. *Phys. Rev. Lett.* **92**, 153001 (2004).
45. Ni, K. *et al.* “[A High Phase-Space-Density Gas of Polar Molecules](#)”. *Science* **322**, 231 (2008).
46. Danzl, J. G. *et al.* “[Quantum Gas of Deeply Bound Ground State Molecules](#)”. *Science* **321**, 1062– (2008).
47. Bethlem, H. L., Berden, G. & Meijer, G. “[Decelerating neutral dipolar molecules](#)”. *Phys. Rev. Lett.* **83**, 1558–61 (1999).
48. van de Meerakker, S. Y., Smeets, P. H., Vanhaecke, N., Jongma, R. T. & Meijer, G. “[Deceleration and Electrostatic Trapping of OH Radicals](#)”. *Phys. Rev. Lett.* **94**, 023004 (2005).
49. Hudson, E. R., Lewandowski, H. J., Sawyer, B. C. & Ye, J. “[Cold Molecule Spectroscopy for Constraining the Evolution of the Fine Structure Constant](#)”. *Phys. Rev. Lett.* **96**, 143004 (2006).
50. Osterwalder, A., Meek, S. A., Hammer, G., Haak, H. & Meijer, G. “[Deceleration of neutral molecules in macroscopic traveling traps](#)”. *Phys. Rev. A* **81**, 051401 (2010).
51. Vanhaecke, N., Meier, U., Andrist, M., Meier, B. H. & Merkt, F. “[Multistage Zeeman deceleration of hydrogen atoms](#)”. *Phys. Rev. A* **75**, 031402 (2007).
52. Narevicius, E. *et al.* “[Stopping Supersonic Beams with a Series of Pulsed Electromagnetic Coils: An Atomic Coilgun](#)”. *Phys. Rev. Lett.* **100**, 093003 (2008).
53. Narevicius, E. *et al.* “[Stopping supersonic oxygen with a series of pulsed electromagnetic coils: A molecular coilgun](#)”. *Phys. Rev. A* **77**, 051401 (2008).
54. Gupta, M. & Herschbach, D. “[A Mechanical Means to Produce Intense Beams of Slow Molecules](#)”. *J. Phys. Chem. A* **103**, 10670–10673 (1999).
55. Strebel, M., Stienkemeier, F. & Mudrich, M. “[Improved setup for producing slow beams of cold molecules using a rotating nozzle](#)”. *Phys. Rev. A* **81**, 033409 (2010).
56. Elioﬀ, M. S., Valentini, J. J. & Chandler, D. W. “[Subkelvin Cooling NO Molecules via “Billiard-like” Collisions with Argon](#)”. *Science* **302**, 1940–1943 (2003).
57. Trottier, A., Carty, D. & Wrede, E. “[Photostop: production of zero-velocity molecules by photodissociation in a molecular beam](#)”. *Mol. Phys.* **109**, 725–733 (2011).
58. Meijer, G., van de Meerakker, S. Y. T. & Bethlem, H. L. in *Cold Molecules: Theory, Experiment, Applications* (eds Krems, R. V., Stwalley, W. C. & Friedrich, B.) 509–552 (CRC Press, Boca Raton, 2009).
59. Tarbutt, M. R. *et al.* “[Slowing Heavy, Ground-State Molecules using an Alternating Gradient Decelerator](#)”. *Phys. Rev. Lett.* **92**, 173002 (2004).
60. Wall, T. E. *et al.* “[Stark deceleration of CaF molecules in strong- and weak-field seeking states](#)”. *Phys. Chem. Chem. Phys.* **131**, 18991 (2011).
61. van den Berg, J. E., Turkesteen, S. H., Prinsen, E. B. & Hoekstra, S. “[Deceleration and trapping of heavy diatomic molecules using a ring-decelerator](#)”. *European Physical Journal D* **66**, 235 (2012).
62. Fulton, R., Bishop, A. I. & Barker, P. F. “[Optical Stark Decelerator for Molecules](#)”. *Phys. Rev. Lett.* **93**, 243004 (2004).
63. Bishop, A. I., Wang, L. & Barker, P. F. “[Creating cold stationary molecular gases by optical Stark deceleration](#)”. *New J. Phys.* **12**, 073028 (2010).
64. Stuhl, B. K. *et al.* “[Evaporative cooling of the dipolar hydroxyl radical](#)”. *Nature* **492**, 396–400 (2012).

65. Doyle, J. M., Friedrich, B., Kim, J. & Patterson, D. “Buffer-gas loading of atoms and molecules into a magnetic trap”. *Phys. Rev. A* **52**, 2515 (1995).
66. Weinstein, J. D., deCarvalho, R., Guillet, T., Friedrich, B. & Doyle, J. M. “Magnetic trapping of calcium monohydride molecules at millikelvin temperatures”. *Nature* **395**, 148 (1998).
67. Decarvalho, R. *et al.* “Buffer-gas loaded magnetic traps for atoms and molecules: A primer”. *European Physical Journal D* **7**, 289–309 (1999).
68. Patterson, D. & Doyle, J. M. “Bright, guided molecular beam with hydrodynamic enhancement”. *J. Chem. Phys.* **126**, 154307 (2007).
69. Patterson, D., Rasmussen, J. & Doyle, J. M. “Intense atomic and molecular beams via neon buffer-gas cooling”. *New Journal of Physics* **11**, 055018 (2009).
70. Tsikata, E., Campbell, W. C., Hummon, M. T., Lu, H. & Doyle, J. M. “Magnetic trapping of NH molecules with 20 s lifetimes”. *New Journal of Physics* **12**, 065028 (2010).
71. Doret, S. C., Connolly, C. B., Ketterle, W. & Doyle, J. M. “Buffer-Gas Cooled Bose-Einstein Condensate”. *Physical Review Letters* **103**, 103005 (2009).
72. Maxwell, S. E. *et al.* “High-Flux Beam Source for Cold, Slow Atoms or Molecules”. *Phys. Rev. Lett.* **95**, 173201 (2005).
73. Barry, J. F., Shuman, E. S. & DeMille, D. “A bright, slow cryogenic molecular beam source for free radicals”. *Phys. Chem. Chem. Phys.* **13**, 18936–18947 (2011).
74. Hutzler, N. R. *et al.* “A cryogenic beam of refractory, chemically reactive molecules with expansion cooling”. *Phys. Chem. Chem. Phys.* **13**, 18976–18985 (2011).
75. Hutzler, N. R., Lu, H.-I. & Doyle, J. M. “The Buffer Gas Beam: An Intense, Cold, and Slow Source for Atoms and Molecules”. *Chemical Reviews* **112**, 4803–4827 (2012).
76. Tarbutt, M. R. *et al.* “A jet beam source of cold YbF radicals”. *Journal of Physics B: Atomic Molecular Physics* **35**, 5013–5022 (2002).
77. Raymond Ooi, C. H., Marzlin, K.-P. & Audretsch, J. “Laser cooling of molecules via single spontaneous emission”. *Eur. Phys. J. D* **22**, 259–267 (2003).
78. Zeppenfeld, M., Motsch, M., Pinkse, P. W. H. & Rempe, G. “Optoelectrical cooling of polar molecules”. *Phys. Rev. A* **80**, 041401 (2009).
79. Zeppenfeld, M. *et al.* “Sisyphus cooling of electrically trapped polyatomic molecules”. *Nature* **491**, 570–573 (2012).
80. Barry, J. F. & Demille, D. “Low-temperature physics: A chilling effect for molecules”. *Nature* **491**, 539–540 (2012).
81. Englert, B. G. U. *et al.* “Storage and Adiabatic Cooling of Polar Molecules in a Microstructured Trap”. *Physical Review Letters* **107**, 263003 (2011).
82. Lev, B. L. *et al.* “Prospects for the cavity-assisted laser cooling of molecules”. *Phys. Rev. A* **77**, 023402 (2008).
83. Viteau, M. *et al.* “Optical Pumping and Vibrational Cooling of Molecules”. *Science* **321**, 232–234 (2008).
84. Bahns, J. T., Stwalley, W. C. & Gould, P. L. “Laser cooling of molecules: A sequential scheme for rotation, translation, and vibration”. *Journal of Chemical Physics* **104**, 9689–9697 (1996).
85. Allouche, A., Wannous, G. & Aubert-Frcon, M. “A ligand-field approach for the low-lying states of Ca, Sr and Ba monohalides”. *Chemical Physics* **170**, 11–22 (1993).
86. Dagdigian, P. J., Cruse, H. W. & Zare, R. N. “Radiative lifetimes of the alkaline earth monohalides”. *Journal of Chemical Physics* **60**, 2330–2339 (1974).
87. Di Rosa, M. D. “Laser-cooling molecules”. *European Physical Journal D* **31**, 395–402 (2004).
88. Stuhl, B. K., Sawyer, B. C., Wang, D. & Ye, J. “Magneto-optical Trap for Polar Molecules”. *Phys. Rev. Lett.* **101**, 243002 (2008).



89. Berkeland, D. J. & Boshier, M. G. “Destabilization of dark states and optical spectroscopy in Zeeman-degenerate atomic systems”. *Phys. Rev. A* **65**, 033413 (2002).
90. Shuman, E. S., Barry, J. F., Glenn, D. R. & DeMille, D. “Radiative Force from Optical Cycling on a Diatomic Molecule”. *Phys. Rev. Lett.* **103**, 223001 (2009).
91. Brown, J. M. & Carrington, A. *Rotational spectroscopy of diatomic molecules* (Cambridge Univ. Press, 2003).
92. Hamilton, P. *Preliminary results in the search for the electron electric dipole moment in PbO*. PhD thesis (Yale University, 2010).
93. Dunham, J. L. “The Energy Levels of a Rotating Vibrator”. *Physical Review* **41**, 721–731 (1932).
94. Colarusso, P., Guo, B., Zhang, K.-Q. & Bernath, P. “High-Resolution Infrared Emission Spectrum of Strontium Monofluoride”. *Journal of Molecular Spectroscopy* **175**, 158–171 (1996).
95. Steimle, T. C., Domaille, P. J. & Harris, D. O. “Rotational analysis of the  $A^2\Pi-X^2\Sigma$  system of SrF using a CW tunable dye laser”. *Journal of Molecular Spectroscopy* **73**, 441–443 (1978).
96. Steimle, T. C., Fletcher, D. A. & Scurlock, C. T. “A Molecular Beam Study of the (0,0) $A^2\Pi-X^2\Sigma^+$  Band System of SrF”. *J. Mol. Spectrosc.* **158**, 487–488 (1993).
97. Steimle, T. private communication. 2008.
98. Sheridan, P. M., Wang, J.-G., Dick, M. J. & Bernath, P. F. “Optical-Optical Double Resonance Spectroscopy of the  $C^2\Pi-A^2\Pi$  and  $D^2\Sigma-A^2\Pi$  Transitions of SrF”. *Journal of Physical Chemistry A* **113**, 13383–13389 (2009).
99. Ernst, W. & Schröder, J. “The  $B^2\Sigma^+-X^2\Sigma^+$  system of SrF: Precise spectroscopic constants from a combined fit of microwave and sub-doppler optical spectra”. *Chemical Physics* **78**, 363–368 (1983).
100. Domaille, P. J., Steimle, T. C. & Harris, D. O. “The rotational spectrum of the  $X^2\Sigma^+$  state of the SrF radical using laser microwave optical double resonance”. *Journal of Molecular Spectroscopy* **68**, 146–155 (1977).
101. Fowler, C. A. “New Absorption Spectra of the Alkaline Earth Fluorides”. *Physical Review* **59**, 645–652 (1941).
102. Nitsch, C., Schröder, J. O. & Ernst, W. E. “Optical-optical double-resonance spectroscopy of SrF: The  $F^2\Sigma^+-B^2\Sigma^+$  and  $G^2\Pi-B^2\Sigma^+$  systems”. *Chemical Physics Letters* **148**, 130–135 (1988).
103. Childs, W. J., Goodman, L. S. & Renhorn, I. “Radio-frequency optical double-resonance spectrum of SrF: The  $X^2\Sigma^+$  state”. *Journal of Molecular Spectroscopy* **87**, 522–533 (1981).
104. Sauer, B. E., Wang, J. & Hinds, E. A. “Laser-rf double resonance spectroscopy of  $^{174}\text{YbF}$  in the  $X^2\Sigma^+$  state: Spin-rotation, hyperfine interactions, and the electric dipole moment”. *Journal of Chemical Physics* **105**, 7412–7420 (1996).
105. Wall, T. E. *et al.* “Lifetime of the  $A(v' = 0)$  state and Franck-Condon factor of the  $A-X(0-0)$  transition of CaF measured by the saturation of laser-induced fluorescence”. *Phys. Rev. A* **78**, 062509 (2008).
106. Ernst, W. E. “Microwave-optical polarization spectroscopy of the  $X^2\Sigma$  state of SrF”. *Applied Physics B: Lasers and Optics* **30**, 105–108 (1983).
107. Knight, L. B. Jr. & Weltner, W. Jr. “Hyperfine Interaction and Chemical Bonding in MgH, CaH, SrH, and BaH Molecules”. *Journal of Chemical Physics* **54**, 3875–3884 (1971).
108. Huber, K. P. & Herzberg, G. *Constants of Diatomic Molecules* (Van Nostrand Reinhold, 1979).
109. Brown, J. M. & Merer, A. J. “Lambda-type doubling parameters for molecules in  $\Pi$  electronic states of triplet and higher multiplicity”. *Journal of Molecular Spectroscopy* **74**, 488–494 (1979).

110. Mulliken, R. S. & Christy, A. “A-Type Doubling and Electron Configurations in Diatomic Molecules”. *Phys. Rev.* **38**, 87–119 (1931).
111. Kändler, J., Martell, T. & Ernst, W. E. “Electric dipole moments and hyperfine structure of  $\text{SrF } A^2\Pi$  and  $B^2\Sigma^+$ ”. *Chemical Physics Letters* **155**, 470–474 (1989).
112. Rydberg, R. “Graphische Darstellung einiger bandenspektroskopischer Ergebnisse”. *Zeitschrift fr Physik* **73**, 376–385 (1932).
113. Klein, O. “Zur Berechnung von Potentialkurven fr zweiatomige Molekle mit Hilfe von Spektraltermen”. *Zeitschrift fr Physik* **76**, 226–235 (1932).
114. Rees, A. L. G. “The calculation of potential-energy curves from band-spectroscopic data”. *Proceedings of the Physical Society* **59**, 998 (1947).
115. Le Roy, R. J. “Level 8.0: A computer program for solving the radial Schrödinger equation for bound and quasibound levels”. *University of Waterloo Chemical Physics Research Report CP-663* (2007).
116. Stienkemeier, F. *Reaktive und nichtreaktive Streuung con Li, Sr an HF(v=0), HF(v=1,J=1): Rückwärtsglorien, Reaktionsquerschnitte, Produktzustandsverteilungen, sterische Effekte*. PhD thesis (Universität Bielefeld, 1993).
117. Watson, J. K. G. “Honl London factors for multiplet transitions in Hund’s case a or b”. *Journal of Molecular Spectroscopy* **252**, 5–8 (2008).
118. Zanon-Willette, T., de Clercq, E. & Arimondo, E. “Ultrahigh-resolution spectroscopy with atomic or molecular dark resonances: Exact steady-state line shapes and asymptotic profiles in the adiabatic pulsed regime”. *Phys. Rev. A* **84**, 062502 (2011).
119. Lindvall, T., Merimaa, M., Tittonen, I. & Madej, A. A. “Dark-state suppression and optimization of laser cooling and fluorescence in a trapped alkaline-earth-metal single ion”. *Phys. Rev. A* **86**, 033403 (2012).
120. Hummon, M. T. *et al.* “2D Magneto-Optical Trapping of Diatomic Molecules”. *Phys. Rev. Lett.* **110**, 143001 (2013).
121. Dunning, F. B. & Hulet, R. G. *Atomic, Molecular, and Optical Physics: Electromagnetic Radiation* First Edition (Academic Press, Inc., San Diego, 1997).
122. Swain, S. “Generalised multiphoton rate equations”. *Journal of Physics B Atomic Molecular Physics* **13**, 2375–2396 (1980).
123. Grynberg, G., Aspect, A., Fabre, C. & Cohen-Tannoudji, C. *Introduction to Quantum Optics* (2010).
124. Tarbutt, M. R., Sauer, B. E., Hudson, J. J. & Hinds, E. A. “Design for a fountain of  $\text{YbF}$  molecules to measure the electron’s electric dipole moment”. *New Journal of Physics* **15**, 053034 (2013).
125. Pearle, P. “Simple derivation of the Lindblad equation”. *European Journal of Physics* **33**, 805 (2012).
126. Saad, Y. *Iterative Methods for Sparse Linear Systems* (Society for Industrial and Applied Mathematics, Philadelphia, 2003).
127. Moler, C. & Loan, C. V. “Nineteen Dubious Ways to Compute the Exponential of a Matrix, Twenty-Five Years Later”. *SIAM Review* **45**, pp. 3–49 (2003).
128. Mazzi, G. *Numerical Treatment of the Liouville-von Neumann Equation for Quantum Spin Dynamics*. PhD thesis (University of Edinburgh, 2010).
129. AtomicDensityMatrix. *Version 13.07.19*. <<http://budker.berkeley.edu/ADM>> (2013).
130. Mathematica. *Version 9.0.1.0* (Wolfram Research, Inc., Champaign, Illinois, 2013).
131. Happer, W., Yuan-Yu, J. & Walker, T. *Optically Pumped Atoms* (Wiley, New Jersey, 2010).
132. MATLINK. *Version 1.0*. <<http://MATLink.org>> (2013).

133. Higham, N. "The Scaling and Squaring Method for the Matrix Exponential Revisited". *SIAM Journal on Matrix Analysis and Applications* **26**, 1179–1193 (2005).
134. DeMille, D., Barry, J. F., Edwards, E. R., Norrgard, E. B. & Steinecker, M. H. "On the transverse confinement of radiatively slowed molecular beams". *Molecular Physics*. eprint: <http://www.tandfonline.com/doi/pdf/10.1080/00268976.2013.793833> (2013).
135. Vanhaecke, N. & Dulieu, O. "Precision measurements with polar molecules: the role of the black body radiation". *Molecular Physics* **105**, 1723–1731 (2007).
136. Langhoff, S. R., Bauschlicher, C. W. Jr., Partridge, H. & Ahlrichs, R. "Theoretical study of the dipole moments of selected alkaline-earth halides". *Journal of Chemical Physics* **84**, 5025–5031 (1986).
137. Ernst, W., Kändler, J., Kindt, S. & Törring, T. "Electric dipole moment of SrF  $X^2\Sigma^+$  from high-precision stark effect measurements". *Chemical Physics Letters* **113**, 351–354 (1985).
138. DeMille, D., Cahn, S. B., Murphree, D., Rahmlow, D. A. & Kozlov, M. G. "Using Molecules to Measure Nuclear Spin-Dependent Parity Violation". *Phys. Rev. Lett.* **100**, 023003 (2008).
139. Isaev, T. A., Hoekstra, S. & Berger, R. "Laser-cooled RaF as a promising candidate to measure molecular parity violation". *Phys. Rev. A* **82**, 052521 (2010).
140. van den Berg, J. E., Turkesteen, S. H., Prinsen, E. B. & Hoekstra, S. "Deceleration and trapping of heavy diatomic molecules using a ring-decelerator". *European Physical Journal D* **66**, 235 (2012).
141. Wandt, D., Laschek, M., Przyklenk, K., Tünnermann, A. & Welling, H. "External cavity laser diode with 40 nm continuous tuning range around 825 nm". *Optics Communications* **130**, 81–84 (1996).
142. Petridis, C., Lindsay, I. D., Stothard, D. J. M. & Ebrahimzadeh, M. "Mode-hop-free tuning over 80 GHz of an extended cavity diode laser without antireflection coating". *Review of Scientific Instruments* **72**, 3811–3815 (2001).
143. Lonsdale, D. J., Andrews, D. A. & King, T. A. "Single mode operation and extended scanning of anti-reflection coated visible laser diodes in a Littrow cavity". *Measurement Science and Technology* **15**, 933–938 (2004).
144. Trutna, W. R. & Stokes, L. F. "Continuously tuned external cavity semiconductor laser". *Journal of Lightwave Technology* **11**, 1279 (1993).
145. Favre, F., Le Guen, D., Simon, J. C. & Landousies, B. "External-cavity semiconductor laser with 15 nm continuous tuning range". *Electronics Letters* **22**, 795 (1986).
146. Repasky, K. S., Nehrir, A. R., Hawthorne, J. T., Switzer, G. W. & Carlsten, J. L. "Extending the continuous tuning range of an external-cavity diode laser". *Applied Optics* **45**, 9013–9020 (2006).
147. Favre, F. & le Guen, D. "82 nm of continuous tunability for an external cavity semiconductor laser". *Electronics Letters* **27**, 183–184 (1991).
148. Cook, E. C., Martin, P. J., Brown-Heft, T. L., Garman, J. C. & Steck, D. A. "High passive-stability diode-laser design for use in atomic-physics experiments". *Review of Scientific Instruments* **83**, 043101 (2012).
149. Schoof, A., Grünert, J., Ritter, S. & Hemmerich, A. "Reducing the linewidth of a diode laser below 30 Hz by stabilization to a reference cavity with a finesse above  $10^5$ ". *Opt. Lett.* **26**, 1562–1564 (2001).
150. Mehuys, D., Welch, D. & Scifres, D. "1 W CW, diffraction-limited, tunable external-cavity semiconductor laser". *Electronics Letters* **29**, 1254–1255 (1993).
151. Arnold, A. S., Wilson, J. S. & Boshier, M. G. "A simple extended-cavity diode laser". *Review of Scientific Instruments* **69**, 1236–1239 (1998).

152. Hawthorn, C. J., Weber, K. P. & Scholten, R. E. "Littrow configuration tunable external cavity diode laser with fixed direction output beam". *Review of Scientific Instruments* **72**, 4477–4479 (2001).
153. Wieman, C. E. & Hollberg, L. "Using diode lasers for atomic physics". *Review of Scientific Instruments* **62**, 1–20 (1991).
154. Saliba, S. D., Junker, M., Turner, L. D. & Scholten, R. E. "Mode stability of external cavity diode lasers". *Appl. Opt.* **48**, 6692–6700 (2009).
155. Andalkar, A., Lamoreaux, S. K. & Warrington, R. B. "Improved external cavity design for cesium D1 (894 nm) diode laser". *Review of Scientific Instruments* **71**, 4029–4031 (2000).
156. Ricci, L. *et al.* "A compact grating-stabilized diode laser system for atomic physics". *Optics Communications* **117**, 541–549 (1995).
157. Vassiliev, V. V., Zibrov, S. A. & Velichansky, V. L. "Compact extended-cavity diode laser for atomic spectroscopy and metrology". *Review of Scientific Instruments* **77**, 013102 (2006).
158. MacAdam, K. B., Steinbach, A. & Wieman, C. "A narrow-band tunable diode laser system with grating feedback, and a saturated absorption spectrometer for Cs and Rb". *American Journal of Physics* **60**, 1098–1111 (1992).
159. Littman, M. G. & Metcalf, H. J. "Spectrally narrow pulsed dye laser without beam expander". *Applied Optics* **17**, 2224–2227 (1978).
160. Liu, K. & Littman, M. G. "Novel geometry for single-mode scanning of tunable lasers". *Optics Letters* **6**, 117 (1981).
161. McNicholl, P. & Metcalf, H. J. "Synchronous cavity mode and feedback wavelength scanning in dye laser oscillators with gratings". *Applied Optics* **24**, 2757–2761 (1985).
162. Yang, G., Barry, J. F., Shuman, E. S., Steinecker, M. H. & DeMille, D. "A low-cost, FPGA-based servo controller with lock-in amplifier". *Journal of Instrumentation* **7**, 26P (2012).
163. Heine, T. & Heidemann, R. *Tunable diode laser system with external resonator*. Germany Patent: 7970024. 2009.
164. Nilse, L., Davies, H. J. & Adams, C. S. "Synchronous Tuning of Extended Cavity Diode Lasers: The Case for an Optimum Pivot Point". *Applied Optics* **38**, 548–553 (1999).
165. Chiow, S.-W., Long, Q., Vo, C., Müller, H. & Chu, S. "Extended-cavity diode lasers with tracked resonances". *Applied Optics* **46**, 7997–8001 (2007).
166. Mok, C., Weel, M., Rotberg, E. & Kumarakrishnan, A. "Design and construction of an efficient electro-optic modulator for laser spectroscopy". *Canadian Journal of Physics* **84**, 775–786 (2006).
167. Glenn, D. R. *Development of Techniques for Cooling and Trapping Polar Diatomic Molecules*. PhD thesis (Yale University, 2009).
168. Yariv, A. *Quantum Electronics* Second Edition (John Wiley and Sons, Inc., New York, 2003).
169. *Practical Uses and Applications of Electro-Optic Modulators*. New Focus, Inc. <<http://www.physics.montana.edu/oct/ctseminar/Practical%20Uses%20of%20EOMs.pdf>> (1993).
170. Williams, A. *Fundamentals of Magnetics Design: Inductors and Transformers*. Telebyte Inc. <[http://www.ieee.li/pdf/viewgraphs/fundamentals\\_of\\_magnetics\\_design.pdf](http://www.ieee.li/pdf/viewgraphs/fundamentals_of_magnetics_design.pdf)> (2011).
171. Sumpf, B. *et al.* "670 nm tapered lasers and amplifier with output powers  $P \sim 1$  W and nearly diffraction limited beam quality". *Proc. SPIE* **6485**, 648517 (2007).
172. Sumpf, B. *et al.* "670 nm nearly diffraction limited tapered lasers with more than 30% conversion efficiency and 1 W cw and 3 W pulsed output power". *Proc. SPIE* **7953**, 79530Z (2011).
173. Shima, A. *et al.* "High-efficiency and high-power laser diodes for CD-R/RW and DVD-RAM/RW". *Proc. SPIE* **4287**, 48–56 (2001).

174. Meyrath, T. P. *An Analog Current Controller Design for Laser Diodes*. Atom Optics Laboratory, Center for Nonlinear Dynamics, University of Texas at Austin. <<http://george.ph.utexas.edu/~meyrath/informal/laser%20diode.pdf>> (2003).
175. Ferrari, G., Mewes, M.-O., Schreck, F. & Salomon, C. “High-power multiple-frequency narrow-linewidth laser source based on a semiconductor tapered amplifier”. *Optics Letters* **24**, 151–153 (1999).
176. Mahnke, J. *et al.* “Microwave sidebands for laser cooling by direct modulation of a tapered amplifier”. *ArXiv e-prints*. arXiv: [1306.0402](https://arxiv.org/abs/1306.0402) [physics.atom-ph] (2013).
177. Bridge, E. M., Millen, J., Adams, C. S. & Jones, M. P. A. “A vapor cell based on dispensers for laser spectroscopy”. *Review of Scientific Instruments* **80**, 013101 (2009).
178. Culshaw, W. & Kannelaud, J. “Hanle Effect in the He-Ne Laser”. *Physical Review* **136**, 1209–1221 (1964).
179. Sargent, M., Lamb, W. E. & Fork, R. L. “Theory of a Zeeman Laser. I”. *Physical Review* **164**, 436–449 (1967).
180. Sargent, M., Lamb, W. E. & Fork, R. L. “Theory of a Zeeman Laser. II”. *Physical Review* **164**, 450–465 (1967).
181. Voitovich, A. “Magnetooptics of gas lasers”. English. *Journal of Soviet Laser Research* **8**, 551–683 (1987).
182. Ferguson, J. B. & Morris, R. H. “Single-mode collapse in 6328-Å He-Ne lasers”. *Appl. Opt.* **17**, 2924–2929 (1978).
183. Lindberg, A. M. “Mode frequency pulling in He-Ne lasers”. *American Journal of Physics* **67**, 350–353 (1999).
184. Baer, T., Kowalski, F. V. & Hall, J. L. “Frequency stabilization of a 0.633-μm He-Ne longitudinal Zeeman laser”. *Applied Optics* **19**, 3173–3177 (1980).
185. Polanyi, T., Skolnick, M. & Tobias, I. “Frequency stabilization of a gas laser”. *IEEE Journal of Quantum Electronics* **2**, 178–179 (1966).
186. Goldwasser, S. M. *Sam’s Laser FAQ*. <<http://www.repairfaq.org/>> (2013).
187. Lee, W.-K., Suh, H. S. & Kang, C.-S. “Vacuum wavelength calibration of frequency-stabilized He-Ne lasers used in commercial laser interferometers”. *Optical Engineering* **50**, 054301 (2011).
188. Umeda, N., Tsukiji, M. & Takasaki, H. “Stabilized  $^3\text{He}$ - $^{20}\text{Ne}$  transverse Zeeman laser”. *Appl. Opt.* **19**, 442–450 (1980).
189. Zumberge, M. A. “Frequency stability of a Zeeman-stabilized laser”. *Appl. Opt.* **24**, 1902–1904 (1985).
190. Diao, X., Tan, J., Hu, P., Yang, H. & Wang, P. “Frequency stabilization of an internal mirror He-Ne laser with a high frequency reproducibility”. *Appl. Opt.* **52**, 456–460 (2013).
191. Sasagawa, G. S. & Zumberge, M. A. “Five-year frequency stability of a Zeeman stabilized laser”. *Appl. Opt.* **28**, 824–825 (1989).
192. Niebauer, T. M., Faller, J. E., Godwin, H. M., Hall, J. L. & Barger, R. L. “Frequency stability measurements on polarization-stabilized He-Ne lasers”. *Appl. Opt.* **27**, 1285–1289 (1988).
193. Eickhoff, M. & Hall, J. “Optical frequency standard at 532 nm”. *Instrumentation and Measurement, IEEE Transactions on* **44**, 155–158 (1995).
194. Lindsay, B. G., Smith, K. A. & Dunning, F. B. “Control of long-term output frequency drift in commercial dye lasers”. *Review of Scientific Instruments* **62**, 1656–1657 (1991).
195. Riedle, E., Ashworth, S. H., J. T. Farrell, J. & Nesbitt, D. J. “Stabilization and precise calibration of a continuous-wave difference frequency spectrometer by use of a simple transfer cavity”. *Review of Scientific Instruments* **65**, 42–48 (1994).



196. Plusquellic, D. F., Votava, O. & Nesbitt, D. J. “Absolute frequency stabilization of an injection-seeded optical parametric oscillator”. *Appl. Opt.* **35**, 1464–1472 (1996).
197. Zhao, W. Z., Simsarian, J. E., Orozco, L. A. & Sprouse, G. D. “A computer-based digital feedback control of frequency drift of multiple lasers”. *Review of Scientific Instruments* **69**, 3737–3740 (1998).
198. Rossi, A., Biancalana, V., Mai, B. & Tomassetti, L. “Long-term drift laser frequency stabilization using purely optical reference”. *Review of Scientific Instruments* **73**, 2544–2548 (2002).
199. Burke, J. H. T., Garcia, O., Hughes, K. J., Livedalen, B. & Sackett, C. A. “Compact implementation of a scanning transfer cavity lock”. *Review of Scientific Instruments* **76**, 116105 (2005).
200. Bohlouli-Zanjani, P., Afrousheh, K. & Martin, J. D. D. “Optical transfer cavity stabilization using current-modulated injection-locked diode lasers”. *Review of Scientific Instruments* **77**, 093105 (2006).
201. Jaffe, S. M., Rochon, M. & Yen, W. M. “Increasing the frequency stability of single-frequency lasers”. *Review of Scientific Instruments* **64**, 2475–2481 (1993).
202. Black, E. D. “An introduction to Pound-Drever-Hall laser frequency stabilization”. *American Journal of Physics* **69**, 79–87 (2001).
203. DeMille, D., Glenn, D. R. & Petricka, J. “Microwave traps for cold polar molecules”. *European Physical Journal D* **31**, 375–384 (2004).
204. Krems, R., Friedrich, B. & Stwalley, W. C. *Cold Molecules: Theory, Experiment, Applications* (CRC Press, Boca Raton, FL, 2009).
205. Van Buuren, L. D. *et al.* “Electrostatic Extraction of Cold Molecules from a Cryogenic Reservoir”. *Phys. Rev. Lett.* **102**, 033001 (2009).
206. Shuman, E. S., Barry, J. F. & DeMille, D. “Laser cooling of a diatomic molecule”. *Nature* **467**, 820–823 (2010).
207. Ramsey, N. F. *Molecular Beams* (Oxford University Press, London, 1956).
208. Scoles, G. *Atomic and Molecular Beam Methods* (Oxford University Press, New York, 1988).
209. Pauly, H. *Atom, Molecule, and Cluster Beams* (Springer, Berlin, 2000).
210. Lu, M.-J. & Weinstein, J. D. “Cold  $\text{TiO}(\text{X}^3\Delta)$ -He collisions”. *New Journal of Physics* **11**, 055015 (2009).
211. Maussang, K., Egorov, D., Helton, J. S., Nguyen, S. V. & Doyle, J. M. “Zeeman Relaxation of CaF in Low-Temperature Collisions with Helium”. *Phys. Rev. Lett.* **94**, 123002 (2005).
212. Petricka, J. *A New Cold Molecule Source: The Buffer Gas Cooled Molecular Beam*. PhD thesis (Yale University, 2007).
213. Skoff, S. M. *et al.* “Diffusion, thermalization, and optical pumping of YbF molecules in a cold buffer-gas cell”. *Phys. Rev. A* **83**, 023418 (2011).
214. Hamel, W. A., Haverkort, J. E. M., Werij, H. G. C. & Woerdman, J. P. “Calculation of alkali-noble gas diffusion cross sections relevant to light-induced drift”. *Journal of Physics B Atomic Molecular Physics* **19**, 4127–4135 (1986).
215. Hogervorst, W. “Diffusion coefficients of noble-gas mixtures between 300 K and 1400 K”. *Physica* **51**, 59–76 (1971).
216. Davis, G. M., Gower, M. C., Fotakis, C., Efthimiopoulos, T. & Argyrakis, P. “Spectroscopic studies of ArF laser photoablation of PMMA”. *Applied Physics A: Materials Science & Processing* **36**, 27–30 (1985).
217. Hasted, J. B. *Physics of Atomic Collisions* (Elsevier Publishing Company, New York, 1972).
218. Toennies, J. P. & Winkelmann, K. “Theoretical studies of highly expanded free jets: Influence of quantum effects and a realistic intermolecular potential”. *J. Chem. Phys.* **66**, 3965–3979 (1977).

219. Wang, J. *et al.* “Speed ratios greater than 1000 and temperatures less than 1 mK in a pulsed He beam”. *Phys. Rev. Lett.* **60**, 696–699 (1988).
220. Tobin, A. G., Sedgley, D. W., Batzer, T. H. & Call, W. R. “Evaluation of charcoal sorbents for helium cryopumping in fusion reactors”. *J. Vac. Sci. Tech.* **5**, 101–105 (1987).
221. Sedgley, D. W., Tobin, A. G., Batzer, T. H. & Call, W. R. “Characterization of charcoals for helium cryopumping in fusion devices”. *J. Vac. Sci. Tech. A* **5**, 2572–2576 (1987).
222. Dondi, M. G., Scoles, G., Torello, F. & Pauly, H. “Energy Dependence of the Elastic Total Collision Cross Section of Identical Molecules:  $^4\text{He}$ ”. *J. Chem. Phys.* **51**, 392–397 (1969).
223. Ball, C. “Direct observation of A-doublet and hyperfine branching ratios for rotationally inelastic collisions of NO He at 4.2 K”. *Chem. Phys. Lett.* **300**, 227–235 (1999).
224. Budker, D., Kimball, D. F. & DeMille, D. P. *Atomic Physics: An Exploration Through Problems and Solutions*, 2nd. Ed. (Oxford Univ. Press, 2008).
225. Tejeda, G., Maté, B., Fernández-Sánchez, J. M. & Montero, S. “Temperature and Density Mapping of Supersonic Jet Expansions Using Linear Raman Spectroscopy”. *Phys. Rev. Lett.* **76**, 34–37 (1996).
226. Hillenkamp, M., Keinan, S. & Even, U. “Condensation limited cooling in supersonic expansions”. *J. Chem. Phys.* **118**, 8699–8705 (2003).
227. Sherman, F. S. “Hydrodynamical Theory of Diffusive Separation of Mixtures in a Free Jet”. *Physics of Fluids* **8**, 773–779 (1965).
228. Dun, H. “The gas dynamics of a conical nozzle molecular beam sampling system”. *Chemical Physics* **38**, 161–172 (1979).
229. Ramos, A. and Tejeda, G. and Fernández, J. M. and Montero, S. “Nonequilibrium Processes in Supersonic Jets of  $\text{N}_2$ ,  $\text{H}_2$ , and  $\text{N}_2 + \text{H}_2$  Mixtures: (I) Zone of Silence”. *J. Phys. Chem. A* **113**, 8506–8512 (2009).
230. Fernandez de La Mora, J. & Rosell-Llompart, J. “Aerodynamic focusing of heavy molecules in seeded supersonic jets”. *J. Chem. Phys.* **91**, 2603–2615 (1989).
231. Reis, V. H. & Fenn, J. B. “Separation of Gas Mixtures in Supersonic Jets”. *J. Chem. Phys.* **39**, 3240–3250 (1963).
232. Ahern, M. “Rotational relaxation of CO in He, Ar, N<sub>2</sub> and CO free jets”. *Chem. Phys. Lett.* **300**, 681–686 (1999).
233. Mazely, T. L., Roehrig, G. H. & Smith, M. A. “Free jet expansions of binary atomic mixtures: A method of moments solution of the Boltzmann equation”. *J. Chem. Phys.* **103**, 8638–8652 (1995).
234. Abuaf, N., Anderson, J. B., Andres, R. P., Fenn, J. B. & Marsden, D. G. H. “Molecular Beams with Energies above One Electron Volt”. *Science* **155**, 997–999 (1967).
235. De Dea, S., Miller, D. R. & Continetti, R. E. “Cluster and Solute Velocity Distributions in Free-Jet Expansions of Supercritical  $\text{CO}_2$ ”. *J. Phys. Chem. A* **113**, 388–398 (2009).
236. Dietz, T. G., Duncan, M. A., Powers, D. E. & Smalley, R. E. “Laser production of supersonic metal cluster beams”. *J. Chem. Phys.* **74**, 6511–6512 (1981).
237. Fletcher, D. A., Jung, K. Y., Scurlock, C. T. & Steimle, T. C. “Molecular beam pump/probe microwave-optical double resonance using a laser ablation source”. *J. Chem. Phys.* **98**, 1837–1842 (1993).
238. Hopkins, J. B., Langridge-Smith, P. R. R., Morse, M. D. & Smalley, R. E. “Supersonic metal cluster beams of refractory metals: Spectral investigations of ultracold  $\text{Mo}_2$ ”. *J. Chem. Phys.* **78**, 1627–1637 (1983).
239. Tu, M., Ho, J., Hsieh, C. & Chen, Y. “Intense SrF radical beam for molecular cooling experiments”. *Review of Scientific Instruments* **80**, 113111 (2009).

240. Rahmlow, D. *Towards a measurement of parity nonconservation in diatomic molecules*. PhD thesis (Yale University, 2010).
241. Lu, H.-I., Rasmussen, J., Wright, M. J., Patterson, D. & Doyle, J. M. “A cold and slow molecular beam”. *Phys. Chem. Chem. Phys.* **131**, 18986 (2011).
242. Zhelyazkova, V. *et al.* “Laser cooling and slowing of CaF molecules”. *ArXiv e-prints*. arXiv: [1308.0421 \[physics.atom-ph\]](#) (2013).
243. Olivier Emile *et al.* “Magnetically assisted Sisyphus effect”. *J. Phys. II France* **3**, 1709–1733 (1993).
244. Gupta, R., Padua, S., Xie, C., Batelaan, H. & Metcalf, H. “Simplest atomic system for sub-Doppler laser cooling”. *J. Opt. Soc. Am. B* **11**, 537–541 (1994).
245. Plimmer, M. D. *et al.* “2D laser collimation of a cold Cs beam induced by a transverse  $B$ -field”. *JETP Letters* **82**, 18–22 (2005).
246. Barry, J. F., Shuman, E. S., Norrgard, E. B. & Demille, D. “Laser Radiation Pressure Slowing of a Molecular Beam”. *Physical Review Letters* **108**, 103002 (2012).
247. Prodan, J. V., Phillips, W. D. & Metcalf, H. “Laser production of a very slow monoenergetic atomic beam”. *Phys. Rev. Lett.* **49**, 1149–1153 (1982).
248. Zhu, M., Oates, C. W. & Hall, J. L. “Continuous high-flux monovelocity atomic beam based on a broadband laser-cooling technique”. *Phys. Rev. Lett.* **67**, 46–49 (1991).
249. Prodan, J. V. & Phillips, W. D. “Chirping the light—fantastic? Recent NBS atom cooling experiments”. *Prog. Quant. Electr.* **8**, 231–235 (1984).
250. Van de Meerakker, S. Y. T., Jongma, R. T., Bethlem, H. L. & Meijer, G. “Accumulating NH radicals in a magnetic trap”. *Phys. Rev. A* **64**, 041401 (2001).
251. Riedel, J. *et al.* “Accumulation of Stark-decelerated NH molecules in a magnetic trap”. *Eur. Phys. J. D* **65**, 161–166 (2011).
252. Falkenau, M., Volchkov, V. V., Rührig, J., Griesmaier, A. & Pfau, T. “Continuous Loading of a Conservative Potential Trap from an Atomic Beam”. *Phys. Rev. Lett.* **106**, 163002 (2011).
253. Stuhler, J. *et al.* “Continuous loading of a magnetic trap”. *Phys. Rev. A* **64**, 031405 (2001).
254. Meyer, E. R. & Bohn, J. L. “Chemical pathways in ultracold reactions of SrF molecules”. *Phys. Rev. A* **83**, 032714 (2011).
255. Tiwari, V. B., Singh, S., Rawat, H. S. & Mehendale, S. C. “Cooling and trapping of  $^{85}\text{Rb}$  atoms in the ground hyperfine  $F=2$  state”. *Phys. Rev. A* **78**, 063421 (2008).
256. Nasyrov, K. *et al.* “Magneto-optical trap operating on a magnetically induced level-mixing effect”. *Phys. Rev. A* **64**, 023412 (2001).
257. Shang, S.-Q., Lu, Z.-T. & Freedman, S. J. “Comparison of the cold-collision losses for laser-trapped sodium in different ground-state hyperfine sublevels”. *Phys. Rev. A* **50**, 4449 (1994).
258. Prentiss, M., Cable, A., Bjorkholm, J. E., Chu, S. & Raab, E. L. “Atomic-density-dependent losses in an optical trap”. *Optics Letters* **13**, 452–454 (1988).
259. Atutov, S. N. *et al.* “Sodium MOT collection efficiency as a function of the trapping and repumping laser frequencies and intensities”. *European Physical Journal D* **13**, 71–82 (2001).
260. Flemming, J. *et al.* “Magneto-optical trap for sodium atoms operating on the  $D_1$  line”. *Optics Communications* **135**, 269–272 (1997).
261. Williamson, R. S. III & Walker, T. “Magneto-optical trapping and ultracold collisions of potassium atoms”. *Journal of the Optical Society of America B Optical Physics* **12**, 1393–1397 (1995).
262. Lindquist, K., Stephens, M. & Wieman, C. “Experimental and theoretical study of the vapor-cell Zeeman optical trap”. *Phys. Rev. A* **46**, 4082–4090 (1992).
263. Metcalf, H. J. & van der Straten, P. *Laser Cooling and Trapping* (Springer, New York, 1999).



264. Boyd, M. M. *High Precision Spectroscopy of Strontium in an Optical Lattice: Towards a New Standard for Frequency and Time*. PhD thesis (University of Colorado, 2007).
265. Mukaiyama, T., Katori, H., Ido, T., Li, Y. & Kuwata-Gonokami, M. “Recoil-Limited Laser Cooling of  $^{87}\text{Sr}$  Atoms near the Fermi Temperature”. *Physical Review Letters* **90**, 113002 (2003).
266. Anderson, B. P. & Kasevich, M. A. “Enhanced loading of a magneto-optic trap from an atomic beam”. *Phys. Rev. A* **50**, 3581 (1994).
267. Hoffnagle, J. A. “Proposal for continuous white-light cooling of an atomic beam”. *Optics Letters* **13**, 102–104 (1988).
268. Faulstich, A. *et al.* “Strong velocity compression of a supersonic atomic beam using moving optical molasses”. *EPL (Europhysics Letters)* **17**, 393 (1992).
269. Rosin, S. & Rabi, I. I. “Effective Collision Cross Sections of the Alkali Atoms in Various Gases”. *Physical Review* **48**, 373–379 (1935).
270. Rothe, E. W. & Bernstein, R. B. “Total Collision Cross Sections for the Interaction of Atomic Beams of Alkali Metals with Gases”. *Journal of Chemical Physics* **31**, 1619–1627 (1959).
271. Sawyer, B. C., Stuhl, B. K., Wang, D., Yeo, M. & Ye, J. “Molecular Beam Collisions with a Magnetically Trapped Target”. *Phys. Rev. Lett.* **101**, 203203 (2008).
272. Zheng, S. *Conductance Calculation - Molecular Flow, Long Tube of Circular Cross Section*. GEM Vacuum Group. <<http://lss.fnal.gov/archive/other/ssc/ssc-gem-tn-93-382.pdf>> (1993).
273. Blatt, S. *Ultracold Collisions and Fundamental Physics with Strontium*. PhD thesis (University of Colorado, 2011).
274. Belyaev, V., Gotkis, I., Lebedeva, N. & Krasnov, K. “Ionization potentials of MX molecules ( $M = \text{Ca, Sr, Ba}$ ;  $X = \text{F, Cl, Br, I, OH, O}$ )”. *Russ. J. Phys. Chem.* **64**, 773 (1990).
275. Jakubek, Z. J., Harris, N. A., Field, R. W., Gardner, J. A. & Murad, E. “Ionization potentials of  $\text{CaF}$  and  $\text{BaF}$ ”. *Journal of Chemical Physics* **100**, 622–627 (1994).
276. Fellers, T. J. & Davidson, M. W. *Concepts in Digital Imaging Technology*. National High Magnetic Field Laboratory. <<http://learn.hamamatsu.com/articles/ccdsnr.html>> (2013).
277. Semrock, Inc. <[www.semrock.com](http://www.semrock.com)> (2013).
278. Gibble, K. E., Kasapi, S. & Chu, S. “Improved magneto-optic trapping in a vapor cell”. *Optics Letters* **17**, 526–528 (1992).
279. Grimm, R., Weidemüller, M. & Ovchinnikov, Y. B. “Optical Dipole Traps for Neutral Atoms”. *Advances in Atomic Molecular and Optical Physics* **42**, 95–170 (2000).
280. Söding, J., Grimm, R., Ovchinnikov, Y. B., Bouyer, P. & Salomon, C. “Short-Distance Atomic Beam Deceleration with a Stimulated Light Force”. *Physical Review Letters* **78**, 1420–1423 (1997).
281. Chieda, M. A. & Eyler, E. E. “Prospects for rapid deceleration of small molecules by optical bichromatic forces”. *Phys. Rev. A* **84**, 063401 (2011).
282. Sommer, C. *et al.* “Continuous guided beams of slow and internally cold polar molecules”. *Faraday Discussions* **142**, 203 (2009).
283. Merz, S., Vanhaecke, N., Jäger, W., Schnell, M. & Meijer, G. “Decelerating molecules with microwave fields”. *Phys. Rev. A* **85**, 063411 (2012).
284. Tscherbul, T. V., Klos, J., Rajchel, L. & Krems, R. V. “Fine and hyperfine interactions in cold  $\text{YbF-He}$  collisions in electromagnetic fields”. *Phys. Rev. A* **75**, 033416–1–10 (2007).
285. Bethlem, H. L. *et al.* “Electrostatic trapping of ammonia molecules”. *Nature* **406**, 491–494 (2000).

286. Greiner, M., Bloch, I., Hänsch, T. W. & Esslinger, T. “Magnetic transport of trapped cold atoms over a large distance”. *Phys. Rev. A* **63**, 031401 (2001).
287. Tollett, J. J., Bradley, C. C., Sackett, C. A. & Hulet, R. G. “Permanent magnet trap for cold atoms”. *Phys. Rev. A* **51**, 22 (1995).
288. Stellmer, S., Pasquiou, B., Grimm, R. & Schreck, F. “Laser Cooling to Quantum Degeneracy”. *Physical Review Letters* **110**, 263003 (2013).
289. Mayle, M., Quémener, G., Ruzic, B. P. & Bohn, J. L. “Scattering of ultracold molecules in the highly resonant regime”. *Phys. Rev. A* **87**, 012709 (2013).
290. Rio Fernandes, D. *et al.* “Sub-Doppler laser cooling of fermionic  $^{40}\text{K}$  atoms in three-dimensional gray optical molasses”. *EPL (Europhysics Letters)* **100**, 63001 (2012).
291. Grier, A. T. *et al.* “ $\Lambda$ -enhanced sub-Doppler cooling of lithium atoms in  $\text{D}_1$  gray molasses”. *Phys. Rev. A* **87**, 063411 (2013).
292. Lane, I. C. “Ultracold fluorine production via Doppler cooled BeF”. *Physical Chemistry Chemical Physics (Incorporating Faraday Transactions)* **14**, 15078 (2012).
293. Levy, C. D. P. *et al.* “Feasibility study of in-beam polarization of fluorine”. *Nuclear Instruments and Methods in Physics Research A* **580**, 1571–1577 (2007).
294. Wells, N. & Lane, I. C. “Prospects for ultracold carbon via charge exchange reactions and laser cooled carbides”. *Physical Chemistry Chemical Physics (Incorporating Faraday Transactions)* **13**, 19036 (2011).
295. Nicholls, R. W. “Franck-Condon factor formulae for astrophysical and other molecules”. *The Astrophysical Journal Supplement Series* **47**, 279–290 (1981).
296. Wells, N. & Lane, I. C. “Electronic states and spin-forbidden cooling transitions of AlH and AlF”. *Physical Chemistry Chemical Physics (Incorporating Faraday Transactions)* **13**, 19018 (2011).
297. Hunter, L. R., Peck, S. K., Greenspon, A. S., Alam, S. S. & Demille, D. “Prospects for laser cooling TlF”. *Phys. Rev. A* **85**, 012511 (2012).
298. DeMille group website. <<http://www.yale.edu/demillegroup/>> (2013).
299. Ott, M. *Capabilites and Reliability of LEDs and Laser Diodes*. Technology Validation Assurance Group, Swales Aerospace, Component Technologies and Radiation Effects Branch, NASA Goddard Space Flight Center. <<http://nepp.nasa.gov/docuploads/474752B6-45E5-417D-AC105086A372A642/Sources.pdf>> (1997).
300. Eagleyard Photonics. <<http://www.eagleyard.com/en/products/tapered-laser-amplifier/>> (2013).
301. Eagleyard Photonics. <[http://www.eagleyard.com/fileadmin/downloads/data\\_sheets/EYP-MNT-0000-00000-0000-CRM14-0001.pdf](http://www.eagleyard.com/fileadmin/downloads/data_sheets/EYP-MNT-0000-00000-0000-CRM14-0001.pdf)> (2013).
302. Stellmer, S. *Degenerate quantum gases of strontium*. PhD thesis (University of Innsbruck, 2013).
303. Vrijssen, G. *Collective quantum behavior of atomic ensembles in high-finesse optical cavities*. PhD thesis (Stanford University, 2011).
304. Rietzler, A. *Narrow-Line Cooling Light for a Magneto-Optical Trap of Erbium Atoms*. MA thesis (University of Innsbruck, 2012).
305. *LIGO Vacuum Compatible Materials List*. LIGO Laboratory / LIGO Scientific Collaboration. <<https://dcc-llo.ligo.org/public/0003/E960050/011/E960050-v11%20Vacuum%20Compatible%20Materials%20List.pdf>> (2013).
306. Birnbaum, K. M. *Ultra-High Vacuum Chambers*. Norman Bridge Laboratory of Physics 12-33 California Institute of Technology. <<http://sourav-dutta.wikispaces.com/file/view/Ultra-High+Vacuum+Chambers.pdf>> (2005).

307. *Outgassing Data for Selecting Spacecraft Materials Online*. National Aeronautics and Space Administration. <<http://outgassing.nasa.gov/>> (2013).
308. Santeler, D. J. “Estimating the gas partial pressure due to diffusive outgassing”. *Journal of Vacuum Science Technology* **10**, 1879–1883 (1992).
309. Kirilov, E. *Development of necessary ion traps, vacuum and laser systems for photoionization, laser cooling and quantum state engineering of trapped Strontium ions*. PhD thesis (University of California Los Angeles, 2007).
310. Zheng, S. *Black copper oxide coating*. SubsTech. <[http://www.substech.com/dokuwiki/doku.php?id=black\\_copper\\_oxide\\_coating](http://www.substech.com/dokuwiki/doku.php?id=black_copper_oxide_coating)> (2013).
311. Noble, A. & Kasevich, M. “UHV optical window seal to conflat<sup>a</sup>) knife edge”. *Review of Scientific Instruments* **65**, 3042–3043 (1994).
312. Engeser, B. *A novel surface trapping apparatus for ultracold cesium atoms and the investigation of an Efimov resonance*. PhD thesis (University of Innsbruck, 2006).
313. Kim, K. J., Yoshimura, M. & Smiya, S. “Hot pressing of LaF<sub>3</sub>-doped SrF<sub>2</sub> from mixed and hydrothermally pre-reacted powders”. *Journal of the European Ceramic Society* **6**, 187–190 (1990).